

Università degli Studi di Bologna

---

CENTRO DI RICERCA SUI SISTEMI ELETTRONICI  
PER L'INGEGNERIA DELL'INFORMAZIONE E  
DELLE TELECOMUNICAZIONI  
"ERCOLE DE CASTRO" - ARCES

**Mixed-Domain Simulation and  
Hybrid Wafer-Level Packaging of  
RF-MEMS Devices for  
Wireless Applications**

Tesi di Dottorato di: JACOPO IANNACCI

Relatore: Chiar. mo Prof. Ing. ANTONIO GNUDI

Correlatore: Dott. Ing. ROBERTO GADDI

Coordinatore: Chiar. mo Prof. Ing. RICCARDO ROVATTI

**Università degli Studi di Bologna**

FACOLTÀ DI INGEGNERIA

Dottorato di Ricerca in Tecnologie dell'Informazione

XIX ciclo (Anni accademici 2004-2006)

**Mixed-Domain Simulation and  
Hybrid Wafer-Level Packaging of  
RF-MEMS Devices for  
Wireless Applications**

Tesi di Dottorato di: JACOPO IANNACCI

Relatore: Chiar. mo Prof. Ing. ANTONIO GNUDI

Correlatore: Dott. Ing. ROBERTO GADDI

Coordinatore: Chiar. mo Prof. Ing. RICCARDO ROVATTI

**Settore Scientifico Disciplinare: ING-INF/01  
XIX Ciclo - Marzo 2007**



“There is real stagnation only when  
the eagerness to that overcomes  
any other willing...”

*“C’è vera stasi solamente quando  
l’ardore che spinge verso di essa  
supera qualunque altro  
desiderio...”*

J. Iannacci  
*December the 2<sup>nd</sup> 2006*

To my Parents

*Ai miei Genitori*



# Contents

<b>1</b>	<b>State of the Art in Simulation, Packaging and Integration of RF-MEMS Devices</b>	<b>11</b>
1.1	The Finite Elements Method (FEM) Approach . . . . .	11
1.2	Compact Modeling of RF-MEMS . . . . .	12
1.2.1	Model Order Reduction (MOR) Method . . . . .	13
1.2.2	Equivalent Electrical Circuits . . . . .	13
1.2.3	Mixed Domain Electromechanical Simulation Environment . . . . .	14
1.3	Packaging of RF-MEMS Devices . . . . .	15
1.4	Integration of RF-MEMS Packaged Devices: Hybrid Packaging . . . . .	16
<b>2</b>	<b>Theoretical Basis</b>	<b>19</b>
2.1	The Choice of the Reference Systems . . . . .	19
2.1.1	The One Degree of Freedom Rotation Matrix . . . . .	22
2.1.2	The Complete 12 Degrees of Freedom Rotation Matrix . . . . .	26
2.2	Structural Mechanics: the Theory of Elasticity . . . . .	28
2.2.1	The Definition of Mechanical Stress and Strain . . . . .	28
2.2.2	Relations Between Stress and Strain . . . . .	32
2.2.3	Plane Stress and Plane Strain . . . . .	35
2.3	Transmission Line Theory Review: the Scattering Parameters . . . . .	37

<b>3</b>	<b>The Rigid Plate Electromechanical Transducer</b>	<b>43</b>
3.1	Mechanical Model of the Rigid Plate with 4 Degrees of Freedom (DoF's) . . . . .	46
3.2	Extension of the Rigid Plate Mechanical Model to 6 Degrees of Freedom (DoF's) . . . . .	57
3.2.1	Nodes Placement on Rigid Plate Edges . . . . .	64
3.3	Contact Model for the 4 and 6 DoF's Rigid Plate . . . . .	67
3.4	Electrostatic Model for the Rigid Plate . . . . .	73
3.4.1	The Case of 4 DoF's . . . . .	73
3.4.2	Extension to the Case of 6 DoF's . . . . .	81
3.4.3	Electric Field Curved Lines Model . . . . .	85
3.5	Electrostatic Model for the Plate with Holes . . . . .	90
3.6	Electrostatic Model for the Fringing Effect . . . . .	97
3.6.1	Fringing Effect on Plate Vertical Faces . . . . .	106
3.7	Viscous Damping Model . . . . .	112
3.7.1	Squeeze-Film Viscous Damping for the Rigid Plate with Holes . . . . .	112
3.7.2	Viscous Damping Model for Lateral Movements . . . . .	116
3.7.3	Effect of the Gas Molecules Mean Free Path . . . . .	118
3.8	Validation of the Rigid Plate Electrostatic Model . . . . .	119
3.9	Complementary Library Models . . . . .	132
3.9.1	Mechanical Constraints . . . . .	132
3.9.2	Applied Forces and Displacements . . . . .	135
3.9.3	Unconnected Pins . . . . .	138
3.9.4	Interconnects for Rigid Structures . . . . .	139
<b>4</b>	<b>The Flexible Euler Beam</b>	<b>141</b>
4.1	Mechanical Model for the 2 DoF's Flexible Beam . . . . .	141
4.1.1	The Stiffness Matrix . . . . .	144
4.1.2	The Mass Matrix . . . . .	146
4.2	Mechanical Model for the 12 DoF's Flexible Beam . . . . .	148
4.2.1	The 12 DoF's Stiffness Matrix . . . . .	150
4.2.2	The 12 DoF's Mass Matrix . . . . .	156
4.3	Complete Mechanical Model for the 12 DoF's Euler Beam . . . . .	163



4.4	The Electrostatic Model for the 12 DoF's Euler Beam . . . . .	167
4.4.1	Fringing Effect Model . . . . .	177
4.5	Viscous Damping Model . . . . .	181
4.6	Validation of the Euler Beam Model . . . . .	185
4.6.1	Static Validation of the Euler Beam Mechanical Model .	186
4.6.2	Dynamic Validation of the Euler Beam Mechanical Model . . . . .	192
4.6.3	Validation of the Beam Electrostatic Model . . . . .	200
<b>5</b>	<b>Hybrid Wafer-Level Packaging of RF-MEMS</b>	<b>205</b>
5.1	Brief Overview on Packaging Solutions for RF-MEMS . . . . .	205
5.2	Technological Solution for the Package Fabrication . . . . .	208
5.2.1	The Wafer-Level Packaging Concept . . . . .	208
5.2.2	Package Fabrication Process . . . . .	212
5.2.3	Wafer-to-Wafer Bonding Solutions . . . . .	221
5.2.4	Encapsulation of RF-MEMS Devices . . . . .	227
5.2.5	The Issue of Wafer-to-Wafer Alignment . . . . .	228
5.2.6	Hybrid Packaging Solutions for RF-MEMS Devices . . . . .	232
5.3	Fabrication Run of Packaged Test Structures . . . . .	234
5.4	Electromagnetic Characterization of the Package . . . . .	246
5.4.1	The Ansoft HFSS™ Electromagnetic Simulator . . . . .	247
5.5	Uncompressed ACA Influence on RF Performance of Capped MEMS Devices . . . . .	258
<b>6</b>	<b>Simulation of RF-MEMS Devices</b>	<b>267</b>
6.1	Validation of MEMS Compact Model Library for Complex Structures . . . . .	268
6.1.1	The MEMS Flag Implementation . . . . .	268
6.1.2	MEMS Toggle-Switch . . . . .	278
6.1.3	Meander Structure . . . . .	288
6.2	RF-MEMS Varactor . . . . .	292
6.2.1	Pull-In Characterization . . . . .	296

6.2.2	S-parameters Analysis . . . . .	298
6.2.3	Simulation of the Packaged RF-MEMS Varactor . . . . .	311
6.2.4	Transient Analysis . . . . .	318
6.3	An RF-MEMS/CMOS Voltage Controlled Oscillator (VCO) . . . . .	321
<b>A</b>		<b>331</b>
A.1	SpectreHDL <sup>©</sup> Vs. VerilogA <sup>©</sup> . . . . .	331
A.2	Modular Code and Physical Quantities . . . . .	332
A.3	User Interfaces . . . . .	336
<b>B</b>		<b>339</b>
B.1	Modified Process Flow with Wide Recesses . . . . .	339
B.2	Work in Progress . . . . .	345
<b>C</b>		<b>347</b>
C.1	Flexible Plate with 12 DoF's . . . . .	347
	<b>Bibliography</b>	<b>359</b>

# List of Figures

2.1	Cartesian reference system. A generic point $P$ position in space is identified by means of the corresponding three coordinates along the $x, y, z$ axes. . . . .	20
2.2	Spherical coordinates reference system. A generic point $P$ position in space is identified by means of the radius $r$ and two angles ( $\theta$ and $\phi$ ). . . . .	21
2.3	Point $P$ in the global reference system. Its description is the same in the local reference system when no rotation occurs. . . .	23
2.4	Rotation ( $\theta_Z$ ) around the $Z$ axis of the local system with respect to the global one. . . . .	24
2.5	Rotation of the local system around the three axes of the global one ( $\theta_X, \theta_Y, \theta_Z$ ). . . . .	26
2.6	Body with an arbitrary shape. It is divided in two parts $A$ and $B$ by the cross section $mm$ . . . . .	29
2.7	Definition of strain by means of a rectangular body which undergoes deformations. . . . .	31
2.8	Two ports black box. $V_1$ and $I_1$ are the voltage and the current at the port 1, while $V_2$ and $I_2$ are the same magnitudes at the port 2. . . . .	37
2.9	Two ports network also including the terminations at the two ports. . . . .	38
2.10	Two ports network with the reference planes at which the S-parameters are defined. . . . .	41
3.1	Rigid plate with the origin of the reference system defined in its central point. . . . .	44
3.2	The local reference system origin is placed in the plate centre of mass. . . . .	45

3.3	The four plate vertexes with their coordinates in the local reference system. . . . .	48
3.4	Plate after a rotation $\theta_z$ around the $Z$ axis. A force is applied to the bottom-right ( $SE$ ) corner. . . . .	49
3.5	Rigid plate with all the forces and torques applied to the four vertexes. . . . .	54
3.6	Rigid plate (6 DoF's) with all the forces and torques applied to the four vertexes. . . . .	59
3.7	Rigid plate with 8 nodes. The middle point along the four edges have been also introduced. . . . .	65
3.8	Rigid plate with an offset $D_y$ applied to the $NE$ node along the local $y$ axis. . . . .	66
3.9	Collision of the $SE$ plate corner with the bottom substrate plane.	69
3.10	Lateral view of a plate with an initial orientation angle $\theta_{Y_{INIT}}$ different from zero. . . . .	70
3.11	Electrostatic model for two parallel plates. A voltage $V$ is applied.	74
3.12	The two parallel plates with an oxide layer deposited on the lower electrode. Its thickness $Z_{OX}$ is enlarged to make in visible.	75
3.13	Because of the oxide layer, an additional capacitance is in series with the one due to the air gap. . . . .	77
3.14	When large displacements and rotations occur the plate projection on the underneath substrate could fall outside its area. . . .	80
3.15	Definition of the vertical distance between a generic point $P$ on the rotated plate area and the substrate. . . . .	82
3.16	Example of a curved line of the electric field when only $\theta_Y$ has a non-zero value. . . . .	86
3.17	When $\theta_X$ and $\theta_Y$ have non-zero values each point $P$ admits two segments ( $E_{P_x}$ and $E_{P_y}$ ) to determine the arc length. . . . .	88
3.18	The two segments $E_{P_x}$ and $E_{P_y}$ generate two different arc lengths for the same point $P$ . . . . .	89
3.19	The field arc related to the point $P$ is empirically determined with simple trigonometric considerations. . . . .	90
3.20	SEM picture of a suspended plate with holes on its surface. These allow the etching solution to reach the sacrificial layer underneath the plate. . . . .	91
3.21	Plate schematic with holes. Holes are supposed to be $m$ along $x$ and $n$ along $y$ local axis. . . . .	93

3.22	6 DoF's plate schematic with holes. Differently from the 4 DoF's case, each hole gives a different contribution to the electric magnitudes depending on its position. . . . .	94
3.23	Fringing field lines behaviour nearby the edges of the two plates.	97
3.24	Definition of the fringing lines curvature as a function of the gap $Z_P$ and of an empirical coefficient $\gamma$ . . . . .	98
3.25	The fringing field lines are supposed to be confined within a <i>belt</i> wide $\zeta$ starting from the four plate edges. . . . .	100
3.26	Fringing effect due to the vertical faces when $\theta_Y > 0$ . The <i>SW</i> – <i>NW</i> vertical face is shadowed by the lower plate surface.	106
3.27	Fringing effect due to the vertical faces when $\theta_X > 0$ and $\theta_Y > 0$ . The <i>SW</i> – <i>NW</i> and <i>NW</i> – <i>NE</i> vertical faces are shadowed by the lower plate surface. . . . .	107
3.28	When the plate moves laterally the velocity distribution of the fluid underneath it is described by the Couette-type flow. . . . .	116
3.29	Cadence Virtuoso <sup>©</sup> Schematic of the 6 DoF's rigid plate. Six pins corresponding to the 6 DoF's to each node are visible as well as the two electrical pins to apply the control voltage. . . . .	119
3.30	Cadence Virtuoso <sup>©</sup> Schematic for the validation of the rigid plate electrostatic model. The four vertexes are anchored in order to keep the plate in a fixed position in space. . . . .	120
3.31	COMSOL Multiphysics <sup>TM</sup> schematic of a suspended rigid plate for electrostatic simulations. The suspended plate and the underneath electrode are included in an air box. . . . .	121
3.32	Cadence Virtuoso <sup>©</sup> Schematic for the 6 DoF's anchor. Six pins are made available. . . . .	134
3.33	Cadence Virtuoso <sup>©</sup> Schematic for the 6 DoF's anchor including the definition of the fictitious resistance $r_{min}$ . . . . .	134
3.34	Cadence Virtuoso <sup>©</sup> Schematic for the 6 DoF's force (torque) generator. . . . .	136
3.35	Cadence Virtuoso <sup>©</sup> Schematic for the 6 DoF's displacement (linear and angular) generator. . . . .	136
3.36	Definition of a pulse-shaped stimulus. It is defined in terms of minimum and maximum value, rise and fall time, delay, pulse width and period. . . . .	137
3.37	Cadence Virtuoso <sup>©</sup> Schematic for the 6 DoF's block to be connected to floating nodes. . . . .	138

3.38	Cadence Virtuoso <sup>®</sup> Schematic for the 6 DoF's minimum resistance to connect together two rigid plates. . . . .	140
4.1	Schematic of an Euler flexible beam. Beam length (along $x$ axis), width (along $y$ axis) and thickness (along $z$ axis) are $L$ , $W$ and $T$ respectively. . . . .	142
4.2	Euler beam stimulated along the $x$ direction at the ends $A$ and $B$ . The end in which the stimulus is not applied has to be constrained (anchored). . . . .	143
4.3	Euler beam with 12 DoF's. Three linear and three angular deformations are allowed to both $A$ and $B$ ends. . . . .	149
4.4	Configuration of the Euler beam which undergoes a linear deformation $u_{zA}$ applied in $A$ with the $B$ end anchored. . . . .	157
4.5	Configuration of the Euler beam which undergoes an angular deformation $u_{\theta_y A}$ applied around the $y$ axis in $A$ with the $B$ end anchored. . . . .	157
4.6	The Euler beam with $\theta_X$ , $\theta_Y$ and $\theta_Z$ orientation angles. These define the relations between the global reference system ( $X, Y, Z$ ) and the local one ( $x, y, z$ ). . . . .	164
4.7	The vertical displacement of the beam center line (dotted line) is determined by means of the HSF's. . . . .	168
4.8	Beam stimulated in all the DoF's which give contribution along $z$ axis. . . . .	169
4.9	Total displacement of a generic point $\xi$ along the beam length expressed in the global $Z$ direction. . . . .	170
4.10	The beam length is divided into $n$ element of length $\frac{L}{n}$ Each element is assumed to be rigid. . . . .	172
4.11	Local abscissa value along the $x$ axis center line for the discretized beam elements. . . . .	173
4.12	Cross-section of one beam sub-element. The rotation angle around the $Y$ axis is determined with simple calculations. . . . .	174
4.13	Schematic of all the possible configurations in placing the electrode(s) beneath the flexible beam. . . . .	180
4.14	In the squeeze-film damping description the fluid is squeezed as the beam nears the substrate plane. . . . .	182

4.15	Cadence Virtuoso <sup>®</sup> Schematic for the 12 DoF's cantilever. Six pins corresponding to the 6 DoF's are visible at each of the two ends along with the two electrical pins to apply the control voltage. . . . .	185
4.16	Cadence Virtuoso <sup>®</sup> Schematic for the static validation of the Euler beam. One end is anchored while a linear force is applied to the other one. The beam is connected by wires to the anchor, force source and ground. . . . .	186
4.17	COMSOL Multiphysics <sup>®</sup> schematic for the Euler beam. The force is applied to the free end with orientation angles $\theta_{S_Y} = 0^\circ$ and $\theta_{S_Z} = 0^\circ$ . . . . .	187
4.18	Beam displacement along $X$ predicted with the compact models in Spectre <sup>®</sup> . . . . .	188
4.19	COMSOL Multiphysics <sup>®</sup> schematic for the Euler beam. The force is applied to the free end with orientation angles $\theta_{S_Y} = 0^\circ$ and $\theta_{S_Z} = 45^\circ$ . . . . .	189
4.20	COMSOL Multiphysics <sup>®</sup> schematic for the Euler beam. The force is applied to the free end with orientation angles $\theta_{S_Y} = -90^\circ$ and $\theta_{S_Z} = 0^\circ$ . . . . .	190
4.21	COMSOL Multiphysics <sup>®</sup> schematic for the Euler beam. The force is applied to the free end with orientation angles $\theta_{S_Y} = -60^\circ$ and $\theta_{S_Z} = 30^\circ$ . . . . .	191
4.22	Cadence Virtuoso <sup>®</sup> Schematic for the dynamic validation of the Euler beam mechanical model. . . . .	192
4.23	Small signal AC simulation in Spectre <sup>®</sup> from 100 KHz to 100 MHz. The linear $Y$ displacement and the angular rotation around $Z$ are plotted in a logarithmic vs. linear frequency scale. . . . .	193
4.24	Small signal AC simulation in Spectre <sup>®</sup> from 100 KHz to 4 MHz. The linear $Y$ displacement and the angular rotation around $Z$ are plotted in a logarithmic vs. linear frequency scale. . . . .	194
4.25	COMSOL Multiphysics <sup>®</sup> schematic for the fundamental eigenmode (on $XY$ plane) of the Euler beam. . . . .	195
4.26	COMSOL Multiphysics <sup>®</sup> schematic for the first higher eigenmode (on $XY$ plane) of the Euler beam. . . . .	196
4.27	COMSOL Multiphysics <sup>®</sup> schematic for the second higher eigenmode (on $XY$ plane) of the Euler beam. . . . .	196

4.28	Cadence Virtuoso <sup>®</sup> Schematic for two beams of length $75\ \mu\text{m}$ connected in series. . . . .	197
4.29	Small signal AC simulation in Spectre <sup>®</sup> from 100 KHz to 8 MHz for two beams of length $75\ \mu\text{m}$ ) connected in series. The linear $Y$ displacement and the angular rotation around $Z$ are plotted in a logarithmic vs. linear frequency scale. . . . .	197
4.30	COMSOL Multiphysics <sup>®</sup> schematic for the fundamental eigenmode (on $XZ$ plane) of the Euler beam. . . . .	199
4.31	COMSOL Multiphysics <sup>®</sup> schematic for the first higher eigenmode (on $XZ$ plane) of the Euler beam. . . . .	199
4.32	COMSOL Multiphysics <sup>®</sup> schematic for the second higher eigenmode (on $XZ$ plane) of the Euler beam. . . . .	200
4.33	Schematic of the cantilever structure. When the applied voltage reaches the pull-in value the beam collapses onto the substrate. . . . .	201
4.34	Cadence Virtuoso <sup>®</sup> Schematic of the cantilever structure. The left beam end is anchored while the right one is free to move. Note the voltage source connected to the left beam electric pin while the right one represents the lower electrode connected to ground. . . . .	201
4.35	DC simulation of a cantilever in Spectre <sup>®</sup> . The vertical displacement of the free beam end is plotted vs. the linear biasing voltage swept between 0 and 8 Volts. . . . .	202
4.36	Schematic of a cantilever structure in CoventorWare <sup>®</sup> . The beam has one end anchored and the other free to move. . . . .	204
5.1	In wafer-level packaging a capping wafer with an interconnects scheme compatible with the distribution of electrical signal pads onto the RF-MEMS device substrate is necessary. . . . .	209
5.2	After the alignment of the capping part to the MEMS substrate the wafer-to-wafer bonding is performed. After the subsequent singulation the packaged RF-MEMS dies are available for SMT (see Figure 5.3). . . . .	210
5.3	The final step is to flip the packaged MEMS die over the board performing the bonding by solder balls reflow. . . . .	211
5.4	<b>Step 1:</b> The Silicon wafer is polished and prepared for processing.	214
5.5	<b>Step 2:</b> Recesses are etched in the bottom wafer side by using the Bosch DRIE process. . . . .	214



5.6	<b>Step 3:</b> Vertical vias are etched from the top wafer side by using the Bosch DRIE process. . . . .	215
5.7	<b>Step 4:</b> The Silicon wafer is thinned by grinding it from the back side. The bottom vias openings are released. . . . .	215
5.8	<b>Step 5:</b> The seed layer is sputtered on the wafer top side and onto vias sidewalls. Before this step a silicon dioxide (not shown here) is grown on wafer and vias surface. . . . .	216
5.9	<b>Step 6:</b> A photoresist film is deposited on both wafer sides to pattern the top copper pads and bottom bumps which will be subsequently deposited. . . . .	216
5.10	<b>Step 7:</b> Top side copper bumps are electrodeposited exploiting the seed-layer. . . . .	217
5.11	<b>Step 8:</b> Vias are bottom-up filled with electrodeposited copper.	217
5.12	<b>Step 9:</b> Bottom bumps are electrodeposited in correspondence with vias. Depending on the selected wafer-to-wafer bonding solution these will be made of copper or of a special alloy. . . . .	218
5.13	<b>Step 10:</b> Photoresist residues are removed from both wafer faces as well as the seed layer lying underneath it on the top capping side. . . . .	218
5.14	The package is bonded to the RF-MEMS device wafer after having been aligned to it. . . . .	219
5.15	SEM (Scanning Electron Microscopy) photograph of a capping test wafer. The via exhibits an high aspect ratio and a very uniform via copper filling is also noticeable. . . . .	220
5.16	Scheme of the package aligned and in contact with the RF-MEMS device wafer <b>before</b> the reflow of solder bumps is performed. . . . .	222
5.17	Scheme of the package aligned and in contact with the RF-MEMS device wafer <b>after</b> the reflow of solder bumps is performed.	222
5.18	SEM photograph of AuSn bumps on a dummy wafer <b>before</b> the reflow step. . . . .	223
5.19	SEM photograph of AuSn bumps on a dummy wafer <b>after</b> the reflow step. . . . .	224
5.20	When ACA is uncompressed the particles are far from each other and it is electrically insulating (top figure). When ACA is compressed particles get closer and form an electrically conductive path (bottom figure). . . . .	226

5.21	Top-view of a die on the RF-MEMS device wafer surrounded by a protective peripheral ring. Additionally, a protective ring can also be patterned around each MEMS device. . . . .	227
5.22	Top-view of a package electrical interconnect (via plus bump) superposed to a MEMS signal pad. Depending on the severity of the wafer-to-wafer misalignment the bump-to-pad electrical interconnection can be good (top) or poor as well as totally missing (bottom). . . . .	229
5.23	SEM photograph of a preformed windows by etching (Bosch DRIE process) of a narrow groove. The four anchors at the corners are visible. . . . .	230
5.24	SEM photograph of the window after the release by breaking of the anchor points is achieved by ultrasonic cleaning. . . . .	231
5.25	Hybrid packaging solution based on the placement of the CMOS chip upside-down in a cavity through the package. . . . .	232
5.26	Hybrid packaging solution based on the CMOS chip placement in a shallow cavity. Electrical interconnection is ensured by wire bonding. . . . .	233
5.27	Design in Agilent ADS <sup>®</sup> of a 50 $\Omega$ CPW including the package. The two ports for S-parameters simulation are visible. . . . .	235
5.28	Design in Agilent ADS <sup>®</sup> of a short including the package. The port for S-parameters simulation is visible. . . . .	235
5.29	Photograph of an uncapped evaporated gold CPW. The Silicon surface roughness is clearly noticeable. The probes for direct measurement are also visible. . . . .	236
5.30	Photograph of few test structures after de-bonding of the package. The black stains (ICA residues) indicate a very good chip-to-wafer alignment. . . . .	237
5.31	Top-side pads (onto the capping chip) for some of the underneath test structures. . . . .	238
5.32	Experimental comparison of the S11 parameter for an uncapped and capped CPW. . . . .	239
5.33	Experimental comparison of the S21 parameter for an uncapped and capped CPW. . . . .	240
5.34	Experimental comparison of the S11 parameter for an uncapped and capped CPW. . . . .	242

5.35	Experimental comparison of the S21 parameter for an uncapped and capped CPW. . . . .	243
5.36	Experimental comparison of the S11 parameter for an uncapped and capped short. . . . .	244
5.37	Experimental comparison of the S11 parameter Smith chart for an uncapped and capped short. . . . .	245
5.38	Comparison of the experimental S11 parameter already shown in Figure 5.32 with the one predicted by Ansoft HFSS <sup>TM</sup> . . . . .	248
5.39	Comparison of the experimental S21 parameter already shown in Figure 5.33 with the one predicted by Ansoft HFSS <sup>TM</sup> . . . . .	249
5.40	Comparison of the experimental S11 parameter already shown in Figure 5.34 with the one predicted by Ansoft HFSS <sup>TM</sup> . . . . .	250
5.41	Comparison of the experimental S21 parameter already shown in Figure 5.35 with the one predicted by Ansoft HFSS <sup>TM</sup> . . . . .	251
5.42	Schematic view in Ansoft HFSS <sup>TM</sup> of a capped CPW. The capping substrate was made invisible to get a plain view of the underneath CPW as well as of the vertical through-vias. . . . .	252
5.43	Reflection parameter (S11) for the two DoF's optimization performed at 15 GHz with the parameterized model in Ansoft HFSS <sup>TM</sup> . . . . .	253
5.44	Transmission parameter (S21) for the two DoF's optimization performed at 15 GHz with the parameterized model in Ansoft HFSS <sup>TM</sup> . . . . .	254
5.45	Summary of the most important technology DoF's in package fabrication concerning the influence on RF performance of MEMS. . . . .	256
5.46	Ansoft HFSS <sup>TM</sup> 3D view of the open with an uncompressed ACA layer in between the two ports. . . . .	259
5.47	S11 parameter plot for the open structure with the uncompressed ACA layer between the two ports compared with the one for the same structure without ACA layer. . . . .	260
5.48	S21 parameter plot for the open structure with the uncompressed ACA layer between the two ports compared with the one for the same structure without ACA layer. . . . .	261
5.49	Ansoft HFSS <sup>TM</sup> 3D view of a CPW surrounded by an uncompressed ACA layer. . . . .	263
5.50	S11 parameter plot for the CPW surrounded by an uncompressed ACA layer compared with the one for the CPW without ACA. . . . .	264

5.51	S21 parameter plot for the CPW surrounded by an uncompressed ACA layer compared with the one for the CPW without ACA. . . . .	265
6.1	Cadence Virtuoso <sup>®</sup> Schematic of the flag structure. The Euler beam is connected to the bottom left plate corner while the other three are connected to floating structures. . . . .	269
6.2	CoventorWare <sup>®</sup> 3D model of the flag structure. The structure mesh is displayed in this view both for the suspended structure and for the lower electrode. . . . .	270
6.3	Spectre <sup>®</sup> prediction of the pull-in related to the North-East, South-East, South-West and North-West plate corners. . . . .	271
6.4	North-East corner vertical displacement plot for the Spectre <sup>®</sup> and CoventorWare <sup>®</sup> simulation. CoventorWare <sup>®</sup> predicts the pull-in for a voltage between 2.1 V and 2.2 V which corresponds to the result in Spectre <sup>®</sup> of 2.16 V. . . . .	272
6.5	CoventorWare <sup>®</sup> schematic of the flag after the collapse at the North-East and South-East nodes occurs. The color scale represent the vertical displacement. . . . .	273
6.6	CoventorWare <sup>®</sup> schematic of the flag after the collapse of the South-West and North-West nodes occurs. The color scale represent the vertical displacement. . . . .	274
6.7	South-West and North-West corners vertical displacement plot for the Spectre <sup>®</sup> and CoventorWare <sup>®</sup> simulation. CoventorWare <sup>®</sup> predicts the pull-in for a voltage between 9.5 V and 10 V while the corresponding result in Spectre <sup>®</sup> is 7.19 V. . . . .	275
6.8	Schematic top-view of a MEMS toggle-switch. Central switch is connected to two lateral actuation structures. . . . .	278
6.9	Schematic side-view of a MEMS toggle-switch cross-section. The lateral actuation structures are kept suspended by two short flexible beams. . . . .	279
6.10	Schematic of the MEMS toggle-switch inner actuation mechanism.	279
6.11	Schematic of the MEMS toggle-switch outer actuation mechanism.	280
6.12	Schematic view of the toggle-switch implemented within CoventorWare <sup>®</sup> . Symmetry is exploited and half a structure is implemented. . . . .	281
6.13	Cadence Virtuoso <sup>®</sup> Schematic of the toggle-switch. Exploiting the symmetry of the structure half a toggle is implemented. . . . .	282

6.14	Pull-in characteristic of the toggle predicted in Spectre <sup>©</sup> compared with CoventorWare <sup>©</sup> simulation. . . . .	284
6.15	Pull-in characteristic of the toggle predicted in Spectre <sup>©</sup> compared with CoventorWare <sup>©</sup> simulation. The controlling voltage is applied to the outer electrode. . . . .	285
6.16	Schematic view in CoventorWare <sup>©</sup> for the deformed toggle when the controlling voltage is applied to the inner electrode. Color scale represents the vertical displacement. . . . .	286
6.17	Schematic view in CoventorWare <sup>©</sup> for the deformed toggle when the controlling voltage is applied to the outer electrode. Color scale represents the vertical displacement. . . . .	287
6.18	Schematic of the folded beam structure proposed by Peroulis et Al. [81]. In it two vertical beams of length $240 \mu m$ are connected with two horizontal beams of length $20 \mu m$ . . . . .	289
6.19	Cadence Virtuoso <sup>©</sup> Schematic of the basic folded beam structure proposed by Peroulis. . . . .	290
6.20	Comparison of Spectre <sup>©</sup> prediction for the elastic constant along Z referred to the five meander configurations with the data extrapolated from Peroulis paper. . . . .	291
6.21	Schematic top-view of the meander flexible structure connected to the four plate corners. . . . .	292
6.22	Cadence Virtuoso <sup>©</sup> Schematic of the RF-MEMS varactor based on a central rigid plate suspended with four meander structures. . . . .	293
6.23	3D view of the MEMS varactor obtained by means of an optical profiling system. . . . .	294
6.24	Layout (i.e. top-view) of the MEMS varactor. The central plate and the four meanders are visible. . . . .	295
6.25	Comparison of the plate vertical displacement predicted by Spectre <sup>©</sup> with the experimental measurement. . . . .	296
6.26	Comparison of the plate capacitance predicted by Spectre <sup>©</sup> with the experimental values. . . . .	297
6.27	Cadence Virtuoso <sup>©</sup> Schematic of the intrinsic RF-MEMS varactor including all the parasitics. The symbol of the intrinsic varactor corresponds to the scheme of Figure 6.22. . . . .	299
6.28	Comparison of the experimental S11 parameter with the Spectre <sup>©</sup> simulation when a 0 V biasing voltage is applied to the MEMS varactor (up-state). . . . .	301

6.29	Comparison of the experimental S21 parameter with the Spectre <sup>©</sup> simulation when a 0 V biasing voltage is applied to the MEMS varactor (up-state). . . . .	302
6.30	Comparison of the experimental S11 parameter with the Spectre <sup>©</sup> simulation when a 5.6 V biasing voltage is applied to the MEMS varactor (down-state). . . . .	303
6.31	Comparison of the experimental S21 parameter with the Spectre <sup>©</sup> simulation when a 5.6 V biasing voltage is applied to the MEMS varactor (down-state). . . . .	304
6.32	Comparison of the Smith chart of the experimental S11 parameter with the Spectre <sup>©</sup> simulation when a 0 V biasing voltage is applied to the MEMS varactor (up-state). . . . .	305
6.33	Comparison of the Smith chart of the experimental S21 parameter with the Spectre <sup>©</sup> simulation when a 0 V biasing voltage is applied to the MEMS varactor (up-state). . . . .	306
6.34	Comparison of the Smith chart of the experimental S11 parameter with the Spectre <sup>©</sup> simulation when a 5.6 V biasing voltage is applied to the MEMS varactor (down-state). . . . .	307
6.35	Comparison of the Smith chart of the experimental S21 parameter with the Spectre <sup>©</sup> simulation when a 5.6 V biasing voltage is applied to the MEMS varactor (down-state). . . . .	308
6.36	Comparison of the experimental S11 parameter with the Spectre <sup>©</sup> simulation at 10 GHz for a biasing voltage sweeping between 0 and 6 V. . . . .	309
6.37	Comparison of the experimental S21 parameter with the Spectre <sup>©</sup> simulation at 10 GHz for a biasing voltage sweeping between 0 and 6 V. . . . .	310
6.38	Ansoft HFSS <sup>TM</sup> schematic of the vertical vias. A short CPW is placed both on top of the package and on the device wafer plane.	312
6.39	Cadence Virtuoso <sup>©</sup> Schematic of the RF-MEMS varactor also including the parasitics associated to the package vertical through-vias. . . . .	313
6.40	Simulated S11 parameter for the uncapped RF-MEMS varactor (up-state) compared with the one accounting for vertical vias. . . . .	314
6.41	Simulated S21 parameter for the uncapped RF-MEMS varactor (up-state) compared with the one accounting for vertical vias. . . . .	315

6.42	Simulated S11 parameter for the uncapped RF-MEMS varactor (down-state) compared with the one accounting for vertical vias.	316
6.43	Simulated S21 parameter for the uncapped RF-MEMS varactor (down-state) compared with the one accounting for vertical vias.	317
6.44	Experimental transient behaviour of the RF-MEMS varactor compared with the Spectre <sup>®</sup> prediction. The peak value of the biasing voltage is 4 V (lower than the pull-in voltage).	318
6.45	Experimental transient behaviour of the RF-MEMS varactor compared with the Spectre <sup>®</sup> prediction. The peak value of the biasing voltage is 5 V (higher than the pull-in voltage).	320
6.46	Cadence Virtuoso <sup>®</sup> Schematic of the VCO with the CMOS oscillator in AMS technology and the RF-MEMS LC-tank.	322
6.47	Cadence Virtuoso <sup>®</sup> Schematic corresponding to each of the two RF-MEMS varactors in Figure 6.46.	323
6.48	VCO oscillation frequency versus biasing voltage applied to the RF-MEMS varactors (tuning characteristic).	324
6.49	VCO output voltage versus time simulated in Spectre <sup>®</sup> when no biasing voltage is applied to the RF-MEMS varactors.	326
A.1	Mask for the Euler beam parameters definition in Cadence Virtuoso <sup>®</sup> Schematic.	337
A.2	Cadence <sup>®</sup> Analog Design Environment window. This window allows to control the type of simulation as well as to set the desired values for all the parameters.	338
B.1	3D schematic of the package bottom side realized with the process shown in Chapter 6.	340
B.2	3D schematic of the package bottom side realized with the modified process proposed in this section. Wider recesses are achievable.	341
B.3	Reflection parameters (S11) plot for a CPW capped with the packaging solution shown in Chapter 6 compared with the modified solution with larger recess and silicon shafts.	343
B.4	Transmission parameters (S21) plot for a CPW capped with the packaging solution shown in Chapter 6 compared with the modified solution with larger recess and silicon shafts.	344

B.5	Schematic of the hybrid RF-MEMS/CMOS packaged chip demonstrator. Electrical interconnection will be performed by wire bonding. . . . .	346
C.1	Schematic of the flexible plate with 12 DoF's. The vertexes are marked as 1, 2, 3 and 4 and each of them admits a linear deformation along $z$ and two torsions around $x$ and $y$ . . . . .	348
C.2	Cadence Virtuoso <sup>©</sup> Schematic of the flexible plate with 12 DoF's.	354



# Cenni sulla Tesi

## Introduzione e Motivazioni

L'applicazione di dispositivi realizzati in tecnologia MEMS (Sistemi Micro Elettro-Meccanici) in sistemi operanti a Radio Frequenza (RF) ha mostrato negli ultimi anni notevoli potenzialità relativamente alla fabbricazione di componenti passivi (quali induttori, capacità variabili ed interruttori) ad alte prestazioni (ad esempio alto Fattore di Qualità ed ampi range in cui variare la capacità). La tecnologia MEMS implica, per sua natura, una profonda interazione tra discipline differenti, come la meccanica strutturale e la fluidodinamica. Inoltre, il processo di fabbricazione di dispositivi RF-MEMS non è ancora standardizzato, come invece accade per esempio con la tecnologia CMOS. Di conseguenza, la necessità di dover trattare grandezze fisiche appartenenti a domini fisici differenti da un lato, come il fatto di dover gestire un numero solitamente elevato di gradi di libertà nella definizione del design ottimo degli RF-MEMS dall'altro, motivano lo sviluppo di un ambiente di simulazione creato ad-hoc.

Dopo che tutte le questioni relative all'ottimizzazione delle prestazioni RF ed alla fabbricazione dei MEMS sono risolte, un'altro delicato fattore chiave deve essere affrontato prima di arrivare alla completa utilizzazione dei dispositivi RF-MEMS all'interno di blocchi funzionali. Tale punto è rappresentato dal packaging dei dispositivi MEMS da un lato, e dall'integrazione ed interfacciamento degli stessi con la circuiteria CMOS dall'altro, dal momento che i processi di fabbricazione utilizzati per gli RF-MEMS sono incompatibili con la tecnologia CMOS standard. Nonostante l'esistenza di alcune soluzioni per un processo di fabbricazione MEMS/CMOS unificato, il modo migliore per ottenere alte prestazioni da entrambe le parti è ancora rappresentato dal man-

tenere i due processi di fabbricazioni separati e poi integrare la parte MEMS a quella CMOS come ultimo passo. A seconda della soluzione tecnologica con cui le parti MEMS e CMOS sono ottenute, il loro interfacciamento può essere ottenuto sistemando il chip CMOS direttamente sul substrato RF-MEMS. Tuttavia, in altri casi può succedere che gli schemi di interconnessione elettrica dei due blocchi siano incompatibili, rendendo necessaria la redistribuzione dei segnali elettrici. A questo proposito, è possibile sfruttare il substrato di package stesso, il cui compito principale è quello di progettare i dispositivi RF-MEMS da fattori dannosi (come umidità, polvere, urti ecc.), per realizzare tale redistribuzione. Una soluzione di questo tipo, in cui il package riveste un ruolo fondamentale nell'interfacciare parti realizzate con tecnologie differenti, è ben nota in letterature e va sotto il nome di hybrid packaging (packaging ibrido).

## Riassunto della Tesi

In questa tesi verranno trattati sia il problema della creazione di un ambiente di simulazione a domini fisici misti per dispositivi RF-MEMS, che la definizione di un processo di fabbricazione ad-hoc per il packaging e l'integrazione degli stessi.

Riguardo al primo argomento, sarà mostrato nel dettaglio lo sviluppo di una libreria di modelli MEMS all'interno dell'ambiente di simulazione per circuiti integrati Cadence<sup>©</sup>. L'approccio scelto per la definizione del comportamento elettromeccanico dei MEMS è basato sul concetto di modellazione compatta (compact modeling). Questo significa che il comportamento fisico di ogni componente elementare della libreria è descritto per mezzo di un insieme limitato di punti (nodi) di interconnessione verso il mondo esterno. La libreria comprende componenti elementari, come travi flessibili, piatti rigidi sospesi e punti di ancoraggio, la cui opportuna interconnessione porta alla realizzazione di interi dispositivi (come interruttori e capacità variabili) da simulare in Cadence<sup>©</sup>. Tutti i modelli MEMS sono implementati per mezzo del linguaggio VerilogA<sup>©</sup> di tipo HDL (Hardware Description Language) che è supportato dal simulatore circuitale Spectre<sup>©</sup>. Sia il linguaggio VerilogA<sup>©</sup> che il simulatore Spectre<sup>©</sup> sono disponibili in ambiente Cadence<sup>©</sup>. L'ambiente di simulazione multi-dominio (ovvero elettromeccanico) così ottenuto permette di interfacciare i dispositivi MEMS con le librerie di componenti CMOS standard e di con-

seguenza la simulazione di blocchi funzionali misti RF-MEMS/CMOS. Come esempio, un VCO (Voltage Controlled Oscillator) in cui l'LC-tank è realizzato in tecnologia MEMS mentre la parte attiva con transistor MOS di libreria sarà simulato in Spectre<sup>®</sup>.

Inoltre, nelle pagine successive verrà mostrata una soluzione tecnologica per la fabbricazione di un substrato protettivo (package) da applicare a dispositivi RF-MEMS basata su vie di interconnessione elettrica attraverso un wafer di Silicio. La soluzione di packaging prescelta rende possibili alcune tecniche per l'integrazione ibrida delle parti RF-MEMS e CMOS (hybrid packaging). Verranno inoltre messe in luce questioni riguardanti gli effetti parassiti (accoppiamenti capacitivi ed induttivi) introdotti dal package che influenzano le prestazioni RF dei dispositivi MEMS incapsulati. Nel dettaglio, tutti i gradi di libertà del processo tecnologico per l'ottenimento del package saranno ottimizzati per mezzo di un simulatore elettromagnetico (Ansoft HFSS<sup>TM</sup>) al fine di ridurre gli effetti parassiti introdotti dal substrato protettivo. Inoltre, risultati sperimentali raccolti da misure di strutture di test incapsulate verranno mostrati per validare, da un lato, il simulatore Ansoft HFSS<sup>TM</sup> e per dimostrare, dall'altro, la fattibilità della soluzione di packaging proposta.

Aldilà dell'apparente debole legame tra i due argomenti sopra menzionati è possibile identificare un unico obiettivo. Da un lato questo è da ricercarsi nello sviluppo di un ambiente di simulazione unificato all'interno del quale il comportamento elettromeccanico dei dispositivi RF-MEMS possa essere studiato ed analizzato. All'interno di tale ambiente, l'influenza del package sul comportamento elettromagnetico degli RF-MEMS può essere tenuta in conto per mezzo di modelli a parametri concentrati (lumped elements) estratti da misure sperimentali e simulazioni agli Elementi Finiti (FEM) della parte di package. Infine, la possibilità offerta dall'ambiente Cadence<sup>®</sup> relativamente alla simulazione di dispositivi RF-MEMS interfacciati alla parte CMOS rende possibile l'analisi di blocchi funzionali ibridi RF-MEMS/CMOS completi.



# Thesis Overview

## Introduction and Motivations

MEMS (Micro Electro-Mechanical System) technology for Radio Frequency (RF) applications has emerged in recent years as a valuable solution in order to fabricate passive components (e.g. inductors, varactors, switches etc.) with remarkable performances, like very high quality factor (Q-Factor) and wide capacitance tuning ranges. MEMS technology implies for its nature a deep interaction among different disciplines, like for instance structural mechanics and fluidodynamics. Additionally, the process flow in fabricating RF-MEMS is not standardized like it happens for example when dealing with CMOS technology. Consequently, the need for mixed physical domain environments on one side, as well as the issue of dealing with several degrees of freedom (DoFs) in defining the proper design of RF-MEMS devices on the other hand, urge for the availability of an on-purpose simulation tool.

Once all the issues related to the RF performances optimization and fabrication of the MEMS devices are solved, another delicate key-factor must be faced to make the applicability of RF-MEMS successful within functional blocks. This is represented by the packaging of MEMS devices on one side and by their integration and interfacing to the CMOS active circuitry on the other hand. Indeed, RF-MEMS fabrication process is incompatible with standard CMOS technology. Despite the existence of few solutions for a unified MEMS/CMOS fabrication flow, the most valuable way to achieve the best performances for both parts is still represented by keeping the two processes separated and then integrating the MEMS to the CMOS part at last. Depending on the technological solutions selected for both of them the electrical interfacing on the two parts can be performed accommodating the CMOS chip directly onto

the RF-MEMS devices area. Nonetheless, in other cases it happens that the electrical interconnection schemes of the two blocks are incompatible. In this case the redistribution of electrical signals is necessary. On this purpose, one of the possibilities is to exploit the package substrate itself, whose main task is to protect MEMS devices from harmful factors (e.g. moisture, dust particles, shocks etc.), to make available such a signals redistribution scheme. This solution in which the package plays an active role in realizing the interfacing of different parts is well known in literature as hybrid packaging.

## Thesis Outline

In this thesis, both the issues related to the creation of a mixed-domain simulation tool for RF-MEMS as well as the development of suitable fabrication solutions enabling the packaging and integration of such devices will be addressed.

Concerning the first topic, the development of a MEMS model library within the Cadence<sup>©</sup> IC design framework will be shown. The approach in defining the electromechanical behaviour of such models is the compact nodal modeling. This means a limited set of points (nodes) connecting each component to the external world is defined in order to describe its physical properties. The library includes elementary models like flexible beams, suspended rigid plates, anchor points. In such a way, their interconnection leads to complete MEMS structures (e.g. switches and varactors) to be simulated within Cadence<sup>©</sup>. All the MEMS models are implemented in VerilogA<sup>©</sup> which is an HDL (Hardware Description Language)-based language supported by the Spectre<sup>©</sup> simulator. Both VerilogA<sup>©</sup> and Spectre<sup>©</sup> simulator are available within Cadence<sup>©</sup>. The realized multi-domain simulation environment (electrical and mechanical) allows the interfacing of the MEMS part to the CMOS standard libraries. This enables the simulation of mixed RF-MEMS/CMOS functional blocks. As proof of concept a VCO (Voltage Controlled Oscillator) with the LC-tank realized in MEMS technology and the active part implemented with MOS transistors will be simulated in Cadence<sup>©</sup>.

In this thesis a valuable fabrication solution for a capping substrate (i.e. package) based on vertical electrical interconnects through a Silicon wafer is also presented and discussed. The packaging approach enables few techniques for the integration of the RF-MEMS to the CMOS part (hybrid-packaging). All the issues related to the parasitic effects (capacitive and inductive couplings) introduced by the cap and affecting the RF performances of packaged MEMS devices will be highlighted. More in details, all the technology degrees of freedom (DoF's) will be optimized with an appropriate electromagnetic simulator (the Ansoft HFSS<sup>TM</sup>) in order to reduce as much as possible the package-related losses and mismatch. Furthermore, experimental data of packaged test structures will be presented both to validate the Ansoft HFSS<sup>TM</sup> and to show the feasibility of the chosen fabrication process.

Beyond the apparent weak correlation of the two just mentioned topics a common target can be easily aimed. This is based on the development of a unified simulation environment on one side. Within this, RF-MEMS devices of interest can be studied accounting for their electromechanical behaviour (compact models). Moreover, the influence of the package on their RF performances can also be introduced via the extraction of lumped models from the measurements and FEM simulations of the capping part. Beside this, the possibility offered by the Cadence<sup>©</sup> environment of simulating RF-MEMS devices interfaced to the CMOS active part allows the analysis of complete functional hybrid RF-MEMS/CMOS (packaged) blocks.

## Chapters Outline

- **Chapter 1** reports on state of the art in simulation, packaging and integration of RF-MEMS devices. Among the different approaches in simulation of RF-MEMS, implementation of a multi-domain electromechanical environment within Cadence<sup>©</sup> is introduced. This is the chosen solution pursued throughout this thesis. Moreover, a brief overview on packaging and integration methodologies for RF-MEMS devices is given to introduce this important issue also treated in the thesis.
- **Chapter 2** introduces theoretical basis which are necessary for the fast understanding of the following chapters of the thesis. Briefly, the theory of elasticity is introduced along with the definition of the relations between different geometrical reference systems commonly used in robotic applications. Furthermore, scattering parameters theory (S-parameters), frequently used in radiofrequency (RF) engineering, is reviewed.
- **Chapter 3** focuses on the suspended rigid plate electrostatic transducer. Its implementation within MEMS model library is described in details, focusing first on its 4 and 6 degrees of freedom (DoF's) mechanical model and then on the electrostatic effects. Presence of openings on plate surface (due to technological issues) are accounted for as well as viscous damping effect. The electrostatic model is also validated by comparison with FEM-based simulations. Additionally, complementary models implemented in the MEMS library are described. These are necessary to impose appropriate mechanical constraints to the structures to be simulated as well as to apply stimuli like force and deformations.
- **Chapter 4** introduces the Euler flexible beam model. This comes from the structural mechanics theory and is implemented with 6 DoF's for each beam end. The electrostatic and viscous damping models are also implemented. Static and dynamic validation of the mechanical model is presented as well as the validation of the electrostatic model.
- **Chapter 5** deals with the issue of packaging and integration of RF-MEMS devices. A technological solution for the fabrication of the capping substrate is discussed in details. This is a wafer-level solution and fabrication experiments of capped test structures are shown. Starting from measurements of these structures, a proper FEM tool (the Ansoft



HFSS<sup>TM</sup> electromagnetic simulator) is validated. This is subsequently used to define the optimum design of the capping part to reduce the parasitics affecting the RF behaviour of MEMS packaged devices.

- **Chapter 6** reports on a few complete MEMS structures exploited to validate the compact models ahead described in the thesis. Validations are performed both with experimental data and Finite Element Method (FEM)-based simulations. Moreover, simulation of an RF-MEMS varactor also accounting for the package as well as of an RF-MEMS/CMOS hybrid circuit represented by a Voltage Controlled Oscillator (VCO) are presented.
- **Conclusions and Future Works** section reports some final considerations about the work along with possible future developments related to the issues and topics discussed in this thesis.
- **Appendix A** shows some details related to the particular language chosen for implementing MEMS compact models (i.e. VerilogA<sup>©</sup>). Moreover, the approach of modularity in the realization of the library will be discussed. This allows to choose, time after time, the particular features each model has to have for the particular simulation to be performed. Finally, the user interface that allows the parameters setting within Spectre<sup>©</sup> will be shown.
- **Appendix B** focuses on a possible extension of the package process fabrication discussed in Chapter 5. This modified solution introduces some benefits which will be discussed. Moreover, details about the ongoing processing of a package substrate for RF-MEMS devices will be reported.
- **Appendix C** introduces the mechanical model of a flexible thin membrane. This complementary model, implemented in the library, is not used in the complete structures discussed in this thesis.



# Chapter 1

## State of the Art in Simulation, Packaging and Integration of RF-MEMS Devices

In this chapter a broad overview on the state of the art in RF-MEMS technology both concerning the simulation approaches and the packaging and integration issues will be shown.

### 1.1 The Finite Elements Method (FEM) Approach

The correct prediction of the behaviour related to complex systems via the use of appropriate simulation software is not a simple task. This becomes more critical when dealing with MEMS as they require the coupling of different physical domains (e.g. electrical and mechanical). A valuable approach is represented by the use of Finite Element Method (FEM) based software. Briefly, they divide the 3D geometry of the problem in sub-elements (for instance in the shape of tetrahedrons) connected to each other by means of nodes. Within each of these the problem equations are approximated and locally solved, like Maxwell equations for the electromagnetic problem or elasticity theory relations for the mechanical behaviour [1]. Finally, the relations among the set of elements are defined by imposing suitable boundary conditions. FEM tools with two coupled built-in solvers for electromechanical problems are also available

on the market. ConventorWare<sup>®</sup> is likely the most diffused electromechanical coupled FEM tool for RF-MEMS simulations [2].

Despite FEM tools allow very accurate predictions of RF-MEMS electromagnetic and mechanical behaviour, sometimes their use is not a reasonable choice. Indeed, they require large memory amount as well as considerable simulation time. For this reason, when a structure with a complex geometry (e.g. an RF-MEMS switch) has to be optimized to meet certain requirements a reasonably accurate and fast tool rather than a very accurate but slow software would be preferable. This is the main reason why large efforts are being spent by the Scientific Community in developing fast simulation methods to be placed beside FEM tools, widening the choices the designer has depending on his requirements.

## 1.2 Compact Modeling of RF-MEMS

The approach in pursuing a simplified description of certain structures (RF-MEMS) to be analyzed is well-known in literature as *compact modeling*. Basically, compact models are obtained by following numerical or analytical methods. The first ones will not be treated throughout the thesis but are just referenced to cover the whole spectrum of main solutions for the modeling of RF-MEMS [3]. Whereas, analytical methods can be furthermore split in two categories depending on the approaches through which compact models are derived. These are the so called *bottom-up* and *top-down* approaches. Concerning the first one, starting point is the accurate analysis of the entire RF-MEMS devices, including all the mechanical and electrical effects, performed by means of FEM based tools. Hence, through suitable methods a simplified description of the system is derived and its geometry is divided into elementary models with an acceptable accuracy loss within certain analysis ranges. This method is called Model Order Reduction (MOR) and is going to be briefly described below. The other methodology in compact modeling of RF-MEMS, dual with respect to the just mentioned one, is the top-down approach. In this case the analysis commences at system level. The system, for instance a transceiver, is described by means of lumped elements based on analytical models (lumped analytical modeling). When dealing with a single physical domain, i.e. electrical, a network of lumped elements, like capacitors,

inductors etc., is able to describe the behaviour of the entire system with reasonable accuracy. Nevertheless, when different physical domains are involved like it happens with MEMS technology, different strategies must be employed to adapt the lumped elements approach to such a generic problem. One valuable solution is well-known in literature and is based on equivalent electrical circuits. Whereas, the approach chosen in this work is the development of a mixed domain simulation environment based on the concept of hierarchical structural analysis.

### **1.2.1 Model Order Reduction (MOR) Method**

One of the most effective methods to simplify the initial structure employing a bottom-up approach is the Model Order Reduction (MOR). In a FEM simulation of an entire structure (e.g. a MEMS switch) the number of internal nodes is generally very high (for instance 50.000). Within certain ranges most part of them is not critical in determining the behaviour of the structure. Consequently, very limited sets of nodes, like 10 or 20, are sufficient to model each part of the initial topology with small losses in accuracy but very low computational complexity and small simulation times. The MOR allows to identify which nodes are more critical than others in achieving a correct modeling of the structure. Suitable software have been developed to this purpose [4]. These interact with the matrices generated as output of the FEM simulator and following certain criterion reduce their order down to a few tens. After the matrices screening is complete, the more significant nodes (or degrees of freedom, DoF's) in characterizing the behaviour of the structure within defined ranges are figured out. On the other hand, all the others DoF's are neglected [5].

### **1.2.2 Equivalent Electrical Circuits**

The top-down approach based on equivalent electrical circuits is proposed and very well explained in details by Senturia [6]. The elementary models, or lumped elements, exploit the analogy existing between the mechanical and electrical physical domains. Indeed, as shown by Senturia, it is possible to determine an equivalent electric component for each mechanical effect of interest. For instance a spring defines a certain relation between its deformation and the consequent counteracting force (function of the spring constant) in the

mechanical domain. This is analogue to the relation imposed by a capacitor between the applied voltage and the current in the electrical domain. Following the same approach, other mechanical effects, like inertia or viscous damping, are translated in their electric equivalents. Eventually, a complete RF-MEMS device is represented by its equivalent electrical lumped elements network and can be simulated within a commercial electrical domain simulator.

### 1.2.3 Mixed Domain Electromechanical Simulation Environment

The top-down approach for compact modeling of RF-MEMS chosen in this thesis is different from the ones described thus far. It is based on a multi domain simulation environment, which means the electrical and mechanical physical domains are kept separated. In other words, mechanical magnitudes are not transformed in their electrical equivalents.

The implemented simulation environment allows *hierarchical structural analysis*. The entire system is divided into elementary parts that, according to the concept of hierarchy, can be connected together in several fashions to assemble structures reaching more complex topologies [7]. For instance, an RF-MEMS switch based on suspended electrostatic transducer can be decomposed in two parts. One includes the mechanical spring effects and the other one the actual electromechanical transduction. Whether elementary models implementing the first and the second effects are available, like deformable beams and suspended rigid plate electrostatic transducer respectively, their interconnection allows to reconstruct the behaviour of the entire RF-MEMS switch.

Elementary components are based on mathematical models able to characterize their behaviour within certain physical domains. For instance, the behaviour of flexible structures comes from the theory of elasticity and structural mechanics. Differently, the electromechanical transduction model can be easily derived from an electrostatic problem. The validity of such models is verified within rather large ranges, ensuring a certain flexibility in using the basic components. This reflects in a broad variety of complete RF-MEMS devices configurations that can be successfully simulated and characterized following such an approach.

Each component has a limited number of nodes through which it is connected to the other elements forming a complex structure. Nodes also represent the input/output points by which the mathematical model imposes the relations among the involved physical magnitudes. For example, the deformation applied in input to one node of a flexible structure causes a reaction force, defined by the internal model, which is the output of the same node [8]. The co-existence of magnitudes belonging to different physical domains (electrical and mechanical) is worked out by the simulator. Indeed, tools whose simulation machines are based on the resolution of Kirchhoff Flow Law (KFL) and Kirchhoff Voltage Law (KVL) are suitable for multi domain analysis. In other words, two magnitudes are associated to each node: a through and an across value, allowing a generalization of the physical domain they belong to, within the simulator [9]. In the electrical domain the through value is the flowing current while the across magnitude is the applied voltage. Similarly, in the mechanical domain the through value is the force applied to a certain node while the across variable is the displacement of that very node. This is the approach chosen for the development of the mixed domain simulation environment presented in this thesis. The exploited simulator is the Spectre<sup>®</sup> available within the Cadence<sup>®</sup> IC development framework and the language for compact models implementation is the VerilogA<sup>®</sup> [10].

### 1.3 Packaging of RF-MEMS Devices

The other issue this thesis will focus on is the packaging and integration of RF-MEMS devices. This represents a very delicate step in which the research, especially in the last years, is investing large efforts. After all the issues related to the fabrication and performances optimization of RF-MEMS, the further necessary stage to allow their use on a large scale is, indeed, the packaging and integration. Talking more in general about MEMS for various applications (e.g. pressure sensors, accelerometers, MOEMS and so on), several viable technological solutions for their protection and encapsulation have been already presented and tested [11] [12] [13]. However, the application of a package substrate to MEMS devices for RF applications requires additional cares and involves further considerations. Indeed, the packaging step introduces additional losses due to the longer path the electric signals have to travel through (e.g. vertical vias and bonding wires). This also involves an increase of mismatch because

of the capacitive and inductive couplings between the signal lines through the capping. Additionally, packaging of RF-MEMS devices means to apply a protective substrate to the device wafer, reducing the air gap above the MEMS structures themselves. This means the capping interacts with the electric field of RF-MEMS, resulting in an additional source of losses and mismatch. If these issues are not properly taken into account, the packaging step can affect rather largely the RF performances the MEMS are required to have, eventually making them not to meet the specifications for certain applications. Hence, the availability of an accurate prediction related to the package influence on RF behaviour of MEMS devices prior to its fabrication and application to the device wafer would be desirable. In literature a few valuable solutions for the packaging of RF-MEMS including their experimental characterization have been already presented [14] [15] [16]. However, a careful and extensive electromagnetic analysis of the cap by means of appropriate simulation tools has not been carried out yet. This is what will be presented throughout the thesis, which is an extensive electromagnetic optimization of a fabrication process for a package substrate.

Discussing about the proper simulation methodology, this problem requires a rather large accuracy and has not to be performed at system level but rather at device level. Consequently, the most appropriate choice is represented by FEM electromagnetic simulators. In the next chapters the Ansoft HFSS<sup>TM</sup> electromagnetic simulator [17] will be selected as the proper tool in order to perform the optimization of the package fabrication process.

## **1.4 Integration of RF-MEMS Packaged Devices: Hybrid Packaging**

The final step for a full usability of RF-MEMS is their integration with functional blocks obtained by means of other technologies. Talking more in general about integration of different circuitual parts, several reliable assembly solutions are available. These are known as Surface Mount Technologies (SMT) and are referred to the integration of a functional block on a Printed Circuit Board (PCB) [18] [19]. Among the various integration solutions the more widely used are based on the Flip-Chip approach [20], like it happens in the Ball Grid Array (BGA) technique [21], and the wire-bonding [22] [23].



Referring to the integration of RF-MEMS devices, they require to be interfaced to an active control circuitry, realized in CMOS technology, prior to their availability for SMT on a PCB. As a consequence, it would be desirable to have an RF-MEMS/CMOS hybrid chip ready for its integration on the board. This requires a further integration step within the MEMS packaged chip itself. The state of the art in packaging for RF-MEMS is to exploit the protective substrate in order to provide for additional functionalities. This is the base concept of hybrid packaging, in which the capping substrate itself facilitates the co-integration of the CMOS chip to the RF-MEMS part [24]. This is the integration solution that will be furthermore discussed in this thesis.



# Chapter 2

## Theoretical Basis

In this chapter the fundamentals required for a straightforward and rapid understanding of the topics presented throughout the thesis are reported. These include both elements of structural mechanics (i.e. theory of elasticity) and the definition of the scattering parameters (S-parameters) commonly used in radiofrequency engineering.

### 2.1 The Choice of the Reference Systems

Before introducing the theory of elasticity, it is useful to focus on a preliminary issue related to the description of a body in the space. Each object with an arbitrary shape must be represented within an appropriate reference system. Depending on its choice as well as on the topology of the object to be described, the mapping of each point belonging to the body can assume different representation complexities. For instance, a rectangular object is easily described by using a Cartesian reference system (see Figure 2.1). On the other hand, a circular shaped object can be more clearly represented within a spherical coordinates system like it is shown in Figure 2.2. In our case the most reasonable choice is the use of the Cartesian systems since elements of interest are generally rectangular-like objects, as slender beams and thin plates.

In assembling a complete MEMS device (e.g. a switch) several elementary components have to be connected together. It is easier to describe the mechanical behaviour, in terms of deformations, forces and displacements, by defining a local Cartesian reference system for each sub-element. However, a

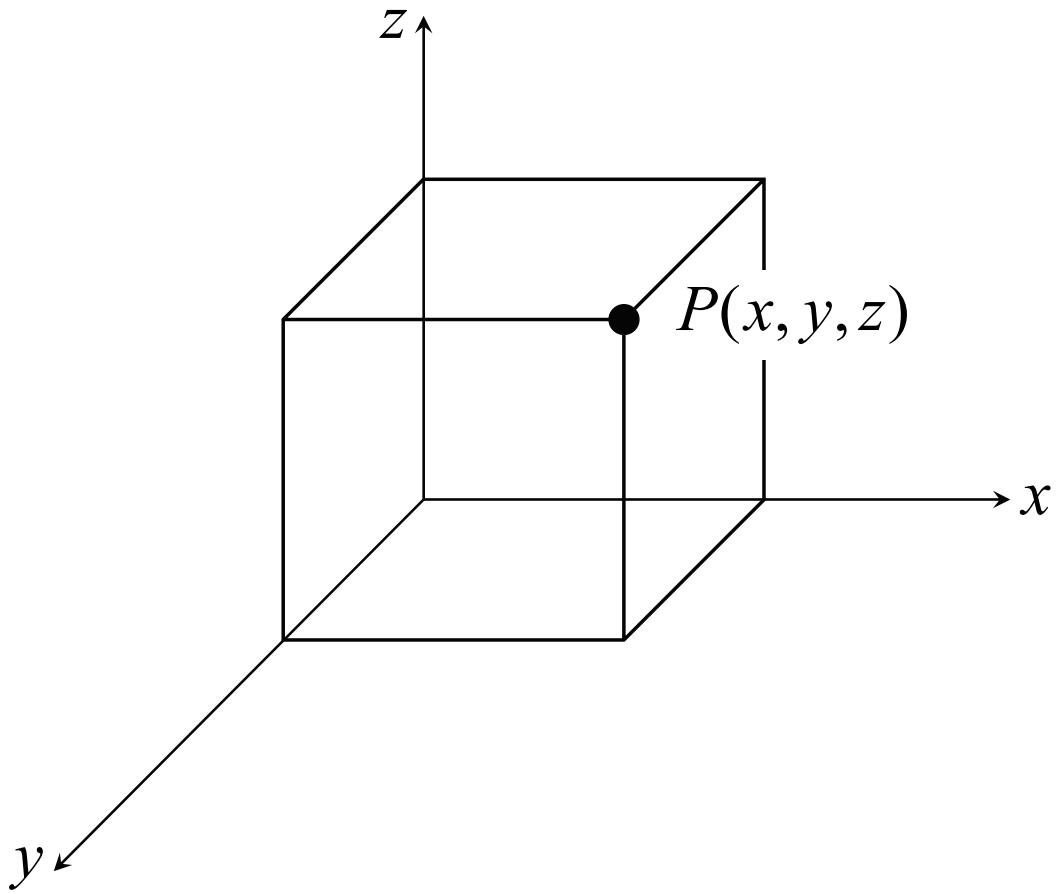


Figure 2.1: Cartesian reference system. A generic point  $P$  position in space is identified by means of the corresponding three coordinates along the  $x, y, z$  axes.

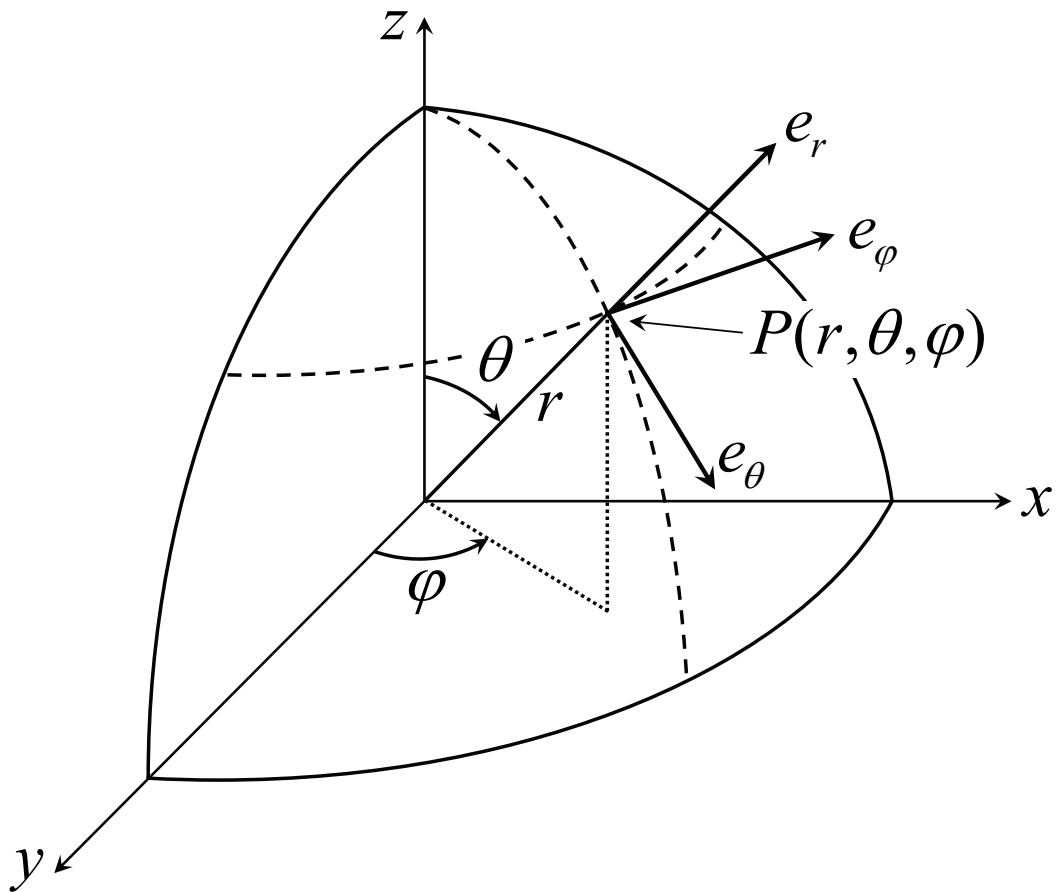


Figure 2.2: Spherical coordinates reference system. A generic point  $P$  position in space is identified by means of the radius  $r$  and two angles ( $\theta$  and  $\phi$ ).

set of relations to maintain consistency in the mapping of the entire system has also to be established. The adopted solution to circumvent this problem is the definition of a local reference system for each elementary component along with the existence of a global one common to the whole hierarchy. Once the mathematical relations between each local system and the global one are defined, the description of each part is made easier and the consistency at system level is also ensured. This mathematical operator which represents the link between different Cartesian systems is a matrix. It is called *rotation matrix*, and its dimension depends on the number of DoF's among the two systems as furthermore described.

### 2.1.1 The One Degree of Freedom Rotation Matrix

To introduce the approach leading to the rotation matrix for multiple DoF's it is appropriate to discuss the very simple case in which a single DoF is allowed between the global and the local Cartesian reference systems. Let the global system be defined by the  $X, Y, Z$  axes, while the local one by the  $x, y, z$  axes as shown in Figure 2.3. The  $Z$  axis direction is perpendicular to the  $xy$  plane and the direction is outgoing the book toward the reader. Let  $P$  be an arbitrary point lying on the  $xy$  plane (i.e.  $z = 0$ ). Its  $X$  and  $Y$  abscissas are  $X_P$  and  $Y_P$  respectively. If there is no rotation of one system with respect to the other one the axes are superposed ( $X = x, Y = y$  and  $Z = z$ ) and the  $P$  abscissas are the same in the two reference systems. Let now  $\theta_Z$  be a rotation angle of the local system with respect to the global one around the  $Z$  axis. After the rotation the point  $P$  is displaced with respect to the fixed system as shown in Figure 2.4. By means of simple calculations the relations between the  $P$  point abscissas in the global system ( $X_P, Y_P$ ) and in the local one ( $x_P, y_P$ ) are derived in equations 2.1 and 2.2:

$$X_P = x_P \cos \theta_Z - y_P \sin \theta_Z \quad (2.1)$$

$$Y_P = x_P \sin \theta_Z + y_P \cos \theta_Z \quad (2.2)$$

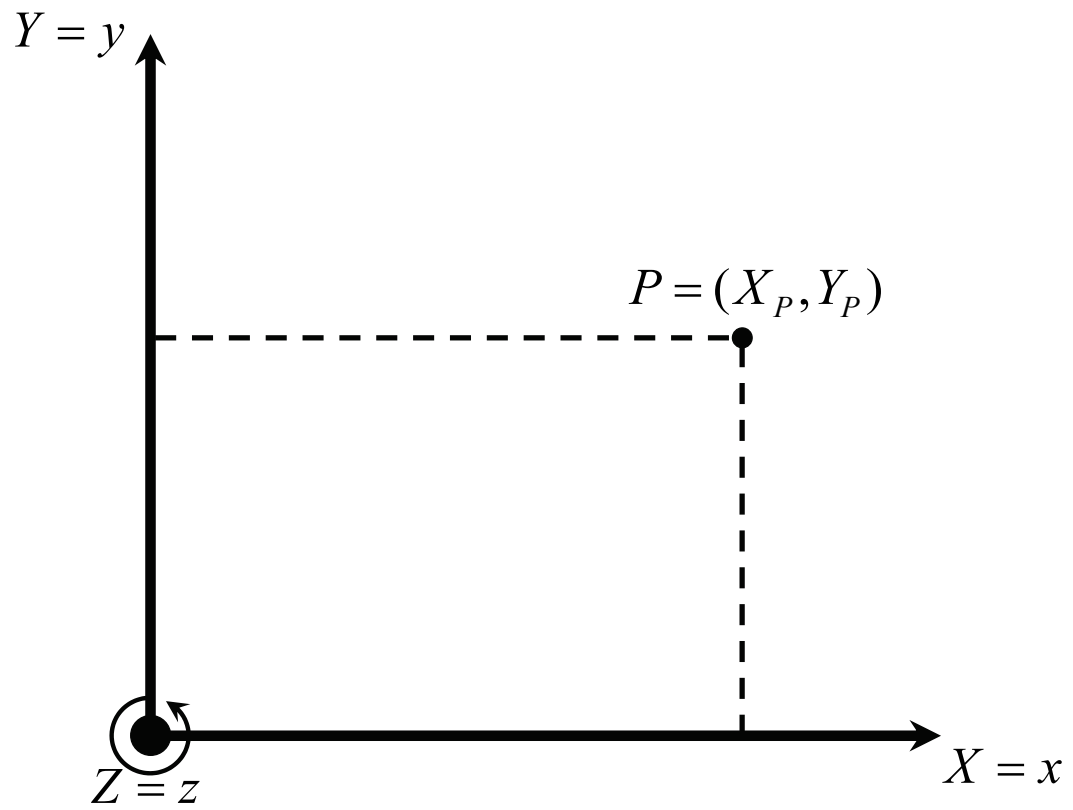


Figure 2.3: Point  $P$  in the global reference system. Its description is the same in the local reference system when no rotation occurs.

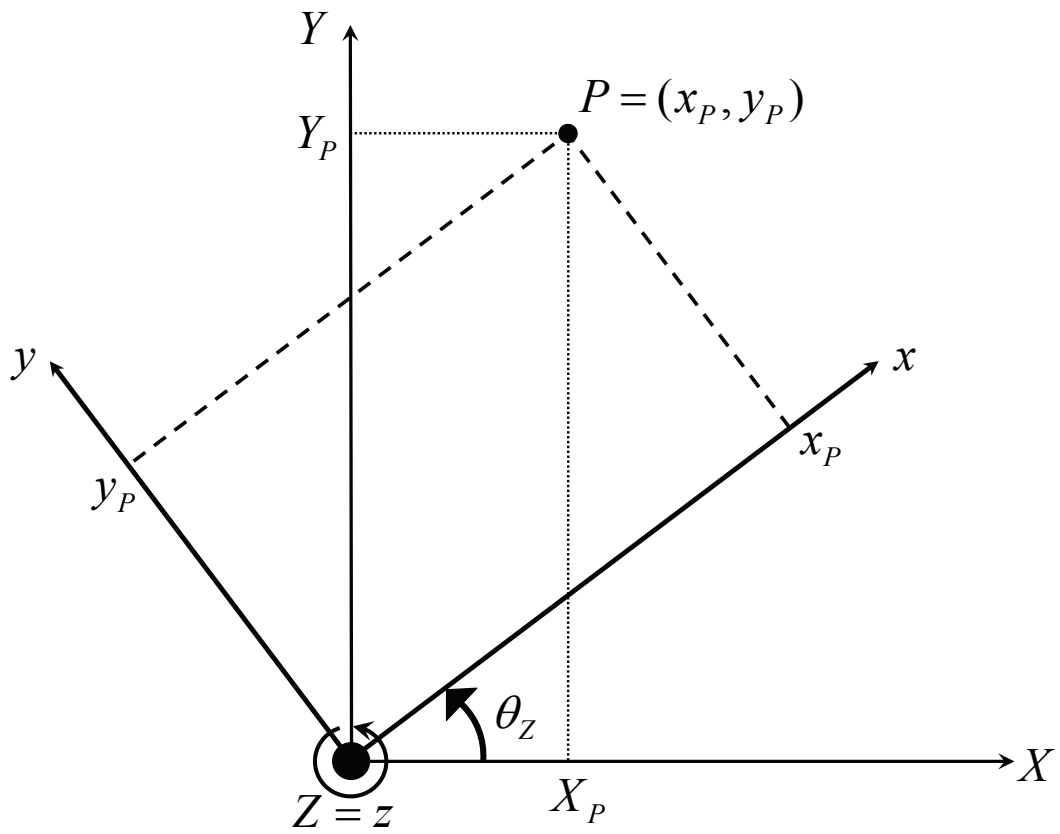


Figure 2.4: Rotation ( $\theta_Z$ ) around the  $Z$  axis of the local system with respect to the global one.



The 2.1 and 2.2 can be written in matrix form:

$$\begin{bmatrix} X_P \\ Y_P \end{bmatrix} = \begin{bmatrix} \cos \theta_Z & -\sin \theta_Z \\ \sin \theta_Z & \cos \theta_Z \end{bmatrix} \begin{bmatrix} x_P \\ y_P \end{bmatrix} \quad (2.3)$$

The rotation matrix will be addressed with the symbol  $\Omega_L$  and in the 2.3 it has the following form:

$$\Omega_L = \begin{bmatrix} \cos \theta_Z & -\sin \theta_Z \\ \sin \theta_Z & \cos \theta_Z \end{bmatrix} \quad (2.4)$$

Looking at the 2.4 it is easy to invert the rotation matrix in order to get the description of the point  $P$  in the local system as a function of its coordinates in the global one:

$$\begin{bmatrix} x_P \\ y_P \end{bmatrix} = \begin{bmatrix} \cos \theta_Z & \sin \theta_Z \\ -\sin \theta_Z & \cos \theta_Z \end{bmatrix} \begin{bmatrix} X_P \\ Y_P \end{bmatrix} \quad (2.5)$$

where the inverted rotation matrix is:

$$\Omega_L^{-1} = \begin{bmatrix} \cos \theta_Z & \sin \theta_Z \\ -\sin \theta_Z & \cos \theta_Z \end{bmatrix} \quad (2.6)$$

It is simple to derive the inverted  $\Omega_L$  (2.6) as it is always verified that for a Cartesian reference system  $\Omega_L^{-1}$  is equal to the transposed rotation matrix  $\Omega_L^T$  [25]:

$$\Omega_L^{-1} = \Omega_L^T \quad (2.7)$$

### 2.1.2 The Complete 12 Degrees of Freedom Rotation Matrix

What we are interested in is the more general case in which the local reference system can rotate around the three axis as reported in Figure 2.5. Following the same approach shown in previous section it is possible to derive the complete rotation matrix that corresponds to the three rotations. In this case the rotation matrix dimension is  $3 \times 3$  and its expression is subsequently reported [25]:

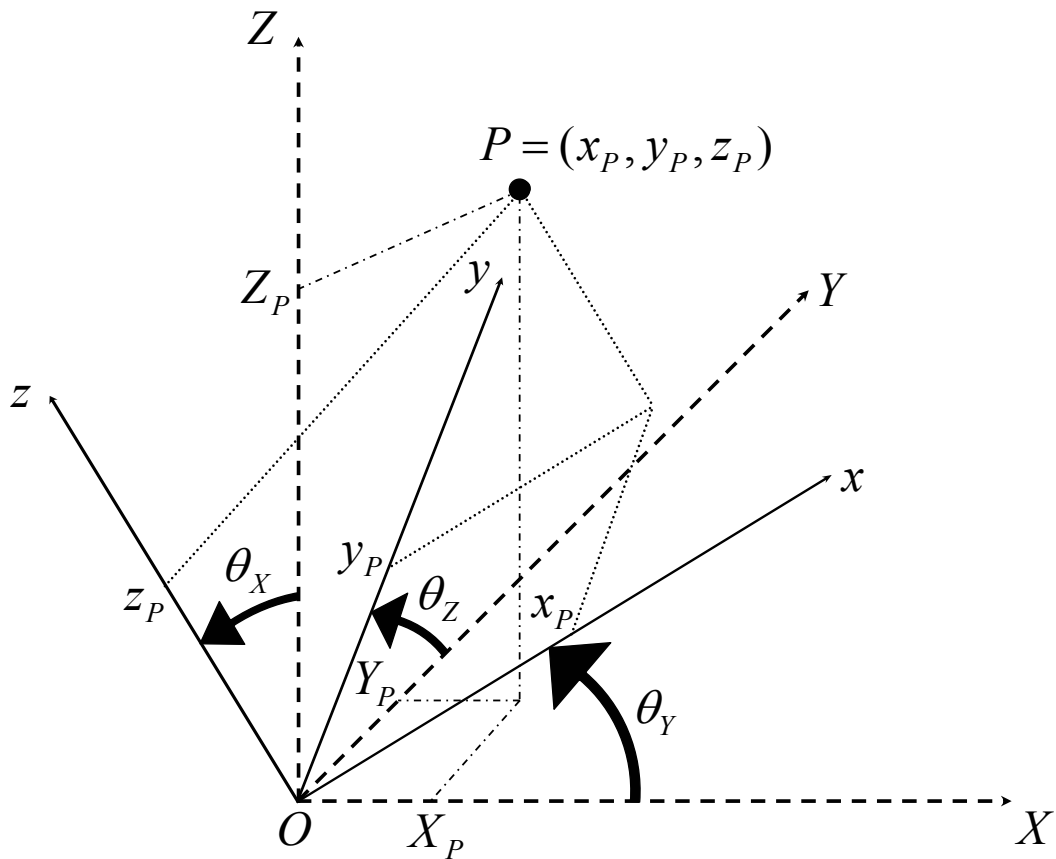


Figure 2.5: Rotation of the local system around the three axes of the global one  $(\theta_X, \theta_Y, \theta_Z)$ .

$$\Omega_L = \begin{bmatrix} C_Y C_Z & (-C_X S_Z + S_X S_Y C_Z) & (S_X S_Z + C_X S_Y C_Z) \\ C_Y S_Z & (C_X C_Z + S_X S_Y S_Z) & (-S_X C_Z + C_X S_Y S_Z) \\ -S_Y & S_X C_Y & C_X C_Y \end{bmatrix} \quad (2.8)$$

where

$$C_X = \cos \theta_X \quad (2.9)$$

$$S_X = \sin \theta_X \quad (2.10)$$

$$C_Y = \cos \theta_Y \quad (2.11)$$

$$S_Y = \sin \theta_Y \quad (2.12)$$

$$C_Z = \cos \theta_Z \quad (2.13)$$

$$S_Z = \sin \theta_Z \quad (2.14)$$

Finally, the relations between the point  $P$  coordinates in the global and local reference system are reported in the equation 2.15 where  $\Omega_L$  is expressed by the 2.8

$$\begin{bmatrix} X_P \\ Y_P \\ Z_P \end{bmatrix} = [\Omega_L] \begin{bmatrix} x_P \\ y_P \\ z_P \end{bmatrix} \quad (2.15)$$

## 2.2 Structural Mechanics: the Theory of Elasticity

In this section introductory elements about the theory of elasticity are shown. By these it will be easy to understand the mechanical model for the flexible beam in the next chapters.

### 2.2.1 The Definition of Mechanical Stress and Strain

First of all two important definitions are to be introduced. These refer to the mechanical stress and strain and are following.

#### Stress

Let a body in equilibrium be represented by the scheme in Figure 2.6. When external forces are applied ( $P_1, P_2, \dots, P_7$ ) internal forces will generate between the parts of the body. In order to identify these forces at any point  $O$  let us imagine the body divided in parts  $A$  and  $B$  by the cross section  $mm$  including this point. Considering for instance the  $A$  part, it can be stated that it is in equilibrium under the action of external forces  $P_1, P_2, \dots, P_7$  and the inner forces distributed onto the cross section  $mm$ . The latter ones represent the action of the material within the part  $B$  on the material of the part  $A$ . It is then assumed that these forces are as continuously distributed over the area  $mm$  as the hydrostatic or wind pressure are continuously distributed over the surfaces they are applied to. The magnitude of such forces is commonly defined by their intensity or, in other words, by the amount of force per area unit of the surface on which they act. In discussing internal forces this intensity is called *stress* [26].

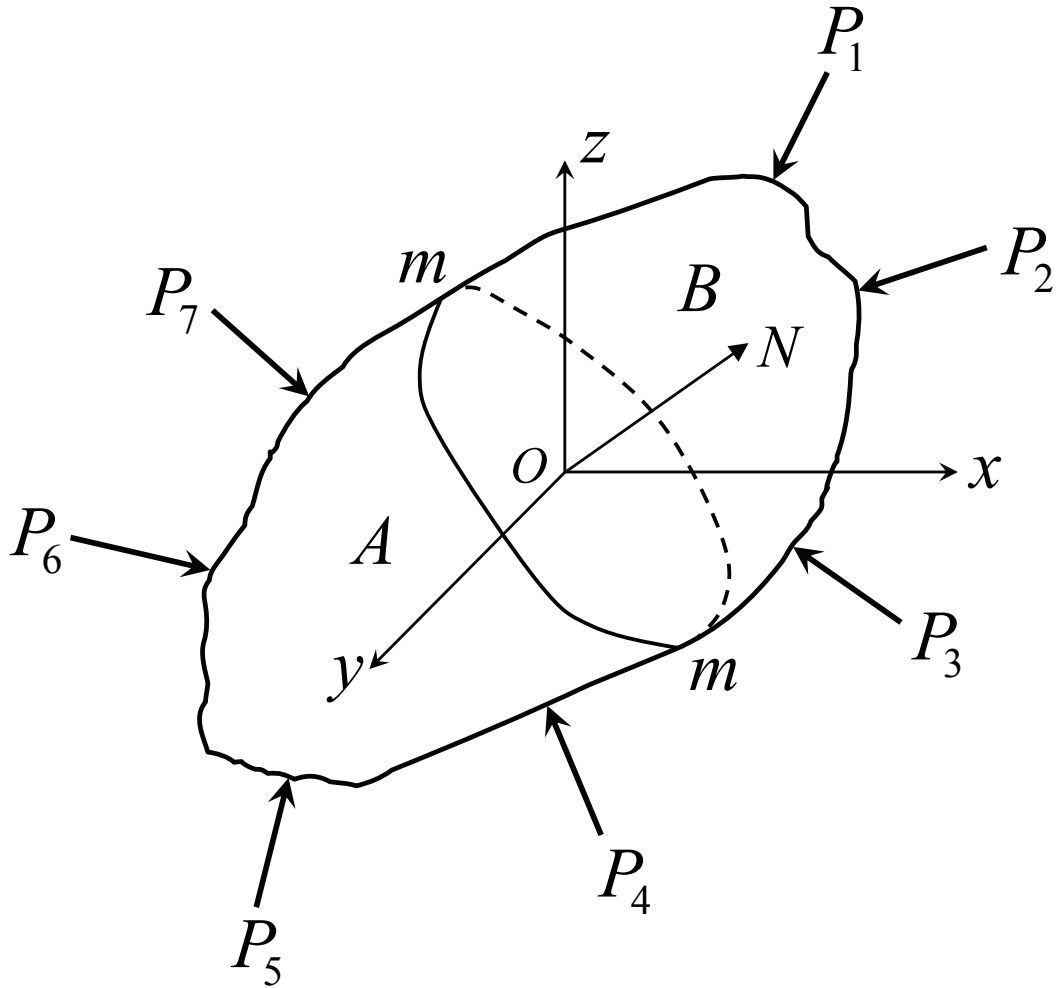


Figure 2.6: Body with an arbitrary shape. It is divided in two parts  $A$  and  $B$  by the cross section  $mm$ .

## Strain

To introduce the concept of strain let us imagine a rectangular deformable body  $ABCD$  like the one shown in Figure 2.7. Imposition of a force on the vertex  $C$  without any constraints will result in a rigid translation of the body equal to  $u_x$  along the  $x$  axis and  $u_y$  along  $y$ . Let us now anchor the  $A$  vertex in the  $A'$  position. The applied stimulus now determines the deformation of the body. The deformed shape of an elastic structure under a given system of loads distribution is described by the three displacements:

$$\begin{aligned}u_x &= u_x(x, y, z) \\u_y &= u_y(x, y, z) \\u_z &= u_z(x, y, z)\end{aligned}\tag{2.16}$$

The vectors related to the three displacements of a given point in the structure are mutually orthogonal and their positive directions correspond to the positive directions of the coordinate axes. The *strains* in the deformed structure are defined as partial derivatives of displacements  $u_x$ ,  $u_y$  and  $u_z$  [27]. For small deformations the strain-displacement relations are linear and the strain components are given by:

$$e_{xx} = \frac{\partial u_x}{\partial x}\tag{2.17}$$

$$e_{yy} = \frac{\partial u_y}{\partial y}\tag{2.18}$$

$$e_{zz} = \frac{\partial u_z}{\partial z}\tag{2.19}$$

$$e_{xy} = e_{yx} = \frac{\partial u_y}{\partial x} + \frac{\partial u_x}{\partial y}\tag{2.20}$$

$$e_{yz} = e_{zy} = \frac{\partial u_z}{\partial y} + \frac{\partial u_y}{\partial z}\tag{2.21}$$

$$e_{zx} = e_{xz} = \frac{\partial u_x}{\partial z} + \frac{\partial u_z}{\partial x}\tag{2.22}$$

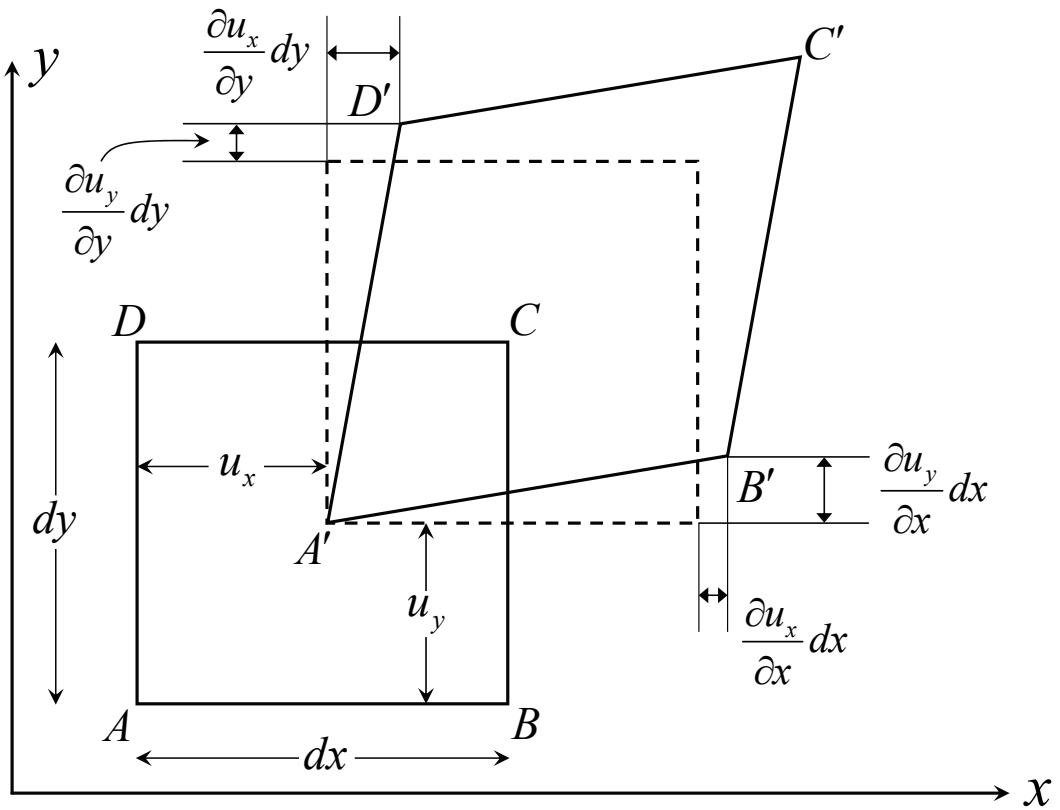


Figure 2.7: Definition of strain by means of a rectangular body which undergoes deformations.

where  $e_{xx}$ ,  $e_{yy}$  and  $e_{zz}$  represent normal strains, while  $e_{xy}$ ,  $e_{yz}$  and  $e_{zx}$  represent shearing strains. From equations 2.20, 2.21 and 2.22 it follows that the symmetry relation

$$e_{ij} = e_{ji} \quad i, j = x, y, z \quad (2.23)$$

is valid for all shearing strains. Therefore, a set of only six strain components is required to describe strain states in three-dimensional elasticity problems. To derive the strain-displacement equations from 2.17 to 2.22 let us now go back to Figure 2.6. The variation in length of  $AB$  is  $(\partial u_x / \partial x)dx$  and whether we define the normal strain as the ratio of the change in length over its original value, it follows that normal strain in the  $x$  direction is  $\partial u_x / \partial x$ , that corresponds to the 2.17. Similarly, the other normal strain components can be derived by following a similar approach. The angular distortion on the element can be derived in terms of angles  $\gamma_1$  and  $\gamma_2$  of Figure 2.6. For small deformations it is  $\gamma_1 = \partial u_y / \partial x$  and  $\gamma_2 = \partial u_x / \partial y$ . Whether the shearing strain  $e_{xy}$  in the  $xy$  plane is defined as the total angular deformation (sum of  $\gamma_1$  and  $\gamma_2$ ) it follows that the shearing-strain component is given by  $\partial u_y / \partial x + \partial u_x / \partial y$ , that corresponds to the 2.20.

## 2.2.2 Relations Between Stress and Strain

Now that both the stress and strain concepts have been introduced, the further step is the definition of their relations. These are defined by the Hooke's Law that, in the case of an elongation of the body along the  $x$  direction is:

$$e_{xx} = \frac{\sigma_{xx}}{E} \quad (2.24)$$

where  $\sigma_{xx}$  is the normal stress along the  $x$  direction and  $E$  the Young's modulus. Extensions of the body in the  $x$  direction are accompanied by lateral contractions expressed as follows:

$$e_{yy} = -\nu \frac{\sigma_{xx}}{E} \quad (2.25)$$

$$e_{zz} = -\nu \frac{\sigma_{xx}}{E} \quad (2.26)$$

where  $\nu$  is the Poisson's ratio. Whether the element undergoes the action of normal stresses  $\sigma_{xx}$ ,  $\sigma_{yy}$  and  $\sigma_{zz}$  the resultant components of strain can be



obtained by the equations 2.24, 2.25 and 2.26. Indeed, by applying the method of superposition it results:

$$e_{xx} = \frac{1}{E}[\sigma_{xx} - \nu(\sigma_{yy} + \sigma_{zz})] \quad (2.27)$$

$$e_{yy} = \frac{1}{E}[\sigma_{yy} - \nu(\sigma_{zz} + \sigma_{xx})] \quad (2.28)$$

$$e_{zz} = \frac{1}{E}[\sigma_{zz} - \nu(\sigma_{xx} + \sigma_{yy})] \quad (2.29)$$

$$e_{xy} = 2\frac{1+\nu}{E}\sigma_{xy} \quad (2.30)$$

$$e_{yz} = 2\frac{1+\nu}{E}\sigma_{yz} \quad (2.31)$$

$$e_{zx} = 2\frac{1+\nu}{E}\sigma_{zx} \quad (2.32)$$

where  $\sigma_{xy}$ ,  $\sigma_{yz}$  and  $\sigma_{zx}$  are the shearing stresses. It must be stated that in previous notation the thermal effects have been neglected since are not relevant in the applications further presented throughout this thesis. Equations from 2.27 to 2.32 can be solved for the stresses:

$$\sigma_{xx} = \frac{E}{(1+\nu)(1-2\nu)}[(1-\nu)e_{xx} + \nu(e_{yy} + e_{zz})] \quad (2.33)$$

$$\sigma_{yy} = \frac{E}{(1+\nu)(1-2\nu)}[(1-\nu)e_{yy} + \nu(e_{zz} + e_{xx})] \quad (2.34)$$

$$\sigma_{zz} = \frac{E}{(1+\nu)(1-2\nu)}[(1-\nu)e_{zz} + \nu(e_{xx} + e_{yy})] \quad (2.35)$$

$$\sigma_{xy} = \frac{E}{2(1+\nu)}e_{xy} \quad (2.36)$$

$$\sigma_{yz} = \frac{E}{2(1+\nu)}e_{yz} \quad (2.37)$$

$$\sigma_{zx} = \frac{E}{2(1+\nu)}e_{zx} \quad (2.38)$$

Equations from 2.27 to 2.32 can be written in matrix form as follows:

$$\begin{bmatrix} e_{xx} \\ e_{yy} \\ e_{zz} \\ e_{xy} \\ e_{yz} \\ e_{zx} \end{bmatrix} = \frac{1}{E} \begin{bmatrix} 1 & -\nu & -\nu & 0 & 0 & 0 \\ -\nu & 1 & -\nu & 0 & 0 & 0 \\ -\nu & -\nu & 1 & 0 & 0 & 0 \\ 0 & 0 & 0 & 2(1+\nu) & 0 & 0 \\ 0 & 0 & 0 & 0 & 2(1+\nu) & 0 \\ 0 & 0 & 0 & 0 & 0 & 2(1+\nu) \end{bmatrix} \begin{bmatrix} \sigma_{xx} \\ \sigma_{yy} \\ \sigma_{zz} \\ \sigma_{xy} \\ \sigma_{yz} \\ \sigma_{zx} \end{bmatrix} \quad (2.39)$$

Also the equations from 2.33 to 2.38 can be arranged in the same form:

$$\begin{bmatrix} \sigma_{xx} \\ \sigma_{yy} \\ \sigma_{zz} \\ \sigma_{xy} \\ \sigma_{yz} \\ \sigma_{zx} \end{bmatrix} = H \begin{bmatrix} 1-\nu & \nu & \nu & 0 & 0 & 0 \\ \nu & 1-\nu & \nu & 0 & 0 & 0 \\ \nu & \nu & 1-\nu & 0 & 0 & 0 \\ 0 & 0 & 0 & \frac{(1-2\nu)}{2} & 0 & 0 \\ 0 & 0 & 0 & 0 & \frac{(1-2\nu)}{2} & 0 \\ 0 & 0 & 0 & 0 & 0 & \frac{(1-2\nu)}{2} \end{bmatrix} \begin{bmatrix} e_{xx} \\ e_{yy} \\ e_{zz} \\ e_{xy} \\ e_{yz} \\ e_{zx} \end{bmatrix} \quad (2.40)$$

where

$$H = \frac{E}{(1+\nu)(1-2\nu)} \quad (2.41)$$

When necessary, the shear modulus  $G$  can be introduced in these equation using the following expression:

$$G = \frac{E}{2(1+\nu)} \quad (2.42)$$

Finally, in order to get a simplified notation, the matrix relation 2.40 can be substituted by its symbolic expression:

$$\boldsymbol{\sigma} = \mathbf{x} \mathbf{e} \quad (2.43)$$

where the bold letters represent a vector notation. From the 2.43 it results that:

$$\boldsymbol{\sigma} = [ \sigma_{xx} \quad \sigma_{yy} \quad \sigma_{zz} \quad \sigma_{xy} \quad \sigma_{yz} \quad \sigma_{zx} ]^T \quad (2.44)$$

$$\mathbf{e} = [ e_{xx} \quad e_{yy} \quad e_{zz} \quad e_{xy} \quad e_{yz} \quad e_{zx} ]^T \quad (2.45)$$

$$\mathbf{x} = \frac{E}{(1+\nu)(1-2\nu)} \begin{bmatrix} 1-\nu & \nu & \nu & 0 & 0 & 0 \\ \nu & 1-\nu & \nu & 0 & 0 & 0 \\ \nu & \nu & 1-\nu & 0 & 0 & 0 \\ 0 & 0 & 0 & \frac{(1-2\nu)}{2} & 0 & 0 \\ 0 & 0 & 0 & 0 & \frac{(1-2\nu)}{2} & 0 \\ 0 & 0 & 0 & 0 & 0 & \frac{(1-2\nu)}{2} \end{bmatrix} \quad (2.46)$$

### 2.2.3 Plane Stress and Plane Strain

What discussed thus far is a very general description of the theory of elasticity. Nevertheless, in order to define the mechanical behaviour of the structures discussed in this thesis, we are interested in two-dimensional stress distributions. This introduces some simplifications in the just presented method. There are two types of two-dimensional stress distributions, called *plane-stress* and *plane-strain* distributions.

#### Plane Stress

This type of distribution is used for thin flat plates loaded in the plane of the plate. This means that no stress components vary through the plate thickness [27]. This assumption reflects in:

$$\sigma_{zz} = \sigma_{zx} = \sigma_{zy} = 0 \quad (2.47)$$

By introducing this hypothesis in the 2.43 the 2.44, 2.45 and 2.46 become respectively:

$$\boldsymbol{\sigma} = [ \sigma_{xx} \quad \sigma_{yy} \quad \sigma_{zz} ]^T \quad (2.48)$$

$$\mathbf{e} = [ e_{xx} \quad e_{yy} \quad e_{zz} ]^T \quad (2.49)$$

$$\mathbf{x} = \frac{E}{(1-\nu^2)} \begin{bmatrix} 1 & \nu & 0 \\ \nu & 1 & 0 \\ 0 & 0 & (1-\nu)/2 \end{bmatrix} \quad (2.50)$$

and the 2.40 becomes:

$$\begin{bmatrix} \sigma_{xx} \\ \sigma_{yy} \\ \sigma_{zz} \end{bmatrix} = \frac{E}{(1-\nu^2)} \begin{bmatrix} 1 & \nu & 0 \\ \nu & 1 & 0 \\ 0 & 0 & (1-\nu)/2 \end{bmatrix} \begin{bmatrix} e_{xx} \\ e_{yy} \\ e_{zz} \end{bmatrix} \quad (2.51)$$

### Plane Strain

A similar simplification is possible on the other hand when the dimension of the body along the  $z$  direction is large. If a long cylindrical or prismatic body is loaded by forces which are perpendicular to the longitudinal elements and do not vary along its length, it may be assumed that all cross sections are in the same conditions [26]. This leads to the following simplification:

$$\frac{\partial}{\partial z} = u_z = 0 \quad (2.52)$$

The 2.52 applied to the 2.43 allows the subsequent rewriting of the 2.44, 2.45 and 2.46:

$$\boldsymbol{\sigma} = [ \sigma_{xx} \quad \sigma_{yy} \quad \sigma_{zz} ]^T \quad (2.53)$$

$$\mathbf{e} = [ e_{xx} \quad e_{yy} \quad e_{zz} ]^T \quad (2.54)$$

$$\mathbf{x} = \frac{E}{(1+\nu)(1-2\nu)} \begin{bmatrix} 1-\nu & \nu & 0 \\ \nu & 1-\nu & 0 \\ 0 & 0 & (1-2\nu)/2 \end{bmatrix} \quad (2.55)$$

Finally, the 2.40 becomes:

$$\begin{bmatrix} \sigma_{xx} \\ \sigma_{yy} \\ \sigma_{zz} \end{bmatrix} = \frac{E}{(1+\nu)(1-2\nu)} \begin{bmatrix} 1-\nu & \nu & 0 \\ \nu & 1-\nu & 0 \\ 0 & 0 & (1-2\nu)/2 \end{bmatrix} \begin{bmatrix} e_{xx} \\ e_{yy} \\ e_{zz} \end{bmatrix} \quad (2.56)$$

## 2.3 Transmission Line Theory Review: the Scattering Parameters

The analysis of an electrical network can be performed at different levels and in several ways. What is commonly done is to describe the entire network as a *black box*. A schematic example of a two ports black box is reported in Figure 2.8.

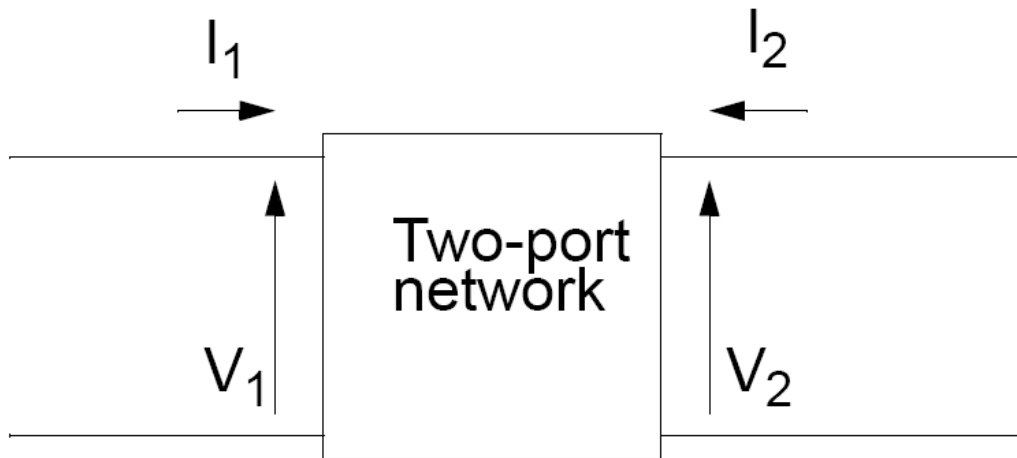


Figure 2.8: Two ports black box.  $V_1$  and  $I_1$  are the voltage and the current at the port 1, while  $V_2$  and  $I_2$  are the same magnitudes at the port 2.

A generic N-ports black box can be described in different fashions by a suitable set of parameters [28]. The most widely used sets are constituted by the Z-, Y- and H-parameters, which correspond to the impedance, admittance and hybrid matrices respectively [29]. These sets represent a valuable choice as long as the operating frequency of the circuit is relatively low (not higher than about 500 MHz). Indeed, several problems arise when moving to higher frequencies. First of all, the equipment is not readily available to measure total voltage and current at the network ports. Furthermore, it is difficult to achieve short and open circuits over a wide frequency range [30]. Because of these considerations an alternative analysis method for networks operating at high frequencies has to be employed. At high frequency it is much convenient to deal with *traveling waves* toward and from the network rather than refer to voltages

and currents. A magnitude and phase are associated to the traveling wave in a given direction. This leads to the definition of the Scattering Parameters (S-parameters). Let us consider the two port network of Figure 2.9.

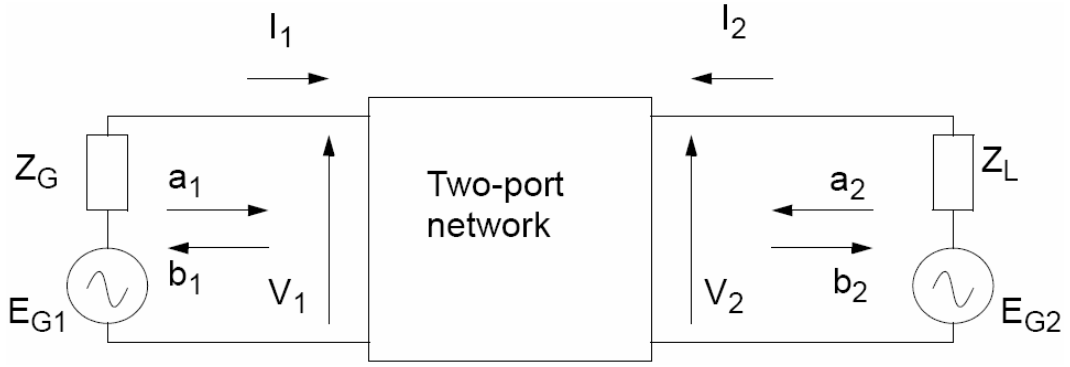


Figure 2.9: Two ports network also including the terminations at the two ports.

In previous Figure  $E_{G1}$  and  $E_{G2}$  are the power sources at the ports 1 and 2 while  $Z_G$  and  $Z_L$  are the load impedance at port 1 and 2 respectively. The  $a_1$ ,  $a_2$ ,  $b_1$  and  $b_2$  parameters definition will be derived soon. First of all the Y-parameter must be introduced:

$$\begin{bmatrix} I_1 \\ I_2 \end{bmatrix} = \begin{bmatrix} Y_{11} & Y_{12} \\ Y_{21} & Y_{22} \end{bmatrix} \begin{bmatrix} V_1 \\ V_2 \end{bmatrix} \quad (2.57)$$

where  $V$  and  $I$  are the total voltages and currents. Replacing  $V$  and  $I$  in terms of traveling voltage and current waves leads to:

$$V_1 = V_1^+ + V_1^- \quad (2.58)$$

$$V_2 = V_2^+ + V_2^- \quad (2.59)$$

$$I_1 = \frac{V_1^+ - V_1^-}{Z_0} \quad (2.60)$$

$$I_2 = \frac{V_2^+ - V_2^-}{Z_0} \quad (2.61)$$

with '+' indicating the ingoing wave, '-' the reflected wave and  $Z_0$  the characteristic impedance of the system.

Substituting the expressions 2.58 - 2.61 in the 2.57 yields:

$$V_1^- = f_{11}(Y, Z_0)V_1^+ + f_{12}(Y, Z_0)V_2^+ \quad (2.62)$$

$$V_2^- = f_{21}(Y, Z_0)V_1^+ + f_{22}(Y, Z_0)V_2^+ \quad (2.63)$$

with the  $f_{ij}$ 's to be functions of the Y-parameters. Let us now introduce the subsequent expressions:

$$s_{11} = f_{11}(Y, Z_0) \quad (2.64)$$

$$s_{12} = f_{12}(Y, Z_0) \quad (2.65)$$

$$s_{21} = f_{21}(Y, Z_0) \quad (2.66)$$

$$s_{22} = f_{22}(Y, Z_0) \quad (2.67)$$

and also the following expressions normalized with respect to  $\sqrt{Z_0}$ :

$$a_1 = \frac{V_1^+}{\sqrt{Z_0}} \quad (2.68)$$

$$a_2 = \frac{V_2^+}{\sqrt{Z_0}} \quad (2.69)$$

$$b_1 = \frac{V_1^-}{\sqrt{Z_0}} \quad (2.70)$$

$$b_2 = \frac{V_2^-}{\sqrt{Z_0}} \quad (2.71)$$

The  $a_1$  and  $a_2$  parameters must be interpreted as the fraction of the wave traveling toward the port 1 and 2 while  $b_1$  and  $b_2$  as the fraction of traveling wave reflected at the port 1 and 2 respectively.

The expressions from 2.64 to 2.71 replaced in the 2.62 and 2.63 lead to:

$$b_1 = s_{11}a_1 + s_{12}a_2 \quad (2.72)$$

$$b_2 = s_{21}a_1 + s_{22}a_2 \quad (2.73)$$

The  $s_{ij}$ 's parameters are defined as follows:

$s_{11}$  is the input reflection coefficient;

$s_{21}$  is the forward transmission coefficient;

$s_{22}$  is the output reflection coefficient;

$s_{12}$  is the reverse transmission coefficient.

The  $s_{ij}$ 's parameters, previously introduced in a generic form with the 2.64 - 2.67, are defined as follows:

$$s_{11} = \left. \frac{b_1}{a_1} \right|_{a_2=0} \quad (2.74)$$

$$s_{21} = \left. \frac{b_2}{a_1} \right|_{a_2=0} \quad (2.75)$$

$$s_{22} = \left. \frac{b_2}{a_2} \right|_{a_1=0} \quad (2.76)$$

$$s_{12} = \left. \frac{b_1}{a_2} \right|_{a_1=0} \quad (2.77)$$

Looking at Figure 2.10 the 2.74, for instance, must be interpreted as the reflected power over the power going through the port 1 when no power is traveling into port 2.



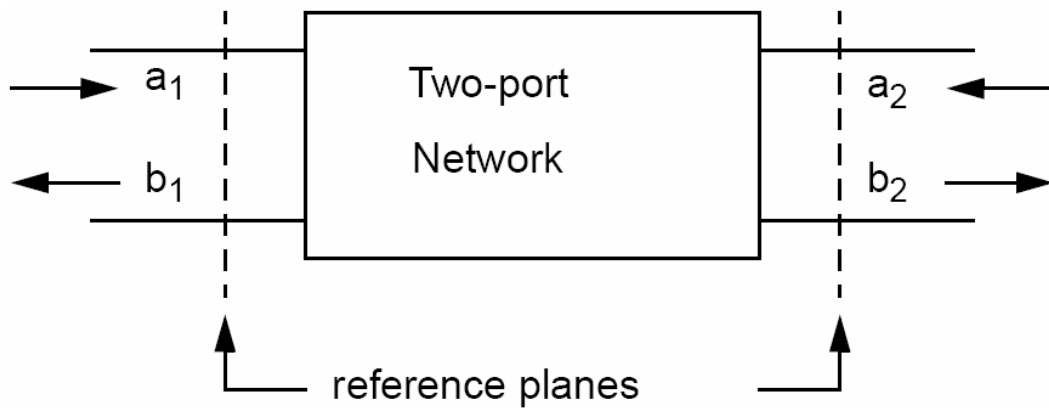


Figure 2.10: Two ports network with the reference planes at which the S-parameters are defined.

The 2.72 and 2.73 can be arranged in matrix form as follows:

$$\begin{bmatrix} b_1 \\ b_2 \end{bmatrix} = \begin{bmatrix} s_{11} & s_{12} \\ s_{21} & s_{22} \end{bmatrix} \begin{bmatrix} a_1 \\ a_2 \end{bmatrix} \quad (2.78)$$

Finally, the theory just presented was shown for the two ports particular case because this represents the one we are interested in. However, the approach can be generalized to the case of a network with N ports. In this case the S-parameter matrix in the 2.78 would have NxN dimensions.



## Chapter 3

# The Rigid Plate Electromechanical Transducer

The compact models included in the previously mentioned MEMS library are being introduced starting from this chapter. In particular, the electromechanical transduction operated by a suspended rigid plate over an electrode is presented. The mechanical model for the plate is discussed along with the implementation of the electrical effects when a biasing voltage between the plate itself and the lower electrode is applied.

First of all let us introduce the description of a rigid plate in a suitable reference system. In Figure 3.1 a rigid plate schematic is reported. The reference system origin is defined in its central point and it is assumed that the local reference system  $(x, y, z)$  and the global one  $(X, Y, Z)$  coincide. The plate dimensions are the width ( $W$ ), length ( $L$ ) and the thickness ( $T$ ) respectively along the  $x$ ,  $y$  and  $z$  axes. As in our case the plate thickness is much lower than the width and length ( $T \ll W, L$ ) it does not matter where the local reference system origin point is taken along  $T$ . We will assume it is the plate centre of mass under the hypothesis it is homogeneous. In other words, the origin is in the middle point of  $W$ ,  $L$  and  $T$ , as shown in Figure 3.2.

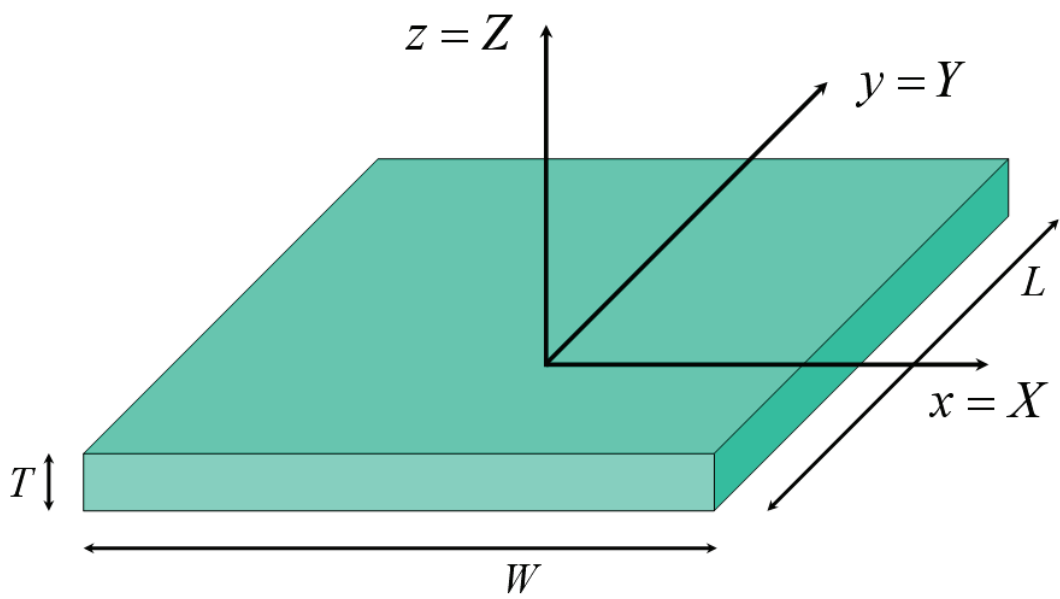


Figure 3.1: Rigid plate with the origin of the reference system defined in its central point.

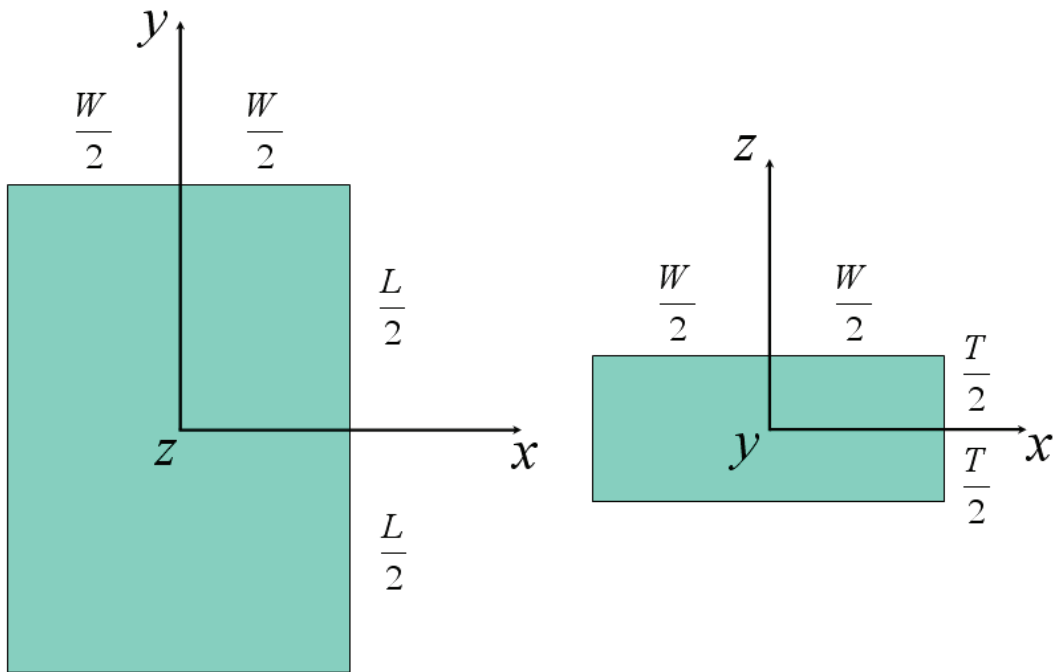


Figure 3.2: The local reference system origin is placed in the plate centre of mass.

The mechanical model of the rigid plate will be now described in details, firstly referring to a simplified model with 4 Degrees of Freedom (DoF's) and subsequently introducing the complete 6 DoF's mechanical model.

### 3.1 Mechanical Model of the Rigid Plate with 4 Degrees of Freedom (DoF's)

First of all the choice of a simplified 4 DoF's model must be introduced and motivated. These are three translational DoF's and one rotational DoF. This means that the plate can translate along the three coordinated axes ( $x, y, z$ ) and can rotate around its vertical axis ( $z$ ). The 4 DoF's plate does not represent just a simple example to explain the chosen approach in its implementation. Indeed, a very common realization of a MEMS switch or varactor is based on a rigid plate suspended above the electrode by means of four flexible beams connected to its four corners and anchored on the other ends. In this case, it can be reasonably assumed that when a biasing voltage is applied between the plate and the electrode, the first one will move downward by keeping a parallel position with respect to the underneath electrode. Therefore, no rotations of the plate will occur around the  $x$  and  $y$  axes and consequently the 4 DoF's model is appropriate at least for a first stage analysis of the entire topology.

The chosen approach to define the mechanical behaviour of the plate is rather simple. Since it is a rigid body the theory of elasticity introduced in the previous chapter is not appropriate to describe it. On the other hand, the main physical effect is the inertia of the body, expressed by the well known formula:

$$F = MA \tag{3.1}$$

where  $F$  is the force applied to the body,  $M$  its mass and  $A$  its acceleration. Thus, the main issue that must be solved is how to compose the set of external forces and torques applied to the plate within this, in order to define their resultants. Let us assume that the only points in which external stimuli can be applied to the plate are its four vertexes (nodes). Looking at Figure 3.3, starting from the top right vertex and proceeding clockwise we will address them as  $NE$  (North-East),  $SE$  (South-East),  $SW$  (South-West) and  $NW$  (North-West). All the external forces and torques will be then referred to

the centre of mass, addressed as  $CM$  point in Figure 3.3 and already defined as the middle point of  $W$ ,  $L$  and  $T$  in Figure 3.2. Consequently, the forces applied to each node have to be decomposed in their contributions along the  $X$  and  $Y$  directions. Finally, the arms of each node with respect to the centre on the  $XY$  plane must be derived to transform the applied force into the corresponding torques in the centre of mass. It is important to notice that the forces components and arms are referred to the global system  $(X, Y, Z)$ . Indeed, as pointed out in the previous chapter (Section 2.1), the consistency in describing different components joined together is maintained when a common reference system for all of them is chosen.

Let us now imagine the plate rotated of a generic angle  $\theta_z$  around the vertical  $Z$  axis like it is shown in Figure 3.4. We will define later the contributions determining the angle  $\theta_z$ . Let us now assume that a force  $F_{SE}$  on the  $XY$  plane is applied at the  $SE$  node. Its two components along the  $X$  and  $Y$  directions are  $F_{X_{SE}}$  and  $F_{Y_{SE}}$  respectively. First of all the part of the force components applied along the  $X$  and  $Y$  axes involved in the torque calculation around the  $Z$  axis must be determined. In other words, a relation between the forces applied in the  $SE$  node and the forces applied in the centre of mass  $CM$  has to be defined.

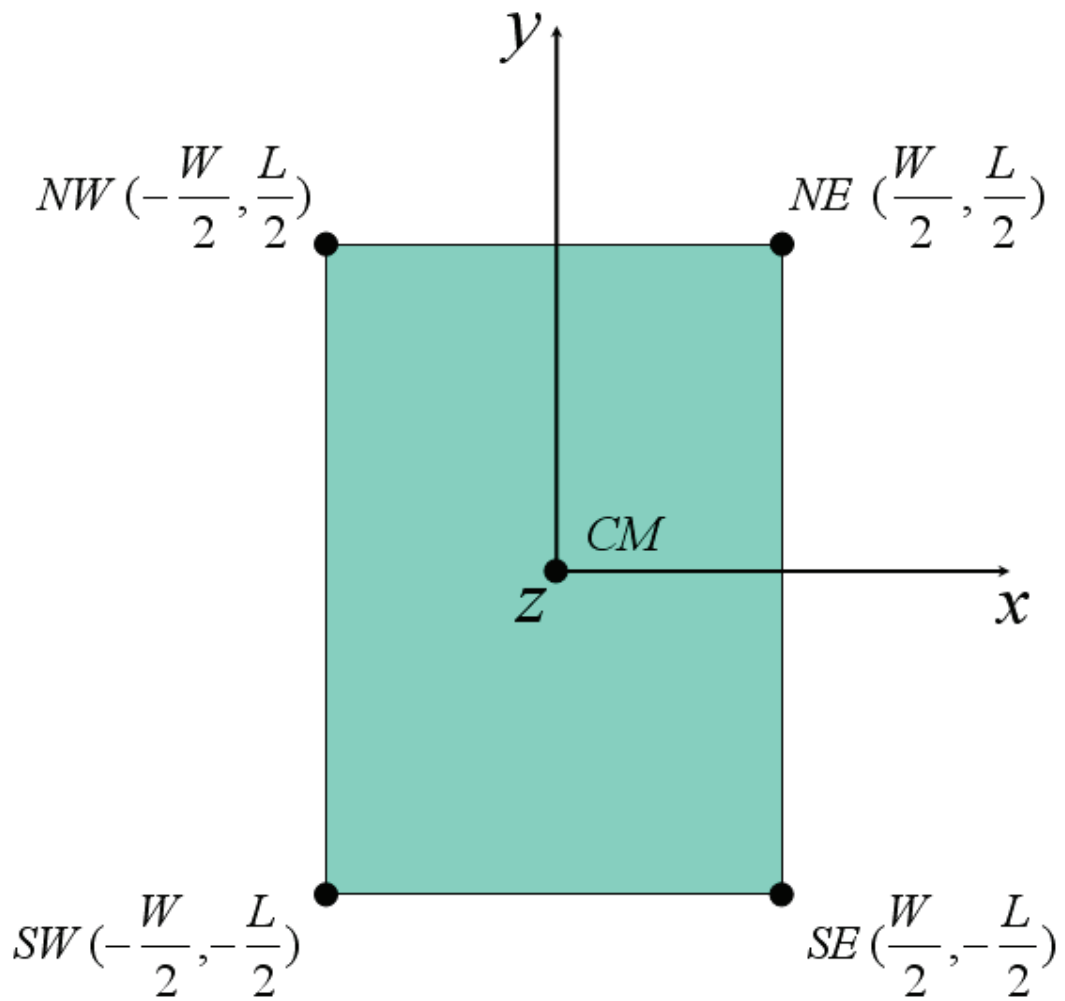


Figure 3.3: The four plate vertexes with their coordinates in the local reference system.



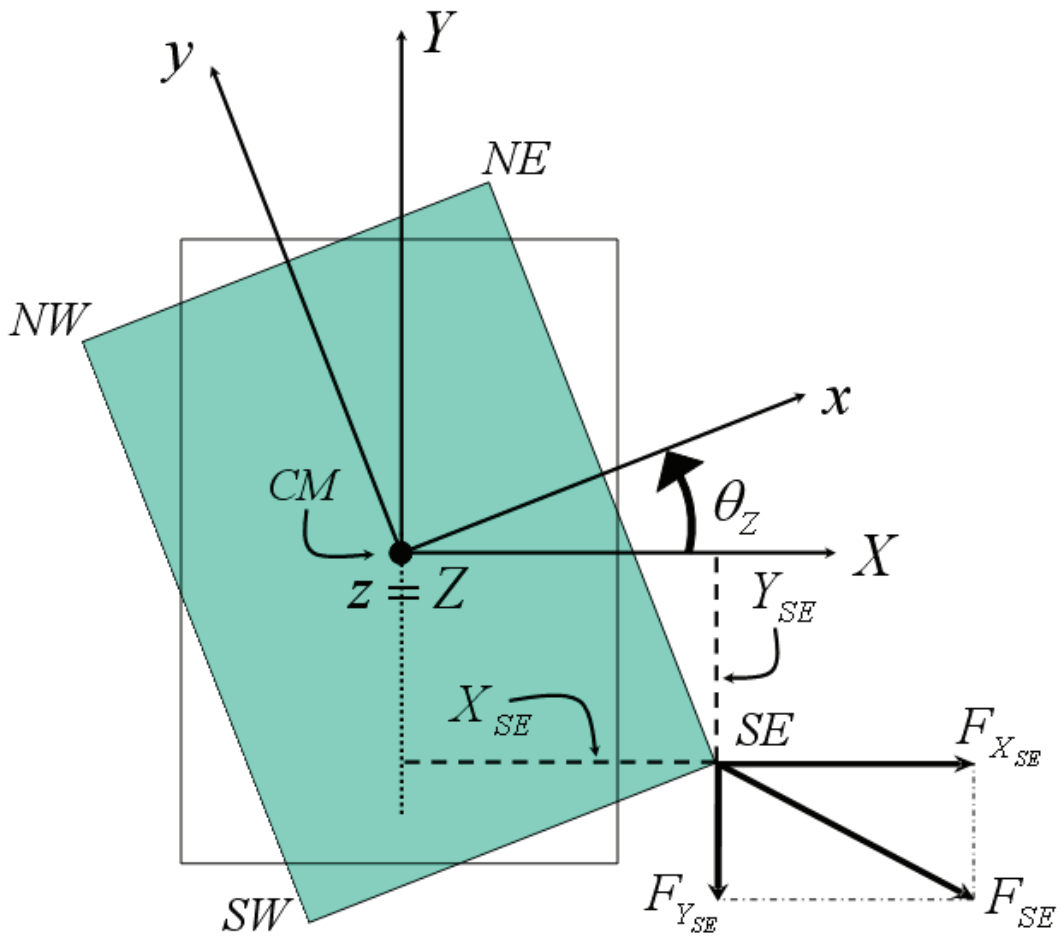


Figure 3.4: Plate after a rotation  $\theta_z$  around the  $Z$  axis. A force is applied to the bottom-right ( $SE$ ) corner.

Taking into account the inertia effects expressed by the 3.1 and applied to the centre of mass  $CM$ , the previously mentioned relations are defined as follow:

$$F_{\Delta X_{SE}} = F_{X_{SE}} - F_{X_{CM}} \quad (3.2)$$

$$F_{\Delta Y_{SE}} = F_{Y_{SE}} - F_{Y_{CM}} \quad (3.3)$$

where  $F_{\Delta X_{SE}}$  and  $F_{\Delta Y_{SE}}$  are the effective forces applied to the  $SE$  node along the  $X$  and  $Y$  direction respectively. These take into account the inertia effect applied to the centre of mass and defined as  $F_{X_{CM}}$  and  $F_{Y_{CM}}$  in the 3.2 and 3.3. Their expression is following:

$$F_{X_{CM}} = -M \frac{d}{dt^2}(P_{X_{CM}}) = -MA_{X_{CM}} \quad (3.4)$$

$$F_{Y_{CM}} = -M \frac{d}{dt^2}(P_{Y_{CM}}) = -MA_{Y_{CM}} \quad (3.5)$$

where  $M$  is the mass of the plate (assuming it made of an homogeneous material) while  $P_{X_{CM}}$  and  $P_{Y_{CM}}$  is the position of the centre of mass  $CM$  along the  $X$  and  $Y$  direction respectively. Their double time derivative leads to the acceleration expressed by  $A_{X_{CM}}$  and  $A_{Y_{CM}}$  in the 3.4 and 3.5. It must be noticed that the second members of these two equations have the minus sign. Indeed, according to the Third Principle of Dynamic the inertia of a body, stimulated with a certain external applied force, tends to counteract the stimulus itself [31]. Finally, as the contribution along the  $Y$  direction of the external force applied to the  $SE$  node is oriented in the negative direction of the axis (see Figure 3.4), the actual expression of the 3.3 is:

$$F_{\Delta Y_{SE}} = -F_{Y_{SE}} - F_{Y_{CM}} \quad (3.6)$$

Now that the relations of the external forces applied to the node and the internal ones related to the centre of mass have been defined let us focus on Figure 3.4 once again. The two segments addressed as  $X_{SE}$  and  $Y_{SE}$  are the projections of the  $SE$  corner in the global reference system  $(X, Y, Z)$  and these depend on the coordinates of the  $SE$  point in the local frame  $(x, y, z)$  and on the angle  $\theta_z$ . These can be very easily determined by using the equation 2.3. Indeed, being the coordinates of the  $SE$  corner equal to  $W/2$  and  $-L/2$  along the  $x$  and  $y$  axes respectively, it is:

$$X_{SE} = \left(\frac{W}{2}\right) \cos \theta_Z + \left(\frac{L}{2}\right) \sin \theta_Z \quad (3.7)$$

$$Y_{SE} = \left(\frac{W}{2}\right) \sin \theta_Z - \left(\frac{L}{2}\right) \cos \theta_Z \quad (3.8)$$

Once the two arms  $X_{SE}$  and  $Y_{SE}$  have been determined, the contributions to the  $Z$  axis torque of the centre of mass due to the external forces applied to the  $SE$  corner are calculated as follows:

$$T_{\theta_{ZCM}} = |Y_{SE}| F_{\Delta X_{SE}} - |X_{SE}| F_{\Delta Y_{SE}} \quad (3.9)$$

In the 3.9  $T_{\theta_{ZCM}}$  represents the  $Z$  axis torque. Moreover, the absolute value of the arms  $X_{SE}$  and  $Y_{SE}$  is taken into account as being projections of a generic point, they can assume negative value. However, in previous equation these are exploited as arms (i.e. segments) in the torque calculation. Consequently, they must always have positive sign. On the other hand, the force components define the sign of each term in the second member of 3.9. According to the right hand rule, when the product of the force by the arm induces an anticlockwise rotation around the  $Z$  axis, its contribution to the torque is positive. This is the case of the first term in the second member of equation 3.9. Differently, as the force applied to the  $SE$  node along the  $Y$  axis is oriented along its negative direction, this brings to a clockwise rotation of the  $Z$  axis. This explains the minus sign of the second term in the second member of previous equation. Equation 3.9 must now be completed by including the momentum of inertia of the plate itself. In this case its form is:

$$T_{\theta_{ZCM}} = -I_Z \frac{d\theta_Z}{dt^2} + |Y_{SE}| F_{\Delta X_{SE}} - |X_{SE}| F_{\Delta Y_{SE}} \quad (3.10)$$

where  $I_Z$  is the momentum of inertia of the plate with respect to the  $Z$  axis expressed as follows [31]:

$$I_Z = \frac{1}{12} M(L^2 + W^2) \quad (3.11)$$

In the 3.11 the inertia momentum is multiplied by the double derivative of  $\theta_Z$  with respect of time. This represents the angular acceleration of the plate around its vertical axis. Furthermore, the sign of the first term in second member of the 3.10 is negative because the Third Principle of Dynamic already mentioned referring to equations 3.4 and 3.5, is also valid when dealing with

the momentum of inertia. Focusing now on the angle  $\theta_Z$ , we must define its contributions. It is defined by two terms:

$$\theta_Z = \theta_{Z_{INIT}} + \theta_{Z_{INST}} \quad (3.12)$$

where  $\theta_{Z_{INIT}}$  is the initial rotation of the plate around the  $Z$  axis as a configuration in which the plate is already not aligned to the global frame  $(X, Y, Z)$  before applying any external stimuli might occur. Whereas,  $\theta_{Z_{INST}}$  is the instantaneous rotation of the  $CM$  around the  $Z$  axis. This depends on all the forces and torques applied to the four plate vertexes (nodes). Before proceeding with further explanations concerning the plate mechanical nodes, it is important to stress an important aspect. As the rigid plate allows translations along the three coordinated axes, the origin of its local frame  $(x, y, z)$  will not be superposed anymore with the origin of the global system  $(X, Y, Z)$ . It does not matter at all since we are interested in the relative displacements of each element as a consequence of the applied stimuli and boundary conditions and not to the absolute position of each device. On the other hand, it is critical to maintain a consistent description of all the magnitudes along the three axes that must be the same for all the devices. This is the reason why the global frame  $X, Y, Z$  is adopted and why all the forces and displacements are referred to it. These considerations are valid for all the structures described in the next chapters as well.

Let us now extend what discussed thus far to the most generic case in which forces with three components along the  $X$ ,  $Y$  and  $Z$  axes as well as torques around the  $Z$  axis are applied to all the four vertexes  $NE$ ,  $SE$ ,  $SW$  and  $NW$  like depicted in Figure 3.5. We have now to rewrite the previous equations in order to include all these stimuli. Starting from the relations among the forces applied to the four nodes and the internal forces related to the centre of mass the 3.2 and 3.3 must be integrated with other expressions as follows:

$$F_{\Delta X_{NE}} = F_{X_{NE}} - F_{X_{CM}} \quad (3.13)$$

$$F_{\Delta Y_{NE}} = F_{Y_{NE}} - F_{Y_{CM}} \quad (3.14)$$

$$F_{\Delta Z_{NE}} = F_{Z_{NE}} - F_{Z_{CM}} \quad (3.15)$$

$$F_{\Delta X_{SE}} = F_{X_{SE}} - F_{X_{CM}} \quad (3.16)$$

$$F_{\Delta Y_{SE}} = F_{Y_{SE}} - F_{Y_{CM}} \quad (3.17)$$

$$F_{\Delta Z_{SE}} = F_{Z_{SE}} - F_{Z_{CM}} \quad (3.18)$$

$$F_{\Delta X_{SW}} = F_{X_{SW}} - F_{X_{CM}} \quad (3.19)$$

$$F_{\Delta Y_{SW}} = F_{Y_{SW}} - F_{Y_{CM}} \quad (3.20)$$

$$F_{\Delta Z_{SW}} = F_{Z_{SW}} - F_{Z_{CM}} \quad (3.21)$$

$$F_{\Delta X_{NW}} = F_{X_{NW}} - F_{X_{CM}} \quad (3.22)$$

$$F_{\Delta Y_{NW}} = F_{Y_{NW}} - F_{Y_{CM}} \quad (3.23)$$

$$F_{\Delta Z_{NW}} = F_{Z_{NW}} - F_{Z_{CM}} \quad (3.24)$$

where  $F_{X_{CM}}$  and  $F_{Y_{CM}}$  are expressed by the 3.4 and 3.5, while  $F_{Z_{CM}}$  follows:

$$F_{Z_{CM}} = -M \frac{d}{dt^2}(P_{Z_{CM}}) = -MA_{Z_{CM}} \quad (3.25)$$

In previous equation  $P_{Z_{CM}}$  is the position of  $CM$  along the  $Z$  direction. Now, a set of similar equations has to be introduced concerning the inertia momentum around the  $Z$  axis. These are expressed as follows:

$$T_{\Delta \theta_{Z_{NE}}} = T_{\theta_{Z_{NE}}} - T_{\theta_{Z_{CM}}} \quad (3.26)$$

$$T_{\Delta \theta_{Z_{SE}}} = T_{\theta_{Z_{SE}}} - T_{\theta_{Z_{CM}}} \quad (3.27)$$

$$T_{\Delta \theta_{Z_{SW}}} = T_{\theta_{Z_{SW}}} - T_{\theta_{Z_{CM}}} \quad (3.28)$$

$$T_{\Delta \theta_{Z_{NW}}} = T_{\theta_{Z_{NW}}} - T_{\theta_{Z_{CM}}} \quad (3.29)$$

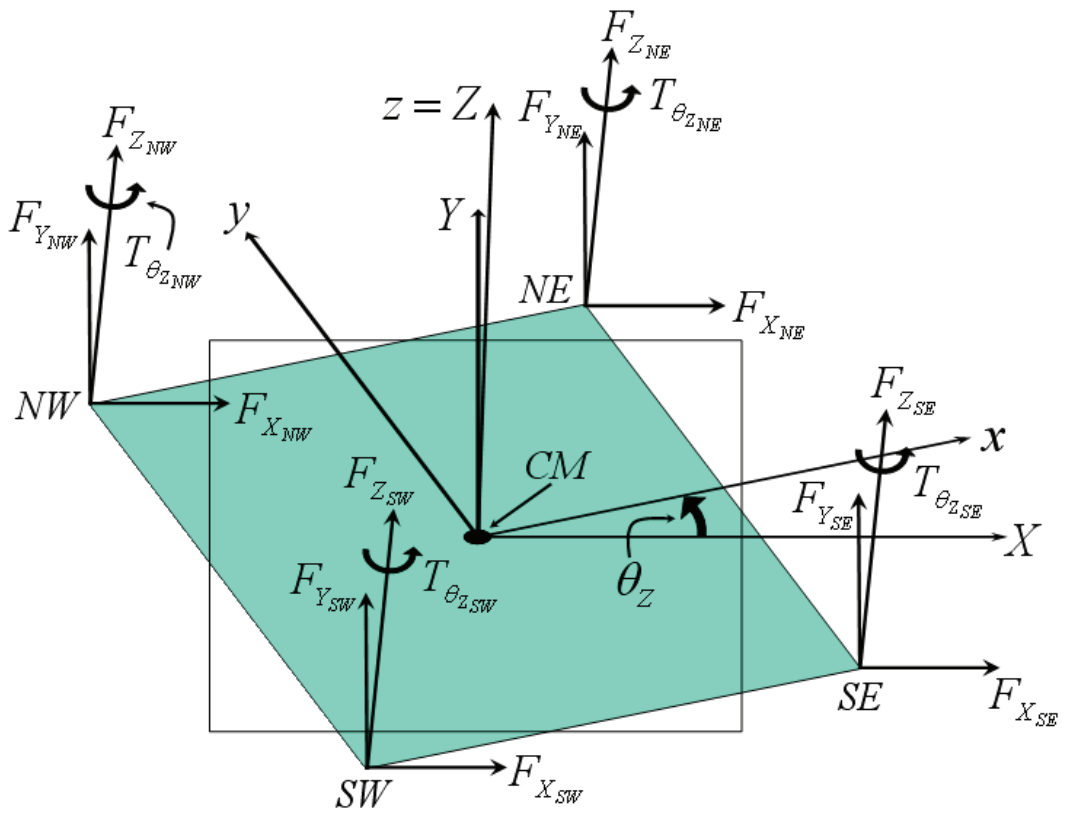


Figure 3.5: Rigid plate with all the forces and torques applied to the four vertices.

where  $T_{\theta_{Z_{NE}}}$ ,  $T_{\theta_{Z_{SE}}}$ ,  $T_{\theta_{Z_{SW}}}$  and  $T_{\theta_{Z_{NW}}}$  are the external torques applied to the North-East, South-East, South-West and North-West nodes respectively. Whereas,  $T_{\theta_{Z_{CM}}}$  corresponds to the equation 3.10. In this case its expression is:

$$\begin{aligned}
T_{\theta_{Z_{CM}}} = -I_Z \frac{d\theta_Z}{dt^2} & - \operatorname{sgn}(Y_{NE}) | Y_{NE} | F_{\Delta X_{NE}} \\
& + \operatorname{sgn}(X_{NE}) | X_{NE} | F_{\Delta Y_{NE}} \\
& - \operatorname{sgn}(Y_{SE}) | Y_{SE} | F_{\Delta X_{SE}} \\
& + \operatorname{sgn}(X_{SE}) | X_{SE} | F_{\Delta Y_{SE}} \\
& - \operatorname{sgn}(Y_{SW}) | Y_{SW} | F_{\Delta X_{SW}} \\
& + \operatorname{sgn}(X_{SW}) | X_{SW} | F_{\Delta Y_{SW}} \\
& - \operatorname{sgn}(Y_{NW}) | Y_{NW} | F_{\Delta X_{NW}} \\
& + \operatorname{sgn}(X_{NW}) | X_{NW} | F_{\Delta Y_{NW}} \quad (3.30)
\end{aligned}$$

where  $X_{NE}$ ,  $Y_{NE}$ ,  $X_{SW}$ ,  $Y_{SW}$ ,  $X_{NW}$  and  $Y_{NW}$  are the arms along the  $X$  and  $Y$  axes for the nodes  $NE$ ,  $SW$  and  $NW$  respectively, calculated with the same approach exploited to obtain the 3.7 and 3.8. The signs of the eight terms related to the forces applied on the  $XY$  plane in previous equation 3.30 are determined with the right hand rule already mentioned for equation 3.9.

To complete the mechanical model of the rigid plate with 4 DoF's we have now to define the relative displacement of each node with respect to the centre of mass  $CM$  in the global frame. The relative displacement of a generic point  $P$  in an arbitrary instant is defined as the difference between its instantaneous position  $P_{INST}$  and initial position  $P_{INIT}$ :

$$\Delta P = P_{INST} - P_{INIT} \quad (3.31)$$

As mentioned before, the angle  $\theta_Z$  is composed by two contributions: one is the initial rotation of the plate  $\theta_{Z_{INIT}}$  and the second is the instantaneous rotation  $\theta_{Z_{INST}}$  (see equation 3.12). Consequently, when the angle  $\theta_{Z_{INIT}}$  has a non-zero value, we have to calculate the position of each node in the global frame and consider this as initial position.

Referring to the  $NE$  vertex and using once again the 2.3, the initial abscissas along the  $X$  and  $Y$  directions are:

$$X_{NE_{INIT}} = \left(\frac{W}{2}\right) \cos \theta_{Z_{INIT}} - \left(\frac{L}{2}\right) \sin \theta_{Z_{INIT}} \quad (3.32)$$

$$Y_{NE_{INIT}} = \left(\frac{W}{2}\right) \sin \theta_{Z_{INIT}} + \left(\frac{L}{2}\right) \cos \theta_{Z_{INIT}} \quad (3.33)$$

Whereas, the instantaneous position of the  $NE$  node is given by:

$$X_{NE_{INST}} = \left(\frac{W}{2}\right) \cos \theta_Z - \left(\frac{L}{2}\right) \sin \theta_Z \quad (3.34)$$

$$Y_{NE_{INST}} = \left(\frac{W}{2}\right) \sin \theta_Z + \left(\frac{L}{2}\right) \cos \theta_Z \quad (3.35)$$

where  $\theta_Z$  is expressed by the 3.12. Finally, the relative displacement of the node  $NE$  with respect to the centre of mass  $CM$  generally expressed by equation 3.31 becomes:

$$\Delta X_{NE} = X_{NE_{INIT}} - X_{NE_{INST}} \quad (3.36)$$

$$\Delta Y_{NE} = Y_{NE_{INIT}} - Y_{NE_{INST}} \quad (3.37)$$

Following the same approach, the proper sets of equations that define the relative displacements along the  $XY$  plane for the nodes  $SE$ ,  $SW$  and  $NW$  can be effortlessly derived. Since this simplified model does not allow any rotation of the plate around the  $X$  and  $Y$  axes (4 DoF's) relative displacement of each node with respect to the centre of mass must never occur. To ensure this condition the subsequent constraints must be imposed:

$$\Delta Z_{NE} = 0 \quad (3.38)$$

$$\Delta Z_{SE} = 0 \quad (3.39)$$

$$\Delta Z_{SW} = 0 \quad (3.40)$$

$$\Delta Z_{NW} = 0 \quad (3.41)$$



Eventually, another condition must be introduced to complete the definition of the plate as rigid body. This is that no relative rotations must ever occur among each node and the *CM*. This results in the following conditions:

$$\theta_{Z_{NE}} - \theta_{Z_{CM}} = 0 \quad (3.42)$$

$$\theta_{Z_{SE}} - \theta_{Z_{CM}} = 0 \quad (3.43)$$

$$\theta_{Z_{SW}} - \theta_{Z_{CM}} = 0 \quad (3.44)$$

$$\theta_{Z_{NW}} - \theta_{Z_{CM}} = 0 \quad (3.45)$$

This completes the 4 DoF's mechanical model for the rigid plate. All the formulas presented so far can be easily implemented in VerilogA<sup>©</sup>.

## 3.2 Extension of the Rigid Plate Mechanical Model to 6 Degrees of Freedom (DoF's)

Extending the 4 DoF's rigid plate model discussed in previous section to the complete one including 6 DoF's for each node is rather simple. Indeed, the approach is the same already introduced. All we have to do is to extend the equations of previous section in order to take into account rotations around the *X* and *Y* axes at each node. Figure 3.6 shows a rigid plate with three translational and three rotational stimuli (forces and torques respectively) applied to all its four nodes. Starting from the relations among the external translational forces at the four nodes and the internal forces on the centre of mass the equations 3.13 - 3.15 and 3.16 - 3.24 are still valid. Whereas, concerning the 3.26 - 3.29, these must be extended as follows:

$$T_{\Delta\theta_{X_{NE}}} = T_{\theta_{X_{NE}}} - T_{\theta_{X_{CM}}} \quad (3.46)$$

$$T_{\Delta\theta_{Y_{NE}}} = T_{\theta_{Y_{NE}}} - T_{\theta_{Y_{CM}}} \quad (3.47)$$

$$T_{\Delta\theta_{Z_{NE}}} = T_{\theta_{Z_{NE}}} - T_{\theta_{Z_{CM}}} \quad (3.48)$$

$$T_{\Delta\theta_{XSE}} = T_{\theta_{XSE}} - T_{\theta_{XCM}} \quad (3.49)$$

$$T_{\Delta\theta_{YSE}} = T_{\theta_{YSE}} - T_{\theta_{YCM}} \quad (3.50)$$

$$T_{\Delta\theta_{ZSE}} = T_{\theta_{ZSE}} - T_{\theta_{ZCM}} \quad (3.51)$$

$$T_{\Delta\theta_{XSW}} = T_{\theta_{XSW}} - T_{\theta_{XCM}} \quad (3.52)$$

$$T_{\Delta\theta_{YSW}} = T_{\theta_{YSW}} - T_{\theta_{YCM}} \quad (3.53)$$

$$T_{\Delta\theta_{ZSW}} = T_{\theta_{ZSW}} - T_{\theta_{ZCM}} \quad (3.54)$$

$$T_{\Delta\theta_{XNW}} = T_{\theta_{XNW}} - T_{\theta_{XCM}} \quad (3.55)$$

$$T_{\Delta\theta_{YNW}} = T_{\theta_{YNW}} - T_{\theta_{YCM}} \quad (3.56)$$

$$T_{\Delta\theta_{ZNW}} = T_{\theta_{ZNW}} - T_{\theta_{ZCM}} \quad (3.57)$$

where  $T_{\theta_{YCM}}$  and  $T_{\theta_{YCM}}$  are the torques in the centre of mass around the  $X$  and  $Y$  axes respectively. Let us now extend the arms definition taking into account out of  $XY$  plane displacements of the nodes. We basically have three segments which identify each node in the global frame  $(X, Y, Z)$  like already shown in Figure 2.5. Taking for instance the  $NE$  vertex and considering its local abscissa along  $z$  axis equal to zero, like already discussed in Figure 3.2, its local coordinates are:

$$NE(x, y, z) = \left(\frac{W}{2}, \frac{L}{2}, 0\right) \quad (3.58)$$

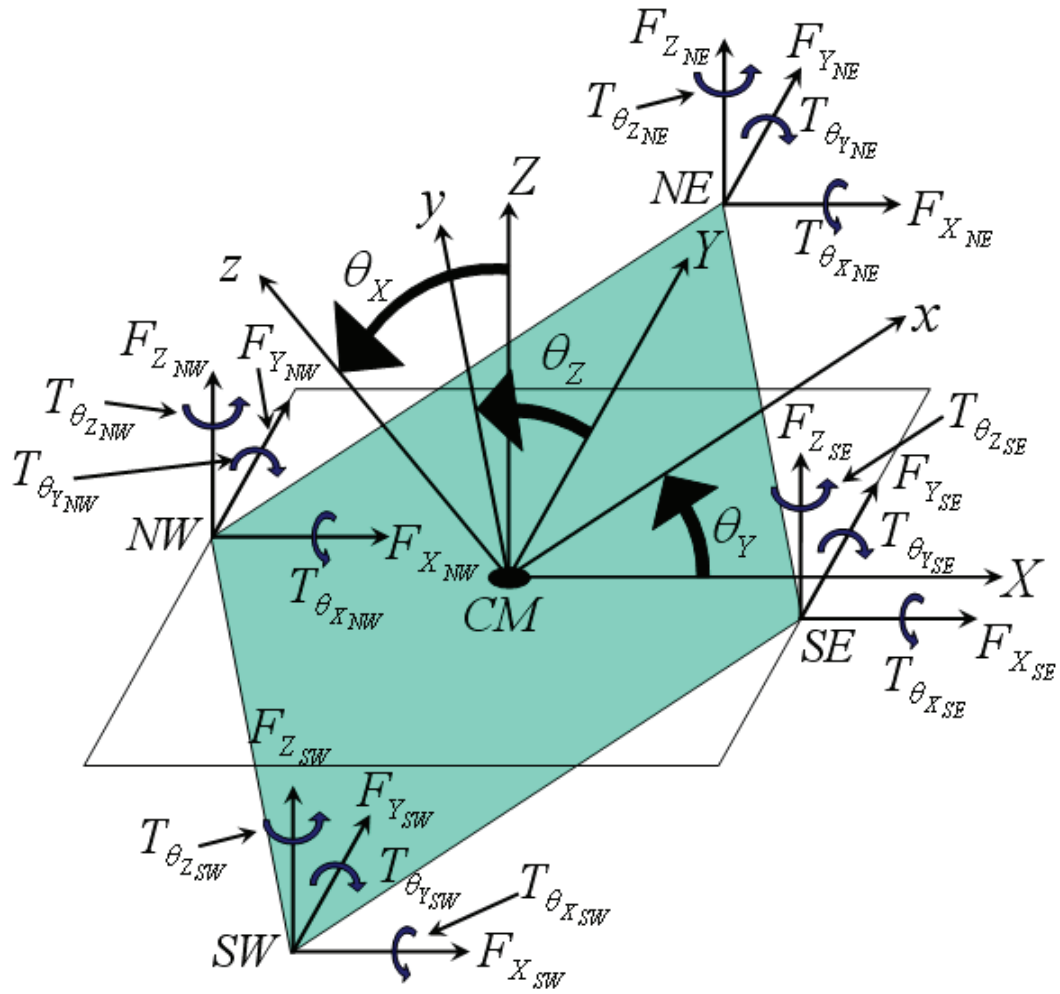


Figure 3.6: Rigid plate (6 DoF's) with all the forces and torques applied to the four vertexes.

In order to derive the three arms  $X_{NE}$ ,  $Y_{NE}$  and  $Z_{NE}$  we have to exploit the complete rotation matrix of equation 2.8. With the same notation of 2.9 - 2.14 it is:

$$X_{NE} = (C_Y C_Z) \frac{W}{2} + (-C_X S_Z + S_X S_Y C_Z) \frac{L}{2} \quad (3.59)$$

$$Y_{NE} = (C_Y S_Z) \frac{W}{2} + (C_X C_Z + S_X S_Y S_Z) \frac{L}{2} \quad (3.60)$$

$$Z_{NE} = -S_Y \frac{W}{2} + (S_X C_Y) \frac{L}{2} \quad (3.61)$$

Following the same approach and substituting in the 3.59 - 3.61 the proper coordinates of the other three nodes all the arms are easily obtained:

$(X_{SE}, Y_{SE}, Z_{SE})$ ,  $(X_{SW}, Y_{SW}, Z_{SW})$  and  $(X_{NW}, Y_{NW}, Z_{NW})$ . Once all the arms are available, the equations for the torque of the centre of mass around the  $X$  and  $Y$  axes ( $T_{\theta_{X_{CM}}}$ ,  $T_{\theta_{Y_{CM}}}$ ) can be written. These complete the 3.30 which is still valid for the 6 DoF's model and their expression is following:

$$\begin{aligned} T_{\theta_{X_{CM}}} = -I_X \frac{d\theta_X}{dt^2} & - \operatorname{sgn}(Z_{NE}) | Z_{NE} | F_{\Delta Y_{NE}} \\ & + \operatorname{sgn}(Y_{NE}) | Y_{NE} | F_{\Delta Z_{NE}} \\ & - \operatorname{sgn}(Z_{SE}) | Z_{SE} | F_{\Delta Y_{SE}} \\ & + \operatorname{sgn}(Y_{SE}) | Y_{SE} | F_{\Delta Z_{SE}} \\ & - \operatorname{sgn}(Z_{SW}) | Z_{SW} | F_{\Delta Y_{SW}} \\ & + \operatorname{sgn}(Y_{SW}) | Y_{SW} | F_{\Delta Z_{SW}} \\ & - \operatorname{sgn}(Z_{NW}) | Z_{NW} | F_{\Delta Y_{NW}} \\ & + \operatorname{sgn}(Y_{NW}) | Y_{NW} | F_{\Delta Z_{NW}} \end{aligned} \quad (3.62)$$

$$\begin{aligned}
T_{\theta_{Y_{CM}}} = -I_Y \frac{d\theta_Y}{dt^2} &+ \operatorname{sgn}(Z_{NE}) | Z_{NE} | F_{\Delta X_{NE}} \\
&- \operatorname{sgn}(X_{NE}) | X_{NE} | F_{\Delta Z_{NE}} \\
&+ \operatorname{sgn}(Z_{SE}) | Z_{SE} | F_{\Delta X_{SE}} \\
&- \operatorname{sgn}(X_{SE}) | X_{SE} | F_{\Delta Z_{SE}} \\
&+ \operatorname{sgn}(Z_{SW}) | Z_{SW} | F_{\Delta X_{SW}} \\
&- \operatorname{sgn}(X_{SW}) | X_{SW} | F_{\Delta Z_{SW}} \\
&+ \operatorname{sgn}(Z_{NW}) | Z_{NW} | F_{\Delta X_{NW}} \\
&- \operatorname{sgn}(X_{NW}) | X_{NW} | F_{\Delta Z_{NW}}
\end{aligned} \tag{3.63}$$

where  $I_X$  and  $I_Y$  are the plate momentum of inertia around the  $X$  and  $Y$  axis which have the following expression:

$$I_X = \frac{1}{12} M(L^2 + T^2) \tag{3.64}$$

$$I_Y = \frac{1}{12} M(W^2 + T^2) \tag{3.65}$$

In equations 3.62 and 3.63,  $I_X$  and  $I_Y$  are multiplied by the angular acceleration of the centre of mass around the  $X$  and  $Y$  axes respectively. The further step is the calculation of the relative displacements of each node with respect to the centre of mass  $CM$ . As reported in the 3.12 for  $\theta_Z$ , the angles  $\theta_X$  and  $\theta_Y$  include an initial and instantaneous contributions as well:

$$\theta_X = \theta_{X_{INIT}} + \theta_{X_{INST}} \tag{3.66}$$

$$\theta_Y = \theta_{Y_{INIT}} + \theta_{Y_{INST}} \tag{3.67}$$

Equation 3.31 is applied also in this case and the instantaneous and initial positions of each node depend on the three rotation angles. The relations are similar to the 3.59 - 3.61 and taking as example the North-East node the initial position along the three coordinated axes ( $X, Y, Z$ ) are given by:

$$\begin{aligned}
X_{NE_{INIT}} &= (C_{Y_{INIT}} C_{Z_{INIT}}) \frac{W}{2} \\
&+ (-C_{Z_{INIT}} S_{Z_{INIT}} + S_{X_{INIT}} S_{Y_{INIT}} C_{Z_{INIT}}) \frac{L}{2}
\end{aligned} \tag{3.68}$$

$$\begin{aligned}
Y_{NE_{INIT}} &= (C_{Y_{INIT}} S_{Z_{INIT}}) \frac{W}{2} \\
&+ (C_{X_{INIT}} C_{Z_{INIT}} + S_{X_{INIT}} S_{Y_{INIT}} S_{Z_{INIT}}) \frac{L}{2} \quad (3.69)
\end{aligned}$$

$$Z_{NE_{INIT}} = -S_{Y_{INIT}} \frac{W}{2} + (S_{X_{INIT}} C_{Y_{INIT}}) \frac{L}{2} \quad (3.70)$$

Whereas, the instantaneous position of the  $NE$  node is given by:

$$\begin{aligned}
X_{NE_{INST}} &= (C_{Y_{INST}} C_{Z_{INST}}) \frac{W}{2} \\
&+ (-C_{Z_{INST}} S_{Z_{INST}} + S_{X_{INST}} S_{Y_{INST}} C_{Z_{INST}}) \frac{L}{2} \quad (3.71)
\end{aligned}$$

$$\begin{aligned}
Y_{NE_{INST}} &= (C_{Y_{INST}} S_{Z_{INST}}) \frac{W}{2} \\
&+ (C_{X_{INST}} C_{Z_{INST}} + S_{X_{INST}} S_{Y_{INST}} S_{Z_{INST}}) \frac{L}{2} \quad (3.72)
\end{aligned}$$

$$Z_{NE_{INST}} = -S_{Y_{INST}} \frac{W}{2} + (S_{X_{INST}} C_{Y_{INST}}) \frac{L}{2} \quad (3.73)$$

Finally, the relative displacements of the node  $NE$  with respect to the centre of mass are expressed as:

$$\Delta X_{NE} = X_{NE_{INIT}} - X_{NE_{INST}} \quad (3.74)$$

$$\Delta Y_{NE} = Y_{NE_{INIT}} - Y_{NE_{INST}} \quad (3.75)$$

$$\Delta Z_{NE} = Z_{NE_{INIT}} - Z_{NE_{INST}} \quad (3.76)$$

By applying the same procedure the relative displacements of the other three nodes are derived.

In the case of 6 DoF's the conditions expressed by the 3.38 - 3.41 must not be imposed as each node of the plate is free to have a different abscissa along  $Z$  due to the rotations  $\theta_X$  and  $\theta_Y$ . Whereas, to ensure the 6 DoF's plate behaves as a rigid body the 3.42 - 3.45 have to be extended as follows:

$$\theta_{X_{NE}} - \theta_{X_{CM}} = 0 \quad (3.77)$$

$$\theta_{Y_{NE}} - \theta_{Y_{CM}} = 0 \quad (3.78)$$

$$\theta_{Z_{NE}} - \theta_{Z_{CM}} = 0 \quad (3.79)$$

$$\theta_{X_{SE}} - \theta_{X_{CM}} = 0 \quad (3.80)$$

$$\theta_{Y_{SE}} - \theta_{Y_{CM}} = 0 \quad (3.81)$$

$$\theta_{Z_{SE}} - \theta_{Z_{CM}} = 0 \quad (3.82)$$

$$\theta_{X_{SW}} - \theta_{X_{CM}} = 0 \quad (3.83)$$

$$\theta_{Y_{SW}} - \theta_{Y_{CM}} = 0 \quad (3.84)$$

$$\theta_{Z_{SW}} - \theta_{Z_{CM}} = 0 \quad (3.85)$$

$$\theta_{X_{NW}} - \theta_{X_{CM}} = 0 \quad (3.86)$$

$$\theta_{Y_{NW}} - \theta_{Y_{CM}} = 0 \quad (3.87)$$

$$\theta_{Z_{NW}} - \theta_{Z_{CM}} = 0 \quad (3.88)$$

### 3.2.1 Nodes Placement on Rigid Plate Edges

Eventually, to complete the mechanical model for the 4 and 6 DoF's rigid plate let us now briefly describe an additional feature included in both of them. Up to now we took into account four nodes on the corners through which external stimuli are applied to the plate. However, four additional nodes have been included in the rigid plate model implemented in VerilogA<sup>©</sup>. This extension is required from the need for a wider spectrum of configurations the hierarchical structures based on MEMS compact models can fit to. Indeed, in several RF-MEMS switch realizations, for instance, suspending springs are not connected to the four corners but in arbitrary positions along the rigid plate edges. The additional nodes mentioned above correspond to the four middle points along the plate edges as shown in Figure 3.7 and, starting from the right edge and proceeding clockwise, these are named as: Middle-East (*ME*), Middle-South (*MS*), Middle-West (*MW*) and Middle-North (*MN*). Moreover, the possibility of having each of these eight nodes displaced with respect to the four corners and four middle points along the local  $x$  or  $y$  axes is also implemented. This allows more flexibility in designing a complete MEMS structure to be simulated as, for instance, it is possible to connect flexible beams basically everywhere along the plate edges. For instance, in Figure 3.8 an offset  $D_y$  has been applied to the North-East node. When the four additional middle nodes are included, the mechanical model of the rigid plate discussed so far is still valid. All we have to do is to extend previous equations (e.g. torques around the axes and displacements) with terms taking into account their presence. Moreover, when an offset is applied to one (or several nodes) we have to calculate its (their) position taking into account the actual local coordinates also including it. For example, referring to Figure 3.8, we have to calculate the 3.59 - 3.61 of the node *NE* by substituting its original set of coordinates 3.58 with the one including the offset  $D_y$ :

$$NE_{D_y}(x, y, z) = \left(\frac{W}{2}, \left(\frac{L}{2} - D_y\right), 0\right) \quad (3.89)$$



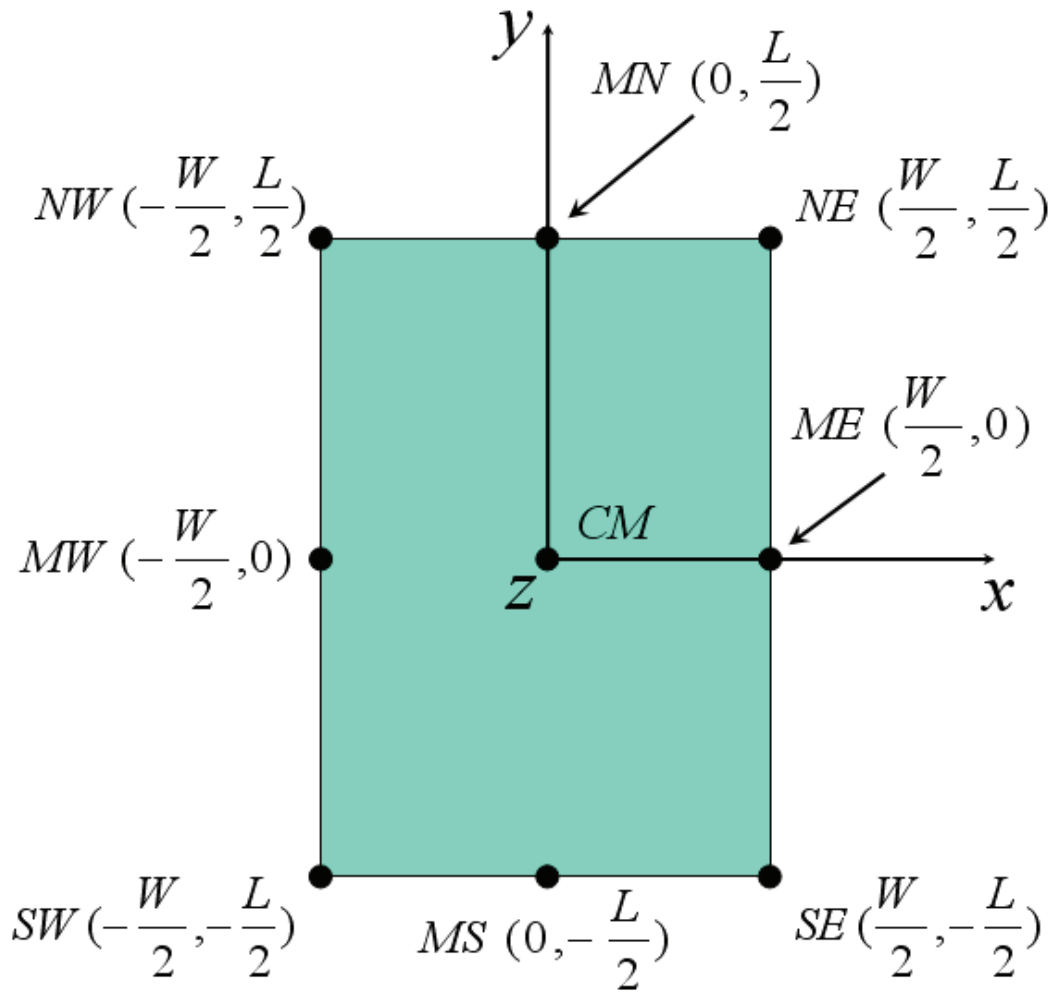


Figure 3.7: Rigid plate with 8 nodes. The middle point along the four edges have been also introduced.

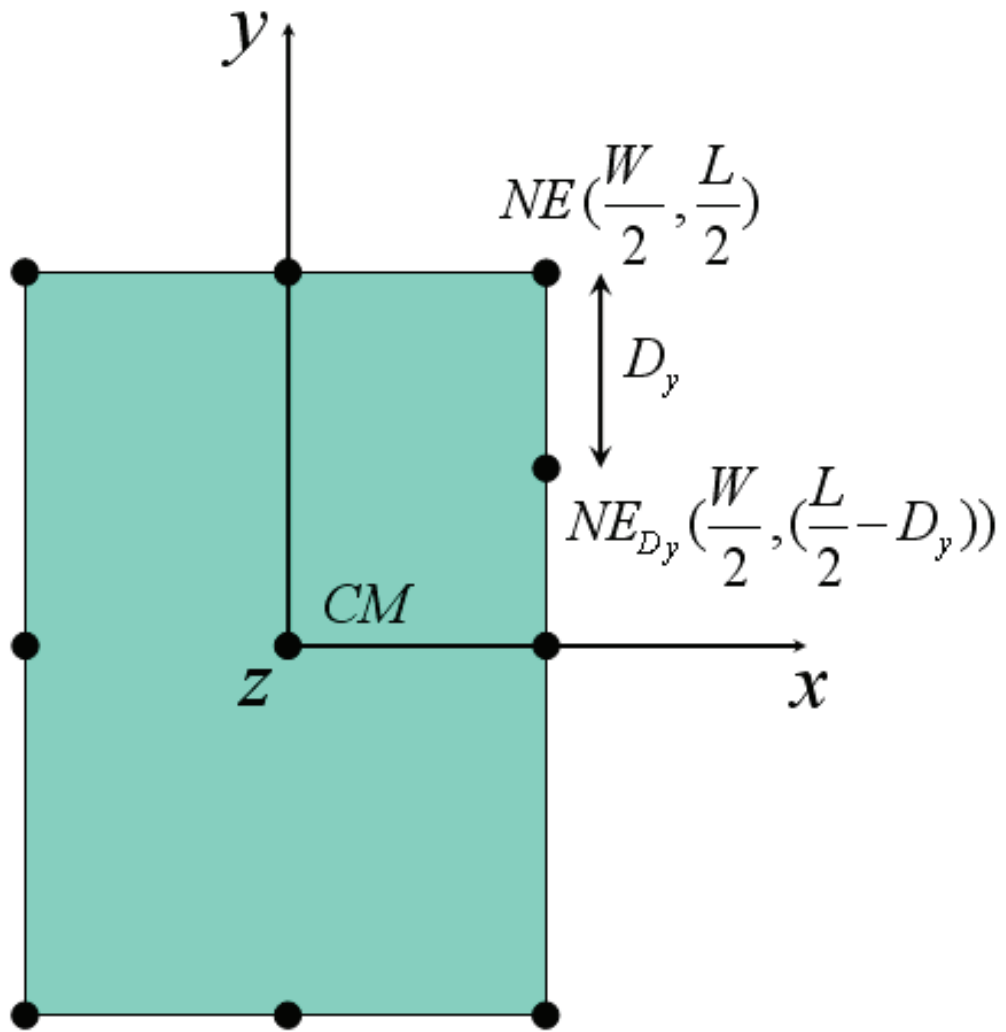


Figure 3.8: Rigid plate with an offset  $D_y$  applied to the  $NE$  node along the local  $y$  axis.

### 3.3 Contact Model for the 4 and 6 DoF's Rigid Plate

An important extension of the mechanical model for the 4 and 6 DoF's rigid plate is the inclusion of the collision effect when a plane is lying underneath the suspended rigid plate. This represents the typical functional condition occurring in MEMS switches. Indeed, when a biasing voltage is applied between the suspended plate and the bottom electrode the electrostatic attractive force makes the plate approach the fixed electrode. Once the bias reaches a critical value the *pull-in* occurs. In other words the plate collapses onto the lower electrode. We will further discuss this effect in details. What we are interested in now is to define a suitable feature in the plate mechanical model taking into account the presence of a surface under the plate. As already done in previous section we will first introduce the collision model for the 4 DoF's rigid plate and subsequently we will extend it to the complete 6 DoF's model.

The approach to model the contact is to introduce a suitable mechanical constraint when a certain condition on the plate vertical displacement is verified. On this purpose, an initial value of the distance between the plate and the underneath plane (called gap) must be defined. In this way the relative vertical displacement of the plate, previously introduced in the mechanical model, is turned into an absolute displacement with respect to the floor plane. When the gap is equal to zero the collision occurs. In order not to allow any further downward movement of the plate, which would imply a physically non-sensible negative gap, an appropriate force must counteract its motion. This is obtained by defining a material with a fictitious elastic constant which is set to a very large value. When the collision occurs, this force is applied to the centre of mass. As a consequence, any further small downward displacement of the plate generates a very large force which counteracts its lowering and eventually stops its movement. Let us now write in formulas what has just been discussed. The contact force called  $F_{Z_{TOUCH}}$  must be added to the 3.25 as follows:

$$F_{Z_{CM}} = -MA_{Z_{CM}} + F_{Z_{TOUCH}} \quad (3.90)$$

In order to distinguish the case in which collision either does or does not occur, a binary flag called  $TC_{FLAG}$  (Touch Flag) is defined as follows:

$$TC_{FLAG} = \begin{cases} 1 & \text{if } (Z_{CM_{INST}} < 0) \text{ and } (|Z_{CM_{INST}}| \geq |Z_{GAP}|) \\ 0 & \text{otherwise} \end{cases} \quad (3.91)$$

where  $Z_{CM_{INST}}$  is the instantaneous displacement of the centre of mass  $CM$  along the  $Z$  direction while  $Z_{GAP}$  is the initial gap between the plate and the substrate. The further step is defining the value of  $F_{Z_{TOUCH}}$  depending on the state of  $TC_{FLAG}$ :

$$F_{Z_{TOUCH}} = \begin{cases} K_{TOUCH}(Z_{GAP} + Z_{CM_{INST}}) & \text{if } TC_{FLAG} = 1 \\ 0 & \text{if } TC_{FLAG} = 0 \end{cases} \quad (3.92)$$

where  $K_{TOUCH}$  is a fictitious elastic constant with a very large value which models the lower contact surface (i.e. underneath electrode).

In the VerilogA<sup>©</sup> implementation of the contact model its magnitude is:

$$K_{TOUCH} = 10^9 \frac{N}{m} \quad (3.93)$$

Extending the contact model to the 6 DoF's rigid plate is rather straightforward. The main difference is that the collision condition must be defined for each node instead of for the only centre of mass. Indeed, collision might occur for instance to one or two nodes depending on the plate orientation around the three axes. Let us suppose that collision occurs to the only South-East ( $SE$ ) corner, as depicted in Figure 3.9. The first step is defining a flag similar to the 3.91 to detect when collision occurs at the  $SE$  corner. Its expression is:

$$TC_{SE_{FLAG}} = \begin{cases} 1 & \text{if } (Z_{SE_{INST}} < 0) \text{ and } (|Z_{SE_{INST}}| \geq |Z_{GAP} + Z_{SE_{INIT}}|) \\ 0 & \text{otherwise} \end{cases} \quad (3.94)$$

where  $Z_{SE_{INIT}}$  and  $Z_{SE_{INST}}$  are the initial and instantaneous positions of the  $SE$  corner along the  $Z$  axis obtained through the relations 3.70 and 3.73 respectively, calculated for the proper coordinates of the  $SE$  corner in the local frame  $(x, y, z)$ .

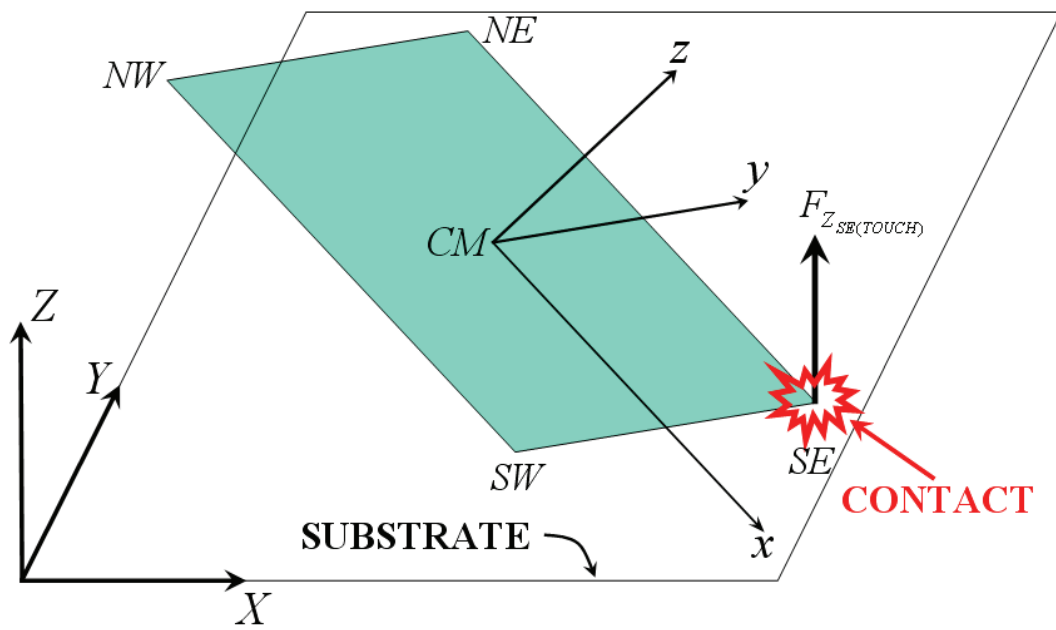


Figure 3.9: Collision of the  $SE$  plate corner with the bottom substrate plane.

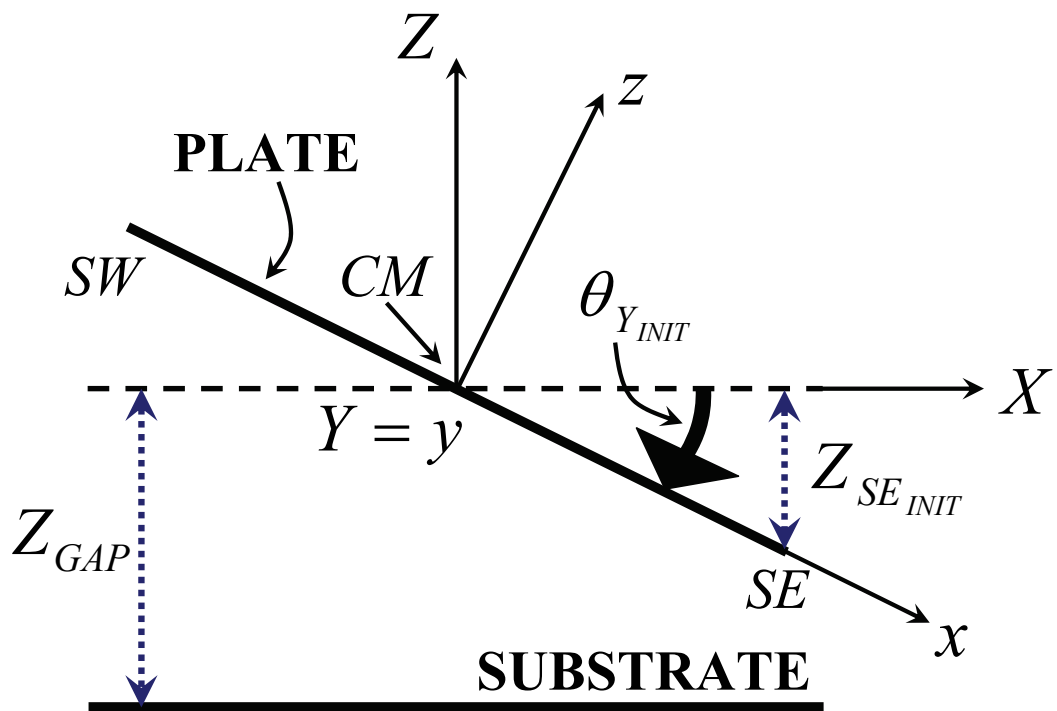


Figure 3.10: Lateral view of a plate with an initial orientation angle  $\theta_{Y_{INIT}}$  different from zero.

Definition of  $Z_{SE_{INIT}}$  is shown in Figure 3.10 where the lateral view of the initial position for a plate rotated around the  $Y$  axis (angle  $\theta_{Y_{INIT}}$ ) is reported. Subsequently, the contact force  $F_{Z_{SE(TOUCH)}}$  of Figure 3.9 is determined and its expression, similar to the 3.92, is:

$$F_{Z_{SE(TOUCH)}} = \begin{cases} K_{TOUCH}(Z_{GAP} + Z_{SE_{INST}} + Z_{SE_{INIT}}) & \text{if } TC_{SE_{FLAG}} = 1 \\ 0 & \text{if } TC_{SE_{FLAG}} = 0 \end{cases} \quad (3.95)$$

Finally, the contribution of  $F_{Z_{SE(TOUCH)}}$  due to the collision of the  $SE$  corner acts on the torques balance in the centre of mass  $CM$ . In particular, the  $F_{Z_{SE(TOUCH)}}$  contributes to the torques around the  $X$  and  $Y$  axes, and consequently the 3.62 and 3.63 have to be rewritten as follows:

$$\begin{aligned} T_{\theta_{X_{CM}}} = -I_X \frac{d\theta_X}{dt^2} & - \operatorname{sgn}(Z_{NE}) | Z_{NE} | (F_{\Delta Y_{NE}}) \\ & + \operatorname{sgn}(Y_{NE}) | Y_{NE} | (F_{\Delta Z_{NE}}) \\ & - \operatorname{sgn}(Z_{SE}) | Z_{SE} | (F_{\Delta Y_{SE}}) \\ & + \operatorname{sgn}(Y_{SE}) | Y_{SE} | (F_{\Delta Z_{SE}} + F_{Z_{SE(TOUCH)}}) \\ & - \operatorname{sgn}(Z_{SW}) | Z_{SW} | (F_{\Delta Y_{SW}}) \\ & + \operatorname{sgn}(Y_{SW}) | Y_{SW} | (F_{\Delta Z_{SW}}) \\ & - \operatorname{sgn}(Z_{NW}) | Z_{NW} | (F_{\Delta Y_{NW}}) \\ & + \operatorname{sgn}(Y_{NW}) | T_{NW} | (F_{\Delta Z_{NW}}) \end{aligned} \quad (3.96)$$

$$\begin{aligned} T_{\theta_{Y_{CM}}} = -I_Y \frac{d\theta_Y}{dt^2} & + \operatorname{sgn}(Z_{NE}) | Z_{NE} | (F_{\Delta X_{NE}}) \\ & - \operatorname{sgn}(X_{NE}) | X_{NE} | (F_{\Delta Z_{NE}}) \\ & + \operatorname{sgn}(Z_{NE}) | Z_{SE} | (F_{\Delta X_{SE}}) \\ & - \operatorname{sgn}(X_{NE}) | X_{SE} | (F_{\Delta Z_{SE}} + F_{Z_{SE(TOUCH)}}) \\ & + \operatorname{sgn}(Z_{NE}) | Z_{SW} | (F_{\Delta X_{SW}}) \\ & - \operatorname{sgn}(X_{NE}) | X_{SW} | (F_{\Delta Z_{SW}}) \\ & + \operatorname{sgn}(Z_{NE}) | Z_{NW} | (F_{\Delta X_{NW}}) \\ & - \operatorname{sgn}(X_{NE}) | X_{NW} | (F_{\Delta Z_{NW}}) \end{aligned} \quad (3.97)$$

Following the same approach, the contact forces are calculated for the other three nodes ( $F_{Z_{NE(TOUCH)}}$ ,  $F_{Z_{SW(TOUCH)}}$  and  $F_{Z_{NW(TOUCH)}}$ ) and the complete expressions for the 3.96 and 3.97 become:

$$\begin{aligned}
T_{\theta_{X_{CM}}} = -I_X \frac{d\theta_X}{dt^2} & - \operatorname{sgn}(Z_{NE}) | Z_{NE} | (F_{\Delta Y_{NE}}) \\
& + \operatorname{sgn}(Y_{NE}) | Y_{NE} | (F_{\Delta Z_{NE}} + F_{Z_{NE(TOUCH)}}) \\
& - \operatorname{sgn}(Z_{SE}) | Z_{SE} | (F_{\Delta Y_{SE}}) \\
& + \operatorname{sgn}(Y_{SE}) | Y_{SE} | (F_{\Delta Z_{SE}} + F_{Z_{SE(TOUCH)}}) \\
& - \operatorname{sgn}(Z_{SW}) | Z_{SW} | (F_{\Delta Y_{SW}}) \\
& + \operatorname{sgn}(Y_{SW}) | Y_{SW} | (F_{\Delta Z_{SW}} + F_{Z_{SW(TOUCH)}}) \\
& - \operatorname{sgn}(Z_{NW}) | Z_{NW} | (F_{\Delta Y_{NW}}) \\
& + \operatorname{sgn}(Y_{NW}) | T_{NW} | (F_{\Delta Z_{NW}} + F_{Z_{NW(TOUCH)}}) \quad (3.98)
\end{aligned}$$

$$\begin{aligned}
T_{\theta_{Y_{CM}}} = -I_Y \frac{d\theta_Y}{dt^2} & + \operatorname{sgn}(Y_{NE}) | Z_{NE} | (F_{\Delta X_{NE}}) \\
& - \operatorname{sgn}(Y_{NE}) | X_{NE} | (F_{\Delta Z_{NE}} + F_{Z_{NE(TOUCH)}}) \\
& + \operatorname{sgn}(Y_{SE}) | Z_{SE} | (F_{\Delta X_{SE}}) \\
& - \operatorname{sgn}(Y_{SE}) | X_{SE} | (F_{\Delta Z_{SE}} + F_{Z_{SE(TOUCH)}}) \\
& + \operatorname{sgn}(Y_{SW}) | Z_{SW} | (F_{\Delta X_{SW}}) \\
& - \operatorname{sgn}(Y_{SW}) | X_{SW} | (F_{\Delta Z_{SW}} + F_{Z_{SW(TOUCH)}}) \\
& + \operatorname{sgn}(Y_{NW}) | Z_{NW} | (F_{\Delta X_{NW}}) \\
& - \operatorname{sgn}(Y_{NW}) | X_{NW} | (F_{\Delta Z_{NW}} + F_{Z_{NW(TOUCH)}}) \quad (3.99)
\end{aligned}$$

To complete the description of the collision effects, a simple model which accounts for the dynamic friction of the plate when touching the lower substrate and moving onto the  $XY$  plane was implemented. It is not shown here for seek of brevity.



## 3.4 Electrostatic Model for the Rigid Plate

We commence now to introduce the electromechanical transduction operated by the suspended rigid plate when a biasing voltage is applied with respect to the lower substrate. As already done in previous sections, we will discuss the most simple case and we will introduce more and more features going ahead.

### 3.4.1 The Case of 4 DoF's

Let us focus on the most simple case first. When the rigid plate allows 4 DoF's only, the two electrodes, i.e. the substrate and the plate itself, are always parallel. In this configuration the electrostatic problem is very simple and the capacitance and the attractive electrostatic force are calculated with the following well-known formulas [6]:

$$C = \varepsilon \frac{A}{g} \quad (3.100)$$

$$F_{EL} = \frac{1}{2} \varepsilon V^2 \frac{A}{g^2} \quad (3.101)$$

In previous 3.100 and 3.101,  $C$  is the capacitance,  $F_{EL}$  the attractive electrostatic force,  $A$  the area of the electrodes,  $g$  the vertical distance in between them,  $V$  the applied voltage and finally  $\varepsilon$  the dielectric constant of the insulator (e.g. air) (see Figure 3.11).

Let us focus on the capacitance. Referring to the 4 DoF's rigid plate model already discussed it is possible to rewrite the 3.100 as follows:

$$C = \varepsilon \frac{WL}{(Z_{GAP} + Z_{CM_{INST}})} \quad (3.102)$$

where the denominator represent the instantaneous gap between the plate and the substrate. In other words, the 3.102 is the expression of the variable capacitance depending on the vertical plate displacement.

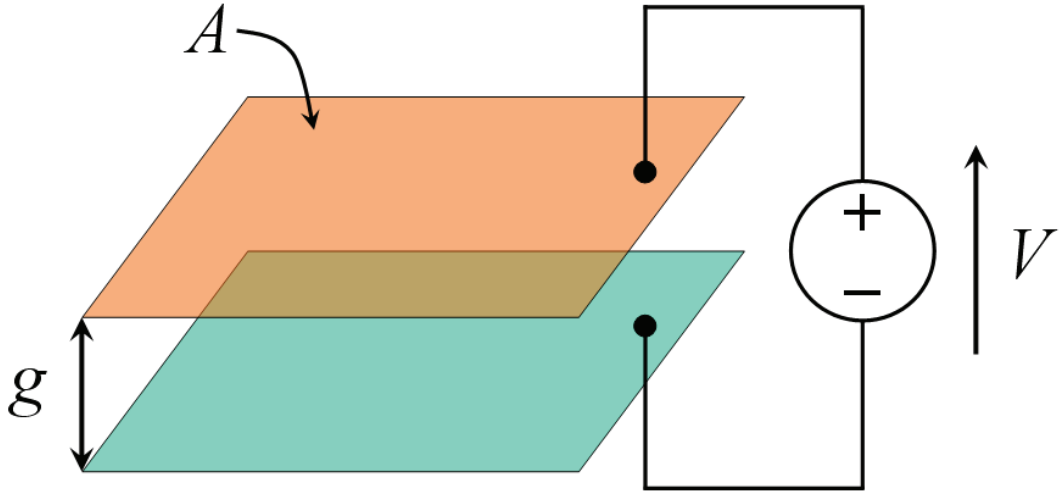


Figure 3.11: Electrostatic model for two parallel plates. A voltage  $V$  is applied.

The current flowing through the suspended plate is then defined as the time derivative of the total accumulated charge on the two faces:

$$I = \frac{dQ}{dt} \quad (3.103)$$

where  $Q$  is:

$$Q = CV \quad (3.104)$$

Concerning the electrostatic force, the 3.101 can be rewritten taking into account the instantaneous gap between the two plates:

$$F_{Z_{EL}} = \frac{1}{2}\epsilon V^2 \frac{A}{(Z_{GAP} + Z_{CM_{INST}})^2} \quad (3.105)$$

With the 3.105 the dependence of the electrostatic force on the instantaneous gap is introduced. In the 3.105 we introduced  $F_{Z_{EL}}$  instead of  $F_{EL}$  because it is oriented along the  $Z$  axis. Finally, the electromechanical transduction is accounted for by introducing the  $F_{Z_{EL}}$  in the forces balance of the centre of mass  $CM$ . This means to rewrite the 3.90 as:

$$F_{Z_{CM}} = -MA_{Z_{CM}} + F_{Z_{TOUCH}} - F_{Z_{EL}} \quad (3.106)$$

Very often during fabrication of MEMS suspended switches a thin insulating layer is deposited onto the lower electrode. This is to prevent from the short-circuit that would occur after the collapse of the suspended plate on the substrate if these stick together. The effect of this additional dielectric layer on the capacitance and electrostatic force is negligible when the gap is large. However, as the air gap between the two plates decrease, the presence of the insulating layer affects the  $C$  and  $F_{Z_{EL}}$  values, especially in the limit-case of pull-in. The model discussed thus far has been extended including also the deposited insulating layer. A schematic view of the suspended plate with an insulating layer onto the lower electrodes is shown in Figure 3.12. In this an oxide (i.e. silicon dioxide) layer has been introduced since this is used in the MEMS fabrication process described ahead in this thesis. The first aspect to take into account is that the gap between the plates is reduced because of the oxide layer. This means that in all previous formulas of the mechanical model we have to replace the initial gap  $Z_{GAP}$  with  $Z_{AIR}$ , whose expression is (see Figure 3.12):

$$Z_{AIR} = Z_{GAP} - Z_{OX} \quad (3.107)$$

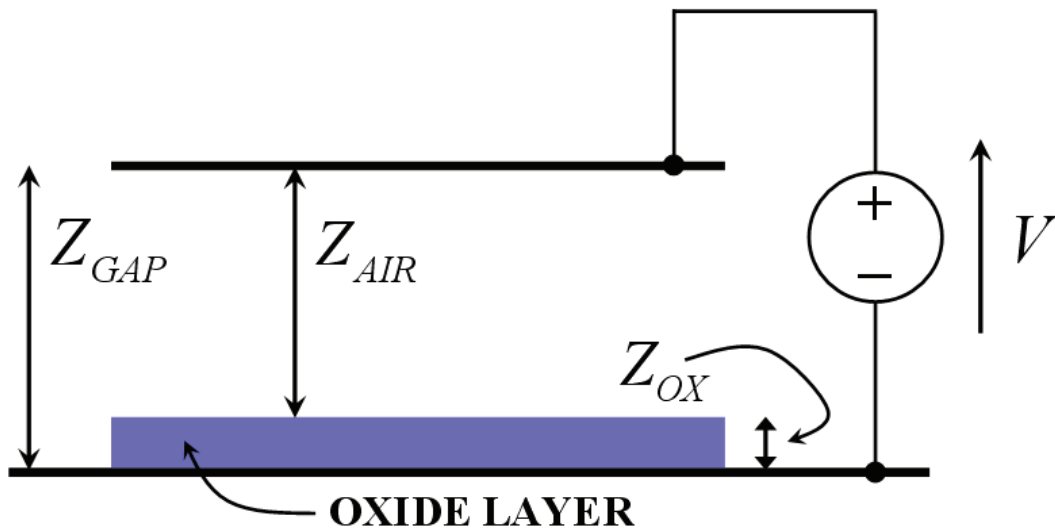


Figure 3.12: The two parallel plates with an oxide layer deposited on the lower electrode. Its thickness  $Z_{OX}$  is enlarged to make in visible.

Now, the capacitance and electrostatic force must be rewritten taking into account the oxide layer. Starting from the first one, the total  $C$  of the entire device is due to two series capacitors: one with air as dielectric ( $C_{AIR}$ ) and the second one with oxide ( $C_{OX}$ ) as shown in Figure 3.13. Subsequently, the  $C$  is defined with the well-known formula:

$$\frac{1}{C} = \frac{1}{C_{AIR}} + \frac{1}{C_{OX}} \quad (3.108)$$

that can be written as:

$$C = \frac{C_{AIR} + C_{OX}}{C_{AIR}C_{OX}} \quad (3.109)$$

where

$$C_{AIR} = \varepsilon_{AIR} \frac{WL}{(Z_{AIR} + Z_{CM_{INST}})} \quad (3.110)$$

and

$$C_{OX} = \varepsilon_{OX} \frac{WL}{Z_{OX}} \quad (3.111)$$

In previous equations 3.110 and 3.111  $\varepsilon_{AIR}$  and  $\varepsilon_{OX}$  represent the dielectric constant of air and oxide respectively.

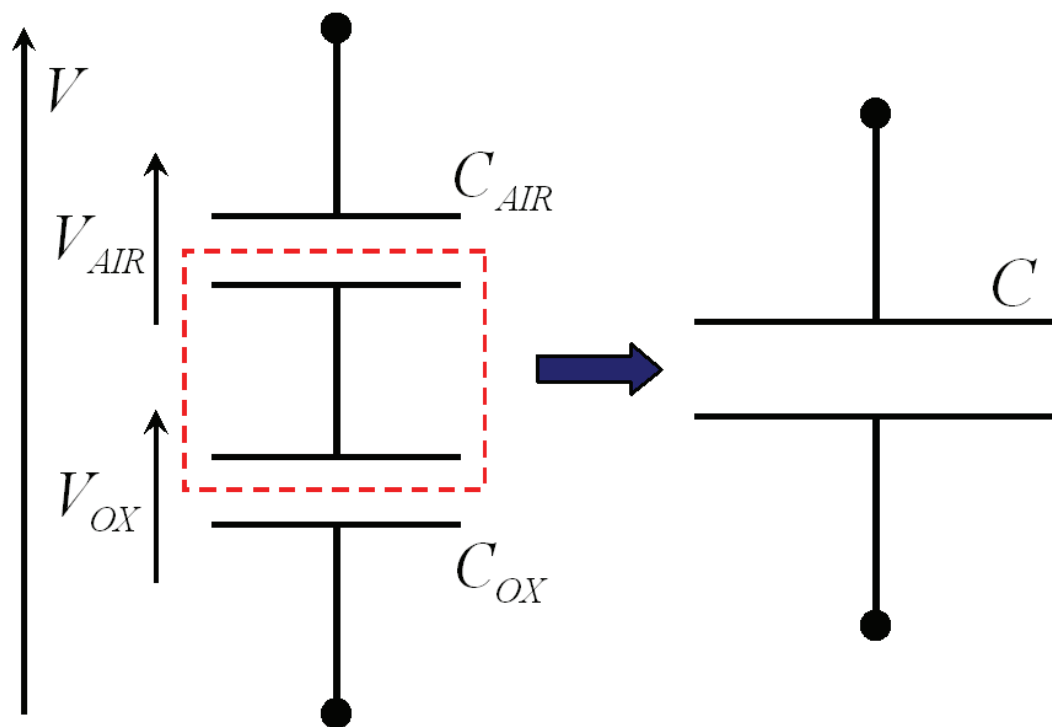


Figure 3.13: Because of the oxide layer, an additional capacitance is in series with the one due to the air gap.

Let us now focus on the electrostatic force. We have to rewrite the 3.105 as a function of the voltage drop across the air gap ( $V_{AIR}$  in Figure 3.13) instead of the total voltage  $V$ . The proper expression for  $V_{AIR}$  can be derived by means of the series capacitors mentioned above. According to the principle of charge conservation and looking at Figure 3.13, the total charge accumulated on one plate must be equal to the charge on the other plate within the dashed box. This means that:

$$Q_{AIR} = Q_{OX} \quad (3.112)$$

According to the 3.104 the 3.112 can be written as:

$$C_{AIR}V_{AIR} = C_{OX}V_{OX} \quad (3.113)$$

However

$$V = V_{AIR} + V_{OX} \quad (3.114)$$

and bringing  $V_{OX}$  at the first member it becomes:

$$V_{OX} = V - V_{AIR} \quad (3.115)$$

Replacing the 3.115 in the 3.113 the expression of  $V_{AIR}$  is carried out as follows:

$$V_{AIR} = \frac{C_{OX}}{C_{AIR} + C_{OX}}V \quad (3.116)$$

Eventually, the actual electrostatic force which accounts for the oxide layer is obtained by replacing  $V$  with the 3.116 in the 3.105 that turns into:

$$F_{ZEL} = \frac{1}{2}\varepsilon_{AIR}V_{AIR}^2 \frac{WL}{(Z_{AIR} + Z_{CMINST})^2} \quad (3.117)$$

Additionally, the total capacitance and electrostatic force accounting for the oxide layer, respectively expressed by equations 3.109 and 3.117, can be expressed as a function of an effective dielectric constant  $\varepsilon_{EFF}$ .

This depends both on  $\varepsilon_{AIR}$  and  $\varepsilon_{OX}$ , and its expression, still taking into account the scheme of Figure 3.13, is:

$$\varepsilon_{EFF} = \frac{\varepsilon_{OX}\varepsilon_{AIR}Z_{GAP}}{Z_{OX}\left(\varepsilon_{AIR} + \varepsilon_{OX}\frac{Z_{AIR}}{Z_{OX}}\right)} \quad (3.118)$$

The 3.118 substituted in the 3.102 and 3.105 gives the complete electrical effects also accounting for the oxide layer.

A further consideration must now be stressed. Both 4 and 6 DoF's rigid plate can translate along the three axes ( $X, Y, Z$ ) and also rotate around them (the 4 DoF's plate only around  $Z$ , while the 6 DoF's one around all of them). It might then happen that, because of large displacements and rotations, the suspended plate ends up in a configuration in which it is partially or not at all superposed to the underneath electrode like shown in Figure 3.14. In this case previous formula for the capacitance and electrostatic force would not be valid anymore. However, we assume that the typical displacements and rotations the plate undergoes are small enough as well as the underneath electrode is large enough so that the suspended plate projection (or shadow) lays always and entirely within its edges.

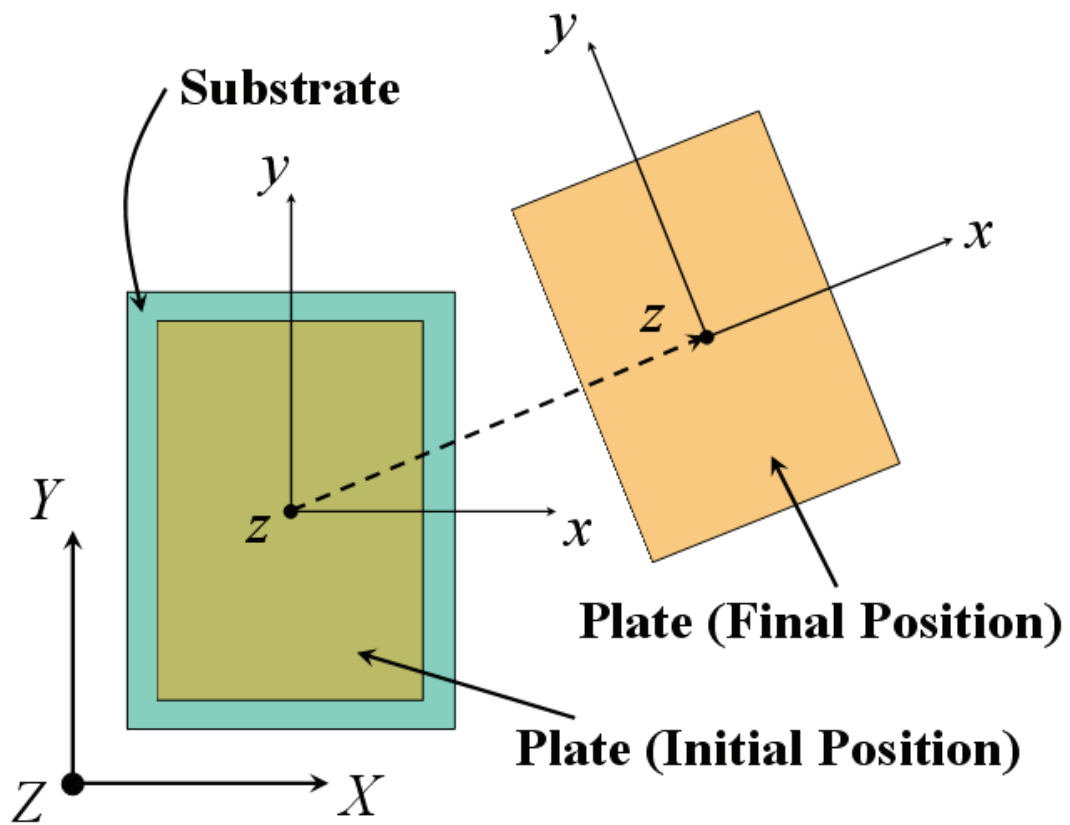


Figure 3.14: When large displacements and rotations occur the plate projection on the underneath substrate could fall outside its area.



### 3.4.2 Extension to the Case of 6 DoF's

Following the usual approach we now extend the electrostatic model for the rigid plate with 6 DoF's. For seek of brevity we will directly take into account the presence of the oxide layer on the lower electrode. The main feature that must be accounted for is that when all the rotation angles ( $\theta_X, \theta_Y, \theta_Z$ ) have non-zero values, every point on plate surface has a different distance from the substrate. In Figure 3.15 a generic point  $P$  with coordinates  $x_P, y_P, z_P$  in the plate local frame is taken as example. Its distance from the substrate is the composition of two contributions. One is the instantaneous distance of the plate centre of mass from the substrate, defined as  $Z_{AIR} + Z_{CM_{INST}}$ . The second segment is the projection along the global  $Z$  axis of the point  $P$  and is expressed by the same formula as the 3.73:

$$Z_{P_{INST}} = -\sin \theta_Y x_P + (\sin \theta_X \cos \theta_Y) y_P + (\cos \theta_X \cos \theta_Y) z_P \quad (3.119)$$

where  $\theta_X$  and  $\theta_Y$  are defined as in the 3.66 and 3.67 respectively. Moreover, in the 3.119 it always is:

$$z_P = -\frac{T}{2} \quad (3.120)$$

Indeed, looking at Figure 3.2 the local reference system origin is superposed to the plate centre of mass. However, the electrical effects must be calculated at its lower face which has a local coordinate as the 3.120 indeed. Looking at equation 3.119 it is noticeable that a rotation of the plate around the  $Z$  global axis does not give any contribution to  $Z_{P_{INST}}$ .

It is now possible to rewrite the equation for the capacitance and electrostatic force in an integral form over the whole plate area (see Figure 3.3). This takes into account the particular gap for each point on its surface. The 3.110 then becomes:

$$C_{AIR} = \varepsilon_{AIR} \int_{-\frac{w}{2}}^{\frac{w}{2}} \int_{-\frac{l}{2}}^{\frac{l}{2}} \frac{dxdy}{(Z_{AIR} + Z_{CM_{INST}} + Z_{P_{INST}})} \quad (3.121)$$

Similarly, the attractive electrostatic force of equation 3.117 becomes:

$$F_{z_{EL}} = \frac{1}{2} \varepsilon_{AIR} V_{AIR}^2 \int_{-\frac{w}{2}}^{\frac{w}{2}} \int_{-\frac{l}{2}}^{\frac{l}{2}} \frac{dxdy}{(Z_{AIR} + Z_{CM_{INST}} + Z_{P_{INST}})^2} \quad (3.122)$$

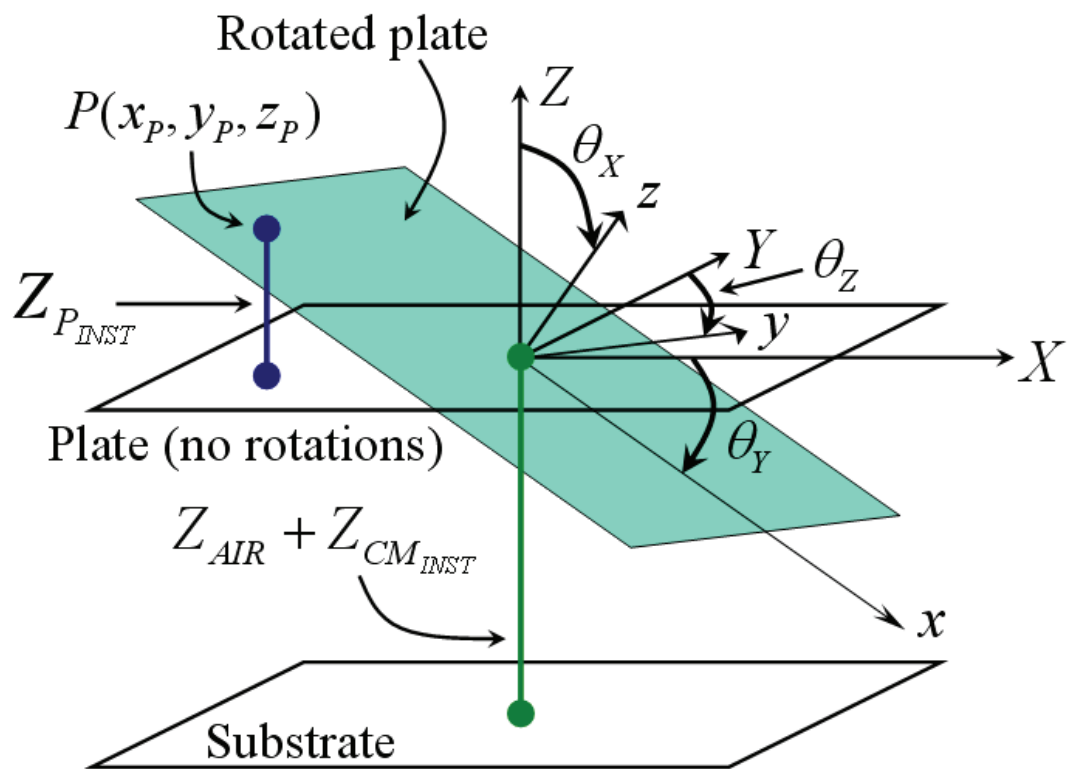


Figure 3.15: Definition of the vertical distance between a generic point  $P$  on the rotated plate area and the substrate.

Both the 3.121 and 3.122 are integrated in a closed form that is implemented in VerilogA<sup>©</sup> without particular issues. Concerning the 3.122, this represents the attractive electrostatic force expressed in the plate local frame  $(x, y, z)$ . Before applying its contribution to the centre of mass, it must then be decomposed in the three corresponding forces in the global frame  $F_{X_{EL}}$ ,  $F_{Y_{EL}}$  and  $F_{Z_{EL}}$  as follows (see equation 2.8):

$$F_{X_{EL}} = (\sin \theta_X \sin \theta_Z + \cos \theta_X \sin \theta_Y \cos \theta_Z) F_{z_{EL}} \quad (3.123)$$

$$F_{Y_{EL}} = (-\sin \theta_X \cos \theta_Z + \cos \theta_X \sin \theta_Y \sin \theta_Z) F_{z_{EL}} \quad (3.124)$$

$$F_{Z_{EL}} = (\cos \theta_X \cos \theta_Y) F_{z_{EL}} \quad (3.125)$$

Now it is possible to apply the electrostatic force contribution to the force balance in the centre of mass rewriting the 3.4, 3.5 and 3.90 as:

$$F_{X_{CM}} = -MA_{X_{CM}} - F_{X_{EL}} \quad (3.126)$$

$$F_{Y_{CM}} = -MA_{Y_{CM}} + F_{Y_{EL}} \quad (3.127)$$

$$F_{Z_{CM}} = -MA_{Z_{CM}} + F_{Z_{TOUCH}} - F_{Z_{EL}} \quad (3.128)$$

The same approach is exploited in order to derive the torque contribution due to the electrostatic force. It is sufficient to include within the integral of formula 3.122 the arm along the local  $x$  and  $y$  directions to get the proper torque expressions:

$$T_{\theta_{x_{EL}}} = \frac{1}{2} \varepsilon_{AIR} V_{AIR}^2 \int_{-\frac{w}{2}}^{\frac{w}{2}} \int_{-\frac{l}{2}}^{\frac{l}{2}} \frac{y_P}{(Z_{AIR} + Z_{CM_{INST}} + Z_{P_{INST}})^2} dx dy \quad (3.129)$$

$$T_{\theta_{y_{EL}}} = \frac{1}{2} \varepsilon_{AIR} V_{AIR}^2 \int_{-\frac{w}{2}}^{\frac{w}{2}} \int_{-\frac{l}{2}}^{\frac{l}{2}} \frac{x_P}{(Z_{AIR} + Z_{CM_{INST}} + Z_{P_{INST}})^2} dx dy \quad (3.130)$$

where  $T_{\theta_{x_{EL}}}$  and  $T_{\theta_{y_{EL}}}$  are the torques due to electrostatic force around the local  $x$  and  $y$  axes respectively. Whereas,  $y_P$  and  $x_P$  are the arm of the generic

point  $P$  on plate surface along  $y$  and  $x$  directions respectively. Also in this case the torques must be decomposed in their contribution in global frame  $(X, Y, Z)$ . Using the same notation of equation 2.8 they are:

$$T_{\theta X_{EL}} = C_Y C_Z T_{\theta x_{EL}} + (-C_X S_Z + S_X S_Y C_Z) T_{\theta y_{EL}} \quad (3.131)$$

$$T_{\theta Y_{EL}} = C_Y S_Z T_{\theta x_{EL}} + (C_X C_Z + S_X S_Y S_Z) T_{\theta y_{EL}} \quad (3.132)$$

$$T_{\theta Z_{EL}} = -S_Y T_{\theta x_{EL}} + S_X C_Y T_{\theta y_{EL}} \quad (3.133)$$

Finally, the 3.131 - 3.133 have to be applied to the torque balance equations referred to the centre of mass. Thus, the 3.30, 3.98 3.99 become:

$$\begin{aligned} T_{\theta Z_{CM}} = -I_Z \frac{d\theta_Z}{dt^2} & - \operatorname{sgn}(Y_{NE}) | Y_{NE} | F_{\Delta X_{NE}} \\ & + \operatorname{sgn}(X_{NE}) | X_{NE} | F_{\Delta Y_{NE}} \\ & - \operatorname{sgn}(Y_{SE}) | Y_{SE} | F_{\Delta X_{SE}} \\ & + \operatorname{sgn}(X_{SE}) | X_{SE} | F_{\Delta Y_{SE}} \\ & - \operatorname{sgn}(Y_{SW}) | Y_{SW} | F_{\Delta X_{SW}} \\ & + \operatorname{sgn}(X_{SW}) | X_{SW} | F_{\Delta Y_{SW}} \\ & - \operatorname{sgn}(Y_{NW}) | Y_{NW} | F_{\Delta X_{NW}} \\ & + \operatorname{sgn}(X_{NW}) | X_{NW} | F_{\Delta Y_{NW}} \\ & - T_{\theta Z_{EL}} \end{aligned} \quad (3.134)$$

$$\begin{aligned} T_{\theta X_{CM}} = -I_X \frac{d\theta_X}{dt^2} & - \operatorname{sgn}(Z_{NE}) | Z_{NE} | (F_{\Delta Y_{NE}}) \\ & + \operatorname{sgn}(Y_{NE}) | Y_{NE} | (F_{\Delta Z_{NE}} + F_{Z_{NE}(TOUCH)}) \\ & - \operatorname{sgn}(Z_{SE}) | Z_{SE} | (F_{\Delta Y_{SE}}) \\ & + \operatorname{sgn}(Y_{SE}) | Y_{SE} | (F_{\Delta Z_{SE}} + F_{Z_{SE}(TOUCH)}) \\ & - \operatorname{sgn}(Z_{SW}) | Z_{SW} | (F_{\Delta Y_{SW}}) \\ & + \operatorname{sgn}(Y_{SW}) | Y_{SW} | (F_{\Delta Z_{SW}} + F_{Z_{SW}(TOUCH)}) \\ & - \operatorname{sgn}(Z_{NW}) | Z_{NW} | (F_{\Delta Y_{NW}}) \\ & + \operatorname{sgn}(Y_{NW}) | Y_{NW} | (F_{\Delta Z_{NW}} + F_{Z_{NW}(TOUCH)}) \\ & - T_{\theta X_{EL}} \end{aligned} \quad (3.135)$$

$$\begin{aligned}
T_{\theta_{Y_{CM}}} = & -I_Y \frac{d\theta_Y}{dt^2} + \operatorname{sgn}(Y_{NE}) | Z_{NE} | (F_{\Delta X_{NE}}) \\
& - \operatorname{sgn}(Y_{NE}) | X_{NE} | (F_{\Delta Z_{NE}} + F_{Z_{NE}(TOUCH)}) \\
& + \operatorname{sgn}(Y_{SE}) | Z_{SE} | (F_{\Delta X_{SE}}) \\
& - \operatorname{sgn}(Y_{SE}) | X_{SE} | (F_{\Delta Z_{SE}} + F_{Z_{SE}(TOUCH)}) \\
& + \operatorname{sgn}(Y_{SW}) | Z_{SW} | (F_{\Delta X_{SW}}) \\
& - \operatorname{sgn}(Y_{SW}) | X_{SW} | (F_{\Delta Z_{SW}} + F_{Z_{SW}(TOUCH)}) \\
& + \operatorname{sgn}(Y_{NW}) | Z_{NW} | (F_{\Delta X_{NW}}) \\
& - \operatorname{sgn}(Y_{NW}) | X_{NW} | (F_{\Delta Z_{NW}} + F_{Z_{NW}(TOUCH)}) \\
& - T_{\theta_{Y_{EL}}} \tag{3.136}
\end{aligned}$$

It is important to stress that the contributions of the electrical torques in previous 3.134 - 3.136 are negative because the electrostatic force is attractive and consequently oriented along the  $z$  axis negative wise.

### 3.4.3 Electric Field Curved Lines Model

An important detail neglected thus far is that when the plate assumes uneven positions in the space (i.e. not parallel to the substrate) the electric field lines are not straight lines. In the model discussed thus far these lines are supposed to be straight segments. This is a reasonable assumption when the plate orientation angles ( $\theta_X, \theta_Y, \theta_Z$ ) are very small [32]. However, it is possible to enhance the accuracy of the plate electrostatic model for larger angles by taking into account the curvature of the field lines as it is being shown in this section.

The hypothesis we will employ assumes the field lines to be orthogonal to both coming-out and coming-in surfaces (i.e. plate area and substrate) [33]. The solution satisfying this condition is to assume the field lines as arcs of circumference. A simplified case in which only  $\theta_Y$  has a non-zero value is shown in Figure 3.16. Given a generic point  $P(x_P, y_P, z_P = -\frac{T}{2})$  on plate surface two new reference systems related to it are defined. One is the local system with the axes oriented as  $x, y, z$  and with origin in the point  $P$ :  $x_P^1, y_P^1, z_P^1$  (see Figure 3.16).

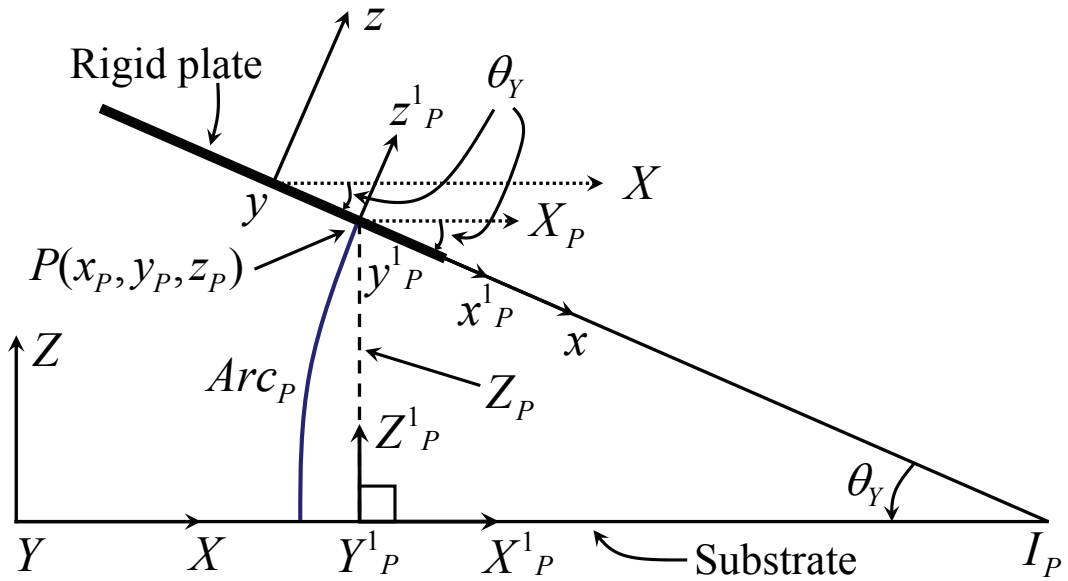


Figure 3.16: Example of a curved line of the electric field when only  $\theta_Y$  has a non-zero value.

Whereas, the second reference system is oriented as the global frame  $X, Y, Z$  and its origin corresponds to the vertical projection along  $Z$  of the point  $P$  on the  $XY$  plane. This system is  $X^1_P, Y^1_P, Z^1_P$  in previous figure. These additional systems are introduced in order to unlink the calculation of the field arc length from the particular set of coordinates for the point  $P$  on  $xy$  plane. Indeed, all we need to know the arc length is the angle  $\theta_Y$  and the segment  $PI_P$ . The coherence among the global  $(X, Y, Z)$  and local  $(x, y, z)$  system is maintained in any case. Indeed, the information about the local coordinates of the point  $P$  is already included in  $Z_P$  (see Figure 3.16) that has been already defined in Figure 3.15 as:

$$Z_P = Z_{AIR} + Z_{CM_{INST}} + Z_{P_{INST}} \quad (3.137)$$

For the properties of triangles the segment  $PI_P$  of Figure 3.16 is:

$$PI_P = \frac{Z_P}{\sin \theta_Y} \quad (3.138)$$

and finally, the field line  $Arc_P$  is:

$$Arc_P = PI_P \theta_Y \quad (3.139)$$

If we now introduce the coefficient  $\sigma_{Arc}$  defined as

$$\sigma_{Arc} = \frac{Arc_P}{Z_P} \quad (3.140)$$

and we replace  $Arc_P$  with the 3.139,  $\sigma_{Arc}$  results to be independent on  $Z_P$  and consequently on the set of coordinates  $(x_P, y_P)$ :

$$\sigma_{Arc} = \frac{\theta_Y}{\sin \theta_Y} \quad (3.141)$$

This allows to define the arc length of each point on plate surface as:

$$Arc_P = \sigma_{Arc} Z_P \quad (3.142)$$

Finally, to include the curvature of the electric field lines within the capacitance and electrostatic force calculation, the denominator of equations 3.121, 3.122, 3.129 and 3.130 has to be multiplied by  $\sigma_{Arc}$  that is constant with respect to the integration variables:

$$C_{AIR} = \frac{\varepsilon_{AIR}}{\sigma_{Arc}} \int_{-\frac{w}{2}}^{\frac{w}{2}} \int_{-\frac{l}{2}}^{\frac{l}{2}} \frac{dxdy}{(Z_{AIR} + Z_{CM_{INST}} + Z_{P_{INST}})} \quad (3.143)$$

$$F_{zEL} = \frac{1}{2} \frac{\varepsilon_{AIR} V_{AIR}^2}{\sigma_{Arc}^2} \int_{-\frac{w}{2}}^{\frac{w}{2}} \int_{-\frac{l}{2}}^{\frac{l}{2}} \frac{dxdy}{(Z_{AIR} + Z_{CM_{INST}} + Z_{P_{INST}})^2} \quad (3.144)$$

$$T_{\theta xEL} = \frac{1}{2} \frac{\varepsilon_{AIR} V_{AIR}^2}{\sigma_{Arc}^2} \int_{-\frac{w}{2}}^{\frac{w}{2}} \int_{-\frac{l}{2}}^{\frac{l}{2}} \frac{y_P}{(Z_{AIR} + Z_{CM_{INST}} + Z_{P_{INST}})^2} dxdy \quad (3.145)$$

$$T_{\theta yEL} = \frac{1}{2} \frac{\varepsilon_{AIR} V_{AIR}^2}{\sigma_{Arc}^2} \int_{-\frac{w}{2}}^{\frac{w}{2}} \int_{-\frac{l}{2}}^{\frac{l}{2}} \frac{x_P}{(Z_{AIR} + Z_{CM_{INST}} + Z_{P_{INST}})^2} dxdy \quad (3.146)$$





Given a generic point  $P(x_P, y_P)$  on plate surface, it now admits two extensions along  $x$  and  $y$  local direction until the intersections with the substrate are reached:  $E_{P_x}$  and  $E_{P_y}$ . This leads to two possible arcs for the same point  $P$ :  $E_{P_x}\theta_Y$  and  $E_{P_y}\theta_X$  in Figure 3.18.

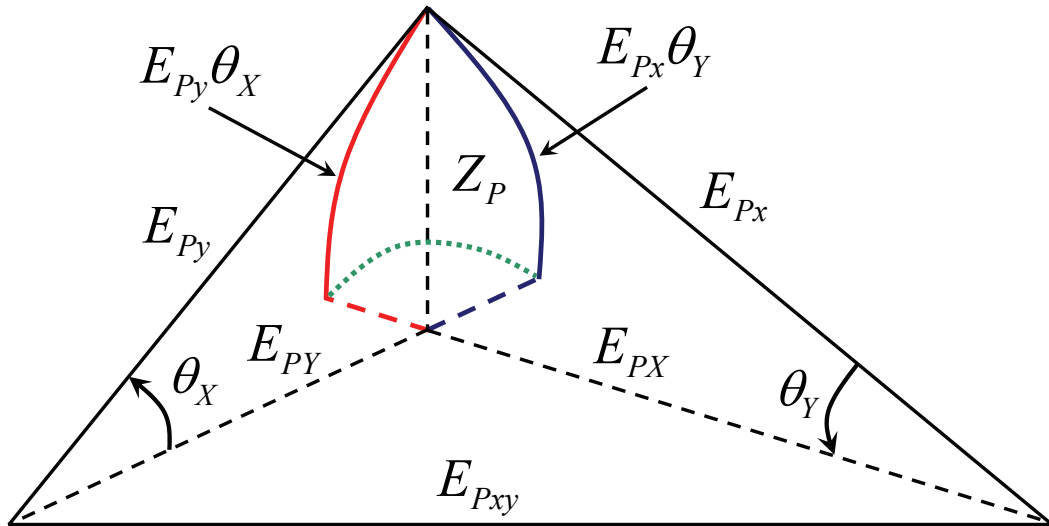


Figure 3.18: The two segments  $E_{P_x}$  and  $E_{P_y}$  generate two different arc lengths for the same point  $P$ .

It is necessary to find a solution to identify the proper arc for the point  $P$ . Following an empirical approach we define the field line arc for the point  $P$  as the one described by the bisector  $E_{P_{Arc}}$  of the  $90^\circ$  angle formed by  $E_{P_x}$  and  $E_{P_y}$  multiplied by the angle  $\theta_{Arc}$  shown in Figure 3.19. Both  $E_{P_{Arc}}$  and  $\theta_{Arc}$  are determined with simple trigonometric calculations on the triangles formed by the edges  $E_{P_x}, E_{P_y}, E_{P_{xy}}$  and  $E_{P_X}, E_{P_Y}, E_{P_{xy}}$  that are not reported here for seek of brevity. Also in this case it is possible to define a suitable coefficient  $\sigma_{Arc}$  independent on  $Z_P$  for which the 3.142 is still valid as well as the 3.143 - 3.146.



with the 3.109 and 3.117 respectively. Subsequently, a contribution of capacitance and electrostatic force due to the *negative* holes surface is calculated and subtracted to the 3.109 and 3.117. This is possible because both the capacitance and electrostatic force are linearly dependent on the area. Finally, the effective value for the two electric magnitudes due to the holes is determined.

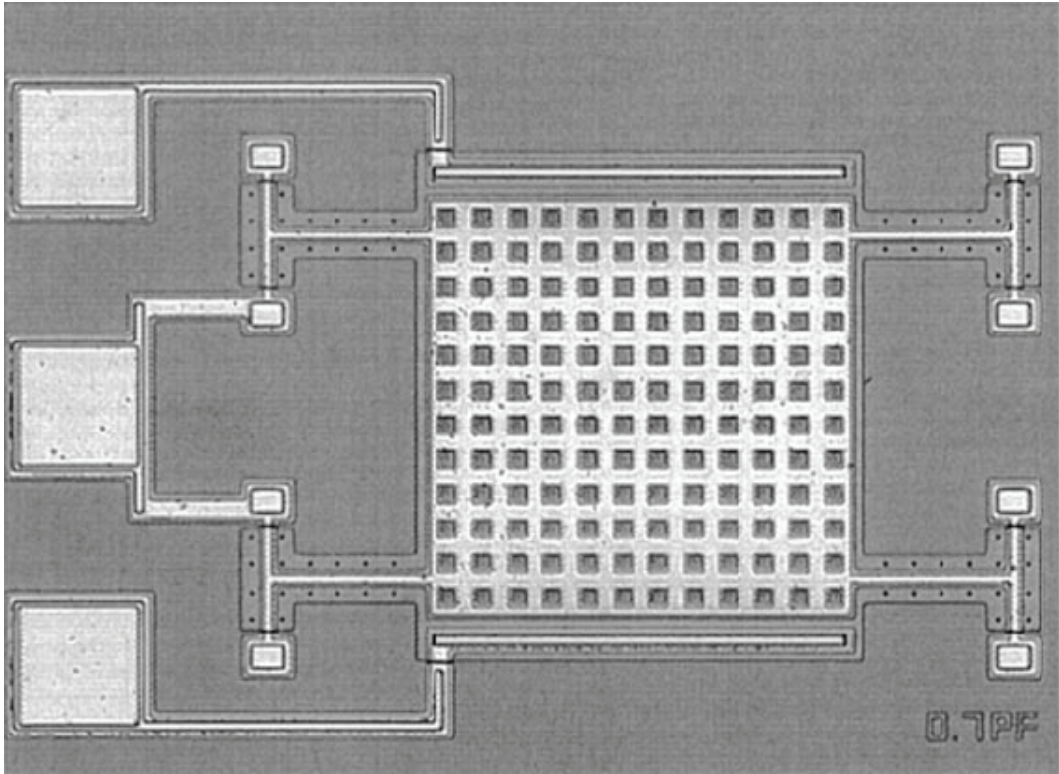


Figure 3.20: SEM picture of a suspended plate with holes on its surface. These allow the etching solution to reach the sacrificial layer underneath the plate.

Let us define the width and length of each hole respectively along the  $x$  and  $y$  axis as  $W_H$  and  $L_H$  as shown in Figure 3.21. If the number of holes along the  $x$  and  $y$  local axes is  $m$  and  $n$  respectively, the total holes surface  $A_{Holes}$  is:

$$A_{Holes} = W_H L_H m n \quad (3.147)$$

First of all, the presence of holes is accounted for in the rigid plate mechanical model by replacing the mass  $M$  in equation 3.1 with an effective value  $M_{EFF}$ . In it, the total holes volume is subtracted to the value for a rigid plate without openings on its surface. The expression is:

$$M_{EFF} = \rho(WLT - W_H L_H T m n) \quad (3.148)$$

where  $\rho$  is the density of the material the rigid plate is made of.

What has to be done next is the calculation of capacitance and electrostatic force due to the area expressed by equation 3.147. Thus, equations 3.110, 3.111 and 3.117 are rewritten as follows:

$$C_{AIR} = \varepsilon_{AIR} \left[ \frac{WL}{(Z_{AIR} + Z_{CM_{INST}})} - \frac{A_{Holes}}{(Z_{AIR} + Z_{CM_{INST}})} \right] \quad (3.149)$$

$$C_{OX} = \varepsilon_{OX} \left[ \frac{WL}{Z_{OX}} - \frac{A_{Holes}}{Z_{OX}} \right] \quad (3.150)$$

$$F_{Z_{EL}} = \frac{1}{2} \varepsilon_{AIR} V_{AIR}^2 \left[ \frac{WL}{(Z_{AIR} + Z_{CM_{INST}})^2} - \frac{A_{Holes}}{(Z_{AIR} + Z_{CM_{INST}})^2} \right] \quad (3.151)$$

Let us apply this approach to the 6 DoF's rigid plate model. In this case there is an important aspect to take into account. As the plate can assume any position in space (as for instance shown in Figure 3.17) each hole gives a different contribution to the capacitance and electrostatic force. Indeed, as the distance from the substrate is unique for each point on plate surface, it is not possible to consider the total holes area, but each of them must be treated separately. Figure 3.22 represents the most general case in which holes are placed unevenly on plate surface. In it, the lateral distance of holes from the four plate edges (left, right, top, bottom) are respectively defined as:  $\Delta_{xL}$ ,  $\Delta_{xR}$ ,  $\Delta_{yT}$  and  $\Delta_{yB}$ .

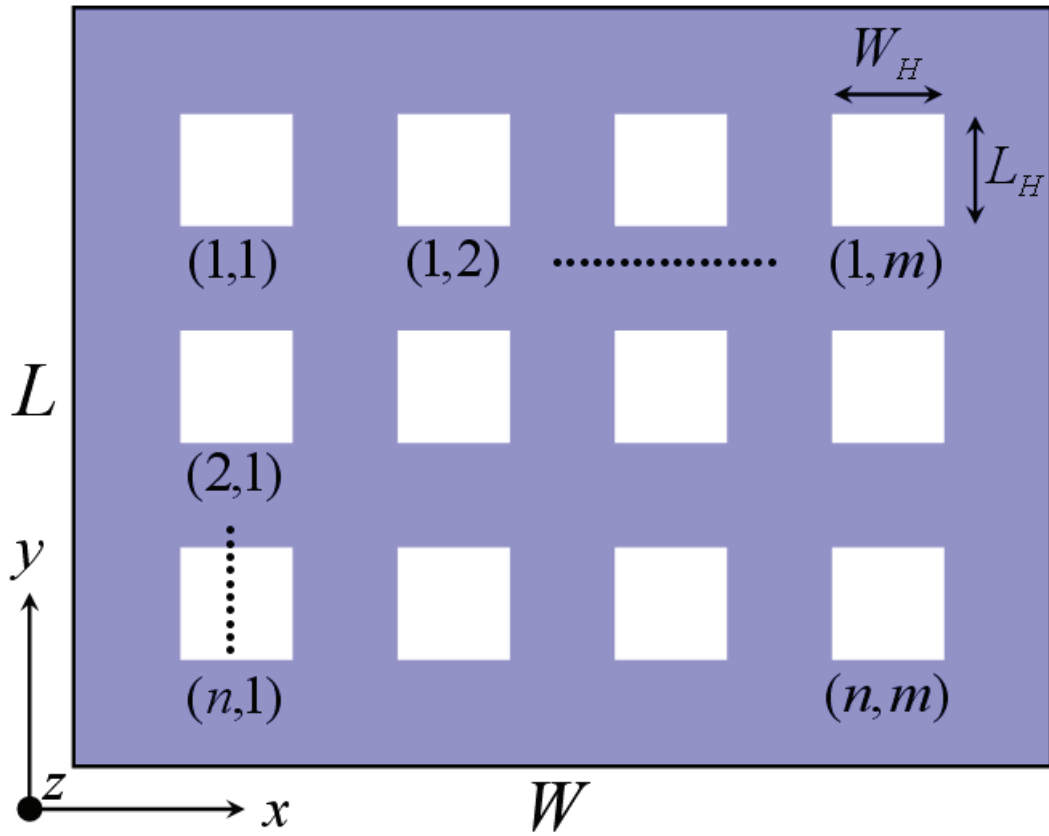


Figure 3.21: Plate schematic with holes. Holes are supposed to be  $m$  along  $x$  and  $n$  along  $y$  local axis.

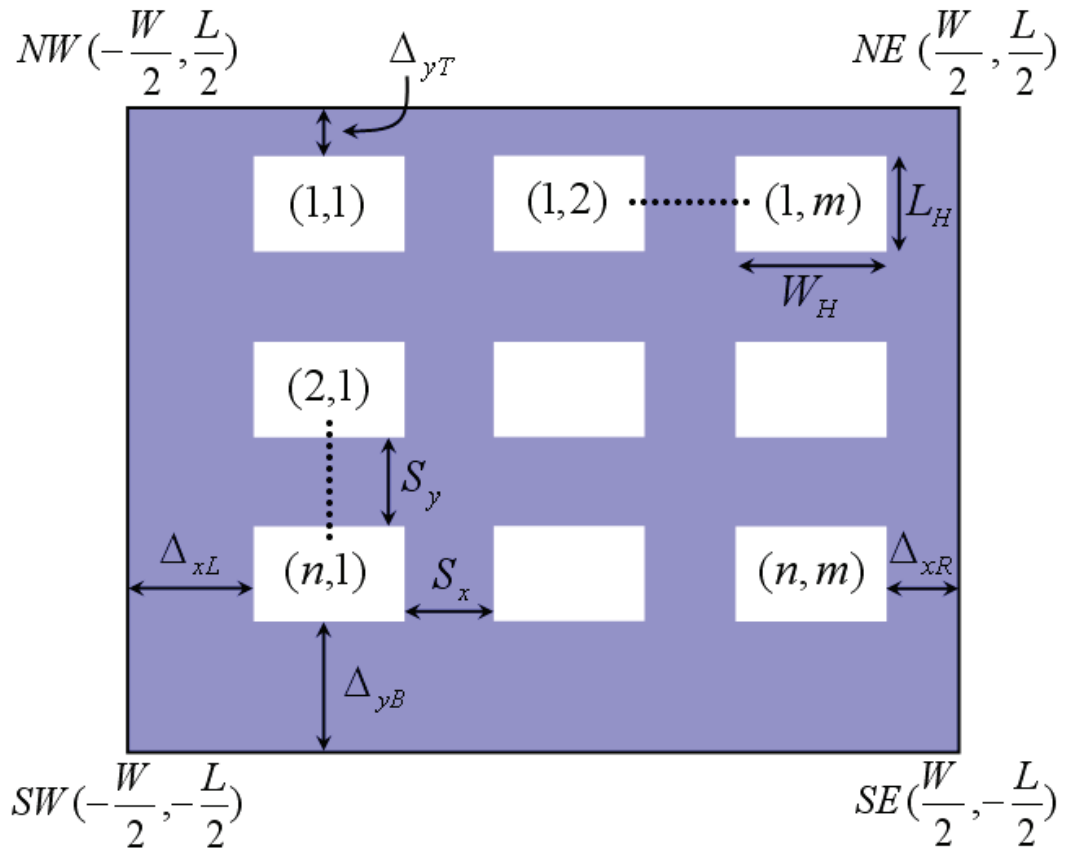


Figure 3.22: 6 DoF's plate schematic with holes. Differently from the 4 DoF's case, each hole gives a different contribution to the electric magnitudes depending on its position.

Given these four parameters, the spacing between adjacent holes along  $x$  and  $y$  local axes, respectively addressed by  $S_x$  and  $S_y$ , are derived as follows:

$$S_x = \frac{W - \Delta_{xL} - \Delta_{xR} - W_H m}{m - 1} \quad (3.152)$$

$$S_y = \frac{L - \Delta_{yT} - \Delta_{yB} - L_H n}{n - 1} \quad (3.153)$$

Now, the holes contribution to the electrical magnitudes is calculated by integrating on the area of each hole in the local coordinates  $x, y$ . By exploiting two indexes  $i, j$  it is possible to sweep the whole plate area and integrate only on the holes area. To do this, a double sum must be introduced in the integral formulas of the capacitance, electrostatic force and torques. Let us now rewrite the equations 3.143 - 3.146 replacing denominators with the 3.137. Their expression taking into accounts the holes contribution becomes:

$$C_{AIR} = \frac{\varepsilon_{AIR}}{\sigma_{Arc}} \left[ \int_{-\frac{W}{2}}^{\frac{W}{2}} \int_{-\frac{L}{2}}^{\frac{L}{2}} \frac{dxdy}{Z_P} - \sum_{i=0}^{m-1} \sum_{j=0}^{n-1} \int_{a^{(i)}}^{b^{(i)}} \int_{c^{(j)}}^{d^{(j)}} \frac{dxdy}{Z_P} \right] \quad (3.154)$$

$$F_{z_{EL}} = \frac{1}{2} \frac{\varepsilon_{AIR} V_{AIR}^2}{\sigma_{Arc}^2} \left[ \int_{-\frac{W}{2}}^{\frac{W}{2}} \int_{-\frac{L}{2}}^{\frac{L}{2}} \frac{dxdy}{Z_P^2} - \sum_{i=0}^{m-1} \sum_{j=0}^{n-1} \int_{a^{(i)}}^{b^{(i)}} \int_{c^{(j)}}^{d^{(j)}} \frac{dxdy}{Z_P^2} \right] \quad (3.155)$$

$$T_{\theta_{x_{EL}}} = \frac{1}{2} \frac{\varepsilon_{AIR} V_{AIR}^2}{\sigma_{Arc}^2} \left[ \int_{-\frac{W}{2}}^{\frac{W}{2}} \int_{-\frac{L}{2}}^{\frac{L}{2}} \frac{y_P}{Z_P^2} dxdy - \sum_{i=0}^{m-1} \sum_{j=0}^{n-1} \int_{a^{(i)}}^{b^{(i)}} \int_{c^{(j)}}^{d^{(j)}} \frac{y_P}{Z_P^2} dxdy \right] \quad (3.156)$$

$$T_{\theta_{y_{EL}}} = \frac{1}{2} \frac{\varepsilon_{AIR} V_{AIR}^2}{\sigma_{Arc}^2} \left[ \int_{-\frac{W}{2}}^{\frac{W}{2}} \int_{-\frac{L}{2}}^{\frac{L}{2}} \frac{x_P}{Z_P^2} dxdy - \sum_{i=0}^{m-1} \sum_{j=0}^{n-1} \int_{a^{(i)}}^{b^{(i)}} \int_{c^{(j)}}^{d^{(j)}} \frac{x_P}{Z_P^2} dxdy \right] \quad (3.157)$$

In previous equations the integral indexes  $a(i)$ ,  $b(i)$ ,  $c(j)$  and  $d(j)$  are expressed as follows:

$$a(i) = -\frac{W}{2} + \Delta_{xL} + i(W_H + S_x) \quad (3.158)$$

$$b(i) = -\frac{W}{2} + \Delta_{xL} + i(W_H + S_x) + W_H \quad (3.159)$$

$$c(j) = \frac{L}{2} - \Delta_{yT} - L_H - j(L_H + S_y) \quad (3.160)$$

$$d(j) = \frac{L}{2} - \Delta_{yT} - j(L_H + S_y) \quad (3.161)$$

Finally, the  $C_{OX}$  expression to be associated to the 3.154 in order to get the total capacitance  $C$  is the 3.150. Plate as well as holes edges introduce boundary effect due to distortion of electric field lines (i.e. fringing) that must be taken into account in order to get an accurate prediction of the electrical effects associated to the rigid plate. This is what is going to be discussed in the following sections.



### 3.6 Electrostatic Model for the Fringing Effect

To complete the electrostatic model for the rigid plate the fringing effect must be taken into account. This is due to the distortion of the electric field lines nearby the boundaries of the plate [35]. Figure 3.23 shows the bent field lines due to fringing effect close to the edges of two parallel plates. These give a contribution of capacitance and electrostatic force which is rather small when the plate dimensions are large and the gap in between the two electrodes is very small so that some Authors decided not to include the fringing effect in their models [32]. However, in order to get an electrostatic model suitable even for more general cases with larger gaps and holes on plate surface we decided to include it in our model. Several approaches to face this issue are available in literature, ranging from fully-empirical to fully-analytical solutions [36] [37].

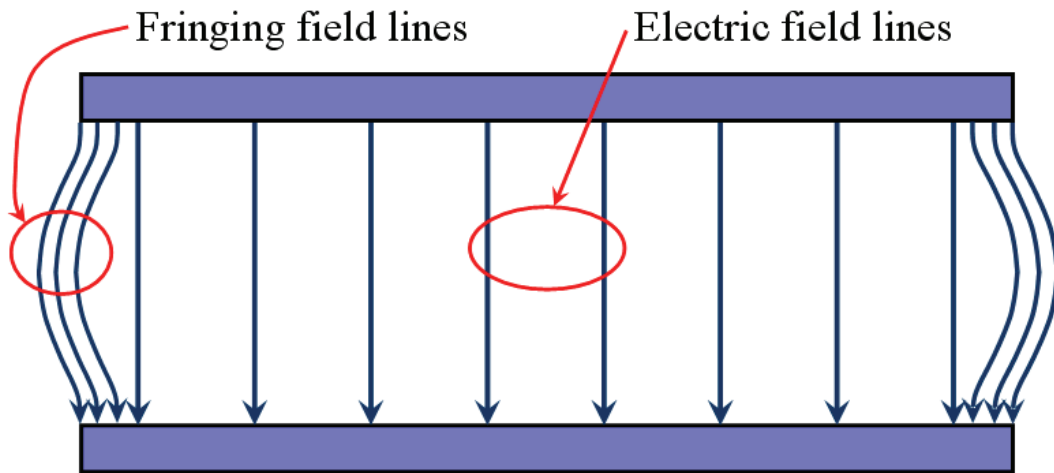


Figure 3.23: Fringing field lines behaviour nearby the edges of the two plates.

The solution we propose is *semi-analytical*. This means it is based on a rather simple analytical model and includes a few empirically determined parameters in order to get an accurate prediction of the fringing effect on a wide range of topologies (i.e. gap, plate features, etc.) on one side, and a light software implementation on the other side. Moreover, the proposed model considers two different fringing contributions which are kept separated. The first is due to the  $xy$  in-plane boundary effects nearby plate edges and is discussed in this section.



Whereas, the second one comes from plate vertical faces when its orientation angles assume non-zero values and is discussed in next section. First of all we determine the proper curvature of the fringing field lines by means of a coefficient  $\gamma$  as shown in Figure 3.24. The coefficient  $\gamma$  swings within the interval  $]0, 1]$ . When  $\gamma = 1$  the fringing line  $ArcF_P$  is half a circumference with diameter  $Z_P$  while when  $\gamma \rightarrow 0$  then  $ArcF_P \rightarrow Z_P$  (see Figure 3.24). The proper value for  $\gamma$  is determined empirically by means of FEM simulations as it will be shown later. Given  $\gamma$ , with simple trigonometric considerations, not shown here, it is possible to determine the coefficient  $\sigma_{ArcF}$  as follows:

$$\sigma_{ArcF} = \frac{1 + \gamma^2}{2\gamma} \arcsin\left(\frac{2\gamma}{1 + \gamma^2}\right) \quad (3.162)$$

by means of what the fringing field arc length is:

$$ArcF_P = \sigma_{ArcF} Z_P \quad (3.163)$$

Once  $ArcF_P$  is determined, another coefficient must be introduced. This is  $\zeta$  and it represents the in-plane depth in which the fringing field is supposed to act, as shown in Figure 3.25. Furthermore,  $\zeta$  will also be empirically determined via FEM simulations. Finally, it is possible to determine the fringing contribution to the capacitance and electrostatic force by determining their value per unit length on each edge and then multiplying them by  $\zeta$ . Let us start from the 4 DoF's plate case. The total capacitance and electrostatic force also including the fringing effect of Figure 3.25 are expressed rewriting the 3.110 and 3.117 as:

$$C_{AIR} = \varepsilon_{AIR} \left[ \frac{WL}{(Z_{AIR} + Z_{CM_{INST}})} + \frac{\zeta(2W + 2L)}{\sigma_{ArcF}(Z_{AIR} + Z_{CM_{INST}})} \right] \quad (3.164)$$

$$F_{Z_{EL}} = \frac{1}{2} \varepsilon_{AIR} V_{AIR}^2 \left[ \frac{WL}{(Z_{AIR} + Z_{CM_{INST}})^2} + \frac{\zeta(2W + 2L)}{\sigma_{ArcF}^2 (Z_{AIR} + Z_{CM_{INST}})^2} \right] \quad (3.165)$$

where the second term of second member represents respectively the fringing capacitance and the fringing electrostatic force.

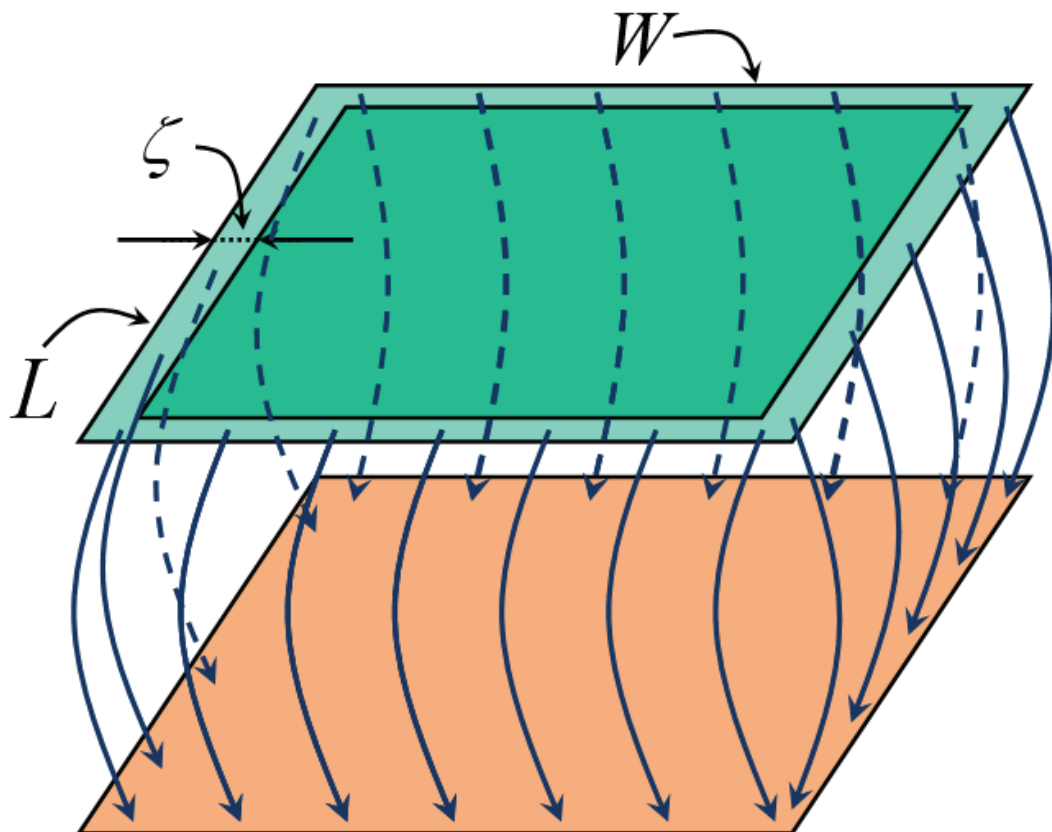


Figure 3.25: The fringing field lines are supposed to be confined within a *belt* wide  $\zeta$  starting from the four plate edges.

In case there are holes on plate surface, we apply the same approach to each hole. Thus, there is a region with  $\zeta$  width around the four edges of each hole within which the fringing field is supposed to be confined [38]. In this case, the 3.149 and 3.151, also including the fringing term of 3.164 and 3.165, can be expressed as follows:

$$\begin{aligned}
C_{AIR} &= \varepsilon_{AIR} \frac{WL}{(Z_{AIR} + Z_{CM_{INST}})} \\
&- \varepsilon_{AIR} \frac{A_{Holes}}{(Z_{AIR} + Z_{CM_{INST}})} \\
&+ \varepsilon_{AIR} \frac{\zeta(2W + 2L)}{\sigma_{ArcF}(Z_{AIR} + Z_{CM_{INST}})} \\
&+ \varepsilon_{AIR} \frac{\zeta(2W_H + 2L_H)mn}{\sigma_{ArcF}(Z_{AIR} + Z_{CM_{INST}})} \tag{3.166}
\end{aligned}$$

$$\begin{aligned}
F_{Z_{EL}} &= \frac{1}{2} \varepsilon_{AIR} V_{AIR}^2 \frac{WL}{(Z_{AIR} + Z_{CM_{INST}})^2} \\
&- \frac{1}{2} \varepsilon_{AIR} V_{AIR}^2 \frac{A_{Holes}}{(Z_{AIR} + Z_{CM_{INST}})^2} \\
&+ \frac{1}{2} \varepsilon_{AIR} V_{AIR}^2 \frac{\zeta(2W + 2L)}{\sigma_{ArcF}^2(Z_{AIR} + Z_{CM_{INST}})^2} \\
&+ \frac{1}{2} \varepsilon_{AIR} V_{AIR}^2 \frac{\zeta(2W_H + 2L_H)mn}{\sigma_{ArcF}^2(Z_{AIR} + Z_{CM_{INST}})^2} \tag{3.167}
\end{aligned}$$

When dealing with the 6 DoF's model the fringing contributions have to be determined for each edge separately because, as already pointed out earlier, each point on plate surface has a unique distance from the substrate. The fringing capacitance and electrostatic force per unit length is calculated on each of four plate edges and then multiplied by  $\zeta$ . Concerning the latter, it is supposed to be small enough to make negligible the vertical distance variations within it. In other words, the  $Z_P$  of each point along an edge is supposed to be constant moving inward on plate area for a distance equal to  $\zeta$ . Given this assumption, we now proceed to calculate the fringing capacitance and electrostatic force referring to the four plate edges starting from the lower

one and proceeding clockwise:  $SW - SE$ ,  $SE - NE$ ,  $NE - NW$  and finally  $NW - SW$ . Looking at Figure 3.3 it results:

$$y_{(SW-SE)} = -\frac{L}{2} \quad (3.168)$$

$$x_{(SE-NE)} = +\frac{W}{2} \quad (3.169)$$

$$y_{(NE-NW)} = +\frac{L}{2} \quad (3.170)$$

$$x_{(NW-SW)} = -\frac{W}{2} \quad (3.171)$$

By exploiting the 3.137 in which we express the dependence on the local coordinates  $(x, y, z)$  of each point (that comes in the 3.119), it is possible to rewrite the 3.143 and 3.144 as follows:

$$\begin{aligned}
C_{AIR} &= \frac{\varepsilon_{AIR}}{\sigma_{Arc}} \int_{-\frac{W}{2}}^{\frac{W}{2}} \int_{-\frac{L}{2}}^{\frac{L}{2}} \frac{dx dy}{Z_P(x, y, -\frac{T}{2})} \\
&+ \zeta \left( \frac{\varepsilon_{AIR}}{\sigma_{ArcF}} \int_{-\frac{W}{2}}^{\frac{W}{2}} \frac{dx}{Z_P(x, -\frac{L}{2}, -\frac{T}{2})} \right) \\
&+ \zeta \left( \frac{\varepsilon_{AIR}}{\sigma_{ArcF}} \int_{-\frac{L}{2}}^{\frac{L}{2}} \frac{dy}{Z_P(\frac{W}{2}, y, -\frac{T}{2})} \right) \\
&+ \zeta \left( \frac{\varepsilon_{AIR}}{\sigma_{ArcF}} \int_{-\frac{W}{2}}^{\frac{W}{2}} \frac{dx}{Z_P(x, \frac{L}{2}, -\frac{T}{2})} \right) \\
&+ \zeta \left( \frac{\varepsilon_{AIR}}{\sigma_{ArcF}} \int_{-\frac{L}{2}}^{\frac{L}{2}} \frac{dy}{Z_P(-\frac{W}{2}, y, -\frac{T}{2})} \right) \tag{3.172}
\end{aligned}$$

$$\begin{aligned}
F_{zEL} &= \frac{1}{2} \frac{\varepsilon_{AIR} V_{AIR}^2}{\sigma_{Arc}^2} \int_{-\frac{W}{2}}^{\frac{W}{2}} \int_{-\frac{L}{2}}^{\frac{L}{2}} \frac{dx dy}{Z_P(x, y, -\frac{T}{2})^2} \\
&+ \zeta \left( \frac{1}{2} \frac{\varepsilon_{AIR} V_{AIR}^2}{\sigma_{ArcF}^2} \int_{-\frac{W}{2}}^{\frac{W}{2}} \frac{dx}{Z_P(x, -\frac{L}{2}, -\frac{T}{2})^2} \right) \\
&+ \zeta \left( \frac{1}{2} \frac{\varepsilon_{AIR} V_{AIR}^2}{\sigma_{ArcF}^2} \int_{-\frac{L}{2}}^{\frac{L}{2}} \frac{dy}{Z_P(\frac{W}{2}, y, -\frac{T}{2})^2} \right) \\
&+ \zeta \left( \frac{1}{2} \frac{\varepsilon_{AIR} V_{AIR}^2}{\sigma_{ArcF}^2} \int_{-\frac{W}{2}}^{\frac{W}{2}} \frac{dx}{Z_P(x, \frac{L}{2}, -\frac{T}{2})^2} \right) \\
&+ \zeta \left( \frac{1}{2} \frac{\varepsilon_{AIR} V_{AIR}^2}{\sigma_{ArcF}^2} \int_{-\frac{L}{2}}^{\frac{L}{2}} \frac{dy}{Z_P(-\frac{W}{2}, y, -\frac{T}{2})^2} \right) \tag{3.173}
\end{aligned}$$

To complete the fringing effect we now introduce the contribution due to the holes for a 6 DoF's rigid plate. With a similar approach to the one just presented, we consider the contribution of all the bottom, right, top and left edges of the holes. More in details, in next formulas holes are treated row by row for the bottom and top edges, and column by column for the right and left edges. Thus, the 3.154 3.155, also taking into account the 3.172 and 3.173, can be written as follows:

$$\begin{aligned}
C_{AIR} = & \frac{\varepsilon_{AIR}}{\sigma_{Arc}} \int_{-\frac{W}{2}}^{\frac{W}{2}} \int_{-\frac{L}{2}}^{\frac{L}{2}} \frac{dxdy}{Z_P(x, y, -\frac{T}{2})} \\
& - \frac{\varepsilon_{AIR}}{\sigma_{Arc}} \sum_{i=0}^{m-1} \sum_{j=0}^{n-1} \int_{a(i)}^{b(i)} \int_{c(j)}^{d(j)} \frac{dxdy}{Z_P(x, y, -\frac{T}{2})} \\
& + \zeta \left( \frac{\varepsilon_{AIR}}{\sigma_{ArcF}} \int_{-\frac{W}{2}}^{\frac{W}{2}} \frac{dx}{Z_P(x, -\frac{L}{2}, -\frac{T}{2})} \right) \\
& + \zeta \left( \frac{\varepsilon_{AIR}}{\sigma_{ArcF}} \int_{-\frac{L}{2}}^{\frac{L}{2}} \frac{dy}{Z_P(\frac{W}{2}, y, -\frac{T}{2})} \right) \\
& + \zeta \left( \frac{\varepsilon_{AIR}}{\sigma_{ArcF}} \int_{-\frac{W}{2}}^{\frac{W}{2}} \frac{dx}{Z_P(x, \frac{L}{2}, -\frac{T}{2})} \right) \\
& + \zeta \left( \frac{\varepsilon_{AIR}}{\sigma_{ArcF}} \int_{-\frac{L}{2}}^{\frac{L}{2}} \frac{dy}{Z_P(-\frac{W}{2}, y, -\frac{T}{2})} \right) \\
& + \zeta \left( \frac{\varepsilon_{AIR}}{\sigma_{ArcF}} \sum_{i=0}^{m-1} \sum_{j=0}^{n-1} \int_{a(i)}^{b(i)} \frac{dx}{Z_P(x, c(j), -\frac{T}{2})} \right) \\
& + \zeta \left( \frac{\varepsilon_{AIR}}{\sigma_{ArcF}} \sum_{i=0}^{m-1} \sum_{j=0}^{n-1} \int_{c(j)}^{d(j)} \frac{dy}{Z_P(b(i), y, -\frac{T}{2})} \right) \\
& + \zeta \left( \frac{\varepsilon_{AIR}}{\sigma_{ArcF}} \sum_{i=0}^{m-1} \sum_{j=0}^{n-1} \int_{a(i)}^{b(i)} \frac{dx}{Z_P(x, d(j), -\frac{T}{2})} \right) \\
& + \zeta \left( \frac{\varepsilon_{AIR}}{\sigma_{ArcF}} \sum_{i=0}^{m-1} \sum_{j=0}^{n-1} \int_{c(j)}^{d(j)} \frac{dy}{Z_P(a(i), y, -\frac{T}{2})} \right) \tag{3.174}
\end{aligned}$$



$$\begin{aligned}
F_{z_{EL}} &= \frac{1}{2} \frac{\varepsilon_{AIR} V_{AIR}^2}{\sigma_{Arc}^2} \int_{-\frac{W}{2}}^{\frac{W}{2}} \int_{-\frac{L}{2}}^{\frac{L}{2}} \frac{dxdy}{Z_P(x, y, -\frac{T}{2})^2} \\
&- \frac{1}{2} \frac{\varepsilon_{AIR} V_{AIR}^2}{\sigma_{Arc}^2} \sum_{i=0}^{m-1} \sum_{j=0}^{n-1} \int_{a(i)}^{b(i)} \int_{c(j)}^{d(j)} \frac{dxdy}{Z_P(x, y, -\frac{T}{2})^2} \\
&+ \zeta \left( \frac{1}{2} \frac{\varepsilon_{AIR} V_{AIR}^2}{\sigma_{ArcF}^2} \int_{-\frac{W}{2}}^{\frac{W}{2}} \frac{dx}{Z_P(x, -\frac{L}{2}, -\frac{T}{2})^2} \right) \\
&+ \zeta \left( \frac{1}{2} \frac{\varepsilon_{AIR} V_{AIR}^2}{\sigma_{ArcF}^2} \int_{-\frac{L}{2}}^{\frac{L}{2}} \frac{dy}{Z_P(\frac{W}{2}, y, -\frac{T}{2})^2} \right) \\
&+ \zeta \left( \frac{1}{2} \frac{\varepsilon_{AIR} V_{AIR}^2}{\sigma_{ArcF}^2} \int_{-\frac{W}{2}}^{\frac{W}{2}} \frac{dx}{Z_P(x, \frac{L}{2}, -\frac{T}{2})^2} \right) \\
&+ \zeta \left( \frac{1}{2} \frac{\varepsilon_{AIR} V_{AIR}^2}{\sigma_{ArcF}^2} \int_{-\frac{L}{2}}^{\frac{L}{2}} \frac{dy}{Z_P(-\frac{W}{2}, y, -\frac{T}{2})^2} \right) \\
&+ \zeta \left( \frac{1}{2} \frac{\varepsilon_{AIR} V_{AIR}^2}{\sigma_{ArcF}^2} \sum_{i=0}^{m-1} \sum_{j=0}^{n-1} \int_{a(i)}^{b(i)} \frac{dx}{Z_P(x, c(j), -\frac{T}{2})^2} \right) \\
&+ \zeta \left( \frac{1}{2} \frac{\varepsilon_{AIR} V_{AIR}^2}{\sigma_{ArcF}^2} \sum_{i=0}^{m-1} \sum_{j=0}^{n-1} \int_{c(j)}^{d(j)} \frac{dy}{Z_P(b(i), y, -\frac{T}{2})^2} \right) \\
&+ \zeta \left( \frac{1}{2} \frac{\varepsilon_{AIR} V_{AIR}^2}{\sigma_{ArcF}^2} \sum_{i=0}^{m-1} \sum_{j=0}^{n-1} \int_{a(i)}^{b(i)} \frac{dx}{Z_P(x, d(j), -\frac{T}{2})^2} \right) \\
&+ \zeta \left( \frac{1}{2} \frac{\varepsilon_{AIR} V_{AIR}^2}{\sigma_{ArcF}^2} \sum_{i=0}^{m-1} \sum_{j=0}^{n-1} \int_{c(j)}^{d(j)} \frac{dy}{Z_P(a(i), y, -\frac{T}{2})^2} \right) \quad (3.175)
\end{aligned}$$

The electrostatic force due to the fringing field has been assumed not large enough to give a significant contribution in terms of torques. This is the reason why there are not expressions like the 3.175 corresponding to the 3.156 and 3.157.

### 3.6.1 Fringing Effect on Plate Vertical Faces

The very last effect to be accounted for is the definition of capacitance and electrostatic force due to the plate vertical faces when  $\theta_X$  and (or)  $\theta_Y$  have non-zero values. This is also considered as a fringing effect as it is not dominant on the final capacitance and electrostatic force values. Moreover, for its nature, this contribution is applied only to the 6 DoF's plate model. The case of  $\theta_X = 0$  and  $\theta_Y > 0$  is shown in Figure 3.26.

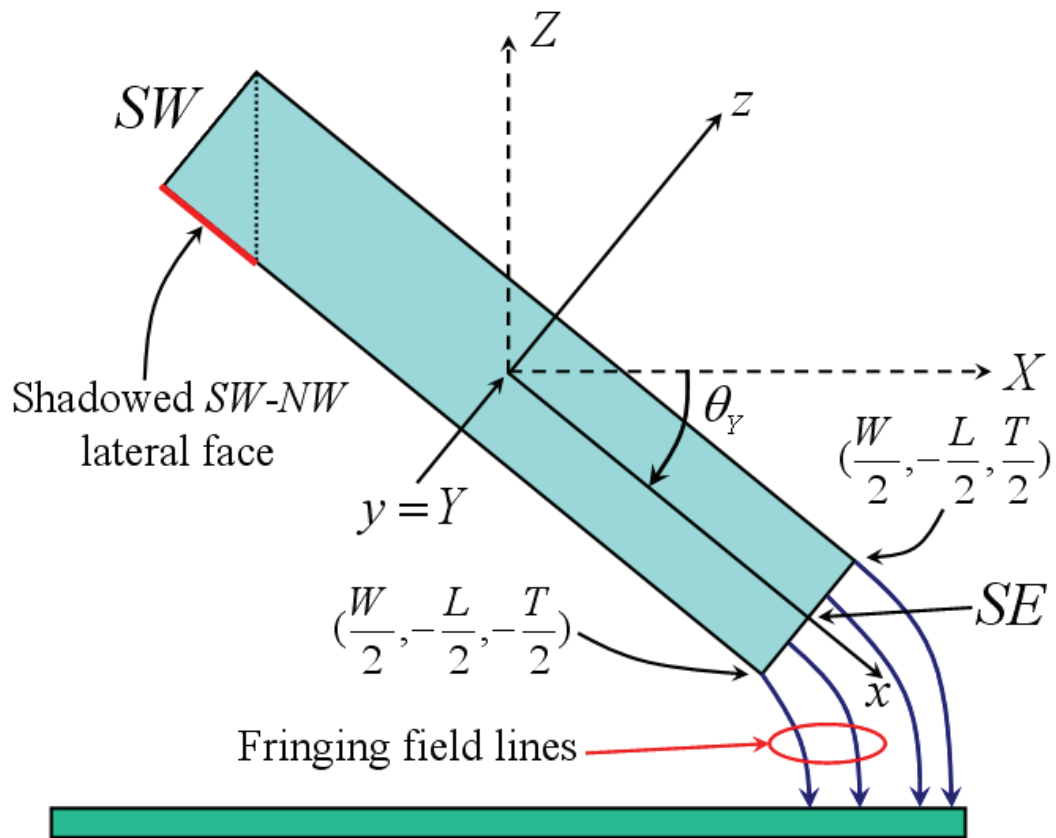


Figure 3.26: Fringing effect due to the vertical faces when  $\theta_Y > 0$ . The SW – NW vertical face is shadowed by the lower plate surface.

The  $SE - NE$  vertical face, i.e. between the  $SE$  and  $NE$  nodes, is exposed to the underneath electrode and consequently it gives a contribution to the electrical magnitudes. On the other hand, the  $SW - NW$  vertical face is shadowed by the lower plate face and consequently its area is not exposed to the substrate. Of course, the other two faces ( $SW - SE$  and  $NW - NE$ ) do not contribute to the capacitance and electrostatic force because when  $\theta_X = 0$  these are perpendicular to the lower electrode. Whereas, the case of either  $\theta_X > 0$  and  $\theta_Y > 0$  is depicted in Figure 3.27.

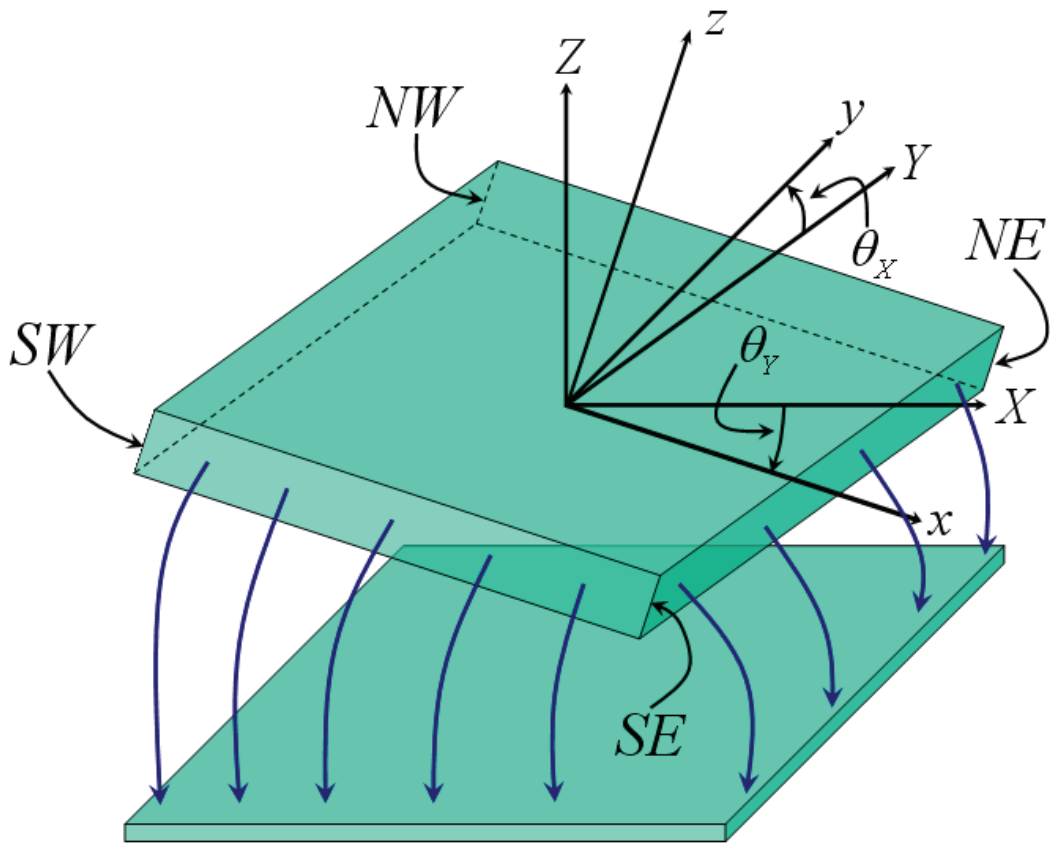


Figure 3.27: Fringing effect due to the vertical faces when  $\theta_X > 0$  and  $\theta_Y > 0$ . The  $SW - NW$  and  $NW - NE$  vertical faces are shadowed by the lower plate surface.

In this case, the  $SW - NW$  and  $NW - NE$  vertical faces are shadowed by the lower plate surface while the other two contribute to the fringing field. Before introducing the mathematical formulation for the capacitance and electrostatic force contributions of vertical faces, let us summarize which face (faces) is (are) involved in the fringing depending on the orientation angles. In table 3.1, depending on all the possible combinations of  $\theta_X$  and  $\theta_Y$ , the face (faces) contributing to the fringing and the others shadowed are listed. Moreover, for each vertical face that generates fringing effects, the direction of  $x$  or  $y$  local axes (positive or negative) along which the electrostatic force acts is reported.

$\theta_X$	$\theta_Y$	$SW - SE$	$SE - NE$	$NE - NW$	$NW - SW$	$x$	$y$
= 0	= 0	Shadowed	Shadowed	Shadowed	Shadowed	No	No
> 0	= 0	Fringing	Shadowed	Shadowed	Shadowed	No	-
< 0	= 0	Shadowed	Shadowed	Fringing	Shadowed	No	+
= 0	> 0	Shadowed	Fringing	Shadowed	Shadowed	+	No
> 0	> 0	Fringing	Fringing	Shadowed	Shadowed	+	-
< 0	> 0	Shadowed	Fringing	Fringing	Shadowed	+	+
= 0	< 0	Shadowed	Shadowed	Shadowed	Fringing	-	No
> 0	< 0	Fringing	Shadowed	Shadowed	Fringing	-	-
< 0	< 0	Shadowed	Shadowed	Fringing	Fringing	-	+

Table 3.1: For each vertical face it is reported if it gives or not contribution to the fringing depending on the value of  $\theta_X$  and  $\theta_Y$  as well as whether the electrostatic force is directed along the positive or negative  $x$  and  $y$  local axes.

Let us refer now to the case of  $\theta_X > 0$  and  $\theta_Y > 0$ . We will proceed to calculate the capacitance and electrostatic force due to the fringing on the  $SW - SE$  and  $SE - NE$  vertical faces. Concerning the capacitance, these two contributions are called  $C_{AIR(SW-SE)}$  and  $C_{AIR(SE-NE)}$  respectively, and their expression is:

$$C_{AIR(SW-SE)} = \frac{\varepsilon_{AIR}}{\sigma_{ArcVF}} \int_{-\frac{W}{2}}^{\frac{W}{2}} \int_{-\frac{T}{2}}^{\frac{T}{2}} \frac{dx dz}{Z_P(x, -\frac{L}{2}, z)} \quad (3.176)$$

$$C_{AIR(SE-NE)} = \frac{\varepsilon_{AIR}}{\sigma_{ArcVF}} \int_{-\frac{L}{2}}^{\frac{L}{2}} \int_{-\frac{T}{2}}^{\frac{T}{2}} \frac{dy dz}{Z_P(\frac{W}{2}, y, z)} \quad (3.177)$$

where  $\sigma_{ArcVF}$  is a coefficient derived for the vertical faces with an approach similar to the one which led to the 3.141. The 3.176 and 3.177 must then be added to the 3.172. Let us now consider the electrostatic force. The two contributions of the  $SW - SE$  and  $SE - NE$  vertical faces are called  $F_{y(SW-SE)}$  and  $F_{x(SE-NE)}$  respectively, and their expression is:

$$F_{y(SW-SE)} = -\frac{1}{2} \frac{\varepsilon_{AIR} V_{AIR}^2}{\sigma_{ArcVF}^2} \int_{-\frac{W}{2}}^{\frac{W}{2}} \int_{-\frac{T}{2}}^{\frac{T}{2}} \frac{dx dz}{Z_P(x, -\frac{L}{2}, z)^2} \quad (3.178)$$

$$F_{x(SE-NE)} = +\frac{1}{2} \frac{\varepsilon_{AIR} V_{AIR}^2}{\sigma_{ArcVF}^2} \int_{-\frac{L}{2}}^{\frac{L}{2}} \int_{-\frac{T}{2}}^{\frac{T}{2}} \frac{dy dz}{Z_P(\frac{W}{2}, y, z)^2} \quad (3.179)$$

Notice that in 3.178 and 3.179 the proper sign of the force according to Table 3.1 has been already taken into account. Now,  $F_{y(SW-SE)}$  and  $F_{x(SE-NE)}$  have to be decomposed in the contribution along global  $X$ ,  $Y$  and  $Z$  axes called respectively  $F_{X(Fring)}$ ,  $F_{Y(Fring)}$  and  $F_{Z(Fring)}$ . Using the 2.8 it is:

$$F_{X(Fring)} = C_Y C_Z F_{x(SE-NE)} + (-C_X S_Z + S_X S_Y C_Z) F_{y(SW-SE)} \quad (3.180)$$

$$F_{Y(Fring)} = C_Y S_Z F_{x(SE-NE)} + (C_X C_Z + S_X S_Y S_Z) F_{y(SW-SE)} \quad (3.181)$$

$$F_{Z(Fring)} = -S_Y F_{x(SE-NE)} + S_X C_Y F_{y(SW-SE)} \quad (3.182)$$

Finally, the 3.180 - 3.182 must be added to the 3.126 - 3.128 in the centre of mass which become:

$$F_{X_{CM}} = -M A_{X_{CM}} - F_{X_{EL}} + F_{X(Fring)} \quad (3.183)$$

$$F_{Y_{CM}} = -M A_{Y_{CM}} + F_{Y_{EL}} + F_{Y(Fring)} \quad (3.184)$$

$$F_{Z_{CM}} = -M A_{Z_{CM}} + F_{Z_{TOUCH}} - F_{Z_{EL}} + F_{Z(Fring)} \quad (3.185)$$

Still referring to the case of  $\theta_X > 0$  and  $\theta_Y > 0$  let us now include the holes in our formulation. Applying the same considerations of Table 3.1 for the  $SW - SE$ ,  $SE - NE$ ,  $NE - NW$  and  $NW - SW$  plate edges to the holes bottom, right, top and left edges respectively and introducing  $C_{AIR(Bottom)}$  and  $C_{AIR(Right)}$  we get:

$$C_{AIR(Bottom)} = \frac{\varepsilon_{AIR}}{\sigma_{ArcVF}} \sum_{i=0}^{m-1} \sum_{j=0}^{n-1} \int_{a(i)}^{b(i)} \int_{-\frac{T}{2}}^{\frac{T}{2}} \frac{dx dz}{Z_P(x, c(j), z)} \quad (3.186)$$

$$C_{AIR(Right)} = \frac{\varepsilon_{AIR}}{\sigma_{ArcVF}} \sum_{i=0}^{m-1} \sum_{j=0}^{n-1} \int_{c(j)}^{d(j)} \int_{-\frac{T}{2}}^{\frac{T}{2}} \frac{dy dz}{Z_P(b(i), y, z)} \quad (3.187)$$

The 3.186 and 3.187, together with the 3.176 and 3.177, added to the 3.174 give the total capacitance accounting for all the effects. Introducing a similar formulation for the electrostatic force we have:

$$F_{y(Bottom)} = -\frac{1}{2} \frac{\varepsilon_{AIR} V_{AIR}^2}{\sigma_{ArcVF}^2} \sum_{i=0}^{m-1} \sum_{j=0}^{n-1} \int_{a(i)}^{b(i)} \int_{-\frac{T}{2}}^{\frac{T}{2}} \frac{dx dz}{Z_P(x, c(j), z)^2} \quad (3.188)$$

$$F_{x(Right)} = \frac{1}{2} \frac{\varepsilon_{AIR} V_{AIR}^2}{\sigma_{ArcVF}^2} \sum_{i=0}^{m-1} \sum_{j=0}^{n-1} \int_{c(j)}^{d(j)} \int_{-\frac{T}{2}}^{\frac{T}{2}} \frac{dy dz}{Z_P(b(i), y, z)^2} \quad (3.189)$$

The 3.180 - 3.182 become:

$$\begin{aligned}
F_{X(Fring)} &= C_Y C_Z (F_{x(SE-NE)} + F_{x(Bottom)}) \\
&+ (-C_X S_Z + S_X S_Y C_Z) (F_{y(SW-SE)} + F_{y(Bottom)}) \quad (3.190)
\end{aligned}$$

$$\begin{aligned}
F_{Y(Fring)} &= C_Y S_Z (F_{x(SE-NE)} + F_{x(Bottom)}) \\
&+ (C_X C_Z + S_X S_Y S_Z) (F_{y(SW-SE)} + F_{y(Bottom)}) \quad (3.191)
\end{aligned}$$

$$\begin{aligned}
F_{Z(Fring)} &= -S_Y (F_{x(SE-NE)} + F_{x(Bottom)}) \\
&+ S_X C_Y (F_{y(SW-SE)} + F_{y(Bottom)}) \quad (3.192)
\end{aligned}$$

Eventually, the 3.190 - 3.192 contribute to the 3.183 - 3.185 in the centre of mass as already shown before.

The effectiveness of the fringing model related to the holes on rigid plate surface will be proven in the section referred to the validation at the end of this chapter.

## 3.7 Viscous Damping Model

Another physical effect related to the plate when it is moving within a fluid, e.g. air, is the viscous damping. This is related to the viscosity of the media within which the body is immersed, as its particles hit the moving structure. Moreover, the viscous damping force depends also on the velocity of the body which is moving within the viscous fluid [39].

In our plate model we distinguish two contributions of the viscous damping. One is due to the vertical movement of the plate and relies on the so-called squeeze-film damping theory, based on the assumption that the fluid is incompressible [34]. On the other hand, the second contribution is given by the in-plane ( $xy$  directions) movement of the plate and is based on the Couette-type damping theory, which employs a laminar flow regime [40].

### 3.7.1 Squeeze-Film Viscous Damping for the Rigid Plate with Holes

The squeeze-film damping model for a rigid plate with holes on its surface which is vertically moving is based on the approach proposed by Bao et Al. [41]. This exploits a modified Reynolds equation which accounts for the presence of openings on plate area. The solution refers to a plate which is parallel to the substrate and the total viscous damping force which counteracts the plate  $z$  motion is:

$$F_{ZVD} = -4Rl^2 \left( \frac{W}{2} - l \right) \left( \frac{L}{2} - l \right) \quad (3.193)$$

where  $R$  represents the resistance of the viscous means which surrounds the moving plate and its expression follows:

$$R = \frac{12\mu}{(Z_{AIR})^3} V_{ZCM} \quad (3.194)$$

In equation 3.194,  $\mu$  is the viscosity of the fluid,  $V_{ZCM}$  is the centre of mass velocity along  $Z$  axis. Whereas,  $l$  is the following form factor:

$$l = \sqrt{\frac{2T(Z_{AIR})^3\eta(\beta)}{3\beta^2 \left( \frac{l_{hole}}{\sqrt{\pi}} \right)^2}} \quad (3.195)$$



In the 3.195 there are two non-dimensional parameters whose expression are:

$$\eta(\beta) = \left( 1 + \frac{3 \left( \frac{l_{hole}}{\sqrt{\pi}} \right)^4 K(\beta)}{16T(Z_{AIR})^3} \right) \quad (3.196)$$

$$K(\beta) = 4\beta^2 - \beta^4 - 4ln\beta - 3 \quad (3.197)$$

where  $\beta$  is the ratio of the hole radius over the radius of the cell containing it on plate surface:

$$\beta = \frac{r_{hole}}{r_{cell}} \quad (3.198)$$

Since we are dealing with squared or rectangular holes instead of circular ones, we have adapted the 3.198 to fit it to our model. Let us refer to the more generic case of rectangular holes. It is possible to write a relation in which the area of the circular hole is set equal to the area of the corresponding rectangular hole (see Figure 3.22). The same relation is then written for the cell surface. It results:

$$\pi(r_{hole})^2 = W_H L_H \quad (3.199)$$

and for the cell it is:

$$\pi(r_{cell})^2 = \frac{W L}{m n} \quad (3.200)$$

Deriving the expression of  $r_{hole}$  and  $r_{cell}$  from the 3.199 - 3.200 and replacing them into the 3.198 the latter becomes:

$$\beta = \sqrt{\frac{mnW_H L_H}{WL}} \quad (3.201)$$

These complete the description of Bao model applied to the 4 DoF's rigid plate model with holes on its surface. In must be stressed that this model has been developed for plates with one in-plane dimension (onto  $xy$  plane) larger than the other one. However, we assume it still valid in our case of interest where the two in-plane features of the plate have comparable value ( $W \sim L$ ). In the end, the viscous damping force of 3.193 must be applied to the force balance in the centre of mass along  $Z$  axis as already shown earlier in this chapter.

We also propose an extension of Bao model to describe the viscous damping effect related to the 6 DoF's rigid plate model. In this case we calculate the local vertical velocity of each cell containing one hole on plate surface. We assume a constant velocity over all the cell area and it is calculated in its middle point. This is the composition of three contributions. One is the velocity of the centre of mass along  $Z$  direction. The other two are tangential contribution and are determined by the angular velocity with which the plate rotates around the  $X$  and  $Y$  axes ( $\dot{\theta}_X$  and  $\dot{\theta}_Y$ ) multiplied by the arms referred to the point of interest on plate surface along  $y$  and  $x$  respectively. Given a generic point  $P$  on plate surface (with coordinates  $x_P, y_P$ ) its velocity along  $Z$  both accounting for the linear movement of the plate centre of mass and the tangential contributions is:

$$V_{Z_P}(x_P, y_P) = V_{Z_{CM}} - x_P \dot{\theta}_Y + y_P \dot{\theta}_X \quad (3.202)$$

In the  $P$  point coordinates we did not introduce the one along  $z$ , usually accounted in the electrostatic model earlier shown in this chapter. This is because we assume the displacement of  $-\frac{T}{2}$  (see Figure 3.15) to give a negligible contribution to the tangential velocity. Moreover, the vertical distance of the point  $P$  from the substrate is still defined as:

$$Z_P(x_P, y_P, z_P) = Z_{AIR} + Z_{CM_{INST}} + Z_{P_{INST}} \quad (3.203)$$

where  $Z_{P_{INST}}$  is defined by the 3.119. Assuming each cell containing an hole quasi-parallel to the substrate and also assuming a small velocity variation between adjacent cells, it is still possible to apply the boundary conditions of Bao model to the plate edges. Consequently, Bao model can be applied also on the plate surface discretized in sub-elements. Given this, the total viscous damping force directed along the local  $z$  axis of the plate can be expressed as follows:

$$F_{z_{VD}} = - \sum_{i=0}^{m-1} \sum_{j=0}^{n-1} \frac{V_{Z_P} \left( \left( -\frac{W}{2} + \frac{W}{m} \left( i + \frac{2}{2} \right) \right), \left( \frac{L}{2} - \frac{L}{n} \left( j + 1 - \frac{1}{2} \right) \right) \right)}{Z_P \left( \left( -\frac{W}{2} + \frac{W}{m} \left( i + \frac{2}{2} \right) \right), \left( \frac{L}{2} - \frac{L}{n} \left( j + 1 - \frac{1}{2} \right) \right), -\frac{T}{2} \right)^3} \Gamma \quad (3.204)$$

where  $\Gamma$  is expressed as follows:

$$\Gamma = 48\mu l^2 \left( \frac{W}{2m} - l \right) \left( \frac{L}{2n} - l \right) \quad (3.205)$$

in which the two parameters  $l$  and  $\eta(\beta)$ , expressed in the 3.195 and 3.196 respectively, are rewritten with  $Z_{AIR}$  replaced by  $Z_P$  with the same expression as at denominator of 3.204. With the same approach already shown before,  $F_{z_{VD}}$  is decomposed in its three contributions in global frame  $(X, Y, Z)$  and applied to the force balance on the centre of mass. Following a similar approach and exploiting the arms on the  $xy$  plane for each cell center point, the torques around the  $X$  and  $Y$  axes due to the viscous damping effect are derived and applied to the torques balance in the centre of mass as well. The latter contribution is not shown here.

### **Squeeze-Film Damping for the Rigid Plate without Holes**

Concerning the case of the rigid plate without holes a model which accounts for the viscous damping effect has been implemented as well. This is also based on the squeeze-film damping assumption but it represents just a first approach assessment of the viscous damping effect for the rigid plate. Indeed, it is based on the reduction of the Reynold equation in the case of a structure characterized by a length much larger than its width ( $L \gg W$ ). Despite in the case of the rigid plate it is  $L \sim W$ , we assume this model can be anyway applied in order to have a rough assessment of the viscous damping influence on the dynamic of this structures. However, since the simplified model mentioned above suits much better to the flexible beam, for which the condition  $L \gg W$  is fully satisfied, the squeeze-film damping model will be explained in details at the end of next chapter about the Euler beam. The total force counteracting the plate dynamic is expressed by the 4.178 and is applied in the centre of mass. Via a similar procedure, and employing the same assumptions stated for the extension of Bao model to the case of 6 DoF's, a viscous damping model for the rigid plate with non-zero orientation angles has been even implemented. The squeeze-film damping model for both the 4 and 6 DoF's rigid plate without holes are not shown in details here.

### 3.7.2 Viscous Damping Model for Lateral Movements

In the case of lateral plate movements on the  $xy$  plane and assuming a laminar behaviour of the fluid underneath the plate, its velocity distribution as the plate moves is reported in Figure 3.28. The fluid behaves as a linear slide-film damper and the viscous damping increases as the ratio of plate area over the distance from the substrate. This behaviour of the fluid is called Couette-type [40].

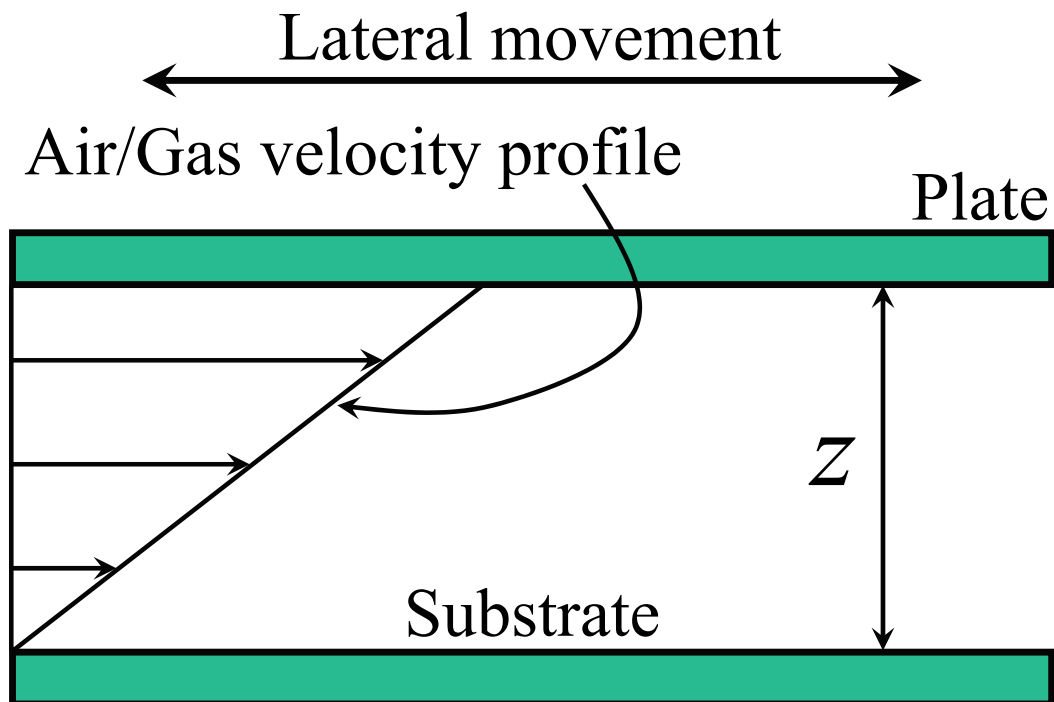


Figure 3.28: When the plate moves laterally the velocity distribution of the fluid underneath it is described by the Couette-type flow.

In the case of a 4 DoF's rigid plate the viscous damping force due to its movement along  $X$  and  $Y$  directions is then expressed as:

$$F_{X_{VD}} = -\mu \frac{LW}{Z_{AIR}} V_{X_{CM}} \quad (3.206)$$

$$F_{Y_{VD}} = -\mu \frac{LW}{Z_{AIR}} V_{Y_{CM}} \quad (3.207)$$

These formulas are supposed to be still valid for the 6 DoF's rigid plate as the orientation angles are assumed to be not large enough to introduce a significant variation on the behaviour of the lateral damping. Consequently, the Couette-type flow regime is assumed to be still valid.

These assumptions are compliant with the qualitative implementation of the viscous damping effect for the rigid plate proposed thus far. All the effects due to air layers on top of the rigid plate are neglected in this viscous damping implementation.

### 3.7.3 Effect of the Gas Molecules Mean Free Path

The viscous damping effect model has been completed taking into account the effect of gas rarefaction on it. Indeed, when the gap between the plate and substrate is small enough to be comparable with the mean free path of the fluid, the latter cannot be considered incompressible anymore [42]. This effect is counted in by replacing the constant value for the fluid viscosity  $\mu$  with an expression which depends on the vertical distance between the plate and the substrate. The expression proposed by Veijola et Al. [43] for the effective viscosity value is:

$$\mu_{eff}(z) = \frac{\mu}{1 + 9.638K_n^{1.159}} \quad (3.208)$$

where  $K_n$  is the Knudsen number defined as the ratio of the gas molecules mean free path  $\lambda$  over the vertical plate distance from the substrate  $z$ :

$$K_n = \frac{\lambda}{z} \quad (3.209)$$

When  $z$  is larger than  $\lambda$  the Knudsen number is very small and consequently  $\mu_{eff}(z)$  can be considered constant and equal to  $\mu$ . Differently, when  $z$  reduces more and more becoming comparable with the mean free path, the denominator of 3.208 becomes larger than 1 and eventually it is  $\mu_{eff}(z) < \mu$ . The 3.208 has to replace  $\mu$  in all equation for the vertical and lateral viscous damping previously shown.

### 3.8 Validation of the Rigid Plate Electrostatic Model

In this section the validation of the rigid plate model discussed so far is shown. Since the plate itself cannot move whether not connected to flexible structures (i.e. the Euler beam presented in next chapter) the validation of the only electrostatic model will be presented here. This is referred to static configurations of the plate in the space that do not imply any displacement. Complete structures for the extensive validation of the plate also including dynamic effects (inertia and viscous damping) will be introduced later throughout the thesis. First of all, the Cadence Virtuoso<sup>®</sup> Schematic of the 6 DoF's rigid plate is shown in Figure 3.29.

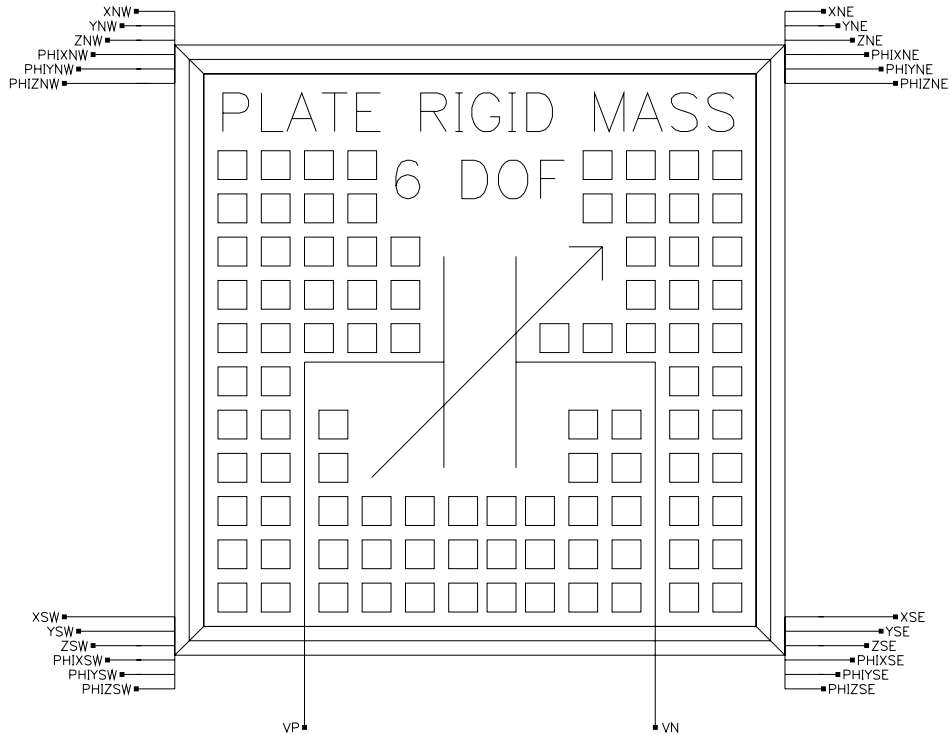


Figure 3.29: Cadence Virtuoso<sup>®</sup> Schematic of the 6 DoF's rigid plate. Six pins corresponding to the 6 DoF's to each node are visible as well as the two electrical pins to apply the control voltage.

Validation of the rigid plate electrostatic model is performed by running steady-state DC simulations in Cadence<sup>®</sup> [9]. The implemented rigid plate compact model includes the feature of making available the readout for the capacitance and electrostatic force values. The Cadence Virtuoso<sup>®</sup> Schematic for the validation is shown in Figure 3.30. The four vertexes are anchored to four elements which impose a mechanical constraint (see the subsequent mechanical constraint elements section and in particular the implementation of a fictitious minimum resistance). In this way the plate remains standing still even when the electrostatic attractive force acts on it. A voltage generator is connected to the left plate electrical node to apply the necessary biasing. Plate position in space with different orientation angles ( $\theta_{X_{INIT}}, \theta_{Y_{INIT}}, \theta_{Z_{INIT}}$ ) and geometrical features, e.g. without holes or with holes of different dimensions and distribution on its surface, can be easily modified within the Cadence Virtuoso<sup>®</sup> Schematic.

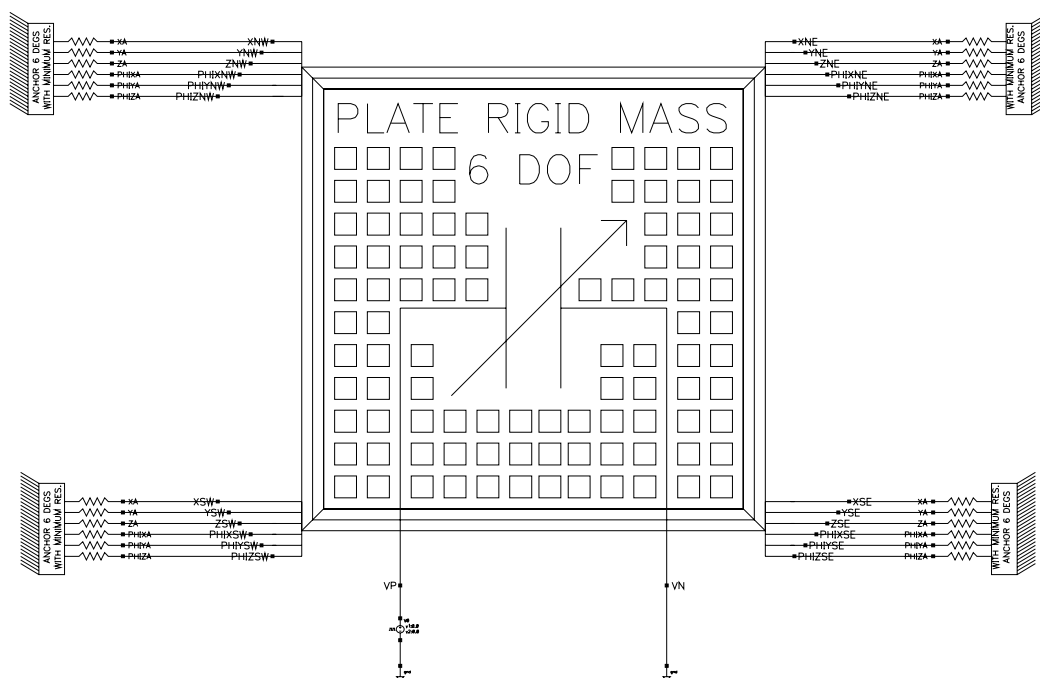


Figure 3.30: Cadence Virtuoso<sup>®</sup> Schematic for the validation of the rigid plate electrostatic model. The four vertexes are anchored in order to keep the plate in a fixed position in space.



The capacitance and electrostatic force values obtained in Spectre<sup>®</sup> are compared with the ones predicted by the FEM simulation of the same rigid plate structure performed within COMSOL Multiphysics<sup>™</sup> [44]. A schematic of a suspended rigid plate with holes within COMSOL Multiphysics<sup>™</sup> is shown in Figure 3.31. The plate and the bottom electrode are contained within a dielectric region which is a box of air. The color scale represents the electrostatic potential.

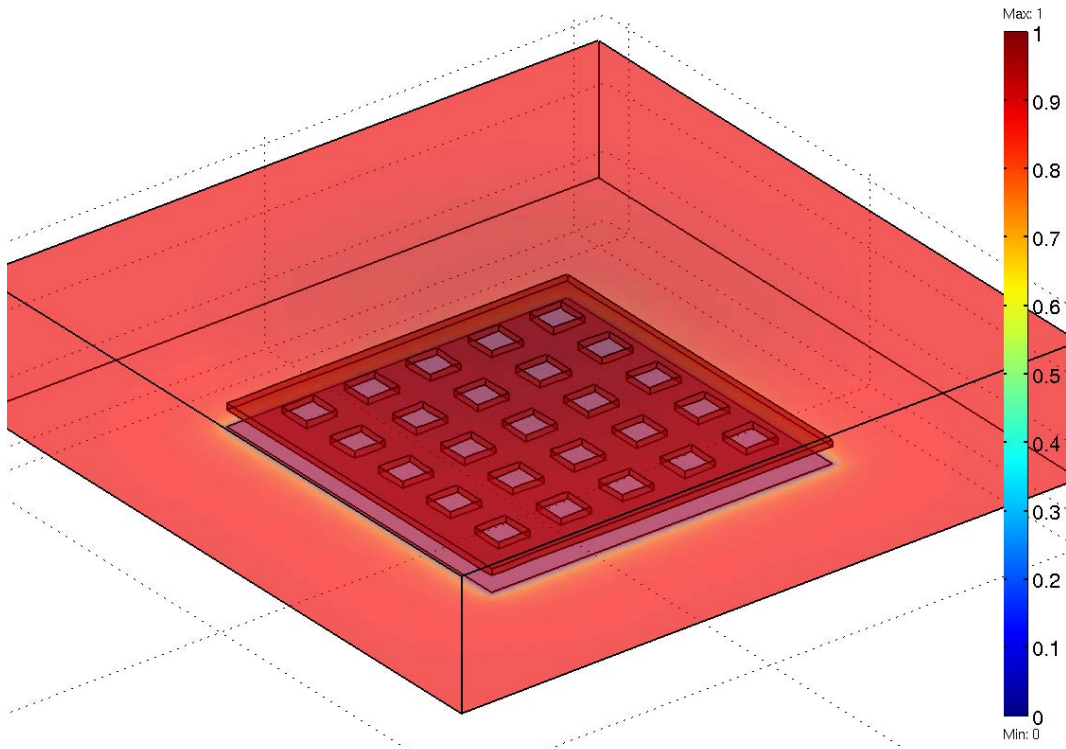


Figure 3.31: COMSOL Multiphysics<sup>™</sup> schematic of a suspended rigid plate for electrostatic simulations. The suspended plate and the underneath electrode are included in an air box.

The compact models implementation is based on the concept of modularity. This means that it is possible to compile the models within Cadence<sup>®</sup> including certain features instead of others depending on the desired specifications (on this purpose see Appendix A). Concerning the plate, this means it can be decided to have a 4 or 6 DoF's mechanical model, or to include or not the

presence of holes on its surface as well as to take into account or to neglect the fringing field. This suggests to perform a comparative validation that, starting from the FEM results, shows the achievable increase of accuracy in predictions of Spectre<sup>©</sup> deriving from the inclusion of additional features (e.g. fringing field model). In all the simulations which are being shown the applied voltage between the plate and the substrate is equal to 1 Volt while permittivity (or dielectric constant) of air ( $\epsilon$ ) is equal to  $8.854 \times 10^{-12} \frac{F}{m}$ . The gap between the plate and the substrate is considered the distance between the plate and the lower electrode ( $Z_{GAP}$  in Figure 3.12). This means the thin oxide layer effects are neglected in all the following comparisons. Different validations are shown below depending on the particular plate features.

### Rigid Plate Without Holes

In the simulations which are going to be compared the case of a plate without holes is considered. Moreover, in the COMSOL Multiphysics<sup>TM</sup> simulations a plate with a zero thickness ( $T = 0$ ) is considered. For this reason the fringing model included in the compact rigid plate model is the one due to the peripheral region of thickness  $\zeta$  shown in previous Section 3.6, while the fringing due to the lateral faces is neglected. In Spectre<sup>©</sup> simulations a plate thickness of  $1 \mu m$  is set but it does not influence the results at all for the just explained reason. The data for each comparison are arranged in tabular format. The top table reports the plate geometry features including the gap and orientation angles. The lower lines compare the results for the capacitance (**C**) and electrostatic force (**F**) also showing the error of the VerilogA<sup>©</sup> model with respect to the FEM simulation prediction. For the plate configurations with uneven positions in space ( $\theta_{X_{INIT}} \neq 0$  and/or  $\theta_{Y_{INIT}} \neq 0$ ) the error we get when a 4 DoF's rigid (parallel) plate model is employed instead of the 6 DoF's complete one (keeping the same gap in the two cases) is also reported.

Length	Width	Thickness	Gap	$\theta_{\mathbf{X}_{\text{INIT}}}$	$\theta_{\mathbf{Y}_{\text{INIT}}}$
$120 \mu m$	$120 \mu m$	$1 \mu m$	$1 \mu m$	$0^\circ$	$0^\circ$

Fringing	C (Cadence)	C (COMSOL)	Error
Yes	$1.279x10^{-13} F$	$1.278x10^{-13} F$	+0.08%
No	$1.275x10^{-12} F$	$1.278x10^{-13} F$	-0.23%

Fringing	F (Cadence)	F (COMSOL)	Error
Yes	$6.406x10^{-8} N$	$6.356x10^{-8} N$	+0.80%
No	$6.375x10^{-8} N$	$6.356x10^{-8} N$	+0.30%

Table 3.2: Comparison No.1 of the rigid plate electrostatic compact model with FEM simulated data in COMSOL Multiphysics<sup>©</sup>.

Length	Width	Thickness	Gap	$\theta_{\mathbf{X}_{\text{INIT}}}$	$\theta_{\mathbf{Y}_{\text{INIT}}}$
$120 \mu m$	$120 \mu m$	$1 \mu m$	$8 \mu m$	$6^\circ$	$0^\circ$

Fringing	Model	C (Cadence)	C (COMSOL)	Error
Yes	6 DoF's	$2.151x10^{-14} F$	$2.197x10^{-14} F$	-2.09%
No	6 DoF's	$2.142x10^{-14} F$	$2.197x10^{-14} F$	-2.50%
Yes	4 DoF's	$1.598x10^{-14} F$	$2.197x10^{-14} F$	-27.3%

Fringing	Model	F (Cadence)	F (COMSOL)	Error
Yes	6 DoF's	$2.608x10^{-9} N$	$2.391x10^{-9} N$	+9.08%
No	6 DoF's	$2.575x10^{-9} N$	$2.391x10^{-9} N$	+7.70%
Yes	4 DoF's	$1.001x10^{-9} N$	$2.391x10^{-9} N$	-58.1%

Table 3.3: Comparison No.2 of the rigid plate electrostatic compact model with FEM simulated data in COMSOL Multiphysics<sup>©</sup>.

Length	Width	Thickness	Gap	$\theta_{\mathbf{X}_{\text{INIT}}}$	$\theta_{\mathbf{Y}_{\text{INIT}}}$
$120 \mu m$	$120 \mu m$	$1 \mu m$	$15 \mu m$	$6^\circ$	$7^\circ$

Fringing	Model	C (Cadence)	C (COMSOL)	Error
Yes	6 DoF's	$1.041x10^{-14} F$	$1.109x10^{-14} F$	-6.13%
No	6 DoF's	$1.037x10^{-14} F$	$1.109x10^{-14} F$	-6.50%
Yes	4 DoF's	$8.524x10^{-15} F$	$1.109x10^{-14} F$	-23.1%

Fringing	Model	F (Cadence)	F (COMSOL)	Error
Yes	6 DoF's	$5.905x10^{-10} N$	$5.331x10^{-10} N$	+10.8%
No	6 DoF's	$5.829x10^{-10} N$	$5.331x10^{-10} N$	+9.34%
Yes	4 DoF's	$2.847x10^{-10} N$	$5.331x10^{-10} N$	-46.6%

Table 3.4: Comparison No.3 of the rigid plate electrostatic compact model with FEM simulated data in COMSOL Multiphysics<sup>©</sup>.

Length	Width	Thickness	Gap	$\theta_{\mathbf{X}_{\text{INIT}}}$	$\theta_{\mathbf{Y}_{\text{INIT}}}$
$120 \mu m$	$120 \mu m$	$1 \mu m$	$3 \mu m$	$0.5^\circ$	$0.5^\circ$

Fringing	Model	C (Cadence)	C (COMSOL)	Error
Yes	6 DoF's	$4.353x10^{-14} F$	$4.349x10^{-14} F$	+0.09%
No	6 DoF's	$4.341x10^{-14} F$	$4.349x10^{-14} F$	-0.19%
Yes	4 DoF's	$4.250x10^{-14} F$	$4.349x10^{-14} F$	-2.28%

Fringing	Model	F (Cadence)	F (COMSOL)	Error
Yes	6 DoF's	$7.593x10^{-9} N$	$7.222x10^{-9} N$	+5.10%
No	6 DoF's	$7.553x10^{-9} N$	$7.222x10^{-9} N$	+4.58%
Yes	4 DoF's	$7.083x10^{-9} N$	$7.222x10^{-9} N$	-1.92%

Table 3.5: Comparison No.4 of the rigid plate electrostatic compact model with FEM simulated data in COMSOL Multiphysics<sup>©</sup>.

In the next simulations a non-zero plate thickness is introduced in the COMSOL Multiphysics<sup>©</sup> simulations. This involves an additional contribution of fringing due to the vertical plate faces. The VerilogA<sup>©</sup> fringing model now accounts also for this contribution.

<b>Length</b>	<b>Width</b>	<b>Thickness</b>	<b>Gap</b>	$\theta_{\mathbf{X}_{\text{INIT}}}$	$\theta_{\mathbf{Y}_{\text{INIT}}}$
$60 \mu m$	$60 \mu m$	$2 \mu m$	$500 nm$	$0^\circ$	$0^\circ$

<b>Fringing</b>	<b>C (Cadence)</b>	<b>C (COMSOL)</b>	<b>Error</b>
Yes	$6.707x10^{-14} F$	$6.415x10^{-14} F$	+4.55%
No	$6.375x10^{-14} F$	$6.415x10^{-14} F$	-0.62%

<b>Fringing</b>	<b>F (Cadence)</b>	<b>F (COMSOL)</b>	<b>Error</b>
Yes	$6.438x10^{-8} N$	$6.369x10^{-8} N$	+1.08%
No	$6.375x10^{-8} N$	$6.369x10^{-8} N$	+0.09%

Table 3.6: Comparison No.5 of the rigid plate electrostatic compact model with FEM simulated data in COMSOL Multiphysics<sup>©</sup>.

Length	Width	Thickness	Gap	$\theta_{\mathbf{X}_{\text{INIT}}}$	$\theta_{\mathbf{Y}_{\text{INIT}}}$
$60 \mu m$	$60 \mu m$	$2 \mu m$	$3 \mu m$	$0^\circ$	$0^\circ$

Fringing	C (Cadence)	C (COMSOL)	Error
Yes	$1.162x10^{-14} F$	$1.102x10^{-14} F$	+5.46%
No	$1.062x10^{-14} F$	$1.102x10^{-14} F$	-3.63%

Fringing	F (Cadence)	F (COMSOL)	Error
Yes	$1.788x10^{-9} N$	$1.763x10^{-9} N$	+1.42%
No	$1.771x10^{-9} N$	$1.763x10^{-9} N$	+0.45%

Table 3.7: Comparison No.6 of the rigid plate electrostatic compact model with FEM simulated data in COMSOL Multiphysics<sup>©</sup>.

Length	Width	Thickness	Gap	$\theta_{\mathbf{X}_{\text{INIT}}}$	$\theta_{\mathbf{Y}_{\text{INIT}}}$
$60 \mu m$	$60 \mu m$	$3 \mu m$	$9 \mu m$	$10^\circ$	$7^\circ$

Fringing	Model	C (Cadence)	C (COMSOL)	Error
Yes	6 DoF's	$5.588x10^{-15} F$	$5.540x10^{-15} F$	+0.87%
No	6 DoF's	$4.704x10^{-15} F$	$5.540x10^{-15} F$	-15.1%
Yes	4 DoF's	$4.089x10^{-15} F$	$5.540x10^{-15} F$	-26.2%

Fringing	Model	F (Cadence)	F (COMSOL)	Error
Yes	6 DoF's	$7.249x10^{-10} N$	$8.488x10^{-10} N$	-14.6%
No	6 DoF's	$6.722x10^{-10} N$	$8.488x10^{-10} N$	-20.8%
Yes	4 DoF's	$1.987x10^{-10} N$	$8.488x10^{-10} N$	-76.6%

Table 3.8: Comparison No.7 of the rigid plate electrostatic compact model with FEM simulated data in COMSOL Multiphysics<sup>©</sup>.

Length	Width	Thickness	Gap	$\theta_{\mathbf{X}_{\text{INIT}}}$	$\theta_{\mathbf{Y}_{\text{INIT}}}$
$80 \mu m$	$80 \mu m$	$2 \mu m$	$1.5 \mu m$	$0.2^\circ$	$0.3^\circ$

Fringing	Model	C (Cadence)	C (COMSOL)	Error
Yes	6 DoF's	$4.039x10^{-14} F$	$3.842x10^{-14} F$	+5.13%
No	6 DoF's	$3.814x10^{-14} F$	$3.842x10^{-14} F$	-0.73%
Yes	4 DoF's	$3.778x10^{-14} F$	$3.842x10^{-14} F$	-1.67%

Fringing	Model	F (Cadence)	F (COMSOL)	Error
Yes	6 DoF's	$1.306x10^{-8} N$	$1.291x10^{-8} N$	+1.16%
No	6 DoF's	$1.296x10^{-8} N$	$1.291x10^{-8} N$	+0.39%
Yes	4 DoF's	$1.259x10^{-8} N$	$1.291x10^{-8} N$	-2.48%

Table 3.9: Comparison No.8 of the rigid plate electrostatic compact model with FEM simulated data in COMSOL Multiphysics<sup>©</sup>.

In conclusion, accuracy of the electrostatic model implemented in VerilogA<sup>©</sup> is rather good. The largest disagreement with respect to the FEM prediction is about 14% concerning the electrostatic force for a configuration with large orientation angles (see Table 3.8) that are not frequently reached in practical applications we are interested in. It is noticeable that, apart from the case of very small orientation angles (about  $0.2 - 0.3^\circ$ ), the use of a 4 DoF's (parallel plate) mechanical model instead of the 6 DoF's one introduces very large underestimations (up to 76%) both for the capacitance and electrostatic force. Finally, the fringing effect model allows in most cases to reduce the disagreement with respect to the FEM results. In the case of the electrostatic force, when the compact model overestimates its value, the fringing model enlarges a bit this disagreement even though it is never larger than 10%.

### Rigid Plate With Holes

In this part the rigid plate electrostatic model including holes on its surface is validated. In all the subsequent simulations squared shaped holes (of side **H Ln.**) are considered and the number of holes along the  $x$  local direction (**H No.**) on plate surface is equal to the one along  $y$ . Moreover, holes are symmetrically distributed on plate area. Hence, looking at Figure 3.22, it is  $\Delta_{xL} = \Delta_{xR}$  and  $\Delta_{xT} = \Delta_{xB}$ . The fringing effects on the plate peripheral border are always included in the following simulations. Each configuration is simulated in Spectre<sup>©</sup> first including all the fringing effects due to the holes and then neglecting them. Moreover, all the simulations are also repeated not including holes at all in order to show the error we would get if the holes electrostatic model was not implemented within the compact rigid plate model in VerilogA<sup>©</sup>.

Length	Width	Thickness	Gap	H No.	H Ln.	$\theta_{X_{INIT}}$	$\theta_{Y_{INIT}}$
110 $\mu m$	110 $\mu m$	2 $\mu m$	2 $\mu m$	5	10 $\mu m$	0°	0°

Holes fringing	Holes	C (Cadence)	C (COMSOL)	Error
Yes	Yes	$5.067x10^{-14} F$	$5.122x10^{-14} F$	-1.07%
No	Yes	$4.500x10^{-14} F$	$5.122x10^{-14} F$	-12.1%
-	No	$5.607x10^{-14} F$	$5.122x10^{-14} F$	+9.47%

Holes fringing	Holes	F (Cadence)	F (COMSOL)	Error
Yes	Yes	$1.086x10^{-8} N$	$1.082x10^{-8} N$	+0.37%
No	Yes	$1.070x10^{-8} N$	$1.082x10^{-8} N$	-1.11%
-	No	$1.346x10^{-8} N$	$1.082x10^{-8} N$	+24.4%

Table 3.10: Comparison No.9 of the rigid plate electrostatic compact model with FEM simulated data in COMSOL Multiphysics<sup>©</sup>.



Length	Width	Thickness	Gap	H No.	H Ln.	$\theta_{\mathbf{X}_{\text{INIT}}}$	$\theta_{\mathbf{Y}_{\text{INIT}}}$
$110 \mu m$	$110 \mu m$	$2 \mu m$	$1 \mu m$	5	$10 \mu m$	$0^\circ$	$0^\circ$

Holes fringing	Holes	C (Cadence)	C (COMSOL)	Error
Yes	Yes	$9.818x10^{-14} F$	$9.718x10^{-14} F$	+1.03%
No	Yes	$8.903x10^{-14} F$	$9.718x10^{-14} F$	-8.39%
-	No	$1.112x10^{-13} F$	$9.718x10^{-14} F$	+14.4%

Holes fringing	Holes	F (Cadence)	F (COMSOL)	Error
Yes	Yes	$4.345x10^{-8} N$	$4.261x10^{-8} N$	+1.97%
No	Yes	$4.279x10^{-8} N$	$4.261x10^{-8} N$	+0.42%
-	No	$5.386x10^{-8} N$	$4.261x10^{-8} N$	+26.4%

Table 3.11: Comparison No.10 of the rigid plate electrostatic compact model with FEM simulated data in COMSOL Multiphysics<sup>©</sup>.

Length	Width	Thickness	Gap	H No.	H Ln.	$\theta_{\mathbf{X}_{\text{INIT}}}$	$\theta_{\mathbf{Y}_{\text{INIT}}}$
$110 \mu m$	$110 \mu m$	$2 \mu m$	$2 \mu m$	5	$10 \mu m$	$0^\circ$	$1^\circ$

Holes fringing	Holes	C (Cadence)	C (COMSOL)	Error
Yes	Yes	$5.613x10^{-14} F$	$5.555x10^{-14} F$	+1.04%
No	Yes	$4.910x10^{-14} F$	$5.555x10^{-14} F$	-11.6%
-	No	$6.111x10^{-14} F$	$5.555x10^{-14} F$	+10.1%

Holes fringing	Holes	F (Cadence)	F (COMSOL)	Error
Yes	Yes	$1.410x10^{-8} N$	$1.415x10^{-8} N$	-0.35%
No	Yes	$1.398x10^{-8} N$	$1.415x10^{-8} N$	-1.20%
-	No	$1.752x10^{-8} N$	$1.415x10^{-8} N$	+23.8%

Table 3.12: Comparison No.11 of the rigid plate electrostatic compact model with FEM simulated data in COMSOL Multiphysics<sup>©</sup>.

Length	Width	Thickness	Gap	H No.	H Ln.	$\theta_{\mathbf{X}_{\text{INIT}}}$	$\theta_{\mathbf{Y}_{\text{INIT}}}$
$110 \mu m$	$110 \mu m$	$2 \mu m$	$2.5 \mu m$	5	$10 \mu m$	$0^\circ$	$1^\circ$

Holes fringing	Holes	C (Cadence)	C (COMSOL)	Error
Yes	Yes	$4.383x10^{-14} F$	$4.384x10^{-14} F$	-0.02%
No	Yes	$3.810x10^{-14} F$	$4.384x10^{-14} F$	-13.1%
-	No	$4.742x10^{-14} F$	$4.384x10^{-14} F$	+8.17%

Holes fringing	Holes	F (Cadence)	F (COMSOL)	Error
Yes	Yes	$8.130x10^{-9} N$	$8.180x10^{-9} N$	-0.61%
No	Yes	$8.052x10^{-9} N$	$8.180x10^{-9} N$	-1.45%
-	No	$1.012x10^{-8} N$	$8.180x10^{-9} N$	+23.7%

Table 3.13: Comparison No.12 of the rigid plate electrostatic compact model with FEM simulated data in COMSOL Multiphysics<sup>©</sup>.

Length	Width	Thickness	Gap	H No.	H Ln.	$\theta_{\mathbf{X}_{\text{INIT}}}$	$\theta_{\mathbf{Y}_{\text{INIT}}}$
$98 \mu m$	$98 \mu m$	$2.5 \mu m$	$8 \mu m$	4	$12 \mu m$	$5^\circ$	$4^\circ$

Holes fringing	Holes	C (Cadence)	C (COMSOL)	Error
Yes	Yes	$1.413x10^{-14} F$	$1.474x10^{-14} F$	-4.14%
No	Yes	$1.156x10^{-14} F$	$1.474x10^{-14} F$	-21.6%
-	No	$1.504x10^{-14} F$	$1.474x10^{-14} F$	+2.03%

Holes fringing	Holes	F (Cadence)	F (COMSOL)	Error
Yes	Yes	$1.372x10^{-9} N$	$1.432x10^{-9} N$	-4.19%
No	Yes	$1.347x10^{-9} N$	$1.432x10^{-9} N$	-5.93%
-	No	$1.890x10^{-9} N$	$1.423x10^{-9} N$	+32.0%

Table 3.14: Comparison No.13 of the rigid plate electrostatic compact model with FEM simulated data in COMSOL Multiphysics<sup>©</sup>.

Length	Width	Thickness	Gap	H No.	H Ln.	$\theta_{\mathbf{X}_{\text{INIT}}}$	$\theta_{\mathbf{Y}_{\text{INIT}}}$
$98 \mu m$	$98 \mu m$	$1.5 \mu m$	$3.5 \mu m$	4	$12 \mu m$	$3^\circ$	$0^\circ$

Holes fringing	Holes	C (Cadence)	C (COMSOL)	Error
Yes	Yes	$2.807x10^{-14} F$	$2.968x10^{-14} F$	-5.42%
No	Yes	$2.470x10^{-14} F$	$2.968x10^{-14} F$	-16.8%
-	No	$3.263x10^{-14} F$	$2.968x10^{-14} F$	+10.0%

Holes fringing	Holes	F (Cadence)	F (COMSOL)	Error
Yes	Yes	$5.839x10^{-9} N$	$5.956x10^{-9} N$	+1.96%
No	Yes	$5.769x10^{-9} N$	$5.956x10^{-9} N$	-3.14%
-	No	$7.586x10^{-9} N$	$5.956x10^{-9} N$	+27.4%

Table 3.15: Comparison No.14 of the rigid plate electrostatic compact model with FEM simulated data in COMSOL Multiphysics<sup>©</sup>.

The electrostatic model which accounts for the holes and the fringing effects related to them allows to achieve very good prediction both for the capacitance and electrostatic force. The largest disagreement with respect to the COMSOL Multiphysics<sup>©</sup> prediction is about 5% (see Table 3.15). When the fringing effects due to holes are not included in the model, underestimations up to about 22% must be paid like Table 3.14 reports. On the other hand, if we think to ignore the presence of holes and to use the simple plate model without openings, the overestimations we would have to deal with are as large as 32%. In conclusion, the results shown above make clear the motivations for which the effort of implementing such an electrostatic model accounting for uneven configurations in space, presence of opening and fringing effect has been spent.

In conclusion, in all previous simulations the value for the empirical coefficients of the fringing model (see Section 3.6) is:  $\zeta = 100 nm$  and  $\gamma = 0.25$ . These have been determined by comparisons with the FEM results and represent the best choice in all the analyzed cases.

## 3.9 Complementary Library Models

The suspended rigid plate, which is one of the most important elementary components implemented within the MEMS model library has been presented thus far through this chapter. The latter, together with the Euler flexible beam (see next chapter), allows to build up more complex structures of interest in RF-MEMS application such as switches and varactors. To make it possible the availability of appropriate modules to impose for instance the mechanical constraints (i.e. anchors) to the free ends of the beams connected to the suspended rigid plate in the switch implementation is necessary. Moreover, mechanical stimuli like force, torque as well as linear and angular displacements, are necessary to extend both the usability and the testability of the implemented compact models. All these complementary structures are discussed below.

### 3.9.1 Mechanical Constraints

The need of applying anchor points to the ends of a structure of interest has just been mentioned. This means to constrain some nodes of a certain hierarchy in order not to allow any displacement on it. The implementation of such a structure is particularly easy as it consist of defining a number of nodes equal to the DoF's which have to be constrained and force their displacement to zero. In case we want to constrain all the 6 DoF's of an Euler beam end the anchor model consist of the subsequent six equations:

$$D_X = 0 \tag{3.210}$$

$$D_Y = 0 \tag{3.211}$$

$$D_Z = 0 \tag{3.212}$$

$$D_{\theta_X} = 0 \tag{3.213}$$

$$D_{\theta_Y} = 0 \tag{3.214}$$

$$D_{\theta_Z} = 0 \tag{3.215}$$

where the 3.210 - 3.212 represent the three linear displacements of the anchor nodes while the 3.213 - 3.215 the three rotations around the global axes.

When the constraints are applied to the nodes of a non-flexible structure like the rigid plate it is not possible to define the anchor like in previous equation. Indeed, thinking in the electrical domain, this would be equivalent to short two voltage generators, the first constituted by the rigidity condition of the plate (equations 3.77 - 3.88) and the second by the anchor itself (equations 3.210 - 3.215). This condition cannot be managed by the simulator. However, it is possible to circumvent the problem by introducing a fictitious resistance  $r_{min}$  with a small value (for instance  $10^{-6}$ ). Then, the constraints on the displacements imposed by the anchor can be defined multiplying the forces and torques applied to the anchor nodes by  $r_{min}$ . Since the latter is very small, not appreciable displacements are allowed by the anchor and at the same time any short condition is prevented by this solution. The 3.210 - 3.215 rewritten as a function of  $r_{min}$  are:

$$D_X = r_{min}F_X \quad (3.216)$$

$$D_Y = r_{min}F_Y \quad (3.217)$$

$$D_Z = r_{min}F_Z \quad (3.218)$$

$$D_{\theta_X} = r_{min}T_{\theta_X} \quad (3.219)$$

$$D_{\theta_Y} = r_{min}T_{\theta_Y} \quad (3.220)$$

$$D_{\theta_Z} = r_{min}T_{\theta_Z} \quad (3.221)$$

The Cadence Virtuoso<sup>®</sup> Schematic for the normal anchor and the one including the fictitious resistance  $r_{min}$  are respectively shown in Figure 3.32 and Figure 3.33.

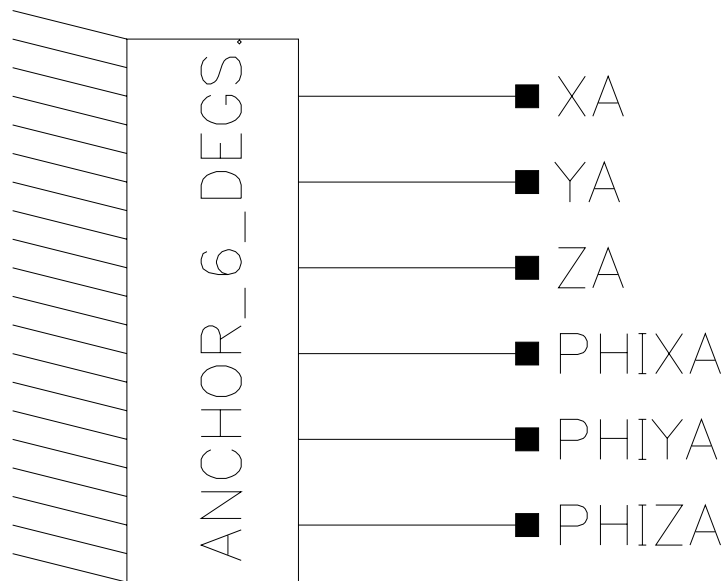


Figure 3.32: Cadence Virtuoso<sup>©</sup> Schematic for the 6 DoF's anchor. Six pins are made available.

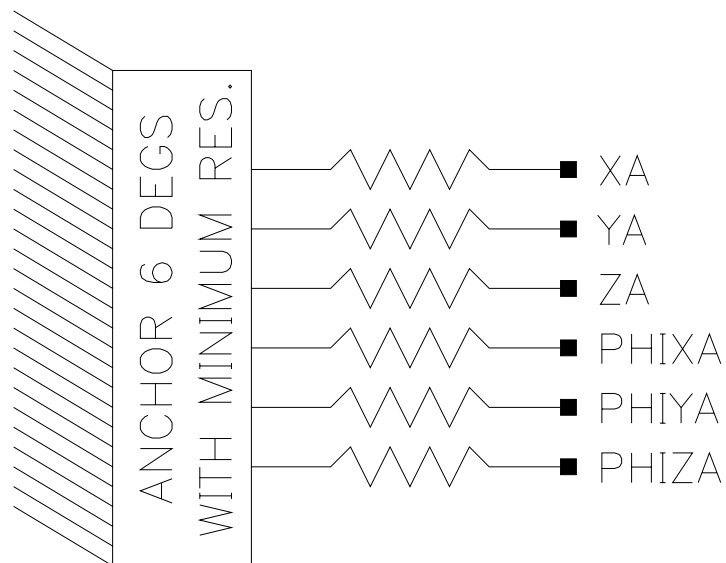


Figure 3.33: Cadence Virtuoso<sup>©</sup> Schematic for the 6 DoF's anchor including the definition of the fictitious resistance  $r_{min}$ .

### 3.9.2 Applied Forces and Displacements

Also the case of defining applied stimuli for a certain structure is rather simple from the viewpoint of the implementation. The magnitude of the applied force or displacement is defined as an initial parameter together with the desired orientation angles. Let  $F_S$  and  $D_S$  be the modulus of the applied force and displacement respectively and let  $\theta_{S_Y}$  and  $\theta_{S_Z}$  be the orientation angles of the stimulus along the axes of the global reference system. By exploiting the 2.8, the components of  $F_S$  imposed by the force generator along the three axes ( $X, Y, Z$ ) are:

$$F_{S_X} = \cos \theta_{S_Y} \cos \theta_{S_Z} F_S \quad (3.222)$$

$$F_{S_Y} = \cos \theta_{S_Y} \sin \theta_{S_Z} F_S \quad (3.223)$$

$$F_{S_Z} = -\sin \theta_{S_Y} F_S \quad (3.224)$$

Similarly, when the applied stimulus is a displacement its three components are:

$$D_{S_X} = \cos \theta_{S_Y} \cos \theta_{S_Z} D_S \quad (3.225)$$

$$D_{S_Y} = \cos \theta_{S_Y} \sin \theta_{S_Z} D_S \quad (3.226)$$

$$D_{S_Z} = -\sin \theta_{S_Y} D_S \quad (3.227)$$

It is also possible to define an applied torque and angular displacement to be imposed by the force and displacement source respectively. These are defined as modulus and then decomposed in the  $X, Y, Z$  contributions as a function of the orientation angles as already shown in equations 3.222 - 3.224 and 3.225 - 3.227. The Cadence Virtuoso<sup>®</sup> Schematic for the force and displacement source are respectively shown in Figure 3.34 and Figure 3.35.

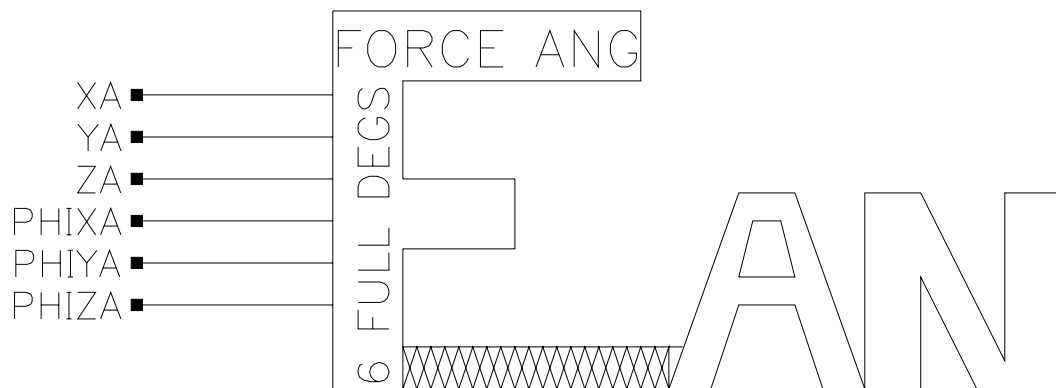


Figure 3.34: Cadence Virtuoso<sup>®</sup> Schematic for the 6 DoF's force (torque) generator.



Figure 3.35: Cadence Virtuoso<sup>®</sup> Schematic for the 6 DoF's displacement (linear and angular) generator.



To complete the overview of stimuli generators, the force and displacement sources have been implemented also in order to allow small signals and transient simulations. In the latter case, the stimulus (force or displacement) is defined in terms of minimum and maximum value, rise and fall time, delay, pulse width and period as shown in Figure 3.36.

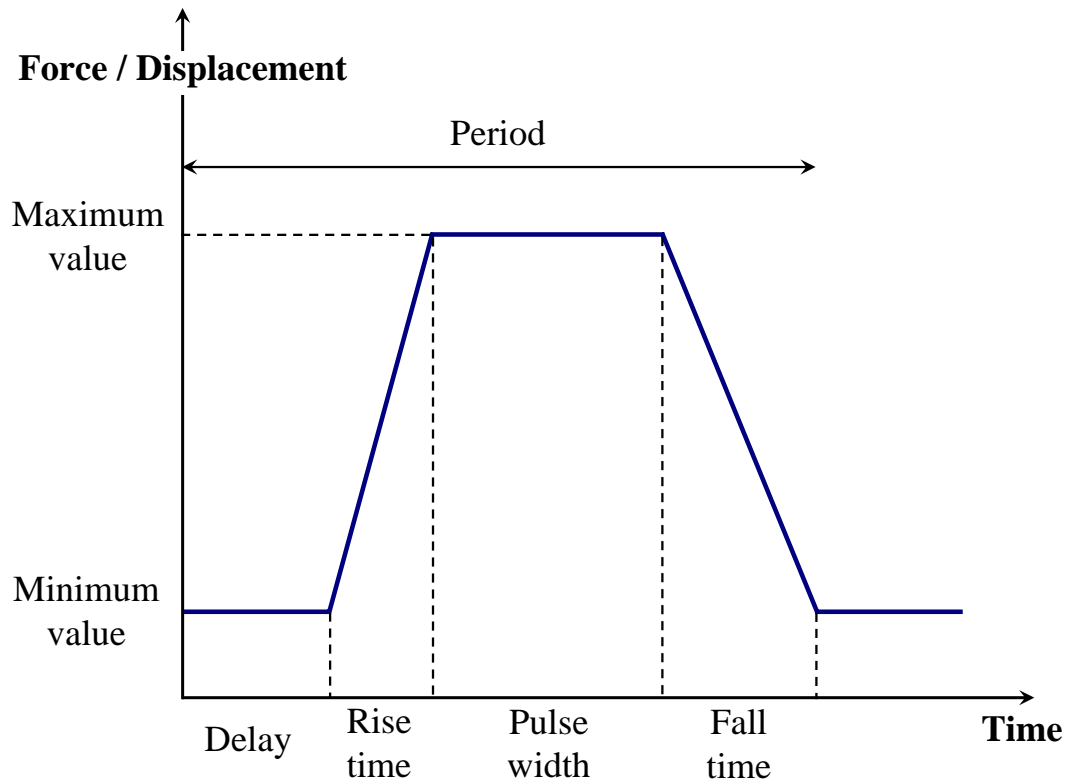


Figure 3.36: Definition of a pulse-shaped stimulus. It is defined in terms of minimum and maximum value, rise and fall time, delay, pulse width and period.

### 3.9.3 Unconnected Pins

Depending on the topology of the analyzed structure it might happen that one or more nodes remain unconnected. Let us imagine for instance to leave one vertex of a rigid plate not connected to any other element. What we get is that the six pins of that corner will remain floating. When the netlist is generated within Spectre<sup>®</sup> a warning message occurs and the software which interprets the Virtuoso<sup>®</sup> Schematic associates by default a fictitious conductance towards ground with a very small value to each floating node. This usually does not represent a real problem. However, an on purpose element has been defined in the library which has to be connected to the floating nodes and is shown in Figure 3.37. Within this model all the forces and torques are forced to zero. This means that no stimuli are applied to these nodes even though they are free to move depending on the forces/torques applied in the other non-floating vertexes.

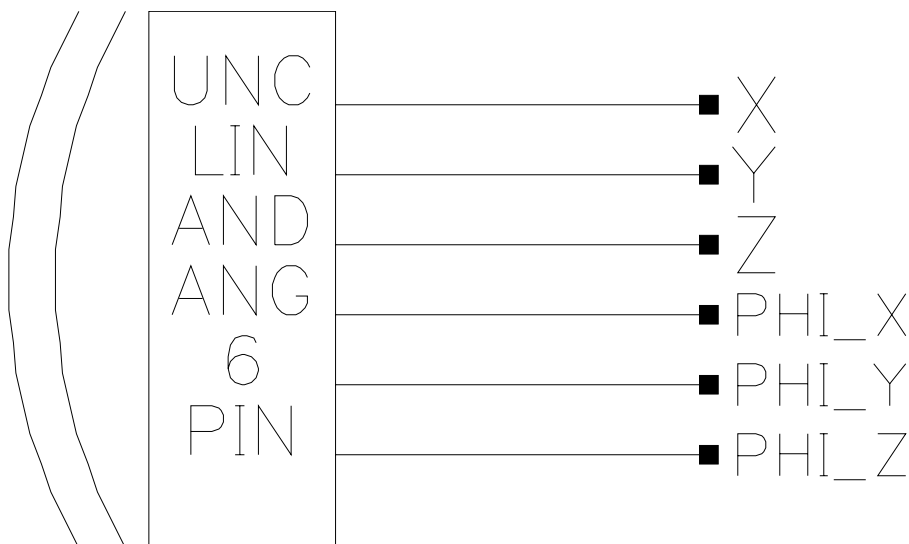


Figure 3.37: Cadence Virtuoso<sup>®</sup> Schematic for the 6 DoF's block to be connected to floating nodes.

Aside the 6 DoF's element for floating pins of previous figure it has been also implemented with just one, two or three linear or angular nodes. This because the number of floating pins can be different from six depending on the topology.

### 3.9.4 Interconnects for Rigid Structures

It can happen that two rigid plates must be connected together, for instance to apply two different biasing signals. However, connecting together two rigid structures means to generate a short condition as already discussed in the section on the mechanical constraints. On this purpose a block that exploits once again the fictitious resistance  $r_{min}$  has been defined. Its Cadence Virtuoso<sup>®</sup> Schematic is shown in Figure 3.38. The relative displacements (linear and angular) at its two ends are defined within the model as the differential forces (torques) multiplied by  $r_{min}$ . If we address its two ports as  $A$  and  $B$ , the just mentioned relations are:

$$D_{X_A} - D_{X_B} = r_{min}(F_{X_A} - F_{X_B}) \quad (3.228)$$

$$D_{Y_A} - D_{Y_B} = r_{min}(F_{Y_A} - F_{Y_B}) \quad (3.229)$$

$$D_{Z_A} - D_{Z_B} = r_{min}(F_{Z_A} - F_{Z_B}) \quad (3.230)$$

$$D_{\theta_{X_A}} - D_{\theta_{X_B}} = r_{min}(T_{\theta_{X_A}} - T_{\theta_{X_B}}) \quad (3.231)$$

$$D_{\theta_{Y_A}} - D_{\theta_{Y_B}} = r_{min}(T_{\theta_{Y_A}} - T_{\theta_{Y_B}}) \quad (3.232)$$

$$D_{\theta_{Z_A}} - D_{\theta_{Z_B}} = r_{min}(T_{\theta_{Z_A}} - T_{\theta_{Z_B}}) \quad (3.233)$$

Also this model has been implemented in additional versions with less than six pins to adapt it to all the possible interconnections.



Figure 3.38: Cadence Virtuoso<sup>®</sup> Schematic for the 6 DoF's minimum resistance to connect together two rigid plates.

# Chapter 4

## The Flexible Euler Beam

In this chapter another important component included in the MEMS compact model library is discussed. This is the flexible Euler beam that, together with the rigid plate of previous chapter, allows to build up more complex structures such as switches and varactors. Following a path similar to the one covered for the rigid plate, we will first introduce the mechanical model starting from a very simple case. Subsequently, the electrostatic model together with the viscous damping model will be described. Finally, the validation of the model will be shown.

### 4.1 Mechanical Model for the 2 DoF's Flexible Beam

In this section a very simple case is taken into account in order to explain in a very straightforward fashion the adopted approach in defining the mechanical model of the Euler beam. First of all, a schematic of an Euler beam with  $W$ ,  $L$  and  $T$  dimensions along the  $x$ ,  $y$  and  $z$  axes respectively is shown in Figure 4.1 The two beam ends  $A$  and  $B$  are also indicated. In this section we will consider a 2 DoF's beam that is stimulated only along the  $x$  direction at the two ends (see Figure 4.2). The first aspect to notice is that the stimuli, i.e. the forces  $F_{xA}$  and  $F_{xB}$ , are applied according to the superposition principle. This means that each stimulus is applied singularly, considering all the others equal to zero. Moreover appropriate mechanical constraints are applied to the not stimulated beam end (see Figure 4.2).

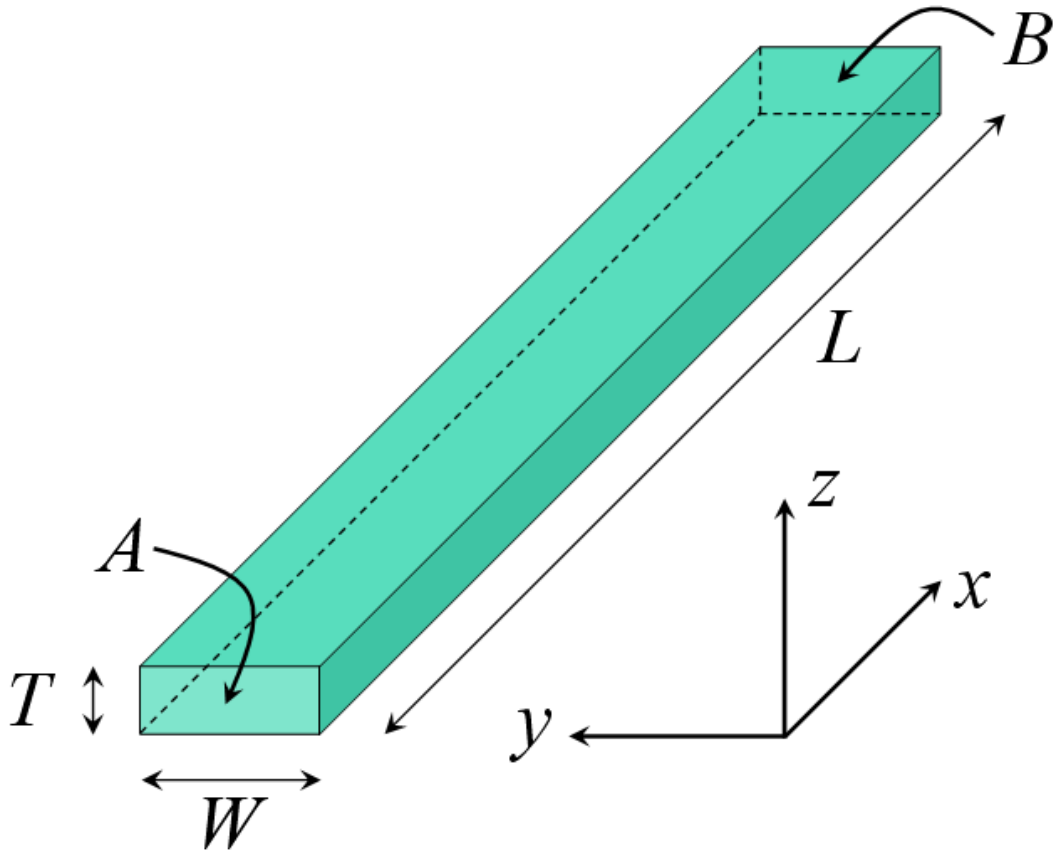


Figure 4.1: Schematic of an Euler flexible beam. Beam length (along  $x$  axis), width (along  $y$  axis) and thickness (along  $z$  axis) are  $L$ ,  $W$  and  $T$  respectively.

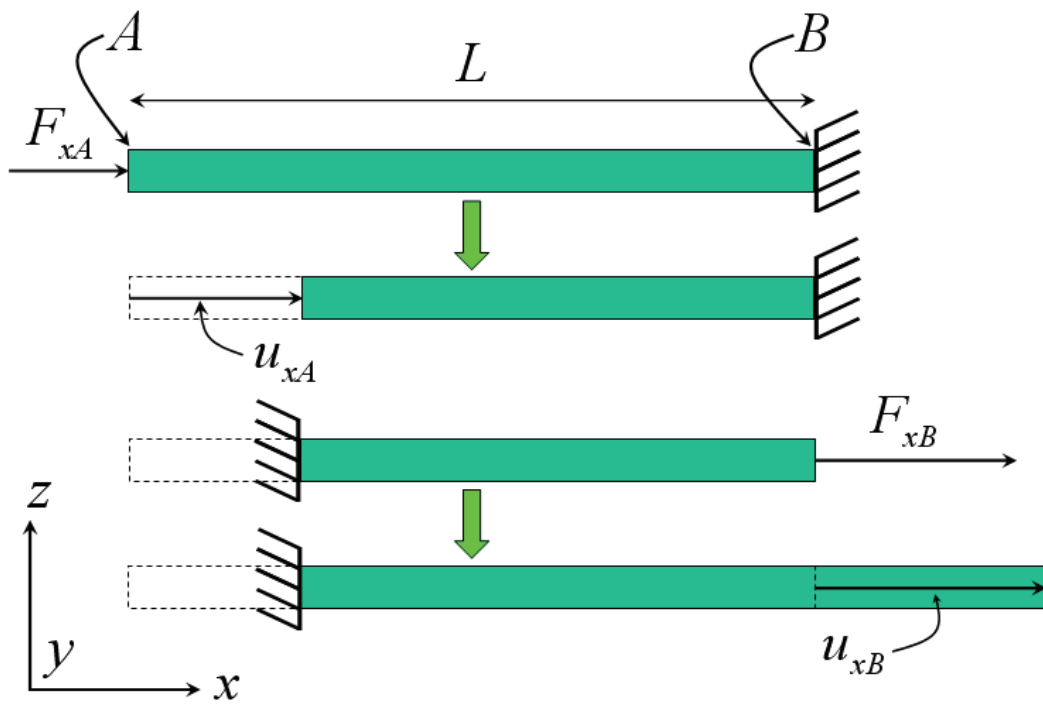


Figure 4.2: Euler beam stimulated along the  $x$  direction at the ends  $A$  and  $B$ . The end in which the stimulus is not applied has to be constrained (anchored).

The force  $F_{xA}$  applied in the beam end  $A$  induces a deformation equal to  $u_{xA}$ . On the other hand, the force  $F_{xB}$  deforms the end  $B$  of  $u_{xB}$ . We will now introduce the procedure in order to derive two matrices called *stiffness* and *mass* matrix. The first one defines the set of relations between the forces and the corresponding deformations for each DoF of the flexible beam. Whereas, the mass matrix describes the inertial behaviour of the beam, defining the relations between the forces and the accelerations to each DoF.

### 4.1.1 The Stiffness Matrix

Before commencing the calculations a consideration has to be done. The Euler beam model is based on the assumption that its length is much larger than the other two dimensions ( $L \gg W, T$ ) [27]. This allows to consider valid the hypothesis of plane stress discussed in Chapter 2. Given this assumption, let us express the set of forces and deformations shown in Figure 4.2 in the form of vectors:

$$\mathbf{F} = \begin{bmatrix} F_{xA} \\ F_{xB} \end{bmatrix} \quad (4.1)$$

$$\mathbf{u} = \begin{bmatrix} u_{xA} \\ u_{xB} \end{bmatrix} \quad (4.2)$$

We now derive an expression that takes into account the punctual deformation  $u_x$  due to  $F_{xA}$  and  $F_{xB}$  in a generic point  $x$  along the beam length. Assuming the local reference system origin in the beam end  $A$  and normalizing the  $u_x$  with respect to its length  $L$  it results:

$$u_x = u_{xA} + (u_{xB} - u_{xA}) \frac{x}{L} \quad (4.3)$$

The first term at the second member of 4.3 is referred to the end  $A$ , while the second one is taken in a generic point  $x$  along  $L$ . Notice that  $x \in [0, L]$  and consequently  $\frac{x}{L} \in [0, 1]$ . Now, applying the 2.17 to the 4.3 it is:

$$e_{xx} = \frac{\partial u_x}{\partial x} = \frac{1}{L}(u_{xB} - u_{xA}) = \frac{1}{L} \begin{bmatrix} -1 & 1 \end{bmatrix} \begin{bmatrix} u_{xA} \\ u_{xB} \end{bmatrix} \quad (4.4)$$



The 4.4 can be expressed in a compact form as:

$$\mathbf{e} = \mathbf{b}\mathbf{u} \quad (4.5)$$

where  $\mathbf{e}$ ,  $\mathbf{b}$  and  $\mathbf{u}$  are:

$$\mathbf{e} = [e_{xx}] \quad (4.6)$$

$$\mathbf{b} = \frac{1}{L} \begin{bmatrix} -1 & 1 \end{bmatrix} \quad (4.7)$$

$$\mathbf{u} = \begin{bmatrix} u_{xA} \\ u_{xB} \end{bmatrix} \quad (4.8)$$

The stiffness matrix  $\mathbf{k}$  can now be introduced and its expression is:

$$\mathbf{k} = \int_v \mathbf{b}^T \mathbf{x} \mathbf{b} dV \quad (4.9)$$

where the integral is calculated over the volume  $v$ . Moreover,  $\mathbf{x}$  is the 2.50 that in this simple case is:

$$\mathbf{x} = E \quad (4.10)$$

Finally, the stiffness matrix  $\mathbf{k}$  expression is:

$$\mathbf{k} = \int_0^L \frac{1}{L} \begin{bmatrix} -1 \\ 1 \end{bmatrix} \frac{E}{L} \begin{bmatrix} -1 & 1 \end{bmatrix} A dx = \frac{AE}{L} \begin{bmatrix} 1 & -1 \\ -1 & 1 \end{bmatrix} \quad (4.11)$$

where, being  $A$  the beam transversal area, it is:

$$dV = A dx \quad (4.12)$$

Once  $\mathbf{k}$  is determined, the relation between the forces applied to the beam and the corresponding deformations is defined as:

$$\mathbf{F} = \mathbf{k}\mathbf{u} \quad (4.13)$$

that written using the complete notation is:

$$\begin{bmatrix} F_{xA} \\ F_{xB} \end{bmatrix} = \frac{AE}{L} \begin{bmatrix} 1 & -1 \\ -1 & 1 \end{bmatrix} \begin{bmatrix} u_{xA} \\ u_{xB} \end{bmatrix} \quad (4.14)$$

### 4.1.2 The Mass Matrix

As already stressed earlier, the mass matrix expresses the set of relations between the forces applied to the beam and the accelerations related to all its DoF's. In formula, this concept is expressed by the well-known following expression:

$$F = ma \quad (4.15)$$

where the acceleration  $a$  is defined as double derivative over time of the displacement  $u$ :

$$a = \ddot{u} = \frac{\partial^2 u}{\partial t^2} \quad (4.16)$$

What we are interested in is to extend the 4.15 to the case of multiple DoF's, which means to express it in vector form:

$$\mathbf{F} = \mathbf{m}\mathbf{a} \quad (4.17)$$

where  $\mathbf{F}$  and  $\mathbf{a}$ , in the simple case depicted in Figure 4.2 are:

$$\mathbf{F} = \begin{bmatrix} F_{xA} \\ F_{xB} \end{bmatrix} \quad (4.18)$$

$$\mathbf{a} = \ddot{\mathbf{u}} = \begin{bmatrix} \ddot{u}_{xA} \\ \ddot{u}_{xB} \end{bmatrix} \quad (4.19)$$

It is now clear that we have now to seek for a matrix form of the mass  $\mathbf{m}$  to be included in the 4.17 that is the mass matrix indeed. To derive  $\mathbf{m}$  we need to express all nodal displacements as already done in equation 4.3. On this purpose let us introduce a non-dimensional variable  $\xi$  as follows:

$$\xi = \frac{x}{L} \quad (4.20)$$

that defines the punctual abscissa  $x$  along the beam, normalized with respect to its length  $L$  [27]. Applying once again the superposition principle (see Figure 4.2) and assuming a unit deformation at both nodes ( $u_{xA} = 1$  and  $u_{xB} = 1$ ), the local displacement in a generic point  $x$  along the beam due to the two just mentioned deformations is expressed by the vector  $\mathbf{a}_m$  as:

$$\mathbf{a}_m = [ 1 - \xi \quad \xi ] \quad (4.21)$$

where the subscript  $\mathbf{m}$  has been introduced in order not to confuse the vector  $\mathbf{a}_m$  of 4.21 with the acceleration (equation 4.19). The interpretation of the geometrical meaning of 4.21 is rather straightforward. Whether we consider the origin  $x = 0$  it results  $\xi = 0$  and consequently:

$$\mathbf{a}_m(\xi = 0) = [ 1 \ 0 ] \quad (4.22)$$

which means the deformation applied to the node  $A$  has its maximum value (i.e. 1) in it while it reduces as  $x$  increases till it reaches 0 in the  $B$  end. The opposite situation is:

$$\mathbf{a}_m(\xi = 1) = [ 0 \ 1 ] \quad (4.23)$$

in which the deformation of end  $B$  does not give any contribution in the node  $A$  while, of course, it is equal to 1 in  $B$ . It is now possible to introduce the mass matrix  $\mathbf{m}$  defined as:

$$\mathbf{m} = \int_v \rho \mathbf{a}_m^T \mathbf{a}_m dV \quad (4.24)$$

where  $v$  is the object volume,  $\rho$  the density of the material of which it is constituted and  $\mathbf{a}_m^T$  is the transposed vector  $\mathbf{a}_m$ . Let us now expand the 4.24:

$$\begin{aligned} \mathbf{m} &= \int_v \rho \begin{bmatrix} 1 - \xi \\ \xi \end{bmatrix} [ 1 - \xi \ \xi ] dV = \\ &= \rho \int_v \begin{bmatrix} (1 - \xi)^2 & \xi(1 - \xi) \\ \xi(1 - \xi) & \xi^2 \end{bmatrix} dV \end{aligned} \quad (4.25)$$

Integrating now each element of the matrix and keeping in mind that

$$dV = Adx = ALd\xi \quad (4.26)$$

it results:

$$\mathbf{m} = L \begin{bmatrix} \int_0^1 \rho A (1 - \xi)^2 d\xi & \int_0^1 \rho A \xi (1 - \xi) d\xi \\ \int_0^1 \rho A \xi (1 - \xi) d\xi & \int_0^1 \rho A \xi^2 d\xi \end{bmatrix} \quad (4.27)$$

Pre-multiplying  $\mathbf{m}$  by the quantity  $\rho AL$  and solving the integrals it results:

$$\mathbf{m} = \rho AL \begin{bmatrix} \left[ \xi - \xi^2 + \frac{\xi^3}{3} \right]_0^1 & \left[ \frac{\xi^2}{2} - \frac{\xi^3}{3} \right]_0^1 \\ \left[ \frac{\xi^2}{2} - \frac{\xi^3}{3} \right]_0^1 & \left[ \frac{\xi^3}{3} \right]_0^1 \end{bmatrix} \quad (4.28)$$

and finally

$$\mathbf{m} = \rho AL \begin{bmatrix} \frac{1}{3} & \frac{1}{6} \\ \frac{1}{6} & \frac{1}{3} \end{bmatrix} \quad (4.29)$$

Eventually, the 4.17 can be now expressed as:

$$\begin{bmatrix} F_{xA} \\ F_{xB} \end{bmatrix} = \rho AL \begin{bmatrix} \frac{1}{3} & \frac{1}{6} \\ \frac{1}{6} & \frac{1}{3} \end{bmatrix} \begin{bmatrix} \ddot{u}_{xA} \\ \ddot{u}_{xB} \end{bmatrix} \quad (4.30)$$

Now that both the stiffness  $\mathbf{k}$  and mass  $\mathbf{m}$  matrices have been introduced, we can combine the effects related to the elasticity and inertial behaviour of the beam in a single constitutive equation which is:

$$\mathbf{F} = \mathbf{k}\mathbf{u} + \mathbf{m}\ddot{\mathbf{u}} \quad (4.31)$$

and that, in the end, expressed in matrix form is:

$$\begin{bmatrix} F_{xA} \\ F_{xB} \end{bmatrix} = \frac{AE}{L} \begin{bmatrix} 1 & -1 \\ -1 & 1 \end{bmatrix} \begin{bmatrix} u_{xA} \\ u_{xB} \end{bmatrix} + \rho AL \begin{bmatrix} \frac{1}{3} & \frac{1}{6} \\ \frac{1}{6} & \frac{1}{3} \end{bmatrix} \begin{bmatrix} \ddot{u}_{xA} \\ \ddot{u}_{xB} \end{bmatrix} \quad (4.32)$$

## 4.2 Mechanical Model for the 12 DoF's Flexible Beam

Now that the stiffness and mass matrices have been introduced, the further step is to extend their formulation, already derived for the 2 DoF's Euler beam in previous section, to the most generic case of the 12 DoF's beam. Its schematic is shown in Figure 4.3 where each beam end admits three linear deformations (along the  $x$ ,  $y$  and  $z$  axes) and three angular deformations (around the  $x$ ,  $y$  and  $z$  axes). Before dealing with calculations a brief consideration must be discussed. We decided to define this element as 12 DoF's beam. However, a Cartesian system admits 6 DoF's. Since the Euler beam is a flexible body deformations at each end are independent on the possible ones to the other

node. Because of this reason, it is more clear to consider 6 DoF's per each node even though the local reference system is unique. For the same reason, in the plate model presented in previous chapter we considered 6 overall DoF's instead of 6 DoF's for each node (i.e. 24 DoF's) because it is a rigid body.

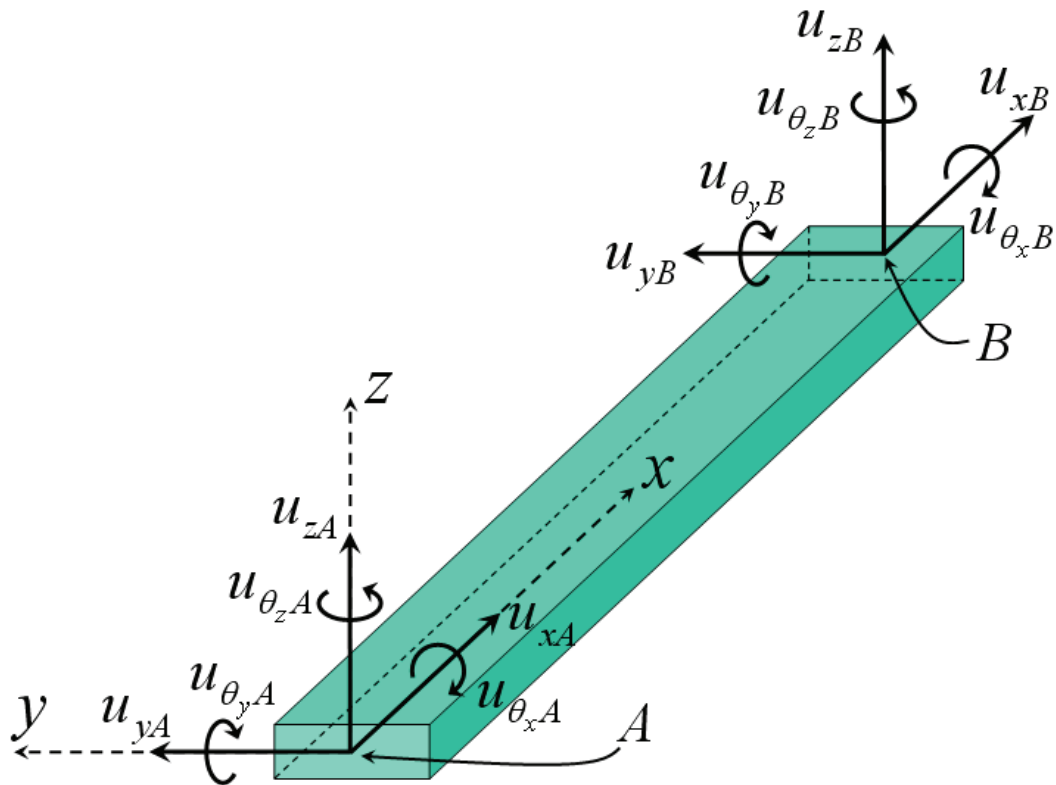


Figure 4.3: Euler beam with 12 DoF's. Three linear and three angular deformations are allowed to both  $A$  and  $B$  ends.

### 4.2.1 The 12 DoF's Stiffness Matrix

Let us now extend the stiffness matrix  $\mathbf{k}$  in order to make it appropriate to describe the whole set of 12 DoF's. First of all, in this case the 4.1 and 4.2 become:

$$\mathbf{F}^T = (F_{xA}, F_{yA}, F_{zA}, T_{\theta_{xA}}, T_{\theta_{yA}}, T_{\theta_{zA}}, F_{xB}, F_{yB}, F_{zB}, T_{\theta_{xB}}, T_{\theta_{yB}}, T_{\theta_{zB}}) \quad (4.33)$$

$$\mathbf{u}^T = (u_{xA}, u_{yA}, u_{zA}, u_{\theta_{xA}}, u_{\theta_{yA}}, u_{\theta_{zA}}, u_{xB}, u_{yB}, u_{zB}, u_{\theta_{xB}}, u_{\theta_{yB}}, u_{\theta_{zB}}) \quad (4.34)$$

We now have to derive a set of relations to link together all the deformations (linear and angular) the beam can undergo. These will be similar to the 4.3 although their expressions are more complicated. In this case, still applying the plane stress hypothesis, the 4.4 becomes:

$$\begin{bmatrix} e_{xx} \\ e_{yy} \\ e_{zz} \end{bmatrix} = \mathbf{b} \begin{bmatrix} u_{xA} \\ u_{yA} \\ u_{zA} \\ u_{\theta_{xA}} \\ u_{\theta_{yA}} \\ u_{\theta_{zA}} \\ u_{xB} \\ u_{yB} \\ u_{zB} \\ u_{\theta_{xB}} \\ u_{\theta_{yB}} \\ u_{\theta_{zB}} \end{bmatrix} \quad (4.35)$$

where  $\mathbf{b}$  is not a vector anymore, but it becomes a 3x12 matrix [27] as follows:

$$\mathbf{b} = \begin{bmatrix} b_{11} & b_{12} & b_{13} & b_{14} & b_{15} & b_{16} & b_{17} & b_{18} & b_{19} & b_{1,10} & b_{1,11} & b_{1,12} \\ b_{21} & b_{22} & b_{23} & b_{24} & b_{25} & b_{26} & b_{27} & b_{28} & b_{29} & b_{2,10} & b_{2,11} & b_{2,12} \\ b_{31} & b_{32} & b_{33} & b_{34} & b_{35} & b_{36} & b_{37} & b_{38} & b_{39} & b_{3,10} & b_{3,11} & b_{3,12} \end{bmatrix} \quad (4.36)$$

By substituting the  $\mathbf{b}$  matrix of equation 4.36 and its transposed  $\mathbf{b}^T$  in the 4.9 the stiffness matrix, whose dimension is 12x12, results to be:

$$\mathbf{k} = [ \mathbf{k}_1 \mid \mathbf{k}_2 ] \quad (4.37)$$

where

$$\mathbf{k}_1 = \begin{bmatrix} k_{11} & 0 & 0 & 0 & 0 & 0 \\ 0 & k_{22} & 0 & 0 & 0 & k_{26} \\ 0 & 0 & k_{33} & 0 & k_{35} & 0 \\ 0 & 0 & 0 & k_{44} & 0 & 0 \\ 0 & 0 & k_{53} & 0 & k_{55} & 0 \\ 0 & k_{62} & 0 & 0 & 0 & k_{66} \\ k_{71} & 0 & 0 & 0 & 0 & 0 \\ 0 & k_{82} & 0 & 0 & 0 & k_{86} \\ 0 & 0 & k_{93} & 0 & k_{95} & 0 \\ 0 & 0 & 0 & k_{10,4} & 0 & 0 \\ 0 & 0 & k_{11,3} & 0 & k_{11,5} & 0 \\ 0 & k_{12,2} & 0 & 0 & 0 & k_{12,6} \end{bmatrix} \quad (4.38)$$

$$\mathbf{k}_2 = \begin{bmatrix} k_{17} & 0 & 0 & 0 & 0 & 0 \\ 0 & k_{28} & 0 & 0 & 0 & k_{2,12} \\ 0 & 0 & k_{39} & 0 & k_{3,11} & 0 \\ 0 & 0 & 0 & k_{4,10} & 0 & 0 \\ 0 & 0 & k_{59} & 0 & k_{5,11} & 0 \\ 0 & k_{68} & 0 & 0 & 0 & k_{6,12} \\ k_{77} & 0 & 0 & 0 & 0 & 0 \\ 0 & k_{88} & 0 & 0 & 0 & k_{8,12} \\ 0 & 0 & k_{99} & 0 & k_{9,11} & 0 \\ 0 & 0 & 0 & k_{10,10} & 0 & 0 \\ 0 & 0 & k_{11,9} & 0 & k_{11,11} & 0 \\ 0 & k_{12,8} & 0 & 0 & 0 & k_{12,12} \end{bmatrix} \quad (4.39)$$

The elements of the 4.37, also accounting for the shear effect, are expressed as follows:

$$k_{11} = \frac{AE}{L} \quad (4.40)$$

$$k_{17} = -\frac{AE}{L} \quad (4.41)$$

$$k_{22} = \frac{12EI_z}{L^3(1 + \Phi_y)} \quad (4.42)$$

$$k_{26} = \frac{6EI_z}{L^2(1 + \Phi_y)} \quad (4.43)$$

$$k_{28} = -\frac{12EI_z}{L^3(1 + \Phi_y)} \quad (4.44)$$

$$k_{2,12} = \frac{6EI_z}{L^2(1 + \Phi_y)} \quad (4.45)$$

$$k_{33} = \frac{12EI_y}{L^3(1 + \Phi_z)} \quad (4.46)$$

$$k_{35} = -\frac{6EI_y}{L^2(1 + \Phi_z)} \quad (4.47)$$

$$k_{39} = -\frac{12EI_y}{L^3(1 + \Phi_z)} \quad (4.48)$$

$$k_{3,11} = -\frac{6EI_y}{L^2(1 + \Phi_z)} \quad (4.49)$$

$$k_{44} = \frac{GJ_x}{L} \quad (4.50)$$

$$k_{4,10} = -\frac{GJ_x}{L} \quad (4.51)$$

$$k_{55} = \frac{(4 + \Phi_z)EI_y}{L(1 + \Phi_z)} \quad (4.52)$$



$$k_{59} = \frac{6EI_y}{L^2(1 + \Phi_z)} \quad (4.53)$$

$$k_{5,11} = \frac{(2 - \Phi_z)EI_y}{L(1 + \Phi_z)} \quad (4.54)$$

$$k_{66} = \frac{(4 + \Phi_y)EI_z}{L(1 + \Phi_y)} \quad (4.55)$$

$$k_{68} = -\frac{6EI_z}{L^2(1 + \Phi_y)} \quad (4.56)$$

$$k_{6,12} = \frac{(2 - \Phi_y)EI_z}{L(1 + \Phi_y)} \quad (4.57)$$

$$k_{77} = \frac{AE}{L} \quad (4.58)$$

$$k_{88} = \frac{12EI_z}{L^3(1 + \Phi_y)} \quad (4.59)$$

$$k_{8,12} = -\frac{6EI_z}{L^2(1 + \Phi_y)} \quad (4.60)$$

$$k_{99} = \frac{12EI_y}{L^3(1 + \Phi_z)} \quad (4.61)$$

$$k_{9,11} = \frac{6EI_y}{L^2(1 + \Phi_z)} \quad (4.62)$$

$$k_{10,10} = \frac{GJ_x}{L} \quad (4.63)$$

$$k_{11,11} = \frac{(4 + \Phi_z)EI_y}{L(1 + \Phi_z)} \quad (4.64)$$

$$k_{12,12} = \frac{(4 + \Phi_y)EI_z}{L(1 + \Phi_y)} \quad (4.65)$$

In previous 4.40 - 4.65,  $G$  is the shear modulus (already expressed in the 2.42), while  $\Phi_y$  and  $\Phi_z$  are:

$$\Phi_y = \frac{12EI_z}{GWT L^2} \quad (4.66)$$

$$\Phi_z = \frac{12EI_y}{GWT L^2} \quad (4.67)$$

Furthermore,  $I_y$ ,  $I_x$  are the moments of inertia referred to the  $y$  and  $z$  axes respectively and  $J_x$  is the second moment of inertia with respect to the  $x$  axis [27]. Their expressions are:

$$I_y = \frac{1}{4} \int_0^W \int_0^T z^2 dz dy = \frac{W^3 T}{12} \quad (4.68)$$

$$I_z = \frac{1}{4} \int_0^T \int_0^W y^2 dy dz = \frac{WT^3}{12} \quad (4.69)$$

$$J_x = \frac{2(WT)^3}{7(W^2 + T^2)} \quad (4.70)$$

Now, by using the transposed of 4.33 and 4.34, and the 4.37, the 4.13 becomes:

$$\begin{bmatrix} F_{xA} \\ F_{yA} \\ F_{zA} \\ T_{\theta xA} \\ T_{\theta yA} \\ T_{\theta zA} \\ F_{xB} \\ F_{yB} \\ F_{zB} \\ T_{\theta xB} \\ T_{\theta yB} \\ T_{\theta zB} \end{bmatrix} = \mathbf{k} \begin{bmatrix} u_{xA} \\ u_{yA} \\ u_{zA} \\ u_{\theta xA} \\ u_{\theta yA} \\ u_{\theta zA} \\ u_{xB} \\ u_{yB} \\ u_{zB} \\ u_{\theta xB} \\ u_{\theta yB} \\ u_{\theta zB} \end{bmatrix} \quad (4.71)$$

Finally, it is possible to write the 4.71 as the corresponding set of equations which are following:

$$F_{xA} = k_{11}u_{xA} + k_{17}u_{xB} \quad (4.72)$$

$$F_{yA} = k_{22}u_{yA} + k_{26}u_{\theta_z A} + k_{28}u_{yB} + k_{2,12}u_{\theta_z B} \quad (4.73)$$

$$F_{zA} = k_{33}u_{zA} + k_{35}u_{\theta_y A} + k_{39}u_{zB} + k_{3,11}u_{\theta_y B} \quad (4.74)$$

$$T_{\theta_x A} = k_{44}u_{\theta_x A} + k_{4,10}u_{\theta_x B} \quad (4.75)$$

$$T_{\theta_y A} = k_{35}u_{zA} + k_{55}u_{\theta_y A} + k_{59}u_{zB} + k_{5,11}u_{\theta_y B} \quad (4.76)$$

$$T_{\theta_z A} = k_{26}u_{yA} + k_{66}u_{\theta_z A} + k_{68}u_{yB} + k_{6,12}u_{\theta_z B} \quad (4.77)$$

$$F_{xB} = +k_{17}u_{xA} + k_{77}u_{xB} \quad (4.78)$$

$$F_{yB} = +k_{28}u_{yA} + k_{68}u_{\theta_z A} + k_{88}u_{yB} + k_{8,12}u_{\theta_z B} \quad (4.79)$$

$$F_{zB} = +k_{39}u_{zA} + k_{59}u_{\theta_y A} + k_{99}u_{zB} + k_{9,12}u_{\theta_y B} \quad (4.80)$$

$$T_{\theta_x B} = +k_{4,10}u_{\theta_x A} + k_{10,10}u_{\theta_x B} \quad (4.81)$$

$$T_{\theta_y B} = k_{3,11}u_{zA} + k_{5,11}u_{\theta_y A} + k_{9,11}u_{zB} + k_{11,11}u_{\theta_y B} \quad (4.82)$$

$$T_{\theta_z B} = k_{2,12}u_{yA} + k_{6,12}u_{\theta_z A} + k_{8,12}u_{yB} + k_{12,12}u_{\theta_z B} \quad (4.83)$$

### 4.2.2 The 12 DoF's Mass Matrix

We now proceed to extend the mass matrix  $\mathbf{m}$  already introduced for the 2 DoF's case (equation 4.29), to the case of 12 DoF's. Doing so, it becomes necessary to introduce a punctual description of the beam depending on all the stimuli (forces and torques) applied to its two ends  $A$  and  $B$ . These information is provided by a set of relations called Hermitian Shape Functions (HRS's) [27]. Each of them describes the deformation in a generic point of the beam, for instance along its length in  $x$ , depending on the deformation applied to one end. Every HSF is defined supposing the superposition principle to be satisfied. In other words, an HFS determines the effect of a particular DoF of a certain beam end, supposing all the other stimuli equal to zero and the other end to be constrained. For instance, if we apply a deformation  $u_{zA}$  to the node  $A$  directed along  $z$  the beam configuration is the one shown in Figure 4.4. Introducing now a suitable Hermitian Shape Function  $\psi_{zA}(x)$  describing the punctual displacement along  $z$  in a generic point on  $x$  axis and supposing  $u_{zA}$  to be equal to 1 it results:

$$\psi_{zA}(x) = 1 - 3\left(\frac{x}{L}\right)^2 + 2\left(\frac{x}{L}\right)^3 \quad (4.84)$$

Reintroducing the non-dimensional variable  $\xi$  already defined in the 4.20 the 4.84 can be written as:

$$\psi_{zA}(\xi) = 1 - 3\xi^2 + 2\xi^3 \quad (4.85)$$

Let us now examine an angular DoF. On this purpose, in Figure 4.5 a rotation  $u_{\theta_y A}$  around the  $y$  axis in the beam end  $A$  is applied. This is also supposed to be equal to 1. Notice that the rotation has been applied in the negative direction of  $y$ . This was done in order not to capsize the schematic in figure. The local displacement along  $z$  in a generic point  $x$  induced by  $u_{\theta_y A}$  is then expressed as:

$$\psi_{\theta_y A}(\xi) = (-\xi + 2\xi^2 - \xi^3)L \quad (4.86)$$

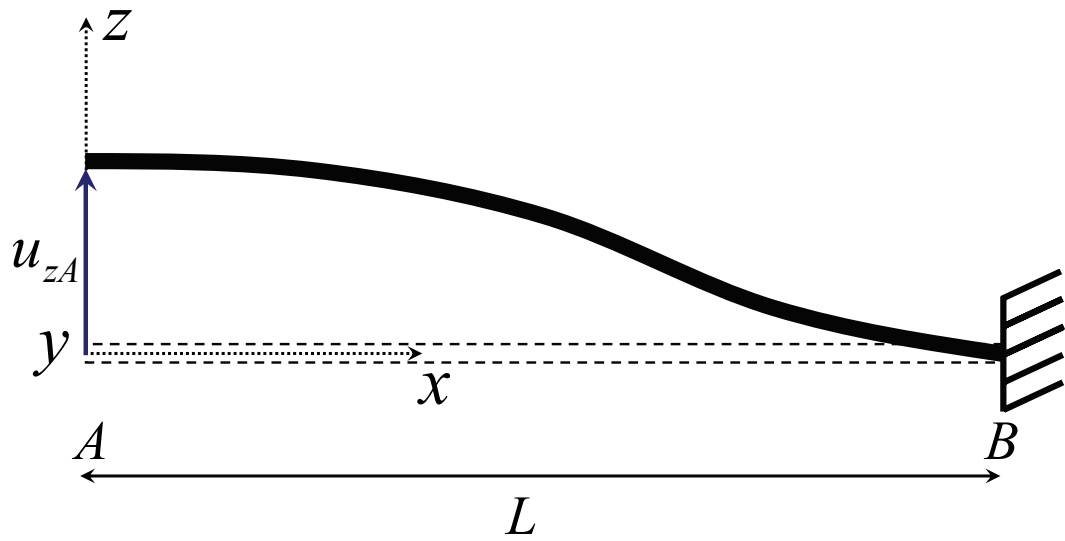


Figure 4.4: Configuration of the Euler beam which undergoes a linear deformation  $u_{zA}$  applied in  $A$  with the  $B$  end anchored.

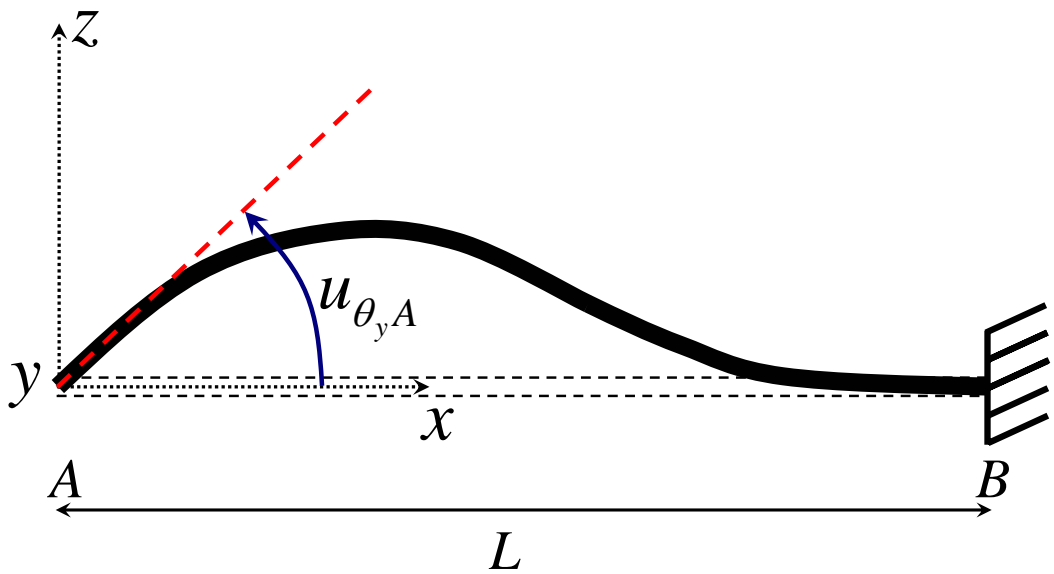


Figure 4.5: Configuration of the Euler beam which undergoes an angular deformation  $u_{\theta_y A}$  applied around the  $y$  axis in  $A$  with the  $B$  end anchored.

By exploiting the same approach for all the 12 DoF's, the vector  $\mathbf{a}_m$  of the 4.21 extends to a 3x12 matrix whose transposed  $\mathbf{a}_m^T$  is [27]:

$$\mathbf{a}_m^T = \begin{bmatrix} 1 - \xi & 0 & 0 \\ 6(\xi - \xi^2)\eta & 1 - 3\xi^2 + 2\xi^3 & 0 \\ 6(\xi - \xi^2)\zeta & 0 & 1 - 3\xi^2 + 2\xi^3 \\ 0 & -(1 - \xi)L\zeta & -(1 - \xi)L\eta \\ (1 - 4\xi + 3\xi^2)L\zeta & 0 & (-\xi + 2\xi^2 - \xi^3)L \\ (-1 + 4\xi - 3\xi^2)L\eta & (\xi - 2\xi^2 + \xi^3)L & 0 \\ \xi & 0 & 0 \\ 6(-\xi + \xi^2)\eta & 3\xi^2 - 2\xi^3 & 0 \\ 6(-\xi + \xi^2)\zeta & 0 & 3\xi^2 - 2\xi^3 \\ 0 & -L\xi\zeta & -L\xi\eta \\ (-2\xi + 3\xi^2)L\zeta & 0 & (\xi^2 - \xi^3)L \\ (2\xi - 3\xi^2)L\eta & (-\xi^2 + \xi^3) & 0 \end{bmatrix} \quad (4.87)$$

In previous 4.87 other two non-dimensional variables similar to the 4.20 have been introduced:

$$\eta = \frac{y}{L} \quad (4.88)$$

$$\zeta = \frac{z}{L} \quad (4.89)$$

It is now possible to derive the mass matrix  $\mathbf{m}$ . Its expression 4.24 can be now rearranged as follows:

$$\mathbf{m} = \rho AL \int_0^1 \int_0^1 \int_0^1 \mathbf{a}^T \mathbf{a} d\xi d\eta d\zeta \quad (4.90)$$

Solving the volume integral 4.90 leads to the mass matrix expressed as:

$$\mathbf{m} = [ \mathbf{m}_1 \mid \mathbf{m}_2 ] \quad (4.91)$$

where

$$\mathbf{m}_1 = \begin{bmatrix} m_{11} & 0 & 0 & 0 & 0 & 0 \\ 0 & m_{22} & 0 & 0 & 0 & m_{26} \\ 0 & 0 & m_{33} & 0 & m_{35} & 0 \\ 0 & 0 & 0 & m_{44} & 0 & 0 \\ 0 & 0 & m_{35} & 0 & m_{55} & 0 \\ 0 & m_{26} & 0 & 0 & 0 & m_{66} \\ m_{17} & 0 & 0 & 0 & 0 & 0 \\ 0 & m_{28} & 0 & 0 & 0 & m_{68} \\ 0 & 0 & m_{39} & 0 & m_{59} & 0 \\ 0 & 0 & 0 & m_{4,10} & 0 & 0 \\ 0 & 0 & m_{3,11} & 0 & m_{5,11} & 0 \\ 0 & m_{2,12} & 0 & 0 & 0 & m_{6,12} \end{bmatrix} \quad (4.92)$$

$$\mathbf{m}_2 = \begin{bmatrix} m_{17} & 0 & 0 & 0 & 0 & 0 \\ 0 & m_{28} & 0 & 0 & 0 & m_{2,12} \\ 0 & 0 & m_{39} & 0 & m_{3,11} & 0 \\ 0 & 0 & 0 & m_{4,10} & 0 & 0 \\ 0 & 0 & m_{59} & 0 & m_{5,11} & 0 \\ 0 & m_{68} & 0 & 0 & 0 & m_{6,12} \\ m_{77} & 0 & 0 & 0 & 0 & 0 \\ 0 & m_{88} & 0 & 0 & 0 & m_{8,12} \\ 0 & 0 & m_{99} & 0 & m_{9,11} & 0 \\ 0 & 0 & 0 & m_{10,10} & 0 & 0 \\ 0 & 0 & m_{9,11} & 0 & m_{11,11} & 0 \\ 0 & m_{8,12} & 0 & 0 & 0 & m_{12,12} \end{bmatrix} \quad (4.93)$$

The elements of 4.91 are expressed as follows:

$$m_{11} = \rho AL \left( \frac{1}{3} \right) \quad (4.94)$$

$$m_{17} = \rho AL \left( \frac{1}{6} \right) \quad (4.95)$$

$$m_{22} = \rho AL \left( \frac{13}{35} + \frac{6I_z}{5AL^2} \right) \quad (4.96)$$

$$m_{26} = \rho AL \left( \frac{11L}{210} + \frac{I_z}{10AL} \right) \quad (4.97)$$

$$m_{28} = \rho AL \left( \frac{9}{70} - \frac{6I_z}{5AL^2} \right) \quad (4.98)$$

$$m_{2,12} = \rho AL \left( -\frac{13L}{420} + \frac{I_z}{10AL} \right) \quad (4.99)$$

$$m_{33} = \rho AL \left( \frac{13}{35} + \frac{6I_y}{5AL^2} \right) \quad (4.100)$$

$$m_{35} = \rho AL \left( -\frac{11L}{210} - \frac{I_y}{10AL} \right) \quad (4.101)$$

$$m_{39} = \rho AL \left( \frac{9}{70} - \frac{6I_y}{5AL^2} \right) \quad (4.102)$$

$$m_{3,11} = \rho AL \left( \frac{13L}{420} - \frac{I_y}{10AL} \right) \quad (4.103)$$

$$m_{44} = \rho AL \left( \frac{J_x}{3A} \right) \quad (4.104)$$

$$m_{4,10} = \rho AL \left( \frac{J_x}{6A} \right) \quad (4.105)$$

$$m_{55} = \rho AL \left( \frac{L^2}{105} + \frac{2I_y}{15A} \right) \quad (4.106)$$

$$m_{59} = \rho AL \left( -\frac{13L}{420} + \frac{I_y}{10AL} \right) \quad (4.107)$$

$$m_{5,11} = \rho AL \left( -\frac{L^2}{140} - \frac{I_y}{30A} \right) \quad (4.108)$$

$$m_{66} = \rho AL \left( \frac{L^2}{105} + \frac{2I_z}{15A} \right) \quad (4.109)$$

$$m_{68} = \rho AL \left( \frac{13L}{420} - \frac{I_z}{10AL} \right) \quad (4.110)$$

$$m_{6,12} = \rho AL \left( -\frac{L^2}{140} - \frac{I_z}{30A} \right) \quad (4.111)$$



$$m_{77} = \rho AL \left( \frac{1}{3} \right) \quad (4.112)$$

$$m_{88} = \rho AL \left( \frac{13}{35} + \frac{6I_z}{5AL^2} \right) \quad (4.113)$$

$$m_{8,12} = \rho AL \left( -\frac{11L}{210} - \frac{I_z}{10AL} \right) \quad (4.114)$$

$$m_{99} = \rho AL \left( \frac{13}{35} + \frac{6I_y}{5AL^2} \right) \quad (4.115)$$

$$m_{9,11} = \rho AL \left( \frac{11L}{210} + \frac{I_y}{10AL} \right) \quad (4.116)$$

$$m_{10,10} = \rho AL \left( \frac{J_x}{3A} \right) \quad (4.117)$$

$$m_{11,11} = \rho AL \left( \frac{L^2}{105} + \frac{2I_y}{15A} \right) \quad (4.118)$$

$$m_{12,12} = \rho AL \left( \frac{L^2}{105} + \frac{2I_z}{15A} \right) \quad (4.119)$$

The 4.17 for the 12 DoF's case becomes:

$$\begin{bmatrix} F_{xA} \\ F_{yA} \\ F_{zA} \\ T_{\theta_x A} \\ T_{\theta_y A} \\ T_{\theta_z A} \\ F_{xB} \\ F_{yB} \\ F_{zB} \\ T_{\theta_x B} \\ T_{\theta_y B} \\ T_{\theta_z B} \end{bmatrix} = \mathbf{m} \begin{bmatrix} \ddot{u}_{xA} \\ \ddot{u}_{yA} \\ \ddot{u}_{zA} \\ \ddot{\theta}_{xA} \\ \ddot{\theta}_{yA} \\ \ddot{\theta}_{zA} \\ \ddot{u}_{xB} \\ \ddot{u}_{yB} \\ \ddot{u}_{zB} \\ \ddot{\theta}_{xB} \\ \ddot{\theta}_{yB} \\ \ddot{\theta}_{zB} \end{bmatrix} \quad (4.120)$$

Finally, the set of equations coming from the mass matrix which represent the relation 4.30 are:

$$F_{xA} = m_{11}\ddot{u}_{xA} + m_{17}\ddot{u}_{xB} \quad (4.121)$$

$$F_{yA} = m_{22}\ddot{u}_{yA} + m_{26}\ddot{u}_{\theta_z A} + m_{28}\ddot{u}_{yB} + m_{2,12}\ddot{u}_{\theta_z B} \quad (4.122)$$

$$F_{zA} = m_{33}\ddot{u}_{zA} + m_{35}\ddot{u}_{\theta_y A} + m_{39}\ddot{u}_{zB} + m_{3,11}\ddot{u}_{\theta_y B} \quad (4.123)$$

$$T_{\theta_x A} = m_{44}\ddot{u}_{\theta_x A} + m_{4,10}\ddot{u}_{\theta_x B} \quad (4.124)$$

$$T_{\theta_y A} = m_{35}\ddot{u}_{zA} + m_{55}\ddot{u}_{\theta_y A} + m_{59}\ddot{u}_{zB} + m_{5,11}\ddot{u}_{\theta_y B} \quad (4.125)$$

$$T_{\theta_z A} = m_{26}\ddot{u}_{yA} + m_{66}\ddot{u}_{\theta_z A} + m_{68}\ddot{u}_{yB} + m_{6,12}\ddot{u}_{\theta_z B} \quad (4.126)$$

$$F_{xB} = m_{17}\ddot{u}_{xA} + m_{77}\ddot{u}_{xB} \quad (4.127)$$

$$F_{yB} = m_{28}\ddot{u}_{yA} + m_{68}\ddot{u}_{\theta_z A} + m_{88}\ddot{u}_{yB} + m_{8,12}\ddot{u}_{\theta_z B} \quad (4.128)$$

$$F_{zB} = m_{39}\ddot{u}_{zA} + m_{59}\ddot{u}_{\theta_y A} + m_{99}\ddot{u}_{zB} + m_{11,9}\ddot{u}_{\theta_y B} \quad (4.129)$$

$$M_{\theta_x B} = m_{4,10}\ddot{u}_{\theta_x A} + m_{10,10}\ddot{u}_{\theta_x B} \quad (4.130)$$

$$M_{\theta_y B} = m_{3,11}\ddot{u}_{zA} + m_{5,11}\ddot{u}_{\theta_y A} + m_{9,11}\ddot{u}_{zB} + m_{11,12}\ddot{u}_{\theta_y B} \quad (4.131)$$

$$M_{\theta_z B} = m_{2,12}\ddot{u}_{yA} + m_{6,12}\ddot{u}_{\theta_z A} + m_{8,12}\ddot{u}_{yB} + m_{12,12}\ddot{u}_{\theta_z B} \quad (4.132)$$

### 4.3 Complete Mechanical Model for the 12 DoF's Euler Beam

Now that all the relations referring to the elastic and inertial behaviour of the Euler beam have been defined, we have to link its model to the global reference system to make it consistent to the other MEMS library components. First of all, the beam can have an orientation in the space like shown in Figure 4.6 where it admits three non-zero orientation angles around the global frame axes ( $\theta_X$ ,  $\theta_Y$  and  $\theta_Z$ ). Moreover, since we are dealing with a deformable body, the rotations of one end around the global frame axes  $X, Y, Z$  can be different from the ones to the other end. Let  $u_{\theta_{XA}}, u_{\theta_{YA}}, u_{\theta_{ZA}}$  be the triad of angles referred to the end  $A$  and  $u_{\theta_{XB}}, u_{\theta_{YB}}, u_{\theta_{ZB}}$  the one related to the other end  $B$ . If we now introduce three initial orientation angles for the beam around the global system and we address them as  $\theta_{X_{INIT}}, \theta_{Y_{INIT}}$  and  $\theta_{Z_{INIT}}$ , we can define the three instantaneous angles of the end  $A$  around the global axes as:

$$\theta_{XA} = \theta_{X_{INIT}} + u_{\theta_{XA}} \quad (4.133)$$

$$\theta_{YA} = \theta_{Y_{INIT}} + u_{\theta_{YA}} \quad (4.134)$$

$$\theta_{ZA} = \theta_{Z_{INIT}} + u_{\theta_{ZA}} \quad (4.135)$$

and the other three instantaneous angles referred to the  $B$  end as:

$$\theta_{XB} = \theta_{X_{INIT}} + u_{\theta_{XB}} \quad (4.136)$$

$$\theta_{YB} = \theta_{Y_{INIT}} + u_{\theta_{YB}} \quad (4.137)$$

$$\theta_{ZB} = \theta_{Z_{INIT}} + u_{\theta_{ZB}} \quad (4.138)$$

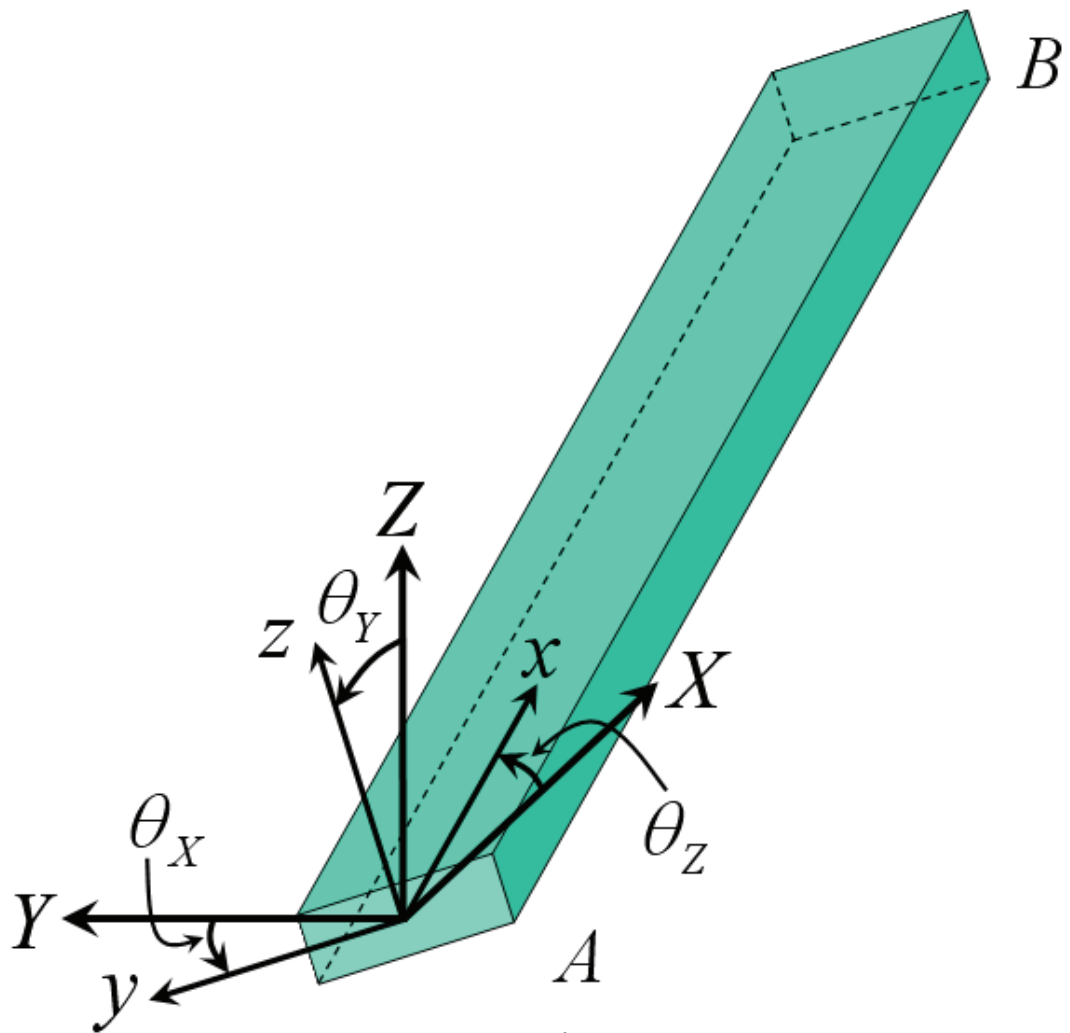


Figure 4.6: The Euler beam with  $\theta_x$ ,  $\theta_y$  and  $\theta_z$  orientation angles. These define the relations between the global reference system  $(X, Y, Z)$  and the local one  $(x, y, z)$ .

Now we have all we need to define the relations between the global reference system and the two local systems linked to the  $A$  and  $B$  beam ends. The approach consist of transforming the linear and angular deformation applied to the two ends in the global frame, in the corresponding deformation in the local system to  $A$  and  $B$  ends. The expression to perform this transformation is:

$$\begin{bmatrix} u_{xA} \\ u_{yA} \\ u_{zA} \\ u_{\theta_x A} \\ u_{\theta_y A} \\ u_{\theta_z A} \\ u_{xB} \\ u_{yB} \\ u_{zB} \\ u_{\theta_x B} \\ u_{\theta_y B} \\ u_{\theta_z B} \end{bmatrix} = \begin{bmatrix} \Omega_{LA}^T & \mathbf{0} & \mathbf{0} & \mathbf{0} \\ \mathbf{0} & \Omega_{LA}^T & \mathbf{0} & \mathbf{0} \\ \mathbf{0} & \mathbf{0} & \Omega_{LB}^T & \mathbf{0} \\ \mathbf{0} & \mathbf{0} & \mathbf{0} & \Omega_{LB}^T \end{bmatrix} \begin{bmatrix} u_{XA} \\ u_{YA} \\ u_{ZA} \\ u_{\theta_X A} \\ u_{\theta_Y A} \\ u_{\theta_Z A} \\ u_{XB} \\ u_{YB} \\ u_{ZB} \\ u_{\theta_X B} \\ u_{\theta_Y B} \\ u_{\theta_Z B} \end{bmatrix} \quad (4.139)$$

where  $\Omega_{LA}^T$  and  $\Omega_{LB}^T$  are the transposed of 2.8 respectively calculated as a function of  $\theta_{XA}, \theta_{YA}, \theta_{ZA}$  at node  $A$  and of  $\theta_{XB}, \theta_{YB}, \theta_{ZB}$  at node  $B$ . Finally,  $\mathbf{0}$  is a 3x3 matrix with all zero elements. For instance, looking at 4.139,  $u_{xA}$  is:

$$u_{xA} = \cos \theta_{YA} \cos \theta_{ZA} u_{XA} + \cos \theta_{YA} \sin \theta_{ZA} u_{YA} - \sin \theta_{YA} u_{ZA} \quad (4.140)$$

When all the deformations are transformed in the local system, the corresponding forces and torques are determined with the 4.72 - 4.83. Eventually, these are transferred back into the global reference system as follows:

$$\begin{bmatrix} F_{XA} \\ F_{YA} \\ F_{ZA} \\ T_{\theta_{xA}} \\ T_{\theta_{yA}} \\ T_{\theta_{zA}} \\ F_{XB} \\ F_{YB} \\ F_{ZB} \\ T_{\theta_{xB}} \\ T_{\theta_{yB}} \\ T_{\theta_{zB}} \end{bmatrix} = \begin{bmatrix} \Omega_{LA} & \mathbf{0} & \mathbf{0} & \mathbf{0} \\ \mathbf{0} & \Omega_{LA} & \mathbf{0} & \mathbf{0} \\ \mathbf{0} & \mathbf{0} & \Omega_{LB} & \mathbf{0} \\ \mathbf{0} & \mathbf{0} & \mathbf{0} & \Omega_{LB} \end{bmatrix} \begin{bmatrix} F_{xA} \\ F_{yA} \\ F_{zA} \\ T_{\theta_{xA}} \\ T_{\theta_{yA}} \\ T_{\theta_{zA}} \\ F_{xB} \\ F_{yB} \\ F_{zB} \\ T_{\theta_{xB}} \\ T_{\theta_{yB}} \\ T_{\theta_{zB}} \end{bmatrix} \quad (4.141)$$

Concerning the inertial effects the approach is the same. First, all linear and angular accelerations are transferred in the local frame:

$$\begin{bmatrix} \ddot{u}_{xA} \\ \ddot{u}_{yA} \\ \ddot{u}_{zA} \\ \ddot{u}_{\theta_{xA}} \\ \ddot{u}_{\theta_{yA}} \\ \ddot{u}_{\theta_{zA}} \\ \ddot{u}_{xB} \\ \ddot{u}_{yB} \\ \ddot{u}_{zB} \\ \ddot{u}_{\theta_{xB}} \\ \ddot{u}_{\theta_{yB}} \\ \ddot{u}_{\theta_{zB}} \end{bmatrix} = \begin{bmatrix} \Omega_{LA}^T & \mathbf{0} & \mathbf{0} & \mathbf{0} \\ \mathbf{0} & \Omega_{LA}^T & \mathbf{0} & \mathbf{0} \\ \mathbf{0} & \mathbf{0} & \Omega_{LB}^T & \mathbf{0} \\ \mathbf{0} & \mathbf{0} & \mathbf{0} & \Omega_{LB}^T \end{bmatrix} \begin{bmatrix} \ddot{u}_{XA} \\ \ddot{u}_{YA} \\ \ddot{u}_{ZA} \\ \ddot{u}_{\theta_{xA}} \\ \ddot{u}_{\theta_{yA}} \\ \ddot{u}_{\theta_{zA}} \\ \ddot{u}_{XB} \\ \ddot{u}_{YB} \\ \ddot{u}_{ZB} \\ \ddot{u}_{\theta_{xB}} \\ \ddot{u}_{\theta_{yB}} \\ \ddot{u}_{\theta_{zB}} \end{bmatrix} \quad (4.142)$$

Then, the 4.121 - 4.132 are calculated and finally transformed in the global frame with the 4.141.

The mechanical model discussed thus far is linear. It is reasonable to assume the elastic behaviour of the beam linear as long as dealing with small deformations. This is what typically happens in the functional situations we are interested in. For instance, in a MEMS switch based on the rigid plate suspended with Euler beams jointed at its corners, a typical plate-to-substrate gap is of a few microns. Whether the beams are relatively long, it is reasonable to assume a vertical deformation of a few microns (due to the pull-in) as lying within their linear elastic regime. However, a model which accounts for the non-linearities due to large deformations has been implemented. This is the one proposed by Jing [32] and it is not shown in this thesis since it has been already discussed, explained in details and validated by the Author.

## 4.4 The Electrostatic Model for the 12 DoF's Euler Beam

Before introducing the electrostatic model for the Euler beam it has to be mentioned that a model taking into account the contact with the substrate has been also implemented for this component. It is the same as the one presented in previous chapter referring to the rigid plate. The contact force is applied to the beam ends  $A$  or/and  $B$  depending on which node(s) the collision occurs. Since this does not represent anything new with respect to the contact model of previous chapter, its formulation will not be reported once again here.

Moving now the focus on the electrostatic model for the Euler beam we need to know the punctual distance between a generic point along the beam length and the substrate. First of all, we will refer to the displacements of the beam center line lying on its lower face, as Figure 4.7 shows. This reports the vertical displacement along  $L$  defined by the HSF  $\psi_{zA}(\xi)$ .

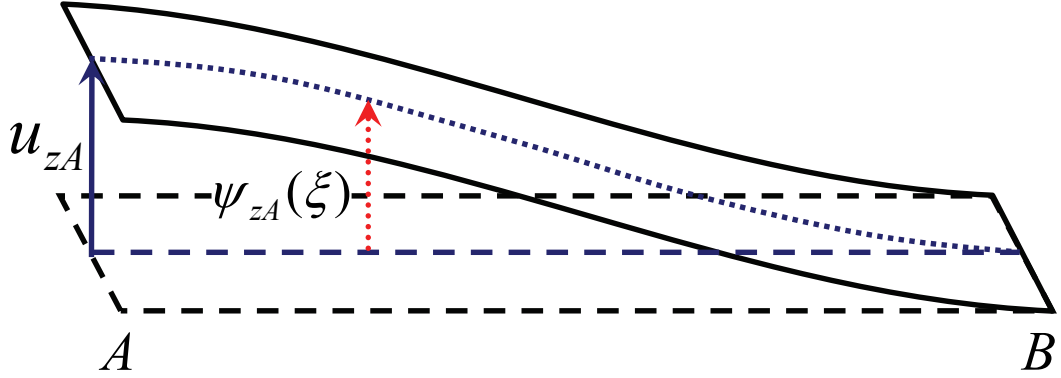


Figure 4.7: The vertical displacement of the beam center line (dotted line) is determined by means of the HSF's.

We are interested in defining the local vertical displacement due to all the stimuli applied to  $A$  and  $B$  ends which give contribution along the  $z$  axis. Looking at the right column of 4.87 (corresponding to the  $z$  direction) and assuming the vertical displacement contribution given by the torsion around the  $x$  axis to be negligible, the local  $z$  displacement is due to the linear deformation along  $z$  and the torsion around  $y$  axis at the  $A$  and  $B$  ends. The corresponding HSF's are respectively:

$$\psi_{zA}(\xi) = 1 - 3\xi^2 + 2\xi^3 \quad (4.143)$$

$$\psi_{\theta_y A}(\xi) = (-\xi + 2\xi^2 - \xi^2)L \quad (4.144)$$

$$\psi_{zB}(\xi) = 3\xi^2 - 2\xi^3 \quad (4.145)$$

$$\psi_{\theta_y B}(\xi) = (\xi^2 - \xi^3)L \quad (4.146)$$

Let us assume the beam stimulated in all the just mentioned DoF's which give deformation contributions along the  $z$  local axis, like shown in Figure 4.8.



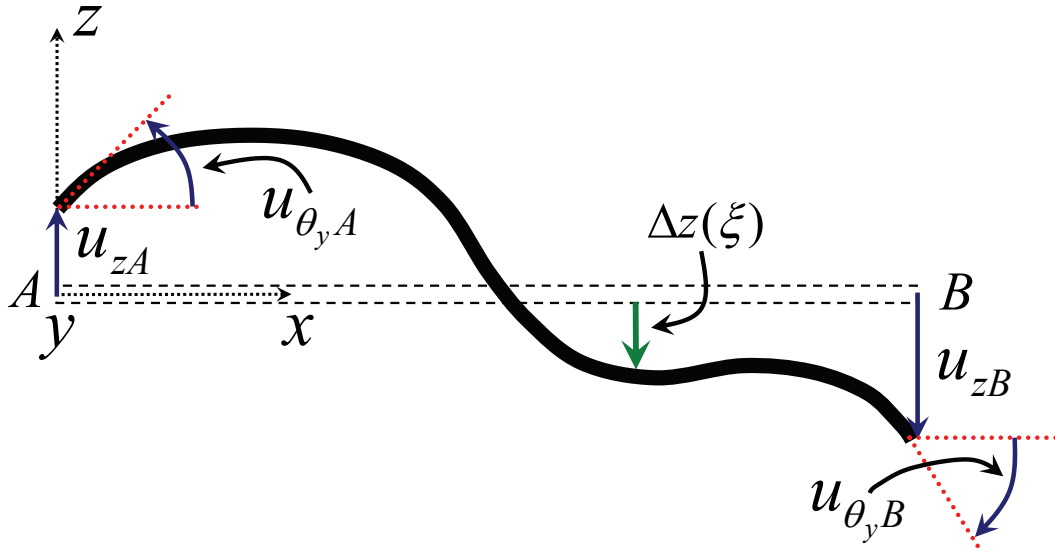


Figure 4.8: Beam stimulated in all the DoF's which give contribution along  $z$  axis.

The local  $z$  displacement  $\Delta z(\xi)$  with respect to the initial beam position (dashed line in previous figure) is given by the sum of the 4.143 - 4.146 multiplied by the corresponding perturbation magnitude:

$$\Delta z(\xi) = \psi_{zA}(\xi)u_{xA} + \psi_{\theta_y A}(\xi)u_{\theta_x A} + \psi_{zB}(\xi)u_{xB} + \psi_{\theta_y B}(\xi)u_{\theta_x B} \quad (4.147)$$

The 4.147 describes the punctual  $z$  deformation of the beam center line of Figure 4.7 in the local system  $x, y, z$ . We now have to derive an expression which defines the vertical distance of each beam center line point with respect to the substrate in the global reference system, as a function of the initial orientation angles  $\theta_{X_{INIT}}$ ,  $\theta_{Y_{INIT}}$  and  $\theta_{Z_{INIT}}$  (see Figure 4.6). The contributions given to the vertical distance between a generic point  $\xi$  and the substrate due to an initial orientation angle  $\theta_{Y_{INIT}}$  are depicted in Figure 4.9.

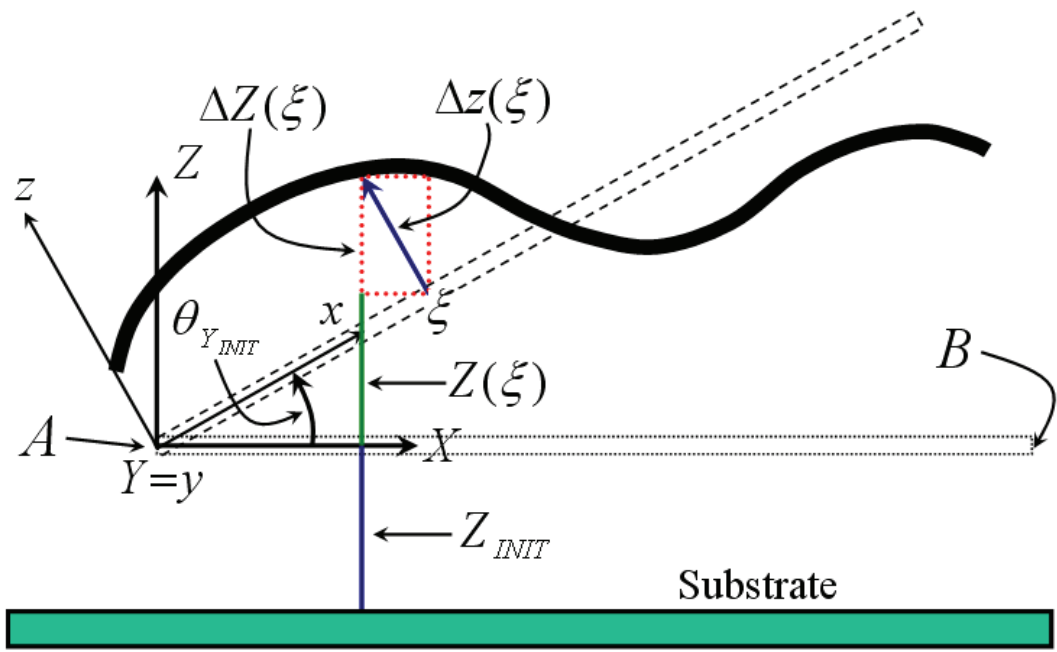


Figure 4.9: Total displacement of a generic point  $\xi$  along the beam length expressed in the global  $Z$  direction.

These are three contributions. The first is the projection of  $\Delta z(\xi)$  along the global  $Z$  axis, called  $\Delta Z(\xi)$ . The second one is the projection of the local  $x$  coordinate of the  $\xi$  point along the  $Z$  axis, and finally the third contribution is the initial gap between the non-displaced and non-deformed beam with respect to the substrate. If we now define  $Z_{AIR}(\xi)$  the total vertical abscissa of the point  $\xi$ , exploiting the 2.8 its expression is:

$$Z_{AIR}(\xi) = \Delta Z(\xi) + Z(\xi) + Z_{INIT} \quad (4.148)$$

where

$$\Delta Z(\xi) = \cos \theta_{X_{INIT}} \cos \theta_{Y_{INIT}} \Delta z(\xi) \quad (4.149)$$

and

$$Z(\xi) = -\sin \theta_{Y_{INIT}} \xi \quad (4.150)$$

Still exploiting the HFS of 4.87 and also accounting for the initial rotation angle around the  $X$  axis  $\theta_{X_{INIT}}$ , we can express the distribution of the total torsion around  $X$  axis as a function of  $\xi$  as follows:

$$\theta_X(\xi) = (1 - \xi)u_{\theta_{XA}} + \xi u_{\theta_{XB}} + \theta_{X_{INIT}} \quad (4.151)$$

Its distribution has been supposed to be similar to the one of the  $x$  deformations reported in 4.87. The problem of calculating the capacitance and electrostatic force is faced considering the beam area partitioned in a suitable number of rectangular sub-elements, assumed to be rigid and with a certain orientation in space like Figure 4.10 shows. Once the local  $x$  abscissa is determined (see Figure 4.11) the orientation angle around the  $Y$  axis for each sub-element can be derived with simple trigonometric considerations. Figure 4.12 shows the cross-section of one element. First of all we need to express the local center line abscissa of each element as a function of  $\xi$ . This means that the generic length of each element

$$x = \frac{L}{n} \quad (4.152)$$

where  $n$  is the number of elements, substituted in the 4.20 becomes:

$$\xi = \frac{1}{n} \quad (4.153)$$

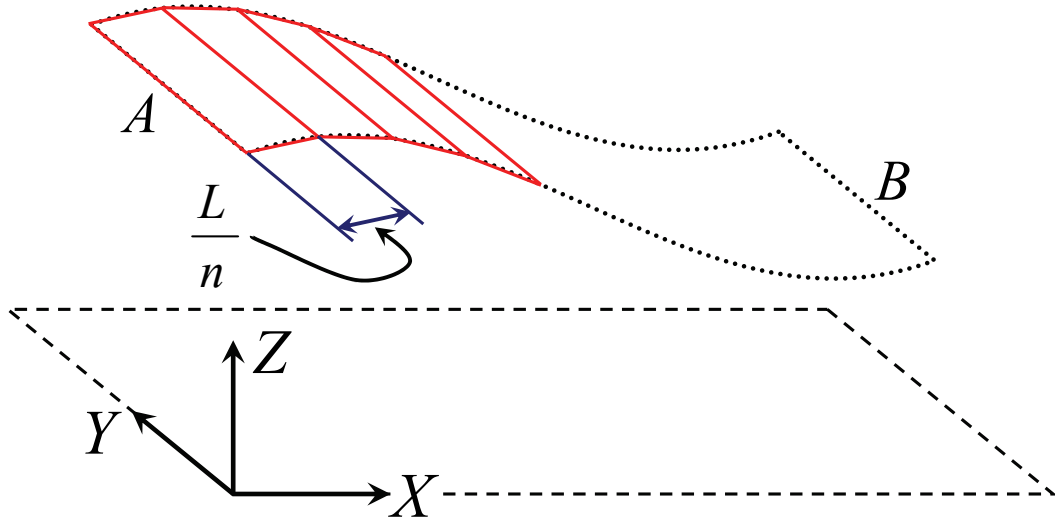


Figure 4.10: The beam length is divided into  $n$  element of length  $\frac{L}{n}$ . Each element is assumed to be rigid.

Given this, let us consider a generic element  $i$ . Its  $\xi$  abscissa referred to the center point along  $x$  is:

$$\xi = \frac{3i}{2n} \quad (4.154)$$

while the abscissa of the  $i$  element edge shared with the  $i + 1$  element is:

$$\xi = \frac{i + 1}{n} \quad (4.155)$$

The distance of the  $i$  element center point and edge along the  $Z$  axis are defined by the 4.148 and are addressed respectively as  $Z_{AIR}(\frac{1}{n}(i + \frac{1}{2}))$  and  $Z_{AIR}(\frac{i+1}{n})$  in Figure 4.12. With the basic triangle relations and considering that half length of each element is equal to  $\frac{1}{2n}$  the  $\theta_{Y_i}$  angle can be determined as:

$$\theta_{Y_i} = \arcsin \left[ 2n \left( Z_{AIR} \left( \frac{1}{n} \left( i + \frac{1}{2} \right) \right) - Z_{AIR} \left( \frac{i + 1}{n} \right) \right) \right] \quad (4.156)$$

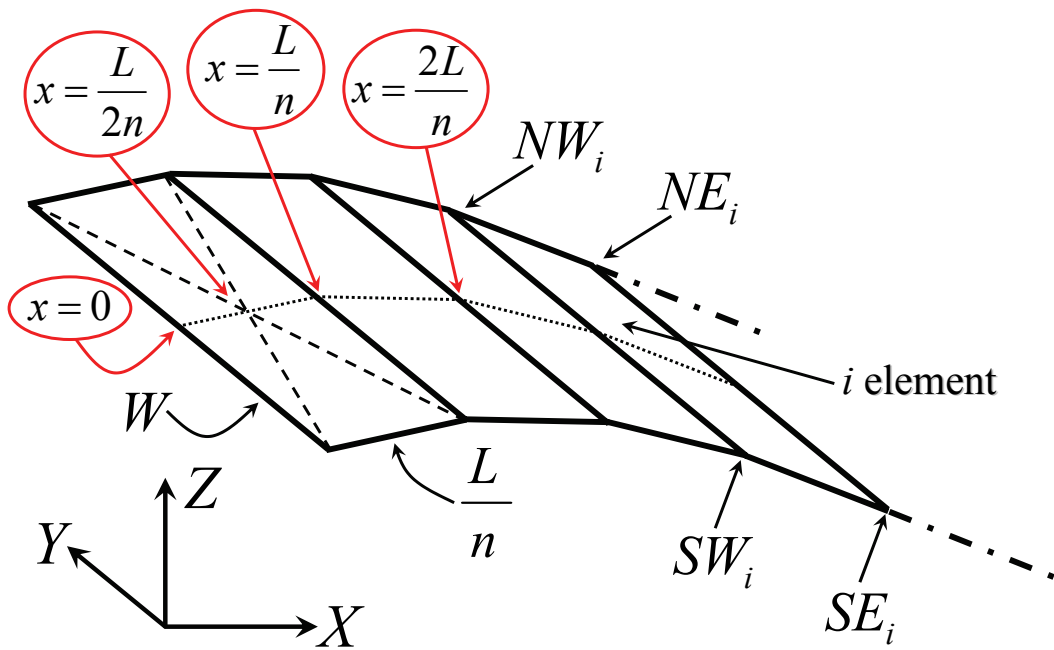


Figure 4.11: Local abscissa value along the  $x$  axis center line for the discretized beam elements.

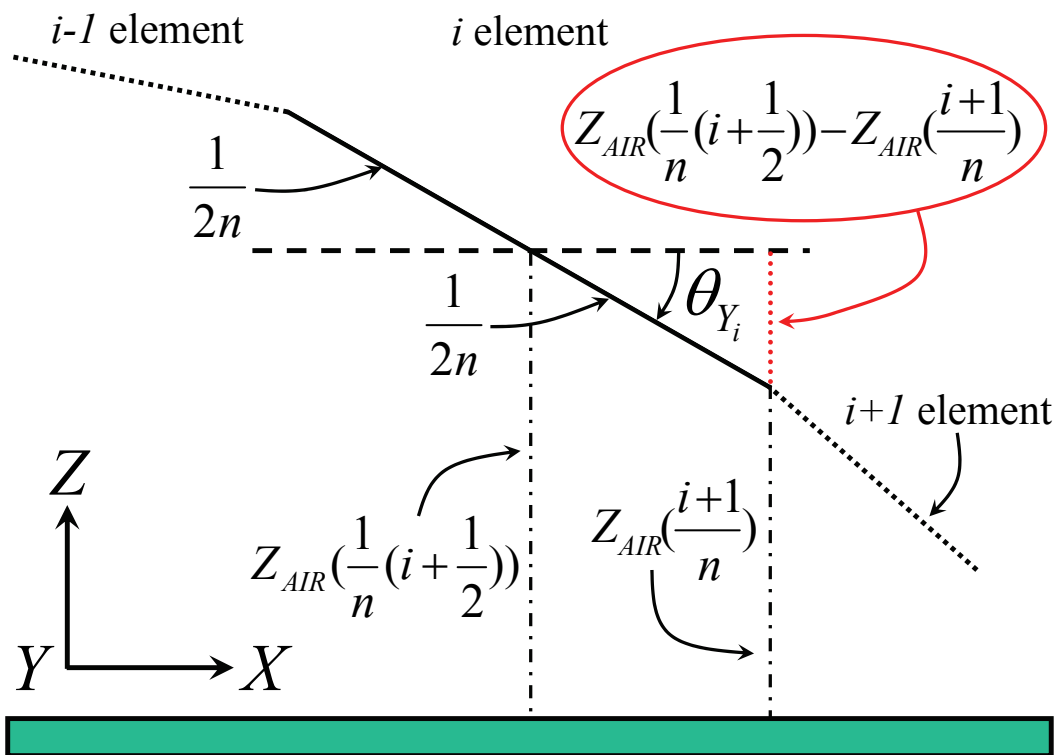


Figure 4.12: Cross-section of one beam sub-element. The rotation angle around the  $Y$  axis is determined with simple calculations.

Finally, the angle around the  $X$  axis is calculated with the 4.151 and, assuming it the one in the center point of each rectangle, for the  $i$  element it is:

$$\theta_{X_i} = \theta_X \left( \frac{1}{n} \left( i + \frac{1}{2} \right) \right) \quad (4.157)$$

As already shown in the rigid plate electrostatic effects calculation, the rotation angle around the  $Z$  axis is not involved in any formula for the capacitance and electrostatic force. This means that the angles  $\theta_{X_i}$  and  $\theta_{Y_i}$  are sufficient to determine the electrostatic effects for each element along the beam. It is possible to apply once again the formulas developed for the capacitance and electrostatic force referring to a rigid plate. Thereby, each beam sub-element is assumed a small rigid plate indeed. Still considering the  $i$  element, the four vertexes local coordinates (see Figure 4.11) are:

$$NE_i(\xi, y) = \left( \frac{i+1}{n}, \frac{W}{2} \right) \quad (4.158)$$

$$SE_i(\xi, y) = \left( \frac{i+1}{n}, -\frac{W}{2} \right) \quad (4.159)$$

$$SW_i(\xi, y) = \left( \frac{i}{n}, -\frac{W}{2} \right) \quad (4.160)$$

$$NW_i(\xi, y) = \left( \frac{i}{n}, \frac{W}{2} \right) \quad (4.161)$$

The capacitance for each element is calculated with the same formula as the 3.143. In this case, to take into account the overall contributions to the capacitance we have to include a sum over the  $n$  sub-elements as follows:

$$C_{AIR} = L \frac{\varepsilon_{AIR}}{\sigma_{Arc}} \sum_{i=0}^{n-1} \int_{\frac{i}{n}}^{\frac{i+1}{n}} \int_{-\frac{W}{2}}^{\frac{W}{2}} \frac{d\xi dy}{Z_L(\xi, y, \theta_{X_i}, \theta_{Y_i})} \quad (4.162)$$

where  $\sigma_{Arc}$  is the coefficient which takes into account the curvature of the electric field lines as already shown for the rigid plate.

Moreover, the local  $Z_L$  is defined as:

$$Z_L = Z_{AIR}\left(\frac{1}{n}\left(i + \frac{1}{2}\right)\right) - \sin \theta_{X_i} L \xi + \sin \theta_{X_i} \cos \theta_{Y_i} y \quad (4.163)$$

where  $Z_{AIR}$  is equal to the 4.148 and is calculated in the middle point of each element ( $\xi = \frac{1}{n}(i + \frac{1}{2})$ ) while the other two terms represent the local  $Z$  displacement of each point on the sub-element surface (see Figure 3.15). Dealing now with the electrostatic force, the 3.144 can be rewritten in the case of the flexible beam divided in sub-elements. It is necessary to take into account that the electrostatic force is a distributed effect even though in the end it has to be punctually applied to the beam nodes  $A$  and  $B$ . Since the beam is a flexible structures, the electrostatic force cannot be directly transferred into the two ends, but it should be somehow weighted by means of suitable functions. The approach proposed by Jing [32] exploits once again the HSF's to weight the electrostatic force to be applied to one beam end depending on the distance of the element where it is calculated from the node of application. This means the electrostatic force must be multiplied by the HSF's which determine the punctual beam displacement along the  $Z$  axis and that the force must be calculated using different functions for the two ends  $A$  and  $B$  as follows:

$$F_{zA_{EL}} = \frac{L \varepsilon_{AIR}}{2 \sigma_{Arc}^2} \sum_{i=0}^{n-1} \left( \psi_{zA}\left(\frac{1}{n}\left(i + \frac{1}{2}\right)\right) \int_{\frac{i}{n}}^{\frac{i+1}{n}} \int_{-\frac{W}{2}}^{\frac{W}{2}} \frac{V_{AIR}^2 d\xi dy}{Z_L(\xi, y, \theta_{X_i}, \theta_{Y_i})^2} \right) \quad (4.164)$$

$$F_{zB_{EL}} = \frac{L \varepsilon_{AIR}}{2 \sigma_{Arc}^2} \sum_{i=0}^{n-1} \left( \psi_{zB}\left(\frac{1}{n}\left(i + \frac{1}{2}\right)\right) \int_{\frac{i}{n}}^{\frac{i+1}{n}} \int_{-\frac{W}{2}}^{\frac{W}{2}} \frac{V_{AIR}^2 d\xi dy}{Z_L(\xi, y, \theta_{X_i}, \theta_{Y_i})^2} \right) \quad (4.165)$$

where  $\psi_{zA}(\frac{1}{n}(i + \frac{1}{2}))$  and  $\psi_{zB}(\frac{1}{n}(i + \frac{1}{2}))$  are the 4.143 and 4.145 respectively, calculated in the middle point of each element along  $\xi$ . The 4.164 and 4.165 must be then added to the respective forces applied at the two nodes along local  $z$  axis in the 4.31. The electrostatic force contribution will be automatically translated back into the global frame together with the elastic and inertial effects by means of the 4.141. With the same approach it is possible to determine the contribution to the torque around the  $x$  and  $y$  by the electrical effect.



Hence, the 3.145 and 3.146 can be rewritten, exploiting the 4.144 and 4.146, as follows:

$$T_{\theta x AEL} = \frac{L \varepsilon_{AIR}}{2 \sigma_{Arc}^2} \sum_{i=0}^{n-1} \left( \left(1 - \frac{1}{n} \left(i + \frac{1}{2}\right)\right) \int_{\frac{i}{n}}^{\frac{i+1}{n}} \int_{-\frac{W}{2}}^{\frac{W}{2}} \frac{V_{AIR}^2 y d\xi dy}{Z_L(\xi, y, \theta_{X_i}, \theta_{Y_i})^2} \right) \quad (4.166)$$

$$T_{\theta x BEL} = \frac{L \varepsilon_{AIR}}{2 \sigma_{Arc}^2} \sum_{i=0}^{n-1} \left( \left(\frac{1}{n} \left(i + \frac{1}{2}\right)\right) \int_{\frac{i}{n}}^{\frac{i+1}{n}} \int_{-\frac{W}{2}}^{\frac{W}{2}} \frac{V_{AIR}^2 y d\xi dy}{Z_L(\xi, y, \theta_{X_i}, \theta_{Y_i})^2} \right) \quad (4.167)$$

$$T_{\theta y AEL} = \frac{L \varepsilon_{AIR}}{2 \sigma_{Arc}^2} \sum_{i=0}^{n-1} \left( \psi_{\theta y A} \left(\frac{1}{n} \left(i + \frac{1}{2}\right)\right) \int_{\frac{i}{n}}^{\frac{i+1}{n}} \int_{-\frac{W}{2}}^{\frac{W}{2}} \frac{V_{AIR}^2 \xi d\xi dy}{Z_L(\xi, y, \theta_{X_i}, \theta_{Y_i})^2} \right) \quad (4.168)$$

$$T_{\theta y BEL} = \frac{L \varepsilon_{AIR}}{2 \sigma_{Arc}^2} \sum_{i=0}^{n-1} \left( \psi_{\theta y B} \left(\frac{1}{n} \left(i + \frac{1}{2}\right)\right) \int_{\frac{i}{n}}^{\frac{i+1}{n}} \int_{-\frac{W}{2}}^{\frac{W}{2}} \frac{V_{AIR}^2 \xi d\xi dy}{Z_L(\xi, y, \theta_{X_i}, \theta_{Y_i})^2} \right) \quad (4.169)$$

In previous 4.166 and 4.167 it has been chosen a torque distribution around  $x$  axis similar to the one for the deformation along  $x$  at the two ends reported in 4.87. Also the 4.166 - 4.169 are transformed back in the global system via the same procedure previously discussed for the electrostatic force.

#### 4.4.1 Fringing Effect Model

In the beam electrostatic model the contribution given by the fringing field has been also introduced. The proposed model is the same presented in details for the rigid plate in previous chapter. All the rigid sub-elements in which the beam is divided are affected by the fringing effect close to the two minor edges, i.e. the ones along  $x$  direction. Furthermore, the first and last elements (which represent the two ends  $A$  and  $B$ ) have one of the two major edges (along  $y$ ) which gives contribution to the fringing field. In next formulas  $\sigma_{ArcF}$  is defined by the 3.162 while the area in which the fringing is confined, that was  $\zeta$  in Chapter 3, is here addressed as  $\lambda$  in order not to confuse it with the 4.89. It

is now possible to rewrite the 4.162 for the capacitance also accounting for the fringing field effect as follows:

$$\begin{aligned}
C_{AIR} &= L \frac{\varepsilon_{AIR}}{\sigma_{Arc}} \sum_{i=0}^{n-1} \int_{\frac{i}{n}}^{\frac{i+1}{n}} \int_{-\frac{W}{2}}^{\frac{W}{2}} \frac{d\xi dy}{Z_L(\xi, y, \theta_{X_i}, \theta_{Y_i})} \\
&+ \lambda \frac{\varepsilon_{AIR}}{\sigma_{ArcF}} \int_{-\frac{W}{2}}^{\frac{W}{2}} \frac{dy}{Z_L(0, y, \theta_{X_i}, \theta_{Y_i})} \\
&+ \lambda \frac{\varepsilon_{AIR}}{\sigma_{ArcF}} \int_{-\frac{W}{2}}^{\frac{W}{2}} \frac{dy}{Z_L(1, y, \theta_{X_i}, \theta_{Y_i})} \\
&+ \lambda L \frac{\varepsilon_{AIR}}{\sigma_{ArcF}} \sum_{i=0}^{n-1} \int_{\frac{i}{n}}^{\frac{i+1}{n}} \frac{d\xi}{Z_L(\xi, -\frac{W}{2}, \theta_{X_i}, \theta_{Y_i})} \\
&+ \lambda L \frac{\varepsilon_{AIR}}{\sigma_{ArcF}} \sum_{i=0}^{n-1} \int_{\frac{i}{n}}^{\frac{i+1}{n}} \frac{d\xi}{Z_L(\xi, \frac{W}{2}, \theta_{X_i}, \theta_{Y_i})} \tag{4.170}
\end{aligned}$$

In previous equation the second and third terms represent the fringing on the boundary major edges of the beam end  $A$  and  $B$  (along  $y$ ) respectively. On the other hand, the fourth and last terms are the fringing capacitance on the lower and upper minor edges (along  $x$ ) of all the elements respectively. Following the same approach the 4.164 and 4.165 become:

$$\begin{aligned}
F_{zAEL} &= \frac{L \varepsilon_{AIR}}{2 \sigma_{Arc}^2} \sum_{i=0}^{n-1} \left( \psi_{zA} \left( \frac{1}{n} \left( i + \frac{1}{2} \right) \right) \int_{\frac{i}{n}}^{\frac{i+1}{n}} \int_{-\frac{W}{2}}^{\frac{W}{2}} \frac{V_{AIR}^2 d\xi dy}{Z_L(\xi, y, \theta_{X_i}, \theta_{Y_i})^2} \right) \\
&+ \lambda \frac{\varepsilon_{AIR}}{\sigma_{ArcF}^2} \int_{-\frac{W}{2}}^{\frac{W}{2}} \frac{V_{AIR}^2 dy}{Z_L(0, y, \theta_{X_i}, \theta_{Y_i})^2} \\
&+ \lambda \frac{L \varepsilon_{AIR}}{2 \sigma_{ArcF}^2} \sum_{i=0}^{n-1} \left( \psi_{zA} \left( \frac{1}{n} \left( i + \frac{1}{2} \right) \right) \int_{\frac{i}{n}}^{\frac{i+1}{n}} \frac{V_{AIR}^2 d\xi}{Z_L(\xi, -\frac{W}{2}, \theta_{X_i}, \theta_{Y_i})^2} \right) \\
&+ \lambda \frac{L \varepsilon_{AIR}}{2 \sigma_{ArcF}^2} \sum_{i=0}^{n-1} \left( \psi_{zA} \left( \frac{1}{n} \left( i + \frac{1}{2} \right) \right) \int_{\frac{i}{n}}^{\frac{i+1}{n}} \frac{V_{AIR}^2 d\xi}{Z_L(\xi, \frac{W}{2}, \theta_{X_i}, \theta_{Y_i})^2} \right) \tag{4.171}
\end{aligned}$$

$$\begin{aligned}
F_{zB_{EL}} &= \frac{L \varepsilon_{AIR}}{2 \sigma_{Arc}^2} \sum_{i=0}^{n-1} \left( \psi_{zB} \left( \frac{1}{n} \left( i + \frac{1}{2} \right) \right) \int_{\frac{i}{n}}^{\frac{i+1}{n}} \int_{-\frac{W}{2}}^{\frac{W}{2}} \frac{V_{AIR}^2 d\xi dy}{Z_L(\xi, y, \theta_{X_i}, \theta_{Y_i})^2} \right) \\
&+ \lambda \frac{\varepsilon_{AIR}}{\sigma_{ArcF}^2} \int_{-\frac{W}{2}}^{\frac{W}{2}} \frac{V_{AIR}^2 dy}{Z_L(1, y, \theta_{X_i}, \theta_{Y_i})^2} \\
&+ \lambda \frac{L \varepsilon_{AIR}}{2 \sigma_{ArcF}^2} \sum_{i=0}^{n-1} \left( \psi_{zB} \left( \frac{1}{n} \left( i + \frac{1}{2} \right) \right) \int_{\frac{i}{n}}^{\frac{i+1}{n}} \frac{V_{AIR}^2 d\xi}{Z_L(\xi, -\frac{W}{2}, \theta_{X_i}, \theta_{Y_i})^2} \right) \\
&+ \lambda \frac{L \varepsilon_{AIR}}{2 \sigma_{ArcF}^2} \sum_{i=0}^{n-1} \left( \psi_{zB} \left( \frac{1}{n} \left( i + \frac{1}{2} \right) \right) \int_{\frac{i}{n}}^{\frac{i+1}{n}} \frac{V_{AIR}^2 d\xi}{Z_L(\xi, \frac{W}{2}, \theta_{X_i}, \theta_{Y_i})^2} \right) \quad (4.172)
\end{aligned}$$

Looking at 4.171, the second term is the fringing field contribution given by the major edge (along  $y$ ) at node  $A$  while the last two terms account for the fringing along  $x$  at the lower ( $y = -\frac{W}{2}$ ) and higher ( $y = \frac{W}{2}$ ) beam edges respectively. Whereas, in 4.172 the second term gives the fringing force on the major edge at node  $B$  and the last two terms have the same meaning of 4.171.

To conclude the discussion of the flexible beam electrostatic model an additional feature has to be introduced. Thus far, we have considered the substrate electrode deployed beneath the whole length of the suspended beam. Nonetheless, it is possible to choose a different electrode placement. For instance, it is possible to define a certain region along the beam where there is no electrode below it. Differently, the electrode can be placed in an area along the beam without including one or both the  $A$  and  $B$  ends. Previous formulas for the capacitance and electrostatic force modified to account for this additional feature are not shown here for seek of brevity. All the different possible configurations for the electrode placement are shown in Figure 4.13. Length of the two electrodes including left end ( $A$ ) and the right end ( $B$ ) are respectively  $EL_{lft}$  and  $EL_{rgt}$ . Moreover a boolean parameter is also defined. It is  $AB_{in}$  and when it is true (i.e. equal to 1) electrodes are considered the two segments  $EL_{lft}$  and  $EL_{rgt}$  including  $A$  and  $B$  beam ends. Differently, when  $AB_{in}$  is false (i.e. equal to 0) electrode does not include any beam end.

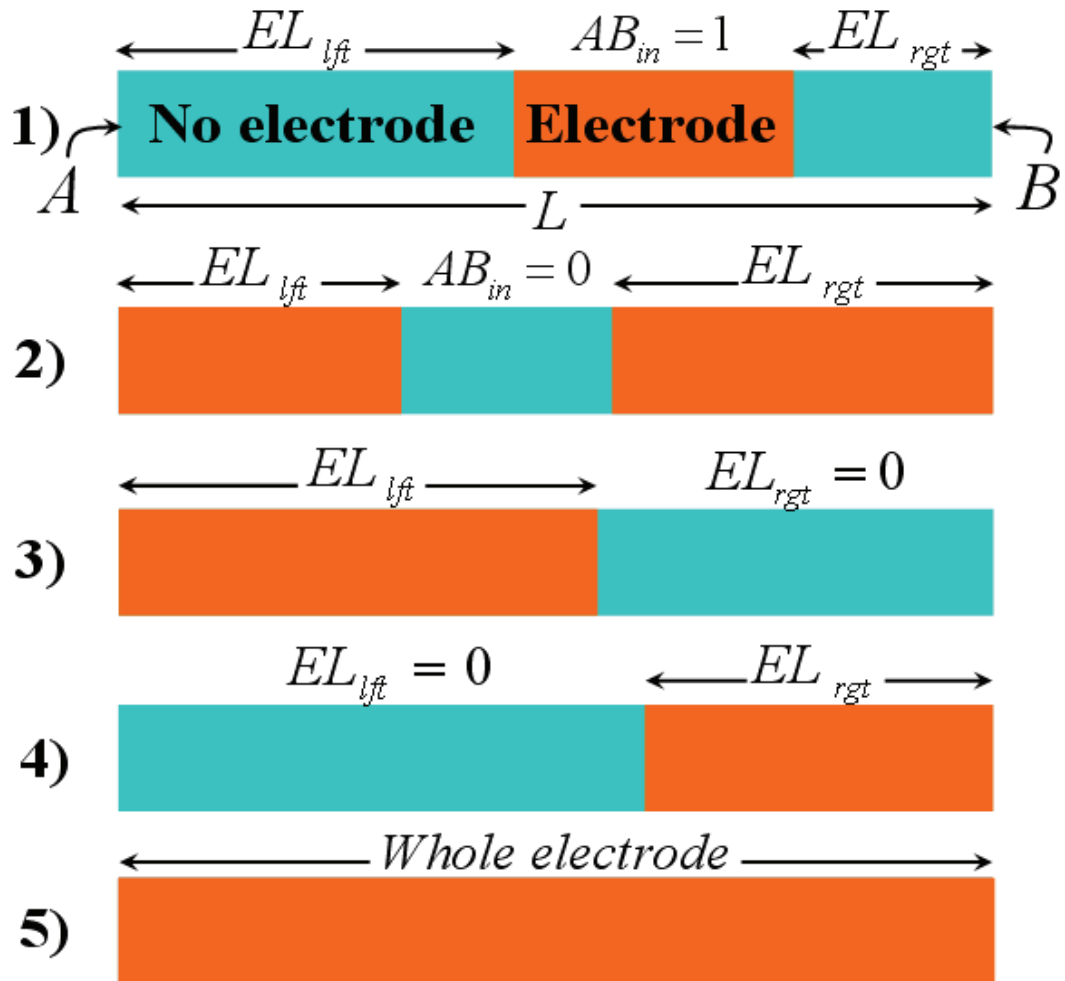


Figure 4.13: Schematic of all the possible configurations in placing the electrode(s) beneath the flexible beam.

## 4.5 Viscous Damping Model

The achievement of a reasonably detailed model for describing the behaviour of the flexible beam also accounting for the dynamic regime requires the inclusion of the viscous damping effect. This results in a force counteracting the motion of a body immersed within a fluid with a certain viscosity (e.g. air) due to the friction of the media particles when touching the body itself.

To ease the introduction and explanation of the viscous damping theory basis let us refer for a short while to a rigid body. The study of the viscous damping effect is based on the Reynolds equation. In the case of a body characterized by certain dimensions on the  $xy$  plane which is moving along the  $z$  direction its expression is:

$$\frac{\partial^2 P}{\partial x^2} + \frac{\partial^2 P}{\partial y^2} = \frac{12\mu}{z^3} \frac{\partial z}{\partial t} \quad (4.173)$$

where  $P$  is the pressure produced by the fluid, whose viscosity is  $\mu$ , on the body surface when its distance from the substrate is  $z$  and it is moving towards it with a velocity which is  $\frac{\partial z}{\partial t}$ . Still referring to a rigid body which is parallel to the substrate, equation 4.173 cannot be easily integrated in a closed form. Nevertheless, in the case of a flexible beam it can be simplified. Indeed, since it is  $L \gg W$  (see Figure 4.1) the pressure variation along the beam length ( $x$  axis) can be assumed negligible with respect to the  $P$  variation along  $y$  [45]. This allows to rewrite the 4.173 as:

$$\frac{\partial^2 P}{\partial y^2} = \frac{12\mu}{z^3} \frac{\partial z}{\partial t} \quad (4.174)$$

that, after integration becomes:

$$P(y) = -\frac{6\mu}{z^3} (W^2 - y^2) V_z \quad (4.175)$$

where

$$V_z = \frac{\partial z}{\partial t} \quad (4.176)$$

The force generated by the pressure applied on the beam surface is derived by its integration over the area:

$$F_z = L \int_{-\frac{w}{2}}^{\frac{w}{2}} P(y) dy \quad (4.177)$$

Replacing the 4.175 in the 4.177 and developing the integral it results:

$$F_z = -\frac{\mu L W^3}{z^3} V_z \quad (4.178)$$

This type of damping is called squeeze-film damping as the fluid, assumed to be incompressible, is squeezed out of the beam as it moves towards the substrate as Figure 4.14 shows [34].

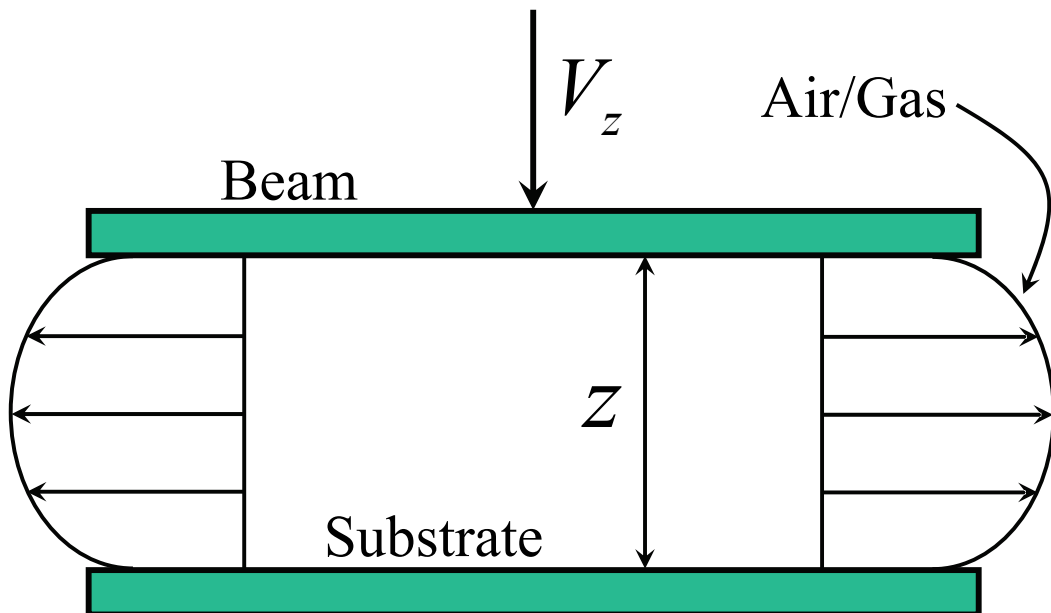


Figure 4.14: In the squeeze-film damping description the fluid is squeezed as the beam nears the substrate plane.

Now that the squeeze-film damping has been expressed in a closed form, we have to cope with the fact that the Euler beam is a flexible structure. Starting from the theory shown above, we propose an extension of this model accounting for the flexibility of the beam. Still exploiting the HSF's as shown in the electrostatic model, it is possible to define a local speed for each sub-element.

The 4.147 can be rewritten replacing the vertical displacements and angular rotation with the corresponding linear and angular velocities at the ends  $A$  and  $B$ :

$$V_z(\xi) = \psi_{zA}(\xi)\dot{u}_{xA} + \psi_{\theta_y A}(\xi)\dot{u}_{\theta_x A} + \psi_{zB}(\xi)\dot{u}_{xB} + \psi_{\theta_y B}(\xi)\dot{u}_{\theta_x B} \quad (4.179)$$

This gives the instantaneous velocity of each point along the beam length depending on the dynamic of both ends. Under appropriate assumptions the squeeze-film damping theory can be applied to the model of the beam divided in sub-elements. First of all we assume an homogeneous vertical velocity over the surface of a rectangular sub-element as well as small orientation angles. Because of these assumptions, we will exploit both the vertical distance of a certain element from the substrate as well as its speed calculated in its center point respectively determined from the 4.163 and the 4.179 calculated for  $\xi = \frac{1}{n}(i + \frac{1}{2})$ . Still assuming each element quasi-parallel to the substrate because of the small  $\theta_{X_i}$  and  $\theta_{Y_i}$  and also assuming the velocity difference among adjacent sub-elements small enough such as there is no need for singularly applying boundary conditions to each element, the 4.178 can still be considered valid. This allows to write the 4.178 with a formulation similar to the 4.164 and 4.165 for the two  $A$  and  $B$  ends as follows:

$$F_{zAVD} = -\mu \sum_{i=0}^{n-1} \psi_{zA} \left( \frac{1}{n} \left( i + \frac{1}{2} \right) \right) \frac{V_z \left( \frac{1}{n} \left( i + \frac{1}{2} \right) \right) \frac{LW^3}{n}}{\left( Z_{AIR} \left( \frac{1}{n} \left( i + \frac{1}{2} \right) \right) - \sin \theta_{X_i} L \left( \frac{1}{n} \left( i + \frac{1}{2} \right) \right) \right)^3} \quad (4.180)$$

$$F_{zBVD} = -\mu \sum_{i=0}^{n-1} \psi_{zB} \left( \frac{1}{n} \left( i + \frac{1}{2} \right) \right) \frac{V_z \left( \frac{1}{n} \left( i + \frac{1}{2} \right) \right) \frac{LW^3}{n}}{\left( Z_{AIR} \left( \frac{1}{n} \left( i + \frac{1}{2} \right) \right) - \sin \theta_{X_i} L \left( \frac{1}{n} \left( i + \frac{1}{2} \right) \right) \right)^3} \quad (4.181)$$

The negative sign of 4.180 - 4.181 is due to the fact that the viscous damping force counteracts the direction in which the beam moves. The corresponding contributions in the global frame are then derived with the usual transformation via the rotation matrix expressed by 4.141. With a similar approach the torques around the  $y$  axis at the two ends produced by the squeeze-film damping have been determined and are not shown here for seek of brevity.

Concerning the lateral movements of the Euler beam ( $xy$  in-plane) the proposed model is the same shown in previous chapter for the rigid plate. This is based on the assumption of a Couette-type laminar flow distribution of the fluid underneath the beam. Moreover, the beam deformations are supposed to be not too large in order to assume the Couette hypothesis still valid. Given this, the viscous damping force for the in-plane movements are expressed by the 3.206 - 3.207.

Finally, the gas rarefaction effect for very small gaps comparable with the fluid mean free path can be accounted for by replacing  $\mu$  with the 3.208 in all previous formulas.



## 4.6 Validation of the Euler Beam Model

Before introducing the validation of the Euler flexible beam let us introduce its Cadence Virtuoso<sup>®</sup> Schematic. This is shown in Figure 4.15 in which six pins corresponding to the 6 DoF's are provided at each beam end. Moreover there are two electrical pins to apply the biasing controlling voltage. The potential between these two pins is the one applied among the suspended cantilever and the lower electrode.



Figure 4.15: Cadence Virtuoso<sup>®</sup> Schematic for the 12 DoF's cantilever. Six pins corresponding to the 6 DoF's are visible at each of the two ends along with the two electrical pins to apply the control voltage.

First of all mechanical model of the compact Euler beam model will be validated. This is divided in a preliminary static validation in which a force is applied to one cantilever end. Subsequently the dynamic behaviour of the beam will be investigated concerning its resonance modes. Finally, the electrostatic model of the Euler beam will be also validated while the viscous damping effect will be included when dealing with the simulation of complete RF-MEMS structures (next chapter). In all the static and dynamic simulations which are being shown the beam length ( $L$ ), width ( $W$ ) and thickness ( $T$ ) are  $150 \mu m$ ,  $5 \mu m$  and  $3 \mu m$  respectively. The Young modulus of the beam material is equal to  $150 \text{ GPa}$  and the shear effect are not included in the Euler beam model (i.e.  $\nu = 0$ ). Finally, beam orientation angles ( $\theta_X, \theta_Y, \theta_Z$ ) are all equal to zero (see Figure 4.6).

### 4.6.1 Static Validation of the Euler Beam Mechanical Model

The structure chosen for the static validation is an Euler beam with one anchored end (i.e. cantilever). A linear force is then applied to the other node of the structure (see last section of Chapter 3). The Cadence Virtuoso<sup>®</sup> Schematic for such a type of validation is shown in Figure 4.16. Notice that all the components are connected by means of wires like in an electric circuit schematic.

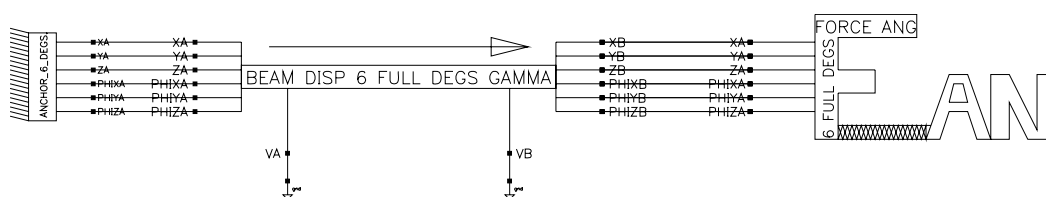


Figure 4.16: Cadence Virtuoso<sup>®</sup> Schematic for the static validation of the Euler beam. One end is anchored while a linear force is applied to the other one. The beam is connected by wires to the anchor, force source and ground.

The results produced by the MEMS compact models by the Spectre<sup>®</sup> simulator are validated by comparisons with the same structure (with the same boundary conditions and applied stimuli) simulated in COMSOL Multiphysics<sup>®</sup> which is a FEM-based tool [44]. For the static validation a linear force is applied to the free end of the beam of Figure 4.16. Its module is swept from 0 to  $1\mu N$  with a step of  $0.1\mu N$ . Different orientation angles  $\theta_{S_Y}$  and  $\theta_{S_Z}$  are imposed to the force in order to have non-zero components along the three axes ( $X, Y, Z$ ). Since for this validation the linear beam model is taken into account, the COMSOL Multiphysics<sup>®</sup> simulation is performed for the maximum value of the applied force (i.e.  $1\mu N$ ). Four simulations are shown here and are presented below.

**Simulation No. 1** ( $\theta_{S_Y} = 0^\circ$  and  $\theta_{S_Z} = 0^\circ$ )

In this case the force is only applied along  $X$  so that all other components are zero. The COMSOL Multiphysics<sup>®</sup> schematic is shown in Figure 4.17. The color scale represents the Von Mises stress [26].

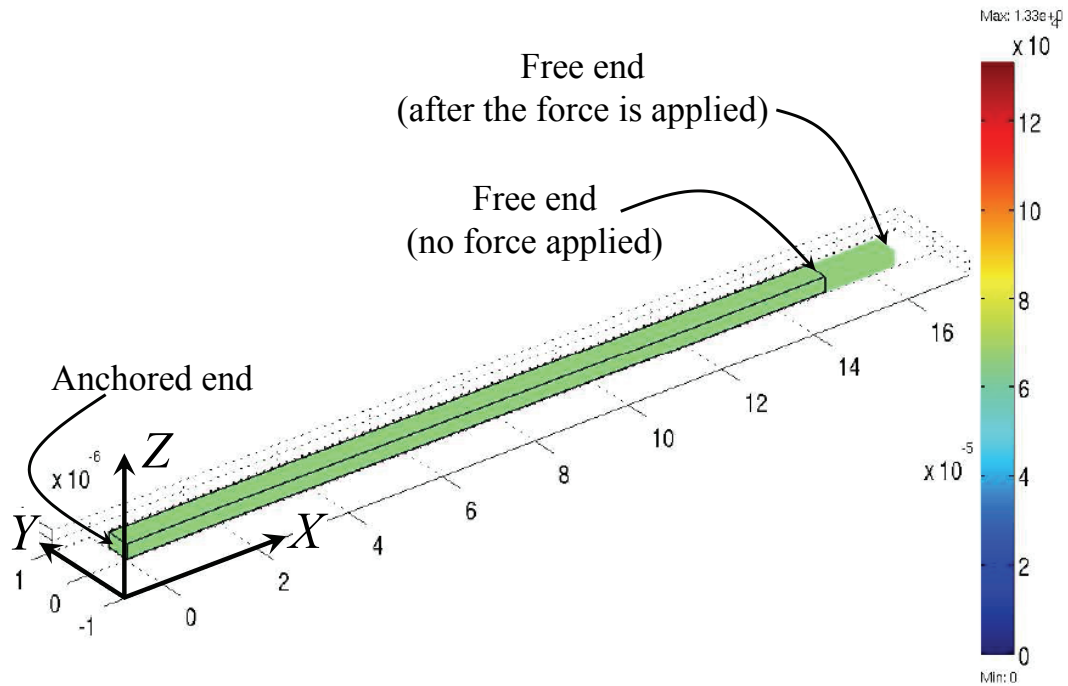


Figure 4.17: COMSOL Multiphysics<sup>®</sup> schematic for the Euler beam. The force is applied to the free end with orientation angles  $\theta_{S_Y} = 0^\circ$  and  $\theta_{S_Z} = 0^\circ$ .

The behaviour of the displacement along  $X$  axis of the free beam end in Spectre<sup>®</sup> is plotted in Figure 4.18. The beam exhibits a linear behaviour versus the applied force as expected. In Table 4.1 the Spectre<sup>®</sup> simulation value for the maximum applied force ( $1 \mu N$ ) is compared with the COMSOL<sup>®</sup> prediction and the analytical value for the deformation showing a very good agreement.

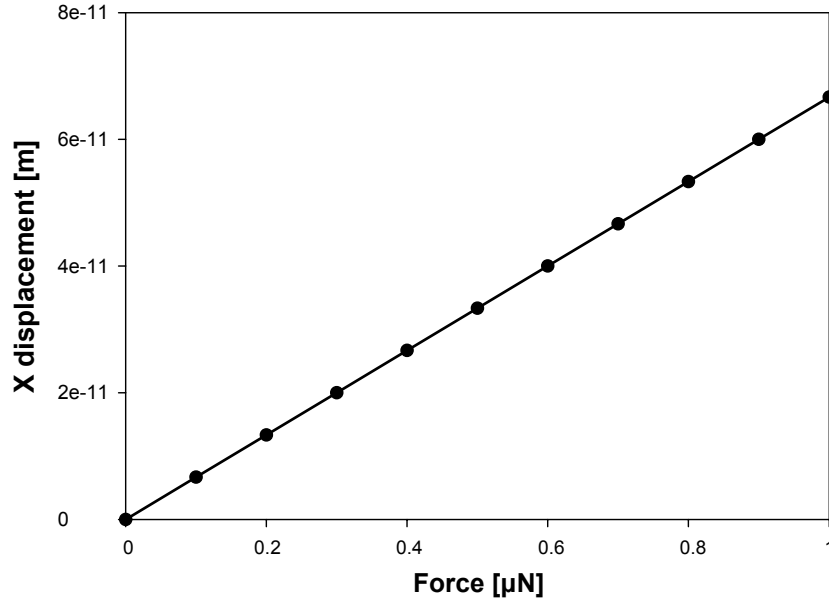


Figure 4.18: Beam displacement along  $X$  predicted with the compact models in Spectre<sup>©</sup>.

Force ( $X$ )	$\Delta X$ (Cadence)	$\Delta X$ (COMSOL)	$\Delta X$ (Theory)
$0.1 \times 10^{-6} \text{ N}$	$6.667 \times 10^{-12} \text{ m}$	-	-
$0.2 \times 10^{-6} \text{ N}$	$13.33 \times 10^{-12} \text{ m}$	-	-
$0.3 \times 10^{-6} \text{ N}$	$20 \times 10^{-12} \text{ m}$	-	-
$0.4 \times 10^{-6} \text{ N}$	$26.67 \times 10^{-12} \text{ m}$	-	-
$0.5 \times 10^{-6} \text{ N}$	$33.33 \times 10^{-12} \text{ m}$	-	-
$0.6 \times 10^{-6} \text{ N}$	$40 \times 10^{-12} \text{ m}$	-	-
$0.7 \times 10^{-6} \text{ N}$	$46.67 \times 10^{-12} \text{ m}$	-	-
$0.8 \times 10^{-6} \text{ N}$	$53.33 \times 10^{-12} \text{ m}$	-	-
$0.9 \times 10^{-6} \text{ N}$	$60 \times 10^{-12} \text{ m}$	-	-
$1 \times 10^{-6} \text{ N}$	$66.67 \times 10^{-12} \text{ m}$	$66.7 \times 10^{-12} \text{ m}$	$66.6667 \times 10^{-12} \text{ m}$

Table 4.1: Beam deformation along  $X$  axis in Spectre<sup>©</sup> compared with the COMSOL<sup>©</sup> prediction and the theoretical value.

**Simulation No. 2** ( $\theta_{S_Y} = 0^\circ$  and  $\theta_{S_Z} = 45^\circ$ )

In this case the applied force has two in-plane components along the  $X$  and  $Y$  axes as the COMSOL Multiphysics<sup>©</sup> schematic of Figure 4.19 shows. Table 4.2 shows the agreement of the  $X$  and  $Y$  deformations in Spectre<sup>©</sup> and COMSOL Multiphysics<sup>©</sup>.

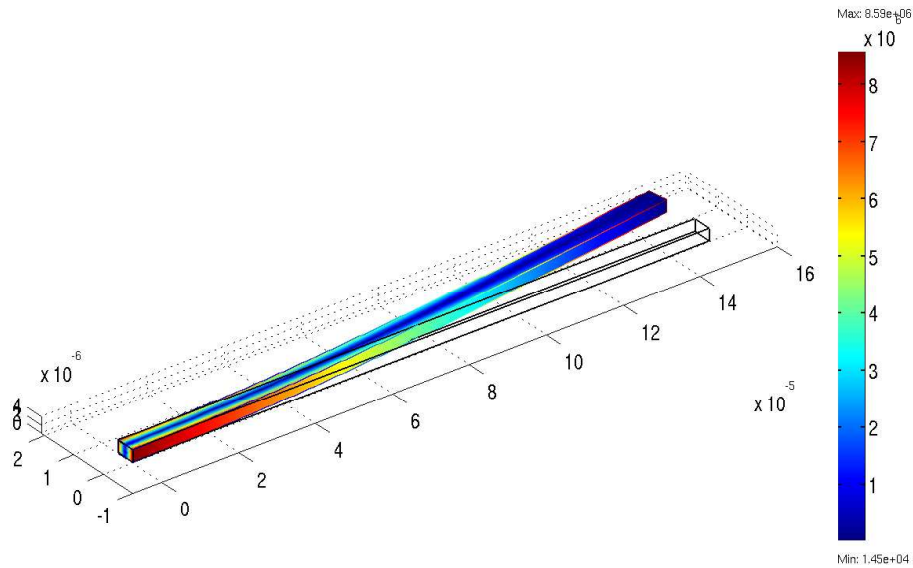


Figure 4.19: COMSOL Multiphysics<sup>©</sup> schematic for the Euler beam. The force is applied to the free end with orientation angles  $\theta_{S_Y} = 0^\circ$  and  $\theta_{S_Z} = 45^\circ$ .

Force (X)	$\Delta X$ (Cadence)	$\Delta X$ (COMSOL)
$707.1x10^{-9} N$	$47.14x10^{-12} m$	$47.1x10^{-12} m$
Force (Y)	$\Delta Y$ (Cadence)	$\Delta Y$ (COMSOL)
$707.1x10^{-9} N$	$169.8x10^{-9} m$	$170x10^{-9} m$

Table 4.2: Beam deformation along  $X$  and  $Y$  axis in Spectre<sup>©</sup> compared with the COMSOL<sup>©</sup> prediction.

**Simulation No. 3** ( $\theta_{S_Y} = -90^\circ$  and  $\theta_{S_Z} = 0^\circ$ )

In this third case the force is all directed along the  $Z$  axis as the COMSOL Multiphysics<sup>®</sup> schematic of Figure 4.20 shows. Table 4.3 shows the agreement of the  $Z$  deformation in Spectre<sup>®</sup> and COMSOL Multiphysics<sup>®</sup>. Concerning the  $X$  deformation it is so small that can be considered negligible. As a consequence, the disagreement in Table 4.3 must not be taken into account.

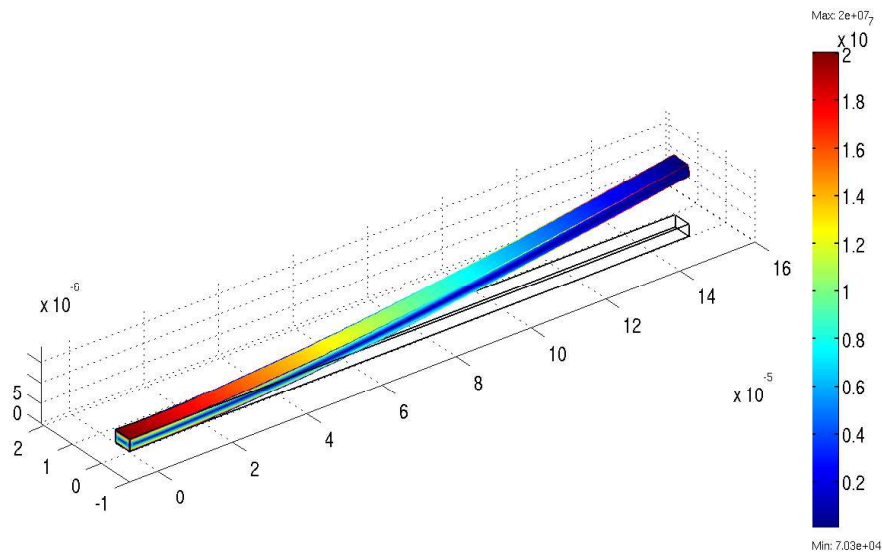


Figure 4.20: COMSOL Multiphysics<sup>®</sup> schematic for the Euler beam. The force is applied to the free end with orientation angles  $\theta_{S_Y} = -90^\circ$  and  $\theta_{S_Z} = 0^\circ$ .

Force (X)	$\Delta X$ (Cadence)	$\Delta X$ (COMSOL)
0 N	$-13.67x10^{-21} m$	$-4x10^{-13} m$
Force (Z)	$\Delta Z$ (Cadence)	$\Delta Z$ (COMSOL)
$1x10^{-6} N$	$667.2x10^{-9} m$	$667x10^{-9} m$

Table 4.3: Beam deformation along  $X$  and  $Z$  axis in Spectre<sup>®</sup> compared with the COMSOL<sup>®</sup> prediction.

**Simulation No. 4 ( $\theta_{S_Y} = -60^\circ$  and  $\theta_{S_Z} = 30^\circ$ )**

In this final simulation the force has components along the  $X$ ,  $Y$  and  $Z$  axes (see Figure 4.21).

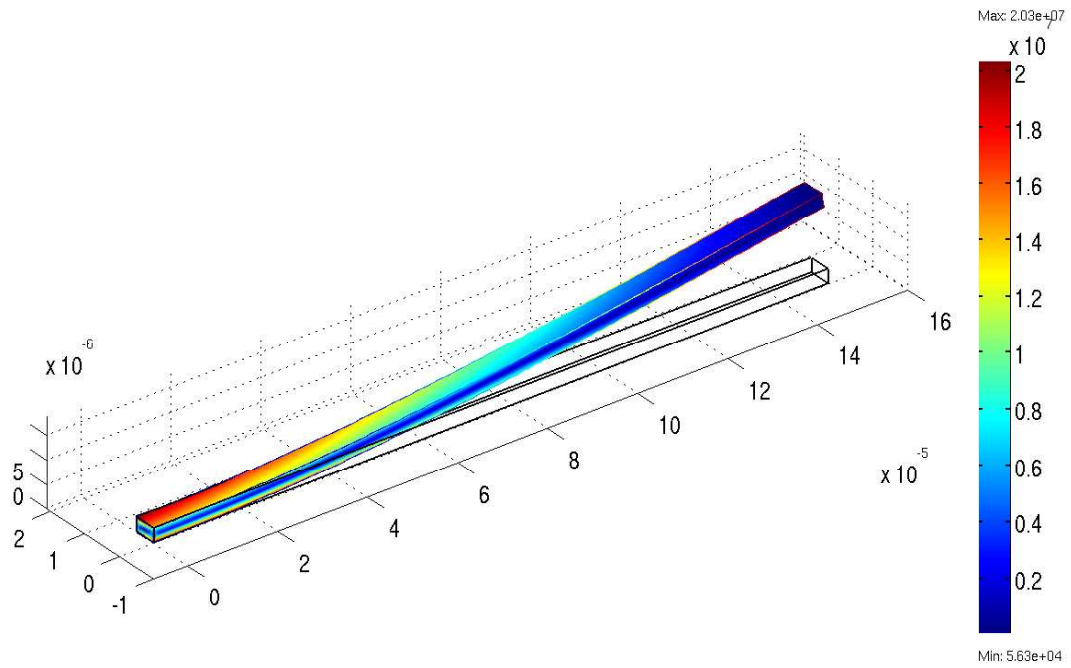


Figure 4.21: COMSOL Multiphysics<sup>®</sup> schematic for the Euler beam. The force is applied to the free end with orientation angles  $\theta_{S_Y} = -60^\circ$  and  $\theta_{S_Z} = 30^\circ$ .

Force (X)	$\Delta X$ (Cadence)	$\Delta X$ (COMSOL)
$433x10^{-9} N$	$28.87x10^{-12} m$	$28.90x10^{-12} m$
Force (Y)	$\Delta Y$ (Cadence)	$\Delta Y$ (COMSOL)
$250x10^{-9} N$	$60.02x10^{-9} m$	$60x10^{-9} m$
Force (Z)	$\Delta Z$ (Cadence)	$\Delta Z$ (COMSOL)
$866x10^{-9} N$	$577.8x10^{-9} m$	$578x10^{-9} m$

Table 4.4: Beam deformation along  $X$  and  $Z$  axis in Spectre<sup>©</sup> compared with the COMSOL<sup>©</sup> prediction.

## 4.6.2 Dynamic Validation of the Euler Beam Mechanical Model

In this section the Euler beam mechanical model will be validated when operating in dynamic regime. The density of the beam material to define its mass is  $2330 \text{ kg / m}^3$  (i.e. poly-silicon). Concerning the compact models within Spectre<sup>©</sup> simulator the type of analysis is the small signals AC simulation. The Virtuoso<sup>©</sup> Schematic of the structure is shown in Figure 4.22. In this one beam end is anchored while at the other node a small signal stimulus (i.e. force) is applied (see stimulus sources in last section of Chapter 3). By sweeping the frequency of the applied force we observe the dynamic response of the beam deformation which will exhibit peaks in correspondence with the resonance frequencies (fundamental and higher modes).

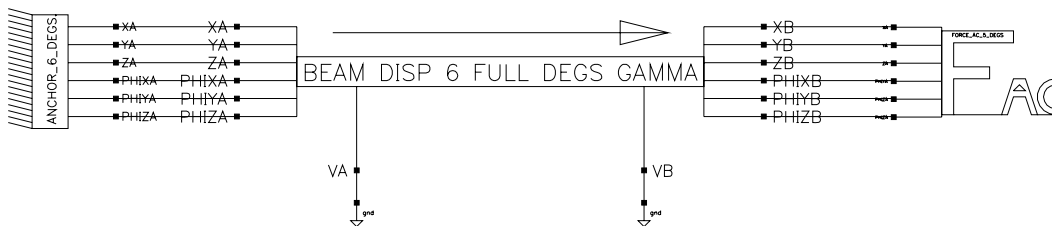


Figure 4.22: Cadence Virtuoso<sup>©</sup> Schematic for the dynamic validation of the Euler beam mechanical model.



On the other hand, the COMSOL Multiphysics<sup>©</sup> analysis of the same structure is based on the eigen resonance frequencies. This means that no stimuli are applied to the beam but its resonance modes are derived as a function of the eigenvalues related to the structure [46].

The force modulus applied to the structure of Figure 4.22 is equal to  $1 \mu N$  and it is all directed along the  $Y$  axis as its orientation angles are  $\theta_{S_Y} = 0^\circ$  and  $\theta_{S_Z} = 90^\circ$ . Consequently, the corresponding DoF's of the free beam end to be stimulated are the  $Y$  linear displacement and the torsion around the  $Z$  axis. The small signal AC simulation response in the frequency range from 100 KHz to 100 MHz is shown in Figure 4.23.

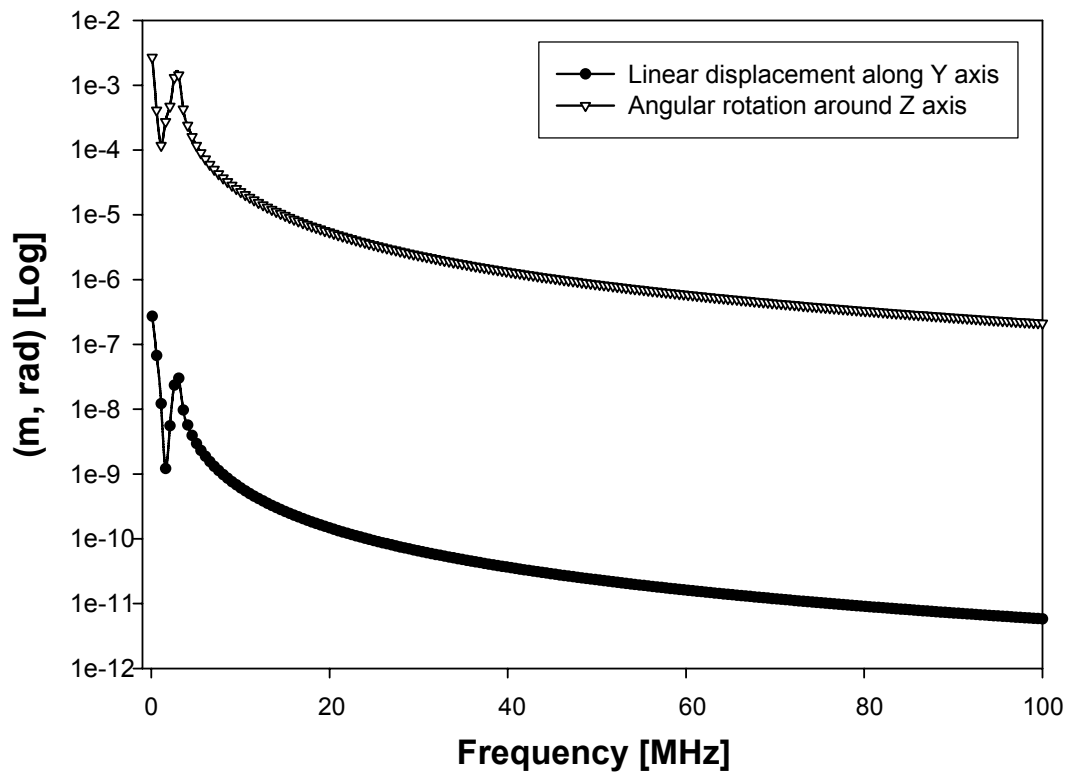


Figure 4.23: Small signal AC simulation in Spectre<sup>©</sup> from 100 KHz to 100 MHz. The linear  $Y$  displacement and the angular rotation around  $Z$  are plotted in a logarithmic vs. linear frequency scale.

The dynamic behaviour of the beam exhibits a low-pass characteristic as the amplitude of the deformations decreases as the frequency raises. Let us now repeat the same simulation within a narrow frequency range (from 100 KHz to 4 MHz) to emphasize the resonance peaks. The plot of Figure 4.24 shows the fundamental resonance frequency for the  $Y$  displacement and rotation around  $Z$  at 289.1 KHz and the first higher mode at 2.852 MHz. The first eigenmode predicted by COMSOL Multiphysics<sup>®</sup>, (the schematic is reported in Figure 4.25) occurs at  $Z$  at 289.69 KHz which is in very good agreement with the Spectre<sup>®</sup> result.

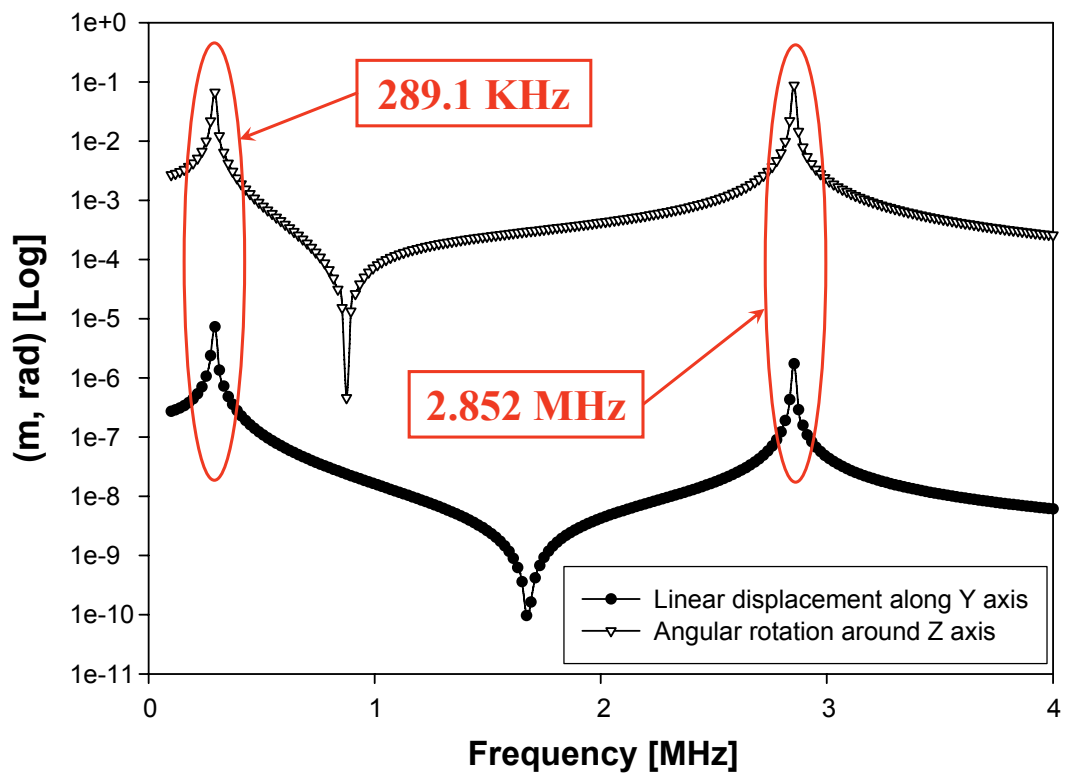


Figure 4.24: Small signal AC simulation in Spectre<sup>®</sup> from 100 KHz to 4 MHz. The linear  $Y$  displacement and the angular rotation around  $Z$  are plotted in a logarithmic vs. linear frequency scale.

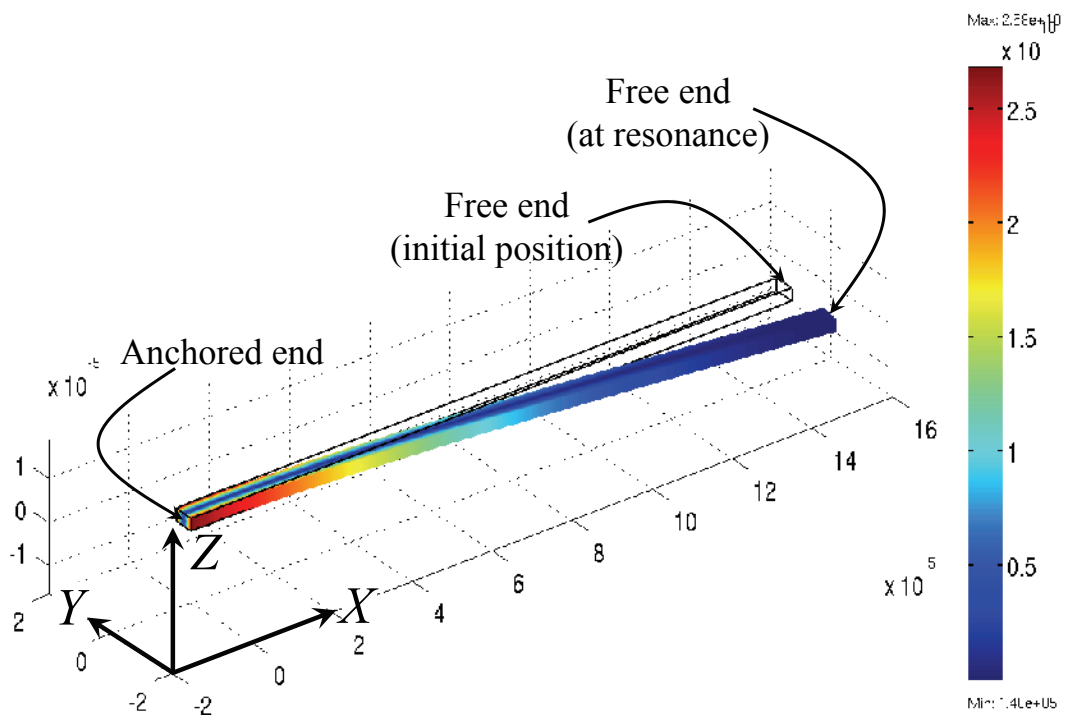


Figure 4.25: COMSOL Multiphysics<sup>®</sup> schematic for the fundamental eigenmode (on  $XY$  plane) of the Euler beam.

Concerning the higher modes, COMSOL Multiphysics<sup>®</sup> predicts the first one at 1.808 MHz (see Figure 4.26) and 5.027 MHz (see Figure 4.27) respectively. Whereas, the Spectre<sup>®</sup> prediction for the first higher mode is 2.852 MHz (see Figure 4.24) and the second one is not predicted at all, as Figure 4.23 shows. However, looking at Figures 4.26 and 4.27 it must be noticed that the beam configurations for the higher modes are incompatible with the ones assumed in the Euler beam mechanical model and based on HSF's. To this purpose see Figures 4.4 and 4.5. This suggests to solve the problem by adding additional degrees of freedom to the Spectre<sup>®</sup> model which means to split the single beam (of length  $L$ ) in two beam (of length  $\frac{L}{2}$ ) connected in series (in our case two beams of length  $75 \mu m$ ). The corresponding Cadence Virtuoso<sup>®</sup> Schematic is shown in Figure 4.28 while the displacement along  $X$  and the rotation around  $Z$  predicted in Spectre<sup>®</sup> are reported in Figure 4.29.

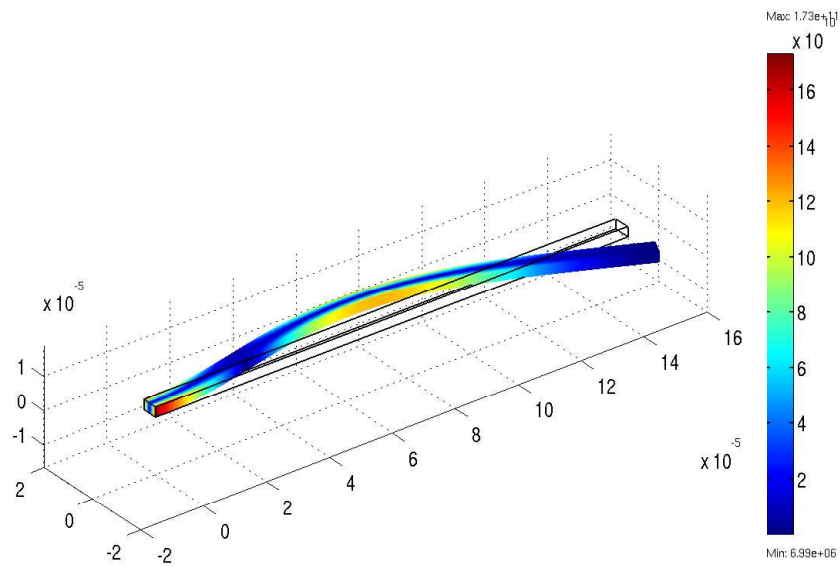


Figure 4.26: COMSOL Multiphysics<sup>®</sup> schematic for the first higher eigenmode (on  $XY$  plane) of the Euler beam.

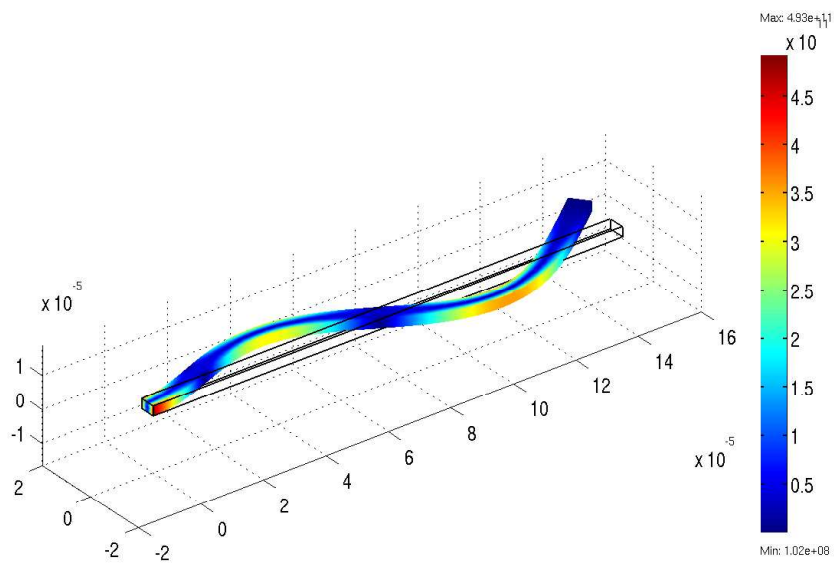


Figure 4.27: COMSOL Multiphysics<sup>®</sup> schematic for the second higher eigenmode (on  $XY$  plane) of the Euler beam.

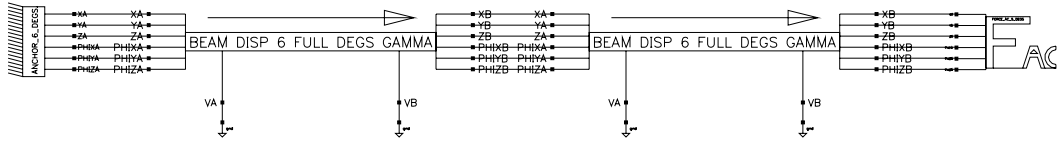


Figure 4.28: Cadence Virtuoso<sup>©</sup> Schematic for two beams of length  $75\ \mu\text{m}$  connected in series.

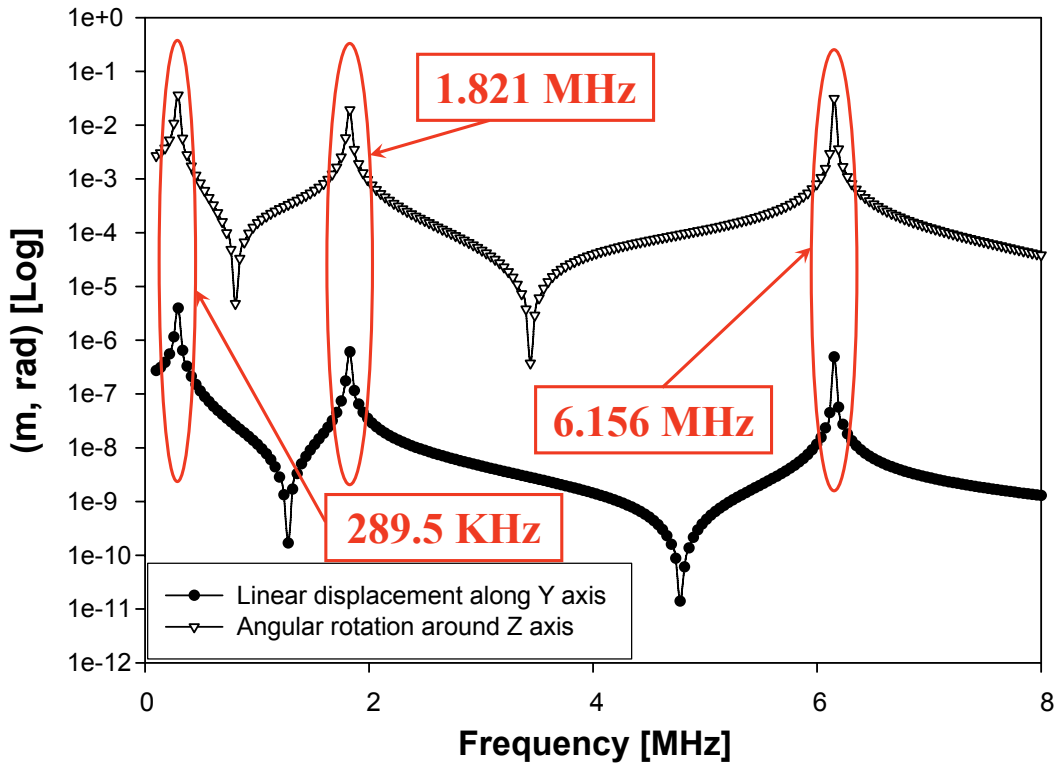


Figure 4.29: Small signal AC simulation in Spectre<sup>©</sup> from 100 KHz to 8 MHz for two beams of length  $75\ \mu\text{m}$  connected in series. The linear  $Y$  displacement and the angular rotation around  $Z$  are plotted in a logarithmic vs. linear frequency scale.

The fundamental resonance mode in Spectre<sup>©</sup> is not affected by the connection of two half-length beams, while the first higher mode now occurs at 1.821 MHz which is very close to the FEM prediction of 1.808 MHz. Concerning the second higher mode, the Spectre<sup>©</sup> result is now 6.156 MHz which is closer to the COMSOL Multiphysics<sup>©</sup> one (5.027 MHz). However, the schematic of Figure 4.28 needs a further degree of freedom along the beam length to be compatible with the configuration of Figure 4.27. To do this, the beam must be split in three shorter beams of length  $\frac{L}{3}$  (i.e.  $50 \mu m$ ). The Cadence Virtuoso<sup>©</sup> Schematic for the three beams in series is not shown here but follows the same principle of the one shown in Figure 4.28. This leads to a prediction in Spectre<sup>©</sup> of the second higher mode which is 5.117 MHz now very close to the one predicted by the FEM software (5.027 MHz). The solution of splitting the beam in shorter devices in order to increase the predictive accuracy of the higher modes is pursuable as long as the single beams are not too short. Indeed the Euler beam model, previously discussed in this chapter, is based on the assumption that the beam length is larger than its width and thickness. Finally, the results shown thus far along with the same analysis performed for the  $XZ$  in-plane resonance modes ( $\theta_{S_Y} = 90^\circ$  and  $\theta_{S_Z} = 0^\circ$ ) are summarized in Table 4.5. The corresponding COMSOL Multiphysics<sup>©</sup> schematics are shown in Figures 4.30, 4.31 and 4.32. The higher order modes are predicted in Spectre<sup>©</sup> by exploiting two and three shorter beams connected in series.

Mode	Cadence	COMSOL	Error
Fundamental ( $XY$ )	289.10 KHz	289.69 KHz	-0.20%
1 <sup>st</sup> higher ( $XY$ )	1.821 MHz	1.808 MHz	+0.72%
2 <sup>nd</sup> higher ( $XY$ )	5.117 MHz	5.027 MHz	+1.79%
Fundamental ( $XZ$ )	173.51 KHz	173.90 KHz	-0.22%
1 <sup>st</sup> higher ( $XZ$ )	1.092 MHz	1.088 MHz	+0.37%
2 <sup>nd</sup> higher ( $XZ$ )	3.069 MHz	3.039 MHz	+0.10%

Table 4.5: Fundamental and higher resonance modes along the  $XY$  and  $XZ$  plane predicted in Spectre<sup>©</sup> are validated by comparison with COMSOL Multiphysics<sup>©</sup> simulations.

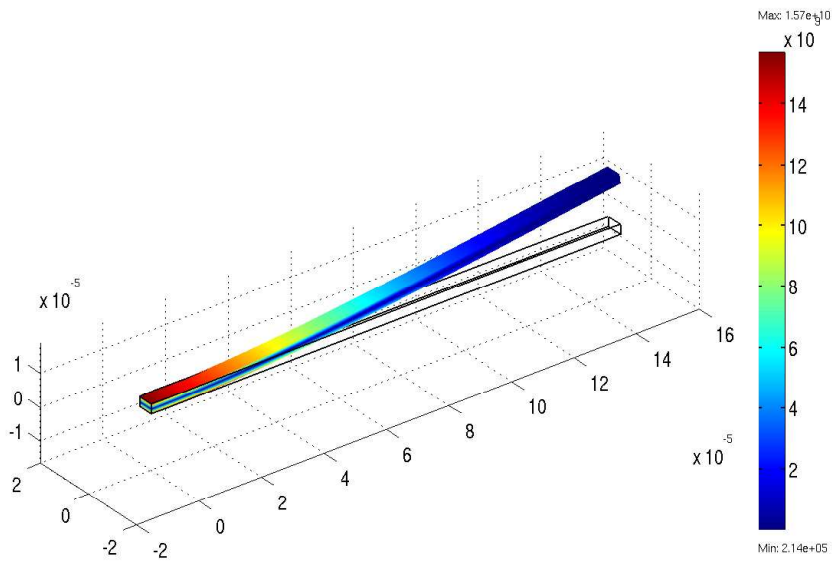


Figure 4.30: COMSOL Multiphysics<sup>®</sup> schematic for the fundamental eigenmode (on  $XZ$  plane) of the Euler beam.

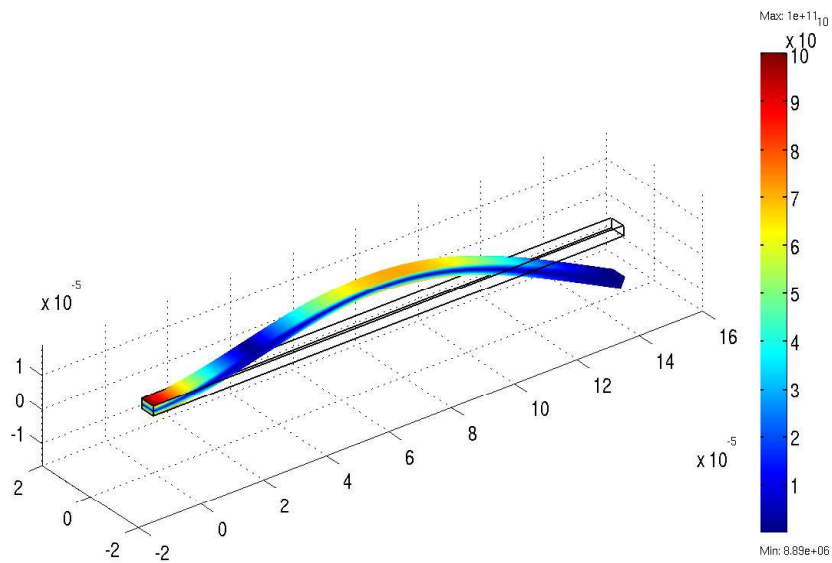


Figure 4.31: COMSOL Multiphysics<sup>®</sup> schematic for the first higher eigenmode (on  $XZ$  plane) of the Euler beam.

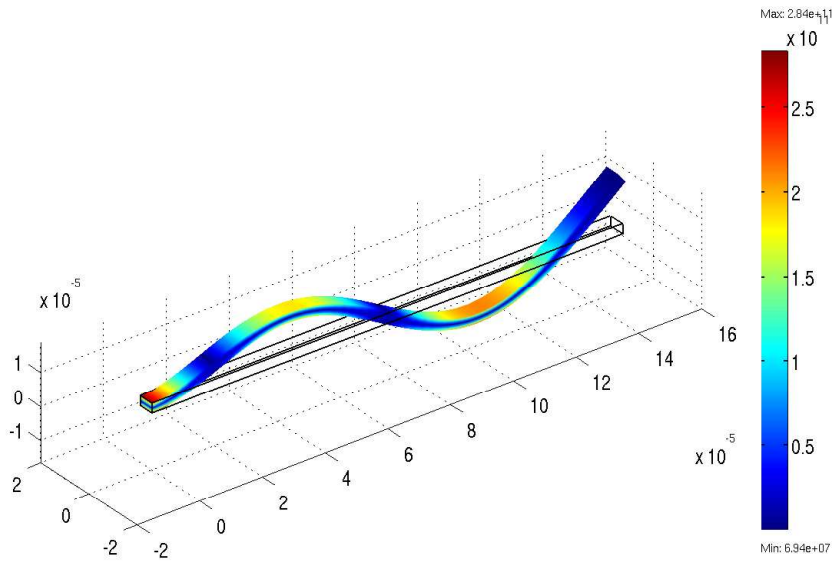


Figure 4.32: COMSOL Multiphysics<sup>®</sup> schematic for the second higher eigenmode (on  $XZ$  plane) of the Euler beam.

### 4.6.3 Validation of the Beam Electrostatic Model

The validation of the beam electrostatic model is based on the electromechanical transduction principle. As the mechanical model for the Euler beam has been already validated, the pull-in effect is observed [34]. To this purpose a cantilever structure is defined within Spectre<sup>®</sup>. This is a suspended beam with one anchored end and the other one free. When a biasing voltage is applied between the beam and the substrate the electrostatic force makes the free end of the beam to bend towards the substrate, and when the pull-in voltage is reached [6] the beam collapses on the substrate as Figure 4.33 shows. The corresponding Cadence Virtuoso<sup>®</sup> Schematic is shown in Figure 4.34. The left beam end is anchored while in the right one pins are terminated in a module which does not apply any force to it in order not to leave the six right nodes floating. For more details about these elements see the last section of Chapter 3. Finally, a voltage generator is connected to one of the two beam electrical nodes to apply the control biasing signal.



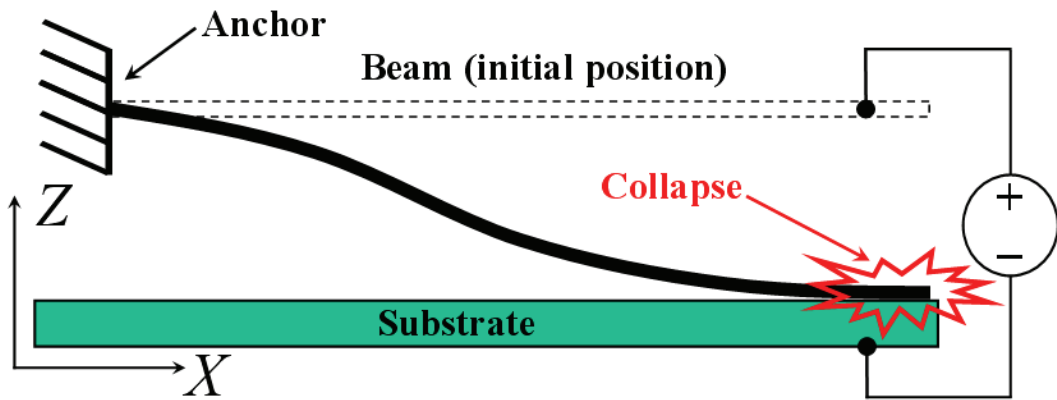


Figure 4.33: Schematic of the cantilever structure. When the applied voltage reaches the pull-in value the beam collapses onto the substrate.

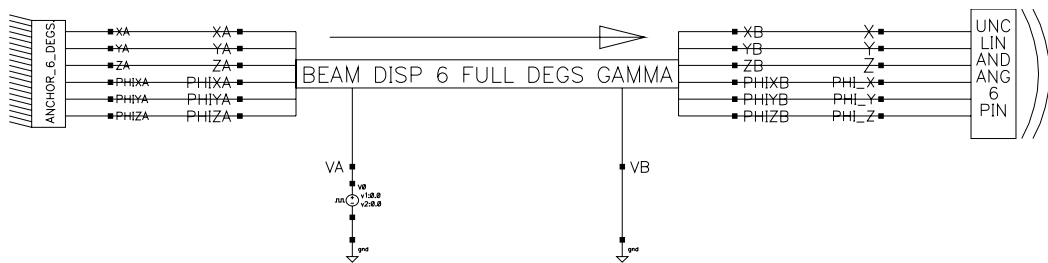


Figure 4.34: Cadence Virtuoso<sup>®</sup> Schematic of the cantilever structure. The left beam end is anchored while the right one is free to move. Note the voltage source connected to the left beam electric pin while the right one represents the lower electrode connected to ground.

The simulation performed in Spectre<sup>®</sup> is a DC [9] with a linear sweep applied to the biasing voltage. The typical vertical displacement behaviour of the free beam end versus the biasing voltage is shown in Figure 4.35 and is simulated in Spectre<sup>®</sup>. This represents the first example of multi-domain (electro-mechanical) simulation performed with the MEMS library compact models discussed thus far. The curve is referred to a beam with length ( $L$ ), width ( $W$ ) and thickness ( $T$ ) respectively equal to  $250\ \mu m$ ,  $2.5\ \mu m$  and  $1\ \mu m$ . Moreover, the gap between the beam and the top-side of the insulating oxide-layer onto the substrate electrode (see Figure 3.12) is  $3.5\ \mu m$ . Finally, the Young modulus of the beam material is 118 GPa.

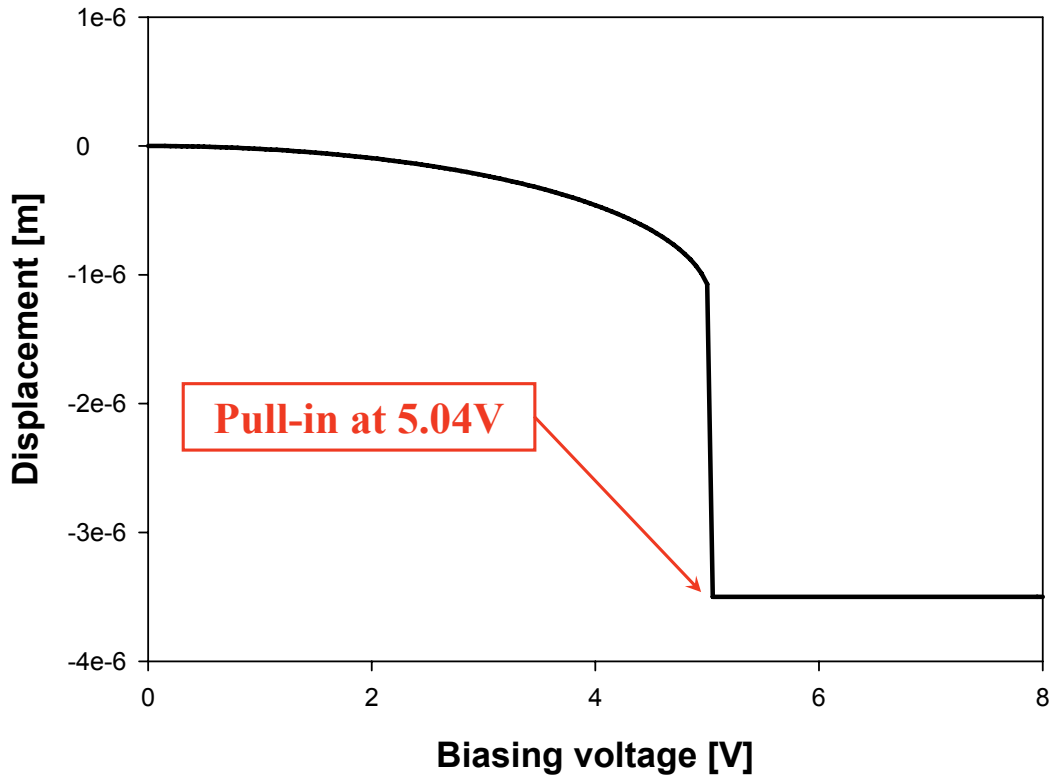


Figure 4.35: DC simulation of a cantilever in Spectre<sup>®</sup>. The vertical displacement of the free beam end is plotted vs. the linear biasing voltage swept between 0 and 8 Volts.

Validation is performed by comparing the results produced in Spectre<sup>®</sup> with the FEM predictions obtained within CoventorWare<sup>®</sup> [47] which is able to solve coupled electro-mechanical problems. A schematic of a cantilever structure in CoventorWare<sup>®</sup> is shown in Figure 4.36.

The comparisons of the Spectre<sup>®</sup> pull-in voltage predictions for some cantilever geometries, compared with the corresponding CoventorWare<sup>®</sup> simulations are summarized in Table 4.6. The accuracy of the compact models predictions is acceptable and comparable with the one of the rigid plate electrostatic model shown in previous chapter. Indeed, the largest disagreement among the simulation in Spectre<sup>®</sup> and CoventorWare<sup>®</sup> is around 11%.

Length	Width	Thickness	Gap	Cadence	CoventorWare	Error
50 $\mu m$	1.5 $\mu m$	1 $\mu m$	400 nm	6.76 V	6.13 V	+10.3%
75 $\mu m$	5 $\mu m$	3 $\mu m$	400 nm	15.82 V	14.78 V	+7.0%
250 $\mu m$	5 $\mu m$	3 $\mu m$	500 nm	360 mV	350 mV	+2.9%
250 $\mu m$	5 $\mu m$	3 $\mu m$	3.5 $\mu m$	5.04 V	5.25 V	-4.0%
250 $\mu m$	4 $\mu m$	2 $\mu m$	2.0 $\mu m$	6.38 V	5.94 V	+7.4%
300 $\mu m$	6 $\mu m$	4 $\mu m$	1.3 $\mu m$	6.86 V	7.75 V	-11.5%

Table 4.6: Comparisons of the pull-in voltage for some typical cantilever geometries predicted in Spectre<sup>®</sup> with FEM simulation results obtained in CoventorWare<sup>®</sup>.

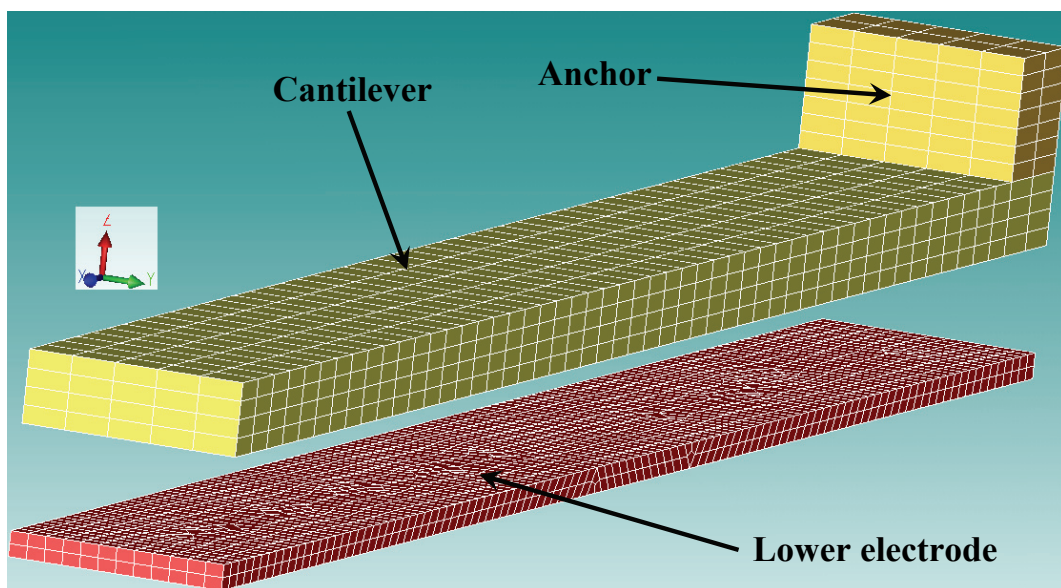


Figure 4.36: Schematic of a cantilever structure in CoventorWare<sup>®</sup>. The beam has one end anchored and the other free to move.

## Chapter 5

# Hybrid Wafer-Level Packaging of RF-MEMS

In this chapter, issues related to the development of a methodology for the packaging and integration of RF-MEMS devices will be discussed.

Basically, two targets will be aimed through the next sections. The first is the definition of a proper technological solution for fabricating the protective substrate, which has to be compatible and applicable to the RF-MEMS part. Moreover, issues related to the influence of the cap on the electromagnetic behaviour of capped devices will be addressed as well. To this purpose, an extensive electromagnetic optimization of the capping part process performed with an appropriate tool will be shown.

### 5.1 Brief Overview on Packaging Solutions for RF-MEMS

In developing a solution for the fabrication of a protective cap to be applied to certain micro-devices several consideration must be taken into account. First of all, the main task of the package is to offer an adequate protection to the devices from harmful factors like mechanical shocks as well as from moisture, dust particles and various contaminants. Of course, depending on the type of devices and on the environment in which these are meant to operate the capping part should be particularly robust with respect to the more harmful ex-

ternal factors [48]. The type of application for which the particular devices are conceived plays also an important role in defining the packaging solution [49].

Concerning issues related to the fabrication of the capping part, different materials are employed to this purpose like Silicon, glass and ceramic compounds [50]. Depending on the particular material chosen for the capping part realization, different techniques can be applied to set up the electrical signals interconnection scheme as well as the necessary space to accommodate the devices to be packaged.

Yun-Kwon Park et Al. demonstrated a packaging solution for RF-MEMS based on a glass substrate [51]. Through-vertical vias are opened in the cap by means of sandblasting. These are then filled with gold to redistribute the electrical signals from the device wafer to the outside world. Another viable solution in order to package RF-MEMS switches has been demonstrated from H. A. Tilmans et Al. [52]. In this a BCB (BenzoCycloButene) ring is patterned around each device to provide the necessary vertical space to house the MEMS itself as well as to isolate it from external dangerous factors. The electrical signals are brought out of the package by means of CPW's (Coplanar Wave Guides) placed on the device wafer and passing underneath the BCB protective ring. Differently, A. Margomenos et Al. presented a packaging solution for RF-MEMS switches in which vertical vias are etched in a Silicon substrate and filled with conductive material prior to the fabrication of the MEMS devices themselves [53]. After a Silicon capping wafer is bonded onto the switches, the electrical signals are accessible on the bottom face of the packaged device wafer.

The final utilization of RF-MEMS implies their integration and interfacing to other functional blocks within a certain system. The packaging represents a delicate step also in the sense of easing the final mounting of a chip including MEMS devices onto a board. Within the scientific community the definitions of *first-level* and *zero-level* packaging have been introduced [54]. The first-level refers to a packaging solution performed on a device chip (i.e. small size). The electrical interconnect scheme is made available the for the final mount of the MEMS chip. This is based for instance on Ball Grid Array (BGA), Dual in-line Package (DiP), Pin Grid Array (PGA) or Leadless Chip Carrier [18]. On the other hand, the zero-level packaging is commonly addressed also as Wafer-Level Packaging (WLP). This means that an entire device wafer has

to be bonded to the package. The wafer-to-wafer bonding can be performed for instance by means of solder reflow, anodic bonding [18] or via the use of adhesive materials like SU-8 [55]. After the bonding step, the capped wafer must be singulated, which means to saw it in dies of smaller size (e.g.  $1 \times 1 \text{cm}^2$ ). Finally, the single die must be made ready for the final on board mounting, for instance by wire-bonding it to a carrier chip provided with leads for DiP or solder balls for Flip-Chip mounting [18]. In other words, a zero-level solution is an intermediate packaging stage which requires additional steps to get a chip ready for standard Surface Mount Technologies (SMT) like the ones mentioned above. This is necessary when dealing with MEMS devices as they need to be protected right after fabrication (for instance during the wafer handling and singulation).

Beside this, still referring to integration of RF-MEMS devices it is very interesting to investigate additional functionalities the package might provide for. One of the most interesting is surely the possibility of interfacing the CMOS circuitry to the passive RF-MEMS part directly on-chip by exploiting the cap to provide the proper housing for the CMOS chip along with an interconnect scheme for the signals interfacing. This allows getting a complete functional block (for instance an oscillator based on a MEMS resonator and a CMOS sustaining circuitry) packaged and ready for SMT. Because the RF-MEMS and CMOS part are obtained via different incompatible technologies, this solution is called Hybrid-Packaging [24].

Another important feature is made available by the package. This is the hermeticity and the vacuum sealing which are possible depending on the particular solution chosen for the bonding of the capping part to the MEMS device part. It has been demonstrated by Nguyen that a MEMS lateral comb-drive resonator exhibits a Q-Factor (Quality Factor) of 27 when is operated in air [56]. The Q-Factor for the same device rises to about 50000 when it is operated in a vacuum environment. Typically it is very tough to maintain the vacuum condition within the packaged cavity over a long period as leakages through the sealing may occur as well as out-gassing phenomena of the materials within the chamber (e.g. the sealing material or the MEMS device itself). This leads to a drift (i.e. degradation) over time of the capped MEMS devices performance. A brilliant solution which leads to a drastic reduction of this problem is offered by the use of the so called *getters* [57]. These are materials which exhibit very

selective absorption properties with respect to certain species which jeopardize the hermetic vacuum of the package. Getter materials are usually arranged in thin films so that they can be easily accommodated within the cavity in which the vacuum condition must be enhanced and maintained. Getters are obtained by sinterisation of different materials to achieve the desired sensitivity to the gaseous species that must be trapped [58]. The effectiveness of getters has been demonstrated by D. Sparks et Al. showing that the Q-Factor of a MEMS resonator operated in vacuum condition is largely more stable over time when a getter layer is added within the chamber [59].

## **5.2 Technological Solution for the Package Fabrication**

After the wide overview on packaging solutions for RF-MEMS devices of previous section let us now introduce the particular methodology chosen in this work. First of all, this is based on a wafer-level packaging (WLP) approach. The material employed for the capping part is Silicon and the redistribution of electrical signals from the MEMS device wafer to the outside world is provided by through-vertical vias etched in the capping substrate and subsequently filled with copper. Recesses are etched in the bottom cap face to accommodate RF-MEMS devices while the wafer-to-wafer bonding can be performed by solder bumps reflow or via the use of Electrically Conductive Adhesives (ECA's) [60]. Moreover, the chosen packaging solution allows the integration of the CMOS circuitry (hybrid packaging). This will be shown in details in the next pages.

### **5.2.1 The Wafer-Level Packaging Concept**

Before going into details of the package fabrication process let us focus on the wafer-level packaging solution. Starting from a devices wafer in which the RF-MEMS are arranged within dies distributed onto the wafer area, a second wafer i.e. the package is necessary. Through it vertical interconnects have to be distributed in correspondence with the signal pads on the dies of the device substrate. A schematic view of both the RF-MEMS device and capping wafers is shown in Figure 5.1.



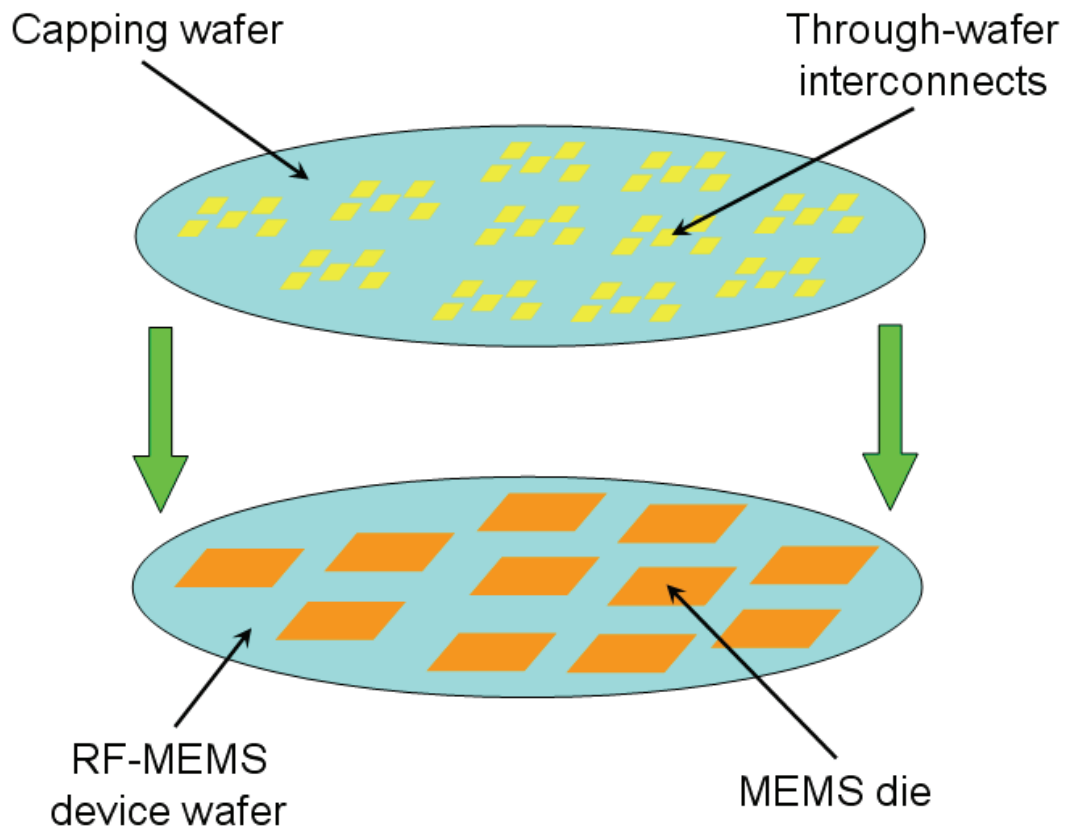


Figure 5.1: In wafer-level packaging a capping wafer with an interconnects scheme compatible with the distribution of electrical signal pads onto the RF-MEMS device substrate is necessary.

After the capping part is aligned to the device wafer the two substrate must be brought in contact. Once the wafer-to-wafer bonding is performed the capped RF-MEMS wafer is ready for subsequent singulation like Figure 5.2 reports. After this step the packaged RF-MEMS dies are ready for the flip-chip on board mount by means of solder balls reflow as it is shown in Figure 5.3.

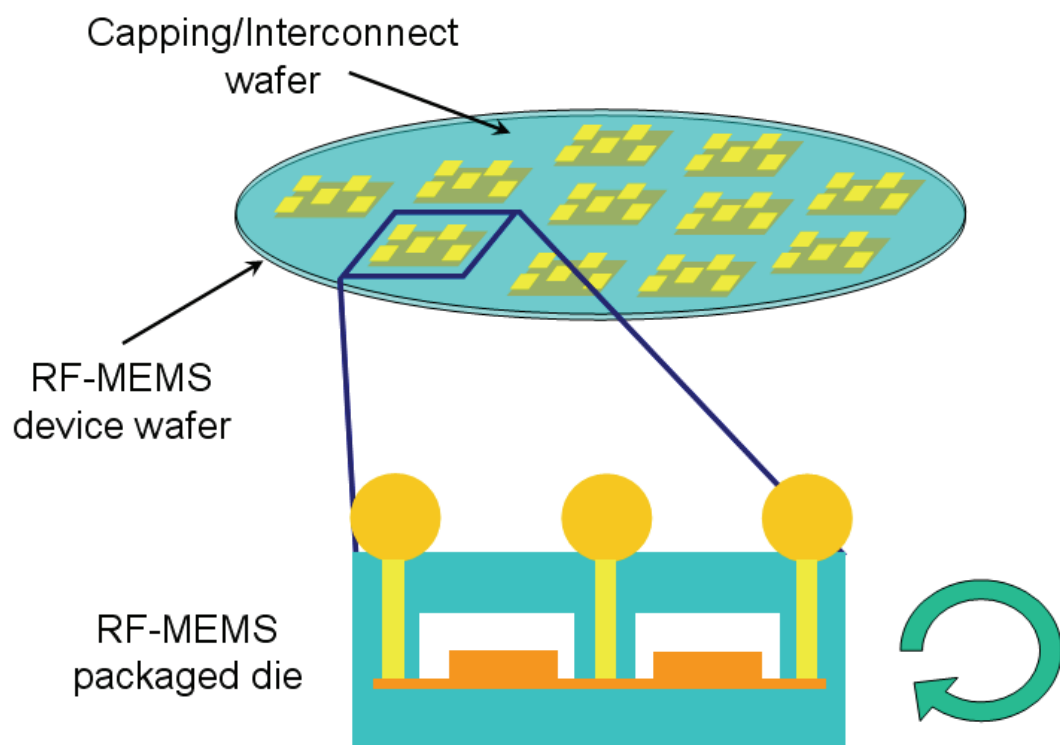


Figure 5.2: After the alignment of the capping part to the MEMS substrate the wafer-to-wafer bonding is performed. After the subsequent singulation the packaged RF-MEMS dies are available for SMT (see Figure 5.3).

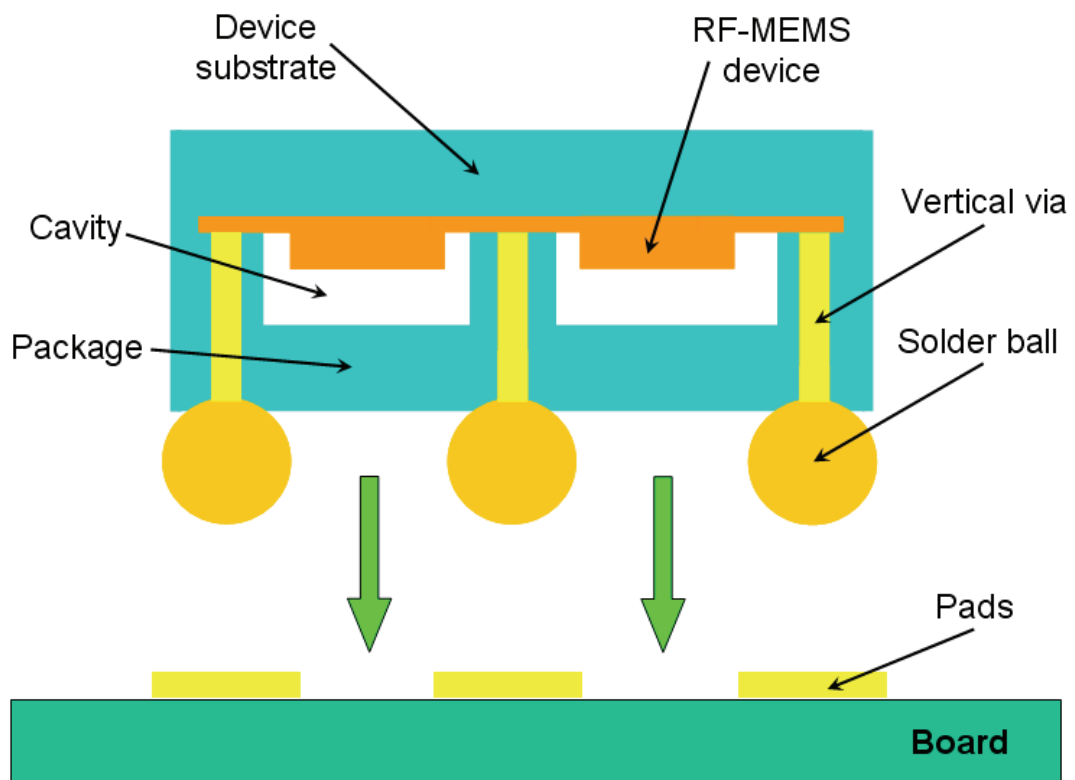


Figure 5.3: The final step is to flip the packaged MEMS die over the board performing the bonding by solder balls reflow.

### 5.2.2 Package Fabrication Process

Let us now go into the details of the fabrication process for the capping part. The process is realized with the facilities available at the HiTeC-DIMES Technology Centre (Technical University of Delft, the Netherlands) and employs a Silicon wafer as starting material. The process flow steps follow:

- **Step 1:** The Silicon wafer is first polished and made ready for the subsequent steps (see Figure 5.4). Its initial thickness is around  $525\ \mu\text{m}$ .
- **Step 2:** Recesses are etched from the bottom wafer side by means of the Bosch DRIE (Deep Reactive Ion Etching) process [61] (see Figure 5.5). Typically the recess depth ranges between a few tens of microns up to  $120 - 150\ \mu\text{m}$ .
- **Step 3:** The Bosch DRIE process is used once again to etch vertical vias from the top wafer side like Figure 5.6 shows. Their diameter ranges from about  $10 - 15\ \mu\text{m}$  up to  $100 - 120\ \mu\text{m}$ . It is not required to etch vias through the whole wafer thickness as the wafer is then grinded from the back side (next step).
- **Step 4:** The wafer with etched recesses and vertical vias is thinned from the bottom side by means of grinding in a lapping machine [62] (see Figure 5.7). Its thickness is reduced at least until when the bottom vias openings are released which corresponds to a wafer height of about  $350\ \mu\text{m}$ . Optionally, it is possible to further thin down the wafer bringing its thickness down to about  $230 - 250\ \mu\text{m}$ .
- **Step 5:** A seed layer is sputtered [18] on the wafer top face and onto vias sidewalls (see Figure 5.8) after a Silicon oxide layer (not shown in figure) is grown on the two wafer sides and vias sidewalls. The seed layer is necessary to perform the subsequent electrodeposition of copper.
- **Step 6:** A photoresist film is patterned on the wafer top side to define the feature of the copper pads which are being electrodeposited and on the bottom side to define where the bumps will be deposited (see Figure 5.9).
- **Step 7:** Top side copper pads are electrodeposited on the Silicon wafer like shown in Figure 5.10. These will ensure the electrical interconnection

with the RF-MEMS devices once the vias are filled with copper. Top side pads can be both used for direct measurements of capped MEMS devices (i.e. probes can be placed on them) and for hosting electrodeposited solder balls for final on board mount (see Figure 5.3).

- **Step 8:** Vertical etched vias are bottom-up filled with copper like Figure 5.11 shows. To perform this step the wafer has to be flipped upside-down and temporary chromium metallization (not shown in figure) are placed on the vertical wafer faces to ensure the electrical connection to the seed layer.
- **Step 9:** Bumps are electrodeposited on the bottom capping side in correspondence with vias (see Figure 5.12). Depending on the solution chosen to perform the wafer-to-wafer bonding these will be made of copper or of a special alloy. More details about the bonding step will be shown later.
- **Step 10:** As final step the photoresist is removed from the top and bottom wafer side as well as the seed layer which was lying below it on the top side (see Figure 5.13).

The capping part is then ready to be aligned with the RF-MEMS device wafer for the wafer-to-wafer bonding. The corresponding scheme is shown in Figure 5.14. A SEM (Scanning Electron Microscopy) photograph of the cross-section of a test capping wafer is shown in Figure 5.15. The test wafer was cut to make the via profile visible. The very high aspect ratio of the via achieved with the Bosch DRIE process as well as the uniform via copper filling are noticeable. The narrowing of the via in the lower part (close to the bump) is an artifact due to the non-parallel direction followed during wafer sawing.

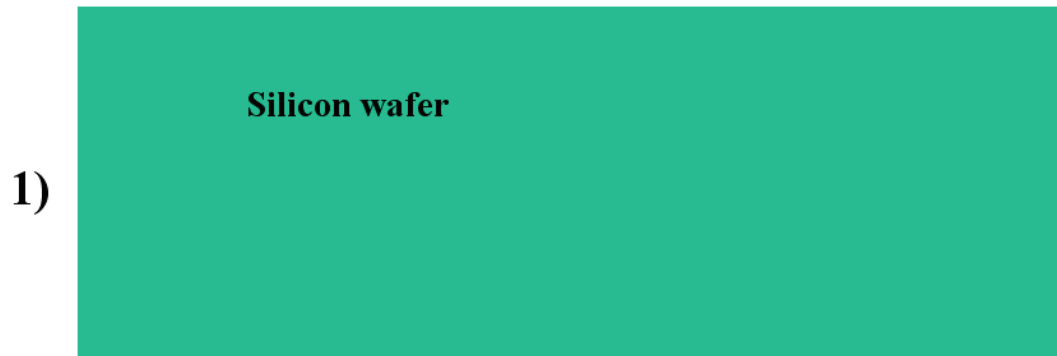


Figure 5.4: **Step 1:** The Silicon wafer is polished and prepared for processing.

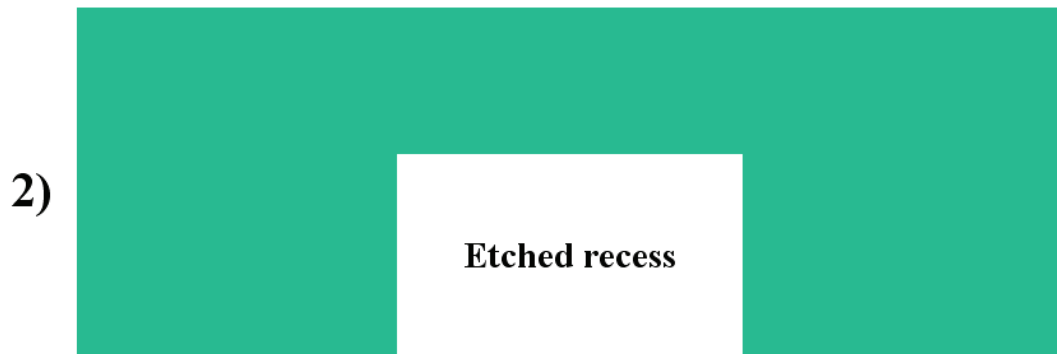


Figure 5.5: **Step 2:** Recesses are etched in the bottom wafer side by using the Bosch DRIE process.

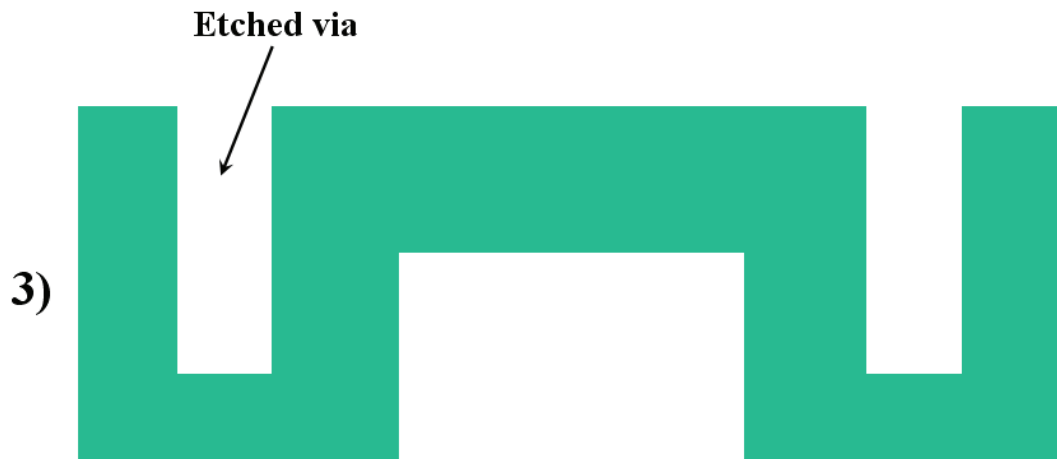


Figure 5.6: **Step 3:** Vertical vias are etched from the top wafer side by using the Bosch DRIE process.

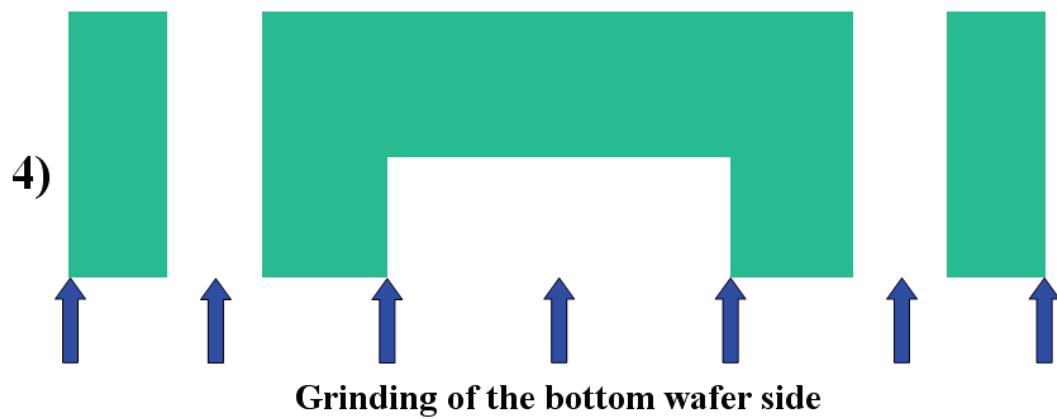


Figure 5.7: **Step 4:** The Silicon wafer is thinned by grinding it from the back side. The bottom vias openings are released.

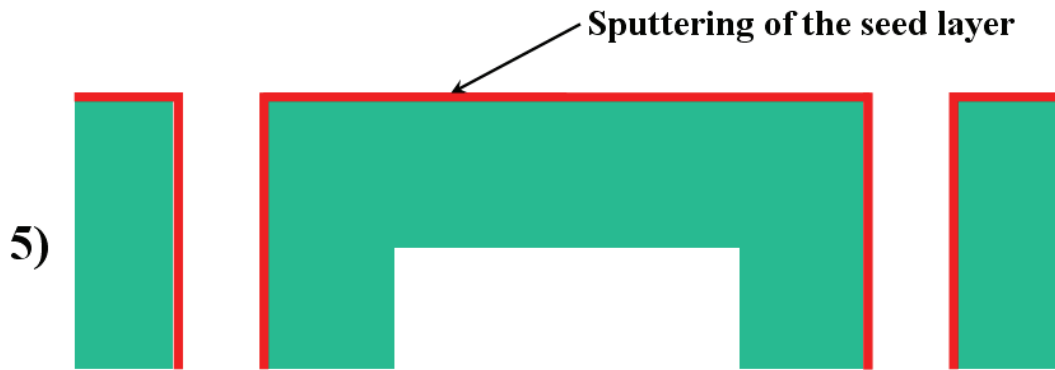


Figure 5.8: **Step 5:** The seed layer is sputtered on the wafer top side and onto vias sidewalls. Before this step a silicon dioxide (not shown here) is grown on wafer and vias surface.

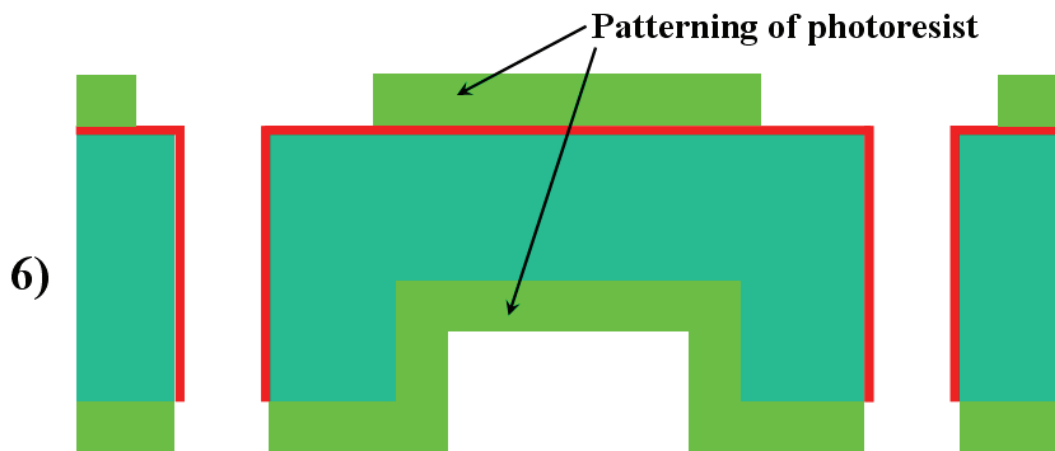


Figure 5.9: **Step 6:** A photoresist film is deposited on both wafer sides to pattern the top copper pads and bottom bumps which will be subsequently deposited.



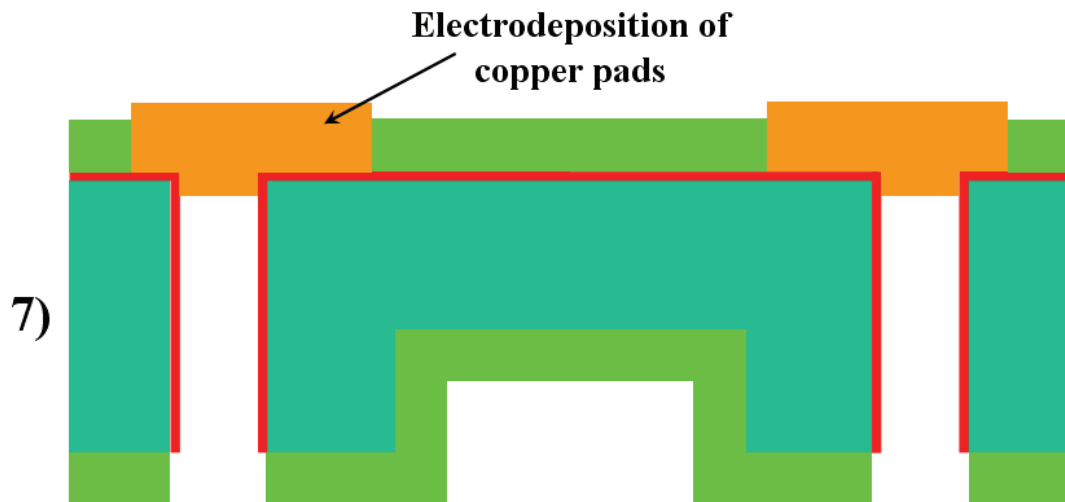


Figure 5.10: **Step 7:** Top side copper bumps are electrodeposited exploiting the seed-layer.

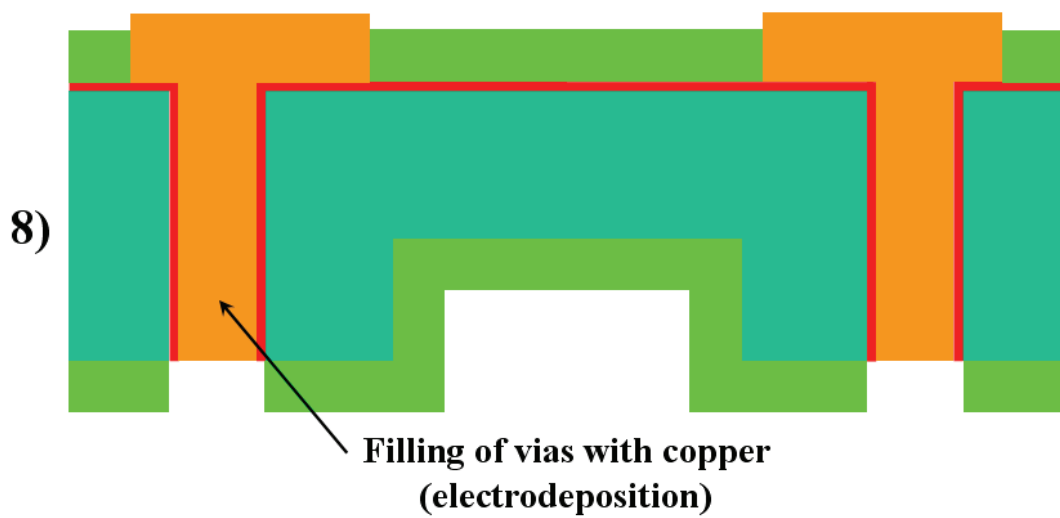


Figure 5.11: **Step 8:** Vias are bottom-up filled with electrodeposited copper.

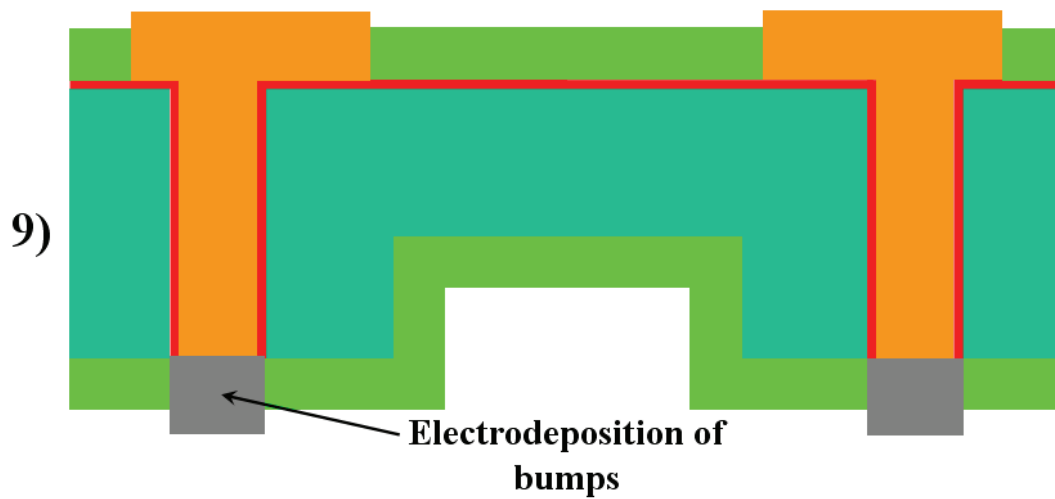


Figure 5.12: **Step 9:** Bottom bumps are electrodeposited in correspondence with vias. Depending on the selected wafer-to-wafer bonding solution these will be made of copper or of a special alloy.

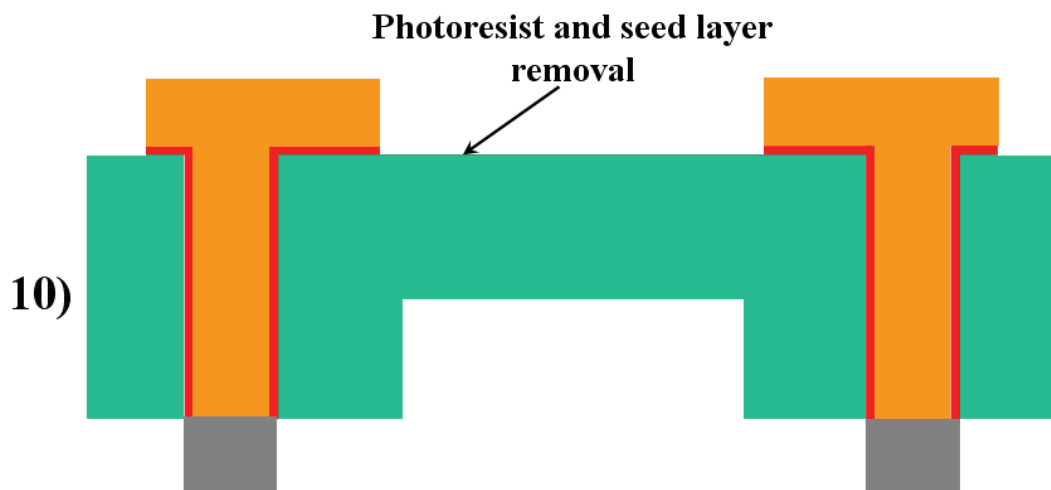


Figure 5.13: **Step 10:** Photoresist residues are removed from both wafer faces as well as the seed layer lying underneath it on the top capping side.

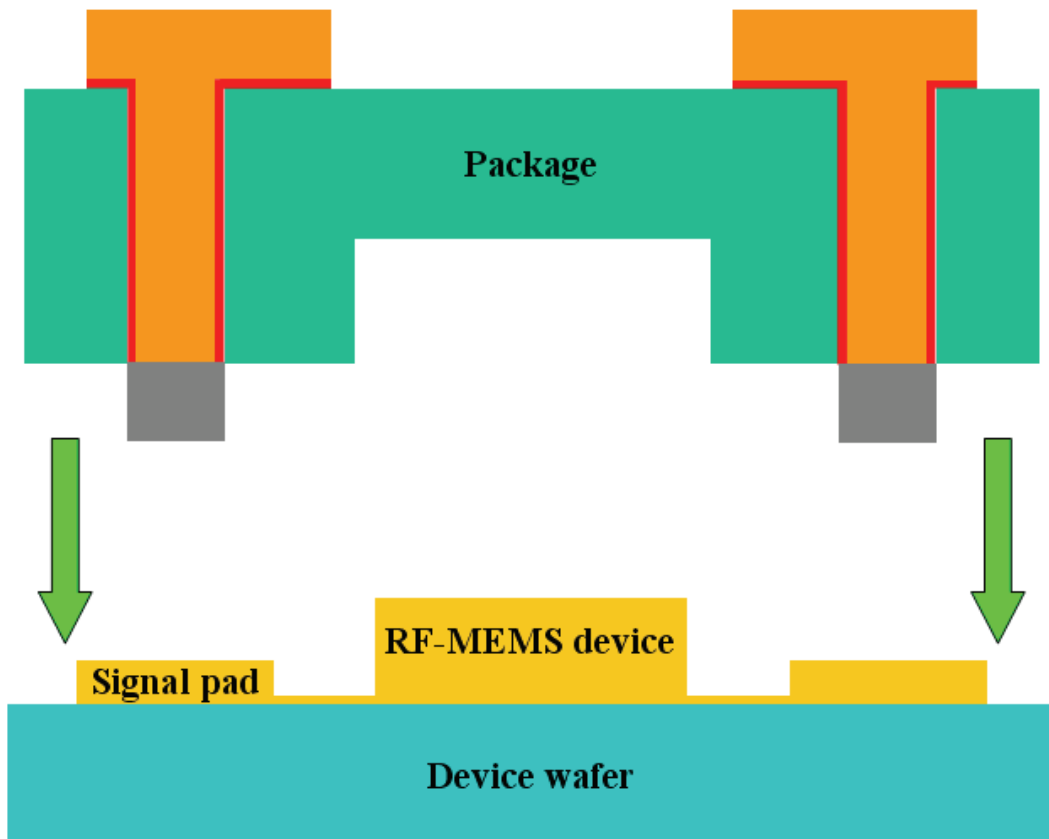


Figure 5.14: The package is bonded to the RF-MEMS device wafer after having been aligned to it.

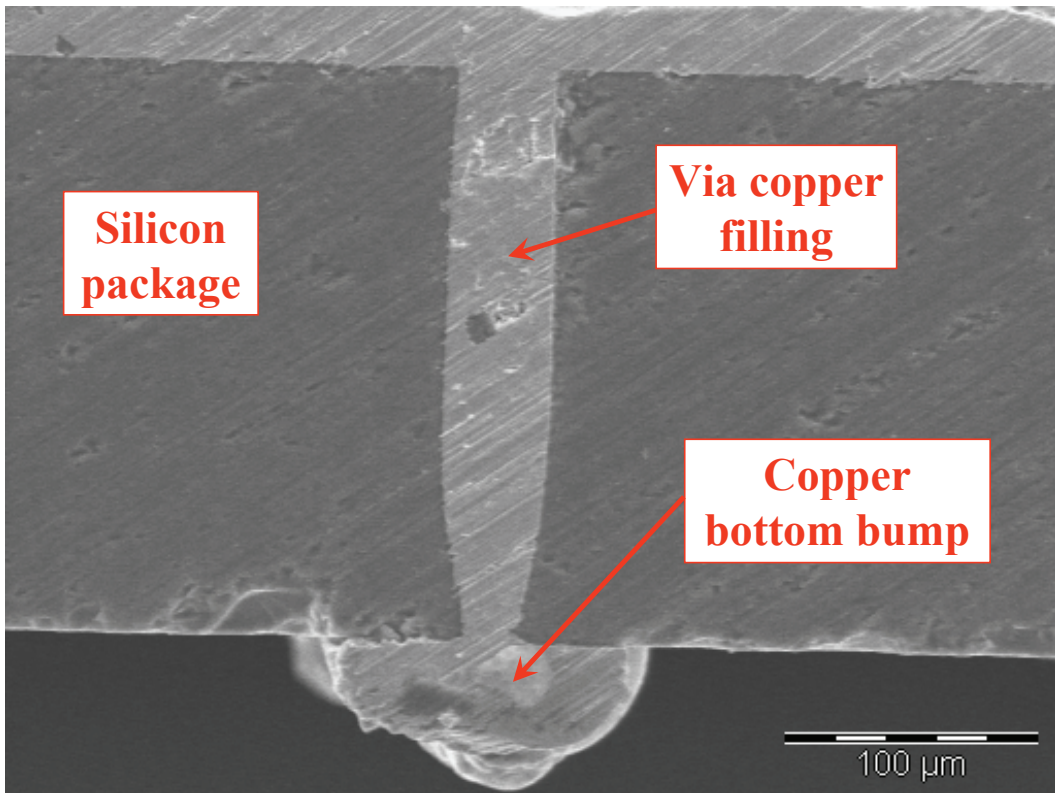


Figure 5.15: SEM (Scanning Electron Microscopy) photograph of a capping test wafer. The via exhibits an high aspect ratio and a very uniform via copper filling is also noticeable.

### 5.2.3 Wafer-to-Wafer Bonding Solutions

It has been briefly mentioned before that the wafer-to-wafer bonding can be performed in two different fashions. The first is based on solder bumps reflow while the second one employs the use of Electrically Conductive Adhesives (ECA). More details about both solutions are being shown below.

#### Solder Bumps Reflow

In the first solution bumps deposited on the bottom capping face (see Figure 5.12) are melted (reflowed) once these are in contact with RF-MEMS signal pads like shown in Figure 5.16. The reflow is achieved by heating up the two wafers until the melting temperature of the bumps is reached [63]. Bumps then commence to spread out enlarging the contact surface of the package-to-device wafers like depicted in Figure 5.17. Subsequent cooling of bumps ensures both the package-to-device wafers adhesion and the proper electrical interconnection. Since the melting temperature of the more commonly used metals (e.g. copper, gold etc.) is generally too high to be tolerated both from the package and device wafers, the bumps material must be chosen trying to minimize the thermal budget for their reflow. This is the reason why suitable alloys composed by different materials to be deposited as bumps are investigated. Indeed, depending on the chosen metals for the alloy and on their relative percentages it is possible to considerably abate the melting temperature of bumps making the bonding step tolerable for the entire capped wafer. This method is well-know in literature as eutectic bonding [64]. In the process discussed in this thesis the alloy is made of Gold (Au) and Tin (Sn). Their percentage in volume is 80% and 20% respectively [65]. This allows to perform the bumps reflow at a temperature of about 300°C. Comparison of SEM pictures taken before and after performing the bumps reflow on a dummy wafer (without applying it to any device wafer) are respectively shown in Figure 5.18 and Figure 5.19.

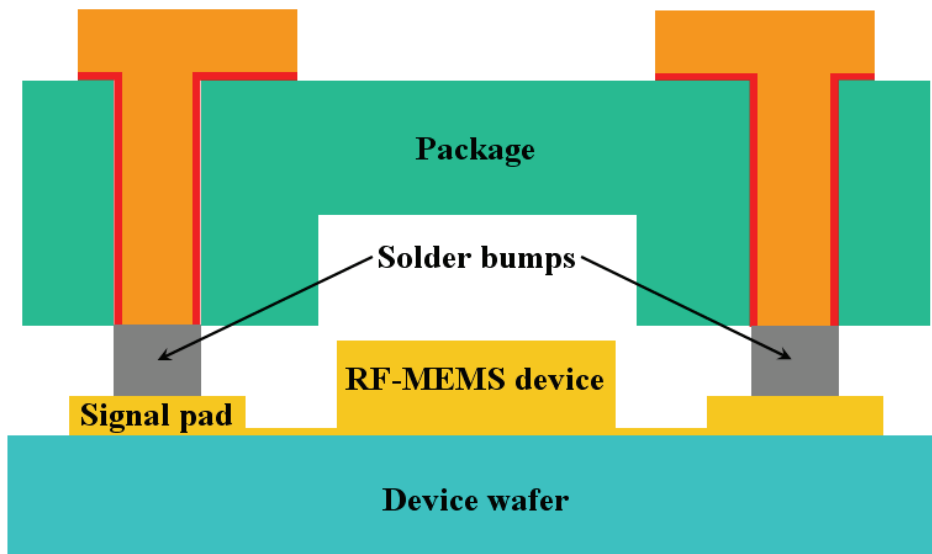


Figure 5.16: Scheme of the package aligned and in contact with the RF-MEMS device wafer **before** the reflow of solder bumps is performed.

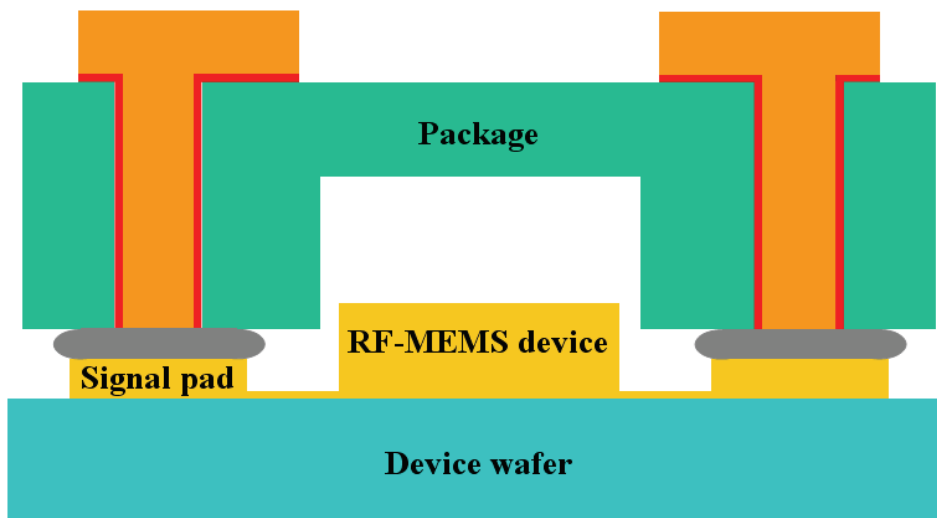


Figure 5.17: Scheme of the package aligned and in contact with the RF-MEMS device wafer **after** the reflow of solder bumps is performed.

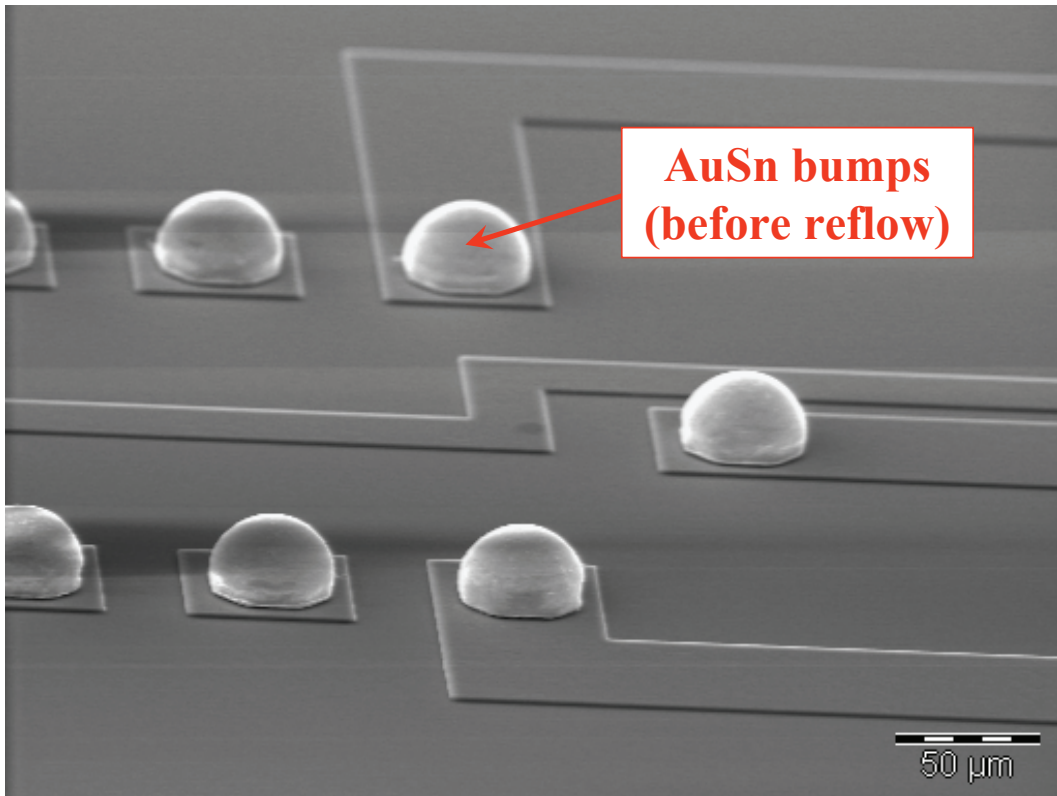


Figure 5.18: SEM photograph of AuSn bumps on a dummy wafer **before** the reflow step.

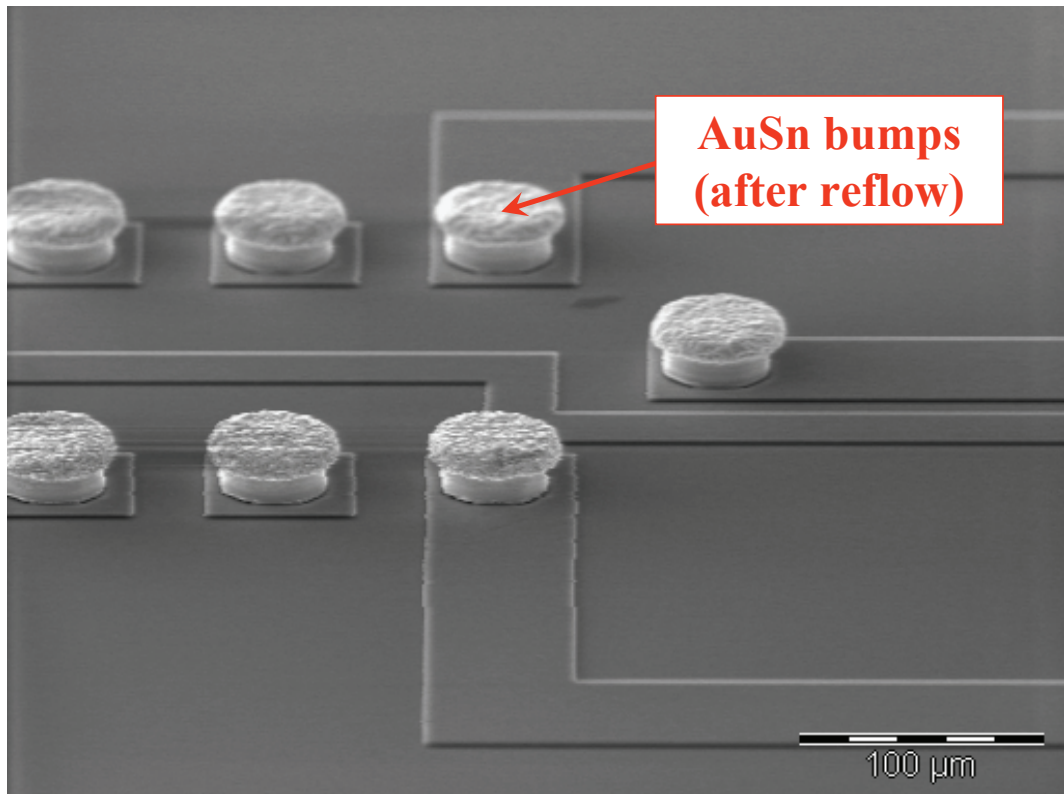


Figure 5.19: SEM photograph of AuSn bumps on a dummy wafer **after** the reflow step.



## Electrically Conductive Adhesives (ECA's)

The other wafer-to-wafer bonding solution relies on the use of special adhesive materials. These are generally called Electrically Conductive Adhesives (ECA's) because are able to ensure both the adhesion and the electrical interconnection of two surfaces. ECA's are constituted of a polymer-based matrix that basically behaves as an electrically insulating glue and are available in the form of pastes or films. Within the matrix a certain amount of conductive particles is distributed [66]. The conductive particles are made of various metals like, for instance, gold, copper or aluminum. Concerning their shape, these can be small spheres (few microns of diameter), flakes or even bigger spheres made of insulating material and coated with a conductive material ( $13 - 15 \mu m$  of diameter) [67]. Depending on the conductive particles dimensions and on their percentage in volume with respect to the insulating glue within which are distributed, ECA's are usually divided in two categories: ACA's (Anisotropic Conductive Adhesives) and ICA's (Isotropic Conductive Adhesives).

If the volume of conductive particles is about 5–10% of the entire ECA volume we are dealing with an ACA material [60]. This means that when the polymer with particles inside is normally uncompressed it behaves as a dielectric material. Whereas, when the ACA is compressed, the conductive particles get closer to each other forming an electrical path through the polymer. A scheme of the ACA in the uncompressed and compressed state is shown in Figure 5.20. The fact that the insulating material can locally become conductive yields the quality of being anisotropic.

On the other hand, when the volume of conductive particles is higher (25–35%) the material is classified as ICA. This means that the distribution of particles is high enough to ensure electrical conductivity independently on the condition of compression or non-compression of the polymer matrix.

Referring to the technological solution shown in previous pages, the use of ACA or ICA involves different solutions for its patterning. Concerning the first, due to its anisotropic conductivity property, it can be patterned (e.g. rolled) over the entire bottom side of the package. When the wafer-to-wafer bonding is performed, the ACA is compressed only in correspondence with the copper bumps on the RF-MEMS signal pads (see Figure 5.14) which is where

the electrical interconnection is needed. On the other hand, the ICA has to be patterned only on the copper bumps (e.g. distributed with a needle or screen printed) otherwise it would cause the shorting of all the electric signals.

In conclusion, ACA/ICA materials require a lower temperature (180 – 200°C) to be cured with respect to the bumps reflow solution and also exhibit good adhesion strength [67].

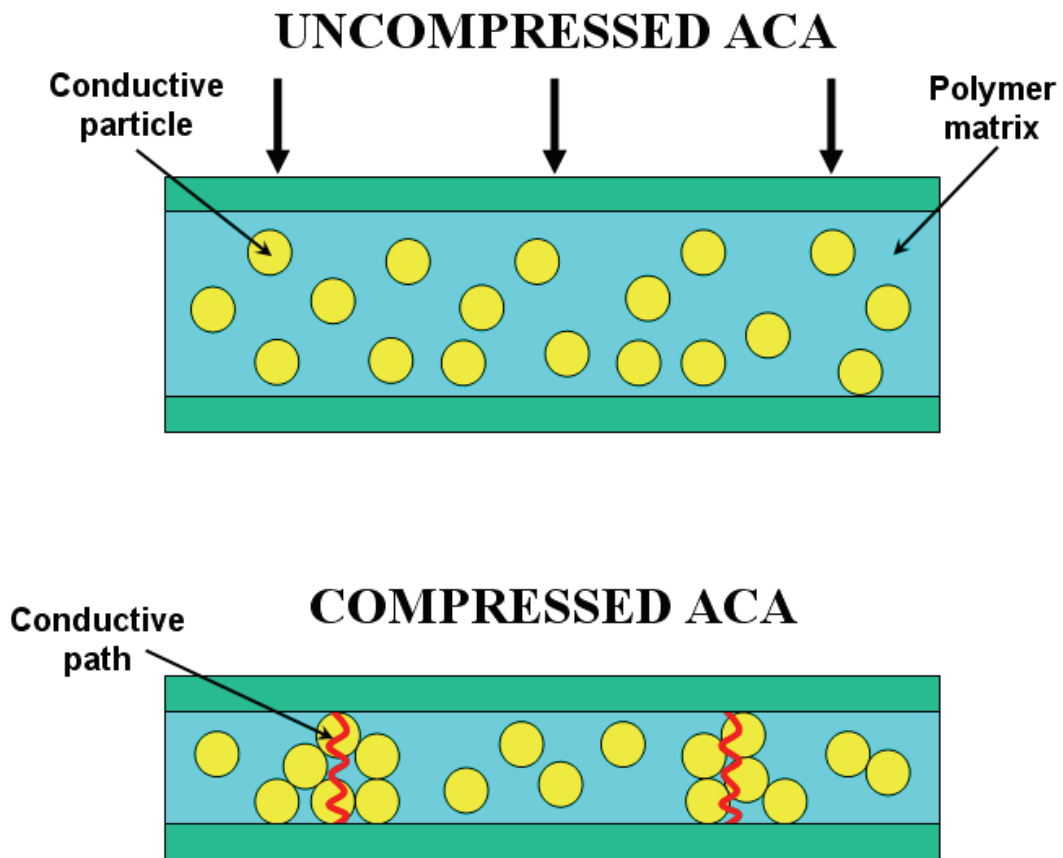


Figure 5.20: When ACA is uncompressed the particles are far from each other and it is electrically insulating (top figure). When ACA is compressed particles get closer and form an electrically conductive path (bottom figure).

### 5.2.4 Encapsulation of RF-MEMS Devices

In the packaging schemes presented thus far the only contact points among the capping-to-device wafers is represented by the bumps onto RF-MEMS signal pads. Of course this is not a complete solution as the vertical gap between the two wafers still remains open and MEMS devices would not be protected at all against external factors like moisture and dust particles. The viable solution we propose in the thesis to solve this issue is to deploy a peripheral ring surrounding the entire RF-MEMS die and, additionally, each single device like the schematic top-view of Figure 5.21 shows.

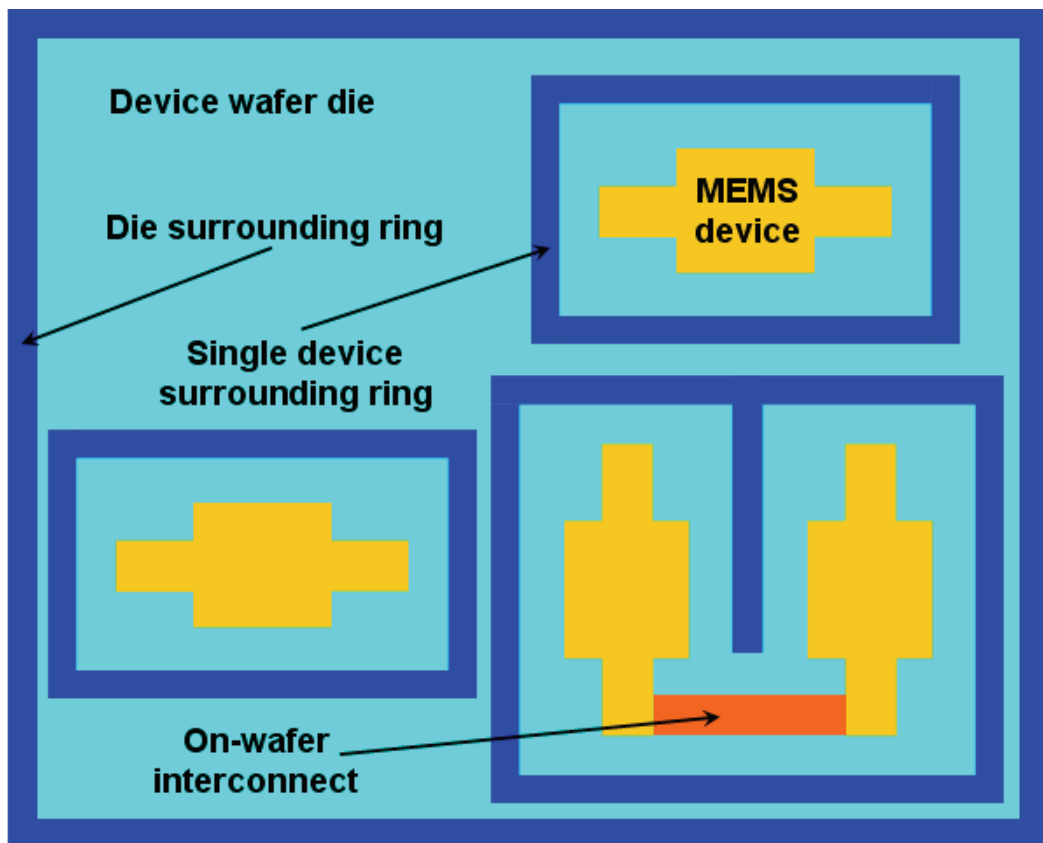


Figure 5.21: Top-view of a die on the RF-MEMS device wafer surrounded by a protective peripheral ring. Additionally, a protective ring can also be patterned around each MEMS device.

Whether more RF-MEMS are electrically connected to each other on the device wafer the protective ring can be patterned in such a way to leave the necessary room for the interconnects. The surrounding ring covers the whole vertical gap between the two wafers ensuring encapsulation of RF-MEMS devices. It can be realized employing different materials like for instance SU-8 [55], BCB [52] or ACA/ICA themselves. All of these solutions ensure the protection of RF-MEMS from direct exposure to harmful factors although, on the other hand, are not able to maintain an hermetic sealing condition (vacuum encapsulation). Nonetheless, if the sealing ring is made of the same alloy used for the solder bumps and if it is reflowed together with them it would be possible to reach a stable hermetic sealing of the packaged cavities [68]. In the applications of interest through this thesis the availability of a vacuum packaging solution is not critical as we will deal mainly with RF-MEMS switches and varactors whose performances are not considerably enhanced when operated in vacuum. However, if the same packaging solution is applied for instance to resonators in MEMS technology, the benefits in terms of RF-performances due to the vacuum condition would be crystal clear [56]. This is the reason why the hermetic packaging solution is mentioned anyway in this work.

### **5.2.5 The Issue of Wafer-to-Wafer Alignment**

The success of the package application to the device substrate is critically dependent on the quality of the wafer-to-wafer alignment reached before the bonding step is performed. If the alignment is coarse it might happen that the vertical vias and bumps are not centered onto the RF-MEMS signal pads. This can lead to a poor quality of the package-to-device wafers electrical interfacing (increased contact resistance) or even, in the most severe cases, to a totally missed interconnection to the RF-MEMS as their pads remain floating. The top-view of Figure 5.22 shows a few possible cases of good, poor and totally missed electrical interconnection. The latter case would compromise the utilization of the capped RF-MEMS. The solution we propose in this thesis to reach a good alignment is rather simple. It is based on direct observation under the microscope of the RF-MEMS device wafer through a window opened in the capping part. This allows to align the two wafers by observing certain structures on the device wafer which have been chosen as alignment marks prior to the window opening. First of all the window is preformed by etching (Bosch DRIE process) a narrow through-wafer peripheral groove. Small tips

(i.e. anchor points) are left non-etched on the four corner to keep the inner Silicon part in-place [69]. Once the wafer is brought out of the DRIE machine the windows are released by ultrasonic cleaning as the anchors break because of the vibrations. A SEM photograph of a cavity after the narrow groove etching is shown in Figure 5.23. The same cavity after the release by ultrasonic cleaning is reported in Figure 5.24.

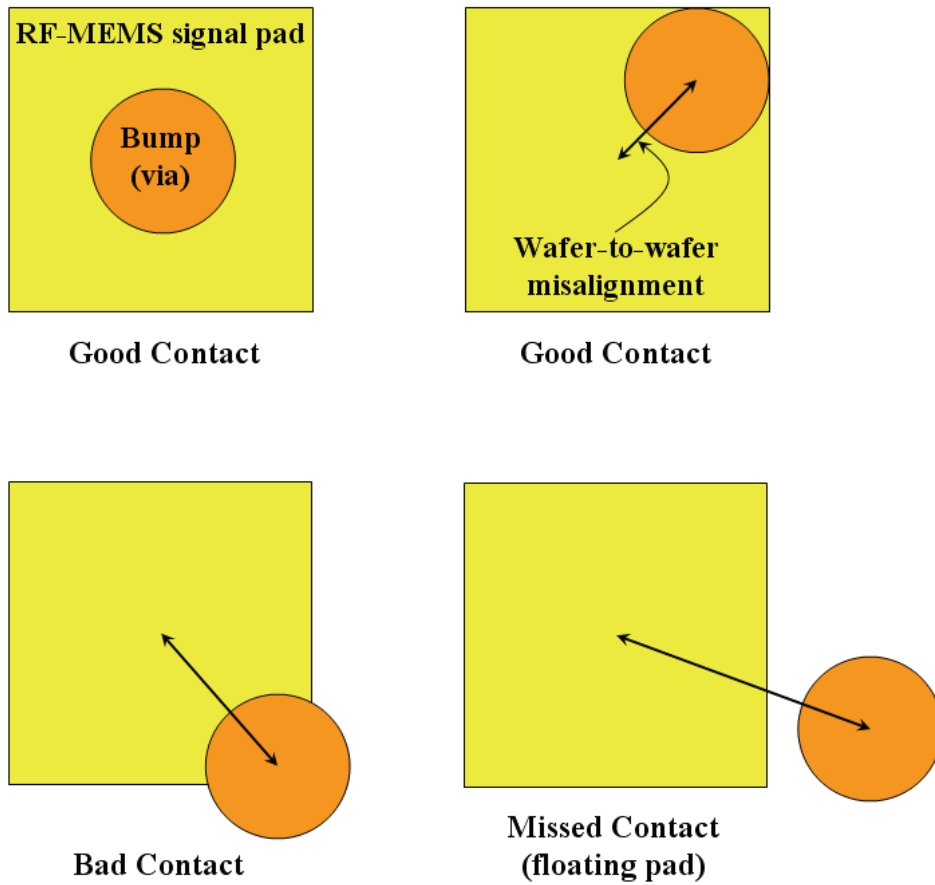


Figure 5.22: Top-view of a package electrical interconnect (via plus bump) superposed to a MEMS signal pad. Depending on the severity of the wafer-to-wafer misalignment the bump-to-pad electrical interconnection can be good (top) or poor as well as totally missing (bottom).

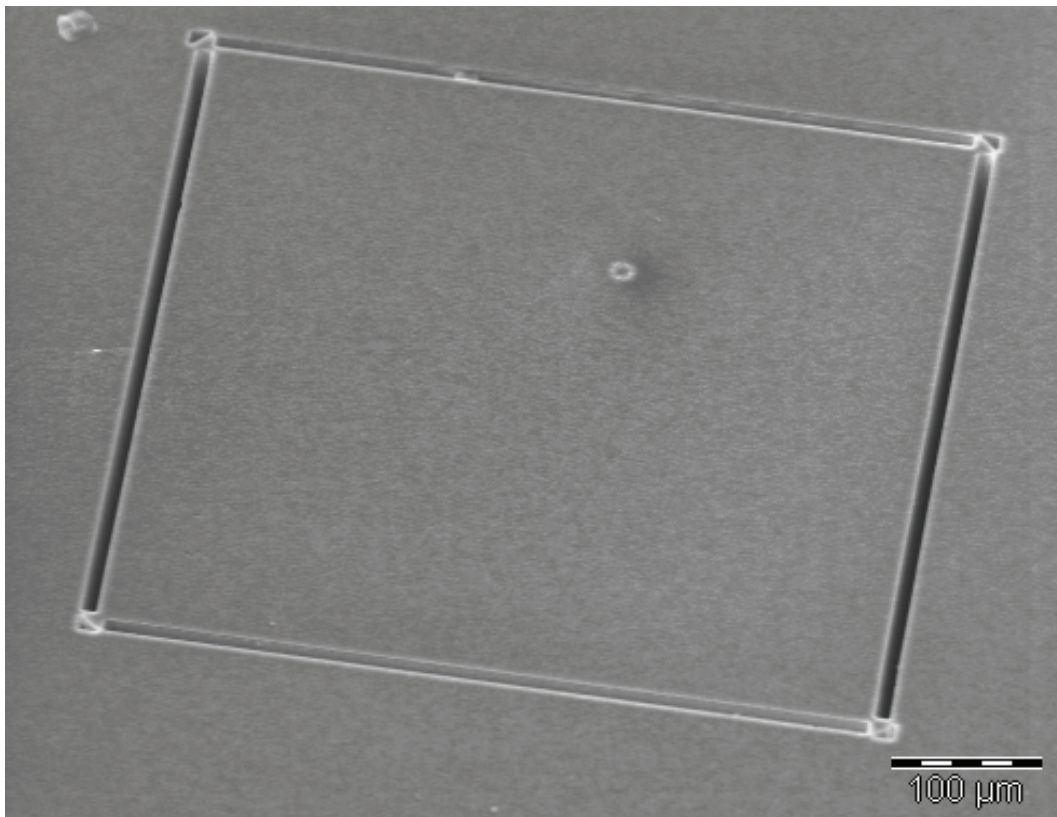


Figure 5.23: SEM photograph of a preformed windows by etching (Bosch DRIE process) of a narrow groove. The four anchors at the corners are visible.

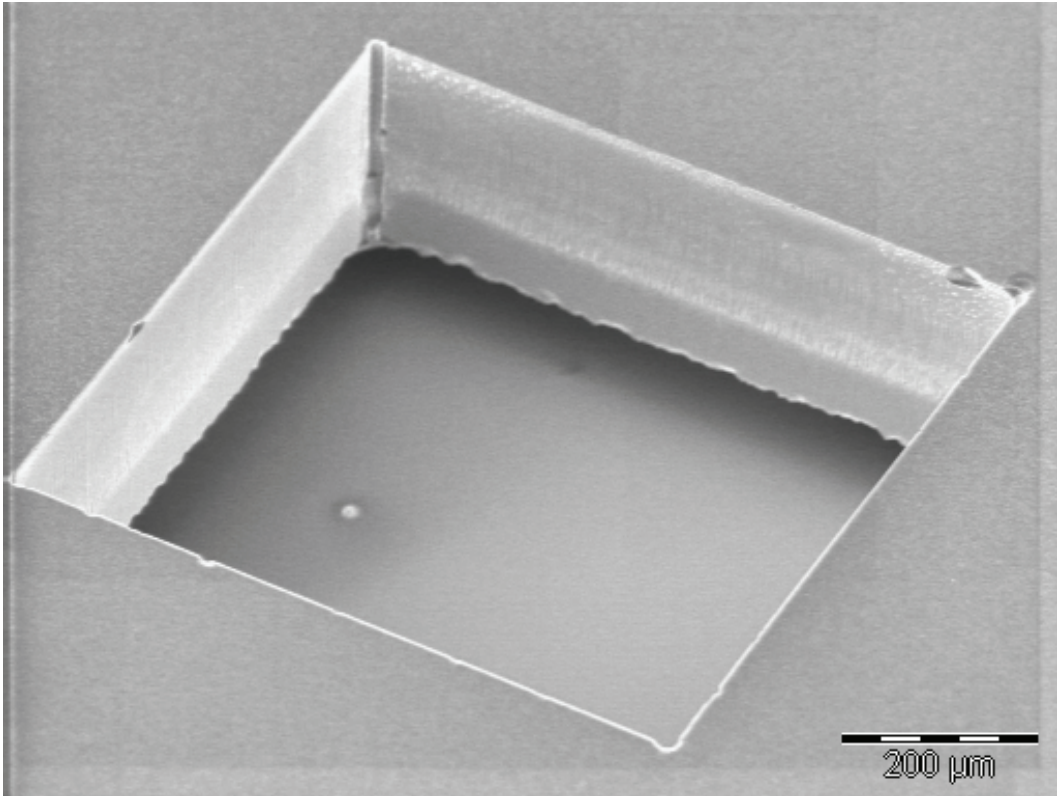


Figure 5.24: SEM photograph of the window after the release by breaking of the anchor points is achieved by ultrasonic cleaning.

## 5.2.6 Hybrid Packaging Solutions for RF-MEMS Devices

The packaging solution proposed in this thesis enables the integration of the capped RF-MEMS devices to the CMOS active circuitry (hybrid packaging). Basically two different approaches are possible in order to exploit the capping part to ease the interfacing of the two parts (RF-MEMS and CMOS). The first one is shown in Figure 5.25 where the CMOS chip is placed upside-down within a through wafer cavity derived in the capping substrate with the same technique shown in the section about the alignment.

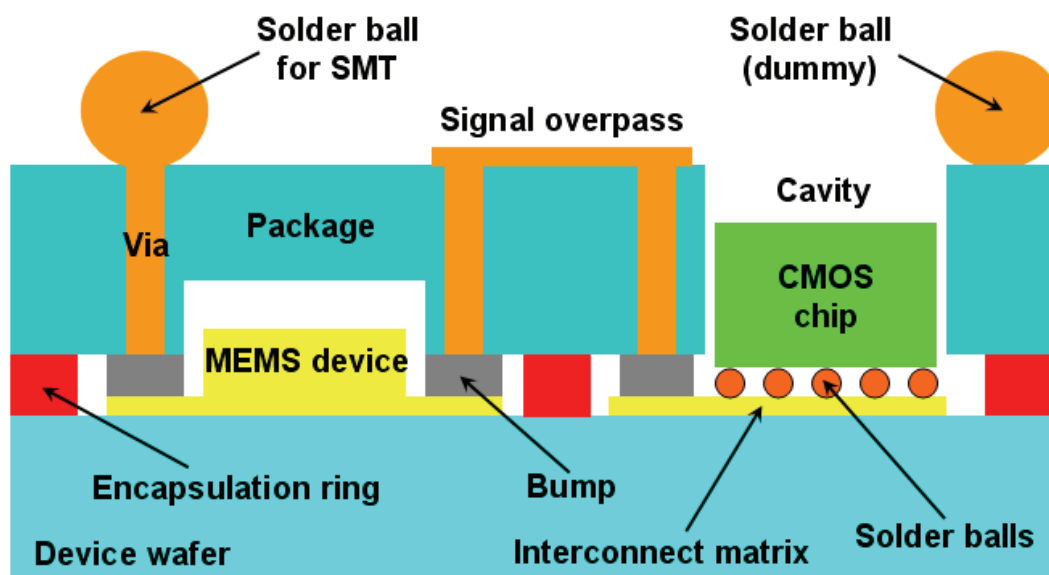


Figure 5.25: Hybrid packaging solution based on the placement of the CMOS chip upside-down in a cavity through the package.

A suitable interconnect matrix must be deployed directly on the device wafer in order to properly contact the CMOS chip signals. This can be patterned at once with the RF-MEMS devices fabrication or can be added later with a metal deposition step (post-processing). The electrical interfacing of the MEMS to the CMOS part is provided by vertical vias and signal overpasses (i.e. CPW's). In this way, the cavities where the RF-MEMS are accommodated are not affected by the opening of the cavity to house the CMOS chip. Hence, whether



a bonding solution which ensures a vacuum sealing is employed, it is possible to keep such an hermetic condition even after the integration with the CMOS part. After solder balls are deposited onto the electrical pads of the hybrid RF-MEMS/CMOS capped die, it is ready to be upside-down mounted on board (see Figure 5.3). In case the electrical signals are unevenly distributed over the capped die surface it is possible to add some dummy solder balls (see Figure 5.25) to enhance the stability and strength of the flip-chip mount on board.

Another possible solution to integrate the RF-MEMS to the CMOS part is shown in Figure 5.26. In this case the CMOS chip is placed upward (and glued) in a shallow etched cavity derived in the package. Electrical interfacing is done by means of wire bonds. In this case it is unnecessary to deploy any a priori interconnect matrix scheme on the device wafer and the CMOS chip can be freely placed anywhere in the package die. The area management could also be improved since it is possible to 3D-stack the CMOS chip on top of RF-MEMS interconnects area by means of waveguides, matching networks, and so on.

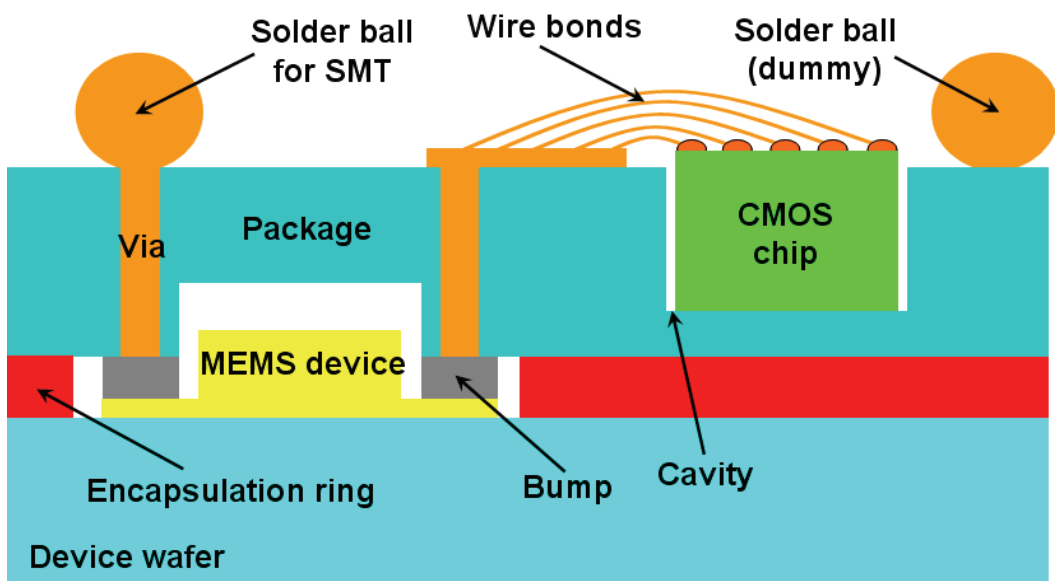


Figure 5.26: Hybrid packaging solution based on the CMOS chip placement in a shallow cavity. Electrical interconnection is ensured by wire bonding.

### 5.3 Fabrication Run of Packaged Test Structures

In order to test the feasibility and viability of the packaging solution discussed thus far a capping substrate to be applied to a wafer of  $50\ \Omega$  coplanar waveguides (CPW's) and shorts has been fabricated at the HiTeC-DIMES Centre. This choice has been done mainly because the influence of the capping substrate is much more straightforward and can easily be interpreted when applied to structures with a very simple frequency response. Indeed, in this preliminary stage of the package process development it would not be useful to focus directly on its influence on the RF-performances of specific MEMS devices. Moreover, there is also a practical reason. In the package process development where several trials are necessary for its optimization, it is preferable to use simple test structures without the need to sacrifice actual RF-MEMS devices, which also represents a low-cost solution.

The  $50\ \Omega$  CPW's and shorts are arranged in a die which is duplicated over the Silicon wafer. The design of these structures as well as of the capping substrate are performed within the Agilent ADS<sup>©</sup> environment [70]. Moreover, the optimization of the CPW's desing to reach the  $50\ \Omega$  matching and a preliminary investigation of the capping influence on the electromagnetic behaviour of such structures are done with the ADS Momentum<sup>©</sup>. Examples of design for a CPW and short including the capping part in ADS<sup>©</sup> are respectively shown in Figure 5.27 and Figure 5.28. The CPW's and shorts are made of evaporated gold onto a Silicon substrate. A photograph of an uncapped gold CPW is shown in Figure 5.29 where it is possible to notice the considerable roughness of the Silicon surface. This first packaging test run is not performed at wafer-to-wafer level. This means that not an entire capping wafer but a single die is bonded to the test device wafer. This is because in this preliminary stage confidence in processing has to be matured and it is easier to perform several trials at chip level instead of at wafer-to-wafer level. The chip-to-wafer bonding is performed by means of ICA (see the section about the bonding techniques) dispensed with a needle onto the capping back side vias. The particular type of utilized ICA is the **CE 3103 WLW** provided by Emerson & Cuming [71].

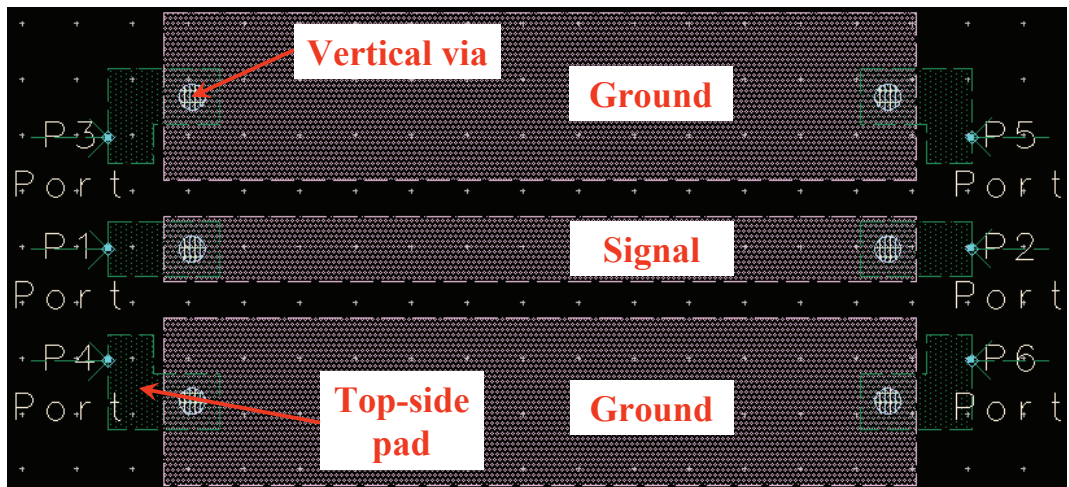


Figure 5.27: Design in Agilent ADS<sup>®</sup> of a 50  $\Omega$  CPW including the package. The two ports for S-parameters simulation are visible.

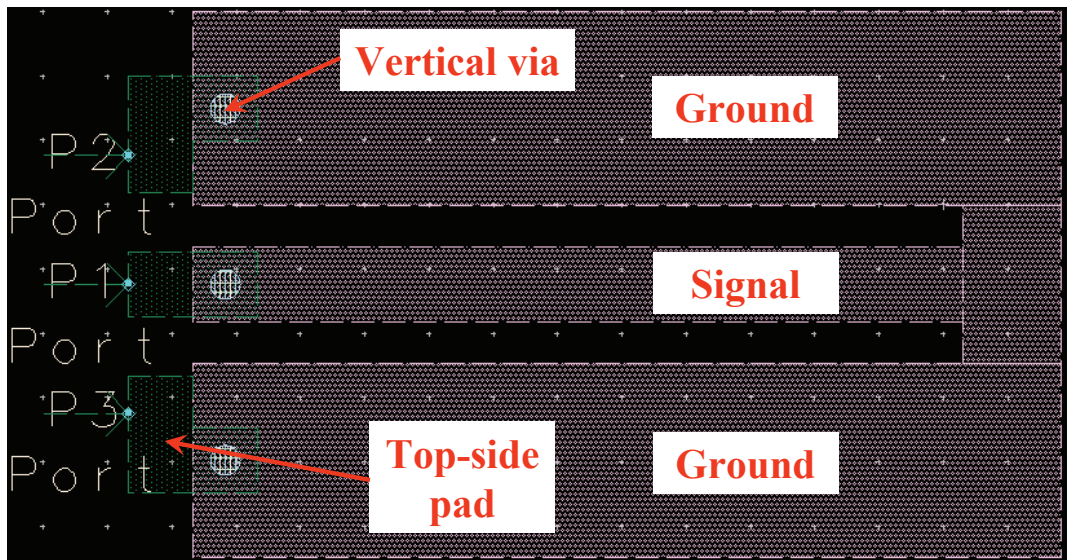


Figure 5.28: Design in Agilent ADS<sup>®</sup> of a short including the package. The port for S-parameters simulation is visible.

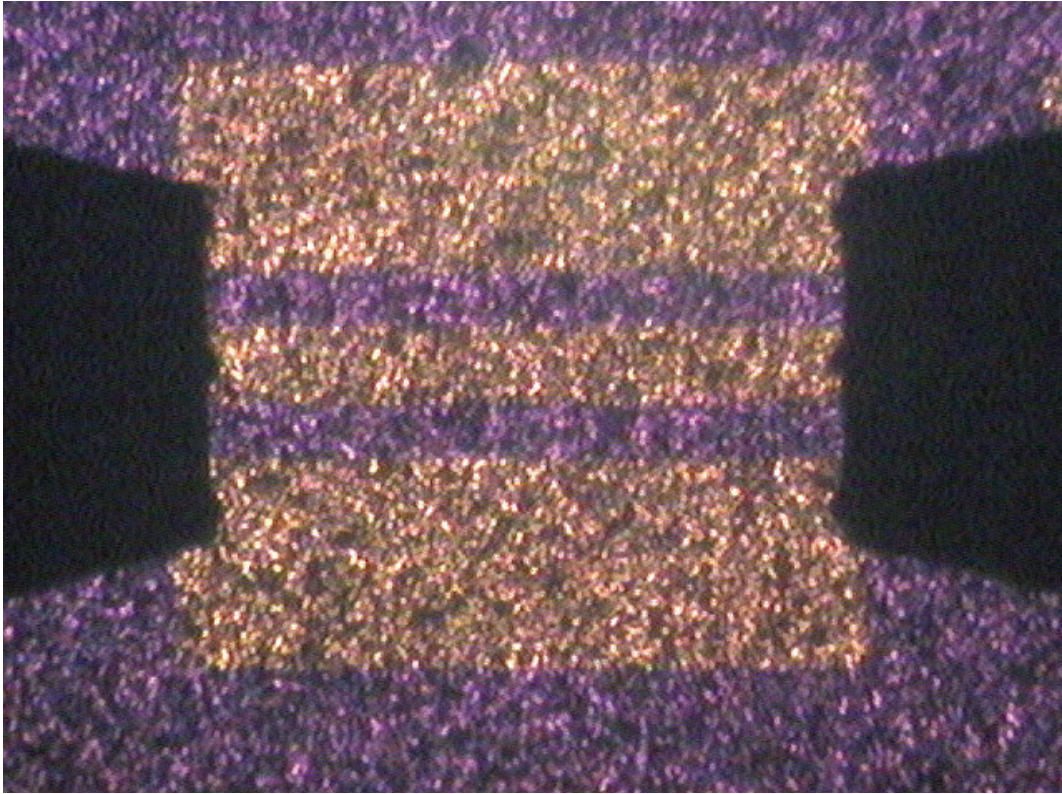


Figure 5.29: Photograph of an uncapped evaporated gold CPW. The Silicon surface roughness is clearly noticeable. The probes for direct measurement are also visible.

In Figure 5.30 a few test structures are shown after de-bonding of the capping chip. The visible black stains are the ICA remains that indicate a very good alignment of the package with the underneath structures. Whereas, Figure 5.31 shows the top-side pads (see Figure 5.10) over the capping chip for some of the packaged test structures.

Experimental data have been collected both for the uncapped and capped test structures mentioned above. The S-parameters (see Chapter 2) for an uncapped transmission line compared to the measurements of the same device after the capping part has been applied are shown in Figure 5.32 (reflection parameter or S11) and Figure 5.33 (transmission parameter or S21). The CPW

length is  $1350\ \mu\text{m}$  while the ground lines and signal line width is  $300\ \mu\text{m}$  and  $116\ \mu\text{m}$  respectively. Finally, the gap between the signal and ground lines is  $65\ \mu\text{m}$  while the evaporated gold layer thickness is around  $500\ \text{nm}$ . Concerning the package, its thickness is around  $280\ \mu\text{m}$ , the top-side pads length is  $200\ \mu\text{m}$  while via diameter is equal to  $50\ \mu\text{m}$ . Bottom recesses are not etched in the package as CPW's and shorts do not require a distance clearance other than the bumps themselves.

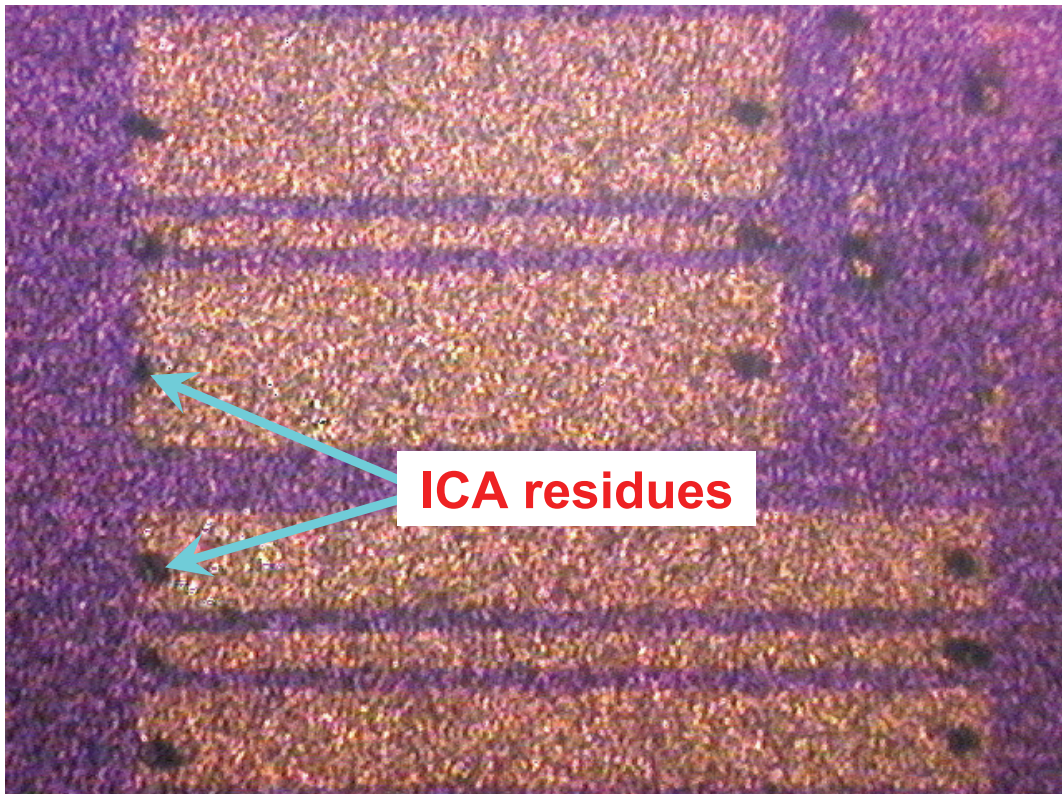


Figure 5.30: Photograph of few test structures after de-bonding of the package. The black stains (ICA residues) indicate a very good chip-to-wafer alignment.

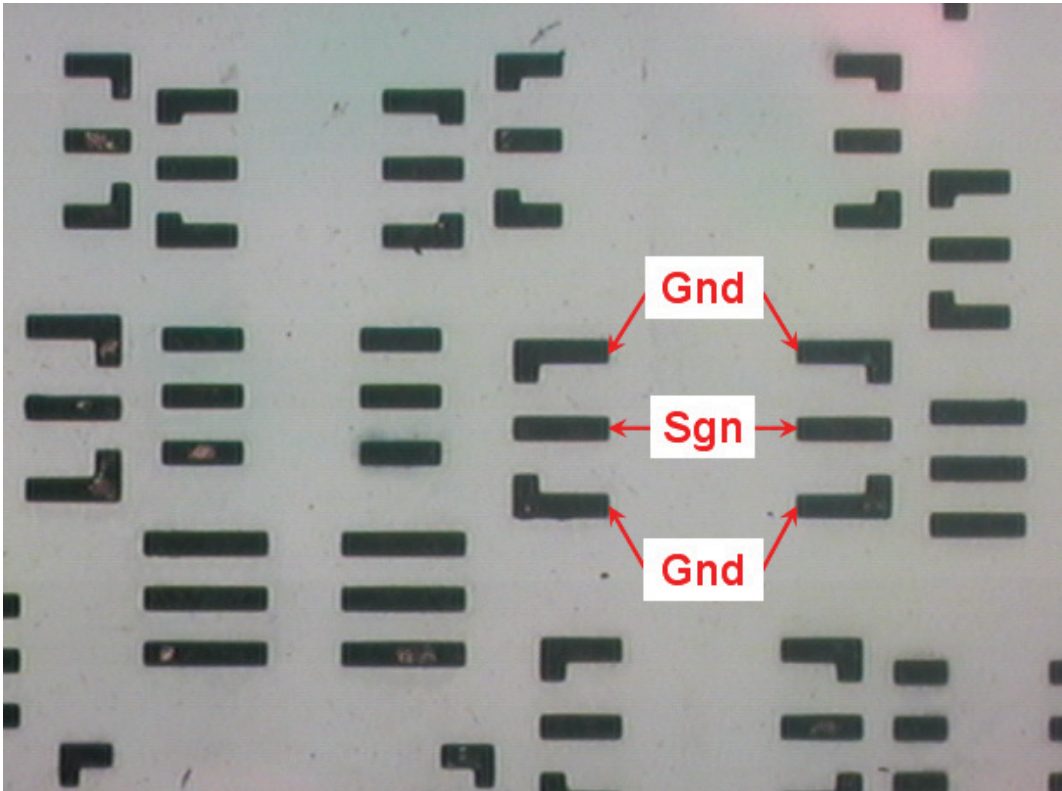


Figure 5.31: Top-side pads (onto the capping chip) for some of the underneath test structures.

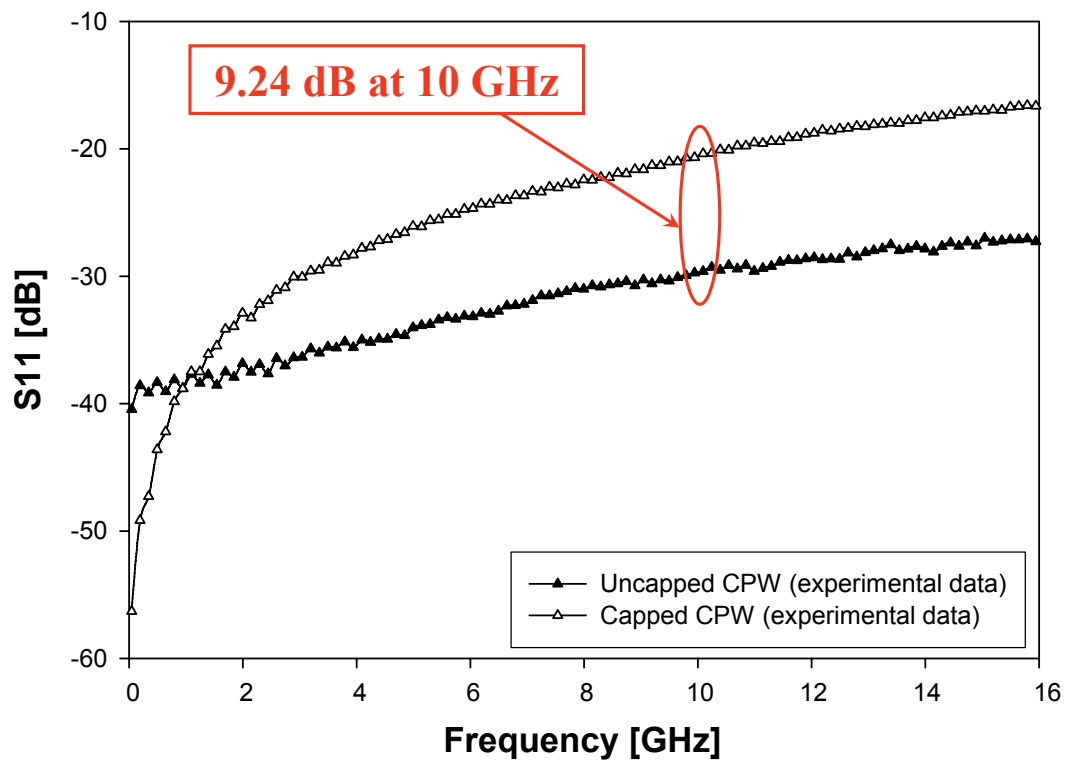


Figure 5.32: Experimental comparison of the S11 parameter for an uncapped and capped CPW.

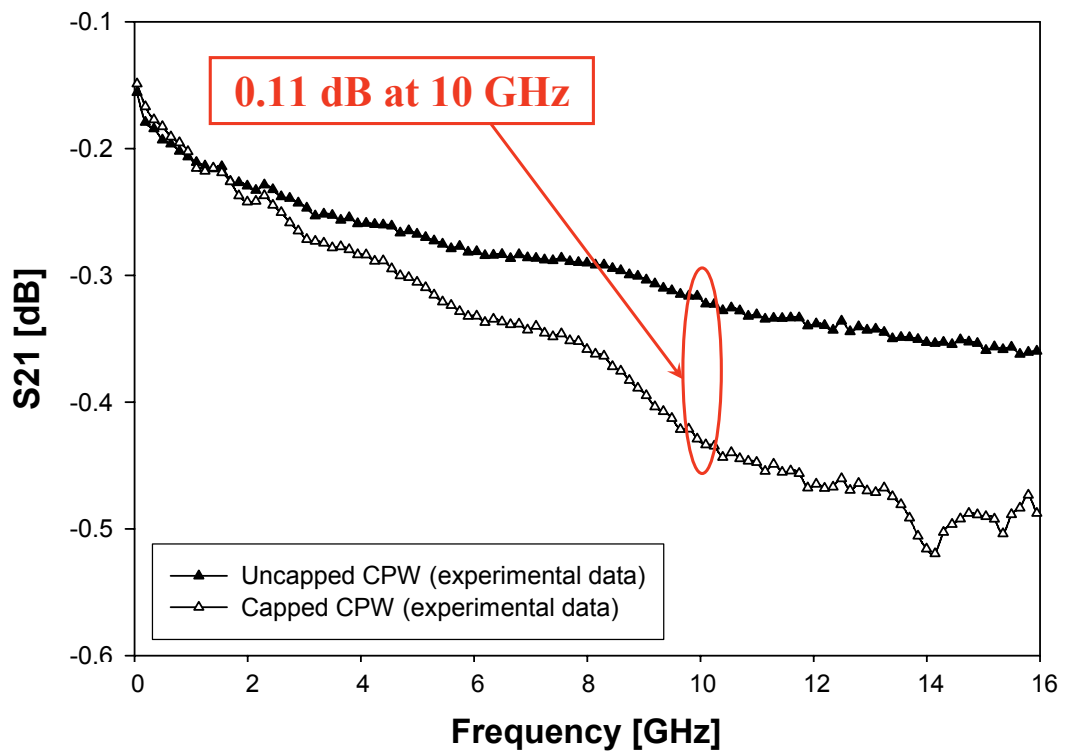


Figure 5.33: Experimental comparison of the S21 parameter for an uncapped and capped CPW.



The just shown S-parameters plots show acceptable offsets introduced by the package. For instance, the reflection parameter increase due to the capping is 9.24 dB at 10 GHz while the transmission parameter decrease is 0.11 dB at the same frequency. This suggests that a not too large influence of the proposed packaging methodology on the RF performances of capped MEMS devices is expectable. The analyzed frequency range is limited to 16 GHz as typically RF application of MEMS we are interested in are in the range of a few GHz. Other comparisons of S-parameters related to an uncapped and capped CPW are shown in Figure 5.34 (reflection parameter) and Figure 5.35 (transmission parameter). In this case the transmission line is 1200  $\mu\text{m}$  long with a signal and ground lines width of 100  $\mu\text{m}$  and 210  $\mu\text{m}$  respectively. The gap is 60  $\mu\text{m}$  while via diameter is 50  $\mu\text{m}$ . Finally, top-side pads length is 200  $\mu\text{m}$ . The S-parameters plots for the uncapped and capped line show an offset of 13.48 dB at 8 GHz for the reflection parameter and of 0.21 dB at 8 GHz for the transmission parameter. Finally, experimental data related to an uncapped and capped short are reported in Figure 5.36 and Figure 5.37. The short length is 1350  $\mu\text{m}$  while the signal and ground lines width is 116  $\mu\text{m}$  and 300  $\mu\text{m}$  respectively. The gap is 65  $\mu\text{m}$  while, concerning the package, via diameter is 50  $\mu\text{m}$  and the top-side pads length is 200  $\mu\text{m}$ . The offset of the reflection parameter referred to the capped short compared with the one of the uncapped one is rather small (see Figure 5.36) and, for instance, it is 0.27 dB at 10 GHz. Looking at the Smith chart for the S11 parameter of Figure 5.37, an extra-rotation is noticeable for the capped short reflection parameter with respect to the uncapped one. Indeed, the electrical signal has to travel through a longer path due to the vertical vias and top-side pads.

In conclusion, experimental data shown above prove the viability of the chosen packaging solution from the technology point of view. Moreover, the data concerning the losses and mismatch introduced by the capping part on the RF performances of test structures are rather promising. This is true especially taking into account that the fabrication process of this run was not optimized in order to reduce the parasitics affecting the electromagnetic behaviour of capped devices. From the point of view of the yield, in all the chip-on-wafer tests a large part of the capped devices were measurable (about 50%) which suggests a rather high level of confidence in technological issues like alignment, bonding and so on.

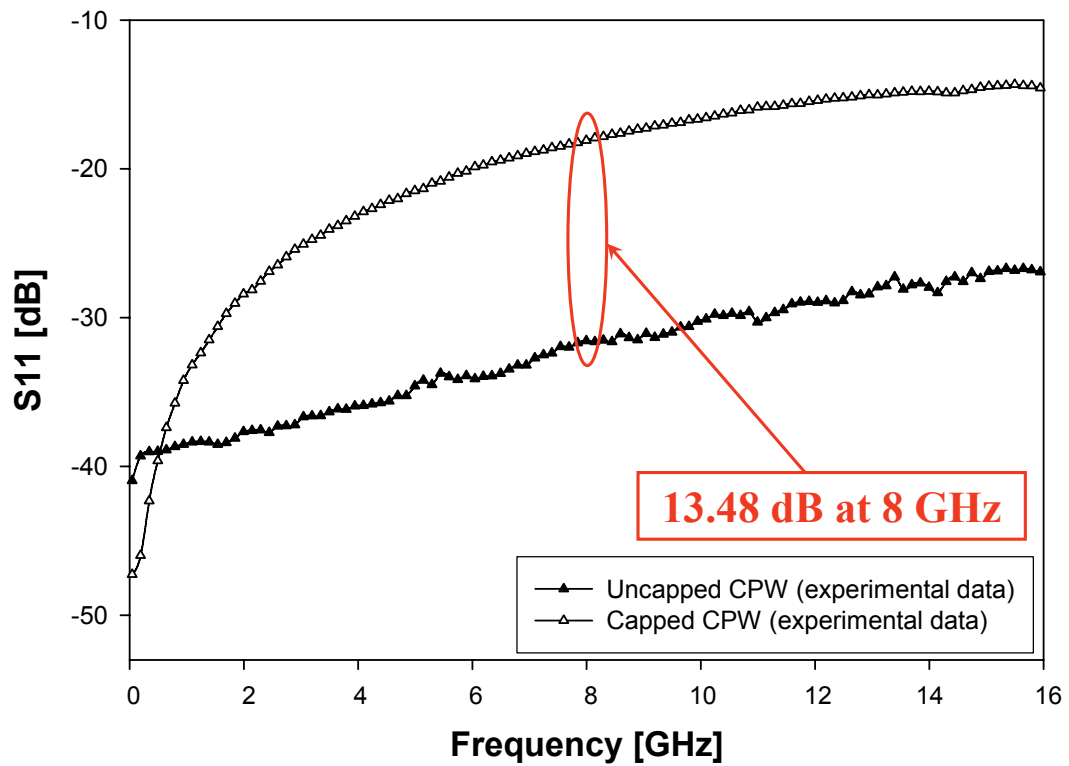


Figure 5.34: Experimental comparison of the S11 parameter for an uncapped and capped CPW.

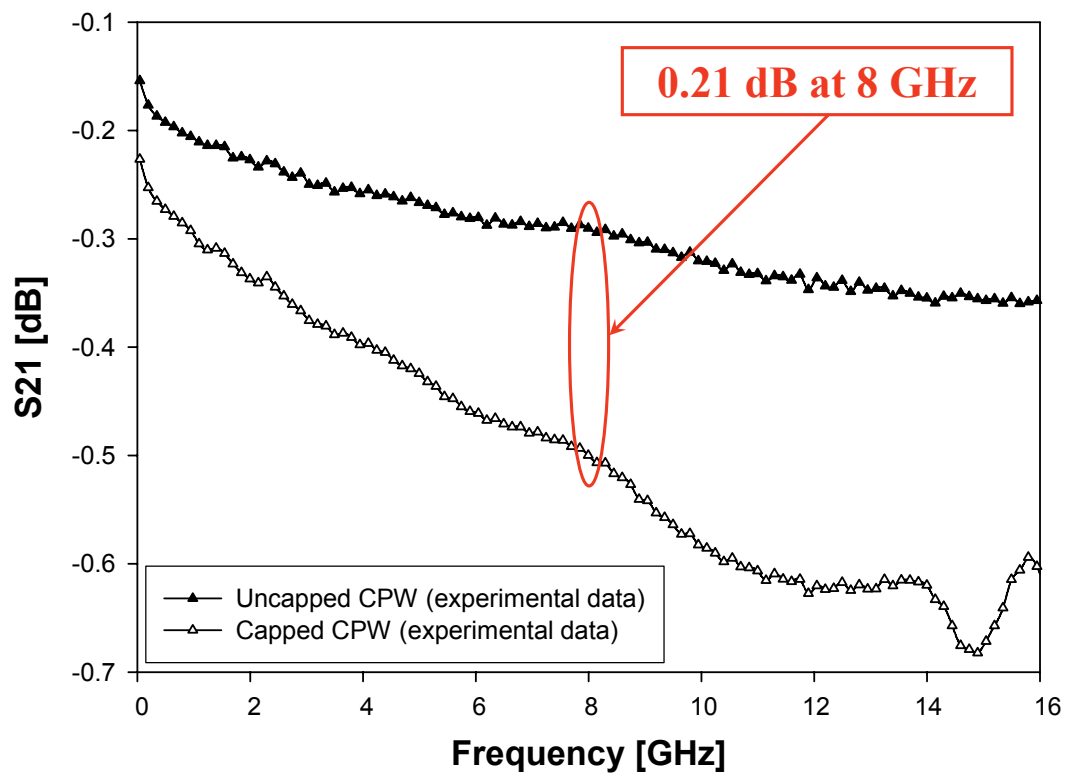


Figure 5.35: Experimental comparison of the S<sub>21</sub> parameter for an uncapped and capped CPW.

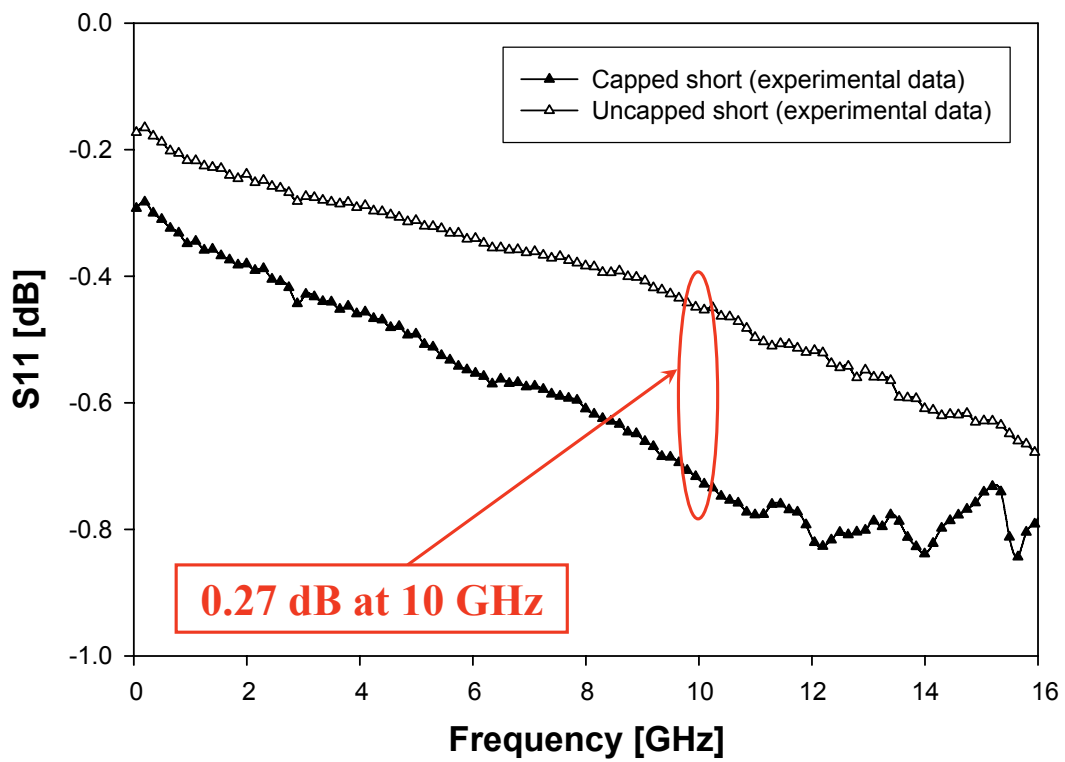


Figure 5.36: Experimental comparison of the S11 parameter for an uncapped and capped short.

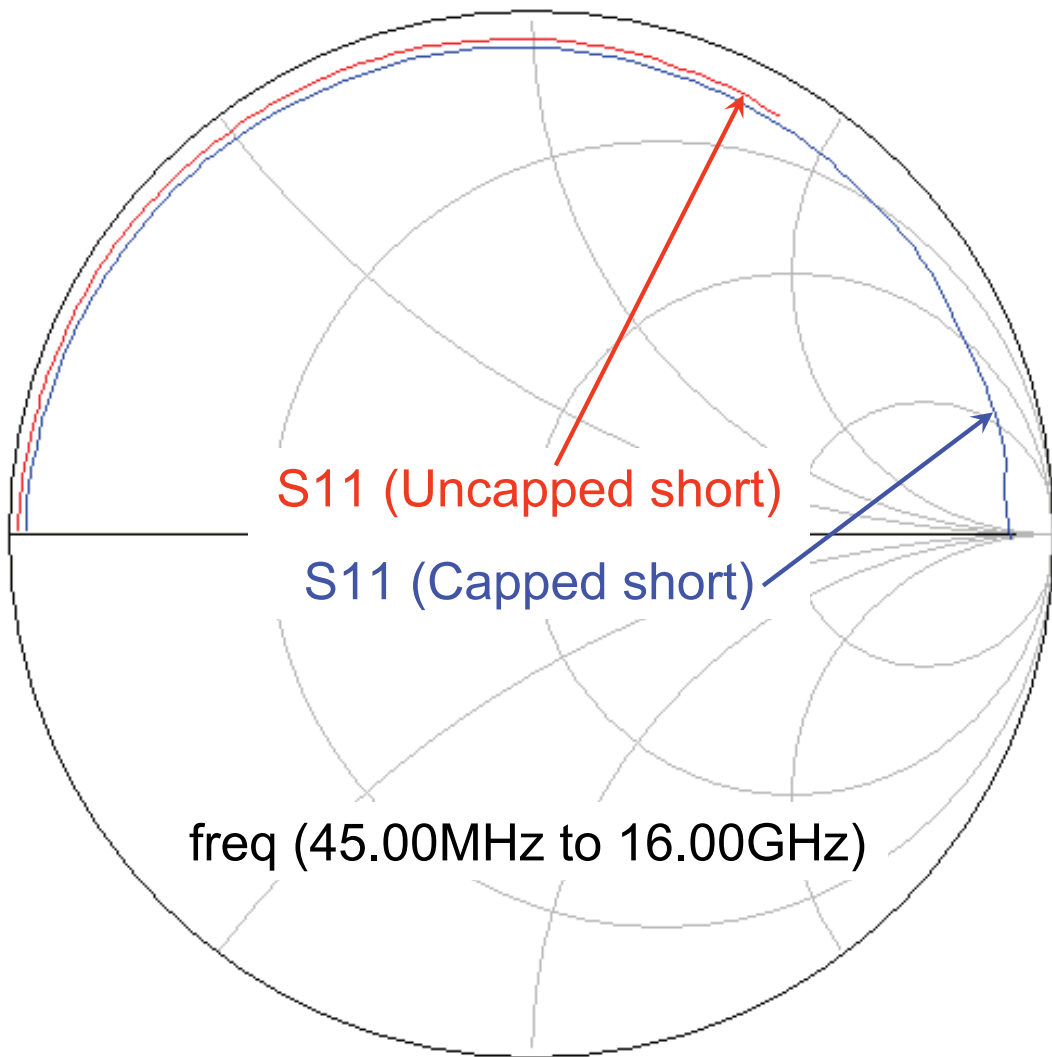


Figure 5.37: Experimental comparison of the S11 parameter Smith chart for an uncapped and capped short.

Also the achieved repeatability of experiments is rather good, as measurement of same capped devices on different dies bonded in different experiments gave very similar results. However, an accurate electromagnetic optimization is the needed further step to enable a successful packaging methodology for RF-MEMS devices and is going to be shown in next section.

## 5.4 Electromagnetic Characterization of the Package

According to what has been shown up to now in this chapter about packaging of RF-MEMS, the capping part has to satisfy several requirements. First of all, its main task is to provide protection to vulnerable devices from factors which represent a jeopardy to them, like moisture, dust particles as well as shocks and vibration. Moreover, it has been also stated that the package substrate must facilitate both the integration with different functional blocks within the packaged chip itself (i.e. hybrid packaging) as well as the final mount by SMT on a board (e.g. flip-chip) to enable the operation of an entire system. Additionally, for certain types of devices for which performances strictly depend on the operation in a vacuum (e.g. MEMS resonators), the establishing of such a condition of hermeticity is even demanded to the package itself. Beside all these consideration, a further requirement is requested to be satisfied from the protective substrate when the latter is conceived for devices operating in the radio-frequency (RF) range [48]. Depending on the type of signals redistribution strategy offered by the packaging solution (e.g. through-vias, underpass, V-grooves etc.) unwanted parasitics (capacitive and inductive couplings) will affect the RF-performances of the capped devices. Additionally, the protective substrate itself interferes with the electromagnetic field of the devices because of its vicinity to them, introducing additional losses and mismatch. Experimental data of the first packaging test run shown above demonstrate that the technological solution presented in this thesis is rather promising concerning its application to RF-MEMS devices. However, a further step will be taken in this sense throughout this section, showing an extensive electromagnetic optimization of the package to reduce as much as possible the losses and mismatch affecting the RF-behaviour of MEMS devices. To do this, a proper simulation tool will be identified first, validating its suitability for this type of problem using the data of previous section as a benchmark.

### 5.4.1 The Ansoft HFSS<sup>TM</sup> Electromagnetic Simulator

The availability of a proper simulation tool is critical in the solution of the electromagnetic problem related to the package as several features related to it can represent a source of unwanted additional parasitics like, for instance, the capacitive coupling between adjacent vias or the resistive losses due to the bumps and the vias themselves. The chosen tool for such a type of analysis is the Ansoft HFSS<sup>TM</sup> Electromagnetic Simulator which is a FEM-based software able to solve 3D electromagnetic problems [73]. It was firstly validated to test its suitability to predict the RF behaviour of MEMS devices by comparing results with experimental data referred to suspended inductors [74]. The latter devices are realized, together with the RF-MEMS switches shown in the next chapter, via a surface micromachining process made available by the ITC-irst Technology Centre in Trento (Italy) [75]. Then, the validation of the Ansoft HFSS<sup>TM</sup> for predicting the electromagnetic behaviour of actual capped structures is performed by comparing experimental data of capped CPW's shown in previous section with the simulated results of the same structures. Comparisons of the S11 and S21 for the capped CPW already shown in Figure 5.32 and Figure 5.33 with the Ansoft HFSS<sup>TM</sup> predictions are reported in Figure 5.38 and Figure 5.39. The offset between the simulated and experimental data is small in the analyzed frequency range both concerning the reflection and transmission parameters. For example, the displacement of the S11 parameter simulated curve is 5.68 dB at 6 GHz while, referring to the S21 parameter it becomes 0.27 dB at 6 GHz. The same type of comparison referred to another capped CPW geometry previously shown in Figure 5.34 and Figure 5.35 is reported in Figure 5.40 and Figure 5.41. In conclusion, this proves the Ansoft HFSS<sup>TM</sup> electromagnetic simulator to be the proper tool to perform the optimization of the package design by exploiting the technology Degrees of Freedom (DoF's) allowed by the fabrication process.

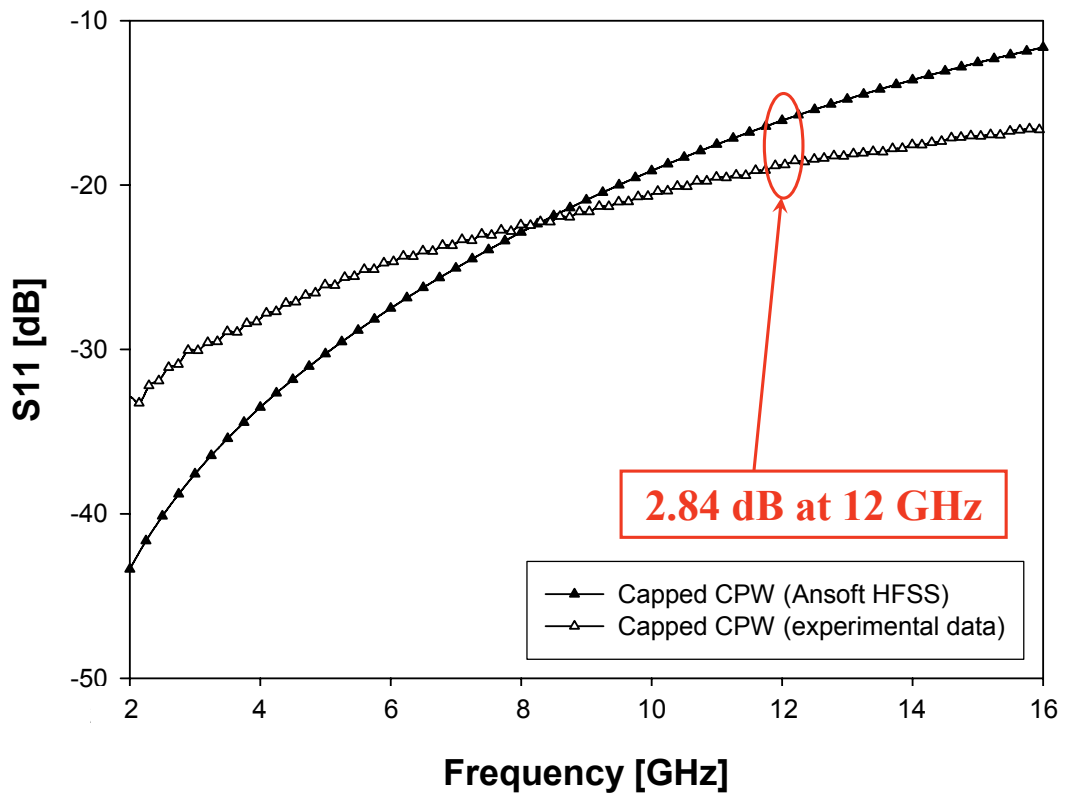


Figure 5.38: Comparison of the experimental S11 parameter already shown in Figure 5.32 with the one predicted by Ansoft HFSS<sup>TM</sup>.



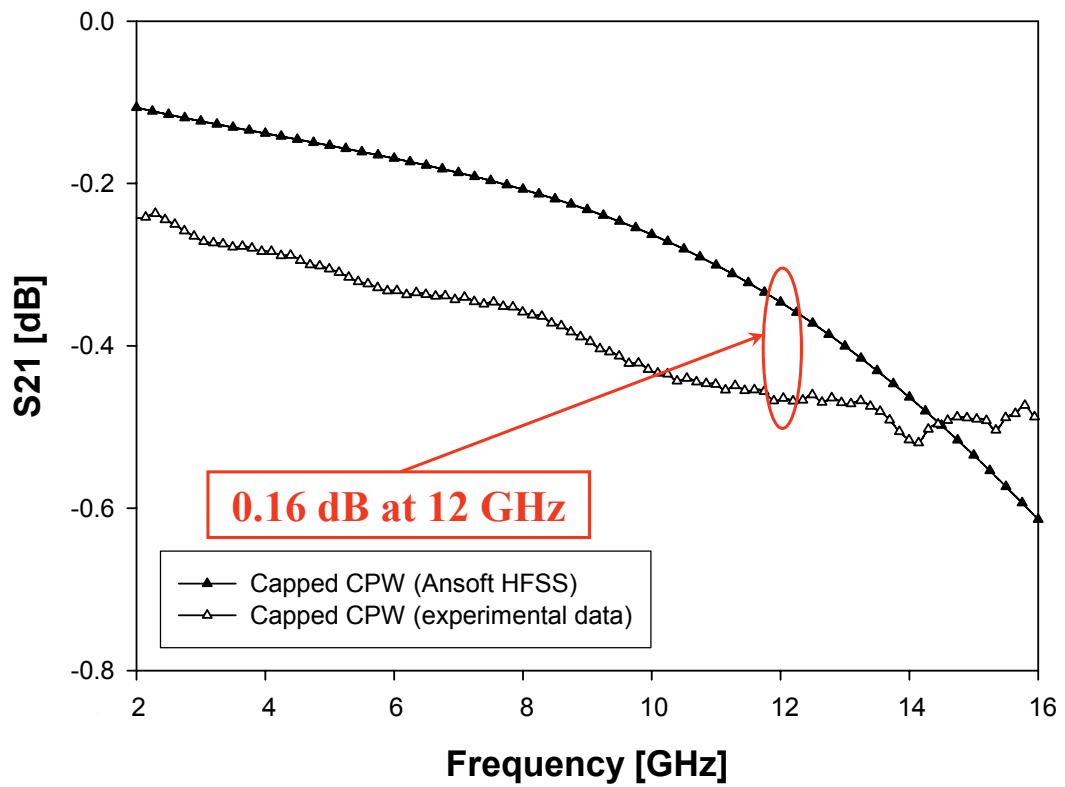


Figure 5.39: Comparison of the experimental S21 parameter already shown in Figure 5.33 with the one predicted by Ansoft HFSS<sup>TM</sup>.

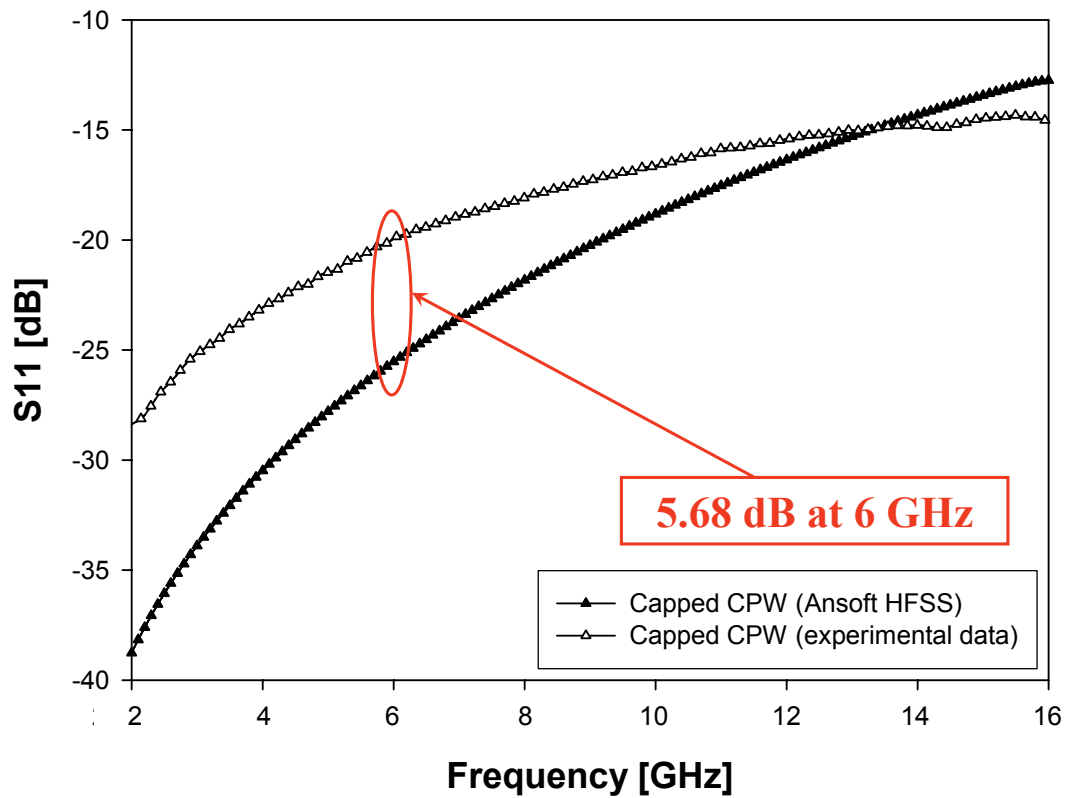


Figure 5.40: Comparison of the experimental S11 parameter already shown in Figure 5.34 with the one predicted by Ansoft HFSS<sup>TM</sup>.

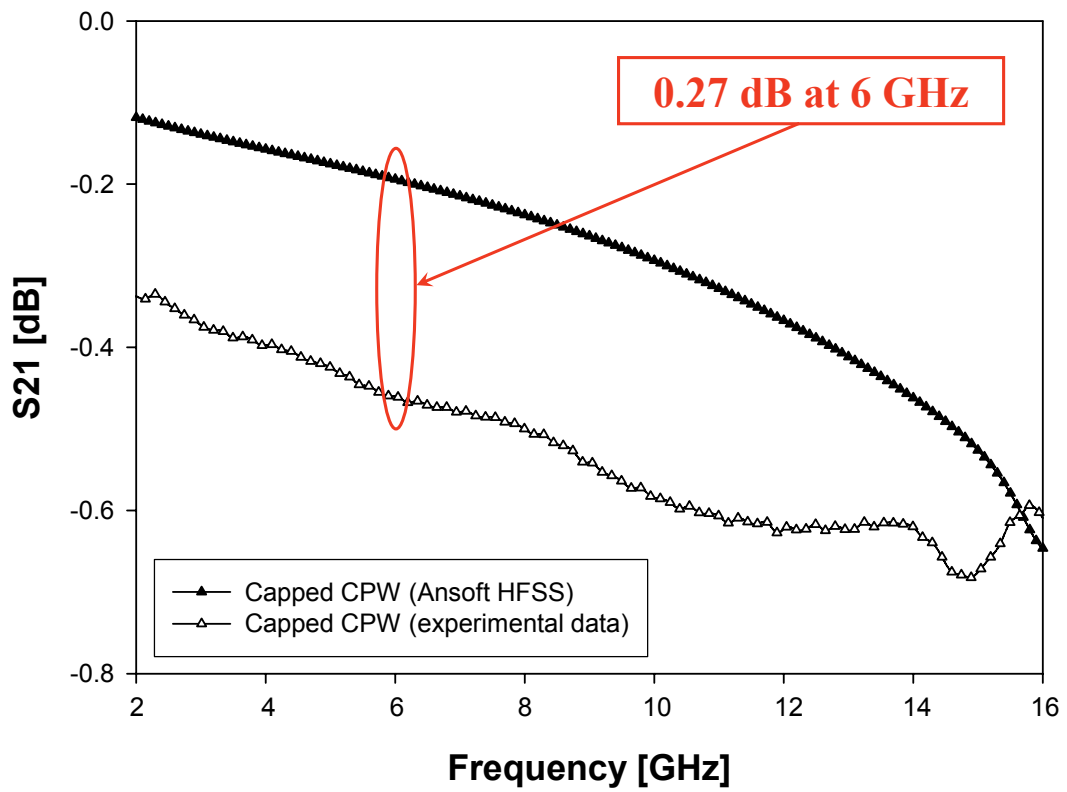


Figure 5.41: Comparison of the experimental S21 parameter already shown in Figure 5.35 with the one predicted by Ansoft HFSS<sup>TM</sup>.

In order to ease the electromagnetic optimization of the capping part a fully parameterized model of a packaged transmission line is implemented within Ansoft HFSS<sup>TM</sup> [74]. Within this all the features of the package fabrication process (i.e. DoF's) which can be modified are included like, for instance, via diameter, capping substrate height, recess depth and so on. These are defined as parameters in such a way that automated (parametric) simulations in which they are modified within ranges defined by the user can be launched. The observation of the results allows to recognize the influence of each variation on the reflection and transmission parameters for each technology DoF leading to the definition of guidelines to be followed to reach the optimum design from the point of view of the electromagnetic losses and mismatch reduction. The schematic view of a capped CPW in Ansoft HFSS<sup>TM</sup> is shown in Figure 5.42.

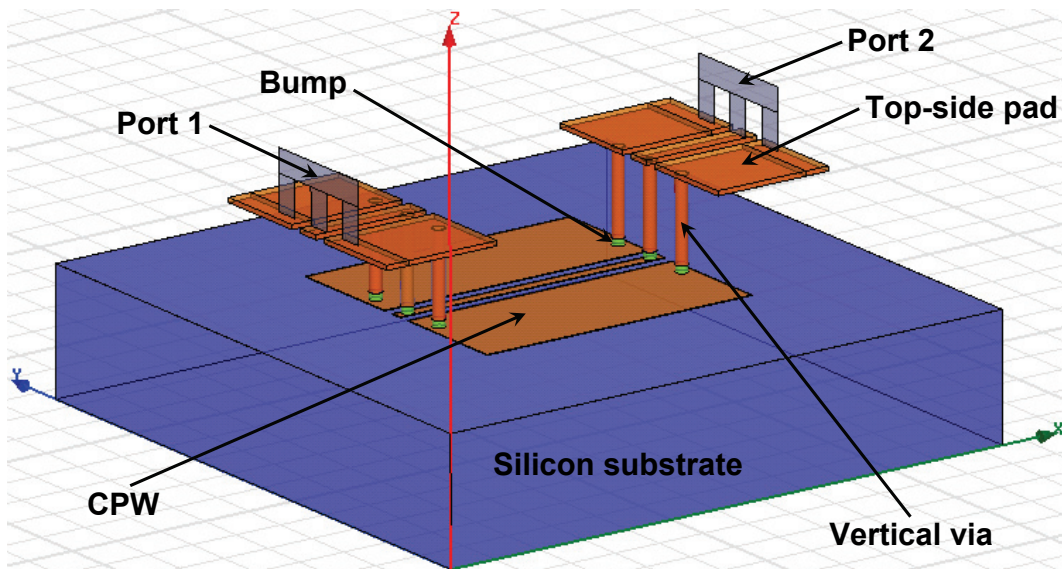


Figure 5.42: Schematic view in Ansoft HFSS<sup>TM</sup> of a capped CPW. The capping substrate was made invisible to get a plain view of the underneath CPW as well as of the vertical through-vias.

An example of two DoF's optimization within Ansoft HFSS<sup>TM</sup> by using the just discussed parameterized model is shown in Figure 5.43 and Figure 5.44.

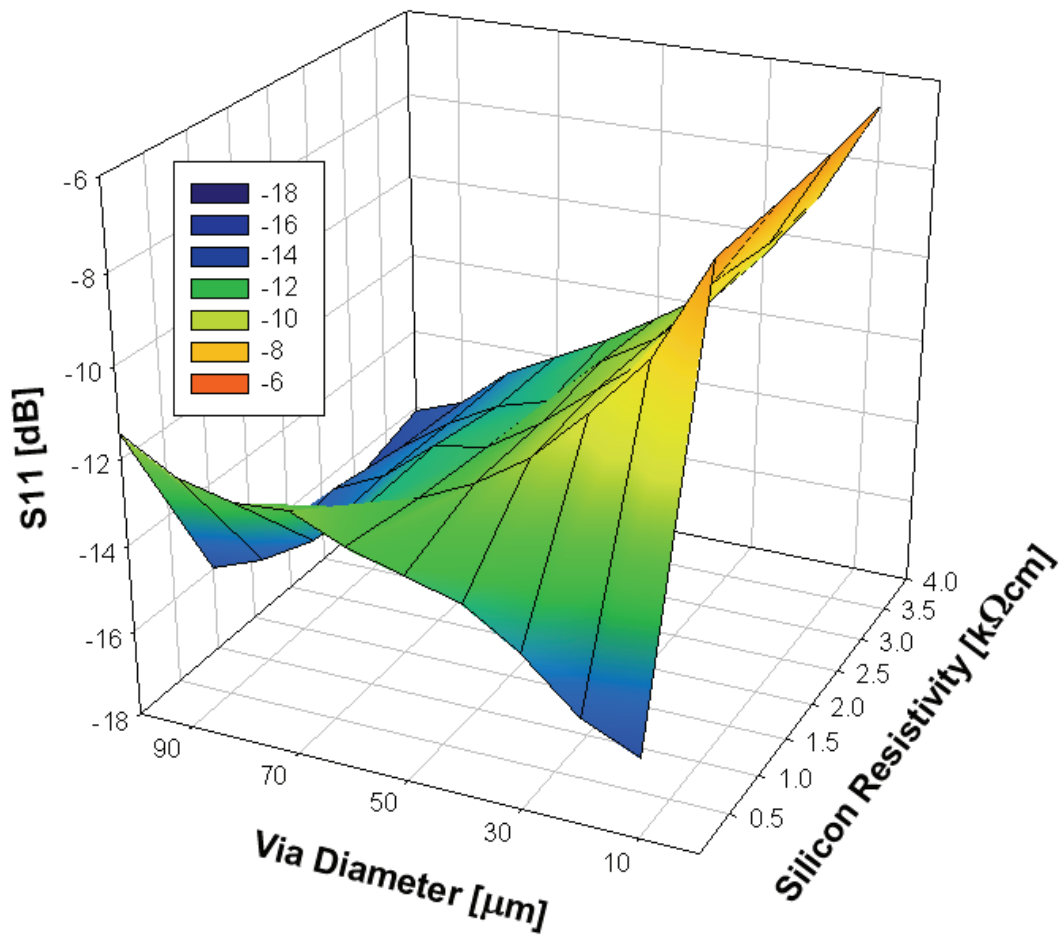


Figure 5.43: Reflection parameter ( $S_{11}$ ) for the two DoF's optimization performed at 15 GHz with the parameterized model in Ansoft HFSS<sup>TM</sup>.

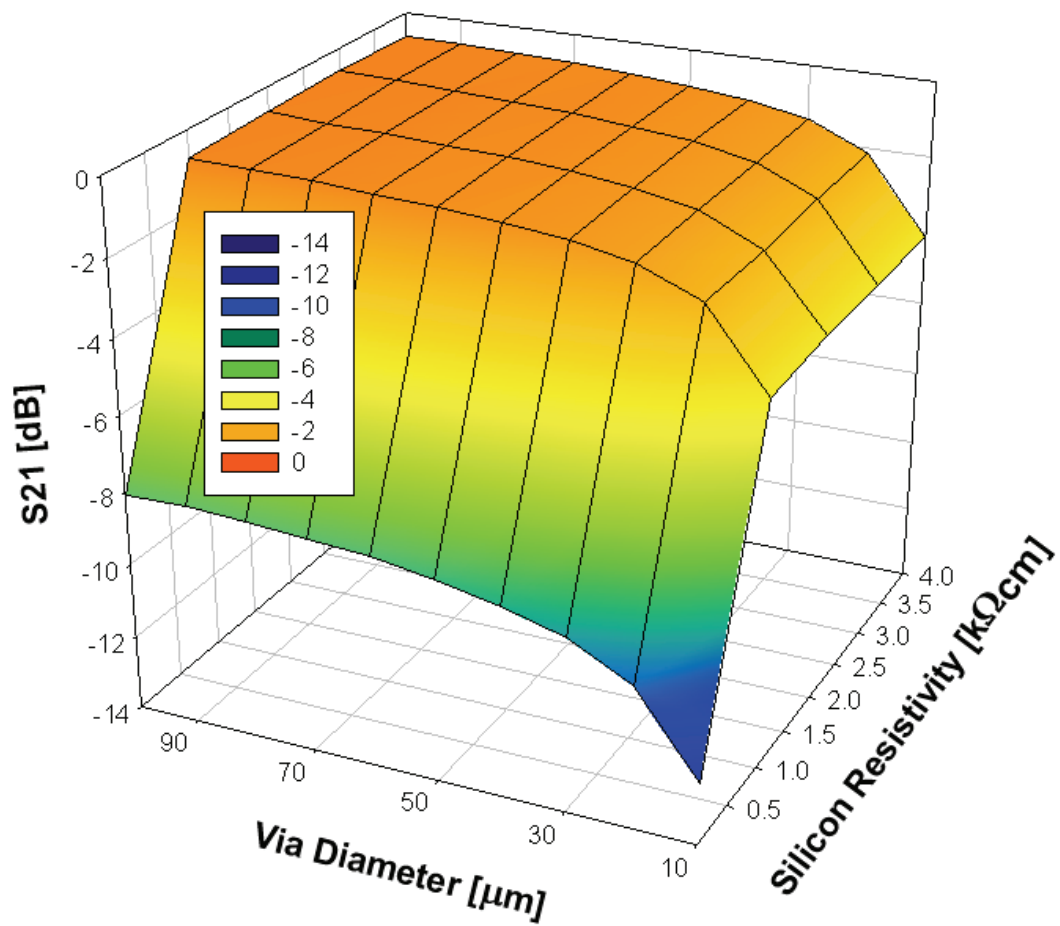


Figure 5.44: Transmission parameter ( $S_{21}$ ) for the two DoF's optimization performed at 15 GHz with the parameterized model in Ansoft HFSS<sup>TM</sup>.

The transmission line is  $2000\ \mu\text{m}$  long. The signal and ground lines width is  $150\ \mu\text{m}$  and  $900\ \mu\text{m}$  respectively while the gap is  $30\ \mu\text{m}$ . The capping part height is  $350\ \mu\text{m}$  and the frequency of this analysis is set at  $15\ \text{GHz}$ . The two technology DoF's taken into account are the via diameter and the resistivity of the Silicon substrate employed for the capping part fabrication. Both these DoF's are reported on the  $xy$  plane of previous 3D plot, while on the vertical abscissa the reflection and transmission parameters are reported. Via diameter is ranged between  $10\ \mu\text{m}$  and  $100\ \mu\text{m}$  which is compatible with the proposed process. Concerning the second DoF, wafers with various resistivities are on stock at the HiTeC-DIMES Centre. It is possible to use e.g. Low Resistivity Silicon (LRS) wafer, whose resistivity is about  $15\ \Omega\text{cm}$ , or four High Resistivity Silicon (HRS) wafers with resistivity of  $1\ \text{K}\Omega\text{cm}$ ,  $2\ \text{K}\Omega\text{cm}$ ,  $3\ \text{K}\Omega\text{cm}$  and  $4\ \text{K}\Omega\text{cm}$ . The 3D plot of Figure 5.43 shows that lower values of the reflection parameter (S11) are achieved for the smaller values of via diameter with the LRS ( $15\ \Omega\text{cm}$ ). For instance, the S11 parameter is  $-16.1\ \text{dB}$  and  $-13.6\ \text{dB}$  at  $15\ \text{GHz}$  for the via diameter value of  $10\ \mu\text{m}$  and  $40\ \mu\text{m}$  respectively. This somehow unexpected result is in fact a false optimum as will be shown from the analysis of the S21 parameter. More appropriately, low values for the S11 parameter are also observable when the chosen via diameter is large (over  $60\ \mu\text{m}$ ) and an high resistivity Silicon substrate is employed ( $1 - 4\ \text{K}\Omega\text{cm}$ ). Indeed, for the  $2\ \text{K}\Omega\text{cm}$  substrate, the reflection parameter ranges between  $-13.4\ \text{dB}$  and  $-16.5\ \text{dB}$  at  $15\ \text{GHz}$  for the via diameter increase from  $60\ \mu\text{m}$  up to  $100\ \mu\text{m}$ . The same analysis is shown for the transmission parameter S21 in the 3D plot of Figure 5.44. Here we verify that the poorest values are obtained for narrow vias etched in a LRS substrate. In general, the  $15\ \Omega\text{cm}$  Silicon must be avoided since when it is used the S21 parameter ranges between  $-12.34\ \text{dB}$  and  $-8.10\ \text{dB}$  at  $15\ \text{GHz}$  for via diameter from  $10\ \mu\text{m}$  to  $100\ \mu\text{m}$  respectively. This complies with the presence of substrate losses due to eddy currents surrounding the vias. Differently, high values of the transmission parameter are achieved for HRS substrate ( $1 - 4\ \text{K}\Omega\text{cm}$ ) in combination with large vias (above  $60\ \mu\text{m}$ ). For instance, it falls into the interval from  $-1\ \text{dB}$  to  $-0.64\ \text{dB}$  at  $15\ \text{GHz}$  for via diameter ranging between  $50\ \mu\text{m}$  and  $100\ \mu\text{m}$ , when a  $2\ \text{K}\Omega\text{cm}$  Silicon substrate is employed. Eventually, optimization of both reflection and transmission parameters within the Ansoft HFSS<sup>TM</sup> shows that the best choice is represented by vias with a diameter of at least  $60\ \mu\text{m}$ . Concerning the type of substrate, while the use of LRS is not an option, the choice of the proper high resistivity substrate brings-up a possible trade-off between the performances and the

costs. In this respect, since the benefits achieved in terms of S-parameters with very high ohmic substrates (3 – 4 KΩcm) are not that large with respect to the 1 KΩcm and 2 KΩcm Silicon wafers, a best choice would probably fall between one of the latter two, being the use of the 2 KΩcm the most reasonable choice.

Running extensive simulations including all the technology DoF's, the ones that exhibit larger influence on the RF behaviour of various capped CPW geometries are identified. These are listed in Figure 5.45 together with the trend of each of them on the additional losses and mismatch introduced by the capping part as a consequence of their increase. For instance, increases of the recess depth as well as of via diameter lead to a reduction of parasitics associated to the package while widening of capping part height leads to an undesired increase of losses and mismatch. This allows to define appropriate ranges within which the package DoF's values should fall to ensure small parasitics affecting the electromagnetic behaviour of capped RF-MEMS devices. Of course, in defining these guidelines for the optimum design of the capping part, issues related to the technology are also accounted for.

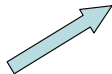

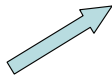

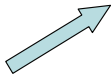

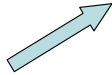

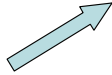

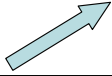

Capping silicon substrate resistivity		Losses & Mismatch	
Capping silicon substrate height		Losses & Mismatch	
Recess depth		Losses & Mismatch	
Via diameter		Losses & Mismatch	
Ground-Signal-Ground vias lateral distance		Losses & Mismatch	
Bumps height		Losses & Mismatch	

Figure 5.45: Summary of the most important technology DoF's in package fabrication concerning the influence on RF performance of MEMS.



For example, the package thinning leads to better RF performance but a trade-off raises with the mechanical strength of the cap itself that lowers with its height. Accounting for this issue, the optimum package height is identified to fall between  $250\ \mu\text{m}$  and  $300\ \mu\text{m}$ . Concerning the substrate resistivity, the choice satisfying the trade-off involving the parasitics reduction and the cost is the  $2\ \text{K}\Omega\text{cm}$  HRS. Moreover, recess height should be large but not too much according to the mechanical strength loss of the cap. When a  $250 - 300\ \mu\text{m}$  thick package is employed, reasonable recess depth should be around  $100\ \mu\text{m}$ . Finally, vias diameter should be as large as possible (not smaller than  $60 - 70\ \mu\text{m}$ ) to reduce their resistance and the horizontal spacing between signal and ground vias has to be large also (more than  $250\ \mu\text{m}$ ) to reduce capacitive couplings. Bumps height must be large (not smaller than  $20 - 40\ \mu\text{m}$ ) in order to keep the largest gap possible between the device and capping wafers. Finally, non-critical DoF's concerning the package-related parasitics are also identified, like the oxide layer thickness on vias sidewalls, which can then be chosen in the process without particular issues. All these considerations are based on the Ansoft HFSS<sup>TM</sup> results of parametric simulations run over the frequency range from 2 GHz to 16 GHz. This is because the mesh of the structure in Ansoft HFSS<sup>TM</sup> was calculated at 16 GHz and consequently it is not appropriate to simulate the low frequency range (below about 2 GHz).

Additionally, the Ansoft HFSS<sup>TM</sup> is exploited to perform a preliminary study on the influence that uncompressed ACA (see section about wafer-to-wafer bonding techniques) can exhibit on RF performances of MEMS devices. This is the topic of next section.

## 5.5 Uncompressed ACA Influence on RF Performance of Capped MEMS Devices

As previously discussed in the section about wafer-to-wafer bonding techniques, one option is the use of Anisotropic Conductive Adhesives (ACA's). The characteristic of such a type of material is to behave as an electrically non-conductive material when is not compressed. However, isolated conductive particles are anyhow distributed within it and this might represent a source of additional unwanted capacitive couplings at high frequency. To this purpose, the Ansoft HFSS<sup>TM</sup> electromagnetic simulator is exploited to carry out a preliminary study to assess whether the presence of conductive particles can affect the RF behaviour of capped MEMS structures.

Very simple test structures are chosen for this analysis, i.e.  $50\ \Omega$  CPW's and opens. These are simulated in Ansoft HFSS<sup>TM</sup> introducing a layer of insulating material with a certain number of conductive spheres (made of Gold) distributed within it. Concerning the percentage of conductive material with respect to the ECA volume it has been assumed to be in the range of 5–10% [60]. Results of simulations for structures including the ACA layer are compared with the simulations of the same structures without it. Typical cases that can occur during the wafer-to-wafer bonding concerning the placement of the uncompressed ACA layer are taken into account.

The first analyzed structure is an open [76]. Its Ansoft HFSS<sup>TM</sup> 3D view with an uncompressed ACA layer in between the two ports is shown in Figure 5.46. Simulations in Ansoft HFSS<sup>TM</sup> are performed from 2 GHz up to 20 GHz. Comparisons of S-parameters plots for the structure of Figure 5.46 with the ones for the same structure without uncompressed ACA layer are reported in Figure 5.47 (reflection parameter) and Figure 5.48 (transmission parameter). It is observable that both the S11 and S21 parameter curves for the open with ACA layer are very close to the ones for the open without uncompressed ACA layer between the two ports. Consequently, not a rather small influence due to the presence of uncompressed ACA layer is expectable when it is placed, for instance, between adjacent RF?MEMS devices.

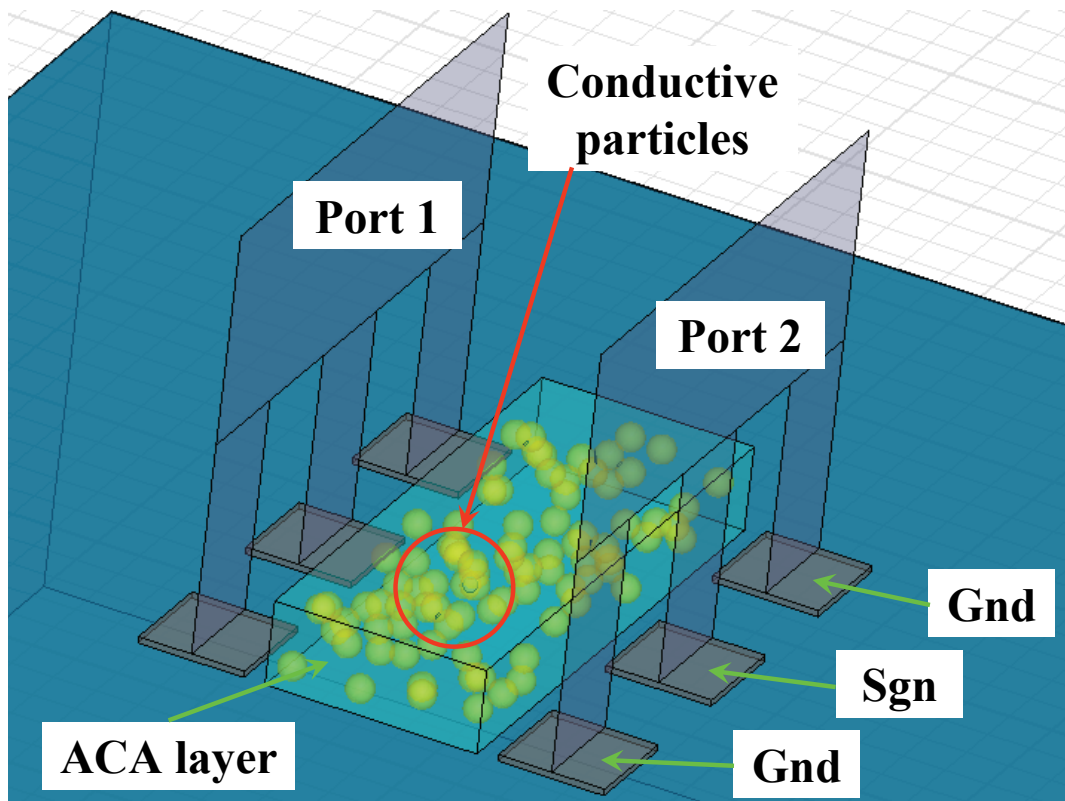


Figure 5.46: Ansoft HFSS™ 3D view of the open with an uncompressed ACA layer in between the two ports.

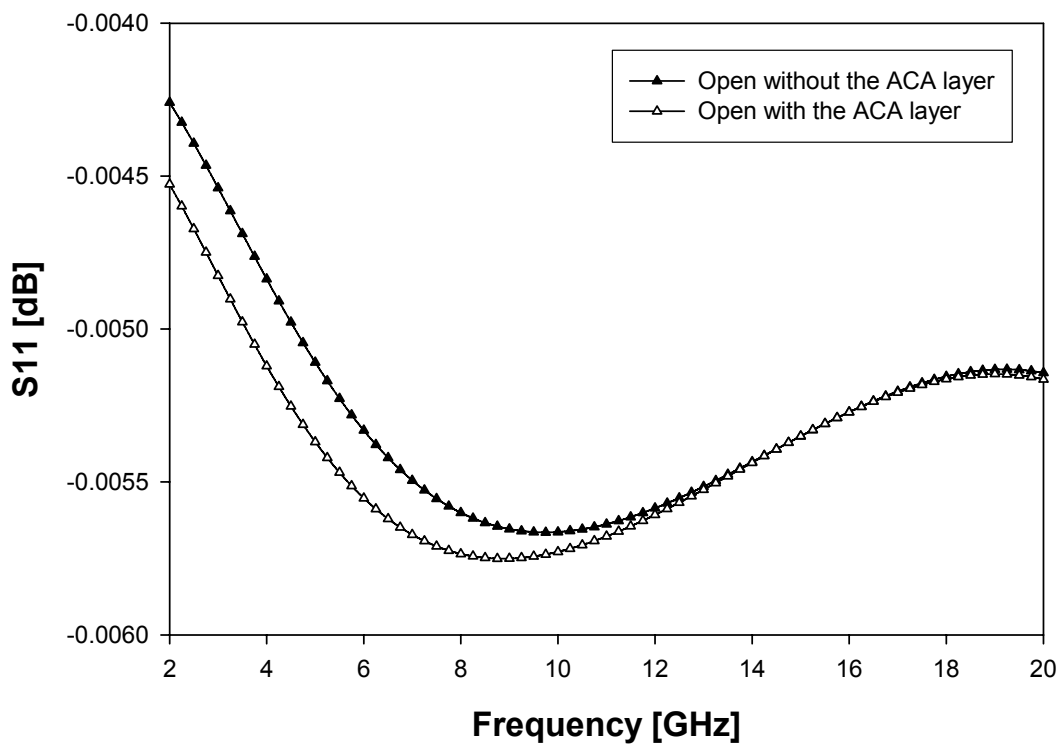


Figure 5.47: S11 parameter plot for the open structure with the uncompressed ACA layer between the two ports compared with the one for the same structure without ACA layer.

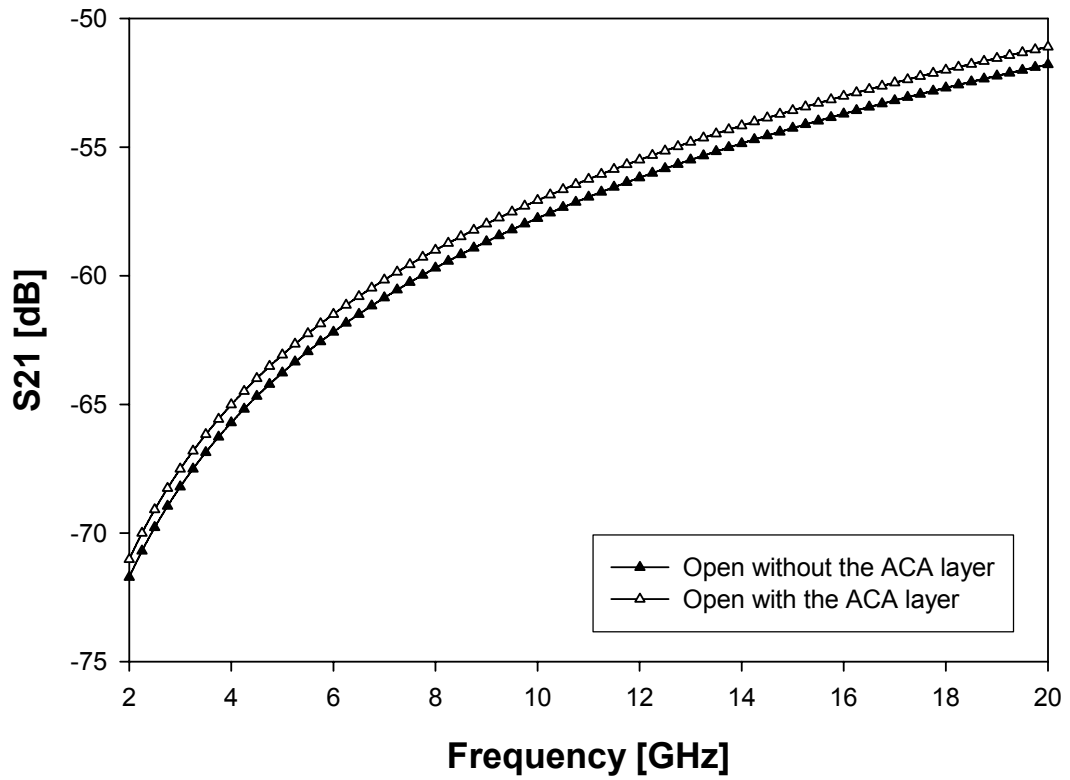


Figure 5.48: S21 parameter plot for the open structure with the uncompressed ACA layer between the two ports compared with the one for the same structure without ACA layer.

Another case that might occur is when an RF-MEMS device is surrounded by a layer of uncompressed ACA. To this purpose, an ACA layer is patterned around a CPW and the Ansoft HFSS<sup>TM</sup> 3D view is shown in Figure 5.49. Also in this case the RF behaviour of the CPW does not seem to be significantly affected by the presence of the uncompressed ACA layer, like it is noticeable from the S-parameters plots of Figure 5.50 and Figure 5.51. Moreover, the case in which an uncompressed ACA layer is suspended above a CPW is also taken into account [76]. The latter is not reported here for seek of brevity.

In conclusion, the presence of uncompressed ACA does not seem to introduce significant additional parasitics to the RF behaviour of capped structures in any of the analyzed cases. However, it has to be considered that this is just a preliminary investigation on this type of problem. Indeed, in the simulations previously shown the presence of the capping substrate above the test structures (open and CPW) was always ignored.

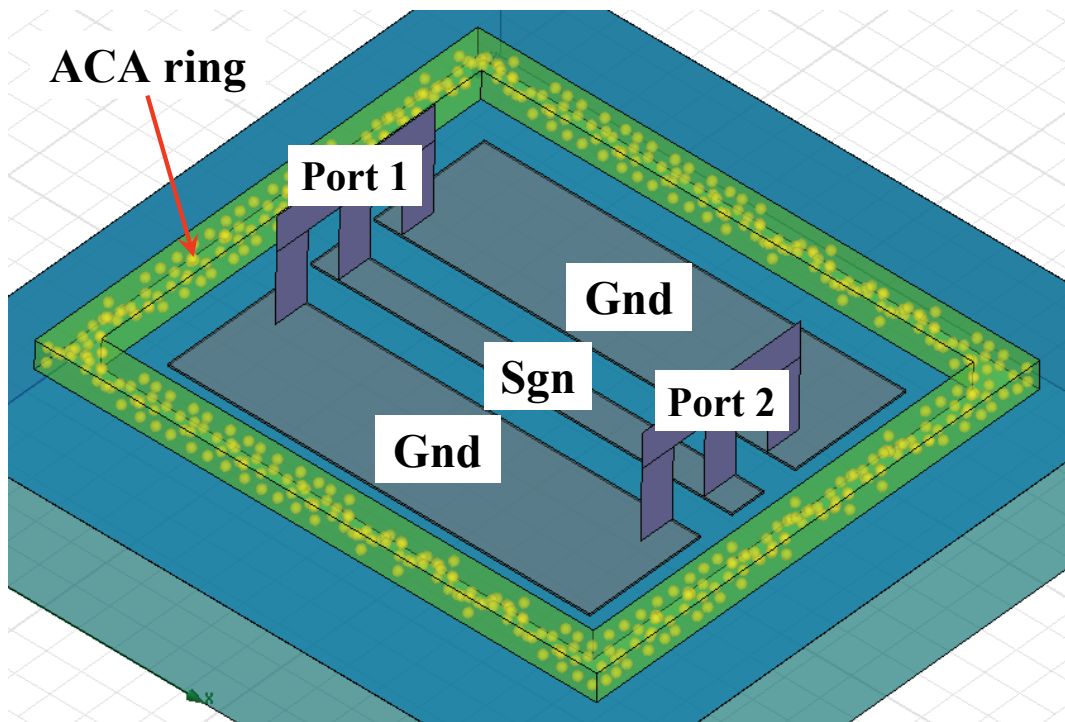


Figure 5.49: Ansoft HFSS™ 3D view of a CPW surrounded by an uncompressed ACA layer.

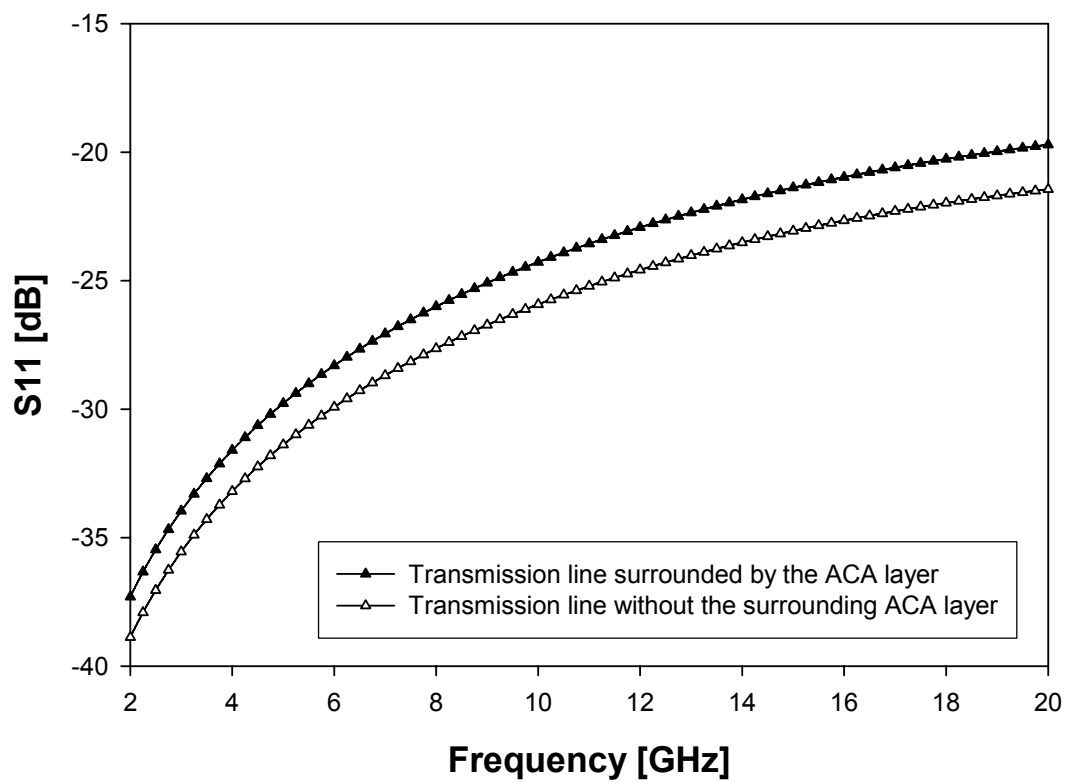


Figure 5.50: S11 parameter plot for the CPW surrounded by an uncompressed ACA layer compared with the one for the CPW without ACA.



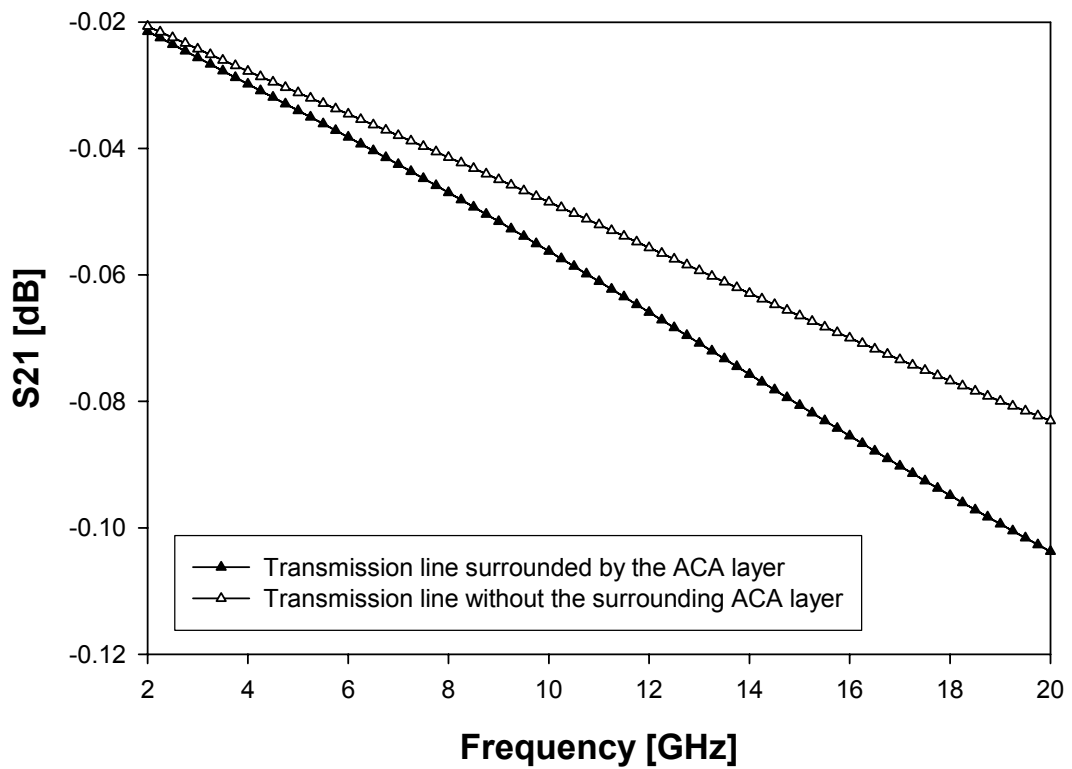


Figure 5.51: S21 parameter plot for the CPW surrounded by an uncompressed ACA layer compared with the one for the CPW without ACA.



## Chapter 6

# Simulation of RF-MEMS Devices

In previous chapters all the necessary elements for the modeling of complete topologies of RF-MEMS devices have been shown in details. Moreover, a suitable technological solution for packaging and integration of these was developed from the point of view of fabrication and has been also characterized concerning the parasitics the cap introduces, affecting the electromagnetic behaviour of RF-MEMS devices.

It is now appropriate to combine all these elements together in order to show the capabilities of the developed mixed domain simulation environment in predicting and characterizing not only the electromechanical but also the radiofrequency behaviour of RF-MEMS complete structures. To this purpose, the first part of the chapter is focused on validation of complex structures in which all the elementary components, singularly validated earlier in the thesis, are combined together. Subsequently, actual RF-MEMS devices (i.e. switches and varactors) simulated within Spectre<sup>©</sup> are compared with experimental data. Furthermore, as a proof of concept of mixed domain structure, a VCO (Voltage Controlled Oscillator) with the LC-tank implemented with RF-MEMS compact models and the active part by means of a commercial CMOS technology library is reported.

## 6.1 Validation of MEMS Compact Model Library for Complex Structures

In this section three complex geometries are presented and discussed. The first one is a structure called *flag* as it is constituted by a suspended rigid plate with just one corner connected to a flexible beam and the other three floating. The second device is a MEMS *toggle-switch*. This is a particular switch implementation with a complex system of actuation. Finally, the last structure is a configuration of Euler beams called *meander*. Flexible beams form a serpentine structure particularly useful for lowering the pull-in voltage of MEMS switches.

### 6.1.1 The MEMS Flag Implementation

As mentioned above, this structure is based on a suspended rigid plate with three floating corners and the fourth connected to an Euler flexible cantilever beam. This configuration, which resembles a flag indeed, is not useful for practical applications, but is very meaningful to validate the 6 DoF's plate and 12 DoF's Euler beam electromechanical models. Indeed, due to the asymmetrical distribution of the spring effect on the rigid plate, when a biasing voltage is applied the latter, initially parallel to the substrate, assumes a tilted position in space, i.e. with non-zero orientation angles. This condition is particularly suitable to validate the electrostatic model for the 6 DoF's rigid plate and 12 DoF's Euler beam. Moreover, the pull-in mechanism is more complicated because of the non-parallel plate configuration which makes the availability of the plate 6 DoF's mechanical model essential. In conclusion, correct prediction of the pull-in voltage represents an extensive validation of MEMS compact model as this effect depends either on the accuracy of the implemented electrostatic model and on the effectiveness of the beam mechanical model in defining the spring constant for each involved DoF.

Cadence Virtuoso<sup>®</sup> Schematic of the flag structure is shown in Figure 6.1 where an Euler flexible beam is connected to the bottom left rigid plate corner while the other end is anchored. The other three plate vertexes are connected to floating structures (see last section of Chapter 3).

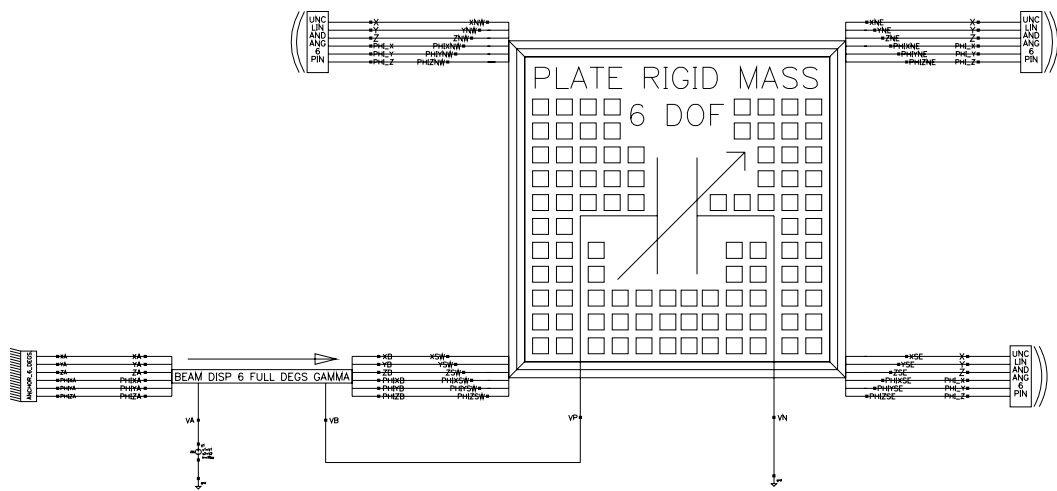


Figure 6.1: Cadence Virtuoso<sup>®</sup> Schematic of the flag structure. The Euler beam is connected to the bottom left plate corner while the other three are connected to floating structures.

Validation of the compact structure is performed by comparing Spectre<sup>®</sup> results with the simulation of the same structure within CoventorWare<sup>®</sup>. The corresponding 3D schematic view is reported in Figure 6.2.

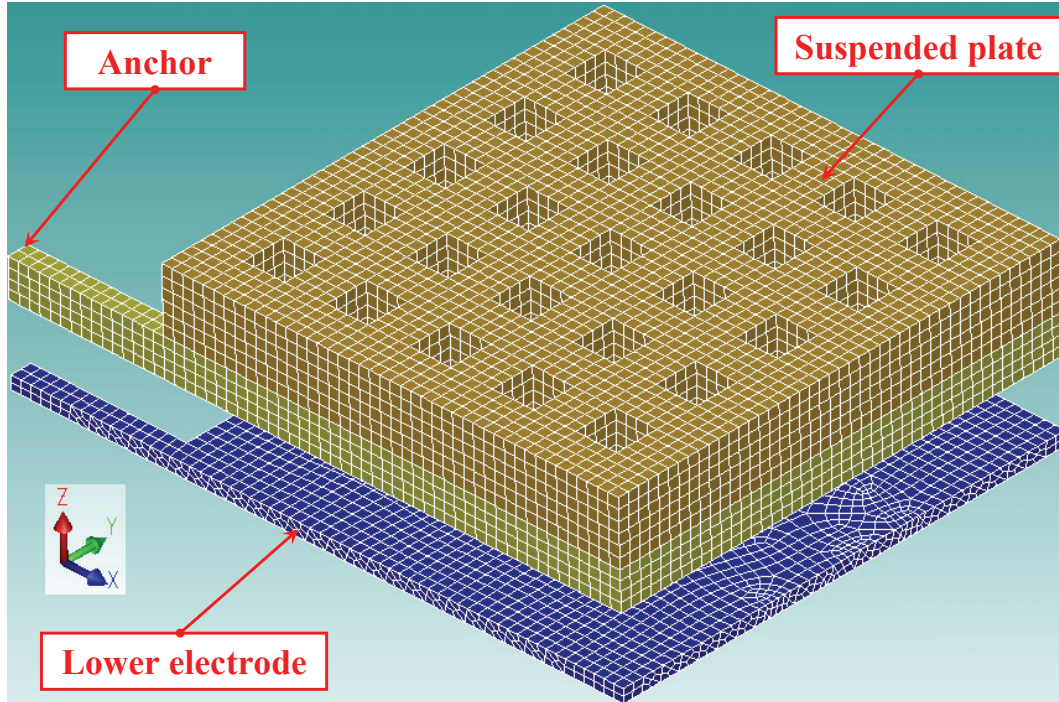


Figure 6.2: CoventorWare<sup>®</sup> 3D model of the flag structure. The structure mesh is displayed in this view both for the suspended structure and for the lower electrode.

Suspended plate width, length and thickness are  $220\ \mu\text{m}$ ,  $220\ \mu\text{m}$  and  $4.8\ \mu\text{m}$  respectively. The offsets between plate edges and holes, addressed as  $\Delta_{xL}$ ,  $\Delta_{xR}$ ,  $\Delta_{yT}$  in Figure 3.22, are all equal to  $20\ \mu\text{m}$ . Moreover, there are 5 holes along  $x$  direction and 5 along  $y$  of dimensions  $20 \times 20\ \mu\text{m}^2$ . The flexible beam is  $75\ \mu\text{m}$  long, the width is  $10\ \mu\text{m}$  and finally the thickness is  $1.8\ \mu\text{m}$ . Gap is equal to  $3\ \mu\text{m}$  and the electrical effects of the insulating layer lying on the lower electrode are ignored. The suspended structure is made of gold and the Young modulus and Poisson's ratio are 98.5 GPa and 0.42 respectively (based on ITC-irst technology [87]). The type of analysis in Spectre<sup>®</sup> is a static DC simulation while in CoventorWare<sup>®</sup> it is an electromechanical coupled analysis.

Because of the uneven distribution of the elastic reactive constraint due to the beam connected to one plate node a complex behaviour of the plate vertexes pull-in is expected. The overall pull-in behaviour referred to the four plate North-East, South-East, South-West and North-West nodes (see Figure 6.1 and Figure 3.3) predicted by Spectre<sup>©</sup> is reported in Figure 6.3.

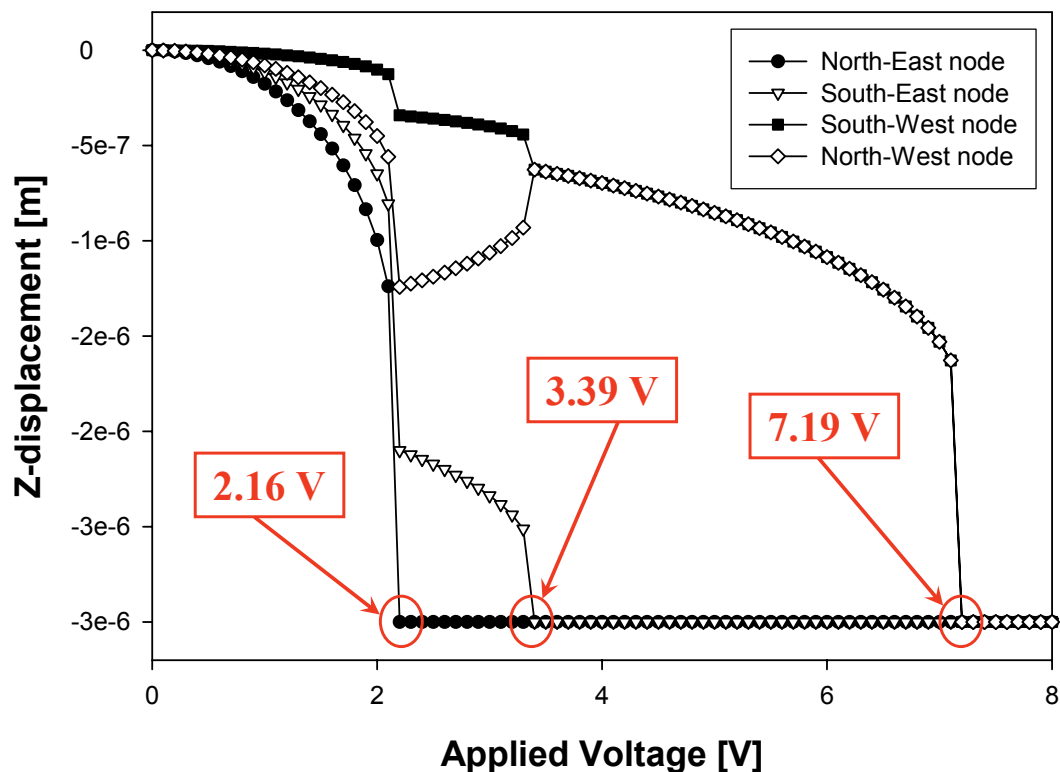


Figure 6.3: Spectre<sup>©</sup> prediction of the pull-in related to the North-East, South-East, South-West and North-West plate corners.

The Spectre<sup>©</sup> simulation predicts the first collapse occurring at the top-right (North-East) corner when the voltage of 2.16 Volts is imposed. On the other hand, CoventorWare<sup>©</sup> predicts the North-East node pull-in for a voltage falling between the interval from 2.1 V to 2.2 V (the voltage step was set to 0.1 V) which is in very good agreement with the Spectre<sup>©</sup> simulation. The North-East corner vertical displacement plot for the Spectre<sup>©</sup> and CoventorWare<sup>©</sup> simulations is reported in Figure 6.4.

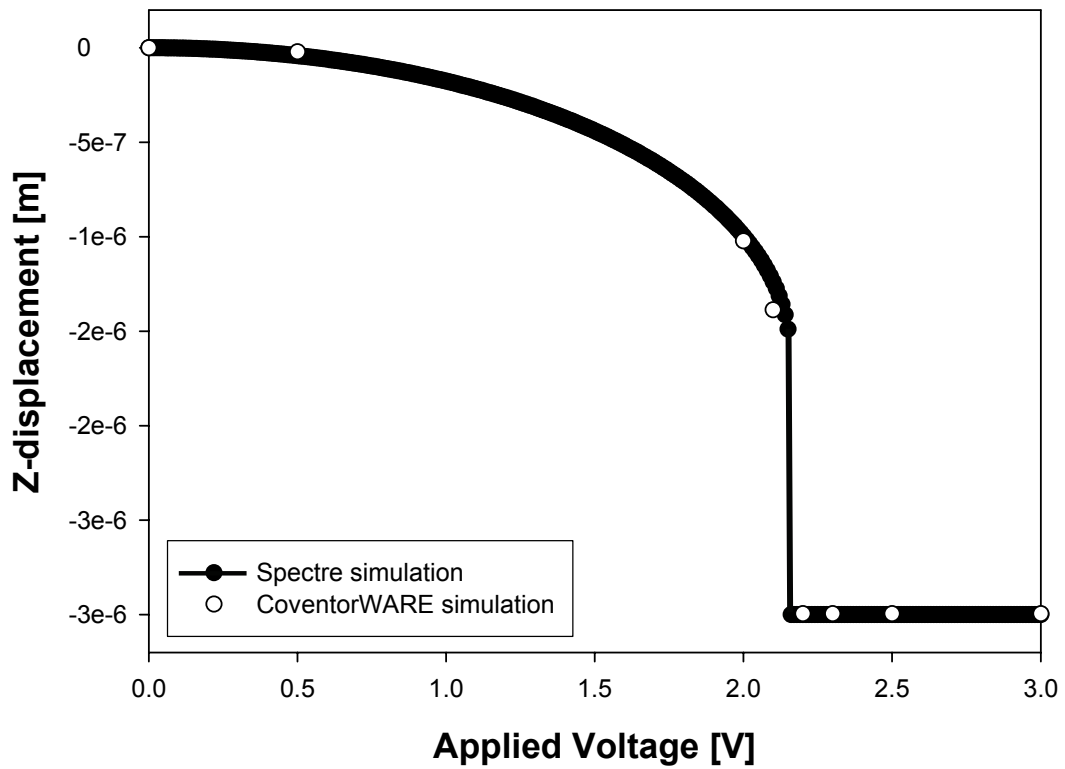


Figure 6.4: North-East corner vertical displacement plot for the Spectre<sup>®</sup> and CoventorWare<sup>®</sup> simulation. CoventorWare<sup>®</sup> predicts the pull-in for a voltage between 2.1 V and 2.2 V which corresponds to the result in Spectre<sup>®</sup> of 2.16 V.



Concerning the other corners, Spectre<sup>®</sup> predicts the second pull-in for the South-East node in correspondence with an applied voltage of 3.39 V (see Figure 6.3). However, the North-East and South-East corners collapse together for a voltage of 2.1–2.2 V in CoventorWare<sup>®</sup>. The corresponding CoventorWare<sup>®</sup> schematic is reported in Figure 6.5 where the color scale represents the vertical displacement.

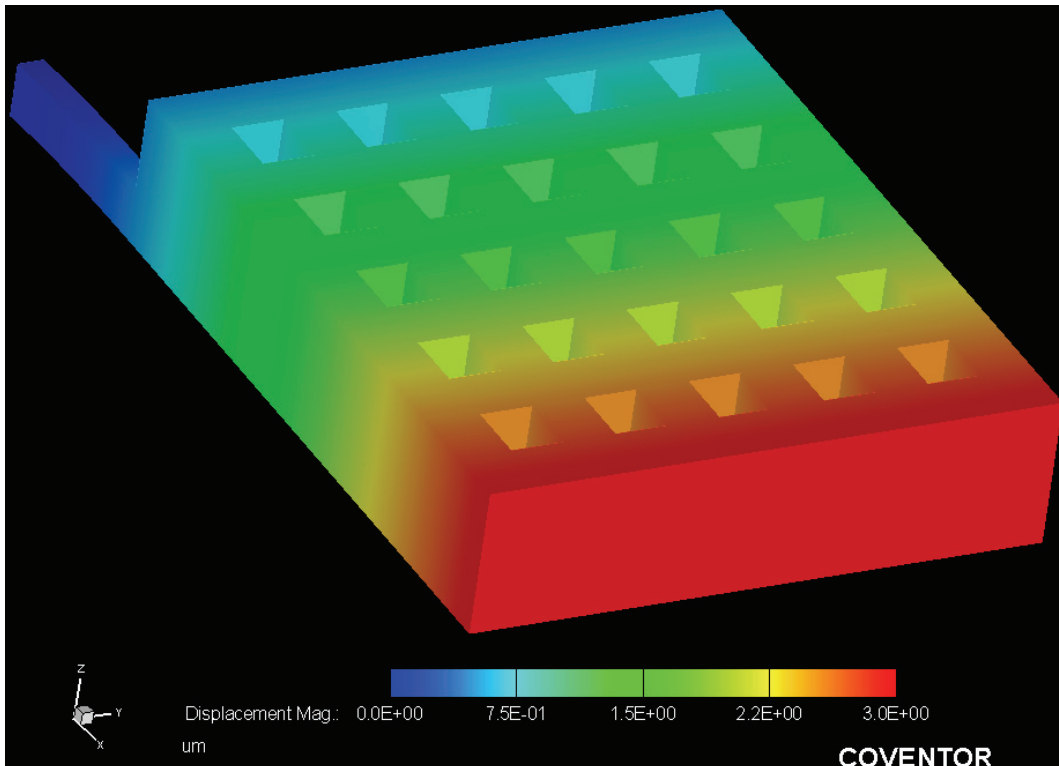


Figure 6.5: CoventorWare<sup>®</sup> schematic of the flag after the collapse at the North-East and South-East nodes occurs. The color scale represent the vertical displacement.

In this case the disagreement with the Spectre<sup>®</sup> prediction is rather large. This can be explained with the fact that the fringing effect becomes dominant when the plate is tilted and just one of its edges (in this case the North-East/South-East one) is very close to the substrate. Consequently, the plate compact model underestimates the fringing effect and this is the reason why

the South-East corner does not collapse together with the North-East but its pull-in occurs for an higher biasing voltage (3.39 V). Finally, let us now refer to the other two nodes (South-West and North-West). CoventorWare<sup>©</sup> schematic is reported in Figure 6.6.

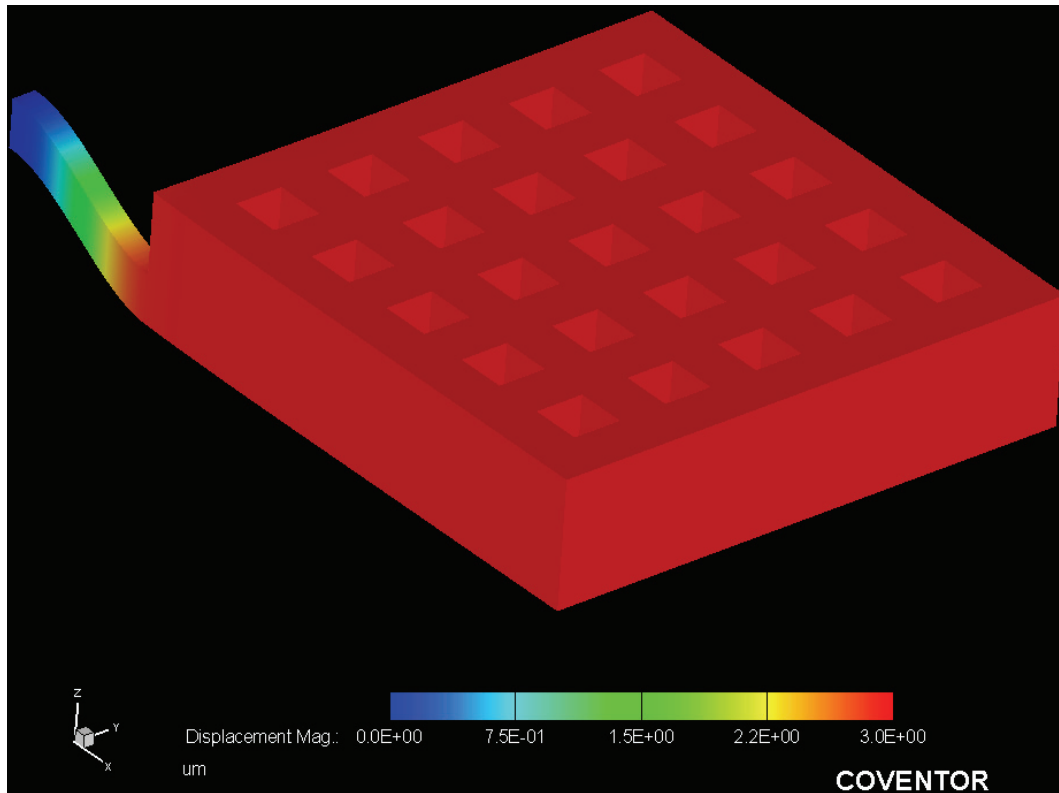


Figure 6.6: CoventorWare<sup>©</sup> schematic of the flag after the collapse of the South-West and North-West nodes occurs. The color scale represent the vertical displacement.

CoventorWare<sup>©</sup> predicts their collapse for a biasing voltage falling in the interval 9.5 – 10 V while in Spectre<sup>©</sup> the pull-in of the South-West and North-West nodes occurs at 7.19 V. The corresponding plot is reported in Figure 6.7.

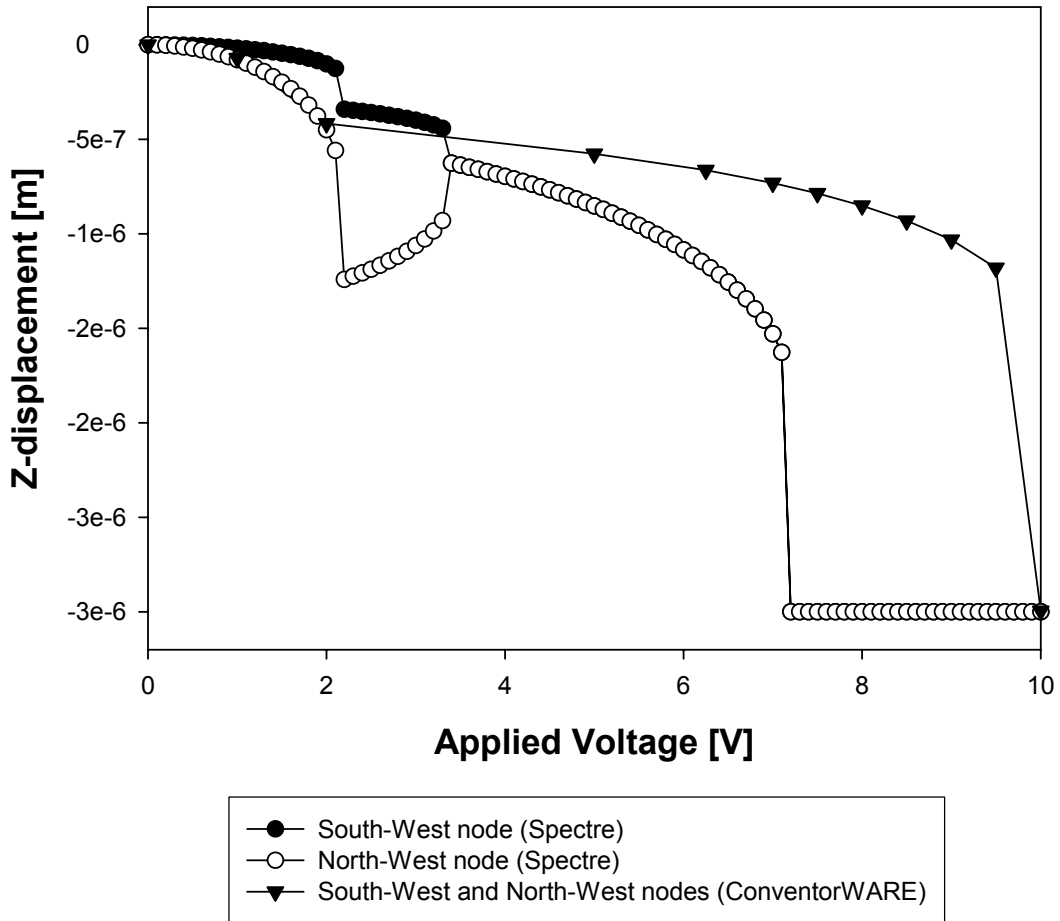


Figure 6.7: South-West and North-West corners vertical displacement plot for the Spectre<sup>®</sup> and CoventorWare<sup>®</sup> simulation. CoventorWare<sup>®</sup> predicts the pull-in for a voltage between 9.5 V and 10 V while the corresponding result in Spectre<sup>®</sup> is 7.19 V.

In this case the compact models seem to overestimate the electrical effect as Spectre<sup>©</sup> predicts a pull-in voltage for the South-West and North-West corners which is more than 2 Volts lower than the CoventorWare<sup>©</sup> one. First of all the qualitative behaviour of the vertical displacement curves in Spectre<sup>©</sup> and CoventorWare<sup>©</sup> is different. Indeed, looking at Figure 6.7 the  $Z$  displacement of the two nodes is superposed over all the voltage range as the South-East and North-East nodes collapse together at a voltage of 2.1 – 2.2 V (see Figure 6.4). This is the reason why the CoventorWare<sup>©</sup> curve of Figure 6.7 exhibits just one knee in correspondence with the first pull-in voltage. Differently, the Spectre<sup>©</sup> curves for the South-West and North-West nodes present two knees corresponding to the pull-in voltage of the North-East and South-East corners. Only after the latter collapse these are superposed. The CoventorWare<sup>©</sup> curve is superposed to the Spectre<sup>©</sup> one for the North-West corner until the first pull-in (East nodes) is reached. After this point the disagreement is rather large as Figure 6.7 reports because of the just discussed reason. Moreover, the compact model for the electrostatic effects of the rigid plate might be not appropriate to describe a complex situation in which two plate corners already collapsed on the bottom electrode while the other two still have a non-zero gap. This could be caused by uneven charge distribution on plate surface in such a condition which are not accounted for in the compact model implemented in VerilogA<sup>©</sup>. Nevertheless, the collapse of the first node (the North-East one) has been predicted with a very good accuracy in Spectre<sup>©</sup>. This must be considered a good result as the analyzed structure represents a very complex problem in which the electric field is not homogeneous over the two faces and also the mechanical constraints are unevenly distributed. Furthermore, such a type of geometry never occurs in practical problems as it has been conceived just to validate MEMS compact models in a limiting case.

A final aspect must be discussed concerning the simulation times. The just shown results obtained in CoventorWare<sup>®</sup> required few simulations depending on which node(s) pull-in had to be analyzed. For the North-East and South-East collapse a simulation from 2 to 4 V with step of 0.1 V was run on a Desktop PC with two 2.8 GHz Intel Pentium<sup>®</sup> IV Processors and 2 GB RAM memory. This simulation had to be interrupted and launched again for a few times to solve some convergence issues. The complete simulation took about 10 hours to be accomplished. Moreover, for the South-West and North-West pull-in another simulation from 0 up to 10 V with 20 steps was run on the same computer described above and required about 24 hours for its completion. On the other hand, the compact models have been simulated in Spectre<sup>®</sup> on a Spark Workstation with one 700 MHz CPU and 1 GB RAM memory. The DC simulation of the flag structure ranging from 0 up to 10 V with 10 mV steps took 34 seconds to be completed.

This shows the effectiveness of the developed compact model library concerning the very small time required to perform the analysis of entire topologies. As already stated before, a fast tool like this is absolutely essential when dealing with several parameters to be analyzed.

### 6.1.2 MEMS Toggle-Switch

The MEMS toggle-switch is a particular switch implementation with a more complex actuation mechanism if compared with a traditional one based on a single suspended rigid plate [77]. A schematic top-view and cross-section of a MEMS toggle-switch are reported in Figure 6.8 and Figure 6.9 respectively.

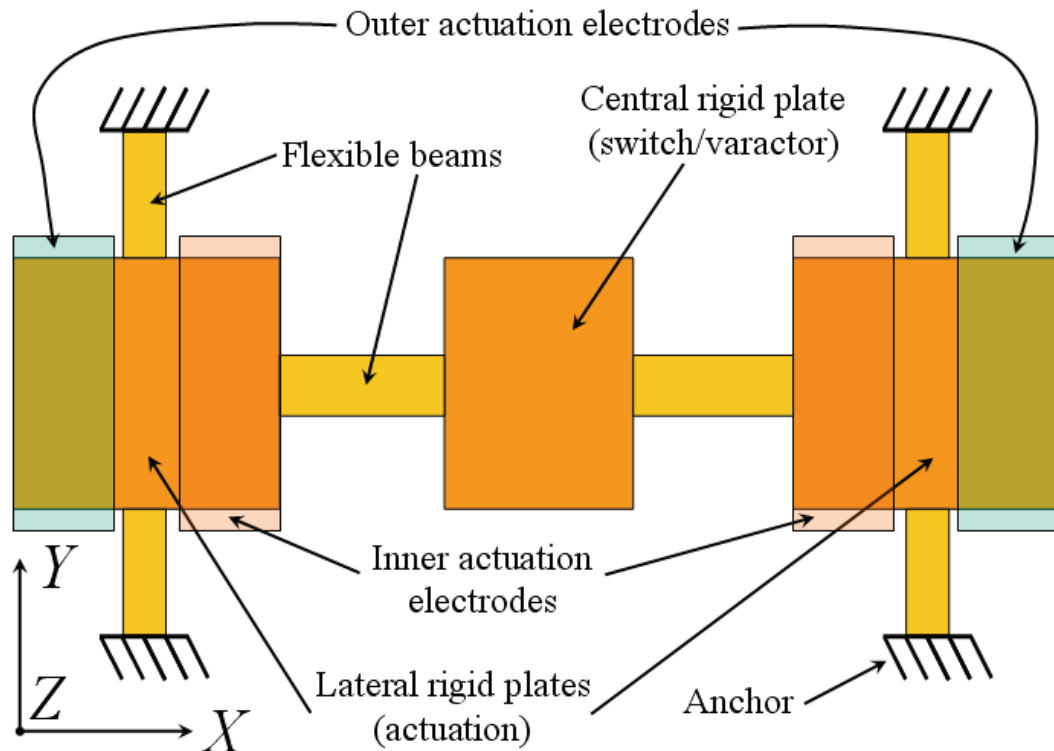


Figure 6.8: Schematic top-view of a MEMS toggle-switch. Central switch is connected to two lateral actuation structures.

It is based on a central suspended rigid plate which implements the switch or varactor function. This is connected by means of flexible beams to two lateral actuation rigid plates. The latter ones are kept suspended by two short flexible beams anchored on the other ends. A pair of electrodes are deployed under each actuation rigid plate, forming a couple of inner and outer controlling electrodes (see Figure 6.9).

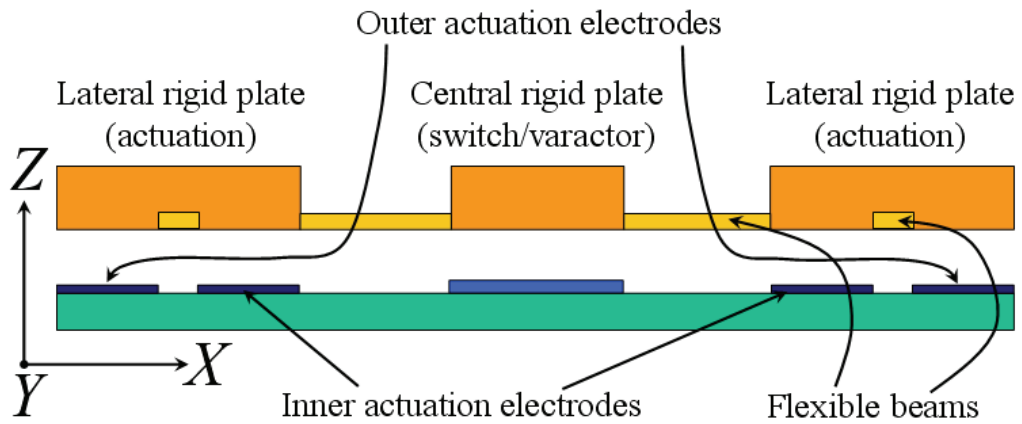


Figure 6.9: Schematic side-view of a MEMS toggle-switch cross-section. The lateral actuation structures are kept suspended by two short flexible beams.

When a biasing voltage  $V$  is applied between the inner electrodes and the two actuation plates, the attractive force acts on their area closer to the central switch/varactor. This causes the two controlling plates rotation like shown in Figure 6.10 and the consequent lowering of central plate towards the underlying electrode.

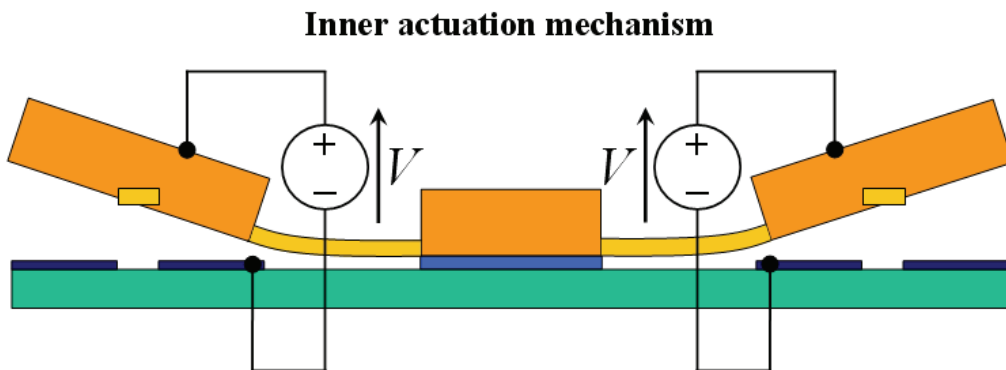


Figure 6.10: Schematic of the MEMS toggle-switch inner actuation mechanism.

On the other hand, when the voltage is applied to the outer electrodes, the actuation structures rotate around the  $Y$  axis in the other direction, like Figure 6.11 shows. This time the central plate moves upward, increasing its gap with respect to the initial position. When the toggle structures is used as a varactor, the last configuration allows to widen the capacitance range with respect to the standard implementation with a single suspended rigid plate with springs connected to its four corners [78].

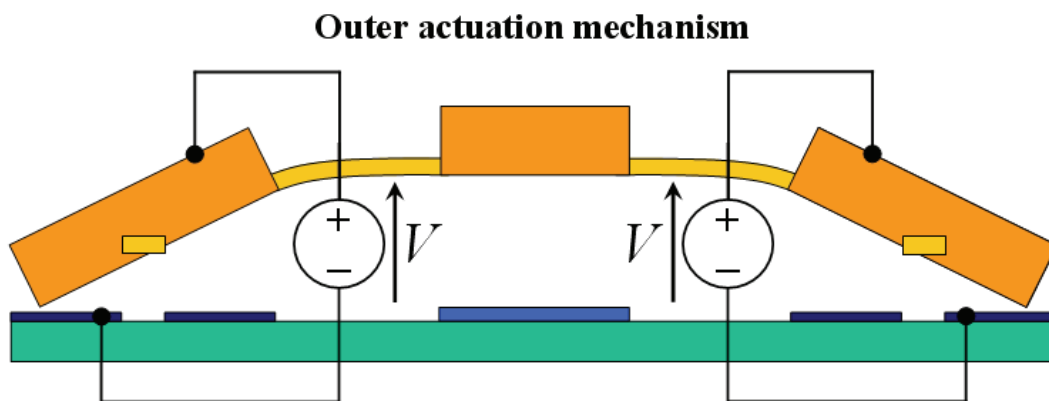


Figure 6.11: Schematic of the MEMS toggle-switch outer actuation mechanism.

The suspending beams must be short enough in order to have a small deformation along  $Z$  axis with respect to the torque around  $Y$  axis.

A toggle structure is implemented in CoventorWare<sup>®</sup> and its 3D FEM model is reported in Figure 6.12. Because of the structure symmetry just one half of the entire structure is simulated in order to reduce both computational complexity and simulation time. Symmetry boundary conditions both for the mechanical and electrostatic simulations are applied in CoventorWare<sup>®</sup> to the plane shown in Figure 6.12. The Cadence Virtuoso<sup>®</sup> Schematic of the half-toggle structure implemented in Spectre<sup>®</sup> is shown in Figure 6.13. Mechanical constraints due to the symmetry condition are applied to the central plate by means of anchors (see last section of Chapter 3). Because of the symmetry condition central plate can only move in the vertical direction ( $Z$  axis), without any in-plane displacement (on the  $XY$  plane) and without any rotation around the three axes (i.e. central plate is always parallel to the substrate).



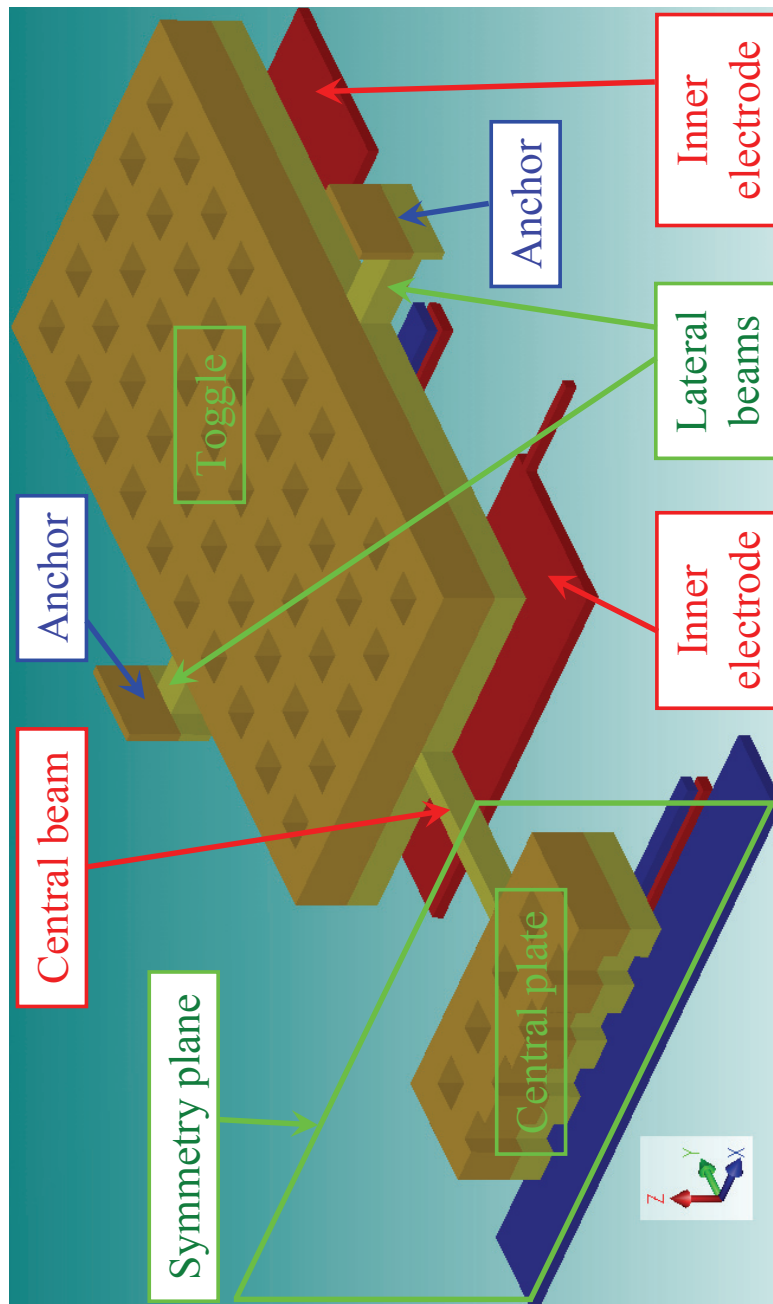


Figure 6.12: Schematic view of the toggle-switch implemented within CoventorWare<sup>®</sup>. Symmetry is exploited and half a structure is implemented.

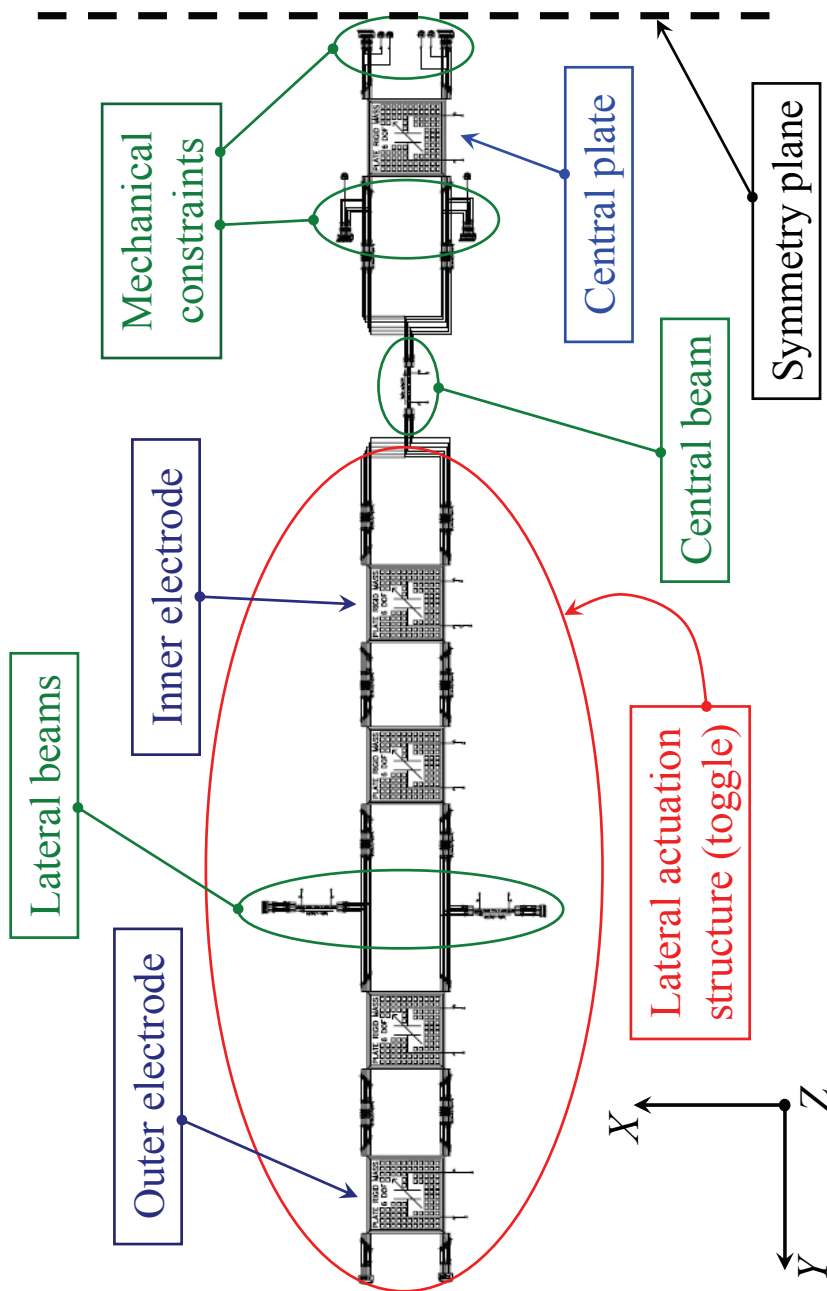


Figure 6.13: Cadence Virtuoso<sup>®</sup> Schematic of the toggle-switch. Exploiting the symmetry of the structure half a toggle is implemented.

Toggle dimensions along  $X$ ,  $Y$  and  $Z$  axes are respectively  $220\ \mu\text{m}$ ,  $420\ \mu\text{m}$  and  $4.8\ \mu\text{m}$ . It has 5 and 10 holes ( $20\times 20\ \mu\text{m}^2$ ) along  $X$  and  $Y$ . Lateral suspending beams are  $60\ \mu\text{m}$  long, while their width and thickness are  $20\ \mu\text{m}$  and  $1.8\ \mu\text{m}$  respectively. The beam connecting the toggle to the central signal plate is  $150\ \mu\text{m}$  long. Its width is  $10\ \mu\text{m}$  and the thickness is  $1.8\ \mu\text{m}$ . Central signal plate  $X$ ,  $Y$  and  $Z$  dimensions are  $180\ \mu\text{m}$ ,  $140\ \mu\text{m}$  and  $4.8\ \mu\text{m}$  respectively ( $4\times 3$  holes of area  $20\times 20\ \mu\text{m}^2$ ). Finally, inner and outer electrodes length is  $100\ \mu\text{m}$  along the  $Y$  axis while these are as wide as the toggle (i.e.  $220\ \mu\text{m}$ ) and the vertical air gap is  $3.23\ \mu\text{m}$ . The suspended structure is made of Gold and the design of the toggle-switch is based on ITC-irst technology [87]).

Static DC simulation of the structure shown in Figure 6.13 is performed in Spectre<sup>©</sup> and compared with the results produced by CoventorWare<sup>©</sup>. First a biasing voltage is applied to the inner electrode (see Figure 6.12) to detect the pull-in of the toggle-switch. Biasing voltage is swept from 0 V up to 12 V with steps of 100 mV in Spectre<sup>©</sup>. Comparison of the static pull-in characteristic simulated with the compact models with CoventorWare<sup>©</sup> prediction is shown in Figure 6.14. The vertical displacement is referred to the edge of the toggle connected to the straight beam going towards the central plate (see Figure 6.12). Spectre<sup>©</sup> predicts the pull-in at 10.6 V which is in very good accordance with CoventorWare<sup>©</sup> pull-in voltage of 10.7 V (that corresponds to an error of  $-0.9\%$  with respect to CoventorWare<sup>©</sup>). Also in this case the simulation time saving introduced by compact models in Spectre<sup>©</sup> with respect to FEM-based software is considerable. The just mentioned simulation took 30 seconds to be completed with the compact models in VerilogA<sup>©</sup>. On the other hand, CoventorWare<sup>©</sup> determined the pull-in in 10 steps and the whole simulation needed about 12 hours to be accomplished. The simulation platforms on which Spectre<sup>©</sup> and CoventorWare<sup>©</sup> simulations were run are the same mentioned in previous section about the MEMS flag validation structure. Finally, the vertical displacement of the same edge of Figure 6.14 is shown in Figure when the controlling voltage is applied to the outer electrode. The same considerations just discussed are still valid for this case. In particular, also in this case the error in Spectre<sup>©</sup> pull-in prediction is  $-0.9\%$  with respect to CoventorWare<sup>©</sup>. Eventually, CoventorWare<sup>©</sup> schematic views of the deformed toggle-switch when a biasing voltage is applied to the inner and outer electrode respectively are shown in Figure 6.16 and 6.17.

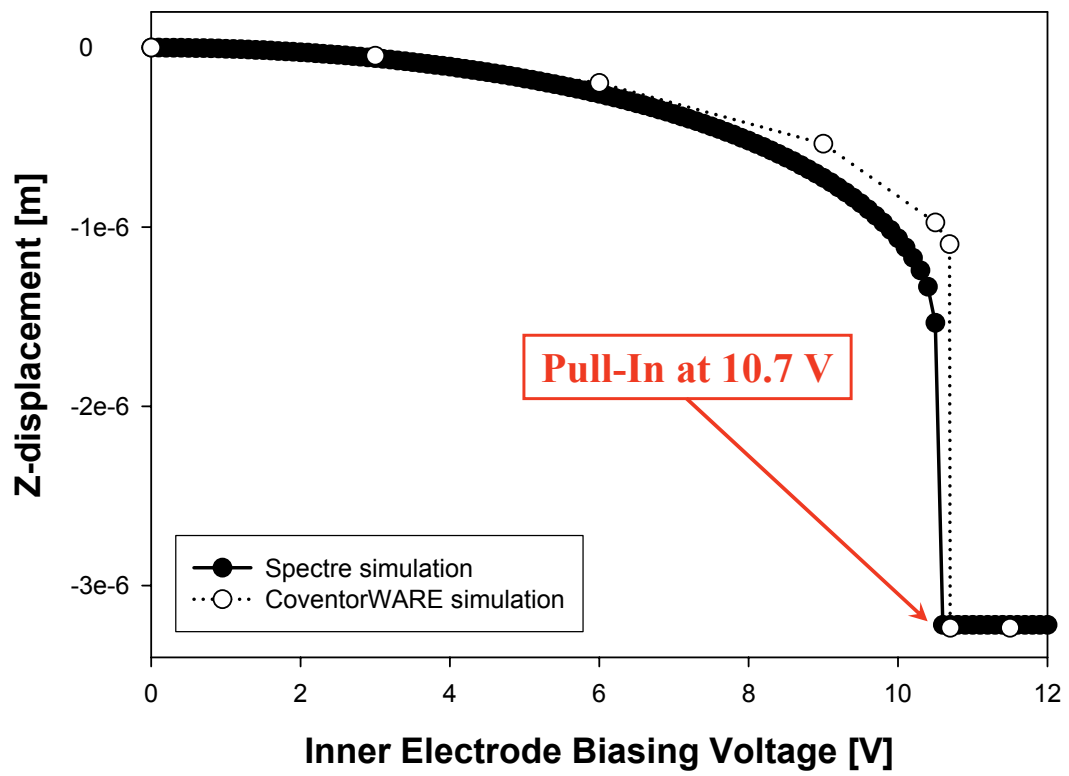


Figure 6.14: Pull-in characteristic of the toggle predicted in Spectre<sup>®</sup> compared with CoventorWare<sup>®</sup> simulation.

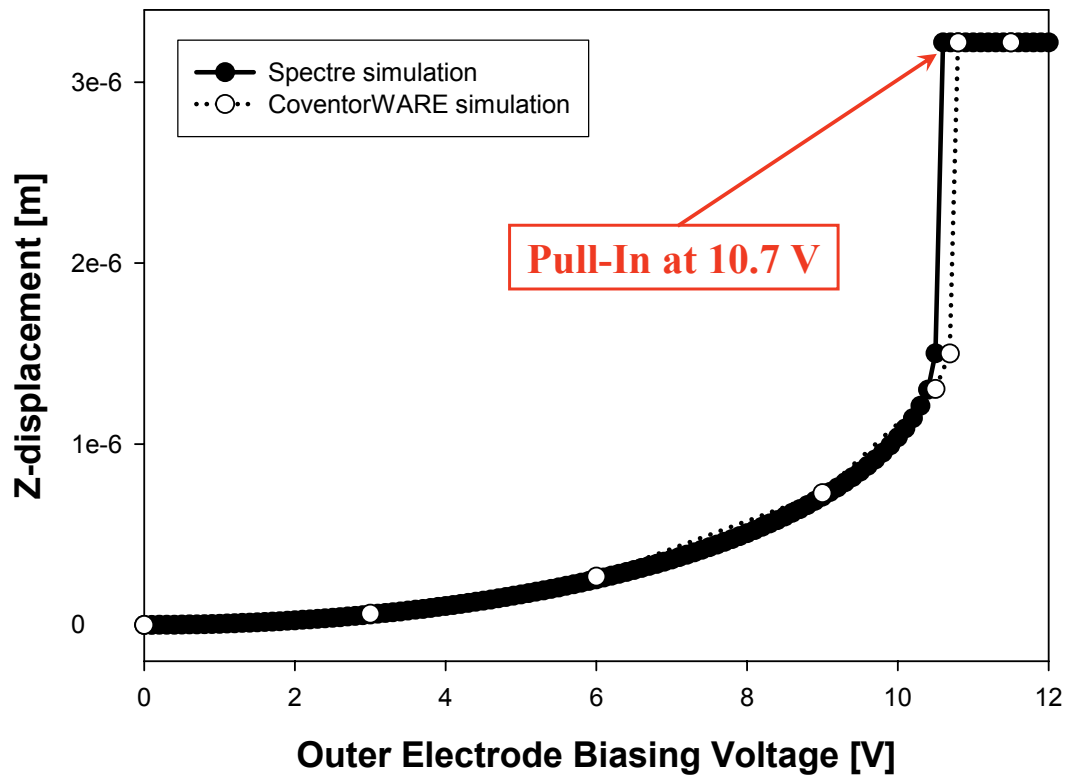


Figure 6.15: Pull-in characteristic of the toggle predicted in Spectre<sup>®</sup> compared with CoventorWare<sup>®</sup> simulation. The controlling voltage is applied to the outer electrode.

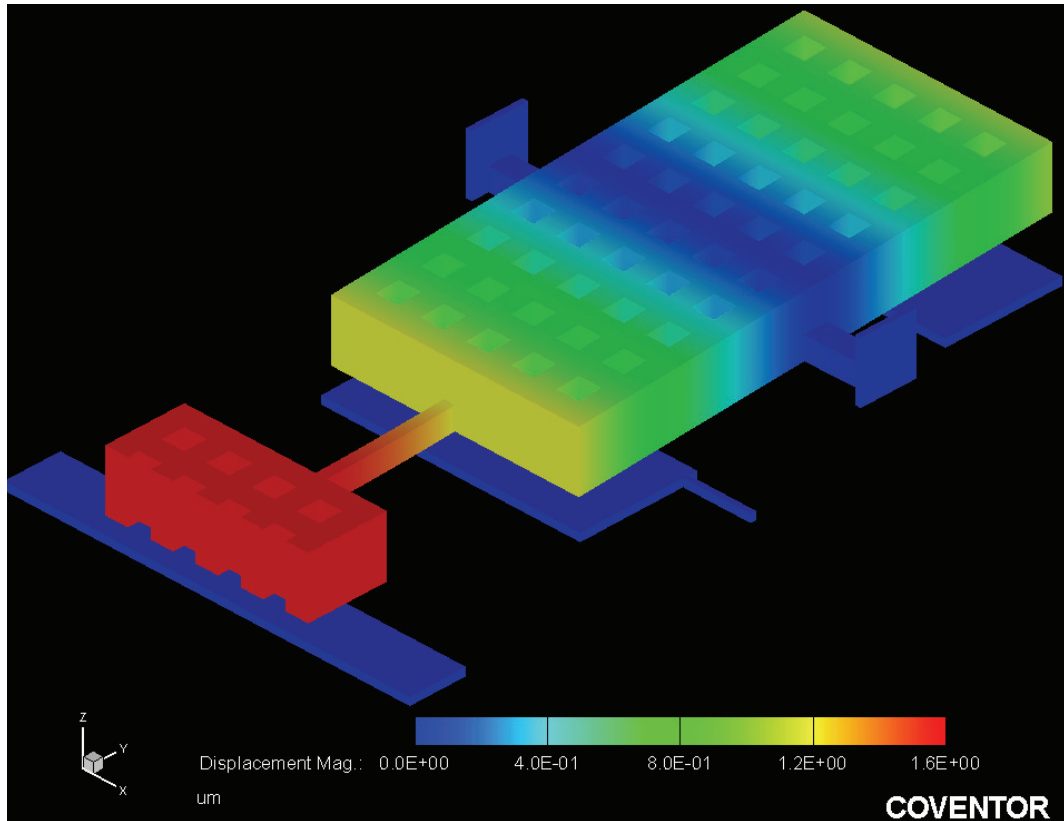


Figure 6.16: Schematic view in CoventorWare<sup>®</sup> for the deformed toggle when the controlling voltage is applied to the inner electrode. Color scale represents the vertical displacement.

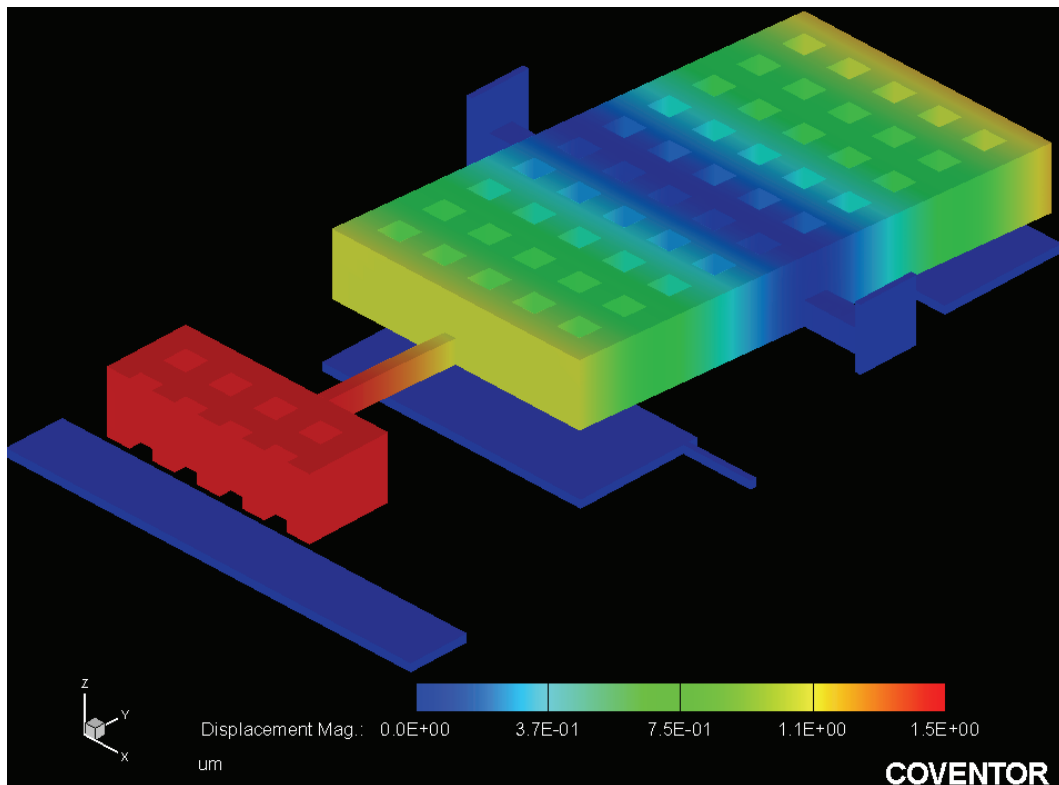


Figure 6.17: Schematic view in CoventorWare<sup>®</sup> for the deformed toggle when the controlling voltage is applied to the outer electrode. Color scale represents the vertical displacement.

### 6.1.3 Meander Structure

Meander configuration of flexible beams is very interesting for its application to RF-MEMS switches topologies. It is based on a serpentine-shaped structure which exhibits a lower spring constant compared to the single straight beam that could be placed within the same area. This allows considerable lowering of the pull-in voltage when applied to RF-MEMS switch geometries [79]. Another important issue linked to the realization of RF-MEMS structures is the residual stress which accumulates within the material of the suspended structure due to high temperature fabrication steps. Residual stress makes the flexible beams stiffer and it results in an increase, sometimes very severe (e.g. 2-3 times), of the pull-in voltage with respect to its theoretical value. Adopting meander springs instead of simple straight beams makes it possible to alleviate the effect of residual stress and to reduce the elastic constant of the entire flexible structure [80].

We report here for validation purposes the comparison of data available in literature for a particular meander configuration with the simulation of the same structure within Cadence<sup>®</sup>. The folded structure, proposed by Peroulis et Al. [81], is shown in Figure 6.18. The basic structure is composed by two vertical beams of length  $240\ \mu m$  connected to two other perpendicular ones of length  $20\ \mu m$ . All the other details concerning the geometry and the material properties are available in the referred publication. The bottom end of one longitudinal beam is anchored while the end of the right transversal beam is free. Peroulis reports a linear analytical model to calculate the spring constant of the structure shown below when all the DoF's of the free end but the vertical displacement along  $Z$  are constrained. The mentioned elastic constant is calculated for the single structure of Figure 6.18 as well as for the connection in series of more of these up to five (serpentine). In the paper, the elastic constant values predicted from the analytical model for the five configurations are compared with FEM simulated results showing an excellent agreement. The latter ones are obtained by deriving  $k$  from the 4.13 when a  $1\ \mu N$  force is applied to the folded structure free end and the corresponding deformation is produced in output.

The same analysis is performed on the structure implemented with the elementary models shown thus far in this thesis. Cadence Virtuoso<sup>®</sup> Schematic



corresponding to the basic folded structure of Figure 6.18 is shown in Figure 6.19. Left bottom end is anchored while a vertical force of  $1\ \mu\text{N}$  (along  $Z$ ) is applied to the right free end as well as mechanical constraints to all the DoF's but the  $Z$  displacement. Simulations in Spectre<sup>®</sup> are repeated also for the multiple configuration of meanders (up to five). Comparison of the elastic constant values for the five structures predicted in Spectre<sup>®</sup> with the corresponding values extrapolated by Peroulis paper are shown in Figure 6.20 demonstrating an excellent superposition.

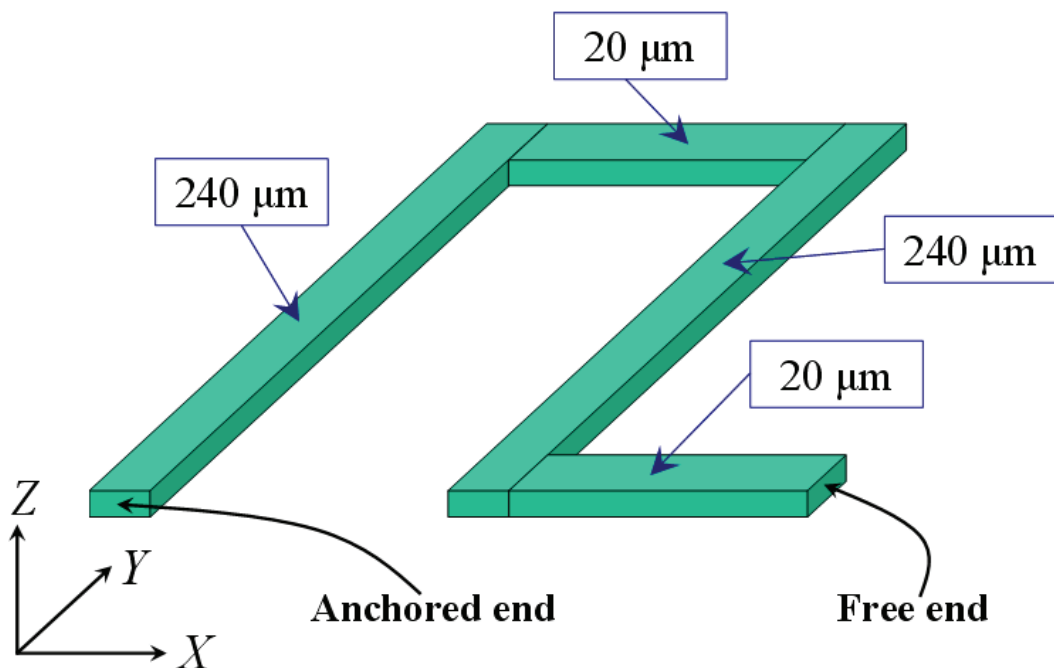


Figure 6.18: Schematic of the folded beam structure proposed by Peroulis et Al. [81]. In it two vertical beams of length  $240\ \mu\text{m}$  are connected with two horizontal beams of length  $20\ \mu\text{m}$ .

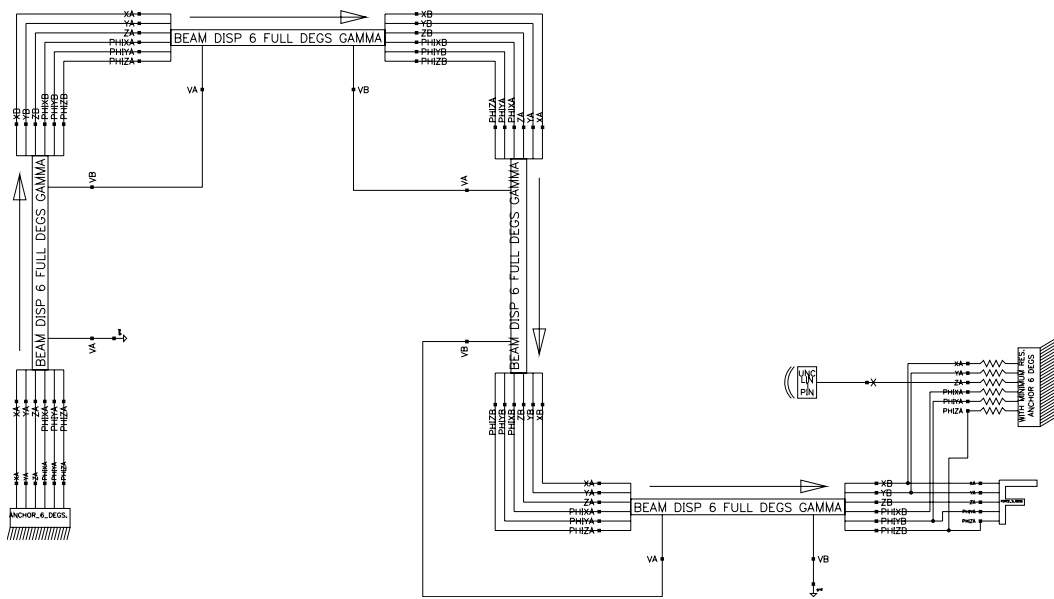


Figure 6.19: Cadence Virtuoso<sup>®</sup> Schematic of the basic folded beam structure proposed by Peroulis.

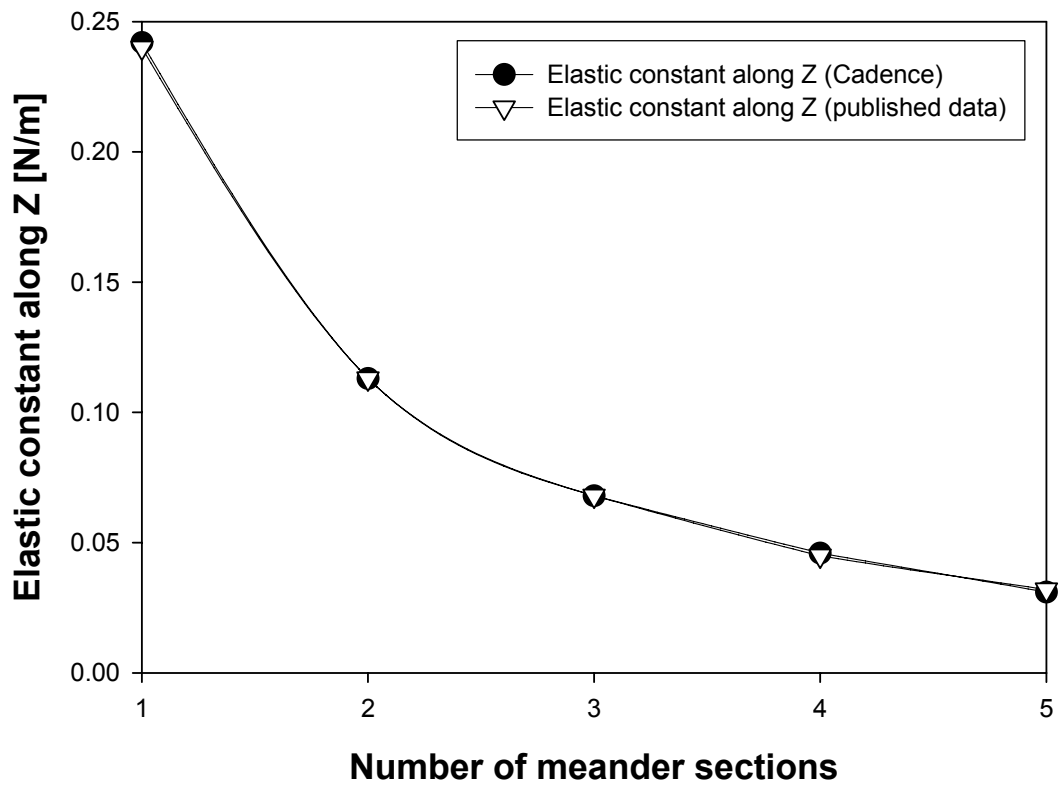


Figure 6.20: Comparison of Spectre<sup>©</sup> prediction for the elastic constant along Z referred to the five meander configurations with the data extrapolated from Peroulis paper.

## 6.2 RF-MEMS Varactor

In this section an RF-MEMS varactor based on a central rigid plate kept suspended by four meander structures connected to its corners is analyzed. These are based on a meander configuration of flexible beams different from the one of previous section. A schematic of the meander used in this MEMS varactor topology is reported in Figure 6.21.

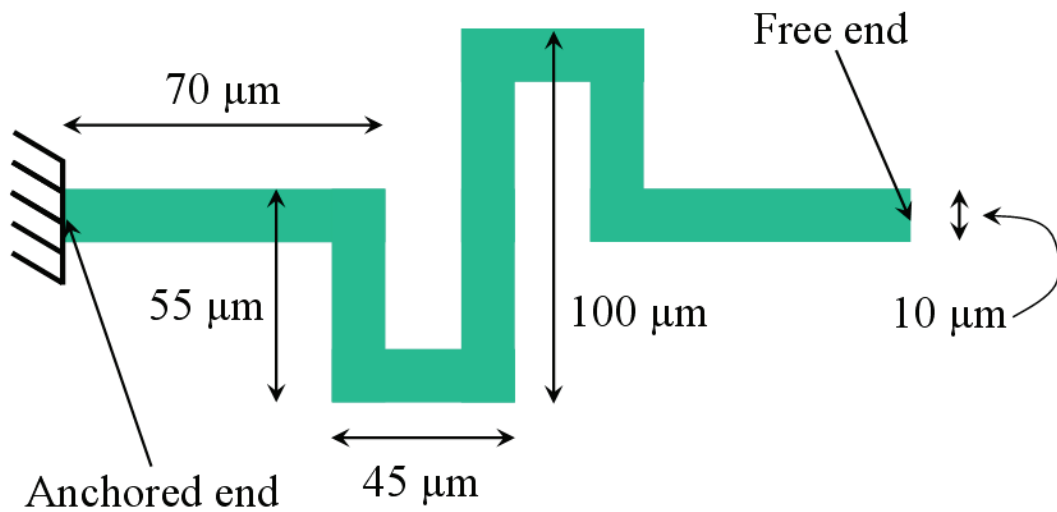


Figure 6.21: Schematic top-view of the meander flexible structure connected to the four plate corners.

The thickness of the meander structure is about  $1.8 \mu m$  while the other dimensions are reported in the previous figure. Concerning the central rigid plate, its width and length are  $220 \mu m$  while the thickness is around  $4.8 \mu m$ . It has 20  $\mu m$  side square holes, 5 along the x axis and 5 along the y axis. Moreover, the distance of holes from plate edges is equal to  $20 \mu m$ . The gap between the plate and the lower electrode is about  $2.2 \mu m$ . The entire suspended structure is made of gold and is realized in ITC-irst technology [75]. The Cadence Virtuoso<sup>©</sup> Schematic of the entire varactor is shown in Figure 6.22. A 3D view of the MEMS structure obtained by means of an optical profiling system provided by Veeco<sup>©</sup> (WYKO NT1100 DMEMS system) [82] is shown in Figure 6.23. Finally, the layout of the varactor is reported in Figure 6.24.

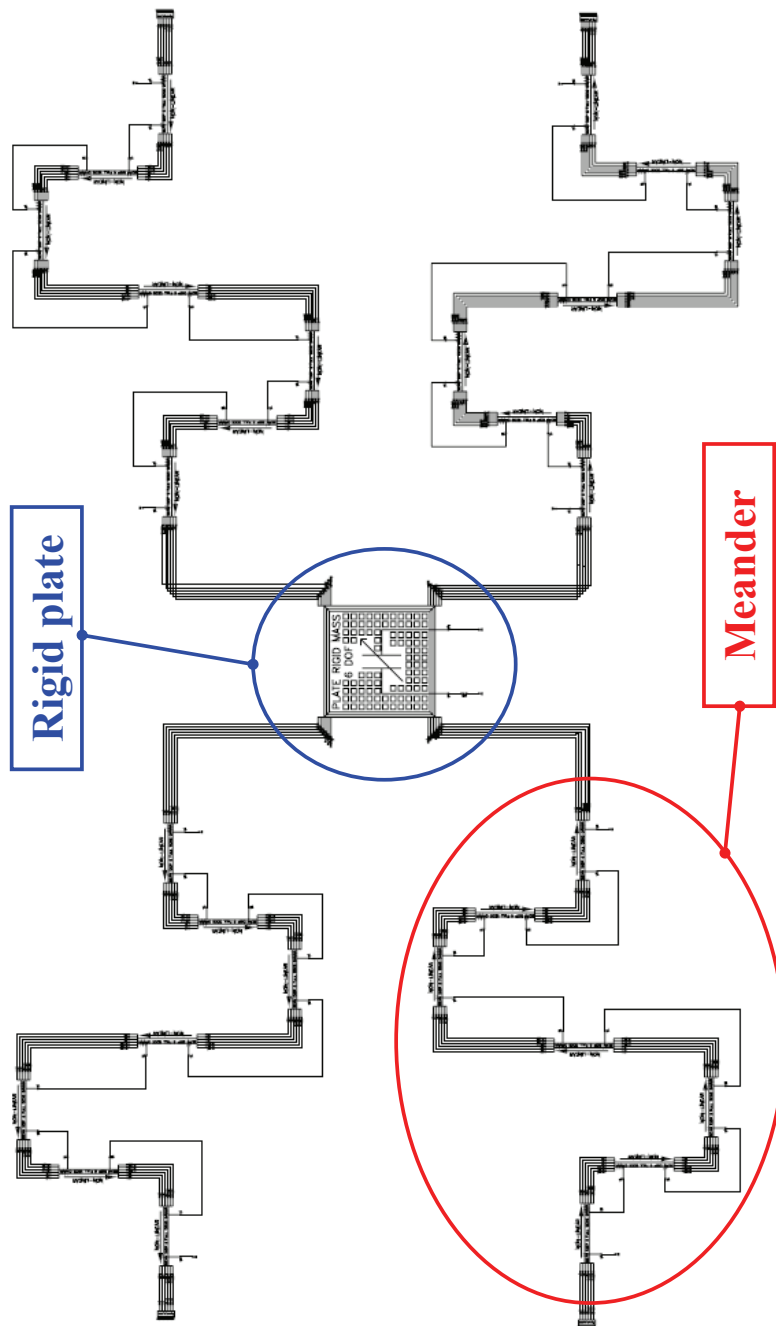


Figure 6.22: Cadence Virtuoso<sup>®</sup> Schematic of the RF-MEMS varactor based on a central rigid plate suspended with four meander structures.

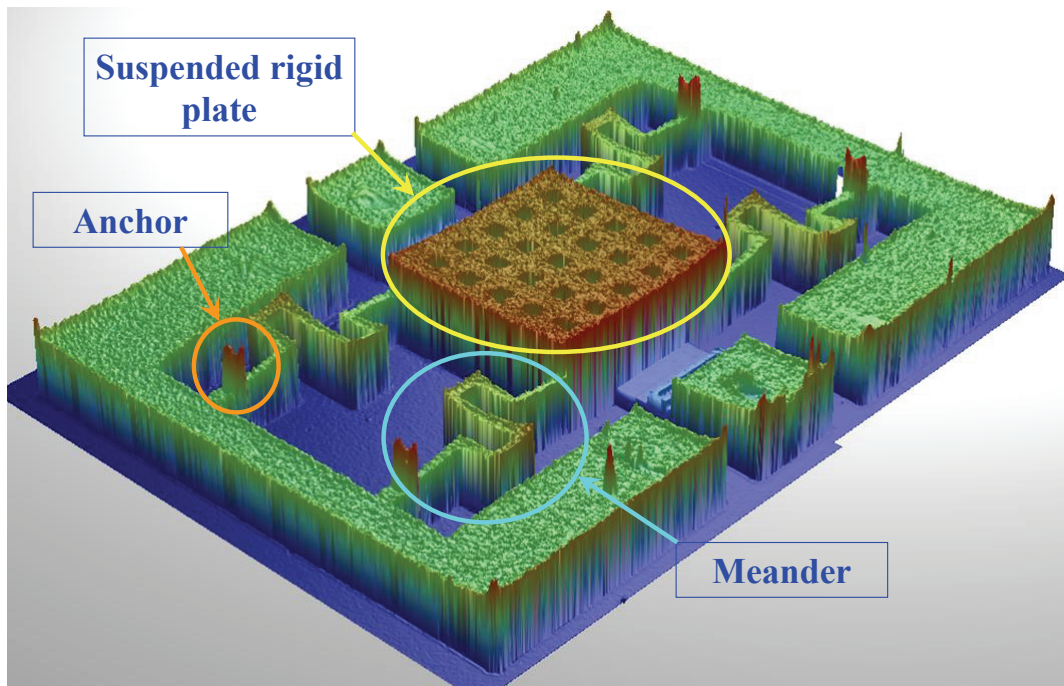


Figure 6.23: 3D view of the MEMS varactor obtained by means of an optical profiling system.

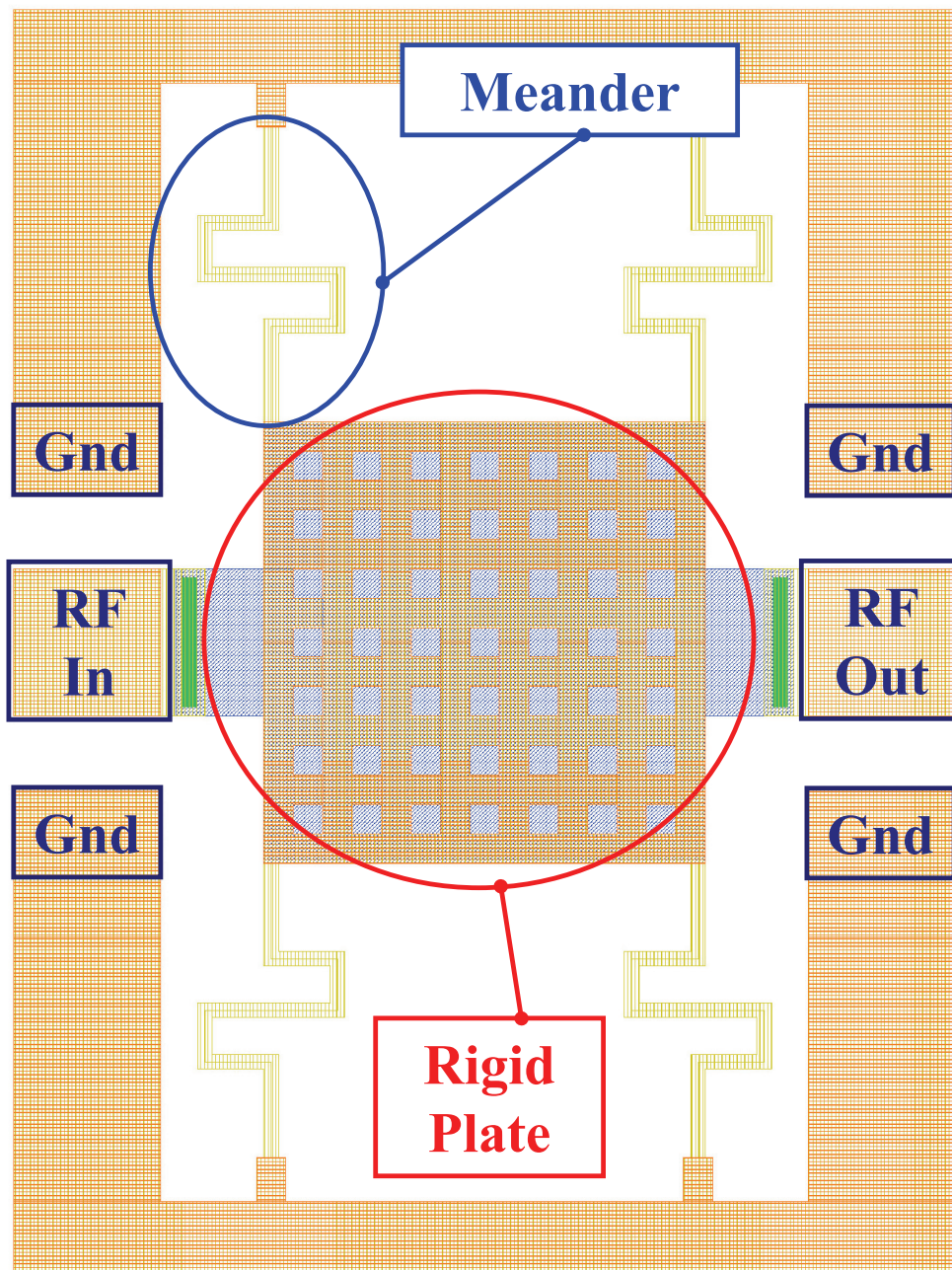


Figure 6.24: Layout (i.e. top-view) of the MEMS varactor. The central plate and the four meanders are visible.

### 6.2.1 Pull-In Characterization

Experimental measurements have been performed on the MEMS varactor shown in previous figure. The applied stimulus is a triangular voltage sweeping both positive and negative voltages with zero average, with a very low frequency (20 Hz) for which the mechanical behaviour of the structure can be assumed static. The corresponding Cadence Virtuoso<sup>®</sup> Schematic (see Figure 6.22) is simulated in Spectre<sup>®</sup> (static DC simulation) and the comparison of the predicted rigid plate vertical displacement with the measured data is shown in Figure 6.25.

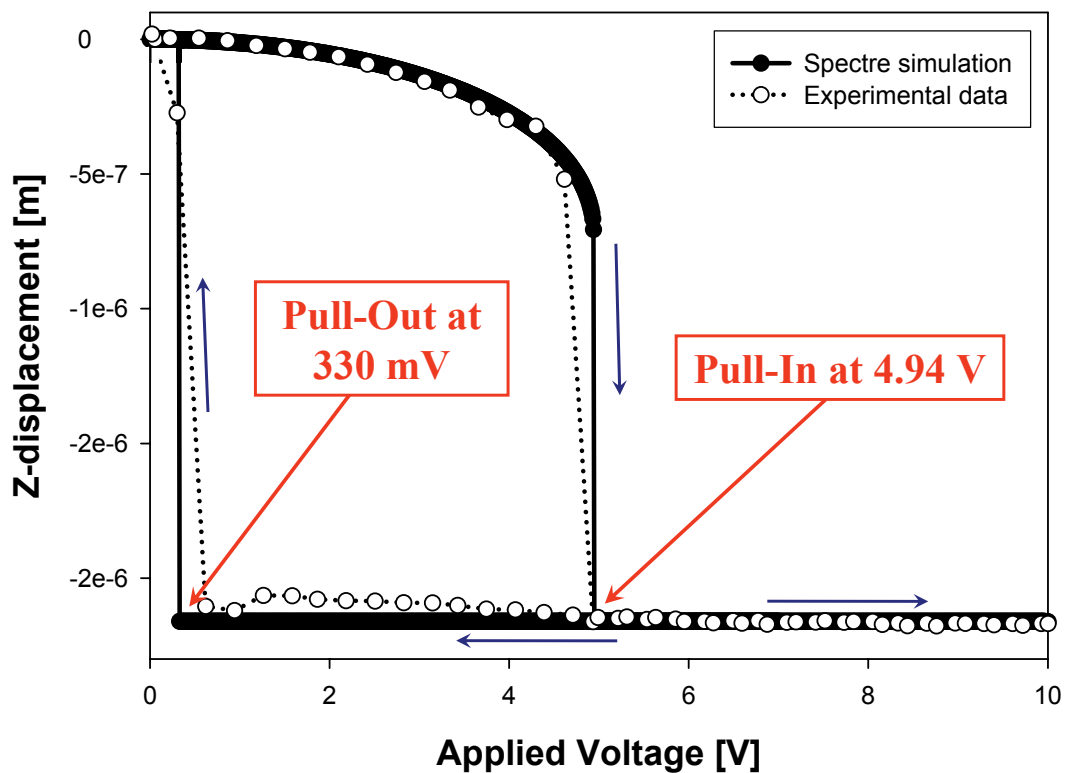


Figure 6.25: Comparison of the plate vertical displacement predicted by Spectre<sup>®</sup> with the experimental measurement.

Both the qualitative and quantitative behaviour of the pull-in and pull-out curves are predicted very well by the compact models in Spectre<sup>®</sup>. The pull-



in occurs for a biasing voltage of 4.94 Volts while the pull-out around 0.33 Volts. Meander structures tend to significantly alleviate the influence of the residual stresses on the stiffness of the flexible structure [81]. This is the reason why the pull-in voltage is accurately predicted by the compact models despite the flexible beam model does not include any accounting for residual stress distribution. The capacitance of the suspended plate depending on the biasing voltage was also experimentally determined and compared with the corresponding values predicted in Spectre<sup>©</sup>. The capacitance comparison is shown in Figure 6.26.

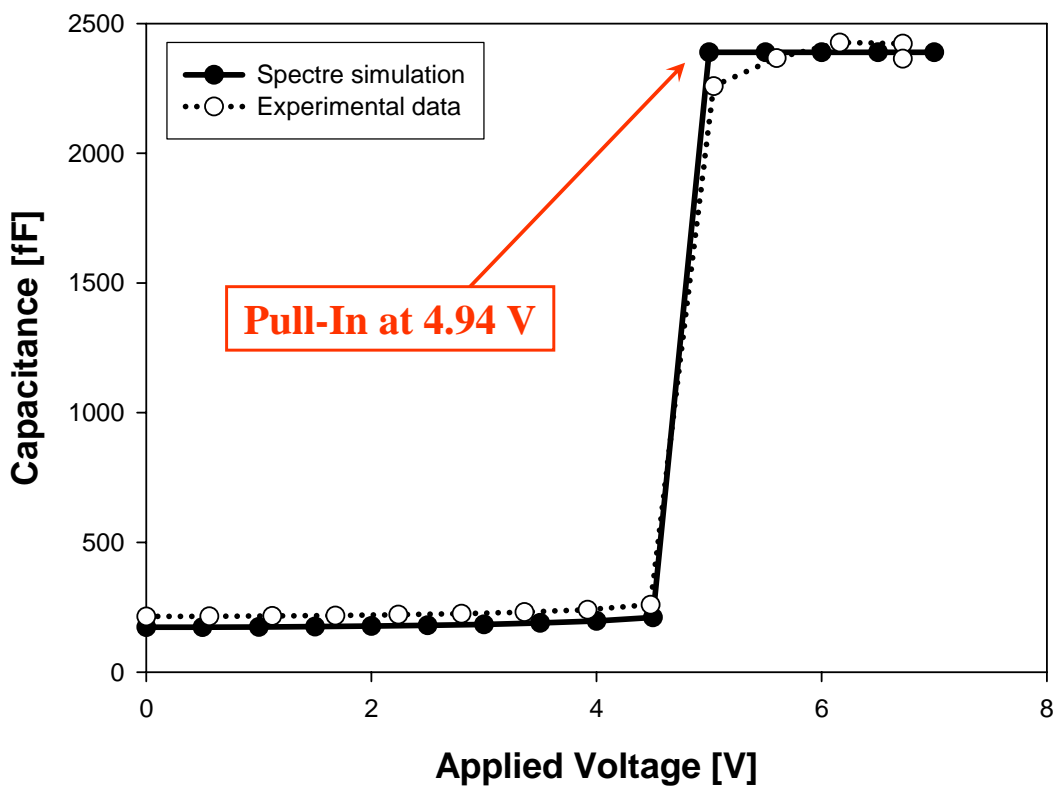


Figure 6.26: Comparison of the plate capacitance predicted by Spectre<sup>©</sup> with the experimental values.

The qualitative behaviour of the capacitance is accurately predicted by the Spectre<sup>©</sup> simulation. However, the model for the capacitance implemented in

VerilogA<sup>®</sup> tends to underestimate its value before the pull-in is reached (i.e. up to about 4.5 V). Indeed, an offset of about 40 fF is noticeable in the plot. On the other hand, the *down-state* capacitance value (i.e. after the pull-in) is accurately predicted in Spectre<sup>®</sup> when a residual mean air gap of about 130 nm is considered between the plate and the substrate after the collapse. This assumption is reasonable taking into account that, because of technological issue, the suspended plate is not perfectly flat but in fact it is slightly bent (upward or downward). Consequently, when the pull-in is reached not the whole plate surface is touching the lower substrate and locally a residual air gap is still present. A further consideration has to be done concerning the RF-MEMS varactor implementation just discussed. The high capacitance value corresponding to the actuated state (i.e. collapsed plate) makes this device usable as a capacitive switch. Indeed, when the pull-in is reached, the intrinsic RF-MEMS varactor behaves as an high capacitance towards ground which diverts to ground the RF signal in input as much as the frequency raises. This characteristic is observable in the S-parameters analysis reported in the following pages.

### 6.2.2 S-parameters Analysis

The intrinsic model has been extended to predict the electromagnetic behaviour of the complete structure, as measured in terms of S-parameters. To this purpose, a network of parasitics lumped circuit elements surrounding the intrinsic RF-MEMS varactor was extracted from the collected S-parameters measurements performed up to 10 GHz. The network accounts for instance for the series inductance of the varactor meanders to ground as well as for the series losses between the input and output ports [88]. It was observed that the lumped elements constituting the parasitics network remain constant over all the analyzed frequency range. The Cadence Virtuoso<sup>®</sup> Schematic of the intrinsic RF-MEMS varactor including all the parasitics is shown in Figure 6.27. In it a symbol is defined for the intrinsic RF-MEMS varactor that corresponds to the Cadence Virtuoso<sup>®</sup> Schematic of Figure 6.22. Moreover, a conductance is connected in parallel to the MEMS varactor and it is set to the mean value of the measured conductance for the up and down state of the suspended plate which is 150  $\mu$ S. Finally, to decouple the biasing voltage from the RF signal an inductor with a large value (1 mH) is connected in series to the voltage generator.

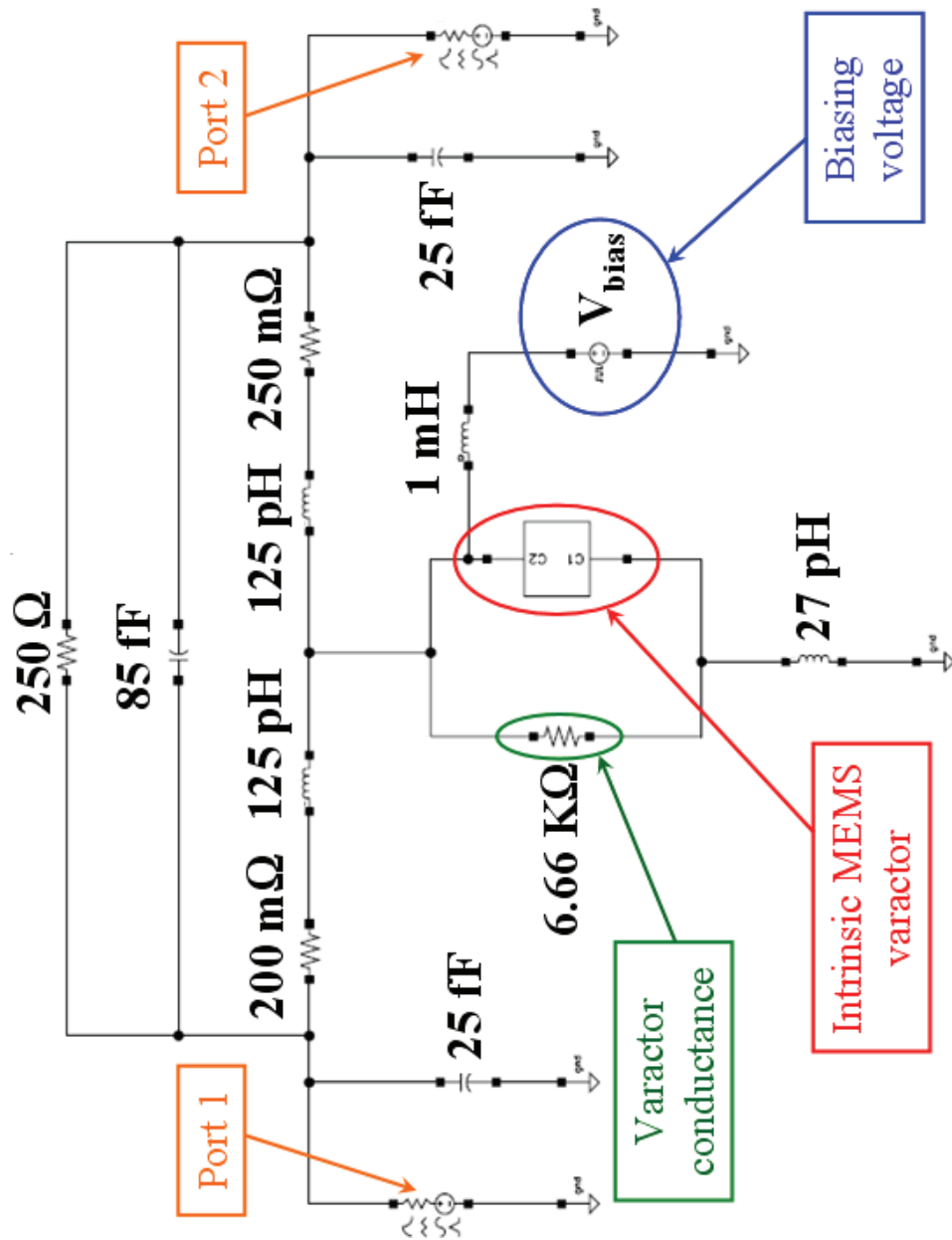


Figure 6.27: Cadence Virtuoso<sup>®</sup> Schematic of the intrinsic RF-MEMS varactor including all the parasitics. The symbol of the intrinsic varactor corresponds to the scheme of Figure 6.22.

S-parameters measurements were performed up to 13.5 GHz for the non-actuated and actuated MEMS varactor state. Among these, experimental S-parameters for a biasing voltage of 0 V (i.e. non actuated varactor) and of 5.6 V (i.e. actuated varactor) are chosen. It must be remembered that the RF-MEMS varactor pull-in voltage is 4.94 V (see Figure 6.25). Spectre<sup>®</sup> S-parameters simulations of the network of Figure 6.27 are performed for the same two biasing voltage values. Comparisons of the measured reflection and transmission parameters for the up-state (0 V) with the Spectre<sup>®</sup> simulations are shown in Figure 6.28 and Figure 6.29 respectively. On the other hand, comparisons of the measured reflection and transmission parameters for the down-state (5.6 V) with the Spectre<sup>®</sup> simulations are shown in Figure 6.30 and Figure 6.31. When the RF-MEMS varactor is in the up-state a small offset between the experimental and simulated curves is observable. Moreover, when the switch is actuated, the curves for the S11 parameters are superposed over all the frequency range, while, concerning the transmission parameter, these begin to divert from each other beyond about 8 GHz.

A good agreement between experimental and simulated data are also noticeable referring to the rotations on the Smith chart. The Smith charts of the S11 and S21 parameters for the switch up-state and down-state are reported in Figures 6.32, 6.33, 6.34 and 6.35 respectively.

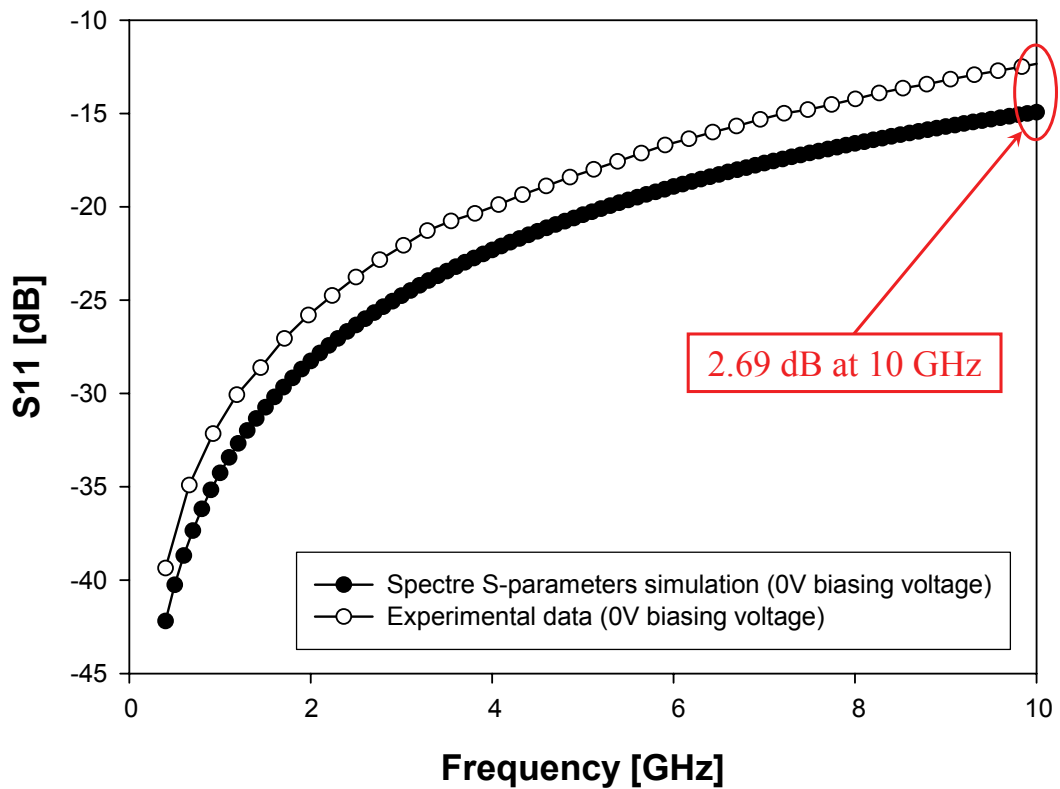


Figure 6.28: Comparison of the experimental S11 parameter with the Spectre<sup>®</sup> simulation when a 0 V biasing voltage is applied to the MEMS varactor (up-state).

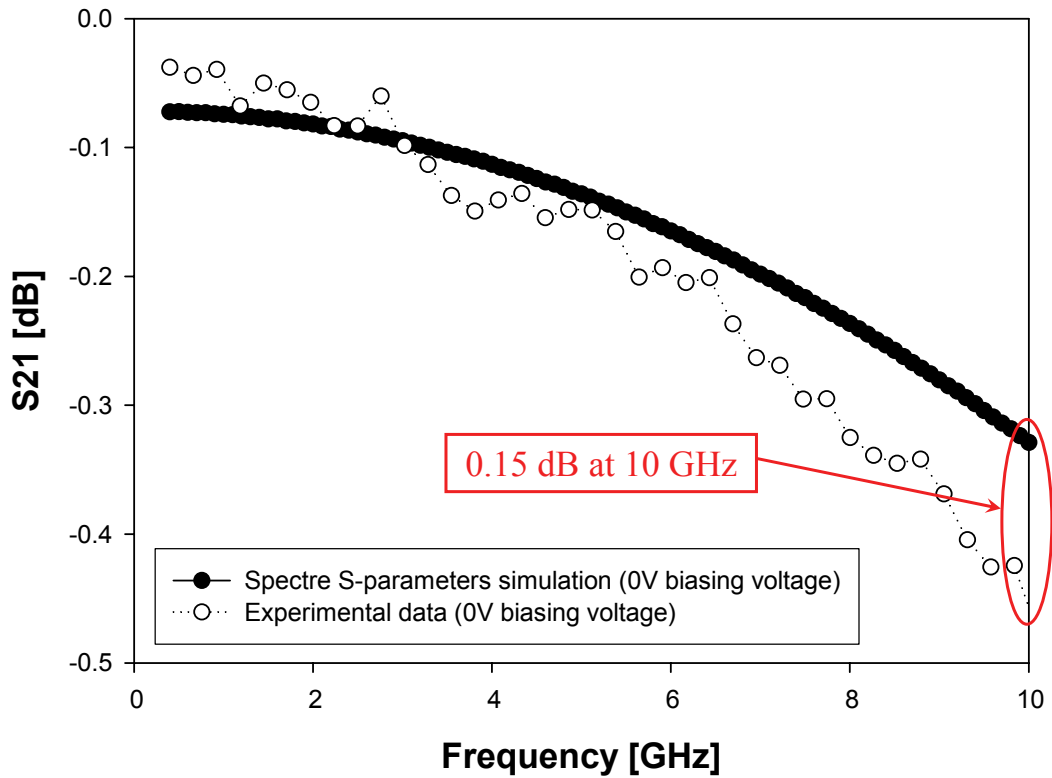


Figure 6.29: Comparison of the experimental S21 parameter with the Spectre<sup>®</sup> simulation when a 0 V biasing voltage is applied to the MEMS varactor (up-state).

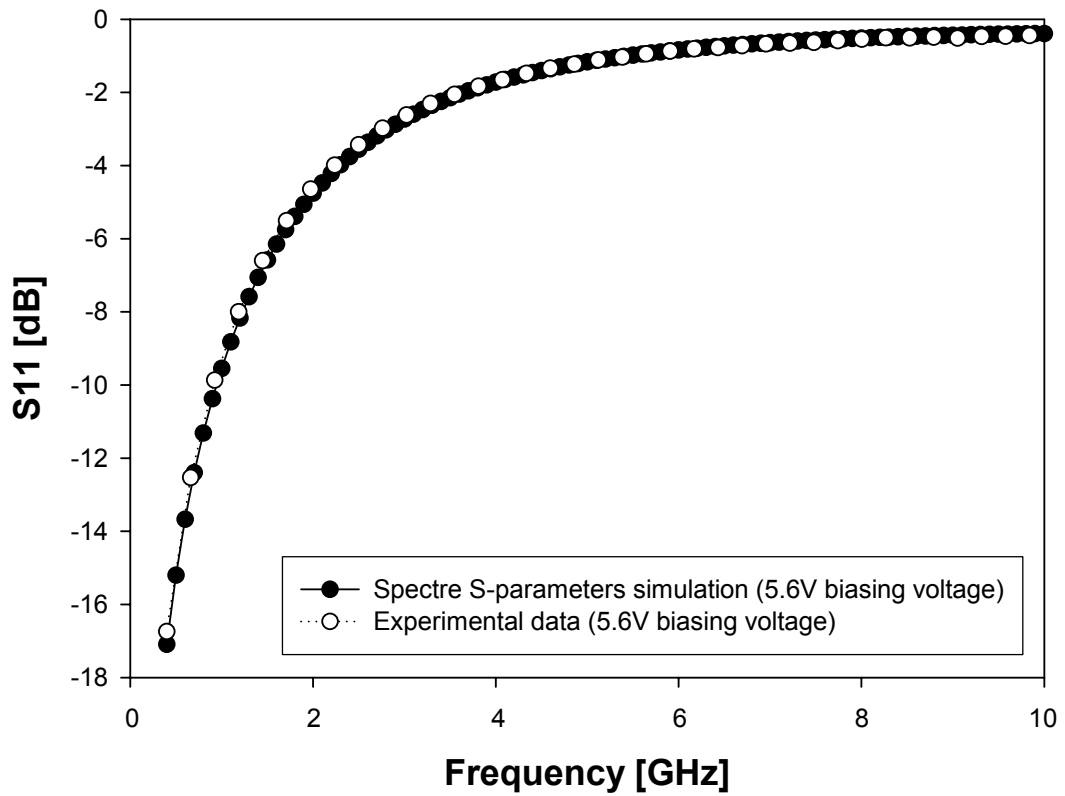


Figure 6.30: Comparison of the experimental S11 parameter with the Spectre<sup>®</sup> simulation when a 5.6 V biasing voltage is applied to the MEMS varactor (down-state).

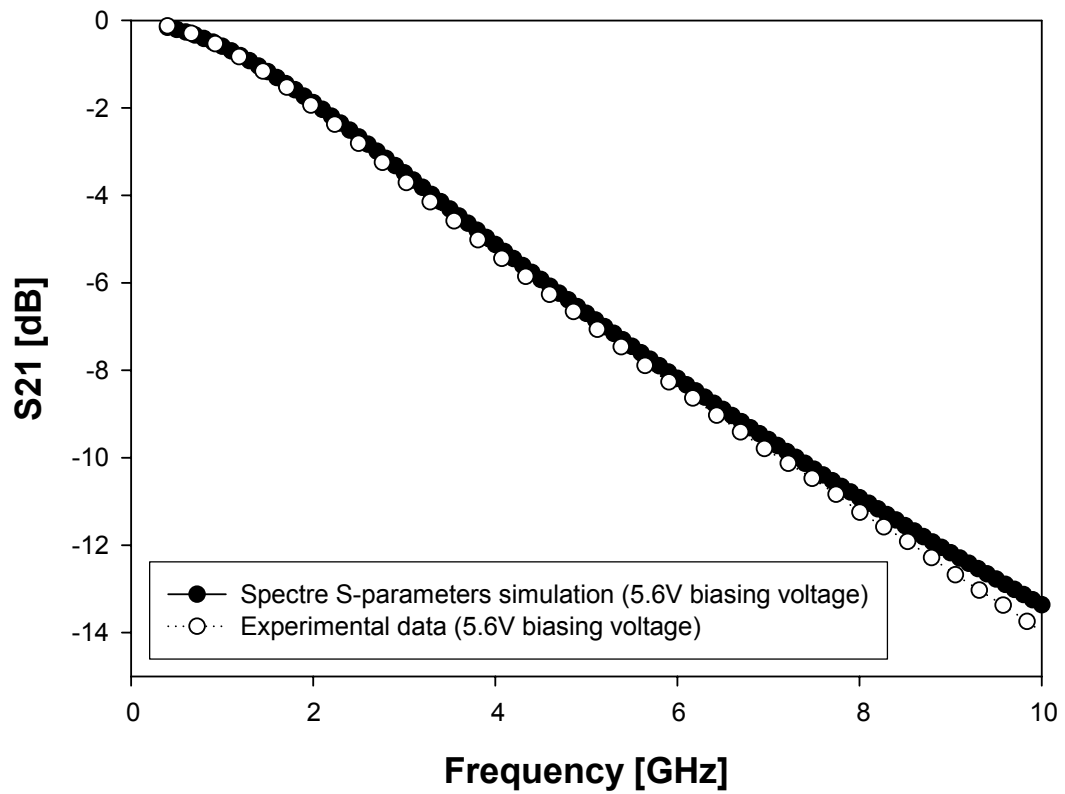


Figure 6.31: Comparison of the experimental S21 parameter with the Spectre<sup>®</sup> simulation when a 5.6 V biasing voltage is applied to the MEMS varactor (down-state).



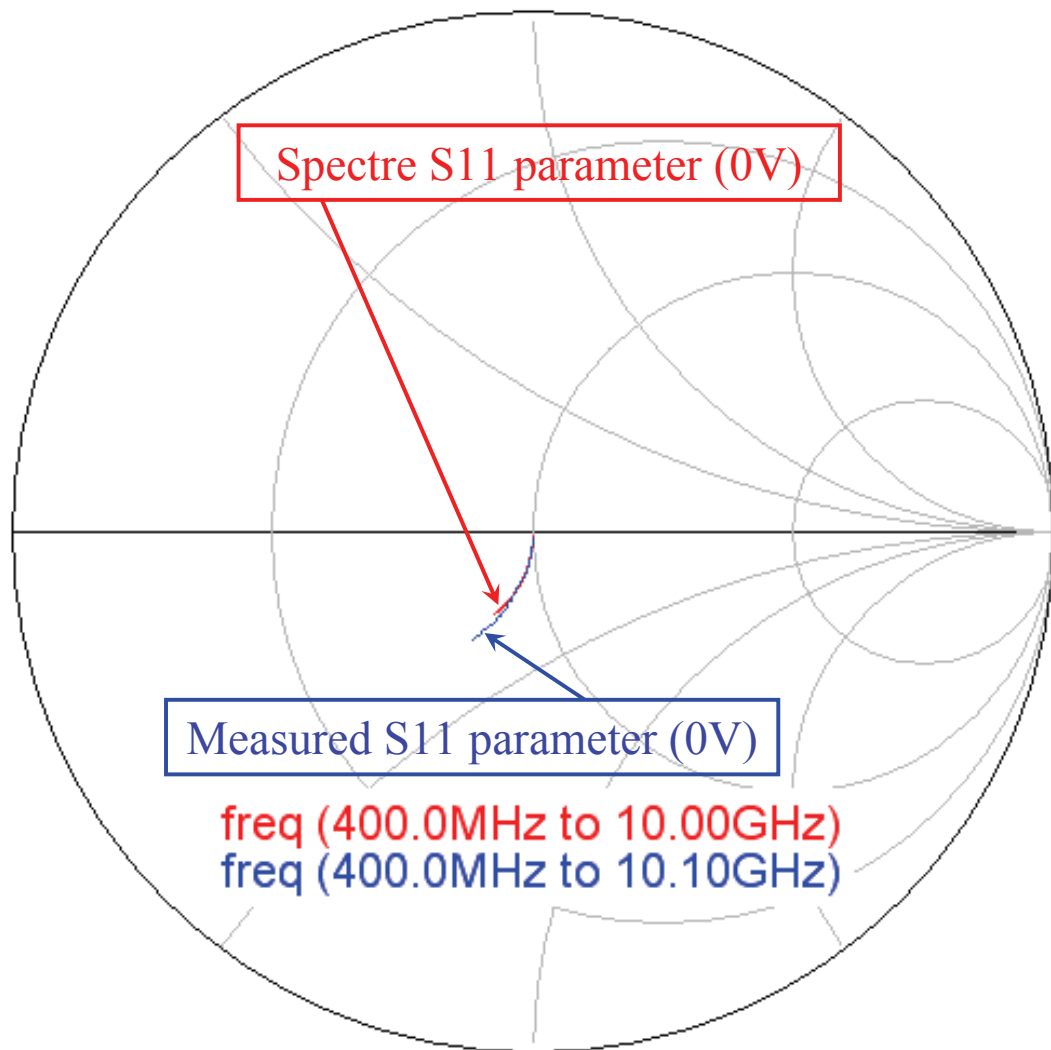


Figure 6.32: Comparison of the Smith chart of the experimental S11 parameter with the Spectre<sup>®</sup> simulation when a 0 V biasing voltage is applied to the MEMS varactor (up-state).

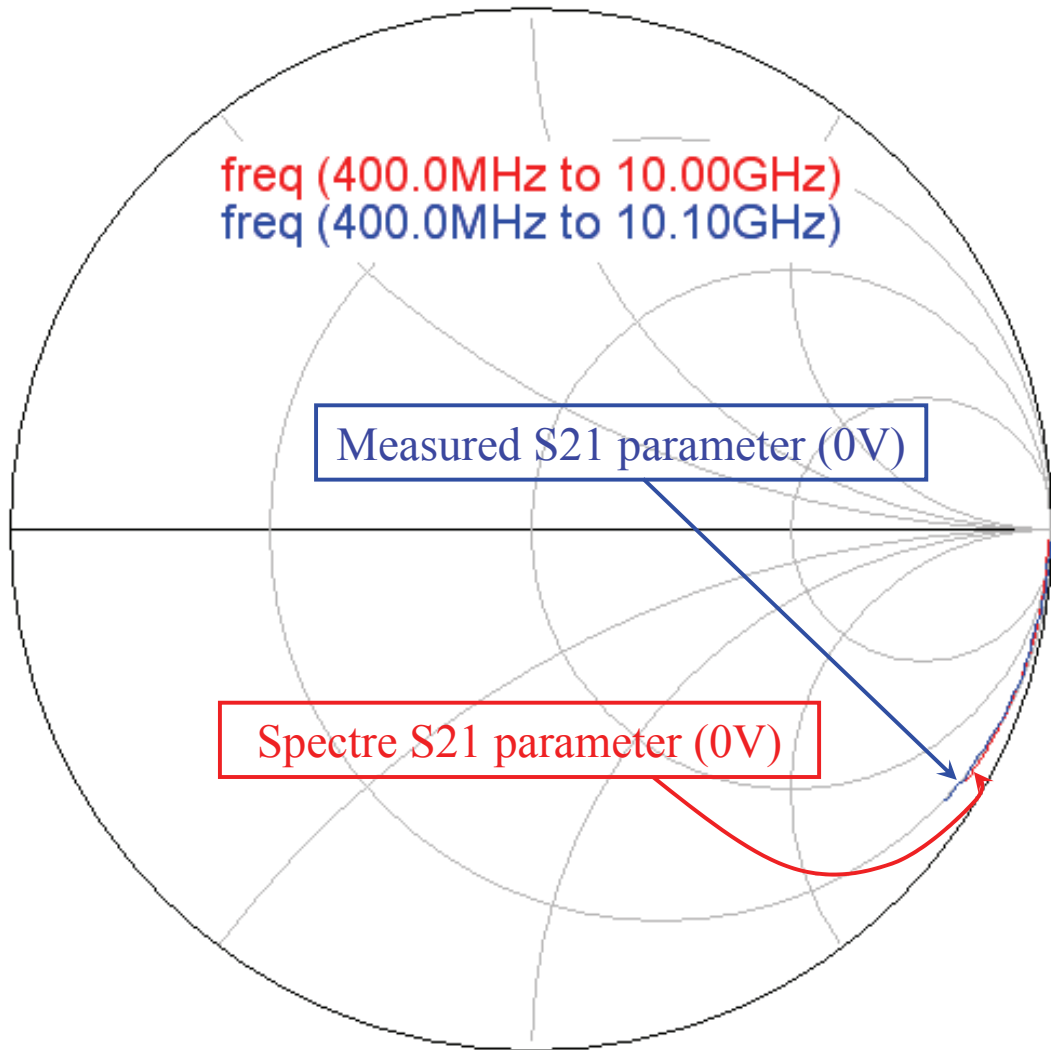


Figure 6.33: Comparison of the Smith chart of the experimental S21 parameter with the Spectre<sup>®</sup> simulation when a 0 V biasing voltage is applied to the MEMS varactor (up-state).

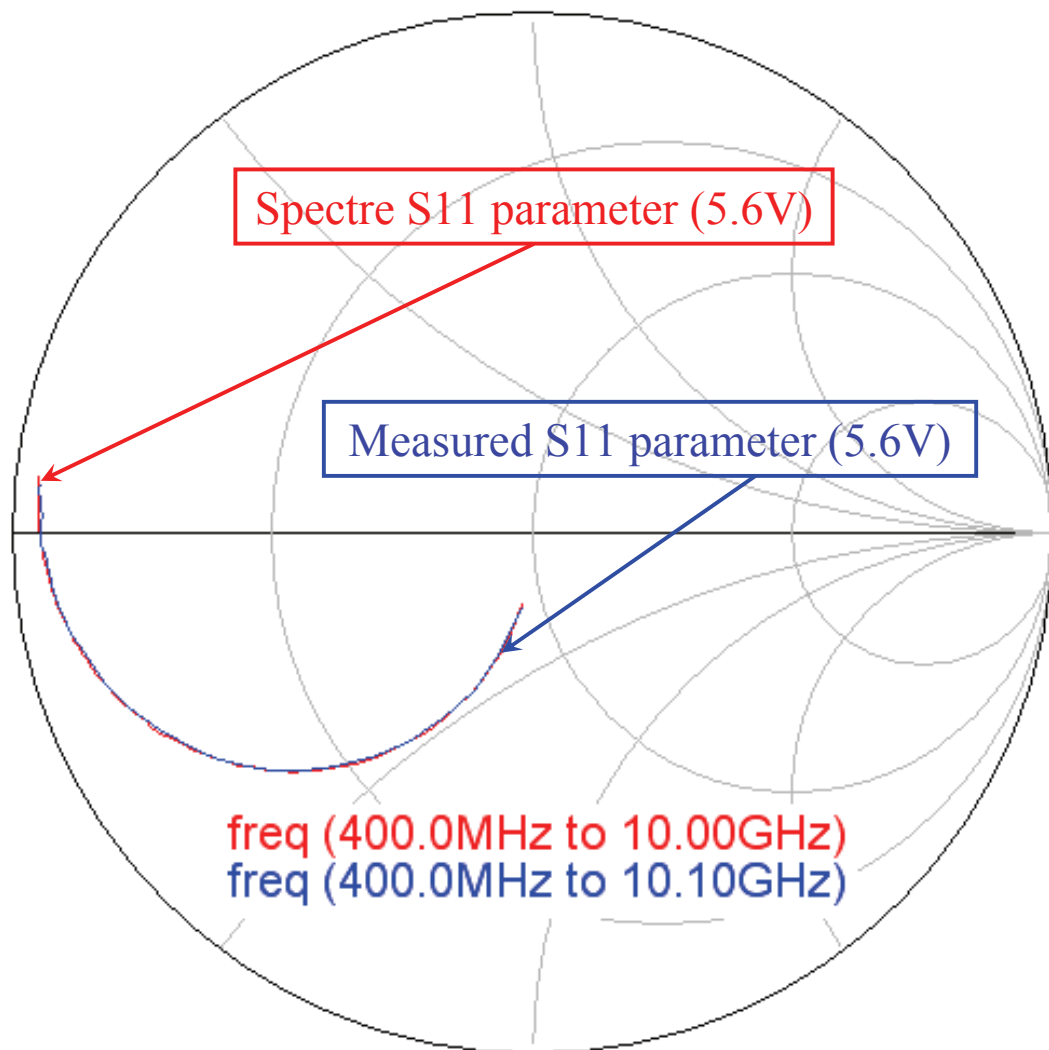


Figure 6.34: Comparison of the Smith chart of the experimental S11 parameter with the Spectre<sup>®</sup> simulation when a 5.6 V biasing voltage is applied to the MEMS varactor (down-state).

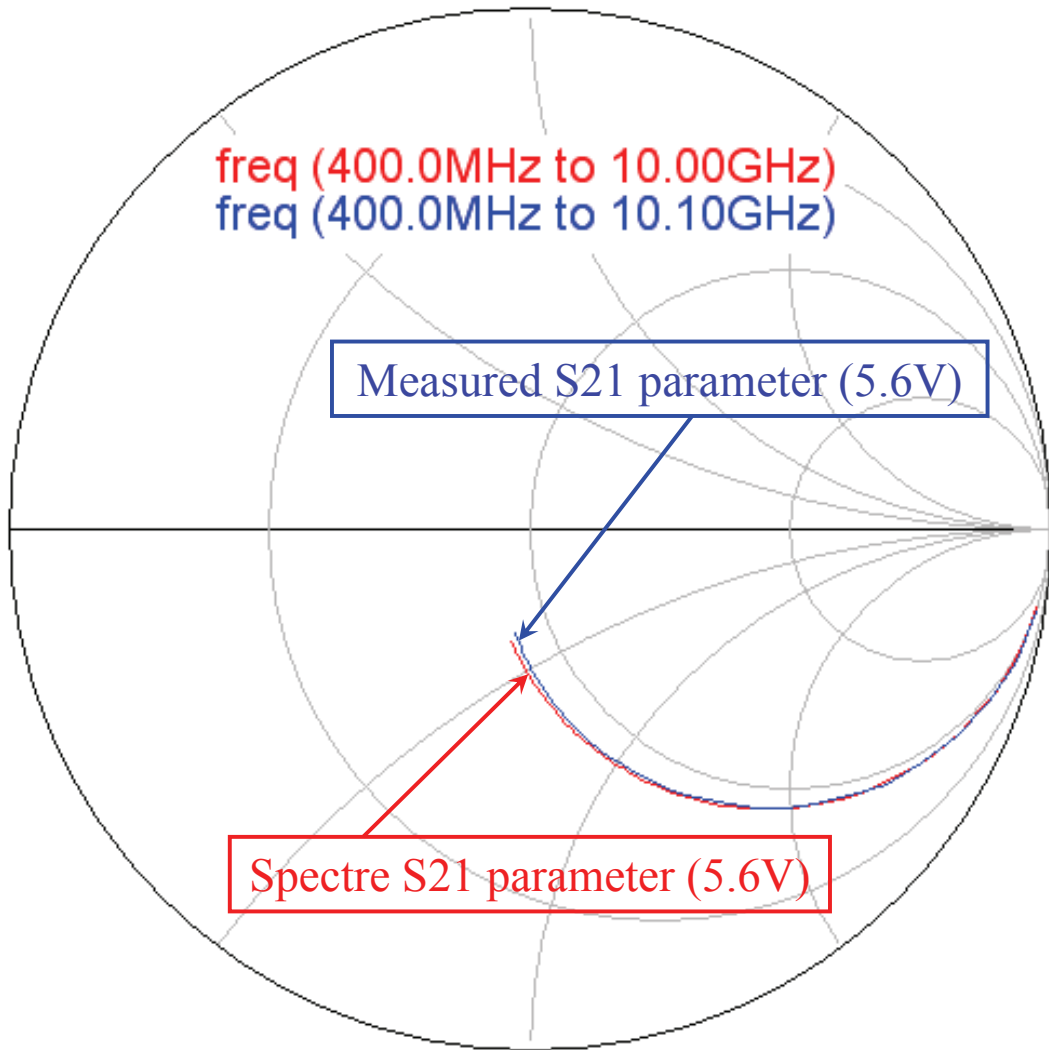


Figure 6.35: Comparison of the Smith chart of the experimental S21 parameter with the Spectre<sup>®</sup> simulation when a 5.6 V biasing voltage is applied to the MEMS varactor (down-state).

The S-parameters have been measured for several values of the biasing voltage. This makes possible to plot the S-parameters at a certain frequency versus the biasing voltage. The frequency of the observation is chosen to be 10 GHz. Concerning the Cadence Virtuoso<sup>®</sup> Schematic of Figure 6.27, it is simulated in Spectre<sup>®</sup> for a fixed frequency of 10 GHz and the biasing voltage is swept between 0 and 6 V. Comparisons of the experimental S11 and S21 parameters with the corresponding ones simulate in Spectre<sup>®</sup> are shown in Figure 6.36 and Figure 6.37 respectively. The agreement of the Spectre<sup>®</sup> simulations with the measurements is rather good. An offset of about 2 dB is noticeable in the low frequency range concerning the S11 parameter plot.

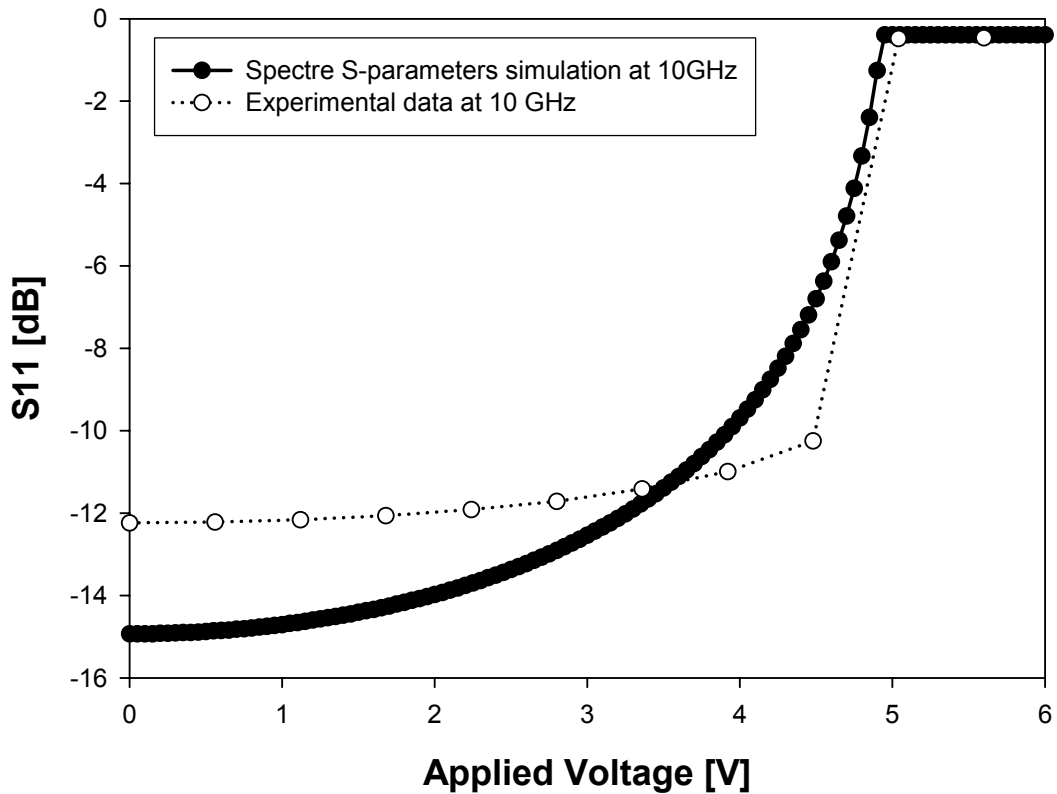


Figure 6.36: Comparison of the experimental S11 parameter with the Spectre<sup>®</sup> simulation at 10 GHz for a biasing voltage sweeping between 0 and 6 V.

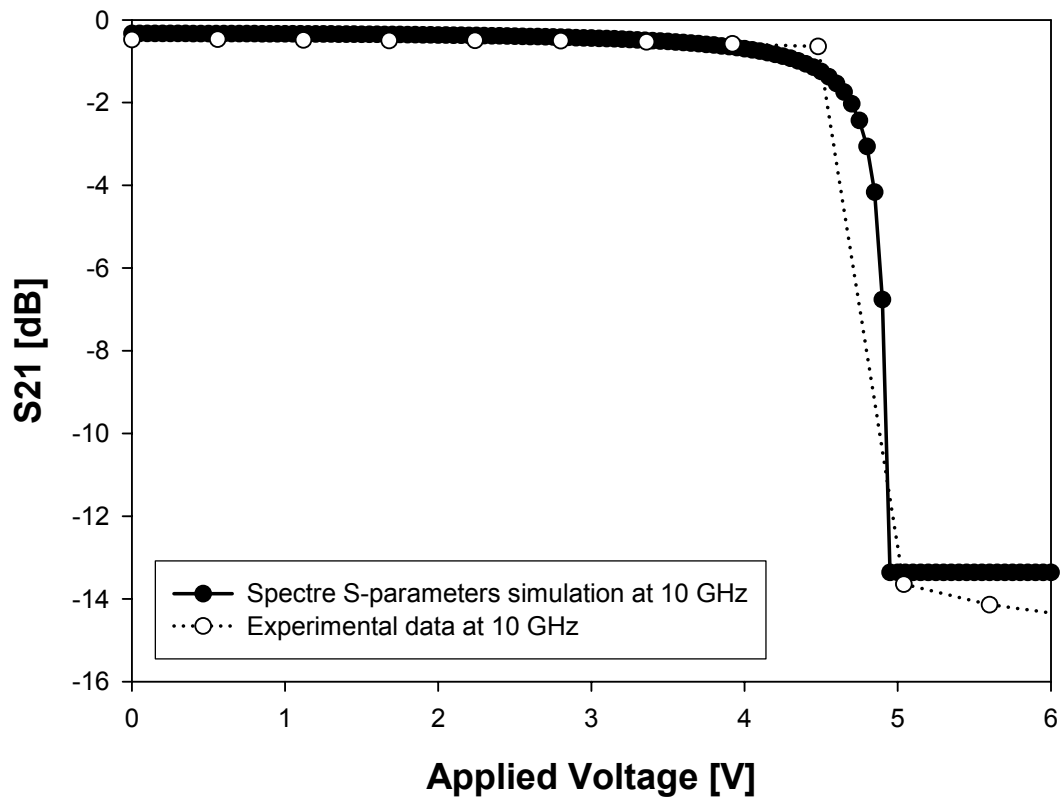


Figure 6.37: Comparison of the experimental S21 parameter with the Spectre<sup>®</sup> simulation at 10 GHz for a biasing voltage sweeping between 0 and 6 V.

The S-parameters plots reported above show the capacitive switch characteristic of the RF-MEMS varactor discussed in earlier. For instance, looking at the transmission parameter plot of Figure 6.37, an offset of about 14 dB of the S21 parameter is observable between the up and down plate positions.

### 6.2.3 Simulation of the Packaged RF-MEMS Varactor

As a proof of concept, a simulation of the RF-MEMS varactor within Spectre<sup>©</sup> also accounting for the presence of the package is set up. On this purpose, a FEM simulation to extract the S-parameters behaviour of through-vertical vias is performed in Ansoft HFSS<sup>TM</sup>. For more details about the packaging solution refer to Chapter 5. The schematic of the vertical via in Ansoft HFSS<sup>TM</sup> is shown in Figure 6.38. Two short CPW's ( $400\ \mu\text{m}$ ) are placed both on top of the package and on the device wafer plane in order to contact both the top and bottom side via sections. Ports are placed on the CPW's. This is done in order not to place ports directly on top and bottom vias openings. Indeed, in the latter case the discontinuities due to the top via connection with the top-side pads as well as the bottom vias connection to the capped device would be neglected. Via diameter is  $70\ \mu\text{m}$  while the capping substrate (not shown in figure) is  $350\ \mu\text{m}$  thick. The S-parameters are exported from Ansoft HFSS<sup>TM</sup> in Touchstone<sup>©</sup> format [83] and imported in Spectre<sup>©</sup> which allows to link this data file to a two-port symbol [9]. To this purpose two two-port blocks are connected to the input and output ports of the network of Figure 6.27. These represent the effect of through vertical vias and the corresponding Spectre<sup>©</sup> network is reported in Figure 6.39.

This implementation does not take into account the additional parasitics due to the vicinity of the capping substrate to the RF-MEMS device. S-parameters simulations are performed in Spectre<sup>©</sup> for the varactor up and down state shown in previous pages, i.e. with a biasing voltage of 0 V and 5.6 V. Simulated reflection and transmission parameters are compared for the uncapped varactor schematic (Figure 6.27) with the corresponding ones for the capped network accounting for vertical vias (Figure 6.39). These are shown for the varactor up and down state in subsequent Figures 6.40, 6.41, 6.42 and 6.43. As it is observable from the S-parameters plots the introduction of the package does not largely affect the RF behaviour of the RF-MEMS varactor. However, it must be taken into account that this simulation is just a proof of concept. Indeed it shows how it is possible to reach a complete description of an RF-MEMS devices both accounting for the parasitics and the package within Spectre<sup>©</sup>. This method is pursuable when experimental data are available.

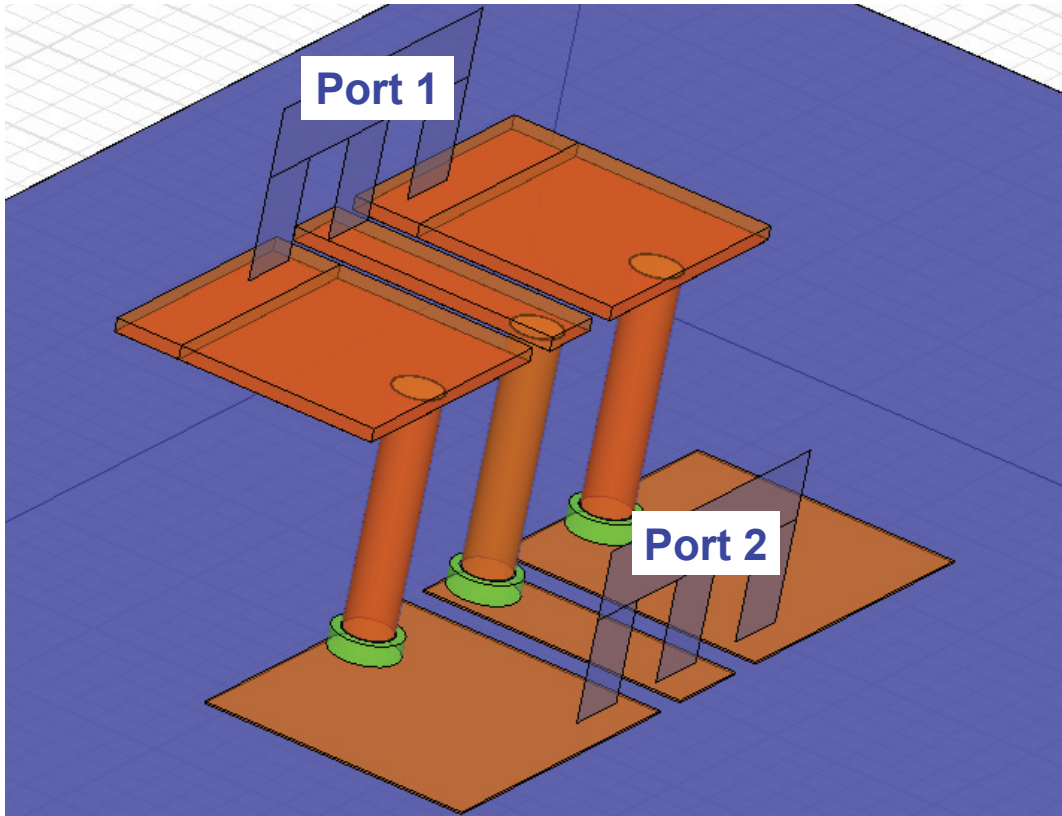


Figure 6.38: Ansoft HFSS™ schematic of the vertical vias. A short CPW is placed both on top of the package and on the device wafer plane.



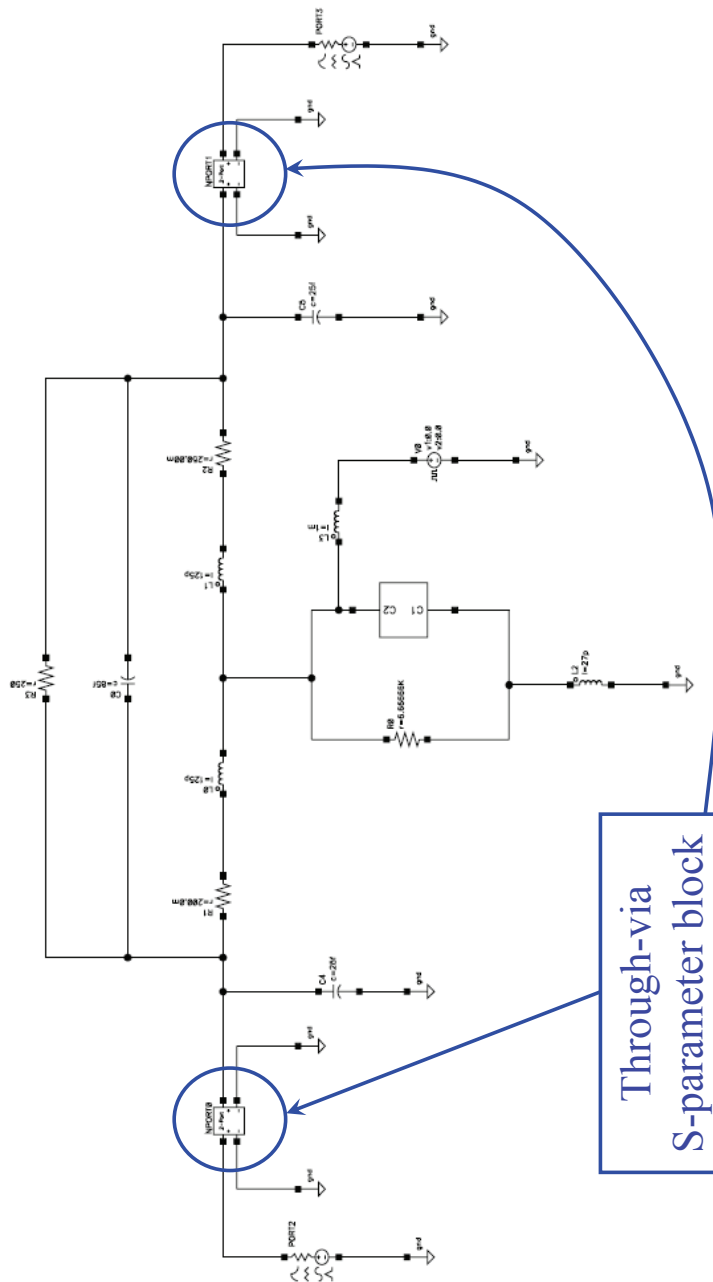


Figure 6.39: Cadence Virtuoso<sup>®</sup> Schematic of the RF-MEMS varactor also including the parasitics associated to the package vertical through-vias.

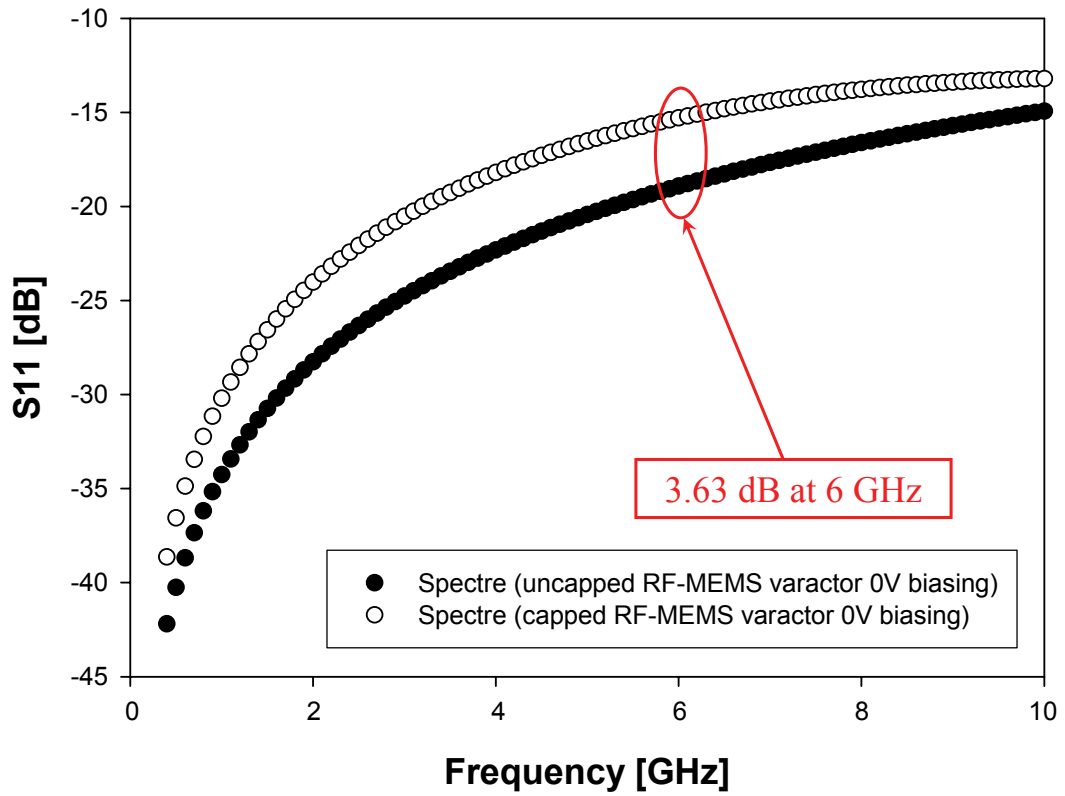


Figure 6.40: Simulated S11 parameter for the uncapped RF-MEMS varactor (up-state) compared with the one accounting for vertical vias.

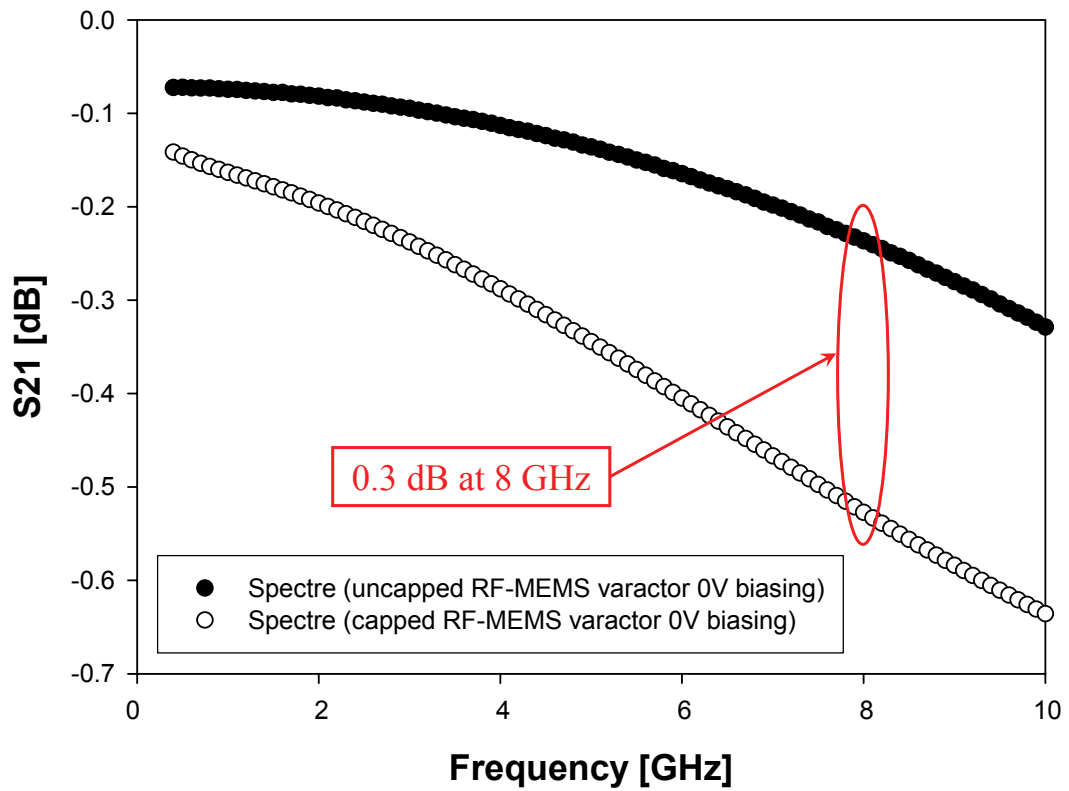


Figure 6.41: Simulated S21 parameter for the uncapped RF-MEMS varactor (up-state) compared with the one accounting for vertical vias.

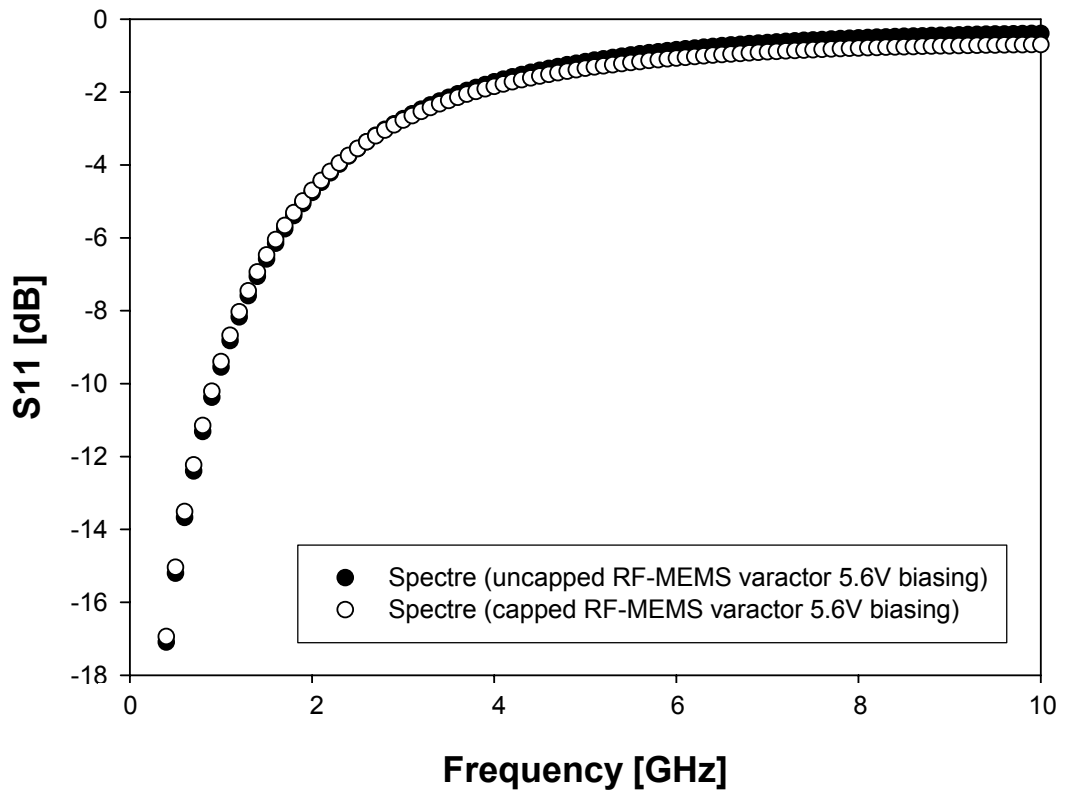


Figure 6.42: Simulated S11 parameter for the uncapped RF-MEMS varactor (down-state) compared with the one accounting for vertical vias.

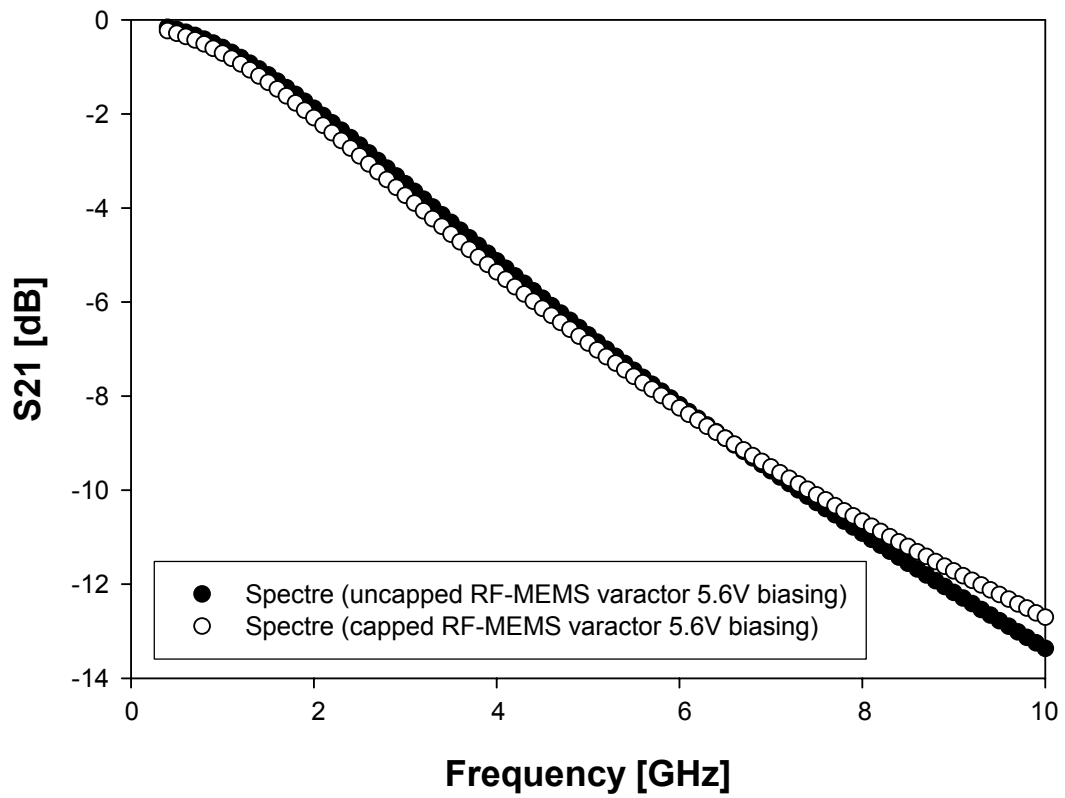


Figure 6.43: Simulated S21 parameter for the uncapped RF-MEMS varactor (down-state) compared with the one accounting for vertical vias.

### 6.2.4 Transient Analysis

The further simulation of the MEMS model library components is performed in dynamic regime. A squared voltage with a period of 2.5 msec (400 Hz) is applied to the suspended plate. The voltage is equal to 4 V for 1.25 msec and equal to 0 V in the other half a period (50% duty-cycle). Since the varactor actuation voltage is 4.94 V (see Figure 6.25) the plate does not collapse on the substrate during this analysis.

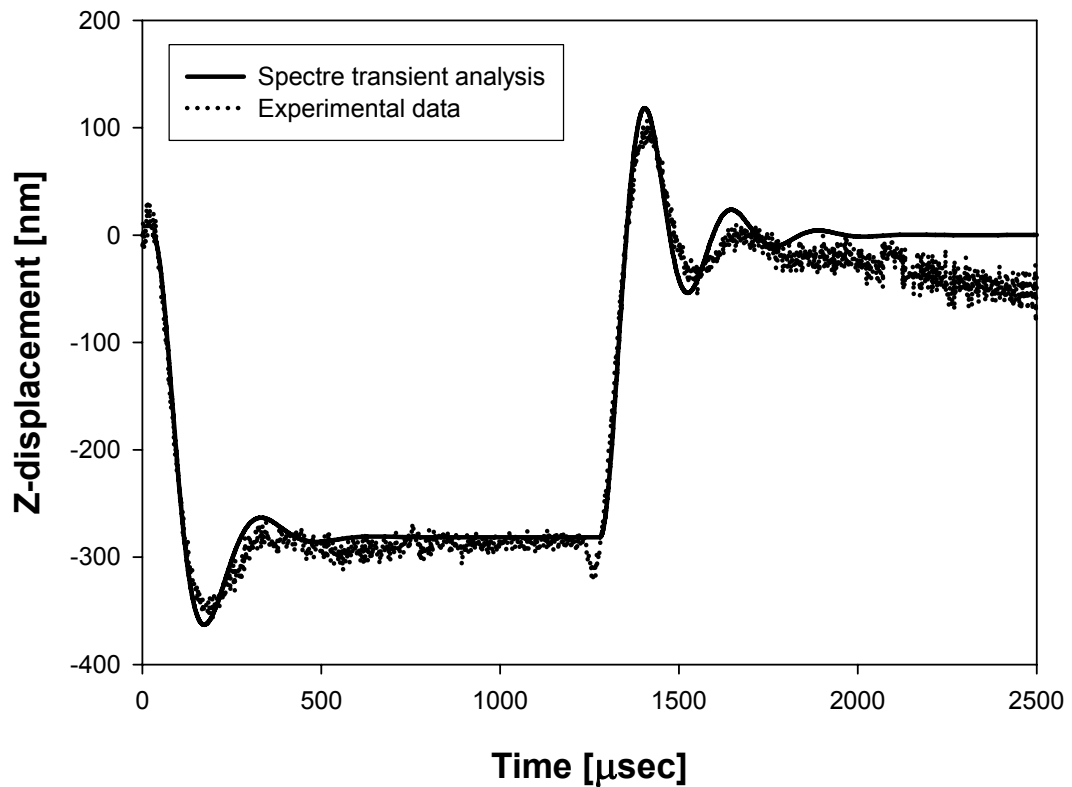


Figure 6.44: Experimental transient behaviour of the RF-MEMS varactor compared with the Spectre<sup>®</sup> prediction. The peak value of the biasing voltage is 4 V (lower than the pull-in voltage).

A transient simulation of the structure shown in Figure 6.22 is performed in Spectre<sup>©</sup> applying the same 400 Hz control voltage mentioned above. The comparison of the simulated and experimental varactor vertical displacement is reported in Figure 6.44. This analysis allows to validate the implemented model for the viscous damping effect related to the plate with holes and to the Euler beam, shown in the corresponding Chapters 3 and 4. The qualitative behaviour of Spectre<sup>©</sup> curve fits very well the experimental data. In particular, the overshoots during the varactor lowering (around 200  $\mu$ sec) and raising (around 1.4 msec) are predicted very accurately by compact models. Moreover, the slopes of the two vertical transitions corresponding to the edges of the biasing voltage correspond to the measured ones. The transient duration before the plate reaches the stable low and high position in Spectre<sup>©</sup> are also very close to the experimental ones. This type of analysis is rather critical as it involves the whole behaviour of the compact models, also including the inertia and the viscous damping effects. Because of this consideration, the obtained results should be considered very good. The small negative peak in the experimental curve of Figure 6.44 corresponding to the lowering of the control voltage (around 1.3 msec) is very likely due to a glitch of the control signal itself. The lowering of the plate after the pull-out and the extinction of oscillations in the experimental curve (Figure 6.45 after about 1.8 msec) is due to a measurement problem. In Spectre<sup>©</sup> simulation viscosity of air was set to 17.9  $\mu$ Pasec. The last performed analysis is carried out applying the control voltage with a peak value of 5 V which is just above the pull-in voltage. The experimental versus simulated behaviour of the varactor vertical displacement is shown in Figure 6.45. Also in this case the agreement of the simulated curve with the experimental one is very good. In this case the effect of gas rarefaction when the air gap is very small was introduced in the plate and beam viscous damping model. The release transient is not analyzed because the corresponding experimental data is not available. A constant delay of about 30  $\mu$ sec of the up and down transitions in the experimental data was observed with respect of the simulations. This is an intrinsic delay within the measurements system setup. For this reason, a delay of 30  $\mu$ sec was applied to the control biasing voltage in Spectre<sup>©</sup> with respect to the initial instant of the transient analysis. Such a delay was applied to both plots of Figures 6.44 and 6.45.

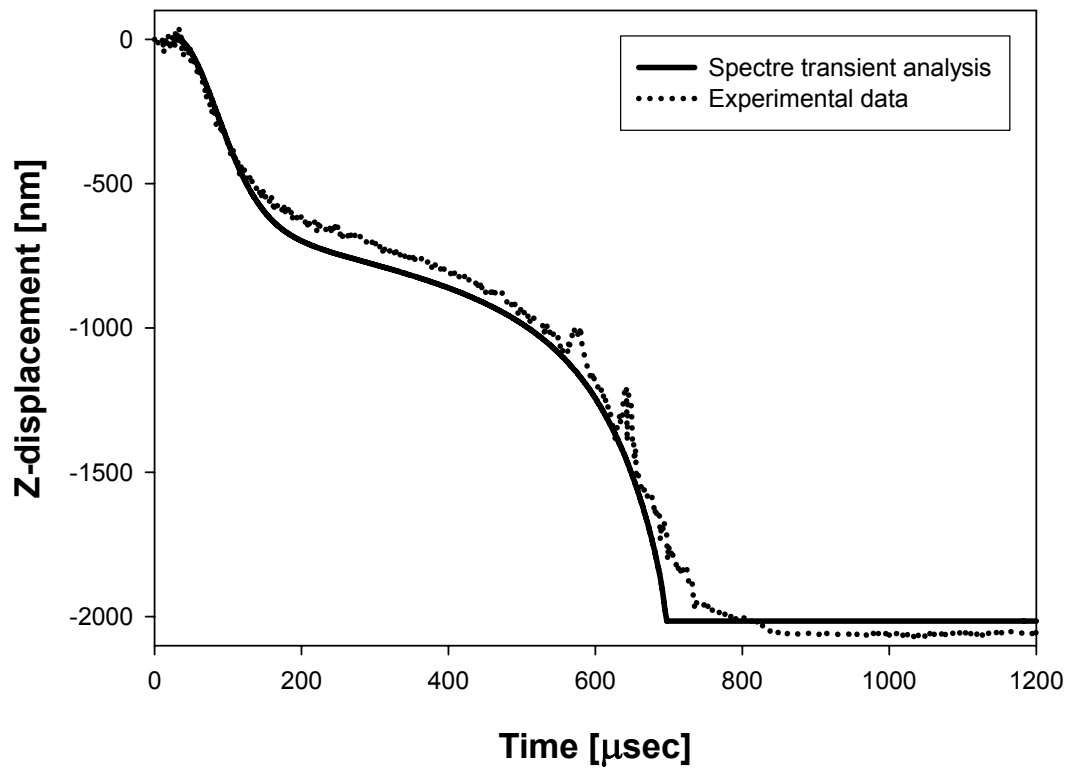


Figure 6.45: Experimental transient behaviour of the RF-MEMS varactor compared with the Spectre<sup>®</sup> prediction. The peak value of the biasing voltage is 5 V (higher than the pull-in voltage).



### 6.3 An RF-MEMS/CMOS Voltage Controlled Oscillator (VCO)

The last section of this chapter reports on an hybrid implementation of a Voltage Controlled Oscillator (VCO) [84]. The oscillator is designed in standard CMOS technology and implemented with the design-kit provided by AMS<sup>©</sup> (0.35  $\mu\text{m}$  HBT BiCMOS S35 technology) [85]. Whereas, the varactors of the LC-tank are implemented in MEMS technology with the compact models previously shown through the thesis. The Cadence<sup>©</sup> Virtuoso Schematic of the VCO is shown in Figure 6.46. The two symbols representing the tunable capacitors are realized with a suspended rigid plate and with four straight beams connected to its corners. Each of them corresponds to the Cadence Virtuoso<sup>©</sup> Schematic of Figure 6.47. The two inductors within the LC-tank in Figure 6.46 are also included in the design-kit provided by AMS<sup>©</sup> and mentioned above. Two RF-MEMS varactors are included in the symmetric LC-tank scheme providing also for decoupling of the controlling voltage from the oscillator RF outputs. For the same reason a capacitor (1 pF) is placed between the controlling voltage generator and the bias voltage supply ( $V_{\text{DD}} = 3.3\text{ V}$ ). Concerning the structure of Figure 6.47 both the central plate width and length are 500  $\mu\text{m}$  while the thickness is 4.8  $\mu\text{m}$ . On its surface 12 holes along  $x$  and 12 along  $y$  are distributed of dimensions 20x20  $\mu\text{m}^2$ . The four straight beams are 75  $\mu\text{m}$  long, while their width and thickness are 10  $\mu\text{m}$  and 1.8  $\mu\text{m}$  respectively. Finally, the gap between the suspended plate and the substrate is 3  $\mu\text{m}$ . Depending on the controlling voltage applied to the common node between the RF-MEMS varactors their capacitance changes and consequently the oscillation frequency of the entire VCO. Transient analyses are performed in Spectre<sup>©</sup> for different controlling voltages lower than the pull-in of the structure in Figure 6.47 (i.e. 15.6 V). The VCO tuning characteristic (frequency versus biasing voltage) is shown in Figure 6.48. The capacitance of each RF-MEMS varactor and the corresponding VCO oscillation frequency are reported in Table 6.1. The VCO output voltage versus time for the transient simulation with zero biasing voltage is shown in Figure 6.49. It is observable that after a few periods the oscillation becomes stable.

The just shown RF-MEMS/CMOS VCO implementation represents a meaningful example about the utilization of the mixed-domain simulation environment (electrical and mechanical) discussed in the thesis.

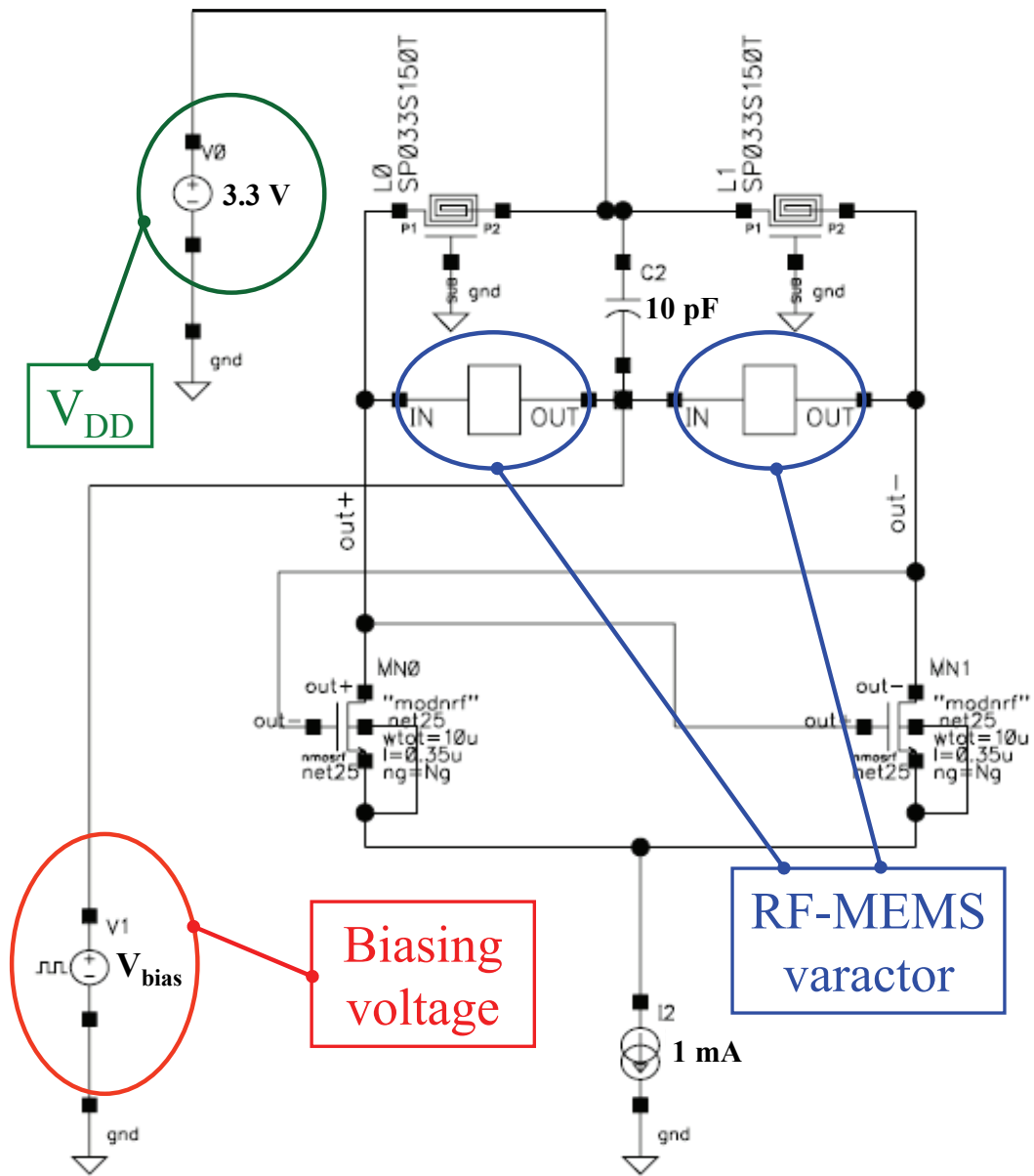


Figure 6.46: Cadence Virtuoso<sup>®</sup> Schematic of the VCO with the CMOS oscillator in AMS technology and the RF-MEMS LC-tank.

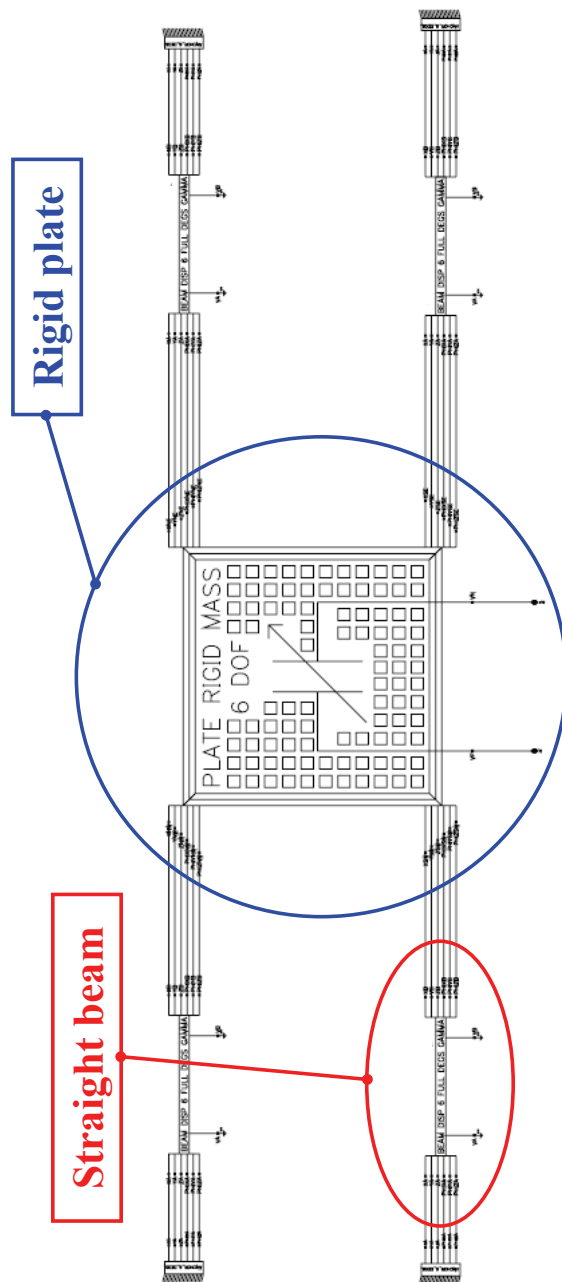


Figure 6.47: Cadence Virtuoso<sup>©</sup> Schematic corresponding to each of the two RF-MEMS varactors in Figure 6.46.

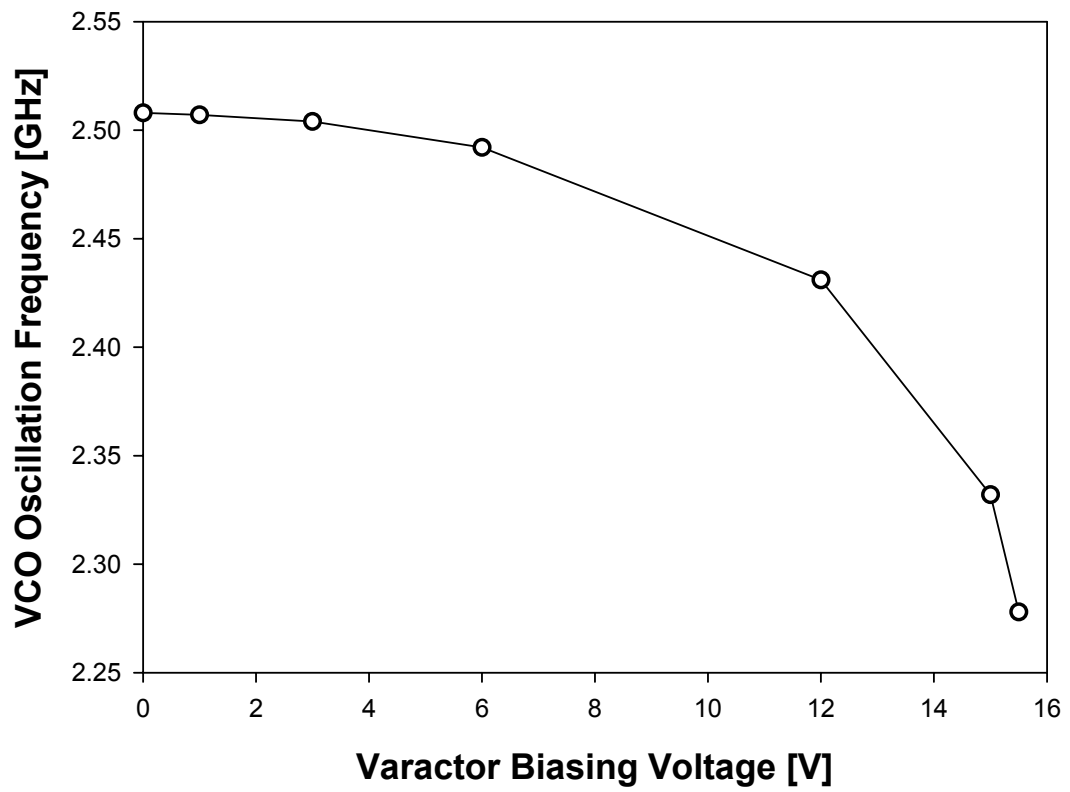


Figure 6.48: VCO oscillation frequency versus biasing voltage applied to the RF-MEMS varactors (tuning characteristic).

Biasing Voltage (V)	Capacitance (fF)	VCO Frequency (GHz)
0	597	2.508
1	598	2.507
3	601	2.504
6	611	2.492
12	671	2.431
15	775	2.332
15.5	838	2.278

Table 6.1: VCO oscillation frequency depending of the biasing voltage applied to the RF-MEMS varactors of the LC-tank.

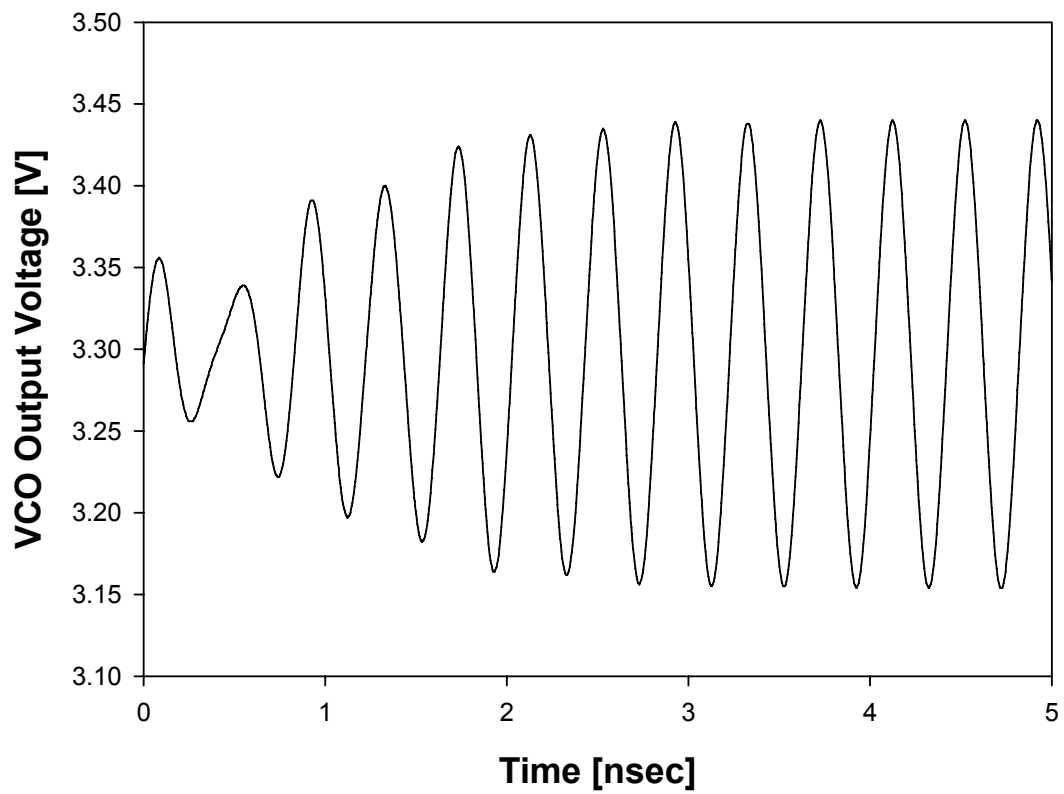


Figure 6.49: VCO output voltage versus time simulated in Spectre<sup>®</sup> when no biasing voltage is applied to the RF-MEMS varactors.

## Conclusions and Further Work

MEMS (Micro Electro-Mechanical System) technology for Radio Frequency (RF) applications has emerged in recent years as a valuable solution in order to fabricate passive components (e.g. inductors, varactors, switches etc.) with remarkable performances, like very high quality factor (Q-Factor) and wide capacitance tuning ranges. However, RF-MEMS technology is not mature yet for a large scale application on the market because of few very important open issues. In this thesis two of them have been addressed in details.

The first one is related to the creation of a multi-domain (electromechanical) fast simulation tool for the analysis of RF-MEMS devices within the Cadence<sup>©</sup> environment. The urge for developing such a simulation environment is due on one side to the need for a unique tool within which parameters belonging both to the mechanical and electrical physical domains can be analyzed. On the other hand, the fact of dealing with very small simulation time and memory use make this tool a valuable alternative to Finite Element (FEM)-based software. Moreover, the availability of the MEMS library within Cadence<sup>©</sup> allows the interfacing of its models to standard CMOS libraries, enabling the simulation of hybrid RF-MEMS/CMOS blocks. MEMS elementary models included in the library are developed according to the concept of compact modeling and are implemented in VerilogA<sup>©</sup> language. Their interconnection allows obtaining of complex topologies for RF-MEMS devices, like varactors and switches, and few significant examples were shown through the thesis.

Compact models available in the MEMS library are appropriate to accurately describe a wide spectrum of cases. However, further efforts should be spent in order to include in the compact models additional physical effects, like residual stress distribution and non-linearity of the material elastic behaviour. Besides, additional models should be developed within the MEMS library (like large flexible membranes). This would make the presented MEMS model library an appropriate tool for the analysis of nearly the whole spectrum of RF-MEMS topologies in different technologies. The further step of including extracted lumped elements networks accounting for the parasitics surrounding intrinsic RF-MEMS devices, could lead to the synthesis of a design-kit for a certain technology.

The second topic treated in the thesis deals with another important aspect related to devices realized in RF-MEMS technology which is the packaging. As RF-MEMS devices are typically very fragile, environmental factors like moisture, dust particles, shocks and so on can compromise their functionality. This requires the application to the RF-MEMS devices of a protective substrate, i.e. the package. In this thesis a feasible methodology for the fabrication of the package along with its application to the MEMS substrate (Wafer-Level Packaging) has been discussed. The capping part is realized with the facilities available at the HiTeC-DIMES Technology Centre (Technical University of Delft, the Netherlands) and is based on vertical through-wafer vias filled with Copper in a Silicon substrate. Experimental data of the first capped test structures (CPW's and shorts) are promising for further development of such a packaging methodology. Moreover, the package fabrication process has been optimized in order to reduce as much as possible the parasitic effects (capacitive and inductive couplings) introduced by the capping part on the RF behaviour of MEMS devices. To this purpose, the Ansoft HFSS<sup>TM</sup> electromagnetic simulator was first validated with the experimental data mentioned above and then exploited in order to determine the critical technology degrees of freedom (DoF's) playing a key-role in reducing the parasitics. A fully optimized package is being fabricated at the HiTeC-DIMES Laboratories at the moment of the thesis writing. This also includes the capping part to be bonded to RF-MEMS devices realized in ITC-irst Technology (already available). As soon as the fabrication of the capping part will be completed the capping part will be applied to RF-MEMS devices and the capped devices experimentally characterized. Moreover, a demonstrator of packaged RF-MEMS/CMOS hy-



brid chip will be obtained by interfacing the capped RF-MEMS devices to an oscillating circuitry realized in CMOS standard technology (hybrid-packaging). Finally, a simulation of an RF-MEMS devices realized with the compact models of this thesis also including the electromagnetic behaviour of through-wafer vias was shown as proof of concept. S-parameters behaviour of vertical vias was determined by simulations in Ansoft HFSS<sup>TM</sup>. An extension of this work in this sense is represented by the extraction of lumped elements networks characterizing the whole package electromagnetic behaviour. To this purpose, ad-hoc structures included in the design currently under fabrication will be exploited.



# Appendix A

In this section some details on the particular implementation chosen for the MEMS compact model library in VerilogA<sup>©</sup> are reported.

## A.1 SpectreHDL<sup>©</sup> Vs. VerilogA<sup>©</sup>

The MEMS compact model library shown discussed in this thesis had been first implemented in SpectreHDL<sup>©</sup> [86]. This is an HDL-based language developed on purpose for the Spectre<sup>©</sup> simulation machine available within the Cadence<sup>©</sup> framework. In the beginning this has been a reasonable choice as MEMS compact models are meant to be simulated by Spectre<sup>©</sup>. However, being the SpectreHDL<sup>©</sup> an on-purpose language, it has the disadvantage of a limited portability in other environments. This is the reason why the MEMS compact model library was translated in VerilogA<sup>©</sup> [10]. The latter is another HDL-based language available within Cadence<sup>©</sup> and supported by Spectre<sup>©</sup> which is more standardized with respect to the SpectreHDL<sup>©</sup>. This allows to exploit the MEMS library within other environments like, for instance, the Agilent ADS<sup>©</sup> framework. Consistency and stability of MEMS compact models has been tested comparing different type of analysis (i.e. DC, AC, Transient) of several structures composed with elementary models of the two libraries (in SpectreHDL<sup>©</sup> and VerilogA<sup>©</sup>). Same results as well as comparable simulation time and convergence robustness are observable proving the implementation in VerilogA<sup>©</sup> to be a viable option for its wider portability and compatibility with other simulation tools.

## A.2 Modular Code and Physical Quantities

Implementation of elementary compact models shown earlier throughout the thesis require rather large code writing to be implemented. For instance, the 6 DoF's rigid plate model including the presence of holes as well as the electrostatic model with fringing effect as well as the viscous damping model, required several thousands of code lines. However, depending on the type of structure and of the analysis to be performed, the availability of *ad hoc* rigid plate models would be desirable. For instance, it could be necessary to use a 4 DoF's plate model instead of the 6 DoF's one as well as a rigid plate without openings on its area. On this purpose the VerilogA<sup>©</sup> code has been arranged in modules. This means that the description of different effects (e.g. presence of holes, fringing effect and so on) is arranged in code modules which can be introduced or not in the plate model utilized in simulations. The selection is done prior to the compilation of the code itself. In this way, time after time the code is optimized for the particular required plate features, as all the unnecessary modules are totally ignored from the compiler. Modularity is achieved by means of *macro variables* supported in VerilogA<sup>©</sup>. Depending on the existence or not of a certain variable an *if then else* macro operation defined in the code includes the desired part of code implementing a certain feature instead of another one. The declaration of the macro controlling variables defining all the possible plate features is included in a header file interpreted from the compiler at the beginning of the correspondent netlist generation. In the subsequent *if then else* structures a true condition (i.e. *if* branch) is recognized if the linked macro variable does exist, while a false condition is encountered (i.e. *else* branch) when the variable does not exist. The header file for the rigid plate model is reported ahead:

```

/// ***** ////////////////////////////////////// ///
/// MODULES INCLUSION. DEFINITION OF A CUSTOM PLATE MODEL ///
/// ***** ////////////////////////////////////// ///

// If a parameter is defined the corresponding module
// is included in the plate model, otherwise is ignored

// ----MECHANICAL-MODEL----- //

'define Model_Reduction_To_4_Degrees_Of_Freedom

// ----ADDITIONAL-FEATURES----- //

//'define Rotation_Matrix_Modified

//'define Offset_Connectivity_Point

'define Contact_Effects

//'define In_Plane_Contact_Effects_Static

//'define In_Plane_Contact_Effects_Dynamic

// ----ELECTROSTATIC-MODEL----- //

//'define Straight_Lines

'define Oxide_Electrical_Effects

'define Electrical_Effects_Capacitance

'define Electrical_Effects_Force

'define Boundary_Fringing_Capacitance

```

```

'define Boundary_Fringing_Electrostatic

'define Lateral_Fringing_Capacitance_Integral

'define Lateral_Fringing_Electrostatic_Integral

'define Manual_Holes_Placement

'define Holes_Capacitance

'define Holes_Electrostatic

'define Holes_Boundary_Fringing_Capacitance

'define Holes_Boundary_Fringing_Electrostatic

'define Holes_Lateral_Fringing_Capacitance_Integral

'define Holes_Lateral_Fringing_Electrostatic_Integral

//'define Electrostatic_Torques

// ----VISCOUS-DAMPING-MODEL----- //

'define Viscous_Damping_Effects

//'define Simplified_Viscous_Damping_Model

//'define Viscous_Damping_Torques_Model

//'define Simplified_Viscous_Damping_Torques_Model

'define Discrete_Damping_Model

'define Mean_Free_Path_Model

```

```

// ----CONVERGENCE-ROBUSTNESS-ENHANCEMENT----- //

//‘define DC_Simulation_Model_Reduction

//‘define Torque_Nodes_Static_Damping_Inclusion

//‘define Torque_Nodes_Dynamic_Damping_Inclusion

‘define Center_Of_Mass_Dynamic_Nodes_For_X

‘define Center_Of_Mass_Dynamic_Nodes_For_Y

‘define Center_Of_Mass_Dynamic_Nodes_For_Z

‘define Center_Of_Mass_Dynamic_Nodes_For_Phi_X

‘define Center_Of_Mass_Dynamic_Nodes_For_Phi_Y

‘define Center_Of_Mass_Dynamic_Nodes_For_Phi_Z

// ----- //

/// ***** ///
/// ----- END OF MODULES INCLUSION ----- ///
/// ***** ///

```

The declaration of certain macro variables can be skipped by commenting (“//” at the line beginning) the corresponding line. Looking at previous file, in the very beginning is the variable which allows to choose between the complete 6 DoF’s and the 4 DoF’s reduced mechanical model. Then there is a section defining various features like the presence or not of a substrate underneath the rigid plate (contact model). The electrostatic model section follows, including or not the electrical effects due to the oxide layer lying on the bottom electrode as well as the presence of holes and of all the possible fringing effects. Next to this there is a section for including the viscous damping model with some extra features like the inclusion of the model which accounts for the air compression (see Equation 3.208). Finally, the last section defines some

features for making the model convergence more robust. For instance, when a DC simulation is performed it is possible to skip the definition of internal nodes for dynamics magnitudes (i.e. time derivatives) which very often cause convergence problems. A similar header file is defined for the Euler flexible beam model.

Additionally, all the material constants definition, like Poisson's ratio, Young Modulus, Sheet resistance and so on, are lumped in a single file and different file for different technologies are defined. In this way, changing the name of the particular file included in the main code it is possible to change the material properties.

### A.3 User Interfaces

Several parameters must be specified in each MEMS elementary component included in a Cadence Virtuoso<sup>®</sup> Schematic prior to the simulation launching. For instance, in an Euler flexible beam the geometrical features (length, width and thickness) must be defined along with the orientation angles. Within Cadence Virtuoso<sup>®</sup> Schematic it is possible to edit the properties of each component. These are available in a window like the one shown in Figure A.1. On the bottom left part of the window there is the name of the parameters to be set. For instance “**w**” is the beam width, “**L**” its length and “**angle z**” the initial orientation angle around  $Z$  axis. In the right fields it is possible to associate a proper numeric value to each parameter or even a parameter, like in Figure A.1. Their value assignment is then done directly within the Cadence<sup>®</sup> Analog Design Environment. In Figure A.2 its window is shown and in its lower left sub-window the some of the beam parameters with the corresponding value are visible. This allows to set a sweep and/or a parametric analysis in which one particular variable is varied within a range defined by the user.



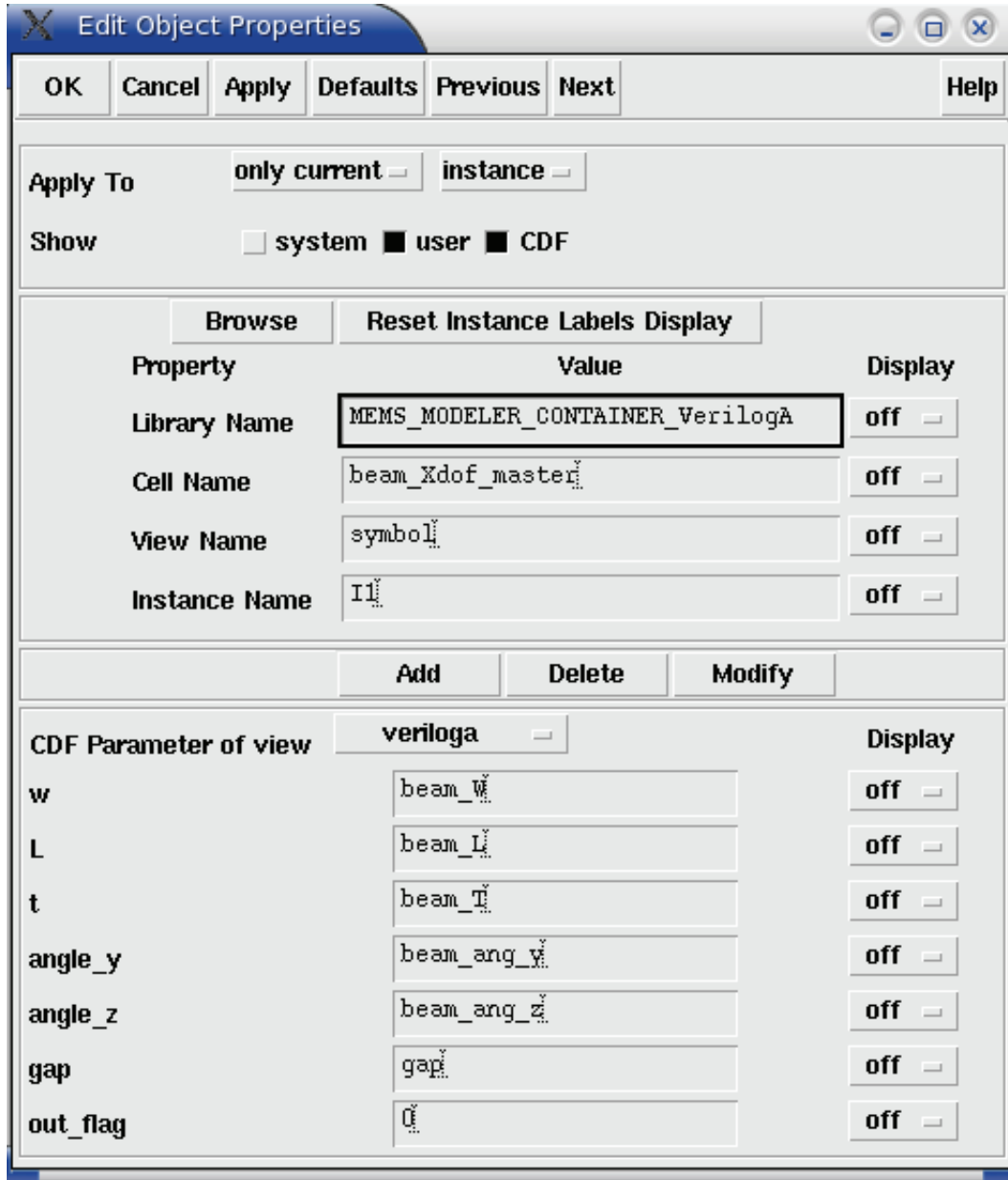


Figure A.1: Mask for the Euler beam parameters definition in Cadence Virtuoso<sup>©</sup> Schematic.

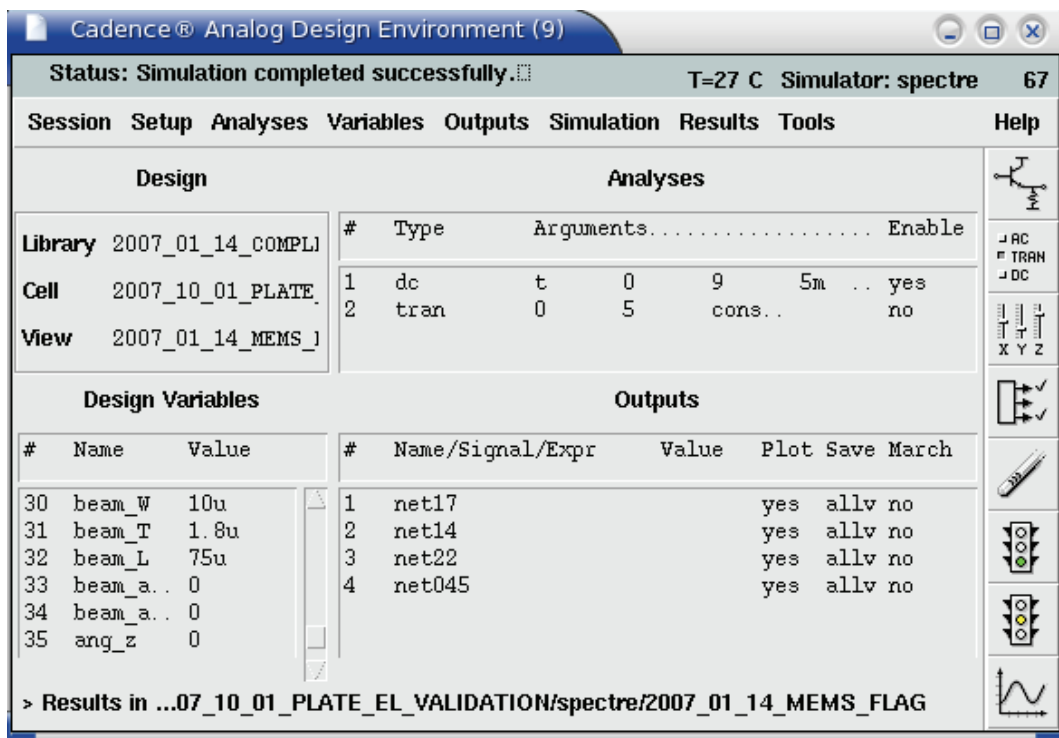


Figure A.2: Cadence® Analog Design Environment window. This window allows to control the type of simulation as well as to set the desired values for all the parameters.

# Appendix B

In this appendix works in progress related to the hybrid wafer level packaging solution for RF-MEMS devices shown in Chapter 6 are being shown.

## B.1 Modified Process Flow with Wide Recesses

In the chapter about packaging for RF-MEMS the chosen process has been described in details. There is a slightly different technological solution that has not been tested yet but that is feasible with the process available at the HiTeC-DIMES Centre. This employs the etching of very wide recesses surrounding the entire devices. Conductive copper interconnect are confined within silicon cylindrical shaft left non-etched. 3D schematic views of the package defined over one single two-ports RF-MEMS device with vias for the Ground-Signal-Ground pads are reported in Figure B.1 (standard process of Chapter 6) and Figure B.2 (modified process with wider recesses). In the latter one the modified process mentioned above is shown. This requires an additional mask for the definition of the wide recess pattern but, on the other hand, introduces some advantages. First of all, a silicon surrounding sidewall is built-in the package substrate itself. This makes unnecessary the patterning of a thick sealing ring around each RF-MEMS devices or at die level like previously shown in Figure 5.21. In this case just a very thin adhesive layer has to be patterned under the silicon sidewalls to ensure wafer-to-wafer bonding, enhancing the encapsulation of RF-MEMS devices and the maintaining of a vacuum in case this solution is needed.

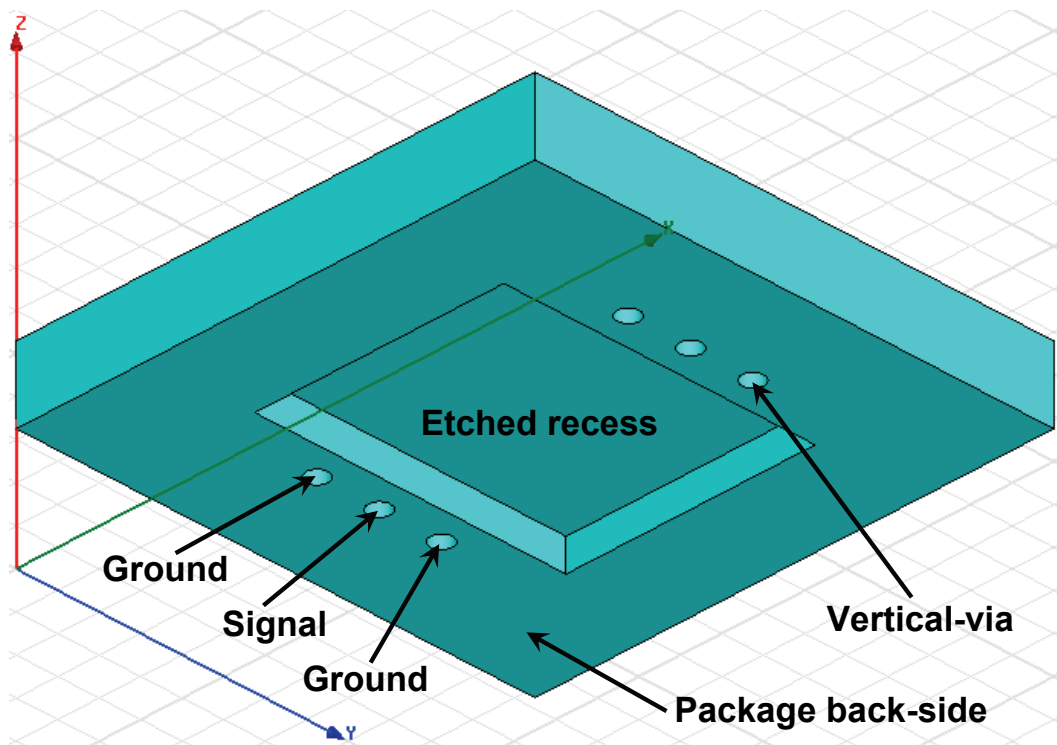


Figure B.1: 3D schematic of the package bottom side realized with the process shown in Chapter 6.

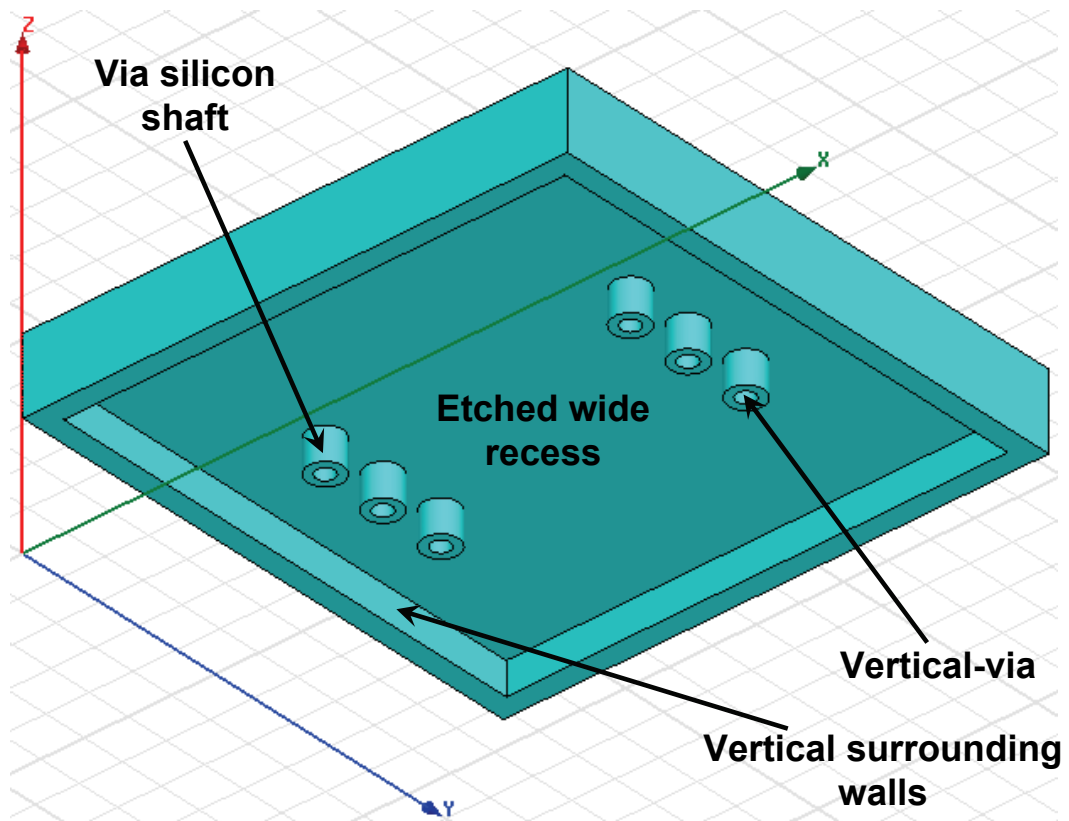


Figure B.2: 3D schematic of the package bottom side realized with the modified process proposed in this section. Wider recesses are achievable.

Another advantage introduced by this modified solution is that more room is available atop and around RF-MEMS devices with respect to the traditional process with small recesses (see Figure B.1). This results in a smaller interference of the package with the electromagnetic field of the capped devices which yield a reduction of losses and mismatch due to the capping substrate. An example is shown below, where the S-parameters of a CPW capped with the traditional solution shown in Chapter 6 are compared with the ones for the same structure capped with the modified solution shown above. CPW is  $800\ \mu\text{m}$  long, while signal and ground lines width is  $140\ \mu\text{m}$  and  $500\ \mu\text{m}$  respectively. Gap is  $50\ \mu\text{m}$  while vertical via diameter is  $70\ \mu\text{m}$ . Moreover, capping substrate height is  $300\ \mu\text{m}$  and the recess depth in the traditional package solution as well as in the modified one is  $100\ \mu\text{m}$ . However, in the first case the recess dimensions are  $500\ \mu\text{m}$  along the CPW length and  $1000\ \mu\text{m}$  over its width, while in the latter the recess is all around the CPW itself ( $2800\ \mu\text{m}$  by  $2800\ \mu\text{m}$ ). Both structures have been simulated within Ansoft HFSS<sup>TM</sup> and results are shown in Figure B.3 (reflection parameter) and Figure B.4 (transmission parameter). Enhancements either concerning the S11 and S21 parameters are visible when the solution with larger recess is employed for the package fabrication.

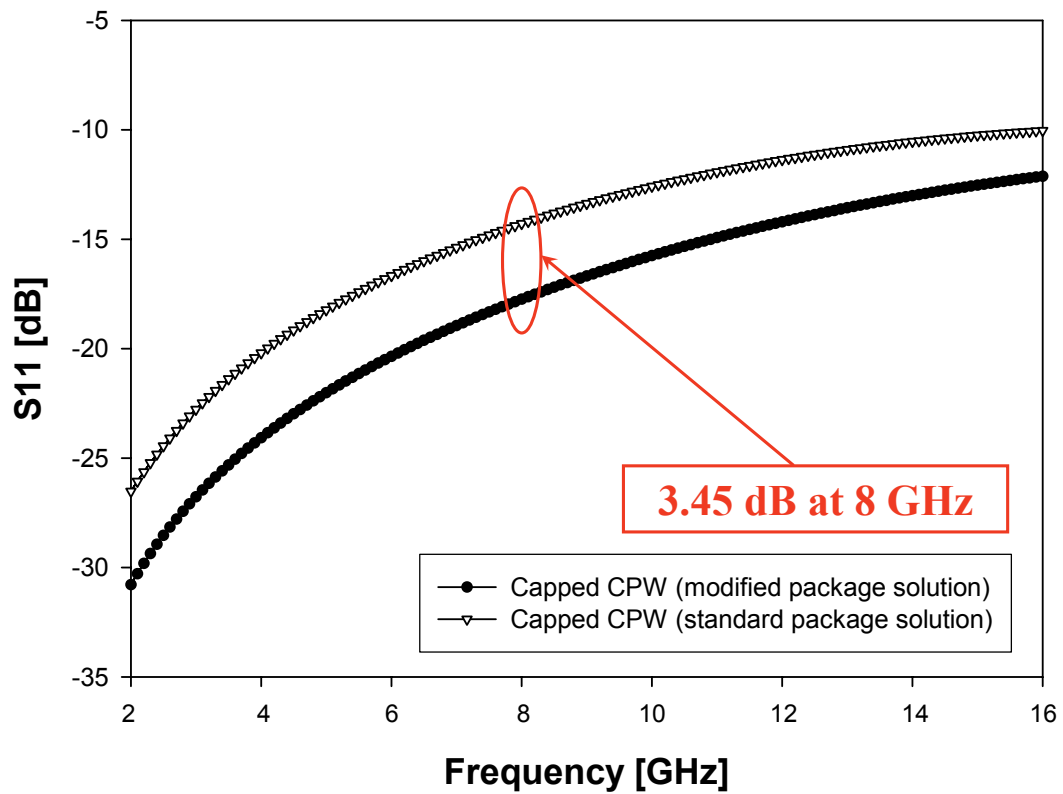


Figure B.3: Reflection parameters (S11) plot for a CPW capped with the packaging solution shown in Chapter 6 compared with the modified solution with larger recess and silicon shafts.

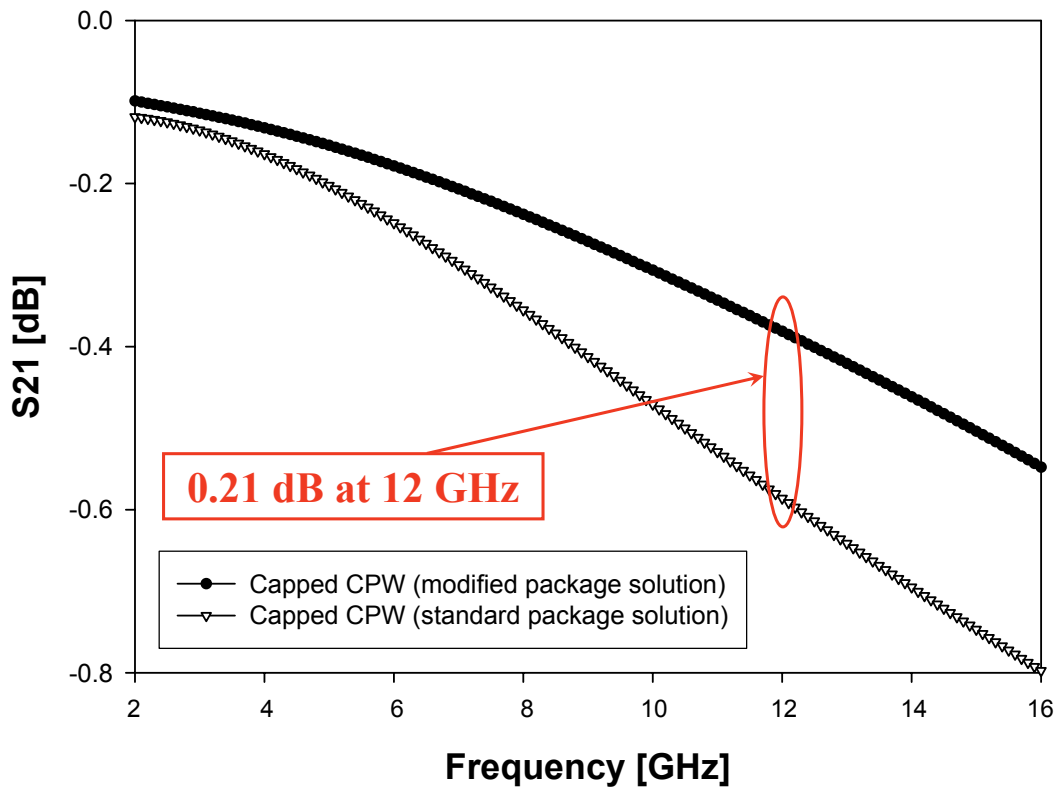


Figure B.4: Transmission parameters (S21) plot for a CPW capped with the packaging solution shown in Chapter 6 compared with the modified solution with larger recess and silicon shafts.



## B.2 Work in Progress

At the moment of the writing of this thesis a package substrate is being processed at the HiTeC-DIMES Technology Centre. The design of the package wafer has been optimized to reduce losses and mismatch according to the results obtained with the Ansoft HFSS<sup>TM</sup> electromagnetic simulator shown in Chapter 6 and summarized in Figure 5.45. The package is meant to be applied to additional test structures, i.e.  $50\ \Omega$  coplanar waveguides (CPW's) and shorts as well as actual RF-MEMS devices. Indeed a part of the capping area has been designed to be bonded to an RF-MEMS LC-tank realized in ITC-irst technology [87]. Once the package will be available and singulated for the RF-MEMS die the chip-to-chip bonding of the latter two will be performed. After this stage, the package LC-tank will be interfaced to an active oscillating block realized in CMOS technology [89]. In this first hybrid RF-MEMS/CMOS packaged chip no accommodation will be derived in the package but the CMOS part will be just lie and glued onto the package like shown in Figure B.5. Electrical interfacing of the RF-MEMS to the CMOS part will be performed by wire-bonding.

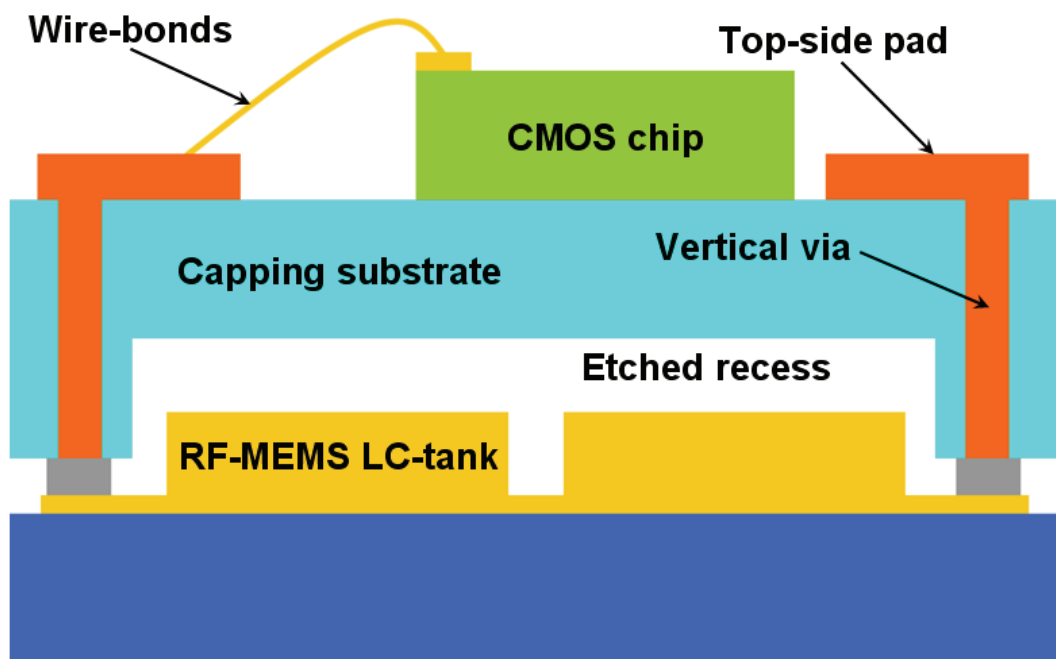


Figure B.5: Schematic of the hybrid RF-MEMS/CMOS packaged chip demonstrator. Electrical interconnection will be performed by wire bonding.

# Appendix C

## C.1 Flexible Plate with 12 DoF's

To conclude the description about the models included in the MEMS library the flexible plate with 12 DoF's is going to be presented. This has been included in this appendix because it has not been included in any of the examples shown in Chapter 6. Moreover, the flexible plate with 12 DoF's at the moments includes only the mechanical model. This means that electromechanical transduction effects are not accounted for in it. A schematic of the flexible plate with all the DoF's is shown in Figure C.1. Its dimensions are  $W$ ,  $L$  and  $T$  respectively along the  $x$ ,  $y$  and  $z$  axes. The four vertexes are labeled by the numbers 1, 2, 3 and 4. Each of them has 3 DoF's that consist of a linear deformation along the  $z$  axis ( $u_{z1}; u_{z2}; u_{z3}; u_{z4}$ ) and two angular deformations around the  $x$  and  $y$  axes ( $u_{\theta_x1}, u_{\theta_y1}; u_{\theta_x2}, u_{\theta_y2}; u_{\theta_x3}, u_{\theta_y3}; u_{\theta_x4}, u_{\theta_y4}$ ). The approach in defining the mechanical model for the flexible plate is the same already shown in details for the 12 DoF's Euler beam. For this reason the only formulation for the stiffness  $\mathbf{k}$  and mass  $\mathbf{m}$  matrix are being reported below.

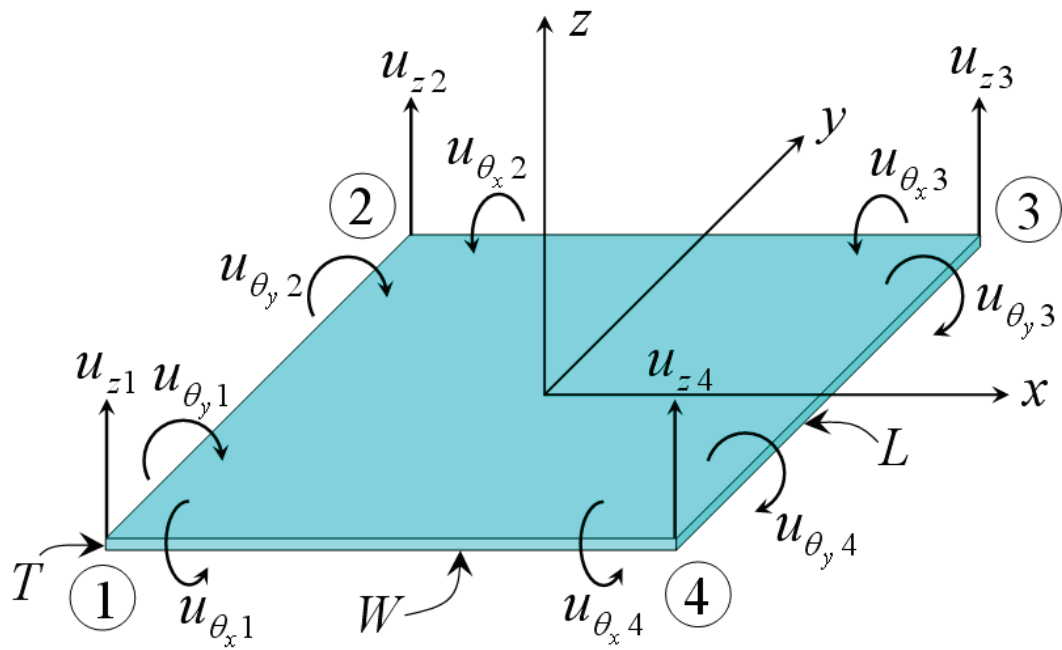


Figure C.1: Schematic of the flexible plate with 12 DoF's. The vertexes are marked as 1, 2, 3 and 4 and each of them admits a linear deformation along  $z$  and two torsions around  $x$  and  $y$ .

The 4.71 rewritten for the indexes shown in Figure C.1 is:

$$\begin{bmatrix} F_{z1} \\ T_{\theta x1} \\ T_{\theta y1} \\ F_{z2} \\ T_{\theta x2} \\ T_{\theta y2} \\ F_{z3} \\ T_{\theta x3} \\ T_{\theta y3} \\ F_{z4} \\ T_{\theta x4} \\ T_{\theta y4} \end{bmatrix} = \mathbf{k} \begin{bmatrix} u_{z1} \\ u_{\theta x1} \\ u_{\theta y1} \\ u_{z2} \\ u_{\theta x2} \\ u_{\theta y2} \\ u_{z3} \\ u_{\theta x3} \\ u_{\theta y3} \\ u_{z4} \\ u_{\theta x4} \\ u_{\theta y4} \end{bmatrix} \quad (\text{C.1})$$

The stiffness matrix  $\mathbf{k}$  [27] can be written as:

$$\mathbf{k} = [ \mathbf{k}_1 \mid \mathbf{k}_2 ] \quad (\text{C.2})$$

where

$$\mathbf{k}_1 = \begin{bmatrix} k_{11} & k_{12} & k_{13} & k_{14} & k_{15} & k_{16} \\ k_{21} & k_{22} & k_{23} & k_{24} & k_{25} & k_{26} \\ k_{31} & k_{32} & k_{33} & k_{34} & k_{35} & k_{36} \\ k_{41} & k_{42} & k_{43} & k_{44} & k_{45} & k_{46} \\ k_{51} & k_{52} & k_{53} & k_{54} & k_{55} & k_{56} \\ k_{61} & k_{62} & k_{63} & k_{64} & k_{65} & k_{66} \\ k_{71} & k_{72} & k_{73} & k_{74} & k_{75} & k_{76} \\ k_{81} & k_{82} & k_{83} & k_{84} & k_{85} & k_{86} \\ k_{91} & k_{92} & k_{93} & k_{94} & k_{95} & k_{96} \\ k_{10,1} & k_{10,2} & k_{10,3} & k_{10,4} & k_{10,5} & k_{10,6} \\ k_{11,1} & k_{11,2} & k_{11,3} & k_{11,4} & k_{11,5} & k_{11,6} \\ k_{12,1} & k_{12,2} & k_{12,3} & k_{12,4} & k_{12,5} & k_{12,6} \end{bmatrix} \quad (\text{C.3})$$

$$\mathbf{k}_2 = \begin{bmatrix} k_{17} & k_{18} & k_{19} & k_{1,10} & k_{1,11} & k_{1,12} \\ k_{27} & k_{28} & k_{29} & k_{2,10} & k_{2,11} & k_{2,12} \\ k_{37} & k_{38} & k_{39} & k_{3,10} & k_{3,11} & k_{3,12} \\ k_{47} & k_{48} & k_{49} & k_{4,10} & k_{4,11} & k_{4,12} \\ k_{57} & k_{58} & k_{59} & k_{5,10} & k_{5,11} & k_{5,12} \\ k_{67} & k_{68} & k_{69} & k_{6,10} & k_{6,11} & k_{6,12} \\ k_{77} & k_{78} & k_{79} & k_{7,10} & k_{7,11} & k_{7,12} \\ k_{87} & k_{88} & k_{89} & k_{8,10} & k_{8,11} & k_{8,12} \\ k_{97} & k_{98} & k_{99} & k_{9,10} & k_{9,11} & k_{9,12} \\ k_{10,7} & k_{10,8} & k_{10,9} & k_{10,10} & k_{10,11} & k_{10,12} \\ k_{11,7} & k_{11,8} & k_{11,9} & k_{11,10} & k_{11,11} & k_{11,12} \\ k_{12,7} & k_{12,8} & k_{12,9} & k_{12,10} & k_{12,11} & k_{12,12} \end{bmatrix} \quad (\text{C.4})$$

Introducing the aspect ratio  $\beta$  defined as

$$\beta = \frac{L}{W} \quad (\text{C.5})$$

the coefficients of previous C.3 - C.4 are:

$$k_{11} = \frac{ET^2}{12(1-\nu^2)WL} \left[ \frac{156}{35} (\beta^2 + \beta^{-2}) + \frac{72}{25} \right] \quad (\text{C.6})$$

$$k_{12} = k_{21} = \frac{ET^2}{12(1-\nu^2)WL} \left[ \left( +\frac{22}{35}\beta^2 + \frac{78}{35}\beta^{-2} + \frac{6}{25}(1+5\nu) \right) L \right] \quad (\text{C.7})$$

$$k_{13} = k_{31} = \frac{ET^2}{12(1-\nu^2)WL} - \left[ \left( +\frac{78}{35}\beta^2 + \frac{22}{35}\beta^{-2} + \frac{6}{25}(1+5\nu) \right) W \right] \quad (\text{C.8})$$

$$k_{14} = k_{41} = \frac{ET^2}{12(1-\nu^2)WL} \left[ +\frac{54}{35}\beta^2 - \frac{156}{35}\beta^{-2} - \frac{72}{25} \right] \quad (\text{C.9})$$

$$k_{15} = k_{51} = \frac{ET^2}{12(1-\nu^2)WL} \left[ \left( -\frac{13}{35}\beta^2 + \frac{78}{35}\beta^{-2} + \frac{6}{25} \right) L \right] \quad (\text{C.10})$$

$$k_{16} = k_{61} = \frac{ET^2}{12(1-\nu^2)WL} \left[ \left( -\frac{27}{35}\beta^2 + \frac{22}{35}\beta^{-2} + \frac{6}{25}(1+5\nu) \right) W \right] \quad (\text{C.11})$$

$$k_{17} = k_{71} = \frac{ET^2}{12(1-\nu^2)WL} \left[ -\frac{54}{35}(\beta^2 + \beta^{-2}) + \frac{72}{25} \right] \quad (\text{C.12})$$

$$k_{18} = k_{81} = \frac{ET^2}{12(1-\nu^2)WL} \left[ \left( +\frac{13}{35}\beta^2 + \frac{27}{35}\beta^{-2} - \frac{6}{25} \right) L \right] \quad (\text{C.13})$$

$$k_{19} = k_{91} = \frac{ET^2}{12(1-\nu^2)WL} \left[ \left( -\frac{27}{35}\beta^2 - \frac{13}{35}\beta^{-2} + \frac{6}{25} \right) W \right] \quad (\text{C.14})$$

$$k_{1,10} = k_{10,1} = \frac{ET^2}{12(1-\nu^2)WL} \left[ -\frac{156}{35}\beta^2 + \frac{54}{35}\beta^{-2} - \frac{72}{25} \right] \quad (\text{C.15})$$

$$k_{1,11} = k_{11,1} = \frac{ET^2}{12(1-\nu^2)WL} \left[ \left( -\frac{22}{35}\beta^2 + \frac{27}{35}\beta^{-2} - \frac{6}{25}(1+5\nu) \right) L \right] \quad (\text{C.16})$$

$$k_{1,12} = k_{12,1} = \frac{ET^2}{12(1-\nu^2)WL} \left[ \left( -\frac{78}{35}\beta^2 + \frac{13}{35}\beta^{-2} - \frac{6}{25} \right) W \right] \quad (\text{C.17})$$

The expression of all the other elements can be found at pp. 123 - 124 of [27]. Let us focus now on the mass matrix  $\mathbf{m}$ . The 4.120 rewritten for the indexes shown in Figure C.1 is:

$$\begin{bmatrix} F_{z1} \\ T_{\theta x1} \\ T_{\theta y1} \\ F_{z2} \\ T_{\theta x2} \\ T_{\theta y2} \\ F_{z3} \\ T_{\theta x3} \\ T_{\theta y3} \\ F_{z4} \\ T_{\theta x4} \\ T_{\theta y4} \end{bmatrix} = \mathbf{m} \begin{bmatrix} \ddot{u}_{z1} \\ \ddot{u}_{\theta x1} \\ \ddot{u}_{\theta y1} \\ \ddot{u}_{z2} \\ \ddot{u}_{\theta x2} \\ \ddot{u}_{\theta y2} \\ \ddot{u}_{z3} \\ \ddot{u}_{\theta x3} \\ \ddot{u}_{\theta y3} \\ \ddot{u}_{z4} \\ \ddot{u}_{\theta x4} \\ \ddot{u}_{\theta y4} \end{bmatrix} \quad (\text{C.18})$$

The mass matrix  $\mathbf{m}$  is then defined as:

$$\mathbf{m} = [ \mathbf{m}_1 \mid \mathbf{m}_2 ] \quad (\text{C.19})$$

where

$$\mathbf{m}_1 = \begin{bmatrix} m_{11} & m_{12} & m_{13} & m_{14} & m_{15} & m_{16} \\ m_{21} & m_{22} & m_{23} & m_{24} & m_{25} & m_{26} \\ m_{31} & m_{32} & m_{33} & m_{34} & m_{35} & m_{36} \\ m_{41} & m_{42} & m_{43} & m_{44} & m_{45} & m_{46} \\ m_{51} & m_{52} & m_{53} & m_{54} & m_{55} & m_{56} \\ m_{61} & m_{62} & m_{63} & m_{64} & m_{65} & m_{66} \\ m_{71} & m_{72} & m_{73} & m_{74} & m_{75} & m_{76} \\ m_{81} & m_{82} & m_{83} & m_{84} & m_{85} & m_{86} \\ m_{91} & m_{92} & m_{93} & m_{94} & m_{95} & m_{96} \\ m_{10,1} & m_{10,2} & m_{10,3} & m_{10,4} & m_{10,5} & m_{10,6} \\ m_{11,1} & m_{11,2} & m_{11,3} & m_{11,4} & m_{11,5} & m_{11,6} \\ m_{12,1} & m_{12,2} & m_{12,3} & m_{12,4} & m_{12,5} & m_{12,6} \end{bmatrix} \quad (\text{C.20})$$

$$\mathbf{m}_2 = \begin{bmatrix} m_{17} & m_{18} & m_{19} & m_{1,10} & m_{1,11} & m_{1,12} \\ m_{27} & m_{28} & m_{29} & m_{2,10} & m_{2,11} & m_{2,12} \\ m_{37} & m_{38} & m_{39} & m_{3,10} & m_{3,11} & m_{3,12} \\ m_{47} & m_{48} & m_{49} & m_{4,10} & m_{4,11} & m_{4,12} \\ m_{57} & m_{58} & m_{59} & m_{5,10} & m_{5,11} & m_{5,12} \\ m_{67} & m_{68} & m_{69} & m_{6,10} & m_{6,11} & m_{6,12} \\ m_{77} & m_{78} & m_{79} & m_{7,10} & m_{7,11} & m_{7,12} \\ m_{87} & m_{88} & m_{89} & m_{8,10} & m_{8,11} & m_{8,12} \\ m_{97} & m_{98} & m_{99} & m_{9,10} & m_{9,11} & m_{9,12} \\ m_{10,7} & m_{10,8} & m_{10,9} & m_{10,10} & m_{10,11} & m_{10,12} \\ m_{11,7} & m_{11,8} & m_{11,9} & m_{11,10} & m_{11,11} & m_{11,12} \\ m_{12,7} & m_{12,8} & m_{12,9} & m_{12,10} & m_{12,11} & m_{12,12} \end{bmatrix} \quad (\text{C.21})$$

the coefficients of previous C.20 - C.21 are:

$$m_{11} = \frac{\rho W L}{176,400} (24, 336) \quad (\text{C.22})$$

$$m_{12} = m_{21} = \frac{\rho W L}{176,400} (3, 432L) \quad (\text{C.23})$$



$$m_{13} = m_{31} = \frac{\rho WL}{176,400}(-3, 432W) \quad (\text{C.24})$$

$$m_{14} = m_{41} = \frac{\rho WL}{176,400}(8, 424) \quad (\text{C.25})$$

$$m_{15} = m_{51} = \frac{\rho WL}{176,400}(-2, 028L) \quad (\text{C.26})$$

$$m_{16} = m_{61} = \frac{\rho WL}{176,400}(-1, 188W) \quad (\text{C.27})$$

$$m_{17} = m_{71} = \frac{\rho WL}{176,400}(2, 916) \quad (\text{C.28})$$

$$m_{18} = m_{81} = \frac{\rho WL}{176,400}(-702L) \quad (\text{C.29})$$

$$m_{19} = m_{91} = \frac{\rho WL}{176,400}(702W) \quad (\text{C.30})$$

$$m_{1,10} = m_{10,1} = \frac{\rho WL}{176,400}(8, 424) \quad (\text{C.31})$$

$$m_{1,11} = m_{11,1} = \frac{\rho WL}{176,400}(1, 188L) \quad (\text{C.32})$$

$$m_{1,12} = m_{12,1} = \frac{\rho WL}{176,400}(2, 028W) \quad (\text{C.33})$$

The expression of all the other elements can be found at page 308 of [27]. The relations among the local and global reference systems are defined following the same approach discussed in the Euler beam beam and is not reviewed here for seek of brevity. The Cadence Virtuoso<sup>©</sup> Schematic of the 12 DoF's flexible plate is reported in Figure C.2.

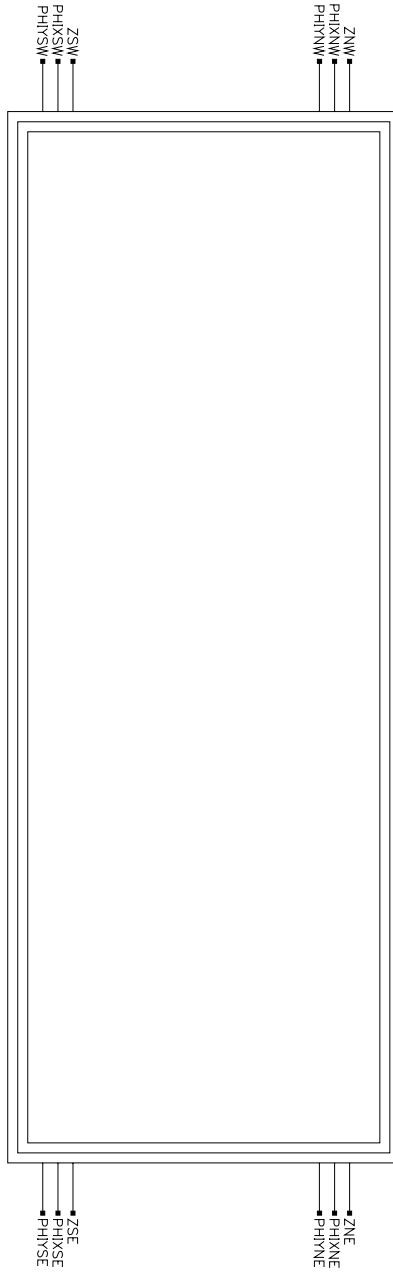


Figure C.2: Cadence Virtuoso<sup>©</sup> Schematic of the flexible plate with 12 DoF's.

# Publications

J. Iannacci, L. Del Tin, M. Bellei, R. Gaddi, A. Gnudi, B. Margesin, F. Giacomozzi, “*Radiofrequency transient behaviour of ohmic RF-MEMS switches*”, Proceedings of the 10<sup>th</sup> Italian Conference Sensors and Microsystems (AISEM 2005), Firenze, IT, 15-17 February 2005.

J. Iannacci, R. Gaddi, A. Gnudi, “*Nodal Modelling of Uneven Electrostatic Transduction in MEMS*”, Proceedings of the 9<sup>th</sup> Italian Conference Sensors and Microsystems (AISEM 2004), Ferrara, IT, 8-11 February 2004.

J. Iannacci, L. Del Tin, R. Gaddi, A. Gnudi, K. J. Rangra, “*Compact modeling of a MEMS toggle-switch based on modified nodal analysis*”, Proceedings of Symposium on Design, Test, Integration and Packaging of MEMS/MOEMS (DTIP 2005), pp. 411-416, Montreux, Switzerland, 01-03 June 2005.

J. Iannacci, J. Tian, S. M. Sinaga, R. Gaddi, A. Gnudi and M. Bartek, “*Parasitic Effects Reduction for Wafer-Level Packaging of RF-MEMS*”, Proc. DTIP 2006 (Symposium on Design, Test, Integration and Packaging of MEMS / MOEMS), 26-28 April 2006, Stresa, Lago Maggiore, Italy, publ. TIMA, ISBN 2-916187-03-0, pp. 1-6.

J. Iannacci, J. Tian, S. M. Sinaga, R. Gaddi, A. Gnudi and M. Bartek, “*Electrical Optimization of a Wafer-Level Package for RF-MEMS Applications*”, Proc. 4<sup>th</sup> European Microelectronic and Packaging Symposium with Table-Top Exhibition (EMPS 2006), May 22-24, 2006, Terme Catez, Slovenia, publ. MIDEM (Ljubljana), eds. D. Belavic, M. Kosec, I. Sorli, ISBN 961-91023-5-5, pp. 79-84.

J. Iannacci and M. Bartek, “*RF Behaviour of Anisotropic Conductive Adhesive in Wafer Level Packaging for RF MEMS*”, Technical Digest The 17<sup>th</sup> Micromechanics Europe Workshop (MME 2006), September 3-5, 2006, Southampton, UK, publ. University of Southampton, ISBN 0-85432-848-3, pp. 93-96.

J. Iannacci and M. Bartek, “*Electromagnetic Optimisation of an RF-MEMS Wafer-Level Package*”, The 20<sup>th</sup> European conference on solid-state transducers (Eurosensors XX) - CD-ROM Proceedings, 17-20 September 2006, Goeteborg, Sweden, ISBN 91-631-9281 0, pp. T2C-04/1-4.

J. Iannacci, M. Bartek, J. Tian and S. Sosin, “*Hybrid Wafer-Level Packaging for RF MEMS Applications*”, Proc. 39<sup>th</sup> International Symposium on Microelectronics (IMAPS 2006), October 9-13, 2006, San Diego, USA, publ. IMAPS (Washington), ISBN 0-930815-80-7, pp. 246-253.

J. Iannacci, J. Tian, S. Sosin, R. Gaddi and M. Bartek, “*Hybrid Wafer-Level Packaging for RF MEMS Applications*”, Proc. IWLPC 2006, November 1-3, 2006, San Jose, Wyndham Hotel, San Jose, CA, publ. SMTA (smta.org, Edina), ISBN 0-9789465-2-9, pp. 106-113.

J. Iannacci, J. Tian, A. Akhnoukh, M. Bartek, R. Gaddi and A. Gnudi, “*Electrical Performance Assessment and Optimization of an RF MEMS Wafer Level Package*”, Proc. 9<sup>th</sup> Annual Workshop on Semiconductor Advances for future Electronics and Sensors (SAFE 2006), 23-24 November 2006, Koningshof, Veldhoven, the Netherlands, publ. STW (Utrecht), ISBN 90-73461-44-8, pp. 512-518.

J. Iannacci, J. Tian, R. Gaddi, A. Gnudi, and M. Bartek, “*A Fully Parameterized FEM Model for Electromagnetic Optimization of an RF-MEMS Wafer Level Package*”, Accepted for the Symposium on Design, Test, Integration and Packaging of MEMS/MOEMS (DTIP 2007), Stresa, Lake Maggiore, Italy, 25-27 April 2007.

J. Iannacci, M. Bartek, J. Tian, R. Gaddi and A. Gnudi, “*Electromagnetic Optimisation of an RF-MEMS Wafer-Level Package*”, Sensors and Actuators Volume A, Special Issue of Eurosensors XX 2006 Conference. Currently under review.

J. Tian, M. Bartek, J. Iannacci, J.N. Burghartz, S. Sosin, “*Low Temperature Wafer Level Packaging of RF-MEMS Using SU-8 Contact Printing*”, Book of Abstracts 2<sup>nd</sup> International Workshop on Wafer Bonding for MEMS Technologies, April 9-11, 2006, Halle, Germany, eds. J. Bagdahn, R. Knechtel, pp. 55-56.

J. Tian, I. Iannacci, R. Gaddi, M. Bartek, “*RF-MEMS Wafer-Level Packaging Using Through-Wafer Interconnect*”, The 20<sup>th</sup> European conference on solid-state transducers (Eurosensors XX) - CD-ROM Proceedings, 17-20 September 2006, Goeteborg, Sweden, ISBN 91-631-9281-0, pp. T2C-P7/1-4.

J. Tian, J. Iannacci, S. Sosin, R. Gaddi, M. Bartek, “*RF-MEMS Wafer-Level Packaging Using Through-Wafer Via Technology*”, Proc. 8<sup>th</sup> Electronics Packaging Technology Conference (EPTC 2006), Vol. 2, 6-8 December 2006, Singapore, eds. J.H.L. Pang, et al., publ. IEEE, ISBN 1-4244-0664-1, pp. 441-447.

R. Gaddi, L. Del Tin, M. Bellei, J. Iannacci, A. Gnudi, B. Margesin, F. Giacomozzi, “*Radiofrequency transient behaviour of ohmic RF-MEMS switches*”, Proceedings of the 10<sup>th</sup> Italian Conference Sensors and Microsystems (AISEM 2005), Firenze, IT, 15-17 February 2005.

R. Gaddi, J. Iannacci, “*Hierarchical Multidomain MEMS Simulation within an IC-Design Framework*”, Proceedings of the 8<sup>th</sup> Italian Conference Sensors and Microsystems (AISEM 2003), Trento, IT, 12-14 February 2003, World Scientific, pp.461-466.

R. Gaddi, J. Iannacci, A. Gnudi, “*Mixed-Domain Simulation of Intermodulation Distortion in RF-MEMS Capacitive Shunt Switches*”, Proceedings of 33<sup>rd</sup> European Microwave Conference 2003, Munich, D, 5-8 October 2003, pp.671-674.

V. Rizzoli, R. Gaddi, J. Iannacci, D. Masotti, F. Mastri, “*Multitone intermodulation and RF stability analysis of MEMS switching circuits by a globally convergent harmonic-balance technique*”, Proceedings of the European Microwave Association, Vol. 1, Issue 1, March 2005, pp. 45-54.

R. Gaddi, A. Gnudi, E. Franchi, M. Bellei, L. Del Tin, J. Iannacci, P. Tortori, D. Guermandi, B. Margesin, F. Giacomozzi, "*Reconfigurable RF-MEMS LC-tanks for multi-band radiofrequency oscillators*", Proceedings of the Wireless Reconfigurable Terminals and Platforms Workshop (WiRTeP), Rome, Italy, 10-12 April 2006.

L. Del Tin, J. Iannacci, R. Gaddi, A. Gnudi, E. B. Rudnyi, A. Greiner and J. G. Korvink, "*Non Linear Compact Modeling of RF-MEMS Switches by Means of Model Order Reduction*", Proceedings of TRANSDUCERS 2007, The 14<sup>th</sup> international Conference on solid-state sensors and actuators 10-14 JUNE 2007 - Lyon, France.

# Bibliography

- [1] Thomas J. R. Hughes, *“The Finite Element Method: Linear Static and Dynamic Finite Element Analysis”*, Courier Dover Publications, 2000.
- [2] *“Reference: MEMS and Microsystems Physical Design”*, CoventorWare DESIGNER Version 2006, Coventor Inc., [www.coventor.com](http://www.coventor.com)
- [3] N. A. Bushyager and M. M. Tenzeris, *“Modeling and Design of RF MEMS Structures Using Computationally Efficient Numerical Techniques”*, Proceedings of the 51<sup>st</sup> Electronic Components and Technology Conference, Las Vegas, NV, USA, 29 May - 1 June 2001.
- [4] E. B. Rudnyi and J. G. Korvink, *“Model Order reduction of MEMS for Efficient Computer Aided Design and System Simulation”*, Proceedings of the 16<sup>th</sup> International Symposium on Mathematical Theory of Networks and Systems, MTNS, Katholieke Universiteit Leuven, Belgium July 5-9, 2004.
- [5] Tamara Bechtold, Evgenii B. Rudnyi and Jan G. Korvink, *“Fast Simulation of Electro-Thermal MEMS, Efficient Dynamic Compact Models”*, Springer, 2007.
- [6] Stephen D. Senturia, *“Microsystem Design”*, Springer, 2000.
- [7] Gary K. Fedder and Qi Jing, *“A Hierarchical Circuit-Level Design Methodology for Microelectromechanical Systems”*, Transactions on Circuits and Systems II: Analog and Digital Signal Processing, IEEE, Volume 46, Pages 1309-1315, October 1999.

- [8] Tamal Mukherjee and Gary K. Fedder, “*Hierarchical Mixed-Domain Circuit Simulation, Synthesis and Extraction Methodology for MEMS*”, Journal of VLSI Signal Processing, Springer Netherlands, Volume 21, Number 3, Pages 233-249, July 1999.
- [9] “*Affirma Spectre Circuit Simulator User Guide*”, Cadence Design Systems, Inc. Product Version 4.4.6, June, 2000.
- [10] “*Affirma VerilogA Language Reference*”, Cadence Design Systems, Inc. Product Version 4.4.5, December, 1999.
- [11] Peter Krulevitch, Paul Bierden, Thomas Bifano, Emily Carr, Clara Dimas, Harold Dyson, Michael Helmbrecht, Peter Kurczynski, Richard Muller, Scot Olivier, Yves-Alain Peter, Bernard Sadoulet, Olav Solgaard, and E.H. Yangh, “*MOEMS spatial light modulator development at the Center for Adaptive Optics*”, MOEMS and Miniaturized Systems III, James H. Smith, Peter A. Krulevitch, Hubert K. Lakner, Editors, Proceedings of SPIE Vol. 4983, 2003.
- [12] Amritsar Jeetender, Ion Stiharu and Muthukumaran Packirisamy, “*MOEMS for Bio-Enzymatic Detection*”, PHOTONS, Tech Review of Canadian Institute of Photonic Innovation, Vol. 1, No. 1, Pages 25-27, Spring 2005.
- [13] Ni Xiao-qi, Wang Ming, Chen Xu-xing, Ge yi-xian and Rong Hua, “*An optical fibre MEMS pressure sensor using dual-wavelength interrogation*”, Measurement Science and Technology Volume 17, Number 9, September 2006 Pages 2401-2404.
- [14] A. Jourdain, K. Vaesen, J.M. Scheer, J.W. Weekamp, J.T.M. van Beek and H.A.C. Tilmans, “*From zero- to second-level packaging of RF-MEMS devices*”, Proceedings of the 18<sup>th</sup> IEEE International Conference on Micro Electro Mechanical Systems MEMS, Pages 36-39, 2005.
- [15] Jae-Hyoung Park, Hee-Chul Lee, Yong-Hee Park, Yong-Dae Kim, Chang-Hyeon Ji, Jonguk Bu and Hyo-Jin Nam, “*A fully wafer-level packaged RF MEMS switch with low actuation voltage using a piezoelectric actuator*”, Journal of Micromechanics and Microengineering, Volume 16, Number 11, November 2006.



- [16] Yun-Kwon Park, Heung-Woo Park, Duck-Jung Lee, Jung-Ho Park, In-Sang Song, Chung-Woo Kim, Ci-Moo Song, Yun-Hi Lee, Chul-Ju Kim and Byeong Kwon Ju, “*A novel low-loss wafer-level packaging of the RF-MEMS devices*”, Proceedings of the 15<sup>th</sup> IEEE International Conference on Micro Electro Mechanical Systems MEMS, Pages 681-684, 2002.
- [17] “*Getting Started with Ansoft HFSS*”, Userguide of Ansoft HFSS, Ansoft Corporation, www.ansoft.com.
- [18] Richard C. Jaeger, “*Microelectronic Circuit Design*”, McGraw-Hill, June 2003.
- [19] “*Leaded Surface Mount Technology (SMT)*”, Intel Packaging Databook, Chapter 7, 2000.
- [20] John H. Lau, “*Flip Chip Technologies*”, McGraw-Hill, 1996.
- [21] “*Ball Grid Array (BGA) Packaging*”, Intel Packaging Databook, Chapter 14, 2000.
- [22] George Harman, “*Wire Bonding in Microelectronics: Materials, Processes, Reliability, and Yield*”, McGraw-Hill, 1997.
- [23] G. E. Servais and S.D. Brandenburg, “*Wire Bonding A Closer Look*”, Proceedings of ISTFA 1991: The 17<sup>th</sup> International Symposium for Testing & Failure Analysis, Pages 525-529, Los Angeles, California, USA, 11-15 November 1991.
- [24] Fred W. Kear, “*Hybrid Assemblies and Multichip Modules*”, Marcel Dekker Editor, 1993.
- [25] Lorenzo Sciavicco, Bruno Siciliano, “*Modelling and Control of Robot Manipulators*”, Technology & Industrial Arts Springer, 2000.
- [26] Stephen P. Timoshenko, “*Theory of Elasticity*”, McGraw-Hill, 1934.
- [27] J. S. Przemieniecki, “*Theory of Matrix Structural Analysis*”, McGraw-Hill, 1968.
- [28] David M. Pozar, “*Microwave Engineering*”, John Wiley & Sons Inc, January 2004.

- [29] Leo C.N. de Vreede, “*Lecture Notes of Microwave circuit design, ET4259*”, Technical University of Delft, the Netherlands, <http://www.dimes.tudelft.nl>
- [30] “*S-Parameter Design*”, Application Note AN 154, Agilent Technologies, Copyright 1990, 2000.
- [31] David Halliday, Robert Resnick, “*Physics*”, John Wiley & Sons Inc, 1966.
- [32] Qi Jing, “*Modeling and Simulation for Design of Suspended MEMS*”, Ph. D. Dissertation in Electrical and Computer Engineering, Carnegie Mellon University Pittsburgh, Pennsylvania 15213, USA, Copyright 2003, Qi Jing.
- [33] “*MEMS and Microsystems System-Level Design*”, Reference of CoventorWare ARCHITECT, Copyright 2006, Coventor Inc.
- [34] Hector J. de Los Santos, “*Introduction to Microelectromechanical (MEM) Microwave Systems*”, Artech House Publishers, First edition, March 1999.
- [35] Orla E. Loper, Edgar Tedsen, “*Direct Current Fundamentals*”, Thomson Delmar Learning, 2000.
- [36] Vitaly Leus and David Elata, “*Fringing Field Effect in Electrostatic Actuators*”, Technion - Israel Institute of Technology, Faculty of Mechanical Engineering, Haifa 32000, Israel, Technical Report ETR-2004-2, May 2004.
- [37] Yuh-Chung Hu and Chung-ShengWei, “*An analytical model considering the fringing fields for calculating the pull-in voltage of micro curled cantilever beams*”, Journal of Micromechanics and Microengineering, Volume 17, Pages 61-67, 2007.
- [38] J.Iannacci, L. Del Tin, R. Gaddi, A. Gnudi and K. J. Rangra, “*Compact Modeling of a MEMS Toggle-Switch Based on Modified Nodal Analysis*”, Proceedings of DTIP 2005, Symposium on Design, Test, Integration and Packaging of MEMS/MOEMS, Pages 411-416, Montreux, Switzerland, 01-03 June 2005.
- [39] Hunter Rouse “*Elementary Mechanics of Fluids Di Hunter Rouse*”, J. Wiley & Sons Inc., 1946.

- [40] Young-Ho Cho, A.P. Pisano and R.T. Howe, “*Viscous damping model for laterally oscillating microstructures*”, Journal of Microelectromechanical Systems, Volume 3, Issue 2, Pages 81-87, June 1994.
- [41] Minhang Bao, Heng Yang and Yuancheng Sun, “*A Modified Reynolds Equation For Squeeze-film Air Damping of Hole-plate*”, Journal of Micromechanics and Microengineering, Volume 13, Number 6, Pages 795-800, November 2003.
- [42] W.S. Griffin, H.H. Richardson and S. Yamanami, “*A study of fluid squeeze-film damping*”, Journal of Basic Engineering, Trans. ASME, Pages 451-456, 1966.
- [43] T. Veijola, H. Kuisma, and J. Lahdenpera, “*Model for gas film damping in a silicon accelerometer*”, Proceedings of the International Conference on Solid-State Sensors Actuators, Volume 4, Pages 1097-1100, June 1997.
- [44] Manuals of COMSOL Multiphysics Version 3.3, COMSOL Inc., [www.comsol.com](http://www.comsol.com)
- [45] Gary Keith Fedder, “*Simulation of Microelectromechanical Systems*”, Ph. D. Dissertation in Engineering-Electrical Engineering and Computer Science, University of California at Berkeley, USA, Copyright 1994, Gary Keith Fedder.
- [46] Igor A. Karnovskii and Olga I. Lebed, “*Free Vibrations of Beams and Frames: Eigenvalues and Eigenfunctions*”, McGraw-Hill, Professional Technology & Industrial Arts, 2004.
- [47] “*Reference: MEMS and Microsystems Design*”, CoventorWare ANALYZER Version 2006, Coventor Inc., [www.coventor.com](http://www.coventor.com)
- [48] Albert C. Imhoff, “*Packaging technologies for RFICs: current status and future trends*”, 1999 IEEE Radio Frequency Integrated Circuits (RFIC) Symposium, Pages 7-10, 1999.
- [49] Ken Gilleo, “*MEMS Packaging Solutions*”, EP & P, Pages 49-56, June 2000.
- [50] Vijay Varadan, K. J. Vinoy, K. A. Jose, Udo Zoelzer, “*Rf-Mems and Their Applications*”, John Wiley & Sons Inc, 2003.

- [51] Yun-Kwon Park, Heung-Woo Park, Duck-Jung Lee, Jung-Ho Park, In-Sang Song, Chung-Woo Kim, Ci-Moo Song, Yun-Hi Lee, Chul-Ju Kim and Byeong-Kwon Ju, “*A Novel Low-Loss Wafer-Level Packaging of the RF-MEMS Devices*”, Proceedings of the 15<sup>th</sup> IEEE International Conference on Micro Electro Mechanical Systems, Pages 681-684, Las Vegas, NV, USA, 20-24 January 2002.
- [52] H. A. C. Tilmans, H. Ziad, H. Jansen, O. Di Monaco, A. Jourdain, W. De Raedt, X. Rottenberg, E. De Backer, A. Decaussemaeker and K. Baert, “*Wafer-level packaged RF-MEMS switches fabricated in a CMOS fab*”, Technical Digest of the International Electron Devices Meeting, 2001, IEDM, Pages 41.4.1-41.4.4, Washington, DC, USA, 2-5 December 2001.
- [53] Alexandros Margomenos, Dimitrios Peroulis, Katherine J. Herrick and Linda P. B. Katehi, “*Silicon Micromachined Packages for RF MEMS Switches*”, Proceedings of Gallium Arsenide Applications Symposium, GAAS 2001, London, 24-28 September 2001.
- [54] F. Niklaus, P. Enoksson, P. Griss, E. Kalvesten, G. Stemme, “*Low-temperature wafer-level transfer bonding*”, Journal of Microelectromechanical Systems, Volume 10, Issue 4, Pages 525-531, December 2001.
- [55] Jun Tian and Marian Bartek, “*Low Temperature Wafer-Level Packaging of RF-MEMS using SU-8 Printing*”, Proceedings of STW Annual Workshop on Semiconductor Advances for Future Electronics and Sensors, SAFE 2005, Veldhoven, the Netherlands, Pages 56-59, 17-18 November 2005.
- [56] Clark Tu-Cuong Nguyen, “*Micromechanical Signal Processors*”, Ph. D. Dissertation in Engineering-Electrical Engineering and Computer Science, University of California at Berkeley, USA, Copyright 1994, Clark Tu-Cuong Nguyen.
- [57] Yufeng Jin, Zhenfeng Wang, Lei Zhao, Peck Cheng Lim, Jun Wei and Chee Khuen Wong, “*Zr/V/Fe thick film for vacuum packaging of MEMS*”, Journal of Micromechanics and Microengineering, Volume 14, Pages 687-692, 2004.

- [58] C. Benvenuti, “*Non-Evaporable Getters: from Pumping Strips to Thin Film Coatings*”, Proceedings of EPAC 1998, Stockholm, Sweden, Pages 200-204, June 1998.
- [59] Douglas Sparks, Sonbol Massoud-Ansari and Nader Najafi, “*Reliable Vacuum Packaging Using NanoGetters<sup>TM</sup> and Glass Frit Bonding*”, Conference on Reliability, Testing and Characterization of MEMS/MOEMS III Editors D.Tanner & R. Ramesham, Proceeding of SPIE Volume 5343, Pages 70-78, January 2004.
- [60] Helge Kristiansen and Johan Liu, “*Overview of Conductive Adhesive Interconnection Technologies for LCDs*”, IEEE Transactions on Components, Packaging and Manufacturing Technology, Part A, Volume 21, Number 2, Pages 208-214, June 1998.
- [61] F. Lrmer et al., US Patent 5,501,893, March 26, 1996.
- [62] Technical Notes of Lapping and Grinding Machines, Logitech Ltd, <http://www.logitech.uk.com/>
- [63] Michael G. Pecht, “*Integrated Circuit, Hybrid, and Multichip Module Package Design Guidelines: A Focus on Reliability*”, John Wiley & Sons Inc-IEEE, 1994.
- [64] Tai-Ran Hsu, “*Mems Packaging*”, IET, 2004.
- [65] Reference of DIMES Technology, DIMES Technology Centre, Technical University of Delft, the Netherlands, <http://www.dimes.tudelft.nl>
- [66] Liqiang Cao, Zonghe Lai and Johan Liu, “*Interfacial Adhesion of Anisotropic Conductive Adhesives on Polyimide Substrate*”, Journal of Electronic Packaging Copyright by ASME, Volume 127, Pages 43-46, March 2005.
- [67] Rolf Aschenbrenner, Andreas Ostmann, Gerald Motulla, Elke Zakel and Herbert Reichl, “*Flip Chip Attachment Using Anisotropic Conductive Adhesives and Electroless Nickel Bumps*”, IEEE Transactions on Components, Packaging and Manufacturing Technology, Part C, Volume 20, Number 2, Pages 95-100, April 1997.

- [68] A. T. Huang, C.-K. Chou, C. Chen, “*Hermetic Packaging Using Eutectic SnPb Solder and Cr/Ni/Cu Metallurgy Layer*”, IEEE Transactions on Advanced Packaging, Volume 29, Number 4, Pages 760-765, November 2006.
- [69] Sebastian Sosin, Jun Tian and Marian Bartek, “*Hybrid Wafer Level Packaging Based on a Capping Substrate with Cavities*”, Proceedings of Eurosensors XX, Goteborg, Sweden, 17-20 September 2006.
- [70] Manuals of Agilent Advanced Design System (ADS), Agilent Technologies, [http://eesof.tm.agilent.com/products/ads\\_main.html](http://eesof.tm.agilent.com/products/ads_main.html)
- [71] Emerson & Cuming, “*CE 3103 WLW Electrically Conductive Adhesive Datasheet*”, <http://www.emersoncuming.com/>
- [72] K.I. Kim, J.Mu Kim, J.Man Kim, G.C. Hwang, C.W. Baek and Y.K. Kim, “*Packaging for RF-MEMS devices using LTCC substrate and BCB adhesive layer*”, Journal of Micromechanics and Microengineering, Volume 16, Pages 150-156, 2005.
- [73] Manuals of Ansoft HFSS Version 10.0, Ansoft Corporation, [www.ansoft.com](http://www.ansoft.com)
- [74] Jacopo Iannacci, Marian Bartek, Jun Tian, Roberto Gaddi and Antonio Gnudi, “*Electromagnetic Optimization of an RF MEMS Wafer Level Package*”, Special Issue of Sensors and Actuators A: Physical for Eurosensors XX Authors, Submitted for review in October 2006.
- [75] Roberto Gaddi, Marco Bellei, Antonio Gnudi, Benno Margesin and Flavio Giacomozzi, “*Interdigitated Low-Loss Ohmic RF MEMS Switches*”, Proceedings of NSTI 2004 Nanotechnology Conference and Trade Show, Nanotech 2004, Boston, MA, Volume 2, Pages 327-330, 7-11 March 2004.
- [76] Jacopo Iannacci and Marian Bartek, “*RF-Behaviour of Anisotropic Conductive Adhesive in Wafer-Level Packaging for RF-MEMS*”, Technical Digest of the 17<sup>th</sup> Micromechanics Europe Workshop (MME 2006), 2006, Southampton, UK, Pages 93-96, 3-5 September, 2006.

- [77] Bernd Schauwecker, Karl M. Strohm, Winfried Simon, Jan Mehner and Johann-Friedrich Luy, “*Toggle-Switch - A new type of RF MEMS switch for power applications*”, Technical Digest of IEEE MTT-S International Microwave Symposium, 2002, Seattle, WA, USA, Volume 1, Pages 219-222, 2-7 June 2002.
- [78] Kamal J. Rangra, et Al., “*Symmetric Toggle Switch - A new type of RF MEMS switch for telecommunication applications*”, Proceedings of XVIII Eurosensors, Rome, IT, Pages 255-256, 12-15 September 2004.
- [79] Devarajan Balaraman, Swapan K. Bhattacharya, Farrokh Ayazi, John Papapolymerou, “*Low-Cost Low Actuation Voltage Copper RF MEMS Switches*”, Technical Digest of the IEEE MTT-S International Microwave Symposium, 2002, Seattle, WA, USA, Volume 2, Pages 1225-1228, 2-7 June 2002.
- [80] Dimitrios Peroulis, Sergio P. Pacheco, Kamal Sarabandi, and Linda P. B. Katehi, “*Alleviating the Adverse Effects of Residual Stress in RF MEMS Switches*”, Proceedings of European Microwave Conference, London, 24-28 September 2001.
- [81] Dimitrios Peroulis, Sergio P. Pacheco, Kamal Sarabandi and Linda P. B. Katehi, “*Electromechanical Considerations in Developing Low-Voltage RF MEMS Switches*”, IEEE Transactions on Microwave Theory and Techniques, Volume 51, Number 1, Pages 259-270.
- [82] Technical Notes of Veeco Profilers, [www.veeco.com](http://www.veeco.com)
- [83] “*Touchstone File Format Specification*”, Copyright by the EIA/IBIS Open Forum, 2002, <http://www.vhdl.org/>
- [84] Marc Tiebout, “*Low Power Vco Design in CMOS*”, Springer Technology & Industrial Arts, 2005.
- [85] “*0.35  $\mu\text{m}$  HBT BiCMOS RF SPICE Models*”, AustriaMircoSystems (AMS), Release date 3 November 2005, [www.austriamicrosystems.com](http://www.austriamicrosystems.com)
- [86] “*SpectreHDL Reference*”, Cadence Design Systems, Inc. Product Version 4.4.5, December, 1999.

- [87] Roberto Gaddi, Antonio Gnudi, Eleonora Franchi, Davide Guermandi, Paola Tortori, Benno Margesin and Flavio Giacomozzi, "*Reconfigurable MEMS-enabled LC-tank for Multi-Band CMOS Oscillator*", IEEE MTT-S 2005 International Microwave Symposium Digest (IMS2005), Long Beach, CA, USA, 12-17 June 2005.
- [88] G. Dambrine, et Al, "*A new method for determining the FET small-signal equivalent circuit*", IEEE Trans. Microwave Theory Tech., Vol. 36, pp.1151-1159, July 1988.
- [89] Paola Tortori, Davide Guermandi, Eleonora Franchi and Antonio Gnudi, "*Quadrature VCO based on direct second harmonic locking*", Proceedings of the 2004 International Symposium on Circuits and Systems, ISCAS 2004, Volume 1, Pages I-169 - I-172, 2004.